

2014

VEHICLE TECHNOLOGIES OFFICE



FY 2014 Annual Progress Report - Energy Storage R&D

This document highlights work sponsored by agencies of the U.S. Government. Neither the U.S. Government nor any agency thereof, nor any of their employees, makes any warranty, express or implied, or assumes any legal liability or responsibility for the accuracy, completeness, or usefulness of any information, apparatus, product, or process disclosed, or represents that its use would not infringe privately owned rights. Reference herein to any specific commercial product, process, or service by trade name, trademark, manufacturer, or otherwise does not necessarily constitute or imply its endorsement, recommendation, or favoring by the U.S. Government or any agency thereof. The views and opinions of authors expressed herein do not necessarily state or reflect those of the U.S. Government or any agency thereof.

U.S. Department of Energy
1000 Independence Avenue, S.W.
Washington, D.C. 20585-0121

Fiscal Year 2014 Annual Progress Report for Energy Storage R&D

March 2015

Approved by
David Howell, Hybrid Electric Systems Program Manager
Vehicle Technologies Office, Energy Efficiency and Renewable Energy

Table of Contents

I. Introduction	1
I.A Vehicle Technologies Office Overview	1
I.B Vehicle Technologies Battery R&D Overview	1
I.B.1 DOE Battery R&D Goals and Technical Targets	1
I.B.2 DOE Battery R&D Plans	2
I.B.3 Energy Storage R&D Programmatic Structure.....	3
I.B.4 Recent <i>EV Everywhere</i> Highlights	5
I.B.5 Organization of this Report	7
II. Advanced Battery Development	11
II.A USABC Battery Development Projects	15
II.A.1 EV Battery Development (Envia Systems)	15
II.A.2 Advanced High-Performance Batteries for Plug-In Hybrid Electric Vehicle Applications (JCI)	19
II.A.3 Development of a High-Performance PHEV Battery Pack (LG Chem, MI).....	26
II.A.4 Development of a PHEV Battery (Xerion).....	31
II.A.5 Energy Storage System for High Power LEESS PAHEV Applications (Maxwell Technologies).....	35
II.A.6 Development of 12V Start-stop Microhybrid Batteries (Saft)	38
II.A.7 Development of 12V Start-stop Microhybrid Batteries (Leyden Energy).....	43
II.A.8 2012 EV Technology Assessment Program (SKI)	47
II.A.9 Multifunctional, Inorganic-Filled Separator Development for Large Format Li-ion Batteries (ENTEK)	50
II.B Advanced Lithium Battery Cell Technology	53
II.B.1 Silicon-nanowire Based Lithium Ion Batteries for Vehicles with Double the Energy Density (Amprius)	53
II.B.2 Development of Large Format Lithium-Ion Cells with Higher Energy Density (XALT Energy).....	56
II.B.3 Innovative Cell Materials and Designs for 300 Mile Range EVs (OneD Material).....	60
II.B.4 Advanced High-energy Li-ion Cell for PHEV and EV (3M)	69
II.B.5 Solid Polymer Batteries for Electric Drive Vehicles (Seeo)	74
II.B.6 Development of High-Energy Lithium-Sulphur Battery Cells (PSU).....	76
II.B.7 Stand Alone Battery Thermal Management System (Denso)	83
II.C Low-cost Processing Research	87
II.C.1 Low Cost Lithium-ion Cell Manufacturing Project (JCI)	87
II.C.2 Ultraviolet Curable Binder Lithium-ion Battery Project (Miltec UV International)	96
II.C.3 High Capacity Alloy Anodes (Applied Materials).....	100
II.C.4 Innovative Manufacturing and Materials for Low Cost Lithium-ion Batteries (Optodot Corporation)	104

Table of Contents

II.C.5 Dry Process Electrode Fabrication (Navitas).....	107
II.D Small Business Innovative Research Projects.....	111
III. Battery Testing, Analysis, and Design.....	115
III.A Cost Assessments and Requirements Analysis	116
III.A.1 Core BatPaC Development and Implementation (ANL).....	116
III.A.2 Battery Ownership Model: A Tool for Evaluating the Economics of Electrified Vehicles and Related Infrastructure (NREL).....	121
III.A.3 PEV Battery Second Use (NREL).....	125
III.A.4 Battery Life Trade-Off Studies (NREL)	128
III.A.5 Battery Production and Recycling Materials Issues (ANL).....	132
III.B Battery Testing Activities	140
III.B.1 Battery Performance and Life Testing (ANL)	140
III.B.2 Battery Performance and Life Testing (INL)	143
III.B.3 Battery Abuse Testing (SNL)	148
III.B.4 Battery Thermal Analysis and Characterization Activities (NREL).....	155
III.C Battery Analysis and Design Activities	161
III.C.1 Battery Multiscale Multidomain Framework & Modeling (NREL)	161
III.C.2 Computer Aided Engineering of Batteries – CAEBAT (NREL)	165
III.C.3 Computer Aided Engineering of Batteries Effort (ORNL).....	170
III.C.4 Development of Computer Aided Design Tools for Automotive Batteries (GM)	174
III.C.5 Development of Computer Aided Design Tools for Automotive Batteries (CD-Adapco).....	182
III.C.6 Development of Computer Aided Design Tools for Automotive Batteries (EC Power)	186
III.C.7 Coupling of Mechanical Behavior of Cell Components to Electrochemical-Thermal Models for Computer-Aided Engineering of Batteries Under Abuse (NREL, MIT, ANSYS).....	190
III.C.8 Mechanistic Modeling Framework for Predicting Extreme Battery Response: Coupled Hierarchical Models for Thermal, Mechanical, Electrical and (Electro)chemical Processes (SNL, ORNL, Col School of Mines)	194
III.C.9 Efficient Safety and Degradation Modeling of Automotive Li-ion Cells and Packs (EC Power, Penn State U).....	199
III.C.10 Significant Enhancement of Computational Efficiency in Nonlinear Multiscale Battery Model for Computer-Aided Engineering (NREL, ANSYS, MIT).....	202
III.C.11 Crash Propagation Simulation and Validation (NREL)	206
IV. Applied Battery Research for Transportation.....	211
IV.A Introduction.....	211
IV.B Core and Enabling Support Facilities	213
IV.B.1 Cell Analysis, Modeling, and Prototyping (CAMP) Facility Production and Research Activities (ANL)	213

IV.B.2 CAMP Materials Benchmarking Activities (ANL)	240
IV.B.3 Impact of Materials on Abuse Response (SNL).....	246
IV.B.4 Post-Test Diagnostic Facility Activities (ANL).....	255
IV.C Critical Barrier Focus —Voltage Fade in Li-ion Battery Cathode Materials	258
IV.C.1 Structure-Electrochemical Activity Relationships in LMR-NMC (ANL)	258
IV.C.2 Spectroscopic and Imaging Characterization of the Voltage Fade Phenomena (ANL, ORNL)	280
IV.C.3 Mitigation Approaches: Synthetic and Coating Strategies (ANL)	317
IV.C.4 Adaptation Approaches: Synthetic and Operational Regime Approaches (ANL)	350
IV.C.5 The Voltage Fade Deep-Dive: Outcomes and Future Directions (ANL)	362
IV.D High Energy Cell R&D: “Improvements in Cell Chemistry, Composition, and Processing”	372
IV.D.1 New High Energy Electrochemical Couple for Automotive Applications (ANL, BNL, LBNL)	372
IV.D.2 High Energy Novel Cathode / Alloy Automotive Cell (3M, GM, Unicore, Leyden, LBNL, ARL)	379
IV.D.3 High Energy Density Li-ion Cells for EVs Based on Novel, High Voltage Cathode Material Systems (Farasis E, ANL, LBNL, Nanosys, Dupont).....	384
IV.D.4 Develop high energy cells for PHEV applications (Envia, LBNL, ORNL, GM)	387
IV.D.5 High Energy, Long Cycle Life Lithium-Ion Batteries for PHEV Application (Penn State U, UT Austin, LBNL, ANL, EC Power)	390
IV.D.6 High Energy High Power Battery Exceeding PHEV40 Requirements (TIAX).....	409
IV.E Process Development and Manufacturing R&D.....	413
IV.E.1 Process Development and Scale up of Advanced Cathode Materials (ANL)	413
IV.E.2 Process Development and Scale up of Advanced Electrolyte Materials (ANL)	424
IV.E.3 Roll-to-Roll Electrode Processing NDE for Advanced Lithium Secondary Batteries (ORNL)	429
IV.E.4 Overcoming Processing Cost Barriers of High Performance Lithium Ion Battery Electrodes (ORNL)	439
IV.E.5 Development of Industrially Viable ALD Electrode Coatings (NREL)	445
V. Focused Fundamental Research	453
V.A Introduction.....	453
V.B Cathode Development.....	456
V.B.1 High Capacity Composite Cathode Materials (ANL).....	456
V.B.2 <i>In situ</i> Solvothermal Synthesis of Novel High Capacity Cathodes (BNL)	461
V.B.3 Design of High Performance, High Energy Cathode Materials (LBNL)	467
V.B.4 Design and Synthesis of Advanced High-Energy Cathode Materials (LBNL).....	471
V.B.5 Studies on High Energy Density Cathodes for Advanced Lithium-ion Batteries (ORNL)	479
V.B.6 Lithium-Bearing Mixed Polyanion (LBMP) Glasses as Cathode Materials (ORNL).....	485
V.B.7 Development of High-Energy Cathode Materials (PNNL)	489
V.B.8 Diagnostics – Optimization of Ion Transport in High-Energy Composite Cathodes (UCSD)	495

V.B.9 Novel Cathode Materials for High-Energy Lithium Batteries (U Texas).....	501
V.C Anode Development	506
V.C.1 Novel Anode Materials (ANL).....	506
V.C.2 Metal-Based High Capacity Li-Ion Anodes (SUNY Binghamton)	510
V.C.3 New Layered Nanolaminates for Use in Lithium Battery Anodes (Drexel U).....	514
V.C.4 A Combined Experimental and Modeling Approach for the Design of High Current Efficiency Si Electrodes (GM, Michigan State U)	519
V.C.5 Hierarchical Assembly of Inorganic/Organic Hybrid Si Negative Electrodes (LBNL).....	524
V.C.6 Electro-Deposition of Silicon and Other Metals for Li-Ion Battery Anodes (NETL).....	529
V.C.7 Atomic Layer Deposition for Stabilization of Amorphous Silicon Anodes (NREL, U Colorado).....	533
V.C.8 Synthesis and Characterization of Structured Si/SiO _x -based Nanocomposite Anodes and Functional Polymer Binders (PS U).....	539
V.C.9 Development of Silicon-Based High Capacity Anodes (PNNL).....	545
V.C.10 Wiring up Silicon Nanoparticles for High Performance Lithium Ion Battery Anodes (Stanford U)	552
V.C.11 First Principles Modeling of SEI Formation on Bare and Surface/Additive Modified Silicon Anode (TAMU)	558
V.C.12 Analysis of Film Formation Chemistry on Silicon Anodes by Advanced <i>In situ</i> and <i>Operando</i> Vibrational Spectroscopy (UCB).....	563
V.C.13 Nanoscale Composite Heterostructures and Thermoplastic Resin Binders: Novel Li-ion Anode Systems (U Pittsburgh)	567
V.C.14 Pre-Lithiation of Silicon Anode for High Energy Li Ion Batteries (Stanford U)	573
V.D Electrolyte Development.....	576
V.D.1 Development of Electrolytes for Lithium Ion Batteries (URI)	576
V.D.2 Fluorinated Electrolyte for 5-V Li-ion Chemistry (ANL, ARL, BNL).....	580
V.D.3 Daikin Advanced Lithium Ion Battery Technology – High Voltage Electrolyte (Daikin)	587
V.D.4 Novel Non-Carbonate Based Electrolytes for Silicon Anodes (Wildcat)	594
V.E Cell Analysis, Modeling, and Fabrication	598
V.E.1 Predicting Microstructure and Performance for Optimal Cell Fabrication (BYU)	598
V.E.2 Assembly of Battery Materials and Electrodes (IREQ)	602
V.E.3 Predicting and Understanding Novel Electrode Materials from First-Principles (LBNL)	608
V.E.4 Electrode Fabrication and Materials Benchmarking (LBNL)	613
V.E.5 First-Principles Calculations of Existing and Novel Electrode Materials (MIT)	617
V.E.6 Design and Scalable Assembly of High Density Low Tortuosity Electrodes (MIT, LBNL)	623
V.E.7 Electrode Materials Design and Failure Prediction (LBNL)	627
V.F Diagnostics	630
V.F.1 Energy Storage Materials Research using DOE's User Facilities (ANL)	630
V.F.2 Advanced <i>In situ</i> Diagnostic Techniques for Battery Materials (BNL).....	635

V.F.3 Interfacial Processes – Diagnostics (LBNL)	640
V.F.4 Microscopy Investigation on the Fading Mechanism of Electrode Materials (PNNL).....	645
V.F.5 NMR and Pulse Field Gradient Studies of SEI and Electrode Structure (Cambridge U)	649
V.F.6 Cell Failure: Electrochemical Diagnostics (LBNL)	654
V.G Beyond Lithium-Ion Battery Technologies	658
V.G.1 Novel Chemistry: Lithium Selenium and Selenium Sulfur Couple (ANL)	658
V.G.2 Development of Novel Electrolytes for Lithium Air (ANL).....	663
V.G.3 Composite Electrolyte to Stabilize Metallic Lithium Anodes (ORNL).....	669
V.G.4 Lithium Dendrite Prevention for Lithium-ion Batteries (PNNL)	673
V.G.5 Development of High Energy Lithium Sulfur Batteries (PNNL)	678
V.G.6 Rechargeable Lithium-Air Batteries (PNNL).....	683
V.G.7 Simulations and X-Ray Spectroscopy of Li-S Chemistry (UCB)	688
V.G.8 Lithium Batteries with Higher Capacity and Voltage (UTA).....	693
V.G.9 Exploratory Studies of Novel Li-Air Battery Systems (BNL, UM Boston)	696
V.G.10 Exploratory Studies of Novel Sodium-Ion Battery Systems (BNL)	700
V.G.11 Nanostructured Design of Sulfur Cathodes for High Energy Lithium-Sulfur Batteries (Stanford U)	705
Appendix A: List of Contributors and Collaborators.....	709
Appendix B: Acronyms	719

List of Figures

Figure I - 1: Battery advancements needed to enable a large market penetration of PEVs	2
Figure I - 2: Amprius' nanowires address swelling issue by allowing Si to swell	6
Figure I - 3: Conceptual view of the ANSYS battery design tool.....	6
Figure I - 4: JCI's cathode slurry processing technique: a) Inline mixer b) Calendared electrode (inline mixed)	6
Figure II - 1: Electrochemical half-cell cycling from different carbon containing SiO _x -based anode composites.....	16
Figure II - 2: DC-Resistance plot for different cathode compositions.....	17
Figure II - 3: Nail penetration results for 20Ah pouch cells incorporating different separators	18
Figure II - 4: Energy Density Roadmap.....	20
Figure II - 5: Final Build Candidate Calendar Life Results	22
Figure II - 6: a) Inline mixer b) Calendared electrode (inline mixed)	22
Figure II - 7: Product Cost Impact Projected from Pilot Trials.....	23
Figure II - 8: a) Mandrel-less cell assembly fixture b) CT images of cycled cells (with and without mandrels)	24
Figure II - 9: Overcharge test comparison for 36 Ah cells.....	24

Table of Contents

Figure II - 10: JCI Pin test	24
Figure II - 11: Beneficial effect of charge voltage and surface coatings on cycle-life. Top: Data show the effect of ALD surface coating on the cycle-life at 45°C. The cell was charged at 0.5C and discharged at 1C. Bottom: When the charge voltage was raised to 4.5V, instead of 4.4V as in Top figure, there is a substantial decline in cycle-life	27
Figure II - 12: Top) Effect of formation voltage on the amount of transition metal deposited on carbon anode. Sample 1 was formed at 4.6V. Sample 2 was formed at 4.4V. Note the significantly large quantity of Mn deposited at 4.6V	28
Figure II - 13: Comparison of the cyclability of 1 st generation blended cathode-based 24Ah and the 60 Ah MRC cells at 45°C. Cycling carried out at 0.5C charge and 1C discharge currents to a discharge voltage of 2.5V	28
Figure II - 14: Schematic of the two generations of packs we delivered to USABC. While the top pack was used to design, develop and optimize the thermal system components, the bottom PHEV- 40 pack used the actual 60 Ah program cells. The thermal chamber containing elements such as the compressor, the cold-plate and the evaporator is on the right while the electrical chamber is on the left of the top packs (top pack). The bottom pack has the thermal and the electrical system both in the same side	28
Figure II - 15: Examples of the thermal performance of the pack using the cooling system we have developed. The top figure shows the average temperature of the modules during US06 cycling at 40°C. The data show that the modules are within 4°C of each other, indicating uniform and efficient cooling. Bottom figure compares three different packs using different compressor ratings (single 12V, dual 12V and a 24V. The associated cold-plate temperatures are also shown in the graph. The cold plate temperature is the bottom curve	29
Figure II - 16: (a) Cross-sectional SEM image of carbon scaffold. (b) Optical image of carbon scaffold fabricated in a scalable and manufacturable method	33
Figure II - 17: (a) SEM image of lithium-rich spinel LMO electroplated on carbon scaffold. (b) Cycle life and charge/discharge voltage profiles (inset) of such cathode	33
Figure II - 18: (a) Charge/discharge voltage profiles of mixed layered (Li ₂ MnO ₃) and spinel (Li ₂ MnO ₄) LMO. (b) Charge/discharge voltage profiles of mixed spinel and γ-MnO ₂ phases electroplated on carbon scaffold	34
Figure II - 19: 3.8 Wh Third Generation HPPC BOL Pulse Power Capability	36
Figure II - 20: Maxwell LEESS Pack	36
Figure II - 21: Cold Crank Results at 0.5 Seconds	40
Figure II - 22: Cold Crank Results at 4.5 Seconds	40
Figure II - 23: SAFT Monoblock Design Concept	40
Figure II - 24: Improvements in 100% SOC -30°C cold-cranking performance over the course of the program; recalculated to pack level	44
Figure II - 25: Rate performance of 2.2Ah prototype cells	44
Figure II - 26: Thermal performance test on 2.2Ah prototype cells	45
Figure II - 27: USABC cycling at 30°C on 2.2Ah cells	45
Figure II - 28: 2.2Ah and 20Ah cell prototype	45
Figure II - 29: Three USABC 12V Start-Stop battery packs	46
Figure II - 30: Bricks construction	46
Figure II - 31: Constant Current Discharge Test for LMO free E400	48
Figure II - 32: C ₃ /3 capacity retention of LMO free E400 in cycle life	48
Figure II - 33: C ₃ /3 Capacity retention of LMO free E400 in calendar life	48
Figure II - 34: OCV fade at 60°C for 18650 cells with silica-filled separators	51
Figure II - 35: Cycle life for silica-filled separator cells compared to control PE separator cells	51
Figure II - 36: Power Capacity Plots for Cells made with silica-filled separator versus those with control separator	52
Figure II - 37: Silicon swelling causes capacity fade and mechanical failure. Amprius' nanowires address swelling by allowing silicon to swell successfully	54

Figure II - 38: Amprius' single-layer cell achieved >700 C/2 cycles at 100% depth of discharge	55
Figure II - 39: Amprius' >2.5 Ah silicon nanowire anode-based cells achieved >330 Wh/kg, >780 Wh/L, and >300 C/2 cycles at 100% depth of discharge.....	55
Figure II - 40: Cycle performance of an HVC / Si-based anode cell	57
Figure II - 41: Energy density of an HVC / Si-based and Graphite sample cell	58
Figure II - 42: Thermal behavior of a high voltage NMC material when charged to various voltages.....	58
Figure II - 43: Baseline SiNANOde/LCO full cell.....	61
Figure II - 44: Voltage hysteresis of SiNANOde and Si powder-graphite full cells.....	62
Figure II - 45: SiNANOde half cell with 700~1000mAh/g	62
Figure II - 46: >1600mAh/g SiNANOde's voltage profile	62
Figure II - 47: Uniform Si Nanowire distribution on graphite powders for 700mAh/g (Left) and >1600mAh/g (Right)	62
Figure II - 48: Voltage profiles and rate capabilities of cathode candidates.....	63
Figure II - 49: Cathode cyclability vs. different electrolyte.....	63
Figure II - 50: Cycle life at 0.3C rate (80% DOD).....	63
Figure II - 51: (a) 1200mAh/g SiNANOde cyclability in half cell; (b) 1400mAh/g SiNANOde cyclability in half cell	64
Figure II - 52: Discharge voltage profiles of various cathode materials	64
Figure II - 53: Cycle life of the pouch cell using 600 mAh/g SiNANOde at 0.5C rate (DOD 100).....	65
Figure II - 54: Thickness change of High Energy Density Pouch Cells: SiNANOde/LCO	65
Figure II - 55: 600mAh/g SiNANOde/NCA full cell cyclability.....	65
Figure II - 56: High capacity SiNANOde/LCO pouch cell performance.....	65
Figure II - 57: High capacity SiNANOde/NCA pouch cell performance	65
Figure II - 58: Low temperature performance of SiNANOde/NCA cell.....	66
Figure II - 59: Pouch Cell Specific Power of SiNANOde vs. Graphite	66
Figure II - 60: New electrolyte enables better cycling performance	67
Figure II - 61: Si Nanowire grown on larger graphite powders (Left) and smaller graphite powders (Right) for >800mAh/g	67
Figure II - 62: Calendered SiNANOde Anode (Left) and Graphite Anode (Right) with 1.5g/cm ³	67
Figure II - 63: Winding on 0.9 mm diameter pin.....	67
Figure II - 64: Reduction in 1 st cycle irreversible capacity by compositional changes to the Si alloy anode.....	70
Figure II - 65: (a) Specific capacity vs. cycle number using different binders (10 wt%) with CV7 alloy (90 wt%). The half cells use EC/DEC=3/7, 30% FEC, 1.2M LiPF ₆ as electrolyte at a 80 mA/g rate, with a cut-off voltage of 0.01V-1V. (b) Adhesion force between silica micron-size probe and polymer-coated silicon wafer in an atomic force microscopy tapping mode, indicating the well-improved adhesion by incorporating catechol functionality in the binder.....	70
Figure II - 66: Comparison of 18650 cell energy with the different cathodes and anodes. Design with 3M lab scale C/S matched to Si anode shows the maximum energy. Umicore scaled C/S & 3M coated 442 show similar energy	71
Figure II - 67: Core-shell NMC precursors of (a), (b) and their final products (c), (d)	71
Figure II - 68: Coin cell (vs. Li) results of final products	71
Figure II - 69: (a) Discharge Capacity vs. Cycles of 'Si alloy NMC'; 4.2-2.8V; 25°C; C/5. (b) Discharge Capacity vs. Cycles of 'High voltage NMC Graphite'; 4.6-3.0V; 25°C; C/5.....	72
Figure II - 70: Coin cell (vs. Li) results of final products	72
Figure II - 71: SEM and elemental analysis of cycled cathode	72
Figure II - 72: Oxygen only observed on the surface of anode	73
Figure II - 73: F and Mn distribution on cycled anode	73

Table of Contents

Figure II - 74: a) Performance of the high-sulfur-loading PSU-5 nitrogen-doped carbon/sulfur cathode with a PSU-5 framework-based interlayer; b) adsorption of lithium polysulfides on different adsorbents, relative to adsorption on Super P carbon; c) rate performance of carbon/sulfur cathodes with different pore properties; and d) 50 th cycle voltage profiles of carbon/sulfur cathodes with different pore properties	78
Figure II - 75: a) Charge/discharge curves,, and c) voltage at 100% state of charge for LiP1 and LiP2 cells with cycling, and d) cycling efficiency of LiP2/Li foil and LiP3/Li foil cells with cycling	78
Figure II - 76: XPS S 2p spectra of PSU-3 cathodes: a) fresh, b) after 1 discharge in baseline electrolyte, c) after 1 cycle in baseline electrolyte, d) after 1 discharge in ANL-E-4 fluorinated electrolyte, and e) after 1 cycles in ANL-E-4 fluorinated electrolyte	80
Figure II - 77: a) Charge/discharge curves of cells with 10% TPPB electrolyte additive and b) cycling and efficiency of cells with 2% LiDFOB additive	80
Figure II - 78: Cycling stability and efficiency of cells with ANL-E-4 electrolyte plus 0.1M LiNO ₃ , with a 10 h rest after the fifth charge, at a) room temperature and b) 55°C, and c) charge discharge curves of cells with baseline electrolyte, baseline electrolyte plus 0.2M LiNO ₃ , PSU-E-6 electrolyte, and PSU-E-6 electrolyte plus 0.2M LiNO ₃ , and their self-discharge after a two week rest at 45°C	81
Figure II - 79: a) Capacity and coulombic efficiency of a 0.39 Ah design capacity cell with ~70% cathode porosity; b) capacity, coulombic efficiency, c) S-specific capacity, and specific energy of a 1.3 Ah design capacity cell with ~60% cathode porosity; and d) S-specific capacity of cells with LiP anodes pressed at 20 MPa and 30 MPa	82
Figure II - 80: Comparing Active Heating Performance of PTC and Heat Pump Systems	84
Figure II - 81: Comparing Heating System Power Consumptions	84
Figure II - 82: Comparing COP of various heating methods	85
Figure II - 83: Thermal System Energy Usage at -20C Driving Conditions.....	85
Figure II - 84: Time to Cool the Battery Pack from Hot Soak.....	85
Figure II - 85: Study of passive heating and cooling; most benefit is found in mild ambient like Seattle	85
Figure II - 86: Relative Capacity of Battery Pack during Battery Life	86
Figure II - 87: Battery Pack Capacity Can Be Reduced 5% and Achieve Life Requirements.....	86
Figure II - 88: 3Ah integrated Cell	88
Figure II - 89: 3Ah Integrated Cell DC Impedance thru HPPC Test; Blue: Baseline cell; Red: Integrated cell	89
Figure II - 90: 3Ah Integrated Cell Rate Capability Test; Blue: Baseline Cell; Red: Integrated Cell	89
Figure II - 91: The Cross-Sectional SEM Images: Baseline Cathode Electrode (Left), Dry Cathode Electrode (Right)	89
Figure II - 92: Integrated Cell Full Cycle Life Test: Capacity Retention (Left), DC Impedance (Right)	90
Figure II - 93: FTA (Fault Tree Analysis) for High Self Discharge.....	90
Figure II - 94: Baseline Cell Full Cycle Life Test.....	91
Figure II - 95: Improved Electrode notching Procedure	91
Figure II - 96: Dry Electrode Cell ASI Test thru HPPC Test; Black: Baseline; Red: Initial Dry Electrode Cell (2013); Blue: Baseline cathode and dry anode electrode	91
Figure II - 97: Dry Electrode Cell Rate Capability Test; Black: Baseline; Red: Initial Dry Electrode Cell (2013); Blue: Baseline cathode and dry anode electrode	91
Figure II - 98: Aqueous Cathode Cell Rate Capability Results; Black: Baseline; Red: A Binder with Additive; Blue: B Binder with Additive; Green: B Binder without Additive	92
Figure II - 99: Aqueous Cathode Cell HPPC Test: Discharge IR (Left), Charge IR (Right)	92
Figure II - 100: Aqueous Cathode Cell Calendar Life	92
Figure II - 101: Aqueous Cathode Cell Cycle Life	92
Figure II - 102: Aqueous Cathode Electrode: Bumpy Surface	92
Figure II - 103: Lamination Cell ASI Results thru HPPC Test; Red: Baseline Cell; Blue: Lamination Separator Cell	93
Figure II - 104: Lamination Cell 5C Rate Discharge Test; Red: Baseline Cell; Blue: Lamination Separator Cell	93

Figure II - 105: Calender Roll Effect for Lamination; Red: Electric Heated Calender Roll; Blue: Oil Heated Calender Roll	93
Figure II - 106: New Activation Process Concept	93
Figure II - 107: DOE Results of New Activation Process	94
Figure II - 108: DOE Results of New Detection Process	94
Figure II - 109: Formation Capacity Comparison; Blue Boxes: Baseline Process; Red Boxes: New Formation Process	94
Figure II - 110: New Formation Cell of DC-IR (Left) and Power (Right); Blue Line: Baseline Process; Red Line: New Formation Process	95
Figure II - 111: New Formation Cell Rate Capability; Blue Line: Baseline Process; Red Line: New Formation Process	95
Figure II - 112: Half cell cycling of 87-5-8 (NMC-C45-UV binder) shows UV coating produced with a slot die has excellent stability and capacity	97
Figure II - 113: Half cell cycling of 87-5-8 (NMC-C45-UV binder). UV coating shows stable capacity with good values	98
Figure II - 114: Half cell cycling of 90-5-5 (NMC-C45-UV binder). UV coating shows good capacity	98
Figure II - 115: UV ceramic coated separators were found have the same capacity as the uncoated separator even at rates as high as 2C	99
Figure II - 116: Schematic diagram of process flows for manufacturing baseline cells, interim cells and final cells with 3D current collector and alloy anodes	101
Figure II - 117: a) Transmission Electron Microscopy (TEM) and b) high resolution Scanning Electron Microscopy (SEM) images of the 3DCuSnFe Material	101
Figure II - 118: Capacity retentions at 5C for half-cells with capacities 3 and 4.3 mAh/cm ² for 3DAloy/Graphite compared to 2.8 mAh/cm ² Graphite anode	101
Figure II - 119: Cycling test results for 3DCuSnFe/Graphite vs. NMC. Measured 80% capacity retention is ~1000 cycles at C/3 rate.....	102
Figure II - 120: Voltage profiles of 1 st formation cycle for 25 SLP cells. Eighteen cells were selected for deliverable	102
Figure II - 121: Anode electrode stack and cathode electrode stack	106
Figure II - 122: (top) a flexible free standing cathode film; (bottom) a cathode by laminating the film to an Al foil	108
Figure II - 123: Rate capability of dry-process cathode in a half cell; the loading is 3 mAh/cm ²	109
Figure II - 124: Cycle life of dry process cathode in a Li ion cell; the cell is with slurry-cast anodes and cycled at C/2 at room temperature	109
Figure II - 125: Rate capability of dry process anode in a half cell; the loading is 3 mAh/cm ²	110
Figure II - 126: Cycle life of a Li ion cell composing both dry process anode and dry process cathode; cycled at C/2 at room temperature	110
Figure III - 1: Electrochemical model simulations of cathode utilization vs. ratio of cathode length to current penetration length for constant C-rate discharges of NCA/Graphite lithium ion cell	118
Figure III - 2: Unit cost per battery pack (including BMS) for LMO-G batteries.....	119
Figure III - 3: Cost of energy storage (including BMS) for LMO-G batteries. These economies of scale were derived in the flex plant by selecting uniform electrode size (length and width) to enable electrode coatings for all four battery packs. Relatively small adjustments in the coating machines can then accommodate the needed variations in coating thicknesses for the different packs. The power, capacity and voltage needs of the packs for the different types of vehicles can be further matched by changing the cell thicknesses, the numbers of cells and modules per pack, and series-parallel configurations	119
Figure III - 4: Cost of energy stored for four types of batteries as plant production level is increased in a flexible plant.....	120
Figure III - 5: Effect of DCFCs and BTMS on battery capacity loss in Seattle	123
Figure III - 6: Effect of DCFCs and BTMS on battery capacity loss in Phoenix	123
Figure III - 7: Additional mileage enabled by fast charger access as a function of vehicle range.....	123
Figure III - 8: Real-time DCM field test response.....	127
Figure III - 9: Change in capacity of 30 cells under test at NREL taken from an aged 10 kW battery pack	127

Table of Contents

Figure III - 10: Damage evolution for 20 constant current discharge/charge simulations using particle fracture model, reduced to a single trend line using fatigue scaling laws	130
Figure III - 11: Cradle-to-gate energy consumption for different cathode materials (NMC= LiNi _{0.4} Co _{0.2} Mn _{0.4} O ₂ , LMR-NMC=0.5Li ₂ MnO ₃ ·0.5LiNi _{0.44} Co _{0.25} Mn _{0.31} O ₂ , LCO=LiCoO ₂ , LFP=LiFePO ₄ , HT=hydrothermal preparation, SS=solid state)	134
Figure III - 12: Cradle-to-gate energy consumption for batteries with different cathode materials (NMC= LiNi _{0.4} Co _{0.2} Mn _{0.4} O ₂ , LMR-NMC=0.5Li ₂ MnO ₃ ·0.5LiNi _{0.44} Co _{0.25} Mn _{0.31} O ₂ , LCO=LiCoO ₂ , LFP=LiFePO ₄ , HT=hydrothermal preparation, SS=solid state)	134
Figure III - 13: Schematic of Processes Avoided by Recycling.....	135
Figure III - 14: GHG emissions associated with producing cathode material	136
Figure III - 15: Energy required to produce battery	136
Figure III - 16: Batteries contribute a significant fraction of life-cycle sulfur emissions. Pioneer plant energy intensity based on Ellingsen et al. N th plant assembly energy intensity based on Dunn et al. (2012) and reflects mature, high-throughput battery assembly facilities	136
Figure III - 17: Cathodes made from recycled materials minimize sulfur emissions	137
Figure III - 18: Fuel cycle and vehicle cycle total energy consumption for BEVs, PHEV50s, and ICVs. The PHEV50 (km) is modelled as being in charge-depleting (CD) and charge-sustaining (CS) modes during 47.5% and 52.5% of operation, respectfully. The PHEV50 is assumed to have a fuel economy of 3.2 and 8.5 gasoline equivalent L/100 km in CD and CS modes, respectively. The BEV is assumed to have a fuel economy of 2.9 gasoline equivalent L/100 km mpg while the ICV operates at 23 mpg. The liquid fuel used by the ICV and the PHEV30 during CS mode is conventional gasoline, 4% of which derives from oil sands recovered via in-situ production	137
Figure III - 19: Relative performance of BEV (NMC cathode) and PHEV50 (LMO cathode) as compared to ICV. Green, orange, black, red, blue, and purple points represent results for vehicles powered with the average U.S. grid, North East Power Coordinating Council regional grid, the California grid, exclusively natural gas-fired power plants, exclusively coal-fired power plants, and hydropower plants, respectively. Hollow and full points represent results generated with the at capacity and low-throughput battery assembly energies, respectively	138
Figure III - 20: Average, relative capacity of cell chemistry A with time and charge rate. The cells were charged from 0 to 100% SOC at the rates given in the legend	141
Figure III - 21: Average, normalized resistance vs. time and charge rate. The cells were charged from 0 to 100% SOC at the rates given in the legend	141
Figure III - 22: Average, normalized resistance vs. time and charge rate. The cells were charged from 40 to 80% SOC at the rates given in the legend	142
Figure III - 23: PHEV Voltage Definitions and Key Concepts	146
Figure III - 24: HPPC Test Profile	147
Figure III - 25: HPPC Test Sequence	147
Figure III - 26: Force-displacement curve for a blunt rod test of a COTS cylindrical cell	149
Figure III - 27: Still photograph of a COTS cylindrical cell blunt rod test.....	149
Figure III - 28: Voltage and temperature as a function of time for a thermal ramp abuse test of a COTS cylindrical cell.....	150
Figure III - 29: Simulated temperature rise from Cell 3 through all five cells in a 1S5P battery (NREL).....	151
Figure III - 30: Experimental (solid lines) and simulated (dotted lines) cell temperature during a propagation test of a 1S5P battery (NREL).....	151
Figure III - 31: Photographs of batteries in the sleeve constraint for mechanical testing in the end and side orientations.....	152
Figure III - 32: Force-displacement curves for batteries crushed in the end orientation using a flat plate (left) and a cylindrical impactor (right)	152
Figure III - 33: Force-displacement curves for batteries crushed in the side orientation using a flat plate (left) and a cylindrical impactor (right)	153

Figure III - 34: Cell heating rate ($^{\circ}\text{C}/\text{min}$) as a function of temperature for the following representative cells: a fresh cell at 100% SOC, a calendar aged cell to 50% capacity fade, and a fresh cell at 50% SOC measured by accelerating rate calorimetry (ARC).....	154
Figure III - 35: Efficiency of cells tested at 30°C in NREL's calorimeter during FY14	156
Figure III - 36: Efficiency of four generations of cells tested at 30°C under a constant current discharge from 100% to 0% SOC	157
Figure III - 37: Normalized heat rate at 30°C for cells discharged from 0% to 100% DOD	157
Figure III - 38: Thermal image of a lithium-ion cell at the end of a constant current discharge from 100% to 0% SOC	158
Figure III - 39: Average cell temperature in a pack with and without cooling. The pack underwent a US06 CD cycle followed by a US06 CS cycle	159
Figure III - 40: NREL's MSMD provides modular architecture, facilitating flexible integration of multiphysics submodels	162
Figure III - 41: Discrete diffusion particle model, a baseline PDM for MSMD multiscale model for better representing complex dynamic behaviors from particulate attributes on kinetics and diffusion dynamics	163
Figure III - 42: Comparison of measured and computed open circuit potential curves for 1:1 LCO-NMC cathode	163
Figure III - 43: Utilization of LCO and NMC particles in 1:1 mixed cathode during 20-minute US06 profile drive of midsize sedan; in PHEV10 (left) and HEV (right) applications.....	164
Figure III - 44: The four elements of CAEBAT activity	166
Figure III - 45: Johnson Controls' 12-cell module, used for validating the Star-CCM+ Battery Model	167
Figure III - 46: Thermal result for a cell within the VL6P module using a standard drive cycle (red dots are simulation, green line is experiment).....	168
Figure III - 47: Validation of externally-shorted 1.6 Ah NMC/graphite 18650 cell; experimental data acquired using RTS sensor.....	168
Figure III - 48: Temperature difference between simulation and test data at three thermocouple locations.	169
Figure III - 49: Automated mesh generation from cell to pack level with corresponding results of thermal solution.....	171
Figure III - 50: Von Mises stress distribution in different domains of a pouch cell under external mechanical loading	171
Figure III - 51: Temperature distribution in a module with asymmetric cooling.....	172
Figure III - 52: Calculated volumetric heat source using loosely and tightly coupled scenarios	172
Figure III - 53: CAEBAT-ICE workflow environment for simulation setup, job launch and data post-processing	173
Figure III - 54: Conceptual view of the ANSYS Battery Design Tool	175
Figure III - 55: Profile Types Selection.....	176
Figure III - 56: Time-Scheduled Profile	176
Figure III - 57: NTGK Model Parameter Estimation Procedure.....	177
Figure III - 58: Virtual Battery Connection	177
Figure III - 59: Thermal Abuse Model in Fluent.....	178
Figure III - 60: The equivalent circuit model with an SEI formation branch.....	178
Figure III - 61: Fit of the ECM life model at the beginning of life	179
Figure III - 62: Comparisons between the ECM life model and experimental cycling data	179
Figure III - 63: A 24-cell module validation test set up for full field simulation against test data for a high-frequency charge/discharge pulse case.....	179
Figure III - 64: Temperature difference between the simulation and the test data at 3 thermocouple locations.....	179
Figure III - 65: Comparison of temperature distribution on the battery surface located in the middle of the module	179
Figure III - 66: Automatic construction of the system model for the 24 cell module from ABDT interface	180
Figure III - 67: Prediction of the battery temperature due to internal heat generation by 1 sec charge/discharge pulses at 3.5 C-rate	180

Table of Contents

Figure III - 68: Comparison of cell temperatures during US06 Drive-Cycle and the heat generation comparison between the test and the prediction	181
Figure III - 69: Voltage response from the created electrochemical model for the JCI VL6P cell over a 30min drive cycle compared to test work (Voltage scale removed)	184
Figure III - 70: Voltage response using the electrochemistry model for the JCI VL41M high energy cell over a 30min drive cycle compared to test work (Voltage scale removed)	184
Figure III - 71: Voltage response using the electrochemistry model for the PL27M cell over a 30min drive cycle compared to test work (Voltage scale removed)	184
Figure III - 72: Comparison of lumped electrochemistry model vs three dimensional electrochemistry model over a 30min drive cycle (Voltage scale removed)	184
Figure III - 73: Johnson Controls 12 cell module ready for testing	184
Figure III - 74: High fidelity finite volume model within STAR-CCM+	184
Figure III - 75: Thermal result for a cell within the VL6P module (red line is simulation, green line is experiment)	185
Figure III - 76: Voltage prediction for WLTP drive cycle as a blind test (Voltage scale removed)	185
Figure III - 77: Thermal result for a cell within the VL6P module using WLTP drive cycle (red dots are simulation, green line is experiment)	185
Figure III - 78: Validation of externally shorted 1.6 Ah NMC/graphite 18650 cell; experimental data acquired using RTS sensor [14,16,17]. (a) voltage, (b) current (C-rate), and (c) cell-internal and surface temperatures	188
Figure III - 79: Cell normalized energy vs. time-averaged current density non-uniformity factor for cells with various tab designs (experiment and simulation results shown) [15]	188
Figure III - 80: Simplified representations of a lithium ion cell used in the mechanical/electrical simulations: the RVE approach is efficient in calibrating the cell response to measured values of the mechanical response of individual layers. The RS model is useful to simulate electrical short-circuit across the different components on the deformed geometry	191
Figure III - 81: Location of crack and comparison of load-displacement curves. Simulations were performed with anisotropic pouch cell model using the RVE at assumed failure strains of 0.15, 0.4 and 1.0	191
Figure III - 82: Current density across the active material before and after a short-circuit at different levels of total strain and the corresponding plot of current vectors during an indentation on a prismatic cell similar to the test shown on the previous figure: the RS model was used to calculate voltage history and evolution of the short-circuit area during the crush	192
Figure III - 83: Comparisons of Dualfoil to 1Delectrode using the OCV fitting capability and recently installed generalized Butler-Voler implementation within Cantera	196
Figure III - 84: Geometry and mesh of the simulated cylindrical cell	196
Figure III - 85: Sample results for cylindrical cell (temperature on the left and the electrical potential on the right)	197
Figure III - 86: Reconstructed anode microstructure from an X-ray tomography experiment (X-ray data courtesy of Prof. Scott Barnett, Northwestern University)	197
Figure III - 87: Methods of upscaling of heat generation tables are being evaluated	197
Figure III - 88: Temperature contours of 6 cell module undergoing nail penetration	200
Figure III - 89: Validation of nail penetration model comparing simulation and experimental data, (a) cell voltage, (b) temperature in nail (blue) and at surface of cell approximately halfway between nail and edge (red)	200
Figure III - 90: Solid diffusivity of NCA cathode material over full depth of discharge (DoD) and temperature	201
Figure III - 91: A diagram of intra- and inter-domain coupling protocols used in NREL's MSMD framework, integrating widely varied scale battery physics in a computationally efficient manner with hierarchical modular architecture (particle, electrode, and cell domains)	203
Figure III - 92: EDM benchmark results show that, without losing accuracy, x100 speed-up is achieved with the new GH-MSMD framework when the most efficient PDM and EDM submodel combination is chosen	205
Figure III - 93: Model versatility - crush response of different types of cells under various load conditions can be studied using the tools developed under this effort; left, a prismatic cell crash on a wall; right, deformed pouch cell geometry after crush	207

Figure III - 94: Short circuit propagation under crash - the conventional approach (a) does not consider the impact of mechanical deformation; so, crash simulations must consider (b) the evolution of geometry along with the thermal/electrical effects that ensue following a crash event	207
Figure III - 95: Propagation of mechanical failure across multiple cells in a module containing 20 prismatic stacked cells (15 Ah each) of the NMC chemistry	208
Figure III - 96: Demonstration of the utility of multi-cell crash-response simulations - two case studies are shown, the first comparing the effect of different locations of impact on temperature rise, and the second comparing two different cooling-fin designs	208
Figure IV - 1: Poly(acrylic acid)	216
Figure IV - 2: Comparison of the formation cycling columbic efficiency of NCM 523 vs. Baseline & Initial xx3450 Silicon-Graphite Pouch Cell Builds. Plots are represented by using average data.....	217
Figure IV - 3: HPPC Discharge ASI values for the NCM 523 vs. Baseline & Initial xx3450 Silicon-Graphite Pouch Cell Builds using a 5C discharge pulse for 10 seconds and 3.75C charge pulse for 10 seconds at each 10 th % state of discharge. Data is averaged and interpolated with 1σ SD error bars.....	218
Figure IV - 4: Discharge capacity in mAh using the same cathode electrodes for NCM 523 vs. Baseline & Initial xx3450 Silicon-Graphite Pouch Cell Build	218
Figure IV - 5: Comparison of the cycle life columbic efficiency performance after formation cycles of NCM 523 vs. Baseline & Initial xx3450 Silicon-Graphite Pouch Cell Builds	218
Figure IV - 6: Averaged discharge capacity and efficiency during formation vs. cycle number and corresponding voltage profile for MAGE graphite only vs. Li metal for comparison to silicon-graphite blends	219
Figure IV - 7: (a) Photo showing the uniformity of the silicon-graphite based electrode in the Electrode Library (A-A006), and (b) Photo of the A-A006 electrode passing a 3 mm diameter pin test without visible cracking or adhesion issues.....	220
Figure IV - 8: Averaged discharge capacity during formation vs. cycle number with inset showing corresponding voltage profile for A-A006 vs. Li metal; 5 cycles @ C/10 from 1.5V to 0.050IV	220
Figure IV - 9: HPPC Discharge and Charge ASI values for A-A006 electrode vs. Li metal. 1C charge (delithiation) pulse for 10 seconds and 0.75C discharge (lithiation) for 10 seconds at each 10 th % state of charge.....	221
Figure IV - 10: Photo image of the Reformulated-1 silicon-graphite electrode (3.7 mAh/cm ²) passing a 3mm diameter pin test without visible cracking or adhesion issues	221
Figure IV - 11: Overlay of NCM 523 vs. Baseline, Initial, and Reformulated-1 silicon-graphite Formation testing in xx3450 pouch cells (NCM 523 vs. Baseline is coin cell data). Cells cycled to 4.1V UCIV	222
Figure IV - 12: Overlay of rate capability for NCM 523 vs. Baseline, Initial, and Reformulated-1 silicon-graphite testing in xx3450 pouch cells cycled to a 4.1V UCIV. Solid lines are trend lines based on rate performance. Open circles are actual data points for discharge capacities with corresponding discharge times for multiple cells	222
Figure IV - 13: Overlay of NCM 523 vs. Baseline, Initial, and Reformulated-1 silicon-graphite HPPC testing in xx3450 pouch cells using a 5C discharge pulse for 10 seconds and 3.75C charge pulse for 10 seconds at each 10 th % state of discharge. Data is averaged with 1σ SD error bars	222
Figure IV - 14: Summary of electrode thickness changes as a function of state of charge for various electrodes with differing active materials.....	223
Figure IV - 15: Chemical structures of additives used in this work	225
Figure IV - 16: Capacity vs. cycle number for full cells cycled at 30°C between 2.2–4.6 V with a 170 mA-g _{oxide} ⁻¹ current and 17 mA-g _{oxide} ⁻¹ current (after every 50 high current cycles). Data for cells with the Gen2 electrolyte (black), with 0.25 wt% PBE (red), and with 0.25 wt% PFO-PBE (blue) electrolyte additives are shown. The capacity and cycling current values are based on Li _{1.2} Ni _{0.15} Mn _{0.55} Co _{0.1} O ₂ content in the positive electrode.....	225
Figure IV - 17: AC impedance data from full cells containing the Gen2 electrolyte (black), 0.25 wt% PBE (red), and with 0.25 wt% PFO-PBE (blue) electrolyte additives after (a) initial cycling and (b) after more than 200 cycles between 2.2–4.6 IV. The cells are charged to 3.75V and held for more than 4h before data are acquired at 30°C in the 100 kHz–10 mHz frequency range.....	225

Table of Contents

Figure IV - 18: Charge and discharge capacities during the first 2.5-4.1V cycle (top) and the corresponding coulombic efficiencies (bottom) as a function of n:p ratio	226
Figure IV - 19: Charge and discharge capacities during the first 2-4.55V cycle (top) and the corresponding coulombic efficiencies (bottom) as a function of the n:p ratio	227
Figure IV - 20: Discharge capacities as a function of the n:p ratio after the rate study.....	227
Figure IV - 21: Discharge capacities as a function of the n:p ratio after cycle life ageing, 100 cycles.....	227
Figure IV - 22: Discharge capacities for electrolyte additives in baseline pouch cell build using HE5050 versus A12 graphite	228
Figure IV - 23: Tap charge voltage profiles for electrolyte additives in baseline pouch cell build using HE5050 versus A12 graphite	228
Figure IV - 24: Tap charge dQ/dV profiles for electrolyte additives in baseline pouch cell build using HE5050 versus A12 graphite	228
Figure IV - 25: Tap charge voltage profiles for electrolyte additives in baseline pouch cell build and coin cells with modified formation protocols using HE5050 versus A12 graphite	229
Figure IV - 26: Life cycle test for electrolyte additives in coin cells with modified formation protocols using HE5050 versus A12 graphite	230
Figure IV - 27: Life cycle test for electrolyte additives in new pouch cell build with modified formation protocols using HE5050 versus A12 graphite	230
Figure IV - 28: Discharge ASI for electrolyte additives in new pouch cell build with modified formation protocols using HE5050 versus A12 graphite	231
Figure IV - 29: Comparison of the coin cell and pouch cell data with modified formation protocols using HE5050 versus A12 graphite	231
Figure IV - 30: Cycle life performance of full cells (A-Top panel) charged at various rates (3C, 1C, C/3) and discharged slowly and (B) charged slowly (C/14) and discharged at various rates	232
Figure IV - 31: AC impedance data (100 kHz-10 mHz, 30°C) from cells charged slowly but discharged rapidly and vice-versa. Impedance is significantly greater for the cell that underwent rapid discharge	233
Figure IV - 32: AC impedance data (100 kHz-10 mHz, 30°C) for LTO-cells from cells charged slowly but discharged rapidly and vice-versa	233
Figure IV - 33: Selected intercalation electrochemical model parameters from longer wait EIS studies on LMR-NMC electrode.....	234
Figure IV - 34: Bulk lithium diffusion coefficient for LMR-NMC active material obtained from micro-reference cell	235
Figure IV - 35: Organizations that have used the CAMP Facility's services over the last several years.	236
Figure IV - 36: Cycle Life Test analysis done with the CAMP Analyzer showing data with statistical error bars present. (8 Cells)	236
Figure IV - 37: Cycle Life Test analysis tracking the dQ/dV plot as a function of cycle number. The cycle numbers are selected by the user in the CAMP Analyzer	237
Figure IV - 38: Voltage profile of silicon alloy electrode received from 3M	242
Figure IV - 39: Voltage profile of silicon alloy electrode received from 3M	242
Figure IV - 40: Cycle performance of silicon electrodes consisting of various particle sizes	242
Figure IV - 41: Voltage profile of silicon electrodes with high loading (top) and low loading (bottom) using 50nm silicon particle from American Element. The PFM binder is provided by LBNL	243
Figure IV - 42: Voltage profile of silicon electrodes with low loading using 50nm silicon particle from NanoAmor. The PFM binder is provided by MERF at ANL	243
Figure IV - 43: Cycle performance of NCM523 half cell with various cut-off voltages	244
Figure IV - 44: Cycle performance of graphite/HE5050 full cell using PVDF separator.....	244
Figure IV - 45: Discharge capacity of NMC 523 18650 cells with graphite (green trace) and XG Si/C composite (blue trace) anodes	247

Figure IV - 46: ARC profiles during thermal runaway from NMC 523/graphite (green trace) and NMC523/Si-C (blue trace) 18650 cells	248
Figure IV - 47: DSC response for NMC graphite (green trace) and Si-C composite (blue trace) anode materials.....	248
Figure IV - 48: Moles of gas as a function of temperature measured during a calorimetry experiment for NMC 523/graphite (green trace) and two NMC523/Si-C (light blue and dark blue traces) 18650 cells	249
Figure IV - 49: Relative compositions of gas species generated from NMC/Si-C (blue) and NMC/graphite (green) cell during thermal runaway collected at 400°C	249
Figure IV - 50: DSC of LiMPO ₄ coated NMC111 (navy blue trace) and uncoated NMC111 (red trace) from 2032 coin cells at 100% SOC (prepared without excess electrolyte)	250
Figure IV - 51: Voltage vs. discharge capacity for LiMPO ₄ -coated and uncoated NMC/graphite 18650 cells	250
Figure IV - 52: ARC profiles of cell heating rate as a function of temperature for LiMPO ₄ -coated and uncoated NMC/graphite 18650 cells	251
Figure IV - 53: 18650 cell discharge capacity of 523 NMC/Graphite cells with 1.0 M ABA-1 in EC:EMC (3:7) (black trace) and 1.2 M LiPF ₆ in EC:EMC (3:7) (red trace) at C/5	252
Figure IV - 54: Thermal runaway profiles of NMC/graphite cells in 1.0 M LiF/ABA-1 in EC:EMC (3:7) (black, gray, and green traces), 1.0 M LiF/ABA-2 in EC:EMC (3:7) (navy blue trace), and in 1.2 M LiPF ₆ in EC:EMC (3:7) (red trace) measured by ARC	252
Figure IV - 55: Cell voltage and temperature during a thermal ramp abuse test for NMC cells with LiPF ₆ (green trace) and LiF/ABA (red trace) electrolytes and a COTS LFP cell (blue)	253
Figure IV - 56: Cell voltage and charging current (left panel) and cell temperature (right panel) as a function of cell state-of-charge (%SOC) during a 1C overcharge abuse test.....	253
Figure IV - 57: Photograph of the electrode and separator materials from cell A, showing staining patterns	256
Figure IV - 58: Photograph of the anode and separator material from cell B.....	256
Figure IV - 59: FT-IR spectra of the colored bands on the anode material from cell A.....	256
Figure IV - 60: Optical micrograph of cell A anode surface showing a white precipitate with metallic-looking crystals.....	256
Figure IV - 61: The first 21 galvanostatic charge/discharge cycles for LMR-NMC vs. Li in the 2.0-4.7V range at 30°C, as-measured (A) and capacity normalized (B). A depression of the voltage profiles is apparent for charge and discharge curves after capacity normalization. A capacity of unity refers to 319 mAh-g _{oxide} -1 (after 1st charge), 277 mAh-g _{oxide} -1 (after 1st discharge), and 248 mAh-g _{oxide} -1 (after 20th discharge). Black arrows indicate the positions of the six current interrupts used to calculate the average resistances. The inset table in 1B table shows cell resistances as a function of the interrupt voltage for the 2 nd and 20 th cycle	261
Figure IV - 62: Average voltages, corrected and uncorrected, as a function of cycle number for the LMR-NMC vs. Li. Average voltages during charge are plotted in light/dark green, and those during discharge are plotted in orange/red. Voltage fade and voltage gap are apparent. Corrected average voltages drop by a total of 185mV during charge and by 124mV during discharge. Thin dotted lines are intended only as a guide to the eye, and are also shown in all subsequent figures. HPPC results of CD sized cells delivered to INL for testing	262
Figure IV - 63: Effect of cycling window on the corrected average voltage and its fade during discharge for the LMR-NMC baseline material. For the first activation cycle, the cycling window is kept constant for all samples, i.e. 2.0V – 4.7IV. During cycling, only the lower cut-off is kept constant at 2IV. The degree of voltage fade increases as the upper cut-off increases. Voltage relaxation at the beginning of discharge down to ~4.5V forces the average voltage after the 2 nd discharge to be nearly the same for the data sets with the three highest cut-off voltages	262
Figure IV - 64: Effect of temperature on the corrected average voltages of the LMR-NMC baseline material under otherwise identical cycling conditions.....	263
Figure IV - 65: Voltage profiles and corrected average voltages as a function of cycle number for selected layered oxides. The cycling window ranges from 2.0V to 4.7IV. On the left hand side, all capacities are normalized. The solid line shows the 1 st (“activation”) cycle; the dotted one the 20 th cycle. On the right	

hand side, the top and bottom curves are the corrected average voltages during charge and discharge, respectively. All materials exhibit some degree of voltage fade if cycled to 4.7V vs. Li	264
Figure IV - 66: Voltage profiles and corrected average voltages as a function of cycle number for NCA and NMC. Both materials are cycled over two different voltage windows, 2.0-4.25V (top panels) and 2.0-4.7V (middle panels), with the first cycle <i>always</i> ranging from 2.0V to 4.7IV. All capacities are normalized. The solid line shows the 1 st cycle; the dashed one the 2 nd (only shown for the 2.0-4.25V window); the dotted one the 20 th cycle. The lower panels show the corrected average discharge voltages for the two voltage ranges. Both materials exhibit some degree of voltage fade only when cycled up to 4.7V vs. Li.....	265
Figure IV - 67: Corrected average voltage gap plotted against the total drop of the corrected average voltage from 2 nd to 20 th charge (ΔU_{corr}). Individual data are collected from the same cells used for Figure IV - 66 through Figure IV - 69. Charge data are chosen because of their overall smaller cell-to-cell variability, as shown in Figure IV - 64. When a linear trend is assumed over this ΔU_{corr} range, an R ² -value of 0.85 is obtained.....	266
Figure IV - 68: Discharge energies as a function of cycle number for the LMR-NMC-based baseline and modified cells. The cycling window is 2.0-4.7IV. The measured energy densities for both cells are given by the x-shaped data points. Energy loss comprises contributions from capacity loss, resistance effects, and voltage fade. Energy loss only due to voltage fade is given by the squared data points. The relative contributions of capacity loss (green), resistance effects (blue), and voltage fade (red) after 20 cycles after activation are measured separately and plotted for each cell in the pie charts. Voltage fade is a significant contributor to the overall energy loss	266
Figure IV - 69: Discharge energies for LMR-NMC (embedded in the modified baseline cell), NCA, and NMC for two voltage windows (2.0-4.25V and 2.0-4.7V) as a function of cycle number. Note that all materials are charged to 4.7V vs. Li/Li ⁺ at 10 mA·g _{oxide} ⁻¹ during the first cycle to ensure consistent testing among all materials and to ensure that the higher capacities of the LMR-NMC are accessed	267
Figure IV - 70: First cycle differential capacity (dQ/dV) plots from $\text{Li}_{1.2}\text{Ni}_{0.15}\text{Mn}_{0.55}\text{Co}_{0.1}\text{O}_2$ vs. Li cells, cycled between 2-4.7 V with a 15 mA·g ⁻¹ current at 30°C (blue) and 55°C (red). Inset shows the corresponding capacity-voltage plots. The columbic efficiency (CE) is the ratio of lithiation to delithiation capacity	268
Figure IV - 71: Selected differential capacity plots from galvanostatic charge/discharge cycles 2 through 20, after initial activation of a $\text{Li}_{1.2}\text{Ni}_{0.15}\text{Mn}_{0.55}\text{Co}_{0.1}\text{O}_2$ vs. Li cell, in the 2.0-4.7V range at 30°C. The arrows indicate changes induced by the cycling. Increasing peak intensities and a shift to lower voltages around 3.1V reveal voltage fade	268
Figure IV - 72: Selected differential capacity plots from a $\text{Li}_{1.2}\text{Ni}_{0.15}\text{Mn}_{0.55}\text{Co}_{0.1}\text{O}_2/\text{Li}_{14}\text{Ti}_5\text{O}_{12}$ cell that was galvanostatically cycled in the 0.75 – 3.15 V (2.3 – 4.7 V vs. Li/Li ⁺) range at 30°C. Growth of the 3.15V charge peak (2.95V discharge peak) indicates voltage fade. Obvious changes are also observed for the other peaks as described in the text.....	269
Figure IV - 73: (a) Capacity-voltage plots obtained by a GITT protocol from $\text{Li}_{1.2}\text{Ni}_{0.15}\text{Mn}_{0.55}\text{Co}_{0.1}\text{O}_2$ vs. Li cells in the (a) 2-4.7V, and (b) 3-4.7V voltage windows; the data were collected both at room-temperature (RT) and at 55°C	270
Figure IV - 74: Capacity-voltage plots, obtained with a room temperature GITT protocol, from a $\text{Li}_{1.2}\text{Ni}_{0.15}\text{Mn}_{0.55}\text{Co}_{0.1}\text{O}_2$ vs. Li cell showing the effect of cycle life aging in the 2-4.7V voltage window. The aged sample shows significant voltage fade; hysteresis persists even after aging.	270
Figure IV - 75: (a) Positive electrode data from a $\text{Li}_{1.2}\text{Ni}_{0.15}\text{Mn}_{0.55}\text{Co}_{0.1}\text{O}_2/\text{Graphite}$ cell showing the voltage-capacity profile after formation cycling. The electrode voltage is shown vs. Li/Li ⁺ . AC impedance data (100 kHz–0.01Hz, 30°C) were obtained at locations A, B and C shown on the plot. Locations A and B are at 3.75V but on charge and discharge, respectively. Locations A and C are at 13.4 mAh but on charge and discharge, respectively. AC impedance data from locations A and B are compared in (b), and from A and C are compared in (c). It is evident that the impedance data are different during charge and discharge even though the cell voltage/cell capacity is similar	271
Figure IV - 76: Evolution of a capacitance vs. voltage profile for TODA HE5050 in a lithium-titanate-oxide (LTO) coin cell. The capacities of the shaded regions are indicated on the plot. Voltages are versus LTO	272
Figure IV - 77: Comparison of the effect of rate on differential capacity plots for post-activated (cycle 21) TODA HE5050 in a Li coin cell. Indicated currents are in mA g ⁻¹ . Voltages are vs. Li	272

Figure IV - 78: Comparison of differential capacity plots in different voltage windows for post-activated (cycle 21) TODA HE5050 in a Li coin cell. Shaded regions represent hypothetical de-convolutions as described in the text. Voltages are vs. Li.....	273
Figure IV - 79: Model-based diagnostic analysis of short-term cycling of TODA HE5050 in an Li coin cell. Voltages are vs. Li.....	274
Figure IV - 80: Model-based diagnostic analysis of long-term cycling of TODA HE5050 in an LTO coin cell. Voltages are vs. LTO.....	275
Figure IV - 81: Growth of voltage fade component	276
Figure IV - 82: Hypothetical maximum TM ion occupations.....	276
Figure IV - 83: Growth curve of voltage fade component for data extracted via model-based analysis	276
Figure IV - 84: Growth curve of voltage fade component for data extracted via measurement-based analysis.....	277
Figure IV - 85: (a) HR-XRD of $0.5\text{Li}_2\text{MnO}_3 \cdot 0.5\text{LiCoO}_2$ quenched and slow-cooled from 850°C . (b) HR-TEM image of a particle from the quenched $0.5\text{Li}_2\text{MnO}_3 \cdot 0.5\text{LiCoO}_2$ showing regions with LiCoO_2 (1) and Li_2MnO_3 (2) ordering. (c) Mn K-edge XANES of quenched and slow-cooled $0.5\text{Li}_2\text{MnO}_3 \cdot 0.5\text{LiCoO}_2$	281
Figure IV - 86: (a) Mn and (b) Co K-edge EXAFS of $0.5\text{Li}_2\text{MnO}_3 \cdot 0.5\text{LiCoO}_2$ quenched and slow-cooled from 850°C . (c) ${}^6\text{Li}$ NMR of the samples in (a) and (b)	282
Figure IV - 87: (a) Mn K-edge EXAFS of $0.5\text{Li}_2\text{MnO}_3 \cdot 0.5\text{LiCoO}_2$ (red) and $0.5\text{Li}_2\text{MnO}_3 \cdot 0.5\text{LiMn}_{0.5}\text{Ni}_{0.5}\text{O}_2$ (black). Both samples were quenched from 850°C . (b) In-situ, HR-XRD during the synthesis of pure Li_2MnO_3	282
Figure IV - 88: (a) Mn K-edge XANES of pure Li_2MnO_3 before (black) and after (red) the first electrochemical cycle between 5-2.0 V (vs. Li) compared with a $0.5\text{Li}_2\text{MnO}_3 \cdot 0.5\text{LiMn}_{0.375}\text{Ni}_{0.375}\text{Co}_{0.25}\text{O}_2$ LMR-NMC (Toda HE5050). (b) Derivative of the pre-edge region shown in (a). (c) EXAFS data of the samples in (a) and (b)	283
Figure IV - 89: EXAFS analysis of fresh Li_2MnO_3 (a), charged to 5.0 V (b), discharged to 2.0 V (d). (c) Detailed analysis of the first-shell Mn-O coordination in Li_2MnO_3 charged to 5.0 V (~94% delithiated)	284
Figure IV - 90: Detailed analysis of the first-shell, Mn-O coordination of in-situ XAS data collected during the first charge of $0.3\text{Li}_2\text{MnO}_3 \cdot 0.7\text{LiMn}_{0.5}\text{Ni}_{0.5}\text{O}_2$	284
Figure IV - 91: Mn (a) and Ni (b) K-edge EXAFS of fresh and cycled $0.5\text{Li}_2\text{MnO}_3 \cdot 0.5\text{LiMn}_{0.5}\text{Ni}_{0.5}\text{O}_2/\text{Li}$ cells	285
Figure IV - 92: Mn (a) and Ni (b) K-edge EXAFS of $x\text{Li}_2\text{MnO}_3 \cdot (1-x)\text{LiMn}_{0.5}\text{Ni}_{0.5}\text{O}_2$ electrode powders. (c) Characteristic LiMn_6 unit of the Li and Mn layers in pure Li_2MnO_3	285
Figure IV - 93: Consecutive cycles to increasing upper cutoff voltages (lower cutoff of 2.0 V) for $x\text{Li}_2\text{MnO}_3 \cdot (1-x)\text{LiMn}_{0.5}\text{Ni}_{0.5}\text{O}_2/\text{Li}$ cells. x values are given in the upper left, magnitude of the hysteresis at 50% SOC denoted as ΔV . All cells were activated between 4.7-2.0V, all cycles done at 5 mA/g at 30°C	286
Figure IV - 94: dQ/dV plots of the window-opening cycles shown in the previous figure for the $x=0.1, 0.3$, and 0.5 $x\text{Li}_2\text{MnO}_3 \cdot (1-x)\text{LiMn}_{0.5}\text{Ni}_{0.5}\text{O}_2/\text{Li}$ cells. Numbers along the oxidation and reduction curves give the capacities obtained in each region (marked by the dashed lines) during charge and discharge, respectively, and are color-coded to match the cycling window used	287
Figure IV - 95: (a) 6 th -cycle charge/discharge for $0.5\text{Li}_2\text{MnO}_3 \cdot 0.5\text{LiMn}_{0.375}\text{Co}_{0.25}\text{O}_2/\text{Li}$, LMR-NMC (Toda HE5050) cells between 4.7-2.0 V (10 mA/g, 30°C). Red dots indicate example points along the curves as which XAS data was collected as shown in the Ni K-edge data of (b) and (c). Inset shows the JT-distorted Ni-O environment of Ni^{3+} with two distinct Ni-O bond lengths	288
Figure IV - 96: Cycling window and calendar time plots (insets) for LMR-NMC cells, cycled as described in the text	288
Figure IV - 97: a) ${}^2\text{H}$ MAS NMR of for acid leached HT- Li_2MnO_3 and $\text{Li}_{1.2}\text{Ni}_{0.2}\text{Co}_{0.2}\text{Mn}_{0.6}\text{O}_2$ powders (* indicates spinning sidebands, 35 kHz spinning speed at 11.7 T) b) XRD diffraction data for acid leached and pristine HT- Li_2MnO_3 ${}^2\text{H}$ MAS NMR data of the cycled, electrochemically active LT- Li_2MnO_3 material is shown in the next figure (b). All spectra contain a single, sharp diamagnetic resonance at 2 ppm indicating non-lattice proton (deuteron) bearing species, presumably due to surface decomposition species. No lattice proton (deuteron) species were observed	290
Figure IV - 98: a) ${}^6\text{Li}$ NMR data for pristine and cycled LT- Li_2MnO_3 (* indicates spinning sidebands, 35 kHz spinning speed at 11.7 T) b) ${}^2\text{H}$ MAS NMR data for cycled LT- Li_2MnO_3 (* indicates spinning sidebands, 25 kHz spinning speed for 1 st and charge and 50 full cycles, 20 kHz for 1 st full cycle data)	290

Table of Contents

Figure IV - 99: ^2H MAS NMR of a) cycled LMR-NMC electrodes. (* indicates spinning sidebands, 20 kHz spinning speed for 1 and 10 cycle data, 25 kHz for 100 cycle data) b) pristine LMR-NMC electrode and charged stages (black 1st charge with 20 kHz spinning speed, red 3rd charge with 30 kHz spinning speed, * indicates spinning sidebands)	291
Figure IV - 100: ^6Li MAS NMR (11.7 Tesla, 30 kHz spinning speed) of pristine and charged LMR-NMC electrodes	291
Figure IV - 101: ^6Li NMR data of pristine LMR-NMC material. Numbers on top of deconvoluted resonances indicate corresponding shift values and italic numbers indicate integral values	291
Figure IV - 102: ^6Li MAS NMR of a) pristine $\text{Li}_{1.2}[\text{Ni}_{0.15}\text{Mn}_{0.55}\text{Co}_{0.10}]_{\text{O}_2}$ and after 1 and 10 cycles b) and c) the deconvoluted ^6Li MAS NMR $\text{Li}_{1.2}[\text{Ni}_{0.15}\text{Mn}_{0.55}\text{Co}_{0.10}]_{\text{O}_2}$ after 1 and 10 cycles, respectively d) comparison of ^6Li MAS NMR data for cycled $\text{Li}_{1.2}[\text{Ni}_{0.15}\text{Mn}_{0.55}\text{Co}_{0.10}]_{\text{O}_2}$ and d) the electrochemical performance	293
Figure IV - 103: Comparison of ^6Li MAS NMR data for cycled $\text{Li}_{1.2}[\text{Ni}_{0.15}\text{Mn}_{0.55}\text{Co}_{0.10}]_{\text{O}_2}$ (top) after 500 cycles, non-enriched sample, (bottom) after 80 cycles for enriched sample	294
Figure IV - 104: a) Li MAS NMR of pristine $\text{Li}_{1.5}[\text{Mn}_{0.5}\text{Co}_{0.5}]_{\text{O}_{2.5}}$ compositions synthesized at 850°C for varying conditions b) electrochemical performance different synthesis condition electrodes. NMR resonances at 0 ppm and at negative shifts are due to diamagnetic Li in LiCoO_2 and spinning sidebands, respectively	295
Figure IV - 105: a) Li MAS NMR of pristine $\text{Li}_{1.2}[\text{Ni}_{0.15}\text{Mn}_{0.55}\text{Co}_{0.10}]_{\text{O}_2}$ compositions synthesized at 850°C for varying conditions, the inset shows X-ray diffraction data for the same samples b) electrochemical performance different synthesis condition electrodes	296
Figure IV - 106: a) Second- cycle $d\text{Q}/dV$ plot with labels corresponding to voltages at which NMR spectra were acquired. Inset shows the schematic representation of electrochemical hysteresis and voltage fade with respect to $d\text{Q}/dV$ during second-cycle charge/discharge. b) and c) show ^6Li MAS-NMR at various SOCs along the second-cycle charge and discharge, respectively	298
Figure IV - 107: a) $d\text{Q}/dV$ plots for several samples charged/discharged to equivalent lithium contents and the corresponding voltages as labeled. Sample numbers correspond to the NMR spectra in b) and c). b) Magnified view of lithium environments in the TM region for points 5 and 10. c) ^6Li MAS-NMR of $0.5\text{Li}_2\text{MnO}_3\bullet0.5\text{LiMn}_{0.5}\text{Ni}_{0.5}\text{O}_2$ comparing samples charged/discharged to equivalent lithium contents	299
Figure IV - 108: ^6Li MAS-NMR of; $0.5^6\text{Li}_2\text{MnO}_3\bullet0.5^6\text{LiMn}_{0.5}\text{Co}_{0.5}\text{O}_2$, (top) charged to 4.3V, 1 st cycle spinning at 67kHz, and (bottom) charged to 4.35V, 1 st cycle spinning at 64kHz. Red arrow highlights \sim 1550ppm resonance due to $\text{LiMn}_6\text{-Mn}_{\text{tet}}$	300
Figure IV - 109: ^6Li MAS-NMR deconvolutions for samples charged to 3.6V at cycles 2,11 and 20. (Right) Li_{TM} region for the same data. Blue and green peaks show the lithium peaks coordinated to octahedral nickel and tetrahedral manganese, respectively. Lithium contents for the specific sites were calculated with the integrated area of the corresponding lithium peak within the mass normalized spectra	301
Figure IV - 110: The voltage-capacity curve during the second (a) and 26 th cycle (b). The HE5050 oxides were collected at the designated cell voltages for characterization. The connected lines represent the samples collected at same voltage or same capacity.....	303
Figure IV - 111: Refined powder neutron diffraction (a) and x-ray diffraction (b) for HE050 by considering a composite monoclinic- Li_2MnO_3 and trigonal LiMO_2 ($\text{M}=\text{Co, Mn, Ni}$) unit cell. The different color of the atoms in the TM layer represents different TM ions (Co, Mn, Ni) present in same site. In figure a, the solid blue arrow shows the cation-ordering peaks exclusively from monoclinic Li_2MnO_3 unit-cell and the dotted arrow represents the (101) reflection in the trigonal phase and (130)/(20 \bullet 1 $\bar{1}$) reflections in the monoclinic phase. (b-c) show the trigonal (101) plane intensity before Li/Ni exchange (b) and after 3% Li/Ni exchange (c).....	304
Figure IV - 112: Voltage profile of a full-pouch cell containing three HE5050 cathodes and three graphite anodes. The arrow shows the voltage fade phenomena.....	305
Figure IV - 113: (108), and (110) peak positions in second (a) and 26 th (b) cycle. The peaks retains the original positions after completion of second cycle, however, changes the positions after 26 th cycle. The New peaks at $d = 1.13 \text{ \AA}$ appear at the 3.2 V discharged state after the 26 th cycle but not observed after the second cycle(c)	305
Figure IV - 114: The refined ND patterns for HE5050 oxide collected after 26 th cycle at 3.2 V discharged state without spinel phase (a), and with the spinel phase (b) in the model. The model includes spinel phase shows better agreement parameter as compared to the model without the spinel phase	306

Figure IV - 115: Percentage of Li_{tet} , Mn_{tet} , Li_{TM} , Ni_{Li} , and Mn_{Li} at different SOCs during second electrochemical cycle(a-b) and 26 th cycle(c-d).....	307
Figure IV - 116: The refined ND patterns for HE5050 oxide collected at 4.1 V charged state without Li in the tetrahedral site of lithium-layer in the trigonal phase, model 2 (a) and with Li in the tetrahedral site of lithium-layer in the trigonal phase, model 3 (b). Presence of Li in tetrahedral sites increases the profile matching	308
Figure IV - 117: Energy along path of Co ion migration from a site near $x/a=0$ toward a Co vacancy at $x/a=1.0$. Insert shows the octahedral coordination of two nearest neighbor Co.....	309
Figure IV - 118: The Li_2MnO_3 supercell used for the DFT calculations (Mn - blue, O - red, Li - purple) with rows of either O (left) or Li (right) vacancies arrowed, and the resulting O K-edge spectra for O atoms either far from the vacancies (black - reference), near the Li vacancies (blue), or near the O vacancies (red). Note that the intensity to the left and to the right of the text labeling each spectrum represents the pre- and the main peak, respectively.....	310
Figure IV - 119: Structure of $\text{Li}_{7/6-x}\text{Co}_{1/2}\text{Mn}_{1/3}\text{O}_2$ composite after delithiation of the Li-layer ($x=1$), AIMD at 1000K, for 0.567ps, followed by the steepest descent relaxation. Migrated Li from the metal-layer is now occupying tetrahedral and octahedral sites in the Li-layer	311
Figure IV - 120: Structure of $\text{Li}_{7/6-x}\text{Ni}_{1/4}\text{Mn}_{7/12}\text{O}_{2-y}$ composite at 70% discharge state ($\text{Li}_{76}\text{Ni}_{24}\text{Mn}_{56}\text{O}_{176}$) ($y=1/6$, $x=3/8$). Some Mn, Ni and O remain in the metal-layer. Mn is shown in dark gray, Ni in green, O in red, and Li in light purple	311
Figure IV - 121: Simulated atomic structure of $\text{Li}_{7/6-x}\text{Ni}_{1/4}\text{Mn}_{7/12}\text{O}_2$ after first charge ($x=1$). The domain "ribbon" is shown on the left side of the figure, and the LiMO_2 ($M=\text{Ni}_{0.5}\text{Mn}_{0.5}$) region is on the right side. Relatively, well-ordered rows of O ions (and NiMn) are seen in the LiMO_2 part of the cell. Oxygen is considerably disordered in the domain, with about 20% of the oxygen in this region (O-O bonds <1.6 Å shown) showing homopolar (O-O) bonding as well as heteropolar (O-M) bonding. Some Mn migrated to the Li layer, in the domain region.....	312
Figure IV - 122: (a) Simplified schematic of hysteresis/voltage fade mechanism as described in the text. (b) octahedral and tetrahedral sites associated with dumbbell configurations in layered Li-TM-oxides	313
Figure IV - 123: Proposed LS transformation mechanism in HE5050 LMR composite oxide via formation of tetrahedral lithium in the lithium layer and migration of Mn from octahedral TM layer to octahedral site of lithium layer.....	314
Figure IV - 124: Cycling between 4.7-2.0 V for $x\text{Li}_2\text{MnO}_3 \bullet (1-x)\text{LiMn}_{0.5}\text{Ni}_{0.5}\text{O}_2/\text{Li}$ cells with $x=0.1$, 0.3 , and 0.5 . Arrows indicate decreasing capacities associated with hysteresis and increasing capacities associated with voltage fade.....	315
Figure IV - 125: Voltage profiles of $\text{Li}/0.5\text{Li}_2\text{MnO}_3 \bullet 0.5\text{Li}[\text{Ni}_{0.375}\text{Mn}_{0.375}\text{Co}_{0.25}]\text{O}_2$ during the first 20 cycles (as labeled). Feature B is the activation plateau	318
Figure IV - 126: O3 stacking arrangements for oxygen closest-packed oxide structures	318
Figure IV - 127: (left) Capacity retention vs. cycle count for coated and uncoated laminates. (right) Capacity retention vs. cycle number for uncoated laminates and mock-coated laminates	319
Figure IV - 128: Rel. cell capacity vs. cycle count, showing capacity decline with cycle count. The capacity of coated materials tended to decline slower than that of uncoated materials. The relative cell capacity vs. cycle count for the 2- and 3-h LiPON coatings behaved similarly to that seen for the 1-h coating. These data were omitted for the sake of clarity.....	321
Figure IV - 129: Cell potential vs. normalized capacity, representing the typical charge and discharge voltage response of a cell containing an uncoated cathode in these experiments. Selected curves were removed for the sake of clarity. During the first charge, the LMR NMC material was activated. With continued cycling, the voltage response for both the charge and discharge subcycles changed. The downward tick marks on the charge curves and upward tick marks on the discharge curves represent current interrupts	321
Figure IV - 130: Cell potential vs. normalized capacity, representing the typical charge and discharge voltage response of a cell containing a coated cathode in these experiments. This particular cell contained a zirconia-coated cathode (150°C). Selected curves were removed for the sake of clarity. During the first charge, the LMR NMC material was activated. With continued cycling, the voltage response for both the charge and	

Table of Contents

discharge subcycles changed. The downward tick marks on the charge curves and upward tick marks on the discharge curves represent current interrupts	322
Figure IV - 131: Relative change in average voltage vs. cycle count. The abbreviations in the legend reflect different Li, Mn, Ni, and Co stoichiometries (see associated table)	327
Figure IV - 132: Change in the relative change in average voltage vs. X_{Co}/X_{Mn}	327
Figure IV - 133: Operando study of the formation of LMR-NMC from hydroxide precursor and lithium carbonate	328
Figure IV - 134: Schematic of honeycomb network for synthesis of modified homogeneously distributed divalent metal precursors	328
Figure IV - 135: (a) Voltage profiles and (b) changes in iR-corrected average discharge voltage in sol-gel prepared and commercial (HE5050, Toda) $Li_{1.2}Ni_{0.15}Mn_{0.55}Co_{0.1}O_2$ baseline samples	329
Figure IV - 136: Particle morphology of (a) pristine $Li_{1.2}Ni_{0.15}Mn_{0.55}Co_{0.1}O_2$, (b) 5% Al-substituted, and (c) 5% Ga-substituted powder samples	330
Figure IV - 137: XRD patterns of (a) Al- and (b) Ga-substituted $Li_{1.2}Ni_{0.15}Mn_{0.55}Co_{0.1}O_2$	331
Figure IV - 138: Plots of lattice parameters in (a) a-axis and (b) c-axis as a function of percent substitution of Al and Ga. For baseline data, three batches of pristine samples are used to obtain average lattice parameter values. The samples containing impurity phases (10% Ga) are marked with hollow symbols. Solid lines are for visual guidance	331
Figure IV - 139: Initial voltage profiles of (a) Al- and (b) Ga-substituted $Li_{1.2}Ni_{0.15}Mn_{0.55}Co_{0.1}O_2$. (Voltage window: 2 – 4.7 V vs. Li; current: 10 mA/g)	332
Figure IV - 140: Capacity retention of (a) Al- and (b) Ga-substituted $Li_{1.2}Ni_{0.15}Mn_{0.55}Co_{0.1}O_2$. (Voltage window: 2 – 4.7 V vs. Li; current: 10 mA/g for the 1 st cycle and 20 mA/g for the following cycles)	332
Figure IV - 141: Normalized voltage profiles (left side) and $(dQ/dV)^{*}1/Q$ plots (right side) for pristine and cation-substituted samples. Arrows indicate the movements of the curves on progressive cycling	333
Figure IV - 142: Plots of (a) iR-corrected average voltage ($V_{avg, iR-corr}$) and (b) relative voltage fade (VF) as a function of cycle number in Al-substituted $Li_{1.2}Ni_{0.15}Mn_{0.55}Co_{0.1}O_2$. The relative voltage fade is defined as the percent decay in $V_{avg, iR-corr}$ relative to $V_{avg, iR-corr}$ at 2 nd cycle	334
Figure IV - 143: Plots of (a) iR-corrected average voltage ($V_{avg, iR-corr}$) and (b) relative voltage fade (VF) as a function of cycle number in Ga-substituted $Li_{1.2}Ni_{0.15}Mn_{0.55}Co_{0.1}O_2$. The relative voltage fade is defined as the percent decay in $V_{avg, iR-corr}$ relative to $V_{avg, iR-corr}$ at 2 nd cycle	335
Figure IV - 144: Schematic illustration of layered to spinel-type phase transition	335
Figure IV - 145: Powder XRD patterns of Cr-substituted $Li_{1.2}Ni_{0.2-x/2}Mn_{0.6-x/2}Cr_xO_2$	336
Figure IV - 146: Electrochemical voltage profile of the first cycle for Cr-subst. LMR-NMC series of compounds with $Li_{1.2}Ni_{0.2-x/2}Mn_{0.6-x/2}Cr_xO_2$	336
Figure IV - 147: Voltage fade percent change as a function of cycle number for $Li_{1.2}Ni_{0.2-x/2}Mn_{0.6-x/2}Cr_xO_2$	336
Figure IV - 148: Schematic of reaction mechanism which represents formation of LMR-NMC materials	337
Figure IV - 149: Schematic of microscopic view of the synthesis of LMR-NMC	337
Figure IV - 150: Synthetic protocol for synthesizing either 'layered-layered' (LL) or 'layered-layered-spinel' (LLS) composites for studying voltage fade behavior in LMR-NMC cathodes	337
Figure IV - 151: Left side: voltage profile (first cycle) of LL and LLS with nominal composition: $Li_{1.2}Mn_{0.55}Co_{0.1}Ni_{0.15}O_{2+\delta}$. Right side; powder XRD patterns of products from LL and LLS synthesis. The LLS or LL can be tuned based on the order of addition of Li salt in the reaction. The arrows in both figures shows the markers for spinel as either a short plateau in the voltage profile at about 2.8 V, and a diffraction peak that corresponds to spinel at about 36 degrees 2-theta	338
Figure IV - 152: Specific capacity of LL and LLS cathode materials (top), and the voltage fade response (lower figure)	338
Figure IV - 153: Amount of nominal lithium retained vs. $1/\sqrt{pO_2}$. The markers represent the data points and the lines, the least-squares fit of those data. The value of the regression coefficient, r^2 , in both cases was 0.98 or greater. High oxygen partial pressures are on the left-hand side of the x-axis	340
Figure IV - 154: A and B) XRD patterns of slow-cooled and quenched HL-NMC cathode materials calcined under different oxygen partial pressures with the patterns are indexed to R3m space group. C and D)	

comparison between slow-cooled and quenched HL-NMC samples showed the effect of quenching rate on the shape of the peak at ~36.5°. ($\lambda = 1.5406 \text{ \AA}$)	340
Figure IV - 155: A and B) XRD patterns of slow-cooled and quenched LL-NMC cathode materials calcined under different oxygen partial pressures. C and D) comparison between slow-cooled and quenched LL-NMC samples showing the effect of quenching rate on the shape of these peaks. ($\lambda = 1.5406 \text{ \AA}$)	341
Figure IV - 156: (a) Cycle life performance; (b) Voltage profiles for the first 7 cycles.....	343
Figure IV - 157: A typical cross-section reconstructed by FBP, approximately through the center of the particle by tomographic reconstruction of the raw data	343
Figure IV - 158: Cropped volume rendered view of the reconstructed data from earlier figure. The data for complete 3D reconstruction were composed of 180 such images as they were collected through a total of 180° rotation	344
Figure IV - 159: 3-D renderings of FP (left), LP (middle), and CLP (right).....	344
Figure IV - 160: (top) Volume to surface area ratios (in pixels) for all nine particles analyzed with nanotomography. (bottom) Three readings of transition metal ratios in each of one particle per type as determined by fluorescence	344
Figure IV - 161: (left) Binarized cross-sections of single particle. (right) A step in the process of overlaying Mn (green) onto the cross section	345
Figure IV - 162: (a) HRTEM image and (b-c) local structural information from Fast-Fourier Transforms of regions 1 and 2. Extra rows of spots indicated by the white arrow in (b) indicate that region 1 contains a spinel structure. (d) EELS data from regions 1 and 2 in (a) and normalized to the Mn edge, indicating that the spinel region contains more Ni than Co.....	346
Figure IV - 163: Electrochemical comparison of 'layered-layered-spinel' electrodes fabricated by the 'oxalate' and 'Li ₂ MnO ₃ ' methods showing (a) discharge capacities as a function of cycle number, and (b) second cycle dQ/dV profiles.....	347
Figure IV - 164: (a) First cycle discharge capacity (■) and first cycle efficiency (□) as a function of x in Li _x Mn _{0.53125} Ni _{0.28125} Co _{0.18750} O ₅ , i.e., the target spinel content in the 'layered-layered-spinel' samples. (b) Discharge capacity for increasing spinel content as a function of increasing current density. (c) Cycle 20 dQ/dV for the series of increasing spinel content when cycled between 2.0 – 4.45 V at 15 mA/g.....	348
Figure IV - 165: (a) Cycle performance for lithium cells with 'layered-layered-spinel' electrodes derived from xLi ₂ MnO ₃ •(1-x)LiMn _y Ni _{1-y} O ₂ compositions with x=0.25 (closed symbols) and x=0.33 (open symbols) for various values of y, and a targeted 15% spinel content. dQ/dV plots for (b) cycle 2 and (c) cycle 20 of the electrochemical data in (a)	348
Figure IV - 166: State-of-charge effects during resting on VF at 30°C after 23 days. Corrected average charge and discharge voltages are plotted against the cycle number	351
Figure IV - 167: Temperature effects on VF for cells rested at 4.45V during discharge after 23 days. Corrected average charge and discharge voltages are plotted against the cycle number	352
Figure IV - 168: The effect of rest time on VF for cells rested at 4.45V during discharge at 65°C. Corrected average charge and discharge voltages are plotted against the cycle number	352
Figure IV - 169: Voltage decay for cells rested at 4.45V during discharge for about 22 days at 30°C and 55°C	353
Figure IV - 170: Effect of multiple rests on VF for two cells rested at 3.55V during charge and at 4.45V during discharge. All testing is done at 55°C	353
Figure IV - 171: View of activated LMR-NMC material	354
Figure IV - 172: Li electrode ASI estimated by comparing half-cell to LMR-NMC electrode reference electrode cell interfacial impedance. Data from two different half-cells are shown	355
Figure IV - 173: Electrochemical model equations for the lithium transport in the LMR-NMC electrode active material.....	356
Figure IV - 174: Assumed open circuit voltage curve as a function of relative lithium concentration in domain. Also the stability ranges of domains 2 and 3 are shown	357
Figure IV - 175: Electrochemical particle model simulation of LMR-NMC standard electrode half-cell charge and discharge curves at a C/300 rate	357

Table of Contents

Figure IV - 176: Volume fraction of domains 2 and 3 in LMR-NMC active material from electrochemical model simulation of charge and discharge at a C/300 rate.....	358
Figure IV - 177: Overlaid selected GITT measurements at indicated voltage on standard LMR-NMC electrode half-cell (600 second C/18 charge pulse and 6000 second relaxation) across full charge. Inset shows expanded view of last hour of relaxation.....	358
Figure IV - 178: Electrochemical model simulation of standard LMR-NMC electrode half-cell GITT experiment (600 second C/18 charge pulse and 6000 second relaxation at about 3.67 volts).....	359
Figure IV - 179: Current pulse experiment on LMR-NMC reference electrode cell (10 minute current pulse and 7 hour relaxation at about 3.3 volts). (a) discharge (b) charge.....	359
Figure IV - 180: Simulation of current pulse experiment on LMR-NMC reference electrode cell (10 minute 5 mA/g charge pulse and 7 hour relaxation at about 3.3 volts). (a) full experiment (b) approximately first 12 minutes.....	360
Figure IV - 181: Charge discharge profile of the LMR-NMC $0.5\text{Li}_2\text{MnO}_3 \bullet 0.5\text{LiMn}_{0.375}\text{Ni}_{0.375}\text{Co}_{0.25}\text{O}_2$, cycled against Li for 20 cycles	364
Figure IV - 182: LMR-NMC cathodes cycled for 1, 300 and 1500 cycles in full cells, cathodes harvested and reassemble in to half cell. Capacity for a fresh electrode 282 mAh/g and a cathode cycled 1500 times is 262 mAh/g	364
Figure IV - 183: Analysis of cell energy loss indicated voltage fade was a significant factor with no known mitigation strategy.....	365
Figure IV - 184: Critical to the team's success was the initial establishment of a unified testing and data analysis protocol which all partners utilized	365
Figure IV - 185: Resistance-corrected average cell potentials versus cycle number. A continuous drop in average potential exceeding 0.1V is apparent during charging and discharging. The drop in average charge potential is larger than the drop in average discharge potential. The average potential is calculated by dividing the measured total energy (current x time x voltage) by the measured cell capacity	366
Figure IV - 186: Discharge capacity after 1st and 6th cycles under various testing conditions	367
Figure IV - 187: Flow chart for consensus decision making within the project	368
Figure IV - 188: (a) Simplified schematic of hysteresis/voltage fade mechanism as described in the text. (b) octahedral and tetrahedral sites associated with dumbbell configurations in layered Li-TM-oxides	368
Figure IV - 189: Proposed LS transformation mechanism in HE5050 LMR composite oxide via formation of tetrahedral lithium in the lithium layer and migration of Mn from octahedral TM layer to octahedral site of lithium layer.....	369
Figure IV - 190: Relative energy densities for cathode materials	370
Figure IV - 191: Relative materials costs for cathode materials is dependent upon energy density and composition. www.cse.anl.gov/batpac	371
Figure IV - 192: Electrochemical performance of baseline cell: (a) capacity for more than 50 cycles and (b) area specific impedance (ASI) vs. depth of discharge (DoD)	374
Figure IV - 193: Schematic of full continuous concentration gradient cathode material (FCG)	374
Figure IV - 194: (a) EDAX of FCG cathode and (b) EPMA result showing the composition gradient at the particle level.....	375
Figure IV - 195: (a) Initial charge and discharge at 30°C and 55°C of half-cell based on FCG cathode and (b) comparison of cycling performance of cell based on FCG cathode and cathode that has the same average formula $\text{LiNi}_{0.6}\text{Mn}_{0.25}\text{Co}_{0.15}\text{O}_2$ with constant composition (core).....	375
Figure IV - 196: SEM images of FCG precursor $\text{Ni}_{0.6}\text{Mn}_{0.2}\text{Co}_{0.2}(\text{OH})_2$ and $\text{LiNi}_{0.6}\text{Mn}_{0.2}\text{Co}_{0.2}\text{O}_2$	375
Figure IV - 197: (a) Initial charge and discharge of half-cell based on FCG cathode prepared by hydroxide process and (b) cycling performance of FCG cathode	376
Figure IV - 198: (a) Contour plots of the TR-XRD patterns at the selected 2θ range for the charged FCG and NCA sample and (b) mass spectroscopy profiles for the oxygen release (O_2 , m/z=32) collected simultaneously during measurement of TR-XRD and the corresponding temperature region of the phase transitions for the FCG and NCA samples.....	376
Figure IV - 199: Scheme for ultra-high energy ball milling machine	377

Figure IV - 200: SEM image (a) and EDX elemental mapping of (b) C, (c) Co, (d) O, (e) Si, and (f) Sn for the UHEM SiO-Sn ₃₀ Co ₃₀ C ₄₀ composite	377
Figure IV - 201: XRD patterns of UHEM sample	377
Figure IV - 202: Charge-discharge curves of cells with UHEM anode cycled at rates of (a) 300 mA g ⁻¹ (~C/3) and (b) 900 mA g ⁻¹ (~1C)	378
Figure IV - 203: Material Validation in coin cells vs. Li.....	380
Figure IV - 204: Snap shot of the dV/DQ software.....	381
Figure IV - 205: High Voltage stability of FEC and L-20446	381
Figure IV - 206: Matching 1st cycle efficiencies maximizes benefit of both materials	382
Figure IV - 207: Cycle life of Core shell Si anode composite	382
Figure IV - 208: Picture of post mortemed 18650 jelly roll	382
Figure IV - 209: Half cell performance of electrodes from the post mortem 18650 cell.....	382
Figure IV - 210: Protocol 2 reduces formation time with similar life performance	383
Figure IV - 211: Voltage windows to yields 60% cell energy	383
Figure IV - 212: Cycle life in 60% energy windows.....	383
Figure IV - 213: Improved cycling stability of a Ti-doped NCM compared to a baseline material.....	385
Figure IV - 214: Materials prepared via ion-exchange exhibit lower impedance, indicated by less voltage relaxation during current interrupts	385
Figure IV - 215: Improved electrolyte formulations lead to extended cycling stability.....	386
Figure IV - 216: Change in useable energy with respect to cycling for HCMR™XLE2 and LiPON coated HCMR™XLE2 cathode materials in a single layer pouch cell configuration	388
Figure IV - 217: DC-R of four select ALD chemistries (AlF ₃ , Al ₂ O ₃ , TiN and AlN) deposited on electrodes at two different thicknesses.....	389
Figure IV - 218: The expected microstructure of the thick-coating electrode and material information of the constituent materials	392
Figure IV - 219: (a) XRD pattern and (b) Raman spectrum of G/Si-C. (c) Low-magnification TEM and (d) SEM image of G/Si-C.....	392
Figure IV - 220: (a) Coulombic efficiency (2nd to 100th cycle) of G/Si-C@high. (b) Impedance spectra of G/Si-C and Si-C at low and high mass loadings. Insets in (b) are the Randles equivalent circuit and enlarged spectra showing difference between G/Si-C@low and G/Si-C@high, respectively.....	393
Figure IV - 221: Cycling performance of G/Si-C (a & b) and Si-C (c & d)	393
Figure IV - 222: Percentage composition of a) the overall electrode and b) the carbon components	393
Figure IV - 223: Electrochemical performance comparison between Umicore Si (a,c,e) and Si-C (b,d,f)	394
Figure IV - 224: (a) SEM and (b) TEM images of B-Si/SiO ₂ /C.....	395
Figure IV - 225: (a) Cycling and (b) rate performance of B-Si/SiO ₂ /C	395
Figure IV - 226: (a) cycling performance and (b) coulombic efficiency of Si electrodes with PAA-PVA, NaCMC, and PAA binders	395
Figure IV - 227: Cycling performance of intermediate B-Si/SiO ₂ /C electrodes with PAA-PVA binder	396
Figure IV - 228: Charge-discharge profiles of the LiNi _{0.62} Mn _{0.24} Co _{0.14} O ₂ cathode at 2.7 – 4.5 V at C/5 rate	396
Figure IV - 229: Cyclability of the LiNi _{0.62} Mn _{0.24} Co _{0.14} O ₂ cathode at 2.7 – 4.5 V at C/5 rate for 100 cycles	396
Figure IV - 230: First three charge-discharge curves of the three Ni-rich samples at 2.7 – 4.5 V: (a) LiNi _{0.8} Co _{0.2} O ₂ , (b) LiNi _{0.62} Mn _{0.24} Co _{0.14} O ₂ , and (c) concentration-gradient Li[Ni _{0.8} Co _{0.2}] _{0.7} [Ni _{0.2} Mn _{0.8}] _{0.3} O ₂	397
Figure IV - 231: Cyclability of the (a) LiNi _{0.8} Mn _{0.1} Co _{0.1} O ₂ , (b) LiNi _{0.7} Mn _{0.15} Co _{0.15} O ₂ , and (c) LiNi _{0.6} Mn _{0.2} Co _{0.2} O ₂ samples with and without coating with various amounts of Al ₂ O ₃ at C/5 rate at 3.0 – 4.5V	397

Table of Contents

Figure IV - 232: Galvanostatic charge-discharge profiles of the $\text{LiNi}_{0.7}\text{Mn}_{0.15}\text{Co}_{0.15}\text{O}_2$ sample (a) without and (b) with 1.0 wt. % Al_2O_3 coating	397
Figure IV - 233: SEM image (a) and EDS pattern (b) of the Al_2O_3 -coated concentration gradient Ni-rich electrode	398
Figure IV - 234: TEM image (a) and HRTEM image (b) of the Al_2O_3 -coated concentration gradient Ni-rich material	398
Figure IV - 235: Cycling performances at 4.5 – 2.7 V of the concentration-gradient (GC) and Al_2O_3 -coated concentration-gradient (Al_2O_3 -CG) at C/5 rate	398
Figure IV - 236: Cyclability at C/5 rate at 3.0 – 4.5 V of the (a) $\text{LiNi}_{0.8}\text{Mn}_{0.1}\text{Co}_{0.1}\text{O}_2$, (b) $\text{LiNi}_{0.7}\text{Mn}_{0.15}\text{Co}_{0.15}\text{O}_2$, and (c) $\text{LiNi}_{0.6}\text{Mn}_{0.2}\text{Co}_{0.2}\text{O}_2$ samples with and without coating with various amounts of Al_2O_3	399
Figure IV - 237: Galvanostatic charge-discharge profiles of the NCM 71151 (Li $\text{Ni}_{0.7}\text{Mn}_{0.15}\text{Co}_{0.15}\text{O}_2$) samples (a) without and (b) with 1 wt. % Al_2O_3 coating	399
Figure IV - 238: (a) Comparison of the cyclability of our Ni-rich cathode ($\text{LiNi}_{0.69}\text{Mn}_{0.23}\text{Co}_{0.08}\text{O}_2$) with that of the commercial Umicore NCM ($\text{LiNi}_{0.5}\text{Mn}_{0.2}\text{Co}_{0.3}\text{O}_2$) at C/5 rate at 2.7 – 4.5V. (b) Cyclability of our Ni-rich cathode with a higher cutoff voltage (2.8 – 4.6 V) at C/5	399
Figure IV - 239: (a) Charge/discharge profiles, (b) cycling performance, (c) capacity retention, and (d) average discharge voltage of $\text{LiNi}_{0.8}\text{Co}_{0.1}\text{Mn}_{0.1}\text{O}_2$ materials prepared at different pH values at C/5 rate over the voltage range of 2.7 - 4.5 IV	400
Figure IV - 240: Comparison of Mn/Ni intensity ratios across the precursor particles of materials prepared at pH = 10.7 and pH = 11.5.....	400
Figure IV - 241: SEM images of three recent batches of the NCM 71151 hydroxide precursor ($\text{LiNi}_{0.7}\text{Mn}_{0.15}\text{Co}_{0.15}\text{O}_2$) with different average particle size: (a) ~ 10 μm , (b) ~ 15 μm , and (c) ~ 20 μm	400
Figure IV - 242: (a) SEM image of the concentration-gradient $\text{LiNi}_{0.62}\text{Co}_{0.08}\text{Mn}_{0.23}\text{O}_2$ prepared at pH = 8.3 and (b) cycling performance of the concentration-gradient $\text{LiNi}_{0.62}\text{Co}_{0.08}\text{Mn}_{0.23}\text{O}_2$ and the constant-concentration material.....	401
Figure IV - 243: SEM images of (a, b) $[\text{Ni}_{0.9}\text{Co}_{0.1}](\text{OH})_2$, (c, d) $[\text{Ni}_{0.9}\text{Co}_{0.1}]_{0.44}[\text{Ni}_{0.7}\text{Co}_{0.08}\text{Mn}_{0.22}]_{0.56}(\text{OH})_2$, and (e, f) $[\text{Ni}_{0.9}\text{Co}_{0.1}]_{0.4}[\text{Ni}_{0.7}\text{Co}_{0.08}\text{Mn}_{0.22}]_{0.5}[\text{Ni}_{0.5}\text{Co}_{0.05}\text{Mn}_{0.45}]_{0.1}(\text{OH})_2$	401
Figure IV - 244: EDS line scan across the $[\text{Ni}_{0.9}\text{Co}_{0.1}]_{0.4}[\text{Ni}_{0.7}\text{Co}_{0.08}\text{Mn}_{0.22}]_{0.5}[\text{Ni}_{0.5}\text{Co}_{0.05}\text{Mn}_{0.45}]_{0.1}(\text{OH})_2$ sample	401
Figure IV - 245: GC-MS of the synthesized new additive	402
Figure IV - 246: LNMO/Li cell capacity retention profile using 1.2 M LiPF ₆ in TFPPCE/EMC (3/7, v/v). Voltage window: 4.95–3.5 V, Current: 0.8 mA (C/3).....	402
Figure IV - 247: Capacity retention and voltage profile of UT-Austin high capacity cathode, UTC#0/Li half cells cycled at RT between 2.7-4.5 V, C/5 using (a), (b) Gen 2 electrolyte and (c), (d) fluorinated electrolyte	403
Figure IV - 248: Capacity retention and voltage profile of UT-Austin high capacity cathode UTC#0/Li half cells cycled at RT between 2.7-4.8 V, C/5 using fluorinated electrolyte	403
Figure IV - 249: Capacity retention profiles of UT-Austin high capacity cathode/Li half cells cycled at RT with cut-off voltage at (a) 2.7 V - 4.5 V and (b) 2.7 V- 4.8 V and at 55 °C with cut-off voltage at (c) 2.7 V - 4.5 V and (d) 2.7 V - 4.8 V using Gen 2 and Gen 2 + 5% F-EPE electrolytes	404
Figure IV - 250: Differential capacity plots of the 1 st cycle formation of Si/Li half cells using (a) Gen 2 electrolyte with LiDFOB, VC, FEC and EPE as additives and (b) HVE1 electrolyte with LiDFOB and VC as additives	404
Figure IV - 251: Capacity retention profiles and Coulombic efficiency of Si/Li half cells at RT using (a) Gen 2 electrolyte and (b) Gen 2 + 10% FEC electrolyte	405
Figure IV - 252: TEM characterization of (a) pristine Si particles and (b) Si anode harvested from Si/Li half cell after formation in Gen 2 + 10% FEC electrolyte; (c) EDS spectrum of the edge coating on cycled Si particles	405
Figure IV - 253: Capacity retention profiles of UT-Austin high capacity cathode/Li half cells cycled with Gen 2 and FEC 2 electrolytes at RT with cut-off voltage at (a) 2.7 V - 4.5 V and (b) 2.7 V- 4.8 V and at 55 °C with cut-off voltage at (c) 2.7 V - 4.5 V and (d) 2.7 V - 4.8 IV	406
Figure IV - 254: (a) Chemical structure of different additives for SiO ₂ -C anode; (b) Differential capacity plots of the 1 st cycle formation of SiO ₂ -C/Li half cells with Gen 2+10% FEC baseline electrolyte and with LiDFOB, 1,3-Propanesultone and N,N-Diethyltrimethylsilylamine as additives	406

Figure IV - 255: Capacity retention and coulombic efficiency of SiO ₂ -C/Li half-cells at RT using baseline plus (a) 0.5% LiDFOB, (b) 1% 1,3-Propanesultone and (c) 0.5% N,N-Diethyltrimethylsilylamine compared with the baseline Gen 2 + 10% FEC electrolyte	407
Figure IV - 256: SEM characterization of cycled SiO ₂ -C anode harvested from SiO ₂ -C /Li half-cells with (a) Gen 2+10% FEC baseline electrolyte, (b) baseline + 0.5% LiDFOB, (c) baseline + 1% 1,3-Propanesultone, and (d) baseline + 0.5% N,N-Diethyltrimethylsilylamine	407
Figure IV - 257: Capacity retention during room temperature cycling of CAM-7/graphite system in baseline 18650 cells fabricated at TIAX. The cells are cycled at C/2 charge rate and discharged at 1C rate between 4.2 to 2.7IV. Every 50 cycles, the C/3 and C/2 capacities are measured	410
Figure IV - 258: Capacity retention during cycling at 45°C of CAM-7/graphite system in 18650 cells fabricated at TIAX. The cells are cycled at C/2 charge rate and discharged at 1C rate between 4.2 to 2.7IV. Every 50 cycles, the C/20 and C/5 capacities are measured	410
Figure IV - 259: Capacity retention during cycling at room temperature of CAM-7/graphite baseline system in 18650 cells fabricated at TIAX. The cells are cycled at C/2 charge rate and discharged at 1C rate between 4.1 to 2.7IV. Note that cycling between 4.1 to 2.7 corresponds to 90% SOC swing during cycling. Every 50 cycles, the C/3 and C/2 capacities are measured	410
Figure IV - 260: Summary data showing the impact of dopant distribution on impedance growth of CAM-7 high-nickel cathode materials. Dopant A is placed in the bulk of the material, and dopant B at the surface. Measurements such as these were performed to develop a new composition of CAM-7 with very low impedance growth specifically for vehicle applications	411
Figure IV - 261: Cycling results of CAM-7/silicon-based anode in coin cells showing the impact of anode to cathode ratio, and pre-lithiation on capacity retention	411
Figure IV - 262: Preliminary synthesis by planetary ball mill.....	415
Figure IV - 263: Preliminary synthesis by hydroxide co-precipitation	415
Figure IV - 264: Preliminary synthesis by carbonate co-precipitation	416
Figure IV - 265: Effect of lithium content on capacity and cyclability	417
Figure IV - 266: Capacity and cyclability summary	418
Figure IV - 267: XRD comparison of bench-scale oxalate, preliminary carbonate and hydroxide cathodes	419
Figure IV - 268: VF protocol comparison of bench-scale oxalate, preliminary carbonate and hydroxide cathodes	419
Figure IV - 269: XRD comparison of bench-scale oxalate, preliminary carbonate and hydroxide cathodes	420
Figure IV - 270: VF protocol comparison of bench-scale oxalate, preliminary carbonate and hydroxide cathodes	421
Figure IV - 271: SEM images of pristine LNO before dry coating	421
Figure IV - 272: SEM images of 1wt% Al ₂ O ₃ coated LNO after dry coating	421
Figure IV - 273: 1C cyclability comparison of pristine and 1wt% Al ₂ O ₃ coated LNO materials.....	422
Figure IV - 274: Advanced Taylor Vortex Reactor	422
Figure IV - 275: Advanced Battery Materials Process R&D Workflow.....	425
Figure IV - 276: Chemical structure of Li-TDI.	426
Figure IV - 277: Chemical structure of PEPM	426
Figure IV - 278: Chemical structures of PEPM co-polymers.....	426
Figure IV - 279: Chemical structure of PFM.....	426
Figure IV - 280: Chemical structure of PFM derivatives	426
Figure IV - 281: Chemical synthesis and structures of GM's separator modifier	427
Figure IV - 282: Chemical structure of PFPBP	427
Figure IV - 283: Chemical structure of Li-FSI.....	427
Figure IV - 284: Examples of different types of NMC 532 electrode defects that were intentionally created during slot-die coating	430

Table of Contents

Figure IV - 285: Optical and IR images of intentionally introduced coating defects: exaggerated non-uniform coating (a, b), metal particle contamination (c, d), large agglomerates (e, f), and pinholes (g, h). The emissivity values in the IR thermographs increase or decrease depending on the nature of defects.....	431
Figure IV - 286: Rate capability (a) and columbic efficiency (b) data from exaggerated non-uniform coating (open symbols) compared with non-defective baseline NMC 532 electrodes (closed symbols). In figure a, blue symbols are full discharge capacity and black symbols are gravimetric capacity	432
Figure IV - 287: Rate capability (a) and columbic efficiency (b) from agglomerated electrodes (open symbols) compared with non-defective baseline NMC 532 electrodes (closed symbols). In figure a, blue symbols are full discharge capacity and black symbols are gravimetric capacity	432
Figure IV - 288: Rate capability (a) and columbic efficiency (b) from metal particle contamination (open symbols) compared with non-defective baseline NMC 532 electrodes (closed symbols). In figure a, blue symbols are full discharge capacity and black symbols are gravimetric capacity	432
Figure IV - 289: Specially designed shim having a 6-mm uncoated stripe (1x large defective area) and three 2-mm uncoated stripes (3x small defective areas). The corresponding optical and IR thermography images are shown on the right.....	433
Figure IV - 290: Rate capability (a) and columbic efficiency (b) from the defective electrodes prepared from the special shim creating Sample 1x (open symbols) compared with non-defective baseline NMC 532 electrode (closed symbols). In figure a, blue symbols are full discharge capacity and black symbols are gravimetric capacity	433
Figure IV - 291: Rate capability (a) and columbic efficiency data from the defective electrode prepared from special shim set creating 3X small defective non-coated area compared with the non-defective baseline NMC 532 electrodes (closed symbols). In figure a, blue color symbols represent full discharge capacity, black symbols represent the gravimetric capacity. The defective electrode shows lower capacity compared to baseline NMC 532 electrode at high-rate.....	433
Figure IV - 292: Short-term capacity fade data for various defective electrodes (open symbols) where defect types are labeled to the left of each figure row compared with non-defective baseline NMC 532 electrodes (closed symbols) at 2C (left column) and 5C (right column) discharge rates. Blue symbols are full-cell discharge capacity and black symbols are gravimetric capacity.....	435
Figure IV - 293: SEM micrographs from non-defective baseline NMC 532 electrode (a) and defective electrode with large agglomerates (b). Carbon-rich areas are highlighted. Corresponding EDS X-ray maps from the respective SEM images are shown below (1 for C, 2 for Co, 3 for Mn, and 4 for Ni).....	436
Figure IV - 294: SEM micrograph from the interfacial length between the coated and uncoated areas from Sample 3x showing less active material at the interface. It is also noted that the z-direction profile of the coated interfacial length is sloped downward towards the uncoated area, which could further alter the local N/P ratio and increase local contact resistance	436
Figure IV - 295: Top – Temperature profile (from IR emissivity) of an A12 anode sample moving right to left past the excitation source (red color) showing a maximum temperature rise of ~27°C. Bottom – “Pseudo-steady-state” temperature profiles of all four anode and cathode samples moving at 0.5 ft/min past excitation source. Dark blue line is A12 anode with high porosity, light blue line is A12 anode with lower porosity, orange line is thick NMC 532 cathode with lower porosity, and green line is thin NMC 532 cathode with high porosity).....	437
Figure IV - 296: Top – Micro-scale model of NMC 532 cathode assuming a thin, uniform binder around active-material/conductive-additive agglomerates deposited on Al foil. Bottom – Preliminary modeling of the effect of line speed on the temperature profile of a given electrode composition	437
Figure IV - 297: Optical reflectance data identifying voids and coating streaks on the surface of a ConocoPhillips A12 anode that are not visible with conventional CCD camera line inspection equipment	438
Figure IV - 298: Comparison of baseline and reduced pack costs (per kWh-usable basis) from the ORNL model. “Reduced” cost is associated with implementing aqueous processing, thick electrode coatings, and reduced wetting and formation times	441
Figure IV - 299: Comparison of baseline NMP/PVDF processed electrodes and <i>all</i> aqueous processed NMC 532 electrodes in full coin cells (CP A12 natural graphite anode).....	442

Figure IV - 300: (a) Aqueous processed NMC 532 rate performance and short-term capacity fade from a 3-Ah pouch cell with JSR Micro TRD202A as the binder; (b) comparison of capacity retention between cell from (a) and six baseline NMC 532 cathodes via PVDF/NMP baseline processing (2σ error bars)	442
Figure IV - 301: (a) Half-cell rate capability of aqueous processed NMC 532 cathodes with different conductive carbon additives; (b) low-rate capacity fade in full coin cells coupled with CP A12 anodes via <i>all</i> aqueous processing	443
Figure IV - 302: A typical ALD chamber with sequentially separated precursor exposures that draws out overall processing time	446
Figure IV - 303: A simplified schematic demonstrating the in-line spatial ALD concept	446
Figure IV - 304: A simple schematic demonstrating the alternate high and low pressure regimes present in the "push-pull" reactor concept.....	446
Figure IV - 305: Schematic representation of the "digital modular" design concept	447
Figure IV - 306: Diagram of drum-in-drum reactor format.....	447
Figure IV - 307: Computational flow dynamic simulation of gas flow through the precursor introduction module and final construction	447
Figure IV - 308: Final construction and sample loading of in-line ALD reactor	448
Figure IV - 309: Measured thickness of aluminum oxide deposited using in-line ALD showing linear film growth at ~400 ft/min line speeds	448
Figure V - 1: BATT approach overview	453
Figure V - 2: BATT focus areas	455
Figure V - 3: (a) Capacity, (b) dQ/dV, and (c) rate data for $0.33\text{Li}_2\text{MnO}_3 \bullet 0.67\text{LiMn}_{0.375}\text{Ni}_{0.375}\text{Co}_{0.25}\text{O}_2$ baseline and Mg^{2+} - and Al^{3+} -doped (2 mol%) electrodes in Li half-cells at RT	457
Figure V - 4: (a) Initial discharge capacities for $x[\text{Li}_{1.2}\text{Mn}_{0.6}\text{Ni}_{0.2}\text{O}_2] \bullet (1-x)\text{LiMn}_{1.5}\text{Ni}_{0.5}\text{O}_4$ electrodes and the corresponding XRD patterns, (b). Dashed lines in (b) mark NiO-like impurities (c) High resolution TEM image of $0.85[0.25\text{Li}_2\text{MnO}_3 \bullet 0.75\text{LiMn}_{0.375}\text{Ni}_{0.375}\text{Co}_{0.25}\text{O}_2] \bullet 0.15\text{LiMn}_{1.5}\text{Ni}_{0.5}\text{O}_4$ particle showing integrated, layered (regions A and C) and spinel (region B) components	458
Figure V - 5: (a) First cycle capacities and efficiencies of $0.05\text{Li}_2\text{MnO}_3 \bullet 0.95\text{LiMn}_{0.5-y}\text{Ni}_{0.5+y/2}\text{Co}_{y/2}\text{O}_2$ with y values from 0-0.3. (b) Specific energy density of the y=0.1 composition for 50 cycles between 4.6-2.0 V (half-cell at 30°C, 15 mA/g)	459
Figure V - 6: Charge and discharge profiles of cycles 5, 25, and 50 (4.4 – 2.5 V, 20 mA/g, half-cells at RT) for (a) bare and (b) ALD AlW_xF_y -coated LiCoO_2 . (c) Comparison of rate capability for bare (black) and AlW_xF_y -coated (red) LiCoO_2	459
Figure V - 7: Local structural ordering of ϵ -CVO by TEM imaging and electron diffraction at pristine state (a, c) and after one cycle (b, d).....	462
Figure V - 8: Lithium reaction pathways and reversibility of ϵ -CVO cathode, via (a) GITT, (b) V K-edge EXAFS.....	463
Figure V - 9: Structural (a) and electrochemical (b) properties of synthesized α - CuVO_3	463
Figure V - 10: Synthesis and structural properties of LVP cathodes, (a) synchrotron XRD patterns recorded from intermediate and final product, (b) <i>in situ</i> synchrotron XRD studies of synthesis reactions, (c) XRD, structure refinement of synthesized LVP, and (d) SEM image of the as-synthesized LVP particles	464
Figure V - 11: Electrochemical properties of LVP particles, shown by (a) galvanostatic cycling at C/10 in two different voltage windows, (b) typical voltage profiles of LVP synthesized via two different routes	465
Figure V - 12: Soft XAS data showing the Ni L-edge of a charged electrode using three different modes. Auger electron yield (AEY) probes the top 1-2 nm of the sample, total electron yield (TEY) the top 2-5 nm, and fluorescence yield (FY) about 50 nm into the bulk	468
Figure V - 13: HR-TEM images of an NMC particle harvested from a charged electrode, showing the formation of a rock salt structure on the surfaces	468
Figure V - 14: Formation energies of the rock salt structure as a function of state-of-charge of baseline and Ti-substituted NMC cathodes, determined by first principles calculations.....	469

Table of Contents

Figure V - 15: Scanning electron micrographs of spray-pyrolyzed NMC samples (left), and electrochemical performance in lithium half-cells (right)	469
Figure V - 16: SEM images of solvothermal synthesized LMNO crystals: a) octahedrons, b) truncated-octahedrons and c) rods; d) rate capability of the crystal samples	473
Figure V - 17: Evolution of the XRD patterns and the expanded view of (311), (400) and (440) peaks during room-temperature storage of fully delithiated LMNO in the electrolyte: a) plates and b) octahedrons	474
Figure V - 18: Li content in the crystal samples as a function of storage time	474
Figure V - 19: XRD patterns collected during: a) <i>in situ</i> electrochemical, b) <i>ex situ</i> electrochemical and c) chemical delithiation of LMNO	475
Figure V - 20: TXRD patterns of selected Li_xMNO crystal samples: a) $x=0.82$, b) $x=0.25$, and c) $x=0$	476
Figure V - 21: Changes in the lattice parameters upon heating the Li_xMNO crystal samples: a) $0.51 \leq x \leq 1$ and b) $0 \leq x \leq 0.40$. Phase I: square; Phase II: circle; Phase III: triangle; solid solution: diamond; spinel-type phase: star	477
Figure V - 22: Phase diagram of Li_xMNO	477
Figure V - 23: Three dimensional morphology of cycled particles and corresponding statistical analysis. Panel a: A selection of typical particles from the $1\times$ -cycled electrode from tomography data acquired at 6630 eV. Panels b, c, d: Views of several particles magnified and virtually sliced/cut, indicating different types of morphology (solid and hollow). Panel e: A plot of ϵ parameter versus particle radius for two groups of particles cycled $1\times$ (green) and $200\times$ (red), indicates that the surface area of the particle structure increases with cycling. A histogram of the data points is plotted on the right hand side of panel e, along with a few selected standard geometric objects and their ϵ values for comparison	481
Figure V - 24: 3D rendering of a selected cathode particle from (a) pristine, (b) $1\times$ -cycled, and (c) $200\times$ -cycled electrodes with elemental distribution resolved from tomography above and below the K-edges of Mn, Co and Ni. The color legend represents relative concentrations of the TM elements	482
Figure V - 25: (a) Average Raman spectra of LMR-NMC cathodes charged to different cut-off voltages during the first cycle. (b) Shift of the A1g and Eg modes with respect to the pristine material as a function of voltage. (c) FWHM of the A1g and Eg modes as a function of voltage	482
Figure V - 26: (Upper panel) SEM picture of as-synthesized Li_2CuO_2 and $\text{Li}_2\text{Cu}_{0.5}\text{Ni}_{0.5}\text{O}_2$ cathode materials. (Lower panel) Initial charge-discharge capacity of Li_2CuO_2 (black) and $\text{Li}_2\text{Cu}_{0.5}\text{Ni}_{0.5}\text{O}_2$ (red)	483
Figure V - 27: Copper (CMP50V) and nickel metaphosphate/ vanadate (NMP50V) glasses demonstrate high-capacity glass-state conversion reactions	486
Figure V - 28: Ni-K edge XANES of nickel metaphosphate/vanadate (NMP50V) glass cathodes confirmed the Ni valence changes associated with a glass-state conversion mechanism	486
Figure V - 29: Electrical conductivity of iron phosphate glasses is strongly dependent on vanadate substitution	487
Figure V - 30: Substantial capacity fade was observed during cycle testing between 4V and 1 V of iron pyrophosphate glasses with 0% vanadate (FPP) and 50% vanadate (FPP50V) substitution	487
Figure V - 31: Z-contrast imaging and XEDS mapping of LMR prepared by different methods. (a) Schematic drawing of the newly developed four-detector system in a TEM, enabling efficient collecting of the EDS signal. Z-contrast images as well as XEDS maps of Mn, Ni and overlaid Mn/Ni maps of (b) coprecipitation-derived, (c) sol-gel method-derived and (d) hydrothermal-assisted method-derived LMR materials	490
Figure V - 32: Charge/discharge characteristics of LMR cathodes prepared by different methods. (a) Initial charge/discharge profiles at C/10 in the voltage range of 2.0–4.8 V. (b) Comparison of rate performance. (c) Cycling performance at C/5 after rate performance tests. Corresponding charge/discharge profile evolutions of materials prepared by the (d) CP method, (e) SG method, and (f) HA method during the long-term cycling	491
Figure V - 33: a) Charge-discharge curves and b) cycling ability of thick LMR electrode (LMR loading: 12.9 mg/cm^2) supplied by ANL. Voltage range: 2.0–4.7 V, current: C/10 for 3 formation cycles followed by C/3 in the subsequent cycling (1C=250 mA/g)	492
Figure V - 34: Characterization of uncoated material after 100 cycles. (a) TEM image showing a thick SEI layer formation. (b) TEM image showing the spinel formation distributed in nanoscale. (c) TEM image magnified	

from the green square in panel (b) showing cubic spinel lattice formation in this region; (d) High resolution Z-contrast image showing the formation of spinel-like phase at particle surface region	492
Figure V - 35: Characterization of AlF ₃ -coated material after 100 cycles. (a) Overview Z-contrast image of coated material after cycling. (b) TEM image showing that the surface region is protected by an AlF ₃ coating layer. (c) Z-contrast image of the cycled particle. (d) Atomic model of the [011] zone projection of a cubic spinel with Fd-3m space group	493
Figure V - 36: a) Voltage profiles and cyclic capacity of untreated (blue) and 1 wt.% AlF ₃ treated (red) LNMO at C/10 with 2.0 - 4.8 voltage range. b, c) Rate profiles for untreated (blue) and treated LNMO (red). d) a-STEM and FFT of uncycled treated LNMO	496
Figure V - 37: a) XRD of Li _{1.133} Ni _{0.3} Mn _{0.567} O ₂ and crystalline LLTO surface modified LNMO. b) First cycle voltage profiles of pristine and LLTO surface modified sample at C/20, voltage range is 2.0-4.8V.....	497
Figure V - 38: a) Cycling stability of Li _{1.133} Ni _{0.3} Mn _{0.567} O ₂ and crystalline LLTO surface modified sample at 1C, voltage range is 2.0-4.8V, b) Comparison of voltage degradations between pristine and LLTO surface modified sample at 1C, voltage range is 2.0-4.8V	497
Figure V - 39: a) dQ/dV profiles for spherical LNMO cycled at C/10 between 2.0 – 4.8V, b) dQ/dV curves of the non-modified LNMO. The first cycle (not depicted) was conducted at a rate of C/20	498
Figure V - 40: a) Cross sectional SEM image of a LMNO particle synthesized by the urea hydrolysis method with labeled EDX point scan locations. b) EDX mapping for Ni. c) EDX mapping for Mn	498
Figure V - 41: FTIR of etched Si wafer (red) compared to etched Si wafer that was exposed in EC:DEC electrolyte (blue).	499
Figure V - 42: Cyclic capacity and coulombic efficiency for the control thin film electrode, and the thin film electrode cycled in electrolyte with the FEC additive	499
Figure V - 43: XPS spectra of a-Si surface after 1 full cycle in 1:1 EC:DEC 1M LiPF ₆ electrolyte (red) and 45:45:10 EC:DEC:FEC 1M LiPF ₆ electrolyte (blue).....	500
Figure V - 44: (a) SEM micrograph of the rod-like LiMn _{0.7} V _{0.20} □ _{0.10} PO ₄ and (b) first charge-discharge profiles of the LiMn _{1-3x/2} V _x □ _{x/2} PO ₄ (0 ≤ x ≤ 0.20) samples, showing the advantage of aliovalent vanadium doping on the performance	502
Figure V - 45: XRD patterns of LiCo _{1-3x/2} V _x □ _{x/2} PO ₄ before and after heating	503
Figure V - 46: FT-IR spectra of LiCo _{1-3x/2} V _x □ _{x/2} PO ₄ after heating at 525°C	503
Figure V - 47: First charge/discharge profiles of LiCo _{1-3x/2} V _x □ _{x/2} PO ₄ after heating at 525°C	503
Figure V - 48: (a) SEM image, (b) CV plots, (c) first charge-discharge profiles at C/20 rate, and (d) cyclability at C/20 and C/10 rates of α ₁ -LiVOPO ₄ /graphene cathodes	504
Figure V - 49: XRD patterns of the α ₁ -LiVOPO ₄ /graphene nanocomposite after various depths of electrochemical discharge and chemical lithiation with n-butyllithium.	505
Figure V - 50: Structural relation showing condensation of molecular [SiO ₄] to chains of [SiO ₃].....	508
Figure V - 51: Solid State ²⁹ Si NMR spectra of mixed Li-Si-O's before and after exposure to DME for 1 week.....	508
Figure V - 52: Capacity of tin-based anodes compared to carbon. The volumetric capacity of Li ≈ Li _{4.4} Sn≈Li _{4.4} Si	511
Figure V - 53: X-ray diffraction pattern performed on operating electrochemical cells as a function of discharge and charge. λ=0.728 Å.....	511
Figure V - 54: (top) First cycle capacity as a function of the Ti/Sn ratio, and (bottom) electrochemical capacity of Sn-Fe-C composites as a function of the Ti/Sn ratio	511
Figure V - 55: Carbon plays a critical role in the maintenance of capacity on cycling	512
Figure V - 56: The volumetric capacity and cycling efficiency of the Sn-Fe-C composite over 100 cycles	512
Figure V - 57: (top) Volumetric capacity comparison of the optimized Sn-Fe-C composite with standard graphite cycled under 1C rate (1C corresponding to a current density of 600 mA/g for Sn-Fe-C, 372 mA/g for standard graphite). The cycling curves of optimized Sn-Fe-C composite (middle) before and (bottom) after replacing lithium the anode in the coin cell	512

Table of Contents

Figure V - 58: Capacity and efficiency versus cycle number of Si-Ti-C between 0.002 and 2 V at C/20 rate (0.4 mA/cm ²).....	513
Figure V - 59: <i>In situ</i> Ti K-edge XANES analysis of lithiation and delithiation of Ti ₃ C ₂	515
Figure V - 60: <i>Ex situ</i> XPS spectra in (A) C1s region and (B) Li1s region for Ti ₃ C ₂ after electrochemical cycling: I – initial Ti ₃ C ₂ soaked in the electrolyte; II – lithiated from OCV to 1 V; III – lithiated from OCV to 5 mV; IV – lithiated from OCV to 5 mV, then delithiated to 3 V	515
Figure V - 61: Areal capacity vs. cycle # for pressed Ti ₃ C ₂ and Nb ₂ C discs with 10 wt.% of different carbon additives at C/3 and C/4, respectively	516
Figure V - 62: Comparison of areal capacities for Ti ₃ C ₂ and Nb ₂ C discs with 10 wt.% of CB with other systems.....	516
Figure V - 63: Electrochemical performance of d-Nb ₂ C/CNT nanocomposite paper: (A) cycling performance compared to d-Ti ₃ C ₂ /CNT paper at 0.5 C; (B) rate performance. Inset in (B) shows a cross-sectional SEM image of d-Nb ₂ C/CNT paper	517
Figure V - 64: Cyclic voltammetry curves of Mo ₂ TiC ₂ recorded at 2 mVs ⁻¹ . Inset shows the galvanostatic charge-discharge curves (5 cycles) at 0.3C recorded after CV measurements	517
Figure V - 65: (a) MD predicted Young's modulus as a function of a-Al ₂ O ₃ film thickness, (b) Experimentally measured the cycle number vs. thickness and calibrated modulus	521
Figure V - 66: The optimized core-size and coating-thickness region for a Si-core and C-shell structure as a function of SOC.....	521
Figure V - 67: (a) Schematic of the finite element model; (b) Snapshots of the finite element results during 1st cycle and 4th cycle, respectively	521
Figure V - 68: MD simulation of the lithiation process of a SiO ₂ covered Si nanowire structure.....	522
Figure V - 69: (a) Chemical structure of PFM conductive polymer binder. (b) HRTEM of the carbon coated SiO pristine particles. (c) cycling performance of the PFM/SiO half cells at C/10 (200 mA/g). (d) cycling performance of the NMC/SiO full cell with or without prelithiation by SLMP, C/20 for 2 cycles, C/10 for 2 cycles and then C/3.....	525
Figure V - 70: (a) Synthetic scheme and the relative molar ratio of four functional block of polymer binders. (b) The swelling tests of polymer films in the EC/DEC (1/1) electrolyte.....	526
Figure V - 71: (a) Cycling performance of graphite half-cells with different binders, C/25 for 2 cycles, C/10 for 5 cycles and then 1C, with the PMAA-based polymer structure embedded. (b) Peel test results of the graphite electrodes using PMAA-based binders	526
Figure V - 72: Cycling performance of graphite (CGP-G8, ConocoPhillips) half-cells based on polyVC or PVDF binder, using 20% PC, 40% EC, 40% DEC and 1 M LiPF ₆ . The cell was put into formation for two cycles C/25, five cycles C/10 before cycling at 1C	527
Figure V - 73: a) Standard input current cycle during pulse electrodeposition and b) input current cycle for pulse current electrodeposition in the current study.....	530
Figure V - 74: SEM images of electrodeposited Si films at (a) 0Hz, (b) 500Hz, (c) 1000Hz and (d) 5000Hz pulse frequency.....	531
Figure V - 75: Charge capacity of a-Si thin films deposited at 500Hz, 1000Hz and 5000Hz current cycle frequencies for Li/Li ⁺ system	531
Figure V - 76: First cycle irreversible loss and Percentage loss per cycle vs Frequency of electrodeposition for a-Si films for Li/Li ⁺ system	531
Figure V - 77: SEM images of amorphous Si films electrodeposited at 1000Hz a) before cycling; b) after 10 and c) after 50 cycles	532
Figure V - 78: TEM images of the bare electrode (a and b) and coated electrode (d and e); schematics of the bare and coated electrodes during lithiation/delithiation (c and f)	535
Figure V - 79: Chemistry structure of TMA-HQ MLD coating: as-prepared coating (top) and the cross-linked coating after annealing at 200°C in Argon.....	535
Figure V - 80: Significantly improved cycling performance achieved in MLD AIGL and AIHQ coated Si anodes.....	536
Figure V - 81: Rate capability of MLD ALHQ coated electrodes under different annealing conditions	536

Figure V - 82: Morphology of as-received (a) and alucone coated Si nanoparticle (b), featuring a native amorphous oxide layer of ~2 nm in the as-received uncoated particle and ~2 nm alucone MLD coating in coated particle. Morphology of lithiated uncoated Si nanoparticle (d) and lithiated coated Si nanoparticle (e), showing the appearance of Li ₂ O islands only in uncoated Si nanoparticle and continuous lithiated-AlGL coating. (f) EDS with elemental line across the coated Si nanoparticle	537
Figure V - 83: (a) SEM image and (b) cycling performance of the hierarchical silicon-carbon (Si-C) composites	540
Figure V - 84: (a) TEM image, (b) Si, (c) Ti and (d) N EDS mapping, and (e) cycling performance of Si@TiN	541
Figure V - 85: (a) TEM image and (b) cycling performance of PSi/C.....	541
Figure V - 86: (a) Voltage profiles of boron doped Si/SiO ₂ /C at different current densities and (b) charge-discharge curves of the hybrid supercapacitor at different current densities	542
Figure V - 87: Chemical structures of carboxylic acid (CA) and nitrile (SPAEN) containing binders.....	542
Figure V - 88: Capacity fade as a function of cycle number for CA and SPAEN binders	543
Figure V - 89: Suzuki graft synthesis of semiconducting side chains and mechanically robust backbones	543
Figure V - 90: Capacity as a function of cycle number for sulfonated semiconducting binder shown in the previous figure	544
Figure V - 91: Cycling stability of a MSS Si anode with a high areal discharge capacity of ~1.5 mAh/cm ²	546
Figure V - 92: Cycling stability of a MSS Si anode with a high areal discharge capacity of ~2.2 mAh/cm ²	547
Figure V - 93: Cycling stability of a MSS Si anode with a high areal discharge capacity of ~3 mAh/cm ²	547
Figure V - 94: Cycling stability of a MSS Si anode with the electrolyte 1M LiFSI in DME with 10 wt% FEC and 1 wt% VC	548
Figure V - 95: Cycling performance of a modified SBG composite anode.....	549
Figure V - 96: Cycling stability of a porous Si anode obtained from the thermite reaction	549
Figure V - 97: (a) Cycling stability of a Si/B ₄ C/graphite composite anode of ~2.4 mg/cm ² between 0.005–1 V. (b) Cycling stability of the Si/B ₄ C/graphite composite anode of ~2.8 mg/cm ² between 0.005–0.6 V.....	550
Figure V - 98: Schematic of the pomegranate-inspired design. (a) Three dimensional view and (b) simplified two-dimensional cross-section view of one pomegranate microparticle before and after electrochemical cycling (in the lithiated state)	553
Figure V - 99: (a) Reversible delithiation capacity for the first 1000 galvanostatic cycles of Si pomegranate and other structures tested with the same conditions. (b) High areal mass loading test (up to 3.12 mg/cm ² active material) of Si pomegranate anodes. (c) Typical SEM images of Si pomegranates after 100 cycles	554
Figure V - 100: (a) A panicle of ripe rice. (b) SEM images of porous Si structure from rice husk. Inset is lithiation/delithiation capacity of the first 100 galvanostatic cycles. The rate was C/20 for the first cycle, then C/2 for the later cycles.....	555
Figure V - 101: (a) Schematic of the aqueous solution process to fabricate flexible electrodes using Si nanoparticles CNT and PEDOT:PSS. (b) TEM image of the composite film. (c) Cycling stability of a thick Si-PEDOT:PSS-CNT electrode at C/10 rate. Cycling result of a control electrode made by simply mixing Si-PEDOT:PSS with CNT is also presented	556
Figure V - 102: Reduction of VC on a Li ₁₃ Si ₄ (010) surface. (a) VC adsorption starts with electrostatic interaction between the negatively charged carbonyl oxygen of the molecule and Li ⁺ ions on the surface (b) A Cc-Si bond is formed (c) Upon adsorption and transfer of 2 e ⁻ from the surface to the molecule a Cc-Oc bond is broken. The resultant adsorbed species is opened VC ²⁻ . (d) The cleavage of a 2 nd Cc-Oc bond is observed upon transfer of 2 additional e ⁻ to the adsorbed VC anion. Color code: Li is purple, Si yellow, O red, C black, and H white	559
Figure V - 103: Reduction mechanisms of FEC on Li _x Si _y surfaces. Color code for the atoms: light blue: F, red: O, yellow: Si, purple: Li, grey: C, white: H	560
Figure V - 104: Schematic of SEI mesoscopic model. Ionic transport may occur through the blocks and/or through the ion channels separating blocks	561

Table of Contents

Figure V - 105: <i>Ex situ</i> ATR-FTIR spectra of Si (100) p-type doped wafer and for Si nanoparticles after 3 CV cycles with 0.1mV/s scan rate (2V-0.01V vs. Li/Li ⁺) and rinsing with DMC to remove residual electrolyte	565
Figure V - 106: (left) ATR geometry of the <i>in situ</i> IR spectroelectrochemical cell using a patterned Si microstructure shown at left (10 micron feature size)	565
Figure V - 107: First cycle galvanostatic curve comparison between Si (100) wafer and 10 µm array on Si (100) wafer; <i>ex situ</i> FTIR spectra of Si (100) wafer and 10 µm array samples after 5 cycles with 5µAcm ⁻² charging rate	566
Figure V - 108: First cycle irreversible loss vs. Si-CVD deposition	568
Figure V - 109: Variation of gravimetric specific capacity vs. cycle number of h-SiNT (15min deposition time).....	569
Figure V - 110: SEM images of h-SiNTs electrodes a) as prepared, b) after lithiation, c) after delithiation, d) before cycling, and e) after 500 cycles	569
Figure V - 111: Specific charge/discharge capacity and coulombic efficiency vs. charge/discharge cycles of carbon coated h-SiNTs (black) and solution treated carbon coated h-SiNTs (violet) electrodes in Li/Li ⁺ battery	570
Figure V - 112: ¹ H-NMR spectra of (a) PVDF before and after cycling; (b) PGG before and after cycling, for 111 cycles in DMSO-d ₆ . Black spectra indicates before cycling and red spectra indicates after cycling. Black arrow indicates the absence of the characteristic peak in PVDF	571
Figure V - 113: (a) Schematic diagrams showing Si NPs react with melted Li to form Li _x Si NPs. A dense passivation layer is formed on the Li _x Si NPs after exposure to trace amounts of oxygen, preventing the Li _x Si alloy from further oxidation in dry air. As-synthesized Li _x Si-Li ₂ O core-shell NPs, compatible with the existing battery manufacturing environment, can be mixed with various anode materials during slurry processing and serve as an excellent prelithiation reagent. (b) STEM image of Li _x Si-Li ₂ O core-shell NPs. (c) Galvanostatic discharge/charge profiles of Li _x Si-Li ₂ O NPs in 1 st and 2 nd cycles	574
Figure V - 114: Discharge capacity vs. cycle number plots and cycling efficiency of Si electrodes	577
Figure V - 115: FT-IR spectra for Si anode before and after 53 cycles	578
Figure V - 116: (a) General synthetic schemes of fluorinated carbonates, (b) structures of the synthesized fluorinated carbonate solvents, and (c) structures of the synthesized fluorinated additives	582
Figure V - 117: Leakage current from the electrochemical floating tests of EC, TFPC, FEC and TFE-PC-E with F-EMC at (a) RT, (b) 55°C; (c) EMC, DMC, F-DEC and (d) F-EPE, F-EEC, F-MiPC with FEC compared with F-EMC/FEC at RT	583
Figure V - 118: Cycle performance of LNMO/A12 cells with cutoff voltage of 3.5-4.9 V at C/3 with (a) HVE 1 electrolyte compared to Gen 2 electrolyte at 55°C, (b) HVE 2 electrolyte compared to Gen 2 electrolyte at RT, (c) HVE 3 electrolyte at RT, and (d) cell self-discharge test at 55°C	584
Figure V - 119: SEM image of (a) a pristine graphite anode and harvested graphite anode from (b) a Gen 2 cell, and (c) a HVE 1 cell; (d) pristine LNMO cathode and harvested LNMO cathode from (e) a Gen 2 cell, and (f) a HVE 1 cell. (100 cycles at 3.5–4.9 V, C/3 and 55°C)	585
Figure V - 120: TEM image of harvested LNMO cathode cycled at 55°C for 20 cycles with (a) Gen 2 electrolyte, (b) HVE 1 electrolyte without additive, and (c) HVE 1 electrolyte with 1% LiDFOB	585
Figure V - 121: Room Temperature C-rate cycling comparison of hydrocarbon (black) vs. fluorocarbon/hydrocarbon (red) electrolyte	588
Figure V - 122: Energy comparison of commercial NMC/graphite cells containing fluorocarbon vs hydrocarbon electrolyte at variable voltage (4.2-4.5 V).....	589
Figure V - 123: Representative property map for FEC/EMC/F-solvent for room temperature conductivity	590
Figure V - 124: Representative additive of property maps to optimize solvent composition of electrolyte	590
Figure V - 125: Comparison of first charge (film formation) curves of FEC, A9 (cyclic fluorocarbonate), VC.....	591
Figure V - 126: Comparison of first charge (film formation) curves of FEC at different FEC concentrations.....	591
Figure V - 127: Comparison of first charge (film formation) at 25, 45, 60, 80 C for several electrolyte compositions	592
Figure V - 128: Cycle behavior of batteries with various electrolytes formed at 80 C (inset shows electrolytes exposed to 60 C and 85 C showing decomposition of electrolyte containing FEC).....	592
Figure V - 129: Category 2 additives improve cycle life in EC/EMC formulations	595
Figure V - 130: Category 3 additives improve cycle life in PC/EMC formulations	595

Figure V - 131: Several HD solvents/EMC blends with single additives perform similarly to baseline EC/EMC electrolyte	596
Figure V - 132: Promising HD solvents/EMC formulations show similar capacity and cycle life to control EC/EMC electrolyte	596
Figure V - 133: Promising non-carbonate HD solvent/LV solvent combinations perform similar to the EC/EMC control.....	597
Figure V - 134: Cycle life of selected non-carbonate electrolyte formulations relative to EC/EMC control.....	597
Figure V - 135: Measurement apparatus for electronic conductivity measurements. The probe wafer is clamped in an inverted orientation to an aluminum block that descends upon the electrode target. Electrical connections are made to the exposed connection pads. The electrode film target is mounted on a disc that is attached to a force gauge to measure and allow the control of the applied pressure.....	599
Figure V - 136: Analysis of Toda 523. (a) Conductivity (with 95% confidence intervals based on repeated sampling) of multiple locations on a 3 mm x 3mm grid (shown on inset). (b) Resulting conductivity map, showing significant spatial variability of the sample electrode compared to probe variability. (c) FIB/SEM cross-section of material used for structure analysis	600
Figure V - 137: Cycle life at C/6 of Li/EC-DEC-1MLiPF ₆ /Si-nano cell at 40% DoD	603
Figure V - 138: Discharge/charge curves at C/6 of Li/EC-DEC-LiPF ₆ /Si-nano cells for cycle 1 and 66 at different %DoD	604
Figure V - 139: Voltage profiles of at C/6 of Li/EC-DEC-LiPF ₆ /Si-nano as function of cycle life.....	604
Figure V - 140: 1 st discharge/charge curves at C/24 of Li/EC-DEC-LiPF ₆ /Si-nano cells with positions where the impedance measurement were taken	605
Figure V - 141: Impedance spectra of Li/EC-DEC-LiPF ₆ /Si-nano cells at different states of discharge or charge	605
Figure V - 142: Slurry and electrode of Si-nano; a) after mixing, b) after 8 hours relaxing for degassing. SEM cross-section of cathode (c) and anode (d) used in 21Ah stacking cells	606
Figure V - 143: Charge/discharge curves of Si-nano/Li/EC-DEC-FEC-LiPF ₆ /LMNO stacking cell (21Ah) between 4.9V and 3.5V at RT	606
Figure V - 144: Illustration of a Mn migration path in Li _x MnO ₃ . Inset shows the Mn4+ activation energy as a function of path coordinate for migrating through the oxygen edge accompanied by a dramatic local oxygen bond stretching.....	609
Figure V - 145: The lowest oxygen formation enthalpy as a function of charge state in Li _x MnO ₃ . Inset illustrates one possible vacancy in the lattice (white circle).....	611
Figure V - 146: Voltage profiles of Li _x MnO ₃ for the first charge (blue lines) and the discharge process (red lines) assuming a structural transformation, originating from Mn migration.....	611
Figure V - 147: LiFePO ₄ half-cell cycled at C/2 with an electrolyte of 1 M LiFePO ₄ in EC:DEC 1:2	614
Figure V - 148: Similar cell as cycled in Figure V - 147 but charged at C/10 and discharged at C/1	614
Figure V - 149: Cycling data of an LFP electrode with increased binder content to eliminate cracking	615
Figure V - 150: Charge, discharge, and coulombic efficiency of the cycling data of an NCM half-cell cycled at difference C-rates.....	615
Figure V - 151: Charge and discharge capacities and the coulombic efficiency of a Graphite/LFP cell at different C-rates	616
Figure V - 152: Charge and discharge capacities and coulombic efficiency of a Si/LFP cell cycled at different C-rates	616
Figure V - 153: (a) XRD pattern of Li _{1.21} Mo _{0.467} Cr _{0.3} O ₂ (LMCO) before and after 1, 2, and 10 cycles. (b) Scanning transmission electron microscopy images of LMCO particles before and after 1 and 10 cycles. (c) The voltage profile of carbon-coated LMCO. The figure has been reproduced from Ref. [1].....	618
Figure V - 154: The c- and a-lattice parameter in disordered-LMCO upon delithiation	619
Figure V - 155: (a). Li migration between two octahedral sites via a tetrahedral activated state. (b.-c.) The three different diffusion channel types that occur in cation-disordered Li metal oxides. The figure has been reproduced from Ref. [1]	619

Table of Contents

Figure V - 156: 0-TM percolation and accessible Li contents as function of the composition and the degree of disorder (cation mixing) in layered Li transition metal oxides ($\text{Li}_x\text{TM}_{2-x}\text{O}_2$). The figure visualizes the results of Monte-Carlo percolation simulations, which has been reproduced from Ref. [1]	620
Figure V - 157: Critical Li concentrations in the most common LiMO_2 crystal phases [2]. The gray region indicates the percolation threshold for 1-TM diffusion (only active in the layered structure), the black region indicates 0-TM percolation, and the hatched region represents the Li content at which 1 Li atom per formula unit becomes 0-TM accessible.....	620
Figure V - 158: (a) 0-TM percolation thresholds and (b)-(d) 0-TM accessible Li content in different LiMO_2 crystal phases as function of Li content and degree of cation mixing (0% = ordered, 100% = cation-disordered) [2]. The thick and thin black lines in panels (b)-(d) indicate the percolation thresholds and the Li content at which 1 Li atom per formula unit is 0-TM accessible, respectively	621
Figure V - 159: Calculated ground state hull for Na_xMnO_2 , including predicted superstructure at $x = 0.625$	621
Figure V - 160: $\text{Na}_{5/8}\text{MnO}_2$ superstructure with vacancy (V_{Na}) ordering, Mn charge and magnetic stripe orderings.	622
Figure V - 161: NCA freeze-cast electrode with 20 mAh/cm ² capacity at C/50 rate	624
Figure V - 162: (a) Dependence of lamellae thickness on cooling rate in the freeze casting process, (b), (c) and (d) SEM micrograph of freeze casted-sintered NCA at three different cooling rates.....	625
Figure V - 163: Voltage vs. capacity of directionally-solidified and sintered NCA electrode of 330 μm thickness, with discharge capacity plotted as area capacity (mAh/cm ²).....	625
Figure V - 164: (a) Voltage vs. time for hybrid pulse power characterization (HPPC) test, (b) Area specific discharge capacity of the freeze-cast and sintered NCA electrode of 300 μm thickness during HPPC test, and (c) Voltage vs. time for hybrid pulse power characterization (HPPC) test of NCA electrode of 300 μm thickness	626
Figure V - 165: Experimental I-V curves for a Li-Li symmetric cell with and without SIC for 0.5M LiPF_6 in EC:DEC (1:1). Also shown are model predictions (solid line) for a Li-Li symmetric cell with SIC (without polarization loss)	628
Figure V - 166: Polarization loss for different concentrations of LiPF_6 in various solvents: ethylene carbonate: diethyl carbonate [EC/DEC(1:1)], dimethyl sulfoxide (DMSO), propylene carbonate (PC)	628
Figure V - 167: Specific energy densities of Li-S batteries with different designs, at a range of C-rates: 0.5 mg/cm ² sulfur loading in batteries without a SIC, 0.5 mg/cm ² loading in batteries with a SIC, and 3 mg/cm ² loading of batteries with a SIC	629
Figure V - 168: Mn K-edge XANES (top) and EXAFS (bottom) data for the samples listed in the Table V - 8	631
Figure V - 169: Ni K-edge XANES (top) and EXAFS (bottom) of the samples listed in Table V - 8	632
Figure V - 170: (a) First-shell, Mn-M Coordination numbers, (b) Mn-M bond distances, and (c) Mn-O bond distances as a function of Li to TM ratios, determined by ICP analysis for the samples listed in Table V - 8.....	632
Figure V - 171: (a) First-shell, Ni-M Coordination numbers, (b) Ni-M bond distances, and (c) Ni-O bond distances as a function of Li to TM ratios, determined by ICP analysis, for the samples listed in Table V - 8	633
Figure V - 172: HR-XRD of the samples listed in Table V - 8	633
Figure V - 173: Electrochemical performance, (a) and (b), of $0.5\text{Li}_2\text{MnO}_3 \bullet 0.5\text{LiMn}_{0.5}\text{Ni}_{0.5}\text{O}_2$ cathodes synthesized via natural $\text{Ni} \rightarrow \text{NiO} \rightarrow \text{Ni}(\text{NO}_3)_2 \rightarrow$ ion-exchange with Li_2MnO_3 . (c) Mn K-edge XANES of $0.5\text{Li}_2\text{MnO}_3 \bullet 0.5\text{LiMn}_{0.5}\text{Ni}_{0.5}\text{O}_2$ with increasing integration of a $\text{LiMn}_{1.5}\text{Ni}_{0.5}\text{O}_4$ spinel component.....	634
Figure V - 174: (a) The first charging curve of $\text{Li}_{1.2}\text{Ni}_{0.15}\text{Co}_{0.1}\text{Mn}_{0.55}\text{O}_2$ during <i>in situ</i> XAS experiment (under constant current), selected XAS scan numbers are marked on the charge curves; (b) Normalized XANES spectra and (c) Magnitude of Fourier transformed Mn, Co and Ni K-edge spectra collected during initial charge. Inset is the schematic view of the coordination environment around transition metal ions	636
Figure V - 175: EXAFS spectra of $\text{Li}_{1.2}\text{Ni}_{0.15}\text{Co}_{0.1}\text{Mn}_{0.55}\text{O}_2$ during constant voltage charging at 5V. Ni, Co, Mn reacted simultaneously using time-resolved XAS technique. Projection view of corresponding Ni-O, Co-O, Mn-O peak magnitudes of the Fourier transformed K-edge spectra as functions of charging time	637
Figure V - 176: <i>In situ</i> XRD spectra for Fe-substituted $\text{LiNi}_{1/3}\text{Fe}_{1/3}\text{Mn}_{4/3}\text{O}_4$ high voltage spinel sample during charge-discharge cycle between 3.6 V to 5.0V	638
Figure V - 177: <i>In situ</i> (a) Fe (b) Mn and (c) Ni K-edge XANES spectra of fully charged $\text{LiNi}_{1/3}\text{Mn}_{4/3}\text{Fe}_{1/3}\text{O}_4$ during heating up to 475°C. (d) illustration of Fe migration to the tetrahedral sites	638

Figure V - 178: Normalized nickel and manganese K-edge transmission XANES spectra of the cycled graphite electrode compared with references	642
Figure V - 179: A) I-V polarization plots,, B) FTIR spectra, C) SEM images, D) EDX and E) XPS analysis of the SEI layer on the Si (100) electrode in 1 M LiPF ₆ , EC/DEC (3:7), electrolyte with VC or FEC additives.....	643
Figure V - 180: a) Double fs-pulse LIBS scheme used for analysis of SEI layers in liquid electrolytes. b) Signal enhancement of Si (100) in 1M LiPF ₆ EC/DEC electrolyte with the double-pulse configuration. c) Comparison of double fs-pulse LIBS signals of Si and SEI on Si in the same electrolyte	643
Figure V - 181: Schematic drawing showing the setup of the liquid cell battery	646
Figure V - 182: Schematics of surface reactions and cycle behaviors of silicon nanoparticles with native oxide layer and artificial coating layer.....	646
Figure V - 183: (a-d) Low magnification STEM-HAADF images to show cycling induced corrosion. Cracks and pits are highlighted by red arrows. (002) surface planes show strong resistance to corrosion. (e-h) [010] zone axis SAED patterns. Extra diffraction spots appeared in cycled samples, which are highlighted by red and blue circles. Red circles indicated the formation of ordered structure. (10-1) ordered plane is clearly seen after cycling. Blue circles come from double diffraction. (i-l) High resolution STEM-HAADF images to show the cycling induced structure change on particle surfaces. Pristine samples (i) shows homogeneous structure from surface to bulk. Dashed lines in (j, k) highlight the thickness of the SRL. In (l), the whole areas were transformed. (m) [101] zone axis STEM-HAADF image and its fast Fourier transformation image. The white arrows indicate the ordered features of (20-2) planes and extra diffraction spots. (n) [010] zone axis STEM-HAADF image to show spinel structure and I41 structure in a 45 cycled sample.....	647
Figure V - 184: Approx. 60 nm Si wires grown on a carbon fiber support	650
Figure V - 185: Galvanostatic (a, b) and SPECS with 50 mV steps (c, d) cycling of Si nanowires. The formation of small Si clusters (P1 resonance) and the overlithiated crystalline phase Li _{15+x} Si (P3) are clearly seen by ⁷ Li NMR. If all the amorphous phase is converted to Li ₁₅ Si (c and d) then the system takes a different path on charge, Li ₁₅ Si reacting to form a low Li content amorphous Si phase (P1 is largely absent)	650
Figure V - 186: Molecules used for Si nanoparticle coating.....	651
Figure V - 187: TEM results of the Si particles before (left) and after (right) Si-TEOOS coating	651
Figure V - 188: Cycling experiments performed with and without the APTES coating	652
Figure V - 189: NMR spectra obtained after 1 charge discharge cycle (right) of a Si:superP carbon electrode (1:1 Si:C ratio by mass). Electrolyte = EC/DMC. Galvanostatic cycling was performed at a rate of C/75 based on a theoretical capacity of 3579 mAhg ⁻¹	652
Figure V - 190: Top: The <i>in situ</i> ⁷ Li NMR signal overlaid on the electrochemical discharge curve for a Li-S bag cell discharged galvanostatically at a rate corresponding to C/20, using a 1 M LiTFSI in DOL/DME electrolyte. A spectrum is recorded every 15 mins. The cell is held at open circuit for 15 min before discharge. The Li metal resonance at ca. +250 ppm is not shown. Bottom: (a) Discharge profile of the same Li-S bag cell. The spectra were fit using three components (two liquid (high and low frequency) and one solid) to extract the changes in (b) chemical shift and (c) integrated intensities as a function of discharge.....	653
Figure V - 191: Charge and discharge capacity and coulombic efficiency vs. cycle number of a pouch cell with graphite/NCM cycled to 4.2 V.....	655
Figure V - 192: The average voltage on charge and on discharge plotted vs. cycle number for a Graphite/NCM pouch cell	655
Figure V - 193: The amount of Mn found at the anode in a NCM half-cell was converted to the amount lost from the cathode while held for two weeks at different voltages	655
Figure V - 194: Nyquist plot of the electrochemical impedance spectroscopy of a Graphite/LiNi _{1/2} Mn _{3/2} O ₄ cell at cycle 1 and cycle 3	656
Figure V - 195: Voltage vs. capacity superimposed on each other where charge is in the positive direction and discharge in the negative direction.....	657
Figure V - 196: Charge (blue diamonds) and discharge (red squares) endpoints vs. time of cycling.....	657

Table of Contents

Figure V - 197: Cycle performance of lithium cells with (a) Se-, (b) SeS ₂ -, and (c) SeS ₇ -carbon composite cathodes in ether-based electrolyte, and voltage profile of Li/Se cell (d)	660
Figure V - 198: HEXRD patterns of Li/Se cell in ether-based electrolyte during the first cycle (a, c) with voltage profile in (b); HEXRD patterns of Li/SeS ₂ cell in the first cycle (d, f) with voltage profile in (e)	660
Figure V - 199: (a) Normalized Se XANES spectra of standard Se and Li ₂ Se, (b) normalized XANES spectra of Li/Se cell during cycling, (c) battery voltage profile, (d) derivative of normalized XANES spectra of Li/Se cell during cycling, and (e) representation of cathode phase evolution during charge and discharge of a Li/Se cell in an ether-based electrolyte.....	661
Figure V - 200: SEM images of discharge products (for (a) Ag ₃ , (b) Ag ₉ , and (c) Ag ₁₅ -based cathodes materials and (d) XRD patterns for the three discharge products from the three cathode materials	665
Figure V - 201: Illustration of two discharge reaction mechanisms based on an initial oxygen reduction at an active site followed by solution phase reactions and growth at a surface nucleation site. Mechanism I involves fast oxygen reduction and formation of a LiO ₂ supersaturated solution, while mechanism II involves slow oxygen reduction and formation of a lithium peroxide supersaturate solution. Growth and nucleation occurs via these supersaturated solutions	665
Figure V - 202: Discharge/charge curves of AC with different discharge current density and the same charge current density	666
Figure V - 203: Raman spectrum of the discharged AC cathode surface showing graphite D (1330 cm ⁻¹), and LiO ₂ -like bands (1123 cm ⁻¹ red trace). Raman spectrum of a similar AC cathode that was discharged and charged back to 3.5 V does not show the LiO ₂ -like band (blue trace).....	666
Figure V - 204: The morphologies of toroids at the same discharge capacity of 1000 mAh/g with different current densities of (a, b) 0.2, (c, d) 0.1 and (e, f) 0.05 mA/cm ²	666
Figure V - 205: Raman spectra of the toroids on the surface of the discharged AC cathode with different current densities of (a) 0.2, (b) 0.1 and (c) 0.05 mA/cm ² . XRD patterns of the discharge AC cathode at the same discharge capacity of 1000 mAh/g with different current densities of (d) 0.2, (e) 0.1 and (f) 0.05 mA/cm ²	666
Figure V - 206: Comparison of the computed B3LYP/6-31G** IR spectra with the experimental FTIR spectra from after the first discharge of the Li-O ₂ cell. The (*) represents the dominant IR peak of lithium oxalate, the (**) indicates the dominant IR peaks of LiBOB, whereas the (Δ) represents the IR signatures of –CH ₃ - and –CH ₂ - groups in the solvent been used	667
Figure V - 207: Impedance of composites assembled in coin cells using a standard (black) and liquid-free (red) glove box. Data were recorded just after assembly and after 3 weeks.....	670
Figure V - 208: Change in conductivity of samples sealed in coin cells. Samples differ in ceramic loading and PEO molecular weight. Some jogs are due to temperature scans	671
Figure V - 209: Conductivity of composites with 50v% Ohara ceramic powder assembled into coin cell in standard glove box (green) and liquid-free glove box (red), compared to pure ceramic and polymer electrolytes (black).....	671
Figure V - 210 Conductivity of composite and polymer electrolytes treated in DMC. Composite is 50v% Ohara ceramic.....	671
Figure V - 211: Long-term cycling performance of Li LFP (a), Li NCA (b) and Li NCM (c) cells with three different electrolytes at C/5 charging and 1C discharging at room temperature	674
Figure V - 212: Surface (a,c,e) and cross-section (b,d,f) SEM images of Li metal anodes in Li LFP cells with three different electrolytes after 150 cycles at C/2 (1.20 mA/cm ²) charging and 1C (2.40 mA/cm ²) discharging. The electrolytes are (a,b) E004; (c,d) X1; and (e,f) X1Cs	675
Figure V - 213: The a.c. impedance spectra of Li LFP coin cells at the discharged state after different cycles. The samples were first charged/discharged at C/10 rate for two cycles, then charged at C/1.5 rate (1.60 mA/cm ²) and discharged at 1C rate (2.40 mA/cm ²) for 200 cycles	676
Figure V - 214: Battery performance of graphite NCA full cells in terms of cycling stability at RT (a) and 60°C (c) and rate capability at RT (d), and discharge voltage profiles of Li graphite cells (b)	676
Figure V - 215: a) Areal specific capacity delivered from sulfur electrodes with different sulfur loadings. b) Rate capability of thick sulfur electrode with 3.5 mg/cm ² loading. 1C=1000 mAh/g (PNNL unpublished results)	679

Figure V - 216: SEM images of lithium metal anode on the a) surface and b) cross-section view and EDS mapping after 100 cycles in Li-S cells comprised of thick sulfur cathode (3.5 mg/cm ²). c) showed the long-term cycling of Li-S cell. (PNNL unpublished results).....	680
Figure V - 217: a) EPR cell design for <i>in situ</i> testing and capturing of radical resonance signals generated throughout the operation of Li-S batteries. b) 3D plot of <i>in situ</i> EPR spectra in a functioning Li-S EPR cell vs. time during CV scan. c) The concentration evolution of sulfur radicals at different time (potentials). d) The 2nd and 3rd CV curves collected concurrently from Li-S EPR cell. Both c) and d) started from the second cycle due to wetting issues. (PNNL unpublished results).....	680
Figure V - 218: Proposed reaction mechanism for Li-S batteries during cycling. The equilibria between S ₆ ²⁻ and S ₃ ^{*-} always existed and shifted at different potentials. S ₆ ²⁻ preferred to stay at relatively high potential (> 2.1 V) while S ₃ ^{*-} was the preferred form at low potential (\leq 2.1 V). Different reaction pathways were suggested for discharge and charge processes. The Li-S cell was tested at C/5 rate between 1 V and 3 V in typical button cells.....	681
Figure V - 219: SEM images of discharged CNTs/Ru electrodes after a) 1 st , b) 5 th , and c) 50 th cycles in the LiTf-tetraglyme electrolyte	684
Figure V - 220: SEM images of charged CNTs/Ru electrodes after a) 1 st , b) 5 th , and c) 50 th cycles in the LiTf-tetraglyme electrolyte	684
Figure V - 221: <i>In situ</i> mass spectroscopic analysis of O ₂ and CO ₂ evolved during charging of the batteries with CNTs/Ru electrode and LiTf-tetraglyme electrolyte at a) 1 st , b) 5 th , and c) 50 th cycles	684
Figure V - 222: Cycling voltammetry (100 mV s ⁻¹) on flat a) glassy carbon and b) Ru electrodes recorded in a LiClO ₄ -DMSO electrolyte bubbled with oxygen	685
Figure V - 223: Cycling Performance of Li-O ₂ Batteries with CNT/Ru electrodes in the LiClO ₄ -DMSO Electrolyte. Capacity limited (1,000 mAh g ⁻¹) cycling was conducted at 80% of the total discharge capacity	686
Figure V - 224: Cycling performance of a Li-O ₂ battery with the electrolyte of 75 wt% LiTFSI in acetonitrile.....	686
Figure V - 225: Sulfur K-edge XAS of Li ₂ S: experimental (black) and theoretical (green – static crystal; gold – 298K)	689
Figure V - 226: Calculated sulfur K-edge XAS of Li ₂ S _x (2 \leq x \leq 8) dissolved in TEGDME.....	690
Figure V - 227: Comparison of peak intensity and area ratios.....	690
Figure V - 228: Calculated sulfur K-edge XAS of S ₃ ²⁻ and S ₃ ^{*-} . Unique radical feature highlighted by arrow	690
Figure V - 229: Effect of LiNO ₃ on Li ₂ S _x , x = 8 X-ray spectrum, where 'r' denotes the ratio of total lithium ions per ethylene oxide monomer	691
Figure V - 230: Modified Li-S pouch cell for <i>in situ</i> XAS experiments.....	691
Figure V - 231: First discharge curve for Li-S cell shown in Figure V - 230.....	691
Figure V - 232: ⁷ Li and ²⁷ Al MAS NMR spectra of LLZT and H-LLZT at room temperature, the line shape of ⁷ Li is fit as a sum of broad and narrow components associated with slow and fast Li-ion domains	694
Figure V - 233: Crosslinked polymer membranes with double vinyl sulfone, double vinyl ester, and perfluorohexane units (from the top)	695
Figure V - 234: ESR signal for the carbon electrode during reduction and oxidation (2 μ A) in a 0.1 M Bu4NBF4 DMSO electrolyte saturated O ₂ (a) before polarization; (b) after reducing for 1000 sec; (c) after reducing for 4800 sec (accumulated); (d) after oxidizing for 1000 sec; (e) after oxidizing for 2000 sec; (f) after re-reducing for 2000 sec.....	697
Figure V - 235: (left) Cyclic voltammograms at 300 mV/sec in 1 M TEABF4 PC electrolyte saturated with O ₂ on a glassy carbon disc electrode, (right) Cyclic voltammograms in 1 M TEABF4 acetonitrile electrolyte (solid line) and 1 M TEABF4 acetonitrile electrolyte containing 40mM TPFPB (dash line) on the same glass disc electrode at 300 mAs ⁻¹ scan rate. The glassy carbon electrode area 0.07 cm ² ; Counter electrode: Pt-mesh; Ag/AgCl as reference electrode.....	698

Table of Contents

Figure V - 236: Left: (a) ESR spectra of O ₂ - in DMSO taken at different times after the addition of TPFPB. Mole ratio of TPFPB and O ₂ - was approximately 1:1. Right: ESR spectra of O ₂ - in DMSO taken at different times after adding PC. Mole ratio of O ₂ - and PC was 1:1	698
Figure V - 237: The evolution of XRD patterns during <i>in situ</i> chemical sodiation of nano-sized (44nm) Li ₄ Ti ₅ O ₁₂ :	
(a) Schematic of the <i>in situ</i> chemical sodiation experiment setup by using a quartz capillary. 1M Na: 1M biphenyl /L 1,2-dimethoxyethane (DME) solution was used as reducing agent; (b) capillaries before (left) and after (right) <i>in situ</i> sodiation; (c) XRD pattern for the Li ₄ Ti ₅ O ₁₂ at the beginning of reaction; (d) contour plot of peak intensities as a function of reaction time; (e) XRD pattern for the final sodiated Li ₄ Ti ₅ O ₁₂ at the end of reaction	701
Figure V - 238: (a) Experimental/calculated Ti K-edge XANES spectra; (b) enlarged view of the XANES pre-edge region as marked by rectangle in panel a; (c) Ti valences of the Li ₄ Ti ₅ O ₁₂ , Li ₇ Ti ₅ O ₁₂ and sodiated Li ₄ Ti ₅ O ₁₂ estimated by comparing with standard titanium oxides; (d) crystal structure of Li ₄ Ti ₅ O ₁₂ and Na ₆ (Li ₆)Li ₇ Ti ₅ O ₁₂ ; and (e) experimental EXAFS spectra of Li ₄ Ti ₅ O ₁₂ , Li ₇ Ti ₅ O ₁₂ (lithiated Li ₄ Ti ₅ O ₁₂), and fully sodiated Li ₄ Ti ₅ O ₁₂ (Li ₇ Ti ₅ O ₁₂ and Na ₆ Li ₇ Ti ₅ O ₁₂ in 1:1 ratio).....	702
Figure V - 239: <i>In situ</i> X-ray diffraction patterns collected during the first charge (up to 3.6 V at C/12 rate) for a NaCrO ₂ /Na cell. Corresponding voltage-composition profile is given on the right of XRD patterns. Oxygen stacking of O ₃ and P ₃ structure is given on the right.....	703
Figure V - 240: (a) Cr K-edge XANES spectra of pristine (x = 0), half charged (x = 0.25), fully charged (x = 0.5) Na _{1-x} CrO ₂ and CrO _x references (Cr ₂ O ₃ , CrO ₂ and CrO ₃); (b) Least-square fits of calculated FT-EXAFS phase and amplitude functions (solid red lines) to the experimental EXAFS spectra (solid and open circles) for pristine (x = 0), half charged (x = 0.25) and fully charged (x = 0.5) Na _{1-x} CrO ₂ . Phase shift was not corrected in the FT magnitude of EXAFS spectra.....	703
Figure V - 241: Schematic illustration of the fabrication process of conductive polymer-coated hollow sulfur nanospheres. RT, room temperature (upper); Cycling performances of the cells made from hollow sulfur nanospheres with PANI, PPY and PEDOT coatings of at C/2 rate for 500 cycles (lower).....	706
Figure V - 242: Schematics and SEM characterizations of the reduced TiO ₂ inverse opal structure before (upper) and after sulfur infusion (lower)	706
Figure V - 243: (a) Cycling performance of the cathodes with different titanium oxides for 100 cycles at C/10. (b) DFT analysis of the adsorption of S species on Ti ₄ O ₇ (1-20) surface. Legend: gray, Ti; pink, O; yellow, S; purple, Li.....	707
Figure V - 244: (a) Schematic Li-S battery model with the conductive surface design of the separator. (b) and (c) Photographs of the pristine separator and the Super P coated separator, respectively.(d) The cycling stability comparison of the Li-S battery (~60 wt% sulfur in the cathode) with different separators at C/10.....	707

List of Tables

Table I - 1: Major Li-ion technology technical challenges and potential pathways to address them.....	3
Table II - 1: Summary of USABC performance targets for EV batteries	12
Table II - 2: Summary of USABC performance targets for PHEV batteries	13
Table II - 3: Summary of USABC performance targets for 12V Start/Stop Vehicle Applications	14
Table II - 4: Version Metrics and Performance	21
Table II - 5: Electrode Design Parameters by Version	23
Table II - 6: 2014 Gap Analysis (note: Selling Price target in the program Statement of Work was \$920).....	37
Table II - 7: SAFT Gap Analysis	41
Table II - 8: Summary of abuse test results of LMO free E400.....	49
Table II - 9: In plant - processable high loading electrode study for high energy cell design.....	64
Table II - 10: SiNANOde Cell Self discharge	66

Table II - 11: Thermal System List	84
Table II - 12: 3Ah / 15Ah Integrated Cell Design	88
Table II - 13: Porosity and Average Pore Size of Dry Electrode	90
Table II - 14: Final Formulation DOE for Aqueous Binder	92
Table II - 15: Anode parameters for 3 mAh/cm ² half-cell capacity including 3DCuSnFe/Graphite material with 20% thickness reduction vs. Graphite anodes (artificial and natural)	101
Table II - 16: Single layer pouch cells (SLP) made with 3D structure CuSnFe/Graphite electrode. Eighteen cells have been shipped to INL for testing according to USABC PHEV manual.....	102
Table II - 17: ICL reduction through anode optimization.....	110
Table III - 1: Distribution of product cost for flexible plant producing LMO-G batteries.....	119
Table III - 2: Stages of development of a flexible plant with increases in production volume, types of batteries, and plant utilization	119
Table III - 3. High volume cost of lithium ion battery materials	120
Table III - 4: Comparison of element values to cathode price.....	135
Table III - 5: Summary List of Tested Batteries.....	140
Table III - 6: Testing activities under the USABC Program.....	144
Table III - 7: Testing activities under the Benchmark Program.....	144
Table III - 8: Testing activities under the FOA-2011 Program.....	145
Table III - 9: Testing activities under the FOA-ARRA Program.....	145
Table III - 10: Anticipated testing activities for FY15.....	145
Table III - 11: Testing activities under the ABR Program	145
Table III - 12: Comparison of model input file lists to run a standalone PDM, EDM and CDM	163
Table IV - 1: Averaged delithiation (charge) capacity for various cycling rates for the A-A006 electrode vs. Li metal. Testing performed at various C-rates ranging from C/24 to 2C using a 1.5V to 0.050V voltage window for 3 cycles at each rate	221
Table IV - 2: Summary of differences between Baseline, Initial, and Reformulated-1 silicon-graphite vs. NCM 523 in xx3450 Pouch Cell Builds. Capacity (mAh/cm ²) range based on cycle rate data	224
Table IV - 3: Positive and Negative Electrode Content.....	226
Table IV - 4: Full cell cycling protocol	226
Table IV - 5: Comparison of electrode areas and electrolyte volumes in different cell formats	229
Table IV - 6: Comparison of electrolyte additive amount to electrode area in different cell formats	229
Table IV - 7: Full-cell cycling protocol for rate effect test	232
Table IV - 8: The composition of silicon alloy electrode from 3M.....	242
Table IV - 9: Average voltage, discharge capacity and energy density of NCM523 with various voltage windows at C/10 rate	243
Table IV - 10: Electrode chemistry and formulation for baseline and modified cells.....	259
Table IV - 11: Cycling conditions and specific capacities for selected layered oxides.....	260
Table IV - 12: Refined crystallographic parameters for HE5050 with combined monoclinic Li ₂ MnO ₃ and trigonal LiMO ₂ (M=Co, Ni, Mn) unit cells	304
Table IV - 13: Cathode compositions used in this work	320
Table IV - 14: Relative change in average voltage in baseline cells and in cells containing an electrolyte additive or a coated cathode	323
Table IV - 15: Group numbers and compositions for this study.....	324
Table IV - 16: Found compositions and phase distribution of materials made for this study	325
Table IV - 17: Elemental analysis of cation-substituted Li _{1.2} Ni _{0.15} Mn _{0.55} Co _{0.1} O ₂	330

Table of Contents

Table IV - 18: Specific capacity at the 2 nd and 20 th cycle number and percent retention.....	332
Table IV - 19: Metals-only composition of materials prepared in this study	339
Table IV - 20: Dependence of charge and discharge capacity on pO ₂ , lithium content and cooling method	342
Table IV - 21: Battery performance based on baseline chemistry determined by BatPAC model.....	374
Table IV - 22: Cathode Energy Factor comparison of different cathodes when matched to graphite or a Si composite.....	380
Table IV - 23: Si alloy anodes developed with DOE support.....	380
Table IV - 24: Summary of hydroxide cathode synthesis.....	416
Table IV - 25: Summary of carbonate precursor synthesis.....	417
Table IV - 26: Summary of carbonate cathode synthesis	418
Table IV - 27: Comparison of bench-scale oxalate, preliminary carbonate and hydroxide cathodes	419
Table IV - 28: Comparison of bench-scale oxalate, preliminary carbonate and hydroxide cathodes	420
Table IV - 29: Milestones and due dates for Li-TDI (electrolyte salt)	425
Table IV - 30: Milestones and due dates for LBNL-PEFM (binder for Si electrode)	426
Table IV - 31: Milestones and due dates for LBNL-PFM (binder for Si electrode).....	426
Table IV - 32: Milestones and due dates for GM Mn-Ion Trap (Separator Modifier).....	427
Table IV - 33: Milestones and due dates for SNL-PFPBO (electrolyte additive, salt)	427
Table IV - 34: Summary of short-term capacity fade data at 2C and 5C discharge rates for non-defective baseline NMC 532 electrode and various defective electrodes	434
Table V - 1: Predicted voltages, specific capacities, and specific energies of glass-state conversion reactions using thermodynamic data from Northwestern's Open Quantum Materials Database	487
Table V - 2: Capacities (mAh.g ⁻¹) corresponding to one Li layer on bare, O- and OH-terminated MXene monolayers.....	516
Table V - 3: DFT calculation for predicting the oxidation potentials of fluorinated molecules.....	581
Table V - 4: ICP-MS results of Mn and Ni dissolution in Gen 2; HVE1 electrolyte with and without LiDFOB additive harvested from LNMO/A12 cells cycled at RT and 55°C	584
Table V - 5: Solvent and additive combinations for electrolyte optimization	589
Table V - 6: Summary of conductive properties and spatial variability for commercial-grade candidate electrodes	600
Table V - 7: Validation of micro-four line probe by other conductivity measurement methods for conductive polymer sheet.....	600
Table V - 8: Sample compositions in layered and composite notation	631
Table V - 9: Effects of Additives on the Average CE of Li.....	674

Introduction

Vehicle Technologies Office Overview

Vehicle Technologies Battery R&D Overview



I. Introduction

I.A Vehicle Technologies Office Overview

The Department of Energy's (DOE's) Vehicle Technologies Office (VTO) develops advanced transportation technologies that would reduce the nation's use of imported oil. Technologies supported by VTO include electric drive components such as advanced energy storage devices (batteries and ultracapacitors), power electronics and drive motors, advanced structural materials, advanced combustion engines, and fuels.¹ VTO is focused on funding high-reward/high-risk research by national laboratories, universities, and industry partners promising improvements in critical components needed for more fuel efficient (and cleaner) vehicles.

VTO works with U.S. automakers through the United States Council for Automotive Research (USCAR)—an umbrella organization for collaborative research consisting of Chrysler LLC, the Ford Motor Company, and the General Motors Company.² Collaboration with automakers through the US DRIVE (Driving Research and Innovation for Vehicle Efficiency and Energy Sustainability) Partnership enhances the relevance and the success potential of such programs.

During the past year, the U.S. government continued its strong R&D support of plug-in electric vehicles (PEVs) such as plug-in hybrids, extended range electric vehicles and all-electric vehicles. Earlier, in March 2012, President Obama announced the *EV Everywhere* Grand Challenge. One of its primary objectives is to enable U.S. innovators rapidly develop/commercialize the next generation of technologies achieving the cost, range, and charging infrastructure necessary for widespread adoption of PEVs. Their significant penetration into the transportation sector would reduce our dependence on foreign oil and any negative economic impacts associated with crude oil price fluctuations, as well as our greenhouse gas emissions.

An important step for the electrification of the nation's light duty transportation sector is the development of more cost-effective, longer lasting, and more abuse-tolerant PEV batteries. In fiscal year 2014, the DOE VTO battery R&D funding totaled nearly \$85 million. R&D continued to focus on the development of high-energy batteries for PEVs and very high power devices for hybrid vehicles. This document summarizes the progress of VTO battery R&D projects supported in FY 2014. An electronic version of this report can be accessed at http://www1.eere.energy.gov/vehiclesandfuels/resources/fcvr_reports.html.

I.B Vehicle Technologies Battery R&D Overview

I.B.1 DOE Battery R&D Goals and Technical Targets

The *EV Everywhere* Grand Challenge³ establishes a vehicle-level framework in which the technological progress toward achieving the Grand Challenge objectives can be evaluated. To meet those objectives, batteries, power electronics, motors, lightweight materials and vehicle structures must see dramatic advances. Performance and cost targets have been established for all the key technical areas associated with a PEV. Achieving those targets will meet the needs for a range of vehicle types including plug-in hybrids as well as short and long range all-electric vehicles. Some of the technology targets, derived from modeling and hardware-in-the-loop simulations of batteries operating in PEVs under multiple drive cycles, are shown in Figure I - 1.

¹ See <http://www1.eere.energy.gov/vehiclesandfuels/> for more information.

² For more information, please see uscar.org/guest/view_partnership.php?partnership_id=1.

³ For more information, please see http://www1.eere.energy.gov/vehiclesandfuels/about/partnerships/ev_everywhere.html.

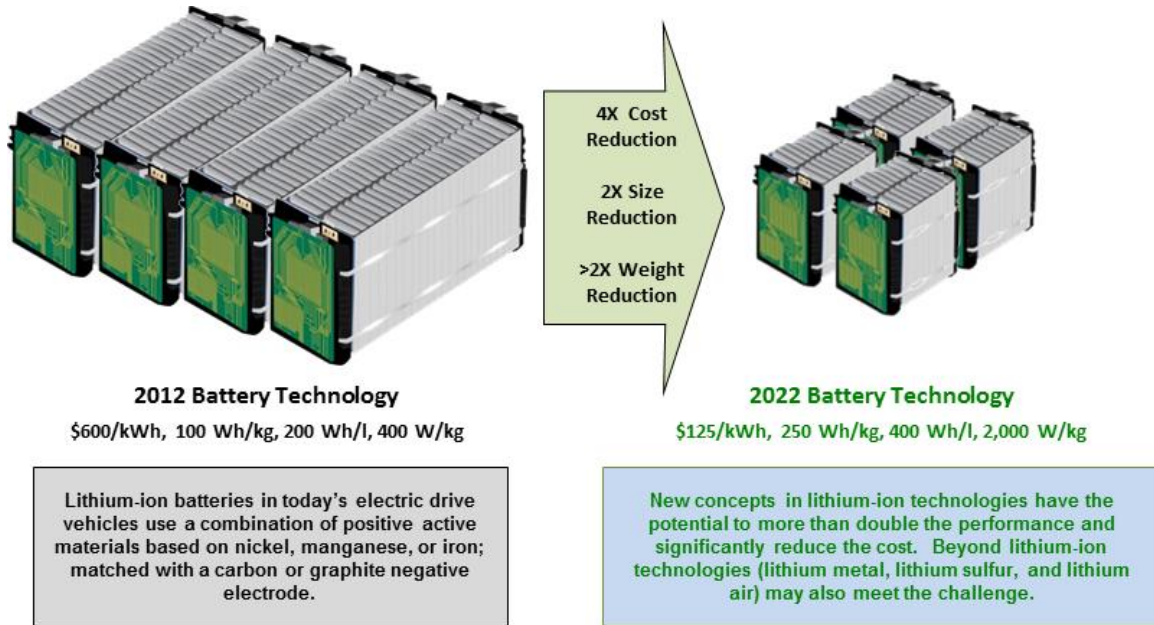


Figure I - 1: Battery advancements needed to enable a large market penetration of PEVs

I.B.2 DOE Battery R&D Plans

The objective of the VTO battery R&D effort is to advance the development of batteries to enable a large market penetration of hybrid and electric vehicles. Program targets focus on overcoming technical barriers to enable market success and they include: (1) significantly reducing battery cost, (2) increasing battery performance (power, energy, durability), (3) reducing battery weight & volume, and (4) increasing battery tolerance to abusive conditions such as short circuit, overcharge, and crush.

Current battery technology performs far below its theoretical limits. For example, in the near-term, with existing lithium-ion technology, there is an opportunity to more than double the battery pack energy density (from 100 Wh/kg to 250 Wh/kg) by using new high-capacity cathode materials, higher voltage electrolytes, and high capacity silicon or tin-based intermetallic alloys to replace graphite anodes. Despite recent promising advances, much more R&D is needed to achieve the performance and lifetime requirements for deploying those advanced technologies in PEVs.

In the longer term, battery chemistries “beyond Li-ion”, such as lithium-sulfur, magnesium-ion, zinc-air, lithium-air, and certain other advanced chemistries; offer the possibility of specific energy levels significantly greater than those for current lithium-ion batteries and they also have the potential of greatly reducing battery cost. However, major shortcomings in cycle life, power density, energy efficiency, and/or other critical performance parameters, including cost, currently hinder commercial introduction of state-of-the-art “beyond Li-ion” battery systems. Therefore, some kind of innovative breakthroughs would be needed for those new battery technologies to enter the market.

The energy density increases described above are critical to achieving the *EV Everywhere* cost and performance targets. Additional R&D efforts, including those related to pack design optimization and simplification, manufacturing improvements at cell/pack levels, production cost reduction for battery materials, and novel thermal management technologies will also help reduce battery cost. The major associated technical challenges and potential solutions to those challenges are listed in Table I - 1.

Table I - 1: Major Li-ion technology technical challenges and potential pathways to address them

Barrier/Challenge	Potential Solutions
<ul style="list-style-type: none"> Reduce the cost and improve the performance of lithium-ion battery technology. 	<ul style="list-style-type: none"> Improved material and cell durability. Improved energy density of active materials. Reduction of inactive material. Improved design tools/design optimization. Improved manufacturing processes.
<ul style="list-style-type: none"> Develop higher energy battery technology such as next generation lithium ion, lithium-sulfur and lithium-air <ul style="list-style-type: none"> Issues with these materials include poor cycle life, low power, low efficiencies, and safety. 	<ul style="list-style-type: none"> Improved electrolyte/separator combinations to reduce dendrite growth for Li metal anodes. Advanced material coatings. New ceramic, polymer, and hybrid structures with high conductivity, low impedance, and structural stability.
<ul style="list-style-type: none"> Improve abuse tolerance performance of battery technology. 	<ul style="list-style-type: none"> Non-flammable electrolytes. High-temperature melt integrity separators. Advanced materials and coatings. Improved understanding of reactions. Battery cell and pack level innovations such as improved sensing, monitoring, and thermal management systems.

I.B.3 Energy Storage R&D Programmatic Structure

The energy storage effort includes multiple activities, ranging from focused fundamental materials research to battery cell and pack development and testing. The R&D activities can involve either short-term directed research by commercial developers and national laboratories or exploratory materials research generally spearheaded by the national laboratories and universities. These consist of four major program elements which are inter-related and complementary, namely:

- Advanced Battery Development.
- Battery Testing, Analysis, and Design.
- Applied Battery Research (ABR).
- Focused Fundamental Research, also called Exploratory Battery Materials Research (BMR)

The *Advanced Battery Development* program's goal is to support the development of a domestic advanced battery industry whose products can meet electric drive vehicle performance targets. Such R&D activity focuses, for example, on the development of robust battery cells and modules to significantly reduce battery cost, increase life, and improve performance. It takes place in close partnership with the automotive industry, through our cooperative agreement with the United States Advanced Battery Consortium (USABC). DOE works in close collaboration with USABC to develop battery and ultracapacitor requirements for various vehicle types⁴ and test procedures.⁵ In FY 2014, the USABC supported 9 cost-shared contracts with developers to further the development of batteries for PEVs and HEVs. Also, DOE often works directly with battery and material suppliers via National Energy Technology Laboratory (NETL) contracts. In FY 2014, NETL managed 20 battery R&D contracts. Chapter III focuses on the battery development program.

The *Battery Testing, Analysis, and Design* activity supports certain complementary aspects of the battery development program. The high-level projects pursued in this area include cost modeling; secondary and other energy storage use and life studies; analysis of the recycling of core materials; requirements analysis for PEVs and HEVs; performance, life and abuse testing of contract deliverables, those of laboratory and university developed cells, and also those of benchmark systems from industry; thermal analysis, thermal testing and modeling; development of new test procedures and maintenance of current test procedures; and finally the development of tools for computer aided engineering of batteries.

⁴ See uscar.org/guest/article_view.php?articles_id=85

⁵ See uscar.org/guest/article_view.php?articles_id=86

Battery technologies are evaluated according to USABC Battery Test Procedures. The manuals for the relevant PEV and HEV applications are available online.^{6,7,8} A benchmark testing of an emerging technology would be performed to remain abreast of the latest industry developments. Within this report, Chapter IV focuses on the *Battery Testing, Analysis, and TestingDesign* activity.

The *Applied Battery Research* (ABR) activity is focused on the optimization of next generation, high-energy lithium-ion electrochemistries that incorporate new battery materials. Its emphasis is on identifying, diagnosing, and mitigating issues that impact the performance and life of cells containing advanced materials. It investigates interaction between all cell components (including the cathode, anode, electrolyte, binders, conductive additives, and separator) which impact performance and life. Typical issues associated with incorporating new material developments into working PEV cells can include: (1) inadequate power capability needed to meet the requirements of PEVs, (2) insufficient cycle life stability to achieve the 1,000 to 5,000 “charge-depleting” deep discharge cycles, and (3) poor performance at lower temperatures. It is conducted by a team which is headed by the Argonne National Laboratory (ANL) and includes five other national labs and several universities. Chapter V lists all the projects under the Applied Battery Research activity.

The *Focused Fundamental Research* activity (alternately called *Exploratory Battery Materials Research* activity which is replacing a previous activity entitled *Batteries for Advanced Transportation Technologies*) addresses fundamental issues of materials and electrochemical interactions associated with lithium batteries. It attempts to develop new and promising materials, to use advanced material models to discover new materials and predict failure modes, and scientific diagnostic tools and techniques to gain insight into why material and systems fail. Battery chemistries are monitored continuously with periodic substitution of more promising components based on advice from within this activity, from outside experts, and from the assessments of world-wide battery R&D. The work is carried out by a team at the Lawrence Berkeley National Laboratory (LBNL) and at several other national labs, universities, and commercial entities. The program is also studying issues critical to the realization of beyond Li-ion technologies. Two of the most promising such technologies are Lithium/Sulfur and Lithium/Air. Some of the main areas of focus are to devise new methods to understand and stabilize lithium metal anodes; to contain Li polysulfides to enable the use of sulfur cathodes; and to develop electrolytes that support Li air and Li/sulfur cells. Chapter VI lists all the projects which are part of the Focused Fundamental Research activity.

Several *Small Business Innovation Research* (SBIR) contracts are also supported by VTO, in addition to the R&D described above. SBIR projects have been the source of new ideas and concepts. These SBIR projects are focused on the development of new battery materials and components.

The Electrochemical Energy Storage Roadmap describes ongoing and planned efforts to develop electrochemical storage technologies for plug-in electric vehicles (PEVs) and can be found at the EERE Roadmap page http://www1.eere.energy.gov/vehiclesandfuels/pdfs/program/eestt_roadmap_june2013.pdf.

Dramatic improvements in battery performance and cost will require a well-coordinated effort across all of the DOE complex and with America’s most innovative researchers and companies. Coordination within DOE and with other government agencies is a key attribute of the VTO energy storage R&D efforts. VTO coordinates efforts on energy storage R&D with the DOE Office of Science, the DOE Office of Electricity, and the Advanced Research Projects Agency – Energy (ARPA-E). Innovations in battery technology occur as a result of fundamental investigations carried out at national labs and universities supported by the DOE Office of Science, through translational research sponsored by ARPA-E, and through applied research and development at labs, universities and industry supported by VTO. Innovations coming from R&D on pre-competitive technologies will be transferred to and implemented by industry partners as a business case develops for these technologies through the US DRIVE public/private partnership. The USABC makes cost-shared, competitively awarded projects to industry to facilitate commercialization of pre-competitive technologies and introduce them into the marketplace.

VTO also has established extensive and comprehensive ongoing coordination efforts in energy storage R&D with other government agencies. Such efforts include membership and participation in the Chemical Working Group of the Interagency Advanced Power Group (IAPG), active participation in program reviews and technical meetings sponsored by

⁶ United States Advanced Batteries Consortium, USABC Electric Vehicle Battery Test Procedure Manual, Rev. 2, U.S. Department of Energy, DOE/ID 10479, January 1996.

⁷ U.S. Department of Energy, PNGV Battery Test Procedures Manual, Rev. 2, August 1999, DOE/ID-10597.

⁸ United States Council for Automotive Research, RFP and Goals for Advanced Battery Development for Plug-in Electric Vehicles, uscar.org.

other government agencies, and coordinating the participation of representatives from other government agencies in the contract and program reviews of DOE-sponsored efforts. DOE also coordinates with the Department of Transportation/National Highway Traffic Safety Administration (DOT/NHTSA), the Environmental Protection Agency (EPA), and with the United Nations Working Group on Battery Shipment Requirements. Additional international collaboration occurs through a variety of programs and initiatives. These include: the International Energy Agency's (IEA's) Implementing Agreement on Hybrid Electric Vehicles (IA-HEV), the eight-nation Electric Vehicle Initiative (EVI), and the Clean Energy Research Center (CERC) bilateral agreement between the U.S. and China.

I.B.4 Recent *EV Everywhere* Highlights

- America is the world's leading market for electric vehicles and is producing some of the most advanced PEVs available today. Consumer excitement and interest in PEVs is growing, with sales continuing to increase, despite the recent drop in gasoline prices. In 2012, PEV sales in the U.S. tripled, with more than 50,000 cars sold. In 2013, PEV sales increased by 85% with over 97,000 vehicles sold. In 2014, PEV sales are on pace to increase by 20%, with annual sales of 117,000 PEVs projected.
- PEVs also have won critical acclaim with awards such as 2011 World Car of the Year (Nissan Leaf), 2013 Motor Trend Car of the Year (Tesla Model S), the 2012 Green Car Vision Award Winner (Ford C-MAX Energi), and a plug-in electric vehicle (Chevrolet Volt) beat all other vehicle models in Consumer Reports' owner satisfaction survey for two consecutive years.
- A 2013 analysis by RTI International in Research Triangle Park, NC determined that the DOE's \$971 million R&D investment in advanced battery technology for electric drive of vehicles (EDVs) from 1991-2012 directly led to the commercialization of the 2.4 million EDVs sold between 1999-2012 that incorporate nickel metal hydride and lithium ion batteries, which are projected to reduce U.S. fuel consumption by \$16.7 billion through 2020. The study also found that VTO-funded research contributed to the knowledge base in energy storage that resulted in 112 patent families in energy storage over the period 1976 to 2012 and is ranked first in patent citations among the top-ten companies.
- Commercial applications of DOE-supported technologies. Several technologies, developed partially under VTO-sponsored projects, have moved into commercial applications. Hybrid electric vehicles on the market from BMW and Mercedes are using lithium-ion technology developed under projects with Johnson Controls Inc. (JCI). JCI will also supply Li-ion batteries to Land Rover for hybrid drive sport utility vehicles. Lithium-ion battery technology developed partially with DOE funding of a USABC project at LG Chem is being used in GM's Chevrolet Volt extended-range electric vehicle (EREV), the Cadillac ELR EREV, and also in the Ford Focus EV battery. LG Chem will also supply Li-ion batteries to Eaton for hybrid drive heavy vehicles.
- The 2014 DOE PHEV Battery Cost Reduction Milestone of \$300/kWh was accomplished. DOE-funded research has helped reduce current cost estimates from three DOE-funded battery developers for a PHEV 40 battery average \$289 per kilowatt-hour of useable energy. This cost projection is derived using material costs and cell and pack designs, provided by the developers, that are then input into ANL's peer reviewed and publically available Battery Production and Cost model (BatPaC); the cost is based on a production volume of at least 100,000 batteries per year. The battery cost is derived for batteries that meet DOE/USABC system performance targets. The battery development projects focus on high voltage and high capacity cathodes, advanced alloy anodes, and processing improvements. Proprietary details of the material and cell inputs and cost models are available in spreadsheet form and in quarterly reports. DOE's goals are to continue to drive down battery cost to \$125/kWh by 2022.
- Amprius Inc's lithium ion battery cells containing silicon nanowire anodes provided 260Wh/kg (~50% more specific energy than SOA cells) and demonstrated good cycle life (less than 5-7% fade after 290 cycles) , see Figure I - 2.

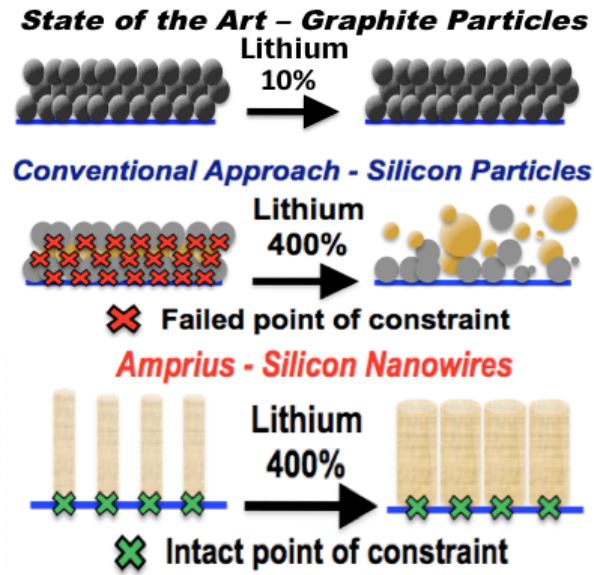


Figure I - 2: Amprius' nanowires address swelling issue by allowing Si to swell

- GM/Ansys/ESim/NREL developed and released a battery design software suite to reduce battery development time and cost. The software package permits thermal response, cycle life modeling, abuse response modeling of battery cells and packs. Customers are currently using tool for battery design, see Figure I - 3.

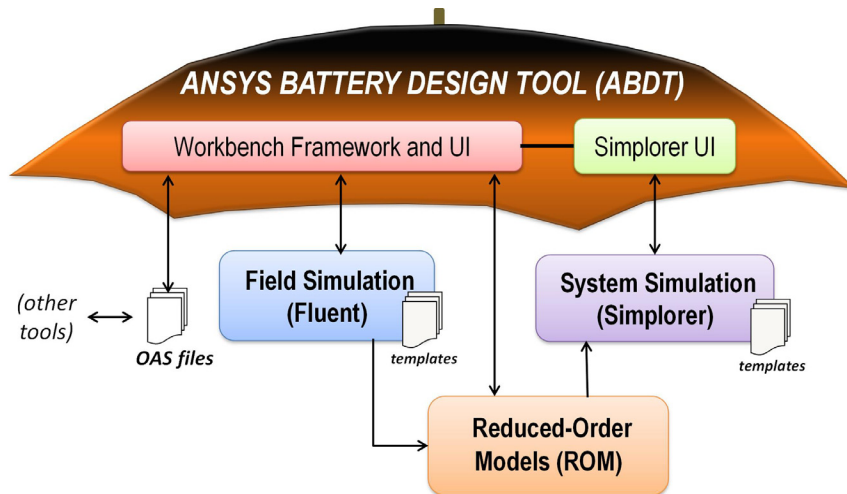


Figure I - 3: Conceptual view of the ANSYS battery design tool

- Johnson Controls Inc. demonstrated novel cathode slurry processing techniques that reduced N-Methylpyrrolidone (NMP) solvent use by 32% and increased coated electrode density by 31%, see Figure I - 4.

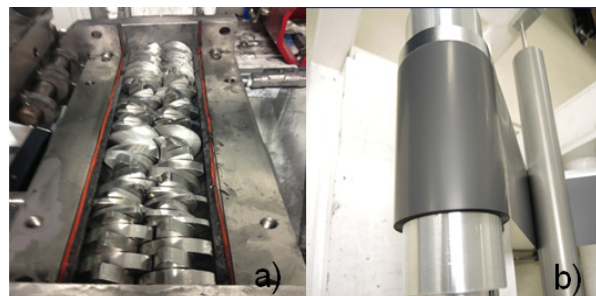


Figure I - 4: JCI's cathode slurry processing technique: a) Inline mixer b) Calendared electrode (inline mixed)

- Miltec International Inc. developed stable, first-of-its-kind, UV curable binders for Li-ion cathodes and demonstrated novel cathode slurry processing techniques. The process reduced NMP solvent use by 100%, achieved cathode containing 87% NMC, and achieved cathode thickness and porosity similar to conventional electrodes (~60 mm and ~25%). Prototype cells retained 50% capacity after 2,000 1C/1C cycles.
- In January 2014, DOE released a Funding Opportunity Announcement (FOA) that solicited proposals in the areas of energy storage, electric drive systems, lightweight materials, and auxiliary load reductions in support of the EV Everywhere Grand Challenge. In August 2014, DOE announced the selection of 19 new projects. The nineteen projects are aimed at reducing the cost and improving the performance of key PEV components. These include improving “beyond lithium-ion technologies” that use higher energy storage materials, and developing and commercializing wide bandgap (WBG) semiconductors that offer significant advances in performance while reducing the price of vehicle power electronics. Other projects focus on advancing lightweight materials research to help electric vehicles increase their range and reduce battery needs, and developing advanced climate control technologies that reduce energy used for passenger comfort and increase the drive range of plug-in electric vehicles. Specifically, in the area of advanced batteries, 9 projects totaling \$11.3 million, were awarded for beyond-lithium-ion battery technologies, including polycrystalline membranes, nanomaterials, high-capacity cathodes, Li-air batteries, Li-sulfur batteries, and electrolyte chemistries. These projects, which were initiated in September 2014, will be described in more detail in next year’s annual report.
- In August 2014, DOE awarded 14 projects under its “Incubator Program” with small businesses and universities. Specifically, in the area of energy storage, DOE awarded 6 projects totaling \$7.4 million related to battery design and manufacturing advancements. Next year’s annual report will describe these in more detail.

I.B.5 Organization of this Report

This report covers all the projects currently ongoing or starting up as part of the energy storage R&D effort in VTO. Chapter II through V contain descriptions and progress of various R&D projects supported through VTO funding. A list of individuals who contributed to this annual progress report (or who are otherwise collaborating with the energy storage R&D effort) appears in Appendix A. A list of acronyms is provided in Appendix B.

We are pleased with the progress made during the year and look forward to continued work with our industrial, government, and scientific partners to overcome the remaining challenges to delivering advanced energy storage systems for vehicle applications.



David Howell
Program Manager, Hybrid and Electric Systems
Vehicle Technologies Office



Tien Q. Duong
Manager, Exploratory Technology Research
Vehicle Technologies Office



Peter W. Faguy
Manager, Applied Battery Research
Vehicle Technologies Office



Brian Cunningham
Lead, Battery Testing, Analysis and Design
Vehicle Technologies Office

II

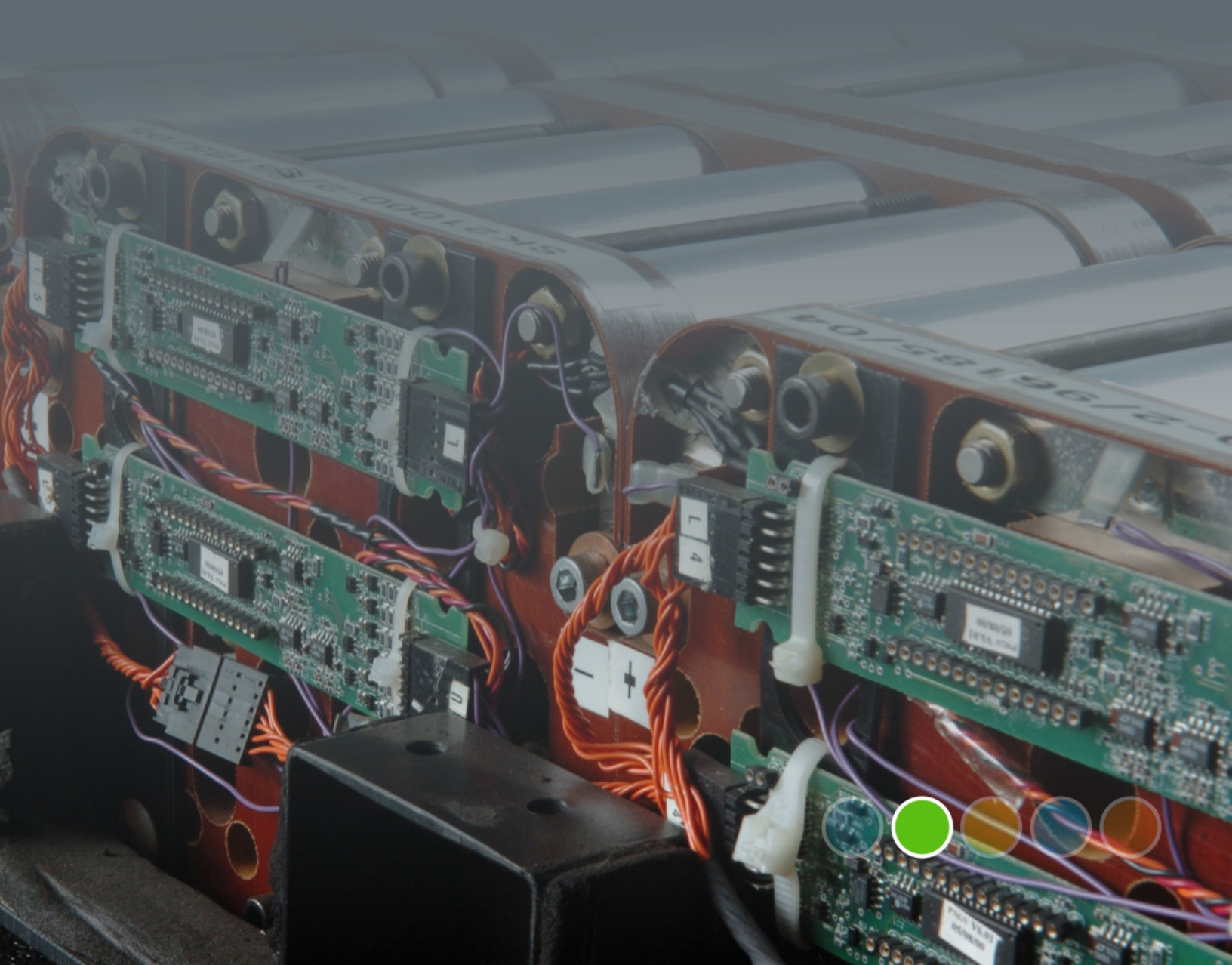
Advanced Battery Development

USABC Battery Development Projects

Advanced Lithium Battery Cell Technology

Low-cost Processing Research

Small Business Innovative Research (SBIR) Projects



II. Advanced Battery Development

One of the primary objectives of the Energy Storage effort is the development of durable and affordable advanced batteries and ultracapacitors for use in advanced vehicles, from start/stop to full-power HEVs, PHEVs, and EVs. The battery technology development activity supports this objective through projects in several areas:

- Full-scale battery R&D under multiple battery development contracts—conducted through the United States Advanced Battery Consortium (USABC),
- Numerous advanced cell, materials and components contracts—administered through the National Energy and Technology Laboratory (NETL), and
- Small Business Innovative Research (SBIR)—to fund early-stage R&D for small businesses/entrepreneurs.

All battery development projects are conducted with a set of technical goals in mind and in order to overcome specific technical barriers which prevent the large-scale commercialization of advanced automotive batteries

Technical Goal

- By 2022, reduce PEV battery cost to \$125/kWh.

Technical Barriers

- **Cost** – The current cost of Li-based batteries is approximately a factor of four too high on a kWh basis for PEVs. The main cost drivers being addressed are the high costs of raw materials and materials processing, cell and module packaging, and manufacturing.
- **Performance** – The performance advancements required include the need for much higher energy densities to meet the volume and weight requirements, especially for the 40 mile PHEV system and longer range EVs, and to reduce the number of cells in the battery (thus reducing system cost).
- **Abuse Tolerance** – Many Li batteries are not intrinsically tolerant to abusive conditions such as a short circuit (including an internal short circuit), overcharge, over-discharge, crush, or exposure to fire and/or other high temperature environments. The use of Li chemistry in the larger (PEV) batteries increases the urgency to address these issues.
- **Life** – A 15-year life with 5,000 HEV cycles or 1,000 EV cycles is unproven.

Technical Targets

- Focus on the small-scale manufacture of cells, batteries, and advanced materials for high-power applications (HEVs) and high-energy applications (e.g., PEVs).
- Attempt to meet the requirements for EVs, PHEVs, HEVs, and 12V start/stop batteries developed with industry – as shown in Table II - 1, Table II - 2, and Table II - 3.

Accomplishments

- The R&D activity remains fully underway with multiple battery development contracts being conducted through the USABC. A revised set of EV battery performance requirements was posted on the USABC site this year. Current USABC-funded projects with Envia Systems, JCI, Xerion, Maxwell Technologies, Saft, Leaden Energy, SKI, and ENTEK are covered in this report.
- Numerous advanced cell, materials, and components contracts are ongoing – administered through the National Energy and Technology Laboratory (NETL). These include projects by Amprius, XALT Energy, OneD Material, 3M, Seeo, Pennsylvania State University, and Denso.

Table II - 1: Summary of USABC performance targets for EV batteries⁹

USABC Goals for Advanced Batteries for EVs – CY 2020 Commercialization			
End of Life Characteristics at 30°C	Units	System Level	Cell Level
Peak Discharge Power Density, 30 s Pulse	W/L	1,000	1,500
Peak Specific Discharge Power, 30 s Pulse	W/kg	470	700
Peak Specific Regen Power, 10 s Pulse	W/kg	200	300
Useable Energy Density @ C/3 Discharge Rate	Wh/L	500	750
Useable Specific Energy @ C/3 Discharge Rate	Wh/kg	235	350
Useable Energy @ C/3 Discharge Rate	kWh	45	N/A
Calendar Life	Years	15	15
DST Cycle Life	Cycles	1,000	1,000
Selling Price @ 100K units	\$/kWh	125	100
Operating Environment	°C	-30 to +52	-30 to +52
Normal Recharge Time	Hours	< 7 Hours, J1772	< 7 Hours, J1772
High Rate Charge	Minutes	80% ΔSOC in 15 min	80% ΔSOC in 15 min
Maximum Operating Voltage	V	420	N/A
Minimum Operating Voltage	V	220	N/A
Peak Current, 30 s	A	400	400
Unassisted Operating at Low Temperature	%	> 70% Useable Energy @ C/3 Discharge rate at - 20 °C	> 70% Useable Energy @ C/3 Discharge rate at - 20 °C
Survival Temperature Range, 24 Hr	°C	-40 to+ 66	-40 to+ 66
Maximum Self-discharge	%/month	< 1	< 1

⁹ For more details and for additional goals, see uscar.org/guest/article_view.php?articles_id=87.

Table II - 2: Summary of USABC performance targets for PHEV batteries

Characteristics at End of Life (EOL)		PHEV-20 Mile	PHEV-40 Mile	xEV-50 Mile
Commercialization Timeframe		2018	2018	2020
AER	Miles	20	40	50
Peak Pulse Discharge Power (10 sec)	kW	37	38	100
Peak Pulse Discharge Power (2 sec)	kW	45	46	110
Peak Regen Pulse Power (10 sec)	kW	25	25	60
Available Energy for CD (Charge Depleting) Mode	kWh	5.8	11.6	14.5
Available Energy for CS (Charge Sustaining) Mode	kWh	0.3	0.3	0.3
Minimum Round-trip Energy Efficiency	%	90	90	90
Cold cranking power at -30°C, 2 sec- 3 Pulses	kW	7	7	7
CD Life/Discharge Throughput	Cycles/MWh	5,000/29	5,000/58	5,000/72.5
CD HEV Cycle Life, 50 Wh Profile	Cycles	300,000	300,000	300,000
Calendar Life, 30°C	Year	15	15	15
Maximum System Weight	kg	70	120	150
Maximum System Volume	Liter	47	80	100
Maximum Operating Voltage	V _{dc}	420	420	420
Minimum Operating Voltage	V _{dc}	220	220	220
Maximum self-discharge	%/month	<1	<1	<1
System Recharge Rate at 30°C (240V/16A)	kW	3.3	3.3	6.6
Unassisted Operating and Charging Temp Range	°C	-30 to +52	-30 to +52	-30 to +52
-30°-52°	%	100	100	100
0°	%	50	50	50
-10°	%	30	30	30
-20°	%	15	15	15
-30°	%	10	10	10
Survival Temperature Range	°C	-46 to +66	-46 to +66	-46 – to +66
Max System Production Price @100,000 units/year	\$	\$2,200	\$3,400	\$4,250

Notes

1. Peak discharge pulse power and peak regen pulse power targets are applicable for the charge- sustaining mode.
2. HPPC-current rate used to approximate the required 10-kW rate during the HPPC test and the static capacity test.
3. With the battery manufacturer's concurrence, an increase recharge rate can be used to accelerate life testing. Maximum system recharge rate refers to the maximum power expected from a standard garage outlet.
4. Values correspond to end-of-life (EOL).
5. PHEV-20 and PHEV-40 targets correspond to commercialization in FY 2018; x-EV targets correspond to commercialization in FY 2020.
6. x-EV cell is intended for architectures that require higher power levels than PHEV-20 and PHEV-40.

Table II - 3: Summary of USABC performance targets for 12V Start/Stop Vehicle Applications

Characteristics	Units	Target	
		Under hood	Not under hood
Discharge Pulse, 1 sec	kW		6
Max discharge current, 0.5 s	A		900
Cold cranking power at -30°C (three 4.5-s pulses, 10s rests between pulses at min SOC)	kW	6 kW for 0.5s, followed by 4 kW for 4s	
Minimum voltage under cold crank	V _{dc}		8.0
Available energy (750W accessory load power)	Wh		360
Peak Recharge Rate, 10s	kW		2.2
Sustained Recharge Rate	W		750
Cycle life, every 10% life RPT with cold crank at min SOC	Engine starts/miles		450k/150k
Calendar life at 30°C, 45°C if under hood	Years	15 at 45°C	15 at 30°C
Minimum round-trip energy efficiency	%		95
Maximum allowable self-discharge rate	Wh/day		2
Peak Operating Voltage, 10s	V _{dc}		15.0
Sustained Operating Voltage - Max	V _{dc}		14.6
Minimum Operating Voltage under Autostart	V _{dc}		10.5
Operating Temperature Range (available energy to allow 6kW, 1s pulse)	°C	-30 to +75	-30 to +52
-30°C to -52°C	Wh	360 (to 75°C)	360
0°C	Wh		180
-10°C	Wh		108
-20°C	Wh		54
-30°C	Wh		36
Survival Temperature Range (24 hours)	°C	-46 to +100	-46 to +66
Maximum System Weight	kg		10
Maximum System Volume	L		7
Maximum System Selling Price (@250k units/year)	\$	\$220	\$180

II.A USABC Battery Development Projects

II.A.1 EV Battery Development (Envia Systems)

Oliver Gross (USABC Program Manager)

Subcontractor: Envia Systems

Herman Lopez (Program Manager)

7979 Gateway Boulevard, Suite 101
Newark, CA 94560

Phone: (510) 962-3687; Fax: (510) 790-7012
E-mail: hlopez@enviasystems.com

Subcontractors:

3M Company, St. Paul, MN
A123 Systems, Waltham, MA
Asahi Kasei, Tokyo, Japan
DuPont, Sunnyvale, CA
Daikin America, Decatur, AL
Nanoscale Components, Hudson, NH

Start Date: June 2014

Projected End Date: July 2017

Objectives

- Develop high capacity silicon-based anodes capable of supporting long cycle life by controlling electrode pulverization, lithium consumption and conductivity loss.
- Develop high capacity Li-rich cathodes capable of supporting cycle life, calendar life, power and low/high temperature cell requirements.
- Develop a manufacturable and cost effective prelithiation process.
- Screen and optimize various electrolyte formulations and coated separators to support meeting the USABC cell targets.
- Design, build, test and deliver large capacity pouch cells integrating high capacity Si-based anodes and Li-rich cathodes along with optimized electrolyte formulations, separators and prelithiation process that meet the USABC cell goals for the CY 2020.

Technical Barriers

There are numerous materials, cell components and cell manufacturing related technical barriers that need to be addressed, in order to develop cells that will meet the aggressive USABC EV cell targets. Advanced materials,

such as anodes, cathodes, high voltage electrolytes, stable separators and processes, such as optimized prelithiation, cell design and cell fabrication will be required to meet the energy, power, cycle life, calendar life, temperature, safety and cost cell targets.

High capacity silicon-based anodes are required to be integrated in the cell in order to meet the high-energy cell targets. Unfortunately silicon-based anodes introduce significant challenges in cycle life, especially at the required high electrode loading and density levels, due to pulverization and lithium consumption.

Pulverization of silicon happens due to the volume expansion of silicon (over 300%) during the lithium insertion process. Pulverization causes the silicon particles to separate from the composite anode coating thus losing contact with the current collector causing severe fade in capacity with cycles. Lithium consumption is another serious issue that causes the battery capacity to fade. Because of the repeated volume expansion and contraction of silicon-based anodes, active silicon surfaces continue to be formed, reacting with the electrolyte to form a new solid-electrolyte interphase (SEI) layer which continuously consumes lithium as the battery cycles. In a full cell, lithium also is consumed by the cathode, and the cell loses capacity with cycling.

High capacity lithium-rich cathodes will also be required to meet the aggressive cell targets. Unfortunately the higher specific capacity lithium-rich cathode materials suffer from a fundamental problem of high resistance and transition metal-ion dissolution, which leads to reduced power, low usable energy, poor cycle life and poor calendar life, all being disadvantageous when considering it for automotive applications.

Technical Targets

- Develop a silicon-based anode formulation able to meet the cycle life and power requirements suitable for EV applications.
- Develop a lithium-rich NMC cathode material with low DC-resistance, voltage fade and good cycling stability.
- Deliver cells that meet the USABC EV battery targets. Cells will be delivered to Idaho National Laboratory (INL), Sandia National Laboratory (SNL) and National Renewable Energy Laboratory (NREL) for independent testing. The project has 3

large format high-capacity pouch cell deliverables, at the beginning, mid point and conclusion of the project.

Accomplishments

- Started to screen silicon-based materials from anode material partners (3M and DuPont).
- Multiple cathode compositions were synthesized and a specific Li, Ni, Co, Mn, and Li_2MnO_3 , formulation was down-selected to continue the doping and coating cathode development.
- Nanoscale has designed and is ahead of schedule constructing a pilot scale version of their electrochemical R&D pre-lithiation line.
- Baseline 20Ah capacity pouch cells were designed and will be built and delivered to INL in Q2 of the project.
- Started screening separators from partner (Asahi Kasei) with different coating layers.



Introduction

Envia has proposed to develop a new battery system based on a novel cathode material and anode formulation that could meet the EV requirements of the USABC while maintaining long life, excellent safety, and low cost. At the conclusion of this program, Envia will demonstrate a lithium ion battery (LIB) with a usable energy density greater than 350 Wh/kg while maintaining other performance requisites of EVs, including usable energy, power, and cycle life of 1000 cycles. This will be achieved through a collaborative effort across several organizations. Each will provide expertise on a specific component of the material and/or cell. Ultimately, large format cells meeting the USABC goals will be built and delivered to the National Laboratories for testing.

Approach

Envia will use a system-level approach to screen, develop and optimize the critical cell components (cathode, anode, electrolyte and separator), cell design (N/P ratio, electrode design, prelithiation, etc.) and cell formation and testing protocols, that will enable meeting the recently released USABC EV commercialization cell level goals for the year 2020. The development will consist of integrating Envia's high capacity lithium rich (HCMRTM) cathodes, prelithiated silicon-based high capacity anodes, high voltage electrolyte and ceramic coated separator into large capacity (1-50Ah) pouch cells. The developed cells will exhibit high energy density and power, good cycle life and calendar life and

acceptable low temperature performance while meeting the cell level cost and safety targets.

Envia will leverage its material, process and cell development expertise to develop, modify and engineer material and cell-level solutions to meet the aggressive cell specifications. During this project, Envia will be partnering with leading chemical companies like 3M, DuPont, Daikin America, Asahi Kasei, Nanoscale Components and A123 Venture Technologies to enable the development of the best anode, electrolyte, separator, prelithiation process and cell manufacturing, respectively. Having the proper partnerships will increase the probability of meeting the USABC project goals, by leveraging the strength of each partner, with Envia mainly focusing on its core strengths of cathode and anode development and cell design. Partnering with large chemical and cell partners also ensures that any technology that is developed will have a clear path to high volume production and commercialization.

Results

Anode development: Envia is developing silicon anodes by integrating commercially available silicon based materials like Si-based alloys and nSi- and SiO_x -based composites. Envia is applying its electrode formulation processing and coating know-how to further improve the performance of the silicon powders. Figure II - 1 shows the half-cell charge discharge cycling performance of two SiO_x -based composite anodes with different amounts of carbon. The C/3 reversible capacity ranges from 1100mAh/g to 1300mAh/g with reasonable cycling performance. Development on Si-based alloys and nano-Si materials are also underway.

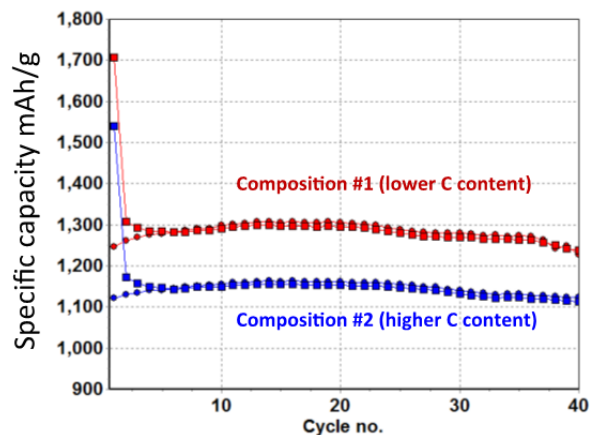


Figure II - 1: Electrochemical half-cell cycling from different carbon containing SiO_x -based anode composites

Cathode development: New cathode compositions, dopants and coatings are being developed in order to deliver a cathode material that will meet the USABC EV cell specifications. Q1 cathode material

development focused mainly on composition engineering to optimize the amount of Li, Ni, Co, Mn and Li_2MnO_3 . A particular cathode composition with 56% Mn showed good capacity and cycling performance with improved usable energy and has been

down-selected to continue the cathode development. Q2 and Q3 will focus on dopant and nanocoating optimization of the down-selected cathode. (See Figure II - 2.)

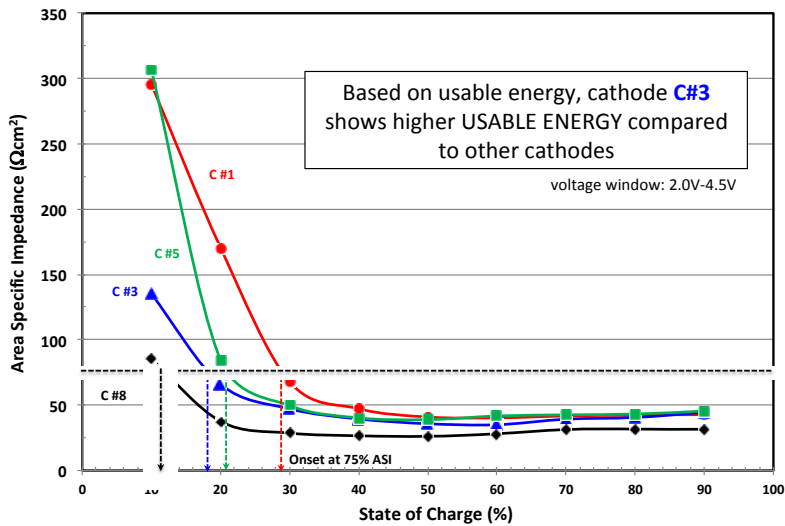


Figure II - 2: DC-Resistance plot for different cathode compositions

Prelithiation development: Electrochemical prelithiation of silicon anodes will be carried out by Nanoscale Components to support the anode material development and scale-up of the process, to enable large cell manufacturing. During Q1 of the program, Nanoscale focused on construction of their pilot level prelithiation line, which will increase linear throughput by 10x and increase roll width by 5x (300mm) from their current R&D line. Construction and debugging of the pilot level production line is ahead of schedule with framing complete. The first anode electrodes and rolls were delivered to Nanoscale late in Q1 and prelithiation development will begin in Q2 of the program.

Separator development: During Q1 of the program, Envia received 3 coated separators from Asahi

Kasei, and preliminary abuse testing was performed. The 3 separators were incorporated into large capacity 20Ah pouch cells, where a nail penetration test was performed. The nail penetration tests were carried out following USABC testing guidelines. Figure II - 3 shows the nail penetration results from the 3 separators under development compared to the current baseline ceramic coated separator (S#1). The nail penetration results show the baseline separator (S#1) and separator #2 & #3 passing the nail penetration test. The cells incorporating separator #4 failed the nail penetration test. The positive results for separator #2 and #3 makes them potential candidates for the next cell build, after further validation of the electrochemical cell performance.

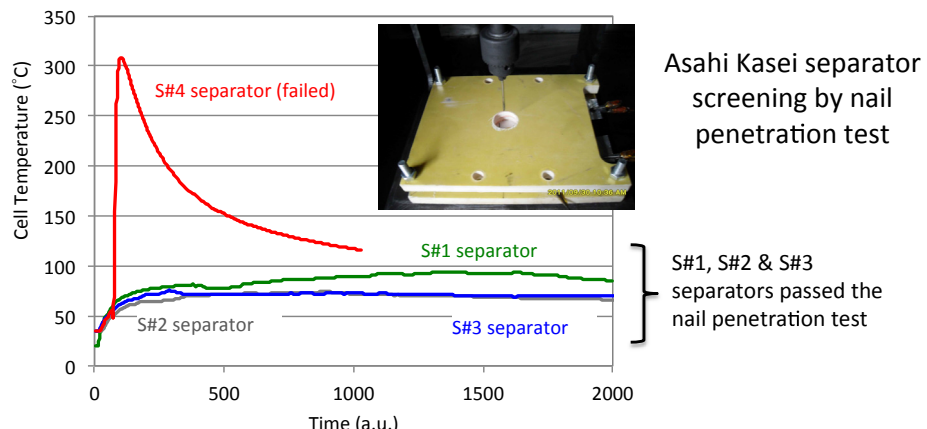


Figure II - 3: Nail penetration results for 20Ah pouch cells incorporating different separators

Cell development: Q1 of the program focused on designing and building baseline 20Ah pouch cells, which integrated Envia's baseline cathode, anode, separator and electrolyte. The baseline cells will benchmark the cell status at the beginning of the program and serve as a reference to evaluate project progress. Two cell designs have been prepared, using two different cathodes and will be tested, in order to down-select to the most optimal baseline cell design. After evaluating the cell performance, the most promising cell design will be down-selected with cells to be made and delivered to INL in Q2 of the program.

Conclusions and Future Directions

Envia will continue to use a system-level approach to screen, develop and optimize the critical cell components (cathode, anode, electrolyte and separator), cell design (N/P ratio, electrode design, prelithiation, etc.) and cell formation and testing protocols that will enable meeting the USABC EV cell targets. All assigned development activities have started, and will continue with the goal of down-selecting the best materials, components and processes to integrate in the next cell deliverable of the project. Close interaction with all development partners will be critical for the success of the project.

FY 2014 Publications/Presentations

No publications or presentations have been made.

II.A.2 Advanced High-Performance Batteries for Plug-In Hybrid Electric Vehicle Applications (JCI)

Renata Arsenault (USABC Program Manager)

Subcontractor: Johnson Controls, Inc.

Avie Judes (Program Manager)

5757 N. Green Bay Road

Glendale, WI 53209

Phone: 414-524-6173

E-mail: avie.judes@jci.com

Team Member:

Argonne National Laboratory

Start Date: April 1, 2012

Projected End Date: March 31, 2014

Objectives

- Build on the prismatic cell platform developed in the previous program and achieve a step-change in energy density from 275 Wh/L to a 375 Wh/L stretch goal.
- Achieve \$250/kWh for the prismatic cell.
- Target EUCAR 4 abuse tolerance rating or better.
- Deliver two generations of prismatic cells.

Technical Barriers

- Higher specific capacity cathode materials of interest have reduced thermal stability (reduced life).
- Novel electrode material processing techniques may have a negative impact on performance and life.
- Lowering the power to energy ratio must not result in an unacceptable reduction in cold temperature power.
- Higher upper voltages adversely affect life and require design countermeasures to stabilize the chemistry.
- Increased cell energy density and total energy require accompanying improvement in abuse tolerance.
- Abuse tolerance improvements require material and process innovation to overcome impact on life and cost.

Technical Targets

- Available Energy (Charge Depleting mode): 5.8 kWh for 20-mile system at End of Life (EOL).
- Energy Density: 375 Wh/L (stretch goal).
- Packaged Energy Cost: \$250/kWh for cell.
- EUCAR 4 abuse tolerance rating or better.

Accomplishments

- Evaluated multiple cathode materials from six suppliers in the $\text{LiNi}_x\text{Mn}_y\text{Co}_z\text{O}_2$ family with stoichiometries ranging from 33% to 60% nickel content and incorporating a range of stabilization techniques.
- Final build cells demonstrated 36% capacity increase, projecting a 40% cost reduction at the system level.
- Dry compounding achieved desired reduction of solvent and binder, but the technique was not pursued due to prohibitive resistance growth and high cost.
- Paste mixing using an in-line compound mixer achieved solvent reduction goals. High electrode densities enabled stretch energy density targets to be met, and yielded cathodes that were used for final deliverables.
- 4.2V and 4.3V upper voltage limits evaluated in parallel with electrolyte development. Enhanced stability demonstrated at 4.2V led to limit increase from 4.1V.
- Mechanical improvement activity resulted in mandrel elimination, can sidewall thinning, collector and coating area optimization, and alternate fill-hole closure design analysis. Results informed final build choices.
- Abuse tolerance improvements focused on Thermal Protective Barrier (TPB), ceramic coating on anode, ceramic separators, electrolytes and cathodes with functional overcharge additives and reduced activation pressure vents, all leading to improved over-charge protection (vs previous program) and enhanced understanding as confirmed by Sandia National Lab.



Introduction

In March 2014, JCI completed a \$4.1 million, 2-year program focused on reducing the cost to capacity ratio of a Gen-1 prismatic NMC-graphite cell developed in the foregoing USABC program. The targeted improvements to the PL27M cell were realized through an orchestrated, multidisciplinary pursuit of increased volumetric energy. Cost reduction was achieved both implicitly from the improved energy density and accompanying BSF (Battery Size Factor) reduction

opportunity, and explicitly through other decoupled mechanical and processing advancements.

The steady, upward march in energy density demonstrated throughout the program reflected the continuous improvements made in process, materials and mechanical design. This is evidenced in Figure II - 4, which traces the volumetric energy density ascent from its baseline value of 275 Wh/L to the achieved stretch target of 375 Wh/L, an increase of almost 40 percent.

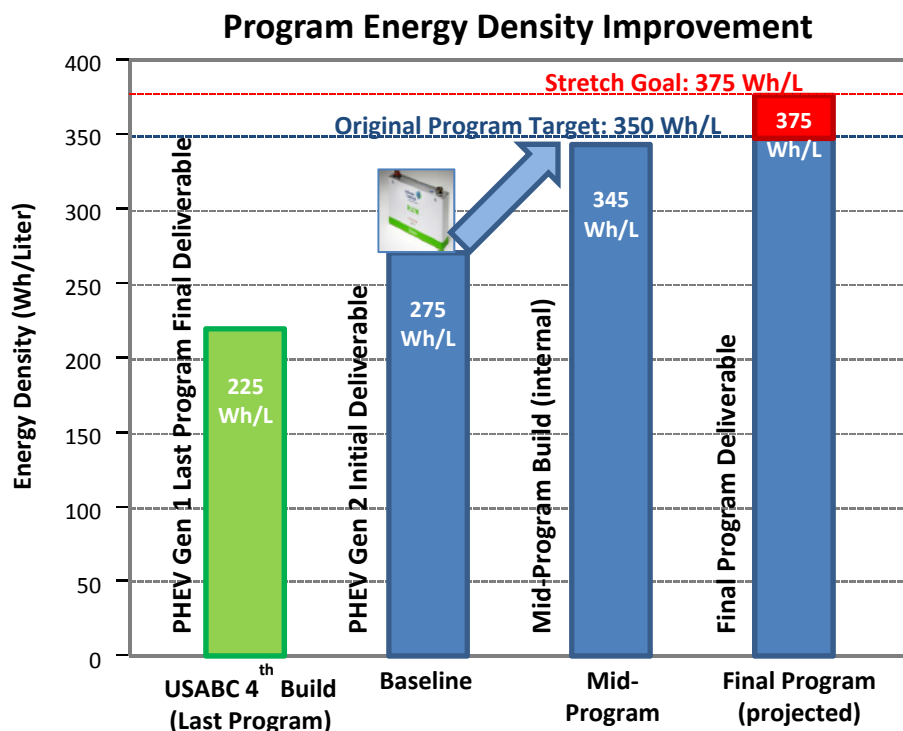


Figure II - 4: Energy Density Roadmap

Approach

The objective of the program was to increase the energy density of the cell and by so doing drive down the cost to capacity ratio, both directly (increased mAh/g, reduced BSF and cost) and indirectly (improved critical enablers: life and abuse tolerance). The focus was on active materials that fall midway on the ‘state-of-the-art’ to ‘high-risk’ continuum, with an effort to exploit their full, unrealized potential through concerted material, process, and mechanical design innovation. The family of $\text{LiNi}_x\text{Co}_y\text{Mn}_z\text{O}_2$ (where $x \geq 1/3$) was targeted for the cathode coupled with a graphitic negative material.

The following six improvement areas formed the framework of the program, all converging toward the central program goal of reducing the \$/kWh metric.

Higher Energy Density Materials: The first part of the program focused on evaluation of higher nickel content $\text{LiNi}_x\text{Mn}_y\text{Co}_z\text{O}_2$ (NMC6/2/2 where $x=6$, $y=2$ & $z=2$, and NMC4/4/2 where $x=4$, $y=4$ & $z=2$) as candidate materials for the positive electrode. Through rigorous testing, the high nickel and variously stabilized materials were shown repeatedly to offer no significant long-term benefits due to higher rates of degradation over time compared to baseline NMC1/1/1. Advantages of the high nickel materials seen at beginning of life were rapidly eroded as aging progressed. Thus, development efforts over the final two quarters focused on the down-selected NMC1/1/1, a second stabilized NMC1/1/1, and the NMC4/4/2.

For the negative electrode, initial approaches were aimed at high density and high compressibility materials, and blends of graphite materials, striving to define the limits of loading level and densification

where no adverse effects on life or abuse tolerance were incurred.

Electrode Processing Optimization: Novel slurry processing techniques were studied with three objectives: 1) reducing the quantity of N-Methyl Pyrrolidinone (NMP) solvent used in the positive electrode manufacturing process, 2) increased ratio of actives to inactives and 3) enabling electrode densification.

Drivers for the amount of solvent, conductive agent and binder used in the current process are intimately linked to the slurry mixing process, and its effectiveness in solids dispersion. Non-traditional mixing strategies of first compounding or pre-mixing active material with the conductive agent were explored as paths to solvent reduction, associated increase in active to inactive material ratios, and increased energy density. Activity during the final two quarters focused on in-line mixing, which proved the most promising of strategies tested.

Electrode Design Optimization: Electrode optimization focused on reducing the power to energy ratio (P:E) to the practical boundary where acceptable performance and life characteristics were maintained. This was achieved by the aforementioned campaigns to increase specific capacity of the active material, increase energy density of the coated electrodes, and increase the loading level itself.

Increased Upper V Limit and Increased SOC Window:

Window: Increasing the upper voltage limit beyond its current value of 4.1 V and expansion of the SOC window beyond 70% represents ‘free’ opportunity to increase energy density, reduce BSF and reduce \$/kWh, but adversely impacts life and abuse tolerance. To surmount these issues, stabilized active materials and stabilization of electrode/electrolyte interfaces were pursued.

Through testing, JCI identified the highest operating voltage limit where inevitable trade-offs in life remained acceptable in magnitude, and expanded

Table II - 4: Version Metrics and Performance

Cell Version	1-C Capacity (Ah)	Energy Density (Wh/L)	Discharge Power (W) (10s, 50% SOC)	Resistance (mOhm)	P/E Ratio
Baseline	27	275	1540	1.92	16
Mid-Program	33.3	345	1800	1.67	15
Final Cell	36.4	375	1970	1.52	15

JCI’s strategy of aggregating improvements from the six work streams introduced in the Approach section culminated in a step-change in energy density accompanied by enhanced understanding of the cell technology, which will benefit related work going forward. Accomplishments made in each work stream over the final two quarters of the program follow:

the voltage window from 25- 95% SOC to a stretch goal of 15-95%.

Mechanical Design and Advanced

Manufacturing: Significant effort was directed at advancing the cell design and manufacturing processes, striving to minimize the void volume in the cell and achieve a commensurate reduction in component and assembly costs. Some of the concepts investigated were:

- Thin wall cans with structural features.
- Mandrel elimination.
- Current collector design optimization.
- Reduced foil margin (wider electrode coated width).
- Alternate electrolyte fill hole closure techniques.
- Alternative internal and external cell insulation.
- Cell to cell interconnect improvements.
- Low cost neutral (plastic) enclosure.

Abuse Tolerance: Abuse tolerance improvement was viewed as a *critical enabler* to all other work aimed at increasing energy content of the cell, and was pursued on multiple parallel fronts;

- High temperature separator co-development with Entek.
- JCI’s Thermal Protective Barrier (TPB) technology.
- Overcharge protection additives. Tested both in the electrolyte and in the electrode itself.
- Low activation pressure vent.
- Mechanical overcharge protection device.

Results

Key design versions built within the program are presented in Table II - 4, which illustrates the notable 36% gain in energy density achieved over the program with no detriment to power capability of the cell technology.

Higher Energy Density Materials: Three NMC materials were down-selected as candidates for the final design; the baseline material (Cat_1), Cat_2 NMC (442) and Cat_4 (improved 111) following extensive testing using pouch cells. Test cells were built using JCI PL27M format and underwent initial capacity checks, power (HPPC), cycling (C/1 discharge, C/2 charge) at

45°C, and calendar life at 60 & 70°C, using the conditions:

- Full charge/discharge voltages: 4.2V, 3.3V.
- Max/min voltage for HPPC pulse: 4.3V, 2.5.
- C/1 discharge; C/2 charge cycling.

Figure II - 5 illustrates the capacity fade observed for the three NMCs that were considered for the final build. At the end of the evaluation period, the baseline material also showed the lowest absolute resistance, and led in cycle life, and was thus selected for the final deliverables.

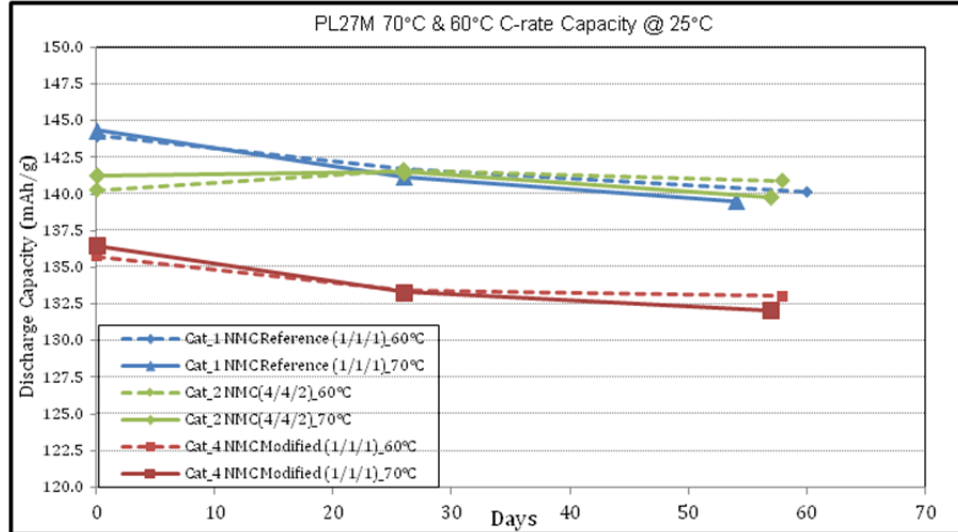


Figure II - 5: Final Build Candidate Calendar Life Results

Electrode Processing Optimization: The main impetus for the mixing work was to reduce the cost of electrode manufacturing by using a reduced amount of solvent, while minimizing the impact on the active and conductive materials. Non-recovered NMP is responsible for 12% of the total cost for production of a positive electrode, making the NMP reduction a clear path to lowering overall cost. In addition to the cost savings, improved cell density was achieved by the higher cathode density processed from high solids mixing.

After the dry compounding (mechanofusion) approach was eliminated in the first half of the program, focus shifted to continuous (in-line) mixing. Rental equipment was used to support a larger scale evaluation, and allowed optimization of feed sequence and strategy that resulted in stabilized feed rates and improved accuracy over several trial iterations. In the final execution, active and conductive materials were combined upstream of an NMP-diluted binder premix stream, and the high viscosity slurry was transferred to the bulk mix tank for final dilution. Scale-up resulted in 12% increase in % solids of the coated slurry, which translated to a final reduction in electrode thickness of

7%. An added benefit of the alternate process was reduced mixing-induced heating of the slurry, with only minimal cooling required. (See Figure II - 6.)

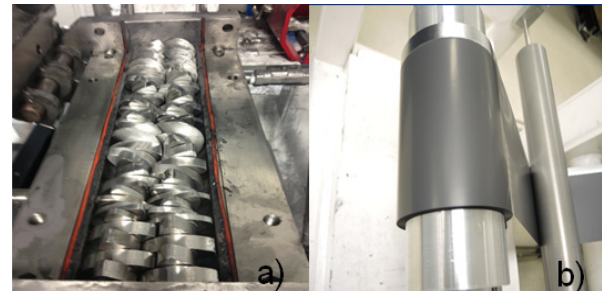


Figure II - 6: a) Inline mixer b) Calendared electrode (inline mixed)

The promising electrochemical results, observable improvement in conductive carbon dispersion degree, and ease of disassembly and clean-up encourage further consideration. A decision for manufacturing implementation will be made in early 2016, following financial payback analysis. Preliminary projections are presented in Figure II - 7 below.

Product	% Solids (relative to baseline)	Density (g/cc) (relative to baseline)	Potential Savings Solvent (only *) per cell
Power Cell - Cylindrical	+13.1%	+9.9%	\$0.05
Energy Cell - Cylindrical	+13.9%	+16.0%	\$0.31
Power Cell - Prismatic	+16.3%	+11.8%	\$0.06
Energy Cell - Prismatic	+8.7%	+7.8%	\$0.14

Figure II - 7: Product Cost Impact Projected from Pilot Trials

Electrode Design Optimization: Development activities falling under electrode design included densification, directly increased loading and formulation optimization, each of which was explored for both electrodes separately. These activities were closely coupled to the processing development work described earlier, whereby slurry manufacturing innovations

enabled exploiting established materials beyond existing boundaries. Over five successive prismatic cell builds, the achievable limits in each of the areas were defined, and informed the final cell design which is detailed in Table II - 5, tracking changes made between key versions.

Table II - 5: Electrode Design Parameters by Version

		Program Baseline	Mid-Program Cell	Cell in Post-Stretch
Cell Capacity		27Ah	33Ah	36Ah
Upper Voltage		4.1V	4.2V	4.2V
Usable SOC Window		70%	80%	80%
Cathode	Processing	Standard	Standard	Paste mix
	Loading	Standard	Standard	Standard
	Density	Standard	Standard	+7%
Anode	Loading	Standard	Standard	Standard
	Density	Standard	+14%	+10%
Electrodes Coating Width		Standard	+1%	+4.5%
Ceramic Coating on Anode		Original	Optimized	Optimized
Separator		Polyolefin	Polyolefin w/ low shutdown T	Polyolefin w/ low shutdown T
Electrolyte		Baseline	Baseline	Baseline + OC Add.
Mechanical Design		Mandrel	No mandrel and thin wall cans	No mandrel, thin wall can, optimized collectors and foil margins

Increased Voltage Limit and SOC Window:

Accelerated testing was conducted with prismatic cells at upper voltages of 4.1, 4.2 and 4.3V. The 4.2 V group showed acceptable power and energy fade, while the first generation (baseline) 4.3 V group was stopped due to poor results. Chemistry stabilization improvements resulted in life at 4.2V that meets EOL targets, and thus 4.2V was qualified as the new upper voltage limit.

To maximize cell utilization, the usable SOC window was expanded from 95-25% to 95-15%, with no adverse impact on life under a PHEV cycle regime.

Mechanical Design and Advanced Manufacturing

Numerous concepts were studied as potential paths to drive down components cost, assembly complexity, and improve cell energy density and performance. Key accomplishments from the final program quarters were:

- Thin-walled cells (0.8 x baseline) were used for final deliverables. Embossed cans with structural

features of varying geometries were shown through testing and simulation to offer some benefits (less thickness variation, reduced clamping force) but not enough to displace spacers used in the existing strategy.

- The assembly process of mandrel-less cells culminated in designs for mid-program and final cell builds, and brought a 3% capacity increase and 8% cost reduction. Controlling the shape of the jelly-roll during the assembly process was found to be critical, and a fixture was developed for this purpose (Figure II - 8a). The performance of mandrel-less cells showed no obvious internal structural difference when compared to baseline after 1000 cycles of C/2 cycling tests at 45°C (Figure II - 8b).

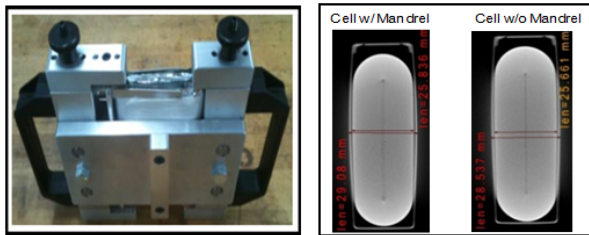


Figure II - 8: a) Mandrel-less cell assembly fixture b) CT images of cycled cells (with and without mandrels)

- Optimizations of foil margin and current collector design delivered another 4.5% capacity increase. Uncoated foil widths for both electrodes were reduced and rigorous component and cell level performance and abuse tests were used to validate the design change. A single-piece current collector design resulted in part reduction and assembly step elimination.
- Many sealing techniques were explored to replace the rivet and eliminate associated void volume. One lead candidate, torsional welding, was tested on the mid-program build, but eliminated (deemed unsuitable as a multi-platform solution). Lateral ultrasonic and pulse laser welding were tested in the final quarters, showing promise for pulse laser welding of an Al disk as a means of providing a robust seal with minimal cell deformation.

Abuse Tolerance: The large increase in energy content of the PHEV cell necessitated work on many fronts to also enhance abuse tolerance. Key

accomplishments of the final quarter are summarized below by area:

- Ceramic-filled separators lack shutdown function, which is considered an essential safety attribute for high energy cells. Efforts with Entek to adjust the ceramic/ polyolefin ratio to achieve full or partial shutdown and retain the life-enhancing properties were not successful. However, excellent performance was found when cells with ceramic filled separators were tested at 4.2V at 70°C. After one year storage, cell resistance only increased 34%, which is an unprecedented result.
- Thermal Protective Barrier (TPB) technology was optimized on thickness, coverage and uniformity, and led to demonstrated improvement in abuse tolerance.
- A low pressure vent was developed (45% baseline activation pressure) to determine if earlier activation and release of thermal energy and fuel might avoid or mitigate thermal runaway. Overcharge tests conducted with early prototypes failed to show a benefit. In a related effort, an overcharge protection device triggered by the low pressure vent was developed, whereby vent activation would support integration of the current interrupt function at the module level.

Additional cells with prototype-level features intended to enhance abuse tolerance were provided to SNL along with final design deliverables for comparative testing. (See Figure II - 9.)

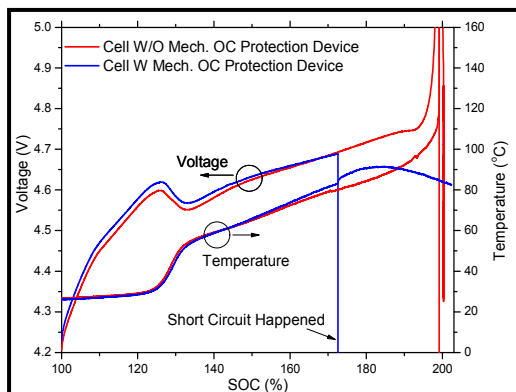


Figure II - 9: Overcharge test comparison for 36 Ah cells

- To accelerate abuse tolerance improvement through component level down-selection, JCI developed a penetration test yielding a higher degree of granularity than existing tests, which was used to elucidate subtle differences between candidate materials such as separators. This will be a valuable tool in future abuse tolerance optimization work at JCI. (See Figure II - 10.)



Figure II - 10: JCI Pin test

SNL's recent testing of JCI's final deliverable cells confirmed the improvement in abuse tolerance achieved

by the program; the 36 Ah cells in all cases exhibited equivalent or more benign EUCAR responses than the 27 Ah baseline cells tested in the previous program.

Conclusions and Future Directions

Fifty-three PHEV2 prismatic cells were delivered to USABC for National Laboratory validation testing; 9 baseline cells, 40 final deliverables, and an additional 4 cells with enhanced abuse tolerance features. All cells were built at JCI's R&D line in Glendale, WI, while a large portion of the continuous electrode material processing work was performed at JCI's Holland, MI Pilot Operation facility. Towards the end of this program a new JCI test facility, also in Holland, was used to conduct some of the final abuse tolerance testing.

In conclusion, the stretch goal of 375 Wh/L was met, up from a 275 Wh/L baseline value. This, along with many component level improvements contributed to a final projected system cost of \$2,460, an impressive 30% reduction over the program. Ultimately, the step change in cell-level energy density yielded a cell that would be better suited for a higher energy application, but the program resulted in enhanced understanding of chemistry and mechanical control factors that will add value to JCI's future development work in the lithium ion battery space.

FY 2014 Publications/Presentations

1. DOE AMR presentation (June 2014, Washington, D.C.)

II.A.3 Development of a High-Performance PHEV Battery Pack (LG Chem, MI)

Chulheung Bae (USABC Program Manager)

Subcontractor: LG Chem Power, Inc.

Mohamed Alamgir (Program Manager)

1857 Technology Drive

Troy, MI 48084

Phone: (248) 291-2375; Fax: (248) 307-1800

E-mail: alamgir@lgcpi.com

Subcontractor:

LG Chem, South Korea

Project Start: April 2010

Project End: December 2013

- Develop a cooling system that is electrically and mechanically robust and efficient.
- Develop a pack design that is modular, easy to manufacture and is close to the USABC cost target.

Accomplishments

- A wide range of material and electrode properties such as morphology, surface area and porosities was carried out to identify formulations optimal from performance and life points of view.
- Significant emphasis was given to optimize process conditions such as cell formation that affect the amount of formation gas and life.
- Cycle-life of the MRC cathode was found to be strongly dependent on the charge voltage as well as the SOC window of operation. Key among the root causes for cell degradation is the dissolution of Mn from the cathode particles and subsequent passivation of the anode.
- Electrolyte additives which enhance the life of the manganese rich cathode (MRC) material were studied and some potential candidates identified.
- Atomic layer deposition (ALD) coating of the cathode particle surface significantly improved the life characteristics.
- Material developed in-house demonstrates state-of-the-art cathode capacity and life. Current estimates show that this material when fully developed will lead to a cell cost <\$200/kWh.
- The thermal system and pack volumetric efficiency were significantly improved by optimizing compressor, evaporator designs as well as by improving the contact between the thermal fins and the cold plate.
- Two generations of large cells (24 and 60 Ah) were fabricated and delivered to National Labs for testing.
- Two generations of battery packs (5 and 18 kWh) were also designed, built and delivered to the National Labs for testing.



Introduction

Development of a cost-effective, high performance battery is a prerequisite for the successful introduction of PHEVs and EVs. The advent of new high specific energy cathode materials has opened up significant

Technical Barriers

The key technical barriers addressed were:

- Validation of the high capacity of new generation of Mn-rich cathode materials.
- Demonstration of cycle-life of > 5,000 cycles.
- Demonstration of calendar-life of 15 years.
- Make significant progress towards achieving the USABC pack cost target of \$3,400.

Technical Targets

- The objective of this project was to establish the high specific energy of new generation of Mn-rich cathode materials.
- Demonstrate both cycle- and calendar-life under USABC test conditions.

opportunities to achieve this objective. Low-cost, high capacity cathode materials using a large operational SOC window will result in the use of less active materials, thus lowering cost. In addition, development of a thermal management system that is more robust and simpler to implement than conventional, liquid cooled system is also important for advanced, next generation battery pack technologies.

Approach

To achieve the proposed objectives for a 40-Mile PHEV program, we have been studying cell chemistries based on next-generation Mn-rich layered-layered compounds, our patented Safety Reinforcing Separator (SRS) and a laminated packaging cell design. The goal is to understand, develop and optimize this cathode chemistry, corresponding anode and electrolyte compositions in order to meet the corresponding USABC targets. Evaluation of critical factors such as cathode and anode compositions, effect of binders and electrolyte compositions as well as the identification of conditions optimum for cycle- and calendar-life were the important tasks of the program.

Another important aspect of the work was to develop a pack that has superior thermal management and packaging using an indirect-cooled, refrigerant-cold plate system. This work was aimed at developing a thermal system that is thermally and mechanically robust with optimized volumetric and gravimetric efficiencies as well as cost.

Results

Material studies of the Mn-rich cathode: The layered-layered compound $x\text{Li}_2\text{MnO}_3(1-x)\text{LiMO}_2$ with reported capacities $> 250 \text{ mAh/g}$. has one of the highest specific energies of any high voltage cathode materials currently being studied. To obtain such high capacity, however, the material needs to be charged to voltages as high as 4.6V. An additional feature of this material is that it is characterized by high surface area and has low conductivity at low SOCs. There is also the phenomenon of voltage fade that lowers cell energy and is also undesirable from the battery control point of view. To improve upon these drawbacks, LG carried out systematic studies to optimize electrode formulations, evaluated cell performance as a function of charge voltages, modified cathode particle surfaces using a variety of approaches, studied a range of electrolytes and optimized cell process parameters such as formation conditions, etc. These studies led to the following key observations.

- Durability of the cell is critically dependent on the charge voltage during cycling/storage. Operation above ~ 4.35 leads to significant

reduction in cycle-life. Cathode surface modification and electrolyte composition appear to mitigate these drawbacks to some extent (Figure II - 11).

- A large amount of gas generation takes place during activation and high voltage operation. This causes significant cell swelling and premature cell failure. Surface treatment of the cathode particle improves this drawback.
- Continuous structural evolution of the cathode during cycling appears to lead to voltage fade. Surface coatings do not appear to be effective in alleviating this disadvantage.
- Dissolution of Mn from the cathode and its migration to and subsequent passivation of the anode remains the key mechanism that controls cell life. Modification of the particle surface with conformal coatings such as ALD appears to significantly improve material durability.

Summary highlights of the above data are shown in Figure II - 11, Figure II - 12, and Figure II - 13.

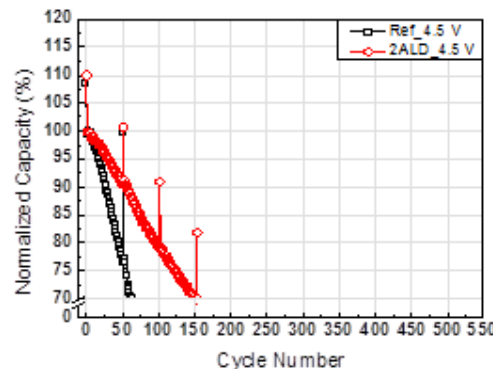
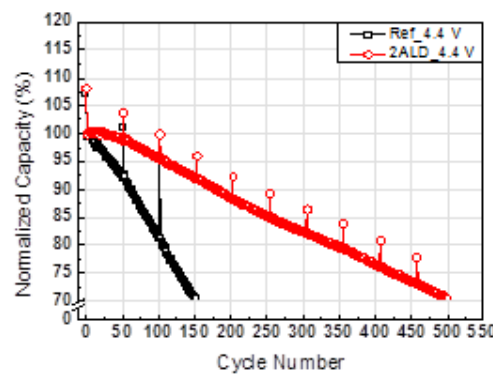


Figure II - 11: Beneficial effect of charge voltage and surface coatings on cycle-life. Top: Data show the effect of ALD surface coating on the cycle-life at 45°C. The cell was charged at 0.5C and discharged at 1C. Bottom: When the charge voltage was raised to 4.5V, instead of 4.4V as in Top figure, there is a substantial decline in cycle-life

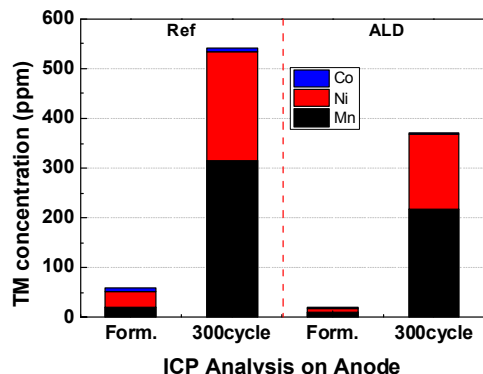
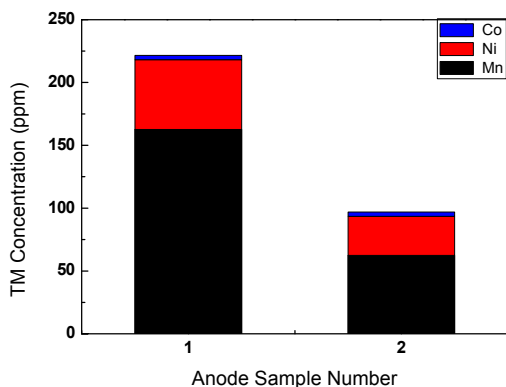


Figure II - 12: Top) Effect of formation voltage on the amount of transition metal deposited on carbon anode. Sample 1 was formed at 4.6V. Sample 2 was formed at 4.4V. Note the significantly large quantity of Mn deposited at 4.6V

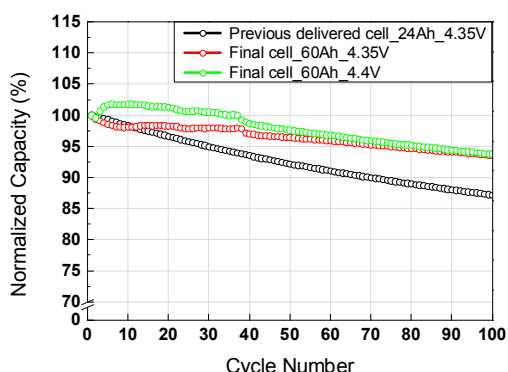


Figure II - 13: Comparison of the cyclability of 1st generation blended cathode-based 24Ah and the 60 Ah MRC cells at 45°C. Cycling carried out at 0.5C charge and 1C discharge currents to a discharge voltage of 2.5V

Pack Development

Two generations of packs (5 and 19 kWh) utilizing a refrigerant-to-coldplate cooling concept were developed (Figure II - 14). The essential components for this self-contained battery pack included solid fins, a cold plate, compressor and evaporator. Studies were carried out to optimize these components with respect to cooling and volumetric efficiency, manufacturability and cost. For example, compressors of different ratings were studied (e.g., 12V, dual 12V or a single 24V) to determine their efficacy in thermally managing the cells during cycling. The second generation of packs contained the 60 Ah cells.

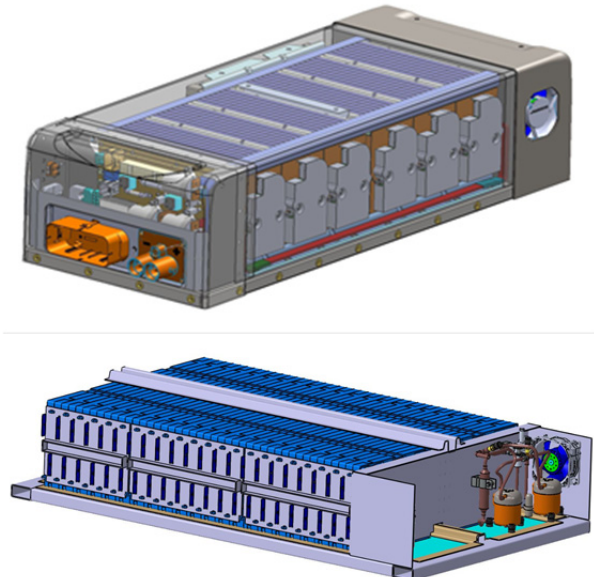


Figure II - 14: Schematic of the two generations of packs we delivered to USABC. While the top pack was used to design, develop and optimize the thermal system components, the bottom PHEV- 40 pack used the actual 60 Ah program cells. The thermal chamber containing elements such as the compressor, the cold-plate and the evaporator is on the right while the electrical chamber is on the left of the top packs (top pack). The bottom pack has the thermal and the electrical system both in the same side

Multiple design iterations led to the development of a pack using an indirect cooling method comprising a refrigerant-to-cold plate system. These packs have been built and delivered to the USABC for testing by the National Labs. Their thermal behavior is summarized in Figure II - 15.

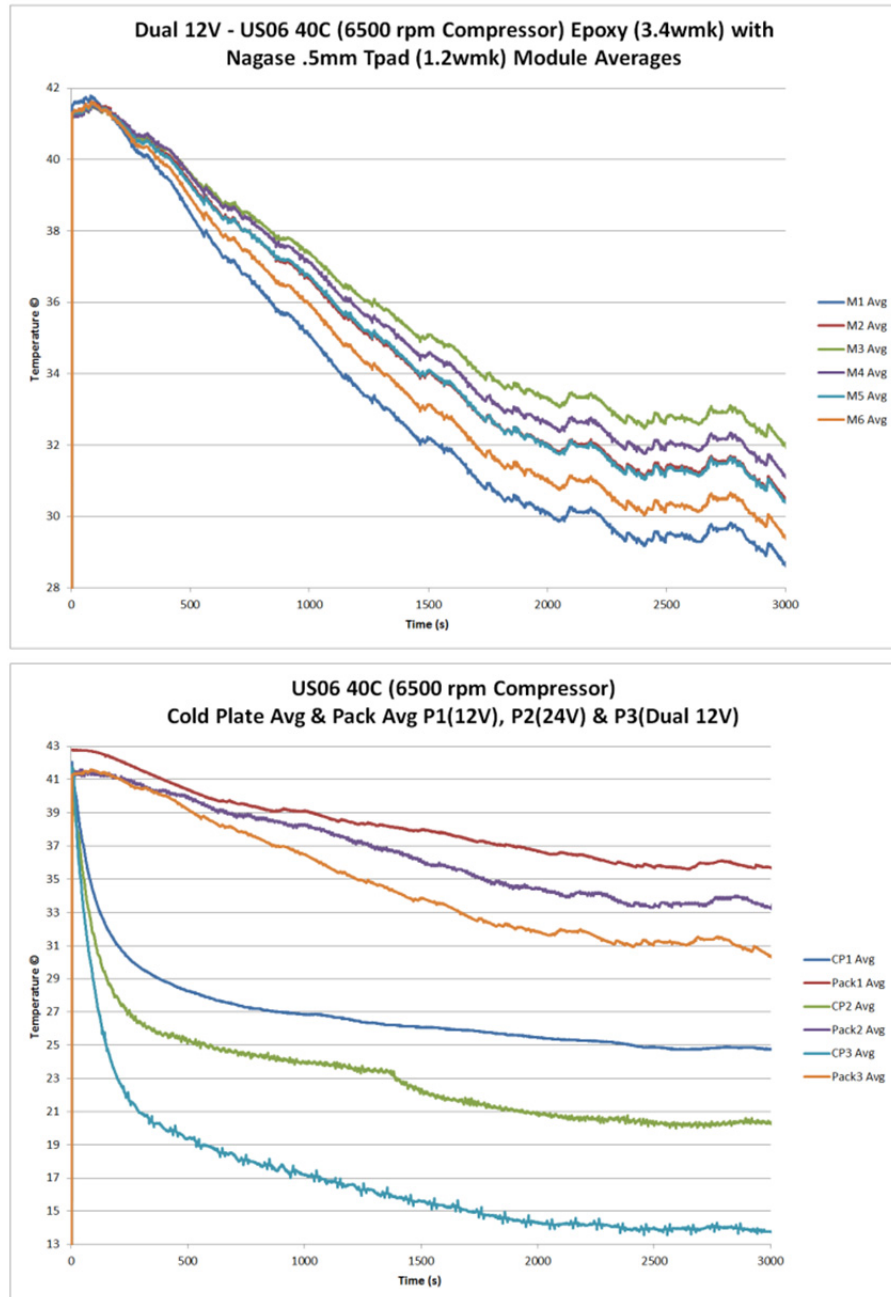


Figure II - 15: Examples of the thermal performance of the pack using the cooling system we have developed. The top figure shows the average temperature of the modules during US06 cycling at 40°C. The data show that the modules are within 4°C of each other, indicating uniform and efficient cooling. Bottom figure compares three different packs using different compressor ratings (single 12V, dual 12V and a 24V). The associated cold-plate temperatures are also shown in the graph. The cold plate temperature is the bottom curve

Conclusions and Future Directions

Comprehensive studies were carried out to utilize the MRC-based cathode to develop a cell that is capable of meeting the PHEV40 mile targets. By first studying its behavior under various test conditions and examining

its failure modes, efforts were made to improve upon the materials properties. We studied the impact of various formation voltages on capacity and cyclability as well as the effect of voltage limits on cyclability. Based on these results, studies were carried out to identify effective solutions such as multi-stage formation and

degassing protocols, doping and coating of cathode powders, use of electrolyte additives, and use of cathode blends. The 1st generation cells consisted of cathode blends, whereas the 2nd generation used an ALD-coated MRC cathode. Although both of the cathodes showed promising initial specific energy and power, both types of cells exhibited less than adequate life characteristics. The cycle-life of the cells was critically dependent on the charge voltage limit. When charged beyond 4.4V to increase the capacity, there was a significant decay in cycle-life. Significant gassing, Mn dissolution and consequent anode passivation were the key failure modes. Conformally coating the cathode particles using ALD considerably enhanced the cycle-life; however, it did not mitigate the voltage fade issue. The cells, though, showed good preliminary abuse characteristics.

Significant efforts were devoted to developing a novel thermal management system based on the concept of indirect cooling using a refrigerant, coldplate and solid fin. Work was carried out to optimally package cells into modules mechanically and electrically, optimize the compressor size, attach fins to the

coldplate, etc. to develop a pack that is volumetrically and gravimetrically efficient. We believe that this cooling system once fully optimized will be highly attractive for PHEV and EV applications.

Considerable insight into the material properties and ways to improve upon them for the MRC cathodes have been obtained in this program that will be highly valuable to the development of a high energy, long-life and low-cost battery for PHEVs. Similarly, the development of a stand-alone, self-contained battery pack provides a good alternative to packs built using conventional cooling methods such as liquid and air.

FY 2014 Publications/Presentations

1. 2014 DOE Annual Peer Review Meeting Presentation.

II.A.4 Development of a PHEV Battery (Xerion)

Renata Arsenault (USABC Program Manager)
Subcontractor: Xerion Advanced Battery Corp.

Dr. John Busbee (Program Manager)
60 Hazelwood Drive
Champaign, IL 61820
Phone: (217) 265-5215; Fax: (866) 242-1069
E-mail: j.busbee@xerionbattery.com

Subcontractor:
Polaris Battery Labs, Portland, OR

Start Date: July 2014
Projected End Date: October 2015

Objectives

Implement StructurePore™ technology to produce low-cost, high-power and high-energy batteries for next generation Plug-in Hybrid Electric Vehicles (PHEV).

- Design and produce cells with maximized energy density at the USABC power density goal by optimizing electrode structural parameters.
- Deliver 36 prototypes (18 Xerion StructurePore™ cathodes with traditional anodes, and 18 optimized cells with Xerion cathodes and Xerion anodes) to USABC.
- Demonstrate the technology's potential for the automotive application space through performance results and cost projections.

Technical Barriers

The StructurePore™ electrode is composed of a thin layer of active material conformally deposited on a 3D nanostructured current collector. The key to the realization of large-format, commercially viable batteries is the capability of producing highly scalable and manufacturable 3D conductive porous scaffold as current collectors. In addition, because the active material is synthesized using a non-conventional, low-temperature method, significant development efforts are needed to ensure that their electrochemical performance (specific capacity, cycle life, etc.) is comparable to or better than those made using conventional methods.

Technical Targets

- Develop a carbon scaffold for both electrodes that has the requisite electrochemical and mechanical properties.
- Develop a PHEV cell parametric design tuned for lower power to energy ratios than the baseline design.
- Demonstrate cycling capability of the proposed chemistry, which falls in the family of lithiated manganese oxides. Both layered and spinel phases are being investigated for data-driven down selection.
- Develop and demonstrate a robust solution for welding to the carbon scaffold, and demonstrate using a multi-layer stack and custom fixture capable of automotive relevant C-rates.
- Develop accurate production cost potential vs standard reference Li-Ion technology.
- Develop scalable and manufacturable processes to produce StructurePore™ electrodes.
- Produce 18 full cells that consist of Xerion StructurePore™ cathodes and traditional graphite anodes. Each cell has a total capacity of > 920 mAh, gravimetric energy density of > 197 Wh/kg, and volumetric energy density of > 350 Wh/L.
- Produce 18 full cells that consist of Xerion StructurePore™ cathodes and Xerion StructurePore™ anodes. Each cell has a total capacity of > 920 mAh, gravimetric energy density of > 197 Wh/kg, and volumetric energy density of > 350 Wh/L.

Accomplishments

- Demonstrated large-scale 3D nanostructured carbonaceous current collectors.
- Demonstrated spinel LMO (lithium manganese oxide) active material made by electrodeposition.
- Demonstrated mixed-phase LMO active material made by electrodeposition.



Introduction

Xerion Advanced Battery Corp (XABC) proposes a 3D electrode technology called StructurePore™, which is composed of a thin layer of active material directly electroplated on a 3D nanoporous current collector. The 3D current collector provides an efficient electron

pathway and a large surface area for high material loading. The pores in the structure enable ions to shuttle quickly in the electrolyte between electrodes, and the thin active material coating significantly reduces the solid-state ion diffusion length compared with the microscaled active material particles in conventional batteries. Thus, the StructurePore™ electrode strives to increase power while maintaining energy. Xerion has initially demonstrated cells with 96 Wh/kg and 161 Wh/L at 1C and exceptional power and rate capability performances, achieving 90% state of charge in five minutes and delivering 30,000 W/kg at a 290C discharge. According to theoretical calculations, a geometrically optimized StructurePore™ can achieve much higher energy densities (>197 Wh/kg and >350 Wh/L).

Since the StructurePore™ electrode utilizes 3D nanostructure templating and low-temperature electrodeposition instead of active material powder processing (high-temperature), it can potentially reduce raw material cost significantly. The process uses a fundamentally different and lower cost bill of materials than traditional lithium ion battery manufacturing, avoiding the lithiated metal oxide powders which are the largest contributor to today's current technology cost. In addition, the reduced internal resistance and porous nature suggest the potential to deliver improved cycle life and enhanced safety for a given commercial battery material. Because of the material-agnostic nature of this architecture based technology, it can also be applied to future, high-energy chemistries, allowing a continued technology development pipeline to ensure high performance as new materials technologies mature.

Approach

Xerion is refining materials and processes for electrodepositing high quality, lithium manganese oxide (LMO) active materials on large-scale 3D carbon scaffolds at a power/energy balance that is optimized for PHEV applications. An array of analytical tools, including scanning electron microscopy (SEM), x-ray diffraction (XRD), transmission electron microscopy (TEM), and x-ray photoelectron spectroscopy (XPS), and elemental analysis are being used to characterize the active materials so as to understand and correlate the observed improvements in cyclability as compared to other developments in these materials as reported in the literature. Initial parametric design of the electrodes and their comprising scaffolds are being performed to at a design point to meet program power and energy goals. Starting material features and final battery performance parameters are being correlated to controllable process variables and in situ variables of interest (such as pore size and surface area) to create process maps to optimize cell performance. Xerion Advanced Battery Corp

(XABC) is also evaluating a selection of commercial electrolytes' and separators' effect on cell performance.

Moving beyond the laboratory scale, Xerion is working with Polaris Battery Labs (Portland, Oregon) on the development of larger-scale, pouch cell prototypes. Polaris specializes in solving problems related to scale-up and the fabrication of pouch cells.

Results

3D Nanostructured Current Collectors: Carbon is lightweight, conductive, and electrochemically inert over a broad voltage window, making it an attractive candidate as a current collector material. XABC has successfully developed a highly scalable and manufacturable method to produce nanostructured 3D carbon current collectors (Figure II - 16). The fabrication utilizes a template inversion process, allowing strategic control of the template structures by the particle size and processing conditions. Increasing through-pore size, as measured by capillary porometry, improves power performance. Increasing surface area, as measured by a BET surface analyzer, enhances energy density for a given power density. Xerion is currently focused on tuning scaffold parameters to a pore size/surface area balance which optimizes the power/energy balance in the region that best meets USABC performance goals, while preserving cost and safety benefits. To maximize the performance of the carbon scaffold, XABC is evaluating a number of polymeric carbon precursors in terms of mechanical robustness and electrical conductivity.

In another work stream, Xerion is conducting development and testing to ensure that welding to the C-scaffold can be achieved and that the aluminum to carbon joint remains robust over time. To this end, XABC is evaluating galvanic corrosion of aluminum with respect to the carbon scaffold in the presence of electrolyte and is additionally examining several welding methods and configurations.

Active Materials: Xerion has previously demonstrated an electroplated lithium cobalt oxide (LCO) system with crystal structure and electrochemical performance similar to commercial LCO materials. Using the same plating method, the team has realized a direct, conformal deposition of LMO on carbon scaffolds (Figure II - 17a). Its charge/discharge voltage curves exhibit a lithium-rich spinel LMO behavior with a 4.1 V average voltage and 103 mAh/g active material based capacity (Figure II - 17b). The electroplated spinel retains at least 90% of the initial capacity after 100 cycles. Compared to the standard spinel, lithium-rich spinel may offer an improved cycle life because the increased manganese valence can reduce both Jahn-Teller distortion and manganese dissolution. Further development on this system will focus on understanding the crystal structure by advanced material

characterization tools, optimizing electrodeposition conditions, and extensive cyclability studies.

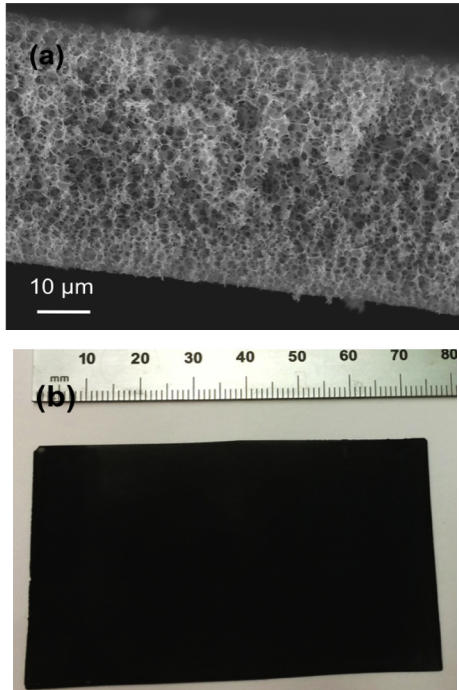


Figure II - 16: (a) Cross-sectional SEM image of carbon scaffold. (b) Optical image of carbon scaffold fabricated in a scalable and manufacturable method

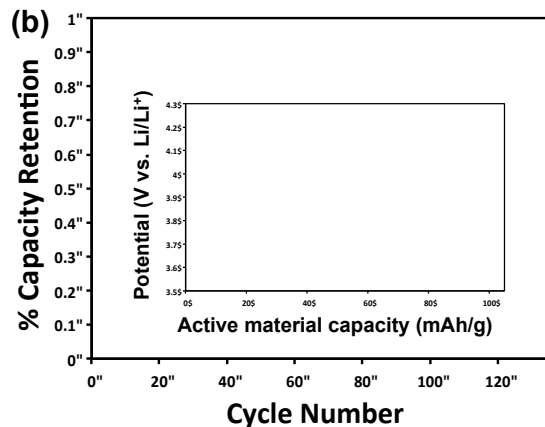
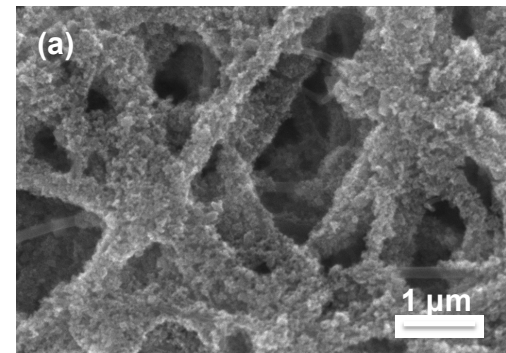


Figure II - 17: (a) SEM image of lithium-rich spinel LMO electroplated on carbon scaffold. (b) Cycle life and charge/discharge voltage profiles (inset) of such cathode

Xerion has also concurrently explored other LMO materials that are electroplated from aqueous solutions. Figure II - 18a shows the voltage profiles of mixed layered (Li_2MnO_3) and spinel (Li_2MnO_4) LMO. The layered component can stabilize the spinel phase, and also provides additional capacity once activated at high voltage (4.6 V). XABC is actively investigating this material system. Initial effort has demonstrated mixed phase LMO with 275 mAh/g active material based capacity. Extensive studies on cycle life will be performed in the beginning of next quarter.

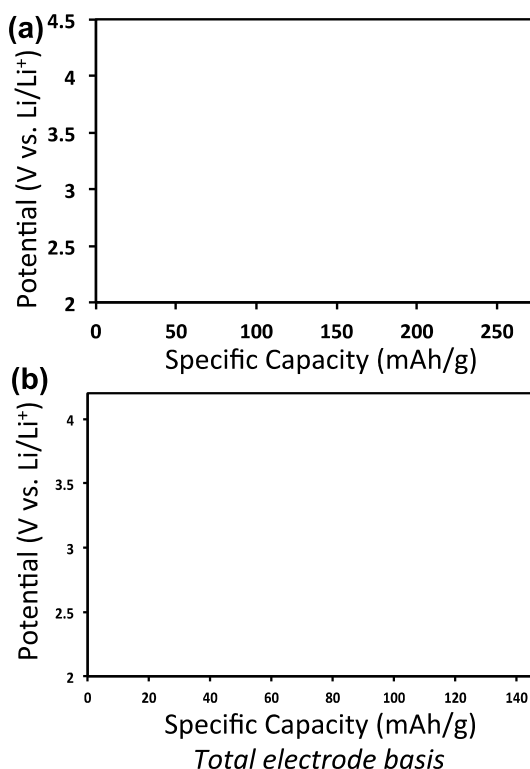


Figure II - 18: (a) Charge/discharge voltage profiles of mixed layered (Li_2MnO_3) and spinel (Li_2MnO_4) LMO.
 (b) Charge/discharge voltage profiles of mixed spinel and $\gamma\text{-MnO}_2$ phases electroplated on carbon scaffold

Another LMO system that Xerion has developed is mixed-phase spinel and $\gamma\text{-MnO}_2$. The spinel phase can significantly improve the cycling stability of $\gamma\text{-MnO}_2$, leading to 90% capacity retention after 100 cycles. Such LMO system has an electrode-based capacity of 140 mAh/g (Figure II - 18b). Because of the relatively low average voltage (2.8 V), further development is needed to enhance its material capacity.

Conclusions and Future Directions

Xerion has developed a scalable and manufacturable method to fabricate large-scale nanostructured carbon current collectors. The team has conducted a series of characterizations and optimizations on the carbon scaffold to maximize energy density of the electrode at the USABC power density goal. In the meanwhile, Xerion has also realized the so-called lithium-rich spinel lithium manganese oxide (LMO) that possesses an encouraging cycle life (> 90% after 100 cycles). Additionally, the team has continued to improve the properties of mixed-phase LMO by refining their electroplating and post treatment conditions. The recent result on the stabilized $\gamma\text{-LMO}$ has shown 140 mAh/g electrode-based capacity and > 90% retention after 100 cycles. Both spinel and mixed-

phase LMO systems are currently selected as candidates for further material characterization and test.

Xerion plans to continue its development of carbon scaffold and LMO active materials to further improve the electrode properties. This effort will produce prototypes to validate the manufacturing processes, performance of the nanostructured cathode versus a traditional carbon anode, and performance of an optimized cell design to simultaneously realize improved energy density, sustained high power, high charge acceptance and cost reduction.

FY 2014 Publications/Presentations

1. Presentation, Integrating Energy Storage Onto the Grid: A JCESR Symposium, Oct 2014.

II.A.5 Energy Storage System for High Power LEESS PAHEV Applications (Maxwell Technologies)

Scott Jorgensen (USABC Program Manager)
Subcontractor: Maxwell Technologies, Inc.

Allen Stoneberg (Program Manager)
3912 Calle Fortunada
San Diego, CA, 92123
Phone: (858) 380-3582
E-mail: astoneberg@maxwell.com

Subcontractor:
University of Rhode Island

Start Date: January 2011
End Date: April 2014

Objectives

- Demonstrate the technical and economic feasibility of advanced capacitors in the Power Assisted Hybrid Electric Vehicle (PAHEV) market.
- Develop and demonstrate a new architecture for cell and system design which is cost effective, compact and light.

Technical Barriers

- Low temperature performance supporting operation at -30°C.
- Improved energy density via an increased stable operating voltage window.
- Major cell and system cost reduction to meet program and USABC gap chart targets.

Technical Targets

- Design, build, and test hybrid advanced capacitor cells and packs capable of meeting USABC goals for LEESS PAHEV applications.
- Develop and utilize a stable electrolyte system that has a voltage window of 4.0 V or higher and can operate in the temperature range of -30 to 52°C per the USABC specification.
- Identify optimal electrode materials for higher energy, lower impedance, and stability at increased potential over lifetime, and lower cost relative to existing commercial capacitive technologies.

- Source a separator that represents a significant cost reduction while maintaining or exceeding existing performance and safety metrics.

Accomplishments

- Completed and shipped the final deliverable Maxwell LEESS packs and sub-modules to Idaho National Laboratory, National Renewable Energy Laboratory, and Sandia National Laboratory for testing.
- Completed RPT6 cell tests at INL and cell abuse tests at SNL on third generation cells.
- Completed the Cost Model with final System Price meeting the program target.
- Submitted Final Program Report.



Introduction

The Maxwell-USABC Low Energy, Energy Storage System (LEESS) Program was initiated to demonstrate the application of advanced capacitors in the Power Assisted Hybrid Electric Vehicle (PAHEV) market. PAHEV applications are well suited to the combined power and energy density afforded by the higher energy density of the advanced capacitor cells.

This program was concluded in April 2014. Over the course of 38 months the research funded by this program resulted in the development of advanced capacitor technology and significantly improved the performance of such devices in areas of operating voltage, low temperature performance, and cost effective manufacturing.

The Maxwell USABC LEESS program was comprised of multiple objectives and has been a challenging effort. Specific technical issues emerged in subjects spanning core cell chemistry to electronic component selection. Those issues were successfully navigated such that the fundamental objective – the technical proof-of-concept of advanced capacitor cells and systems in the PAHEV automotive application – has been demonstrated.

New approaches to cell packaging and system manufacturing were focused on significantly reducing the system selling price.

Approach

Leveraging capabilities in low cost ultracapacitor manufacturing, Maxwell has developed a new large format advanced capacitor cell capable of cycling to at least 4.0 V with good low temperature performance. The compact and economical design of this large cell is key to a pack architecture that combines low cost, weight and size while meeting LEESS power and energy requirements.

Cell performance has been improved by:

- Identifying and selecting the highest performing anode and cathode active materials based on over a decade of previous active material experience.
- Identifying and selecting a stable electrolyte in conjunction with the University of Rhode Island.
- Identifying and characterizing separator materials with good performance.
- Use of a completely dry, solvent-free electrode fabrication process to decrease cell manufacturing cost and increase cell lifetime.
- Quantifying performance/weight/size reduction of new cell architecture via cell-level electrochemical and physical testing

Pack design was based on USABC system performance, physical and cost requirements and incorporated the 2200F advanced capacitor packaged in a pouch cell. The pack design went through several revisions until an optimal configuration of control electronics, cell-string assembly, sub-module design, and thermal control was achieved.

Final configurations of cells, sub-modules and LEESS packs were tested for performance and life at Idaho National Laboratory, for abuse tolerance at Sandia National Laboratories, and for thermal performance at the National Renewable Energy Laboratory.

Results

Electrode Development: The electrode material and processing method was selected earlier in the program. The overall configuration of the 2200F third generation cell was frozen in early-2013 in order to accommodate the time required for the large cell build necessary for the final cell and pack shipments.

The focus of electrode development in 2014 has been on the further optimization of the Maxwell dry process for reduced film thickness, improved electrode formulation and other electrode structural properties.

Electrolyte Development: As reported earlier, after much investigation into alternatives, the current Maxwell control electrolyte was selected for the third generation cell and proved to be stable in a temperature window of -20 to 55°C.

Separator Development: After an exhaustive review of available separators, the Maxwell control separator was selected for the third generation cell and has proven to be stable and cost effective.

Cell Development: In 2013, a sample of 3.8 Wh third generation advanced capacitor cells were produced and shipped to Idaho National Laboratory for testing. Internal HPPC beginning of life data indicated that the cell chemistry meets LEESS performance targets (Figure II - 19). Work continued in 2014 on electrode, separator and electrolyte improvements.

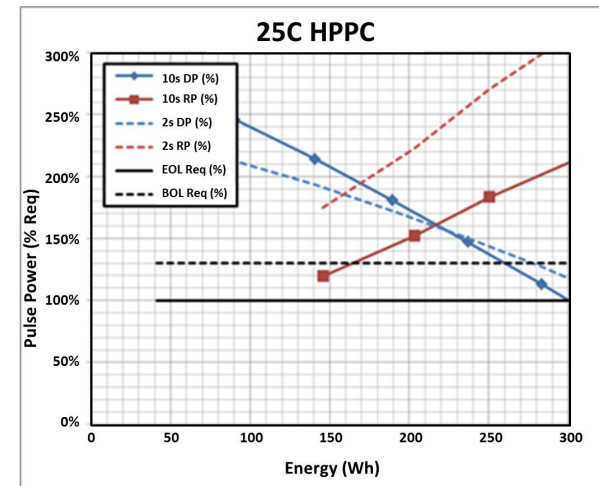


Figure II - 19: 3.8 Wh Third Generation HPPC BOL Pulse Power Capability

LEESS Pack Development. In 2014, Maxwell LEESS packs (Figure II - 20) and sub-modules were produced in quantity to meet shipment deliverables. Packs were shipped to INL (performance) and sub-modules were shipped to NREL (thermal) and SNL (safety) for testing.



Figure II - 20: Maxwell LEESS Pack

Cost Modeling: System cost was a critical program element and all decisions from cell component selection to system design were driven by the cost model. The end-of-program selling price for an annual production rate of 100,000 Maxwell LEESS packs was determined to be \$917 approximately matching the program target of \$920.

Conclusions and Future Directions

Table II - 6 lists the USABC LEESS HEV Gap Analysis showing USABC requirements, end-of-program status and post-program status.

At its conclusion, the system met most program requirements (Table II - 6) with low temperature operation, size, weight and selling price being the remaining gaps. However, cell development and film thickness work that proceeded beyond the configuration freeze of 2013 and throughout 2014 resolved the low temperature operational requirement leaving cost, size and weight as the remaining open items.

The overall program produced the following:

- A 2200F rated 1.1Ah advanced capacitor pouch cell that, in the final configuration based on improvements completed beyond the program, indicates that it can be the basis for a future pack

design that meets all USABC-PAHEV Gap Chart requirements.

- A pack module architecture and design that enabled the testing of the new cells in the full system configuration, demonstrated a sophisticated pack design, and provided a platform for Maxwell automotive pack development experience.
- Lab-scale production equipment and processes to manufacture electrodes, cells and packs in limited quantity and validate key production metrics.
- A fully developed cost model for the third generation cell and Maxwell LEESS pack based on an system annual demand of 100K.

FY 2014 Publications/Presentations

1. 2014 DOE Annual Peer Review Meeting Presentation.

Table II - 6: 2014 Gap Analysis (note: Selling Price target in the program Statement of Work was \$920)

USABC LEESS PAHEV		USABC Required EOL		End of Program 2014 EOL		Post Program 2014 EOL	
End of Life Characteristics		Unit		PA (Lower Energy)		PA (Lower Energy)	
2s / 10s Discharge Pulse Power	kW	55	20	55	20	55	20
2s / 10s Regen Pulse Power	kW	40	30	40	30	40	30
Maximum current		A		300		250	
Energy over which both requirements are met		Wh		26		26	28
Energy Efficiency		%		95		96.1	
Cycle-life		Cycles		300,000 (HEV)		300,000 (HEV)	
Cold-Cranking Power at -30°C		kW		5		3	5.5 kW @ -30 °C
Calendar Life		Years		15		15	
Maximum System Weight		kg		20		35	31.5
Maximum System Volume		Liter		16		33	33
Maximum Operating Voltage		V _{dc}		<=400		320	328 VDC
Minimum Operating Voltage		V _{dc}		>=0.55 V _{max}		0.56	180 VDC
Unassisted Operating Temperature Range		°C		-30° - 52°		-20° - 52°	-30° - 52°
30° - 52°		%		100		67	100%
0°		%		50		37	50%
-10°		%		30		21	30%
-20°		%		15		9	16%
-30°		%		10		6	10%
Survival Temperature Range		°C		-46 to +66		-46 to +66	-46 to +66
Selling Price/System @ 100k/yr)		\$		\$400		\$917 (see note)	\$917 (see note)

II.A.6 Development of 12V Start-stop Microhybrid Batteries (Saft)

Harshad Tataria (USABC Program Manager)
Subcontractor: SAFT

Michael Duffield (Program Manager)
13575 Waterworks Street
Jacksonville, FL 32221-2215
Phone: (904) 861-1521; Fax: (904) 772-1463
E-mail: michael.duffield@saftbatteries.com

Subcontractor:
Wildcat Discovery Technologies,
Virginia Commonwealth University

Start Date: April 2013
End Date: April 2014

Objectives

- To develop an advanced, high-performance battery for 12V Start-Stop (12VSS) vehicle applications based on Saft's advanced NMC-LTO lithium-ion battery technology.

Technical Barriers

The cost of the technology is the single most critical challenging requirement and a generally acknowledged critical path to widespread deployment of the Li-ion battery in the automotive industry. About 20% of the cost of a robust cell design in volume-production today is in the cell hardware. Cell hardware is anything other than electrodes including the foils, separator, and electrolyte. Another 50% cost burden is added as cells are integrated into a turnkey battery pack. Thus, the hardware in a Li-ion battery pack is responsible for a combined 80% of the cost add-on before indirect costs (G&A, O/H, and Profit), and is the single most significant part of the total unit cost.

A dramatically different approach to the way Li-ion cells are fabricated and assembled into a battery is needed for a significant reduction in the hardware cost.

Technical Targets

- Develop a novel cell assembly process which reduces the overall battery cost.
- Reduce elevated temperature impedance growth in order to meet cycle life requirements.

- Identify polymer materials that can hermetically seal the stack from external moisture and prevent electrolyte egress.
- Optimize LTO and electrolytes for -30°C performance, while maintaining calendar life and cycle life up to 75°C.

Accomplishments

- Saft has successfully supplied NMC based Li-ion cells for high power, high temperature automotive application.
- Saft is producing the NMC line of products in two formats, cylindrical and prismatic.
- Saft LTO technology has excellent power capability with a 15s pulse-discharge impedance of around 1.6 mΩ in small cells.



Introduction

Saft's NMC-LTO technology is expected to meet or exceed the USABC requirements for this application, with the exception of cold crank power. Saft can meet all of the performance requirements for power, cycle life, etc. using the LTO technology already demonstrated. Integration of Saft's high temperature stable NMC technology will allow for additional improvements to cell calendar life. Accordingly, a development program is devised and proposed to scale up the Saft LTO technology from the small cells produced to a 10-20Ah prismatic cell to be manufactured in a Saft hard can PHEV-2 VDA size cell as a demonstration of the technology's ability to meet the cost and size requirements.

Approach

A key innovation in the effort, primarily focused on cost reduction, is combining the cell and module packaging in a single injection-molded thermoplastic polymer (IMTP) monoblock. Further proposed cost reductions include optimization of the electrolyte and NMC cathode to meet the cold-cranking requirements and reduction in cost. LTO is a chemistry particularly well suited to this optimization, as the lack of Solid-Electrolyte Interphase (SEI) allows for the use of very low cost, low temperature electrolytes.

In order to reduce the electrode material costs, the LTO manufacturing process is being addressed by large

volume manufacturers of TiO₂ for the paint industry. This could result in extremely low cost LTO, giving a significant cost advantage over graphite-based Li-ion.

With the cost reduction advantages offered by LTO chemistry and the monoblock module design, the proposed NMC-LTO monoblock battery system will meet the USABC cost target.

Results

Polymer Material Study: Saft worked with Virginia Commonwealth University, VCU, to conduct a paper study of potential polymer material candidates for the monoblock housing. The result of this study was a short list of polymers which possessed the desired characteristics for the monoblock and would be evaluated further for compatibility with the proposed electrolyte for this battery.

The polymer to electrolyte study, also conducted by VCU, exposed the polymer candidates to various solvents over a period of time and tests were conducted to quantify the effect of the exposure. The result of this testing was identification of a likely polymer material for the proposed Saft monoblock. This material, which is already being used widely in the automotive industry, is not only strong, stiff and extremely chemically resistant, but also suitable for injection molding.

Electrolyte Development: Initially, cells were built using our low temperature electrolytes which were previously developed for our graphite anode Li-ion cells. The study of novel electrolytes is limited with LTO based Li-ion cells. Saft is investigating numerous typical and atypical solvents along with different salts and molarities. The testing of the electrolytes with SAFT provided electrodes is sub-contracted to Wildcat Discovery Technologies (WDT).

Work was focused on a select set of electrolyte formulations for optimal low temperature performance while maintaining stable high temperature impedance growth. Coin cells were screened for low temperature performance, and gas generation at elevated temperatures.

WDT completed the Phase 1 or “Method Validation” by the end of the second quarter of the program. The WDT results correlated with Saft internal results. In addition, the WDT results proved the validity of the use of coin cells for this study. In phase 2 of the WDT work, WDT would provide cell performance testing with various formulations Saft selected for investigation. This phase was split into 2 sub-phases a & b. These were conducted in series arrangement. The total number of formulations for both is 270 (188 in a & 102 in b).

Wildcat’s high-throughput coin cells (with Saft manufactured positive and negative electrodes) were utilized for the experiment with two replicates for each

formulation. The results of this study were inconclusive due to high standard deviation between replicates on measured power and due to sudden death of the coin cells – perhaps because of electrolyte evaporation from the non-hermetic seals. It was found, however, that the electrolyte chosen for the 2nd deliverable cells was in the high performing group and that MB based electrolytes could provide better stability. Statistical analysis of these results reveals no significance to the controlled variables. No single electrolyte formulation was statistically significantly better than any other electrolyte formulation.

Cell Development: Saft built three distinct LTO-NMC LP10P cell designs for delivery to USABC. Each of the deliverable cell designs builds upon previous work in an effort to reach the USABC requirements.

The first delivery of cells occurred after three months in the program and consisted of five 10Ah cells in PHEV2 hardware. These cells were built and shipped to Idaho National Laboratory (INL) in early August of 2013. This build focused on scaling up the small cylindrical and pouch cells to full 10Ah prismatic cells. Significant process development was required, including coating and welding. A low temperature electrolyte was utilized with a formulation based on our significant prior experience with low temperature capable cells. Positive material formulation was based on existing high temperature capable NMC. Negative formulation was based on prior LTO experience but the production process was modified to maximize available surface area.

The second deliverable cells were a set of fifteen LTO-NMC prismatic cells from the Saft, Cockeysville, low-volume production line and were to be delivered to USABC after approximately nine months in the program for independent testing & evaluation. These prismatic cells would be built in a stacked electrode configuration. This second deliverable which was also assembled in PHEV2 hardware and had a capacity of 10Ah, was built in November of 2013 and the first eight cells were shipped to INL in December of 2013. The remaining seven cells were shipped to INL in January of 2014. This build focused on mitigating the impedance growth observed in the first delivered cells plus switching the design to all aluminum construction (to save cost and weight). Additional coating and welding development was required. The electrolyte formulation was refined based on Wildcat and pouch cell results to improve impedance growth while maintaining low temperature power. Electrode processing was modified to further improve impedance growth.

The third and final deliverable was a set of twenty optimized LTO-NMC cells in PHEV-2 VDA size housings at the end of the program for testing. These prismatic cells were also built in a stacked electrode configuration. Twelve 3rd deliverable cells were shipped to INL in mid-April 2014, four cells were

shipped to Sandia National Laboratories (SNL) at the end of March 2014 and four cells were shipped to National Renewable Energy Laboratory (NREL) also at the end of March 2014. This build focused on further improving impedance growth via optimization of the electrolyte additive and implementation of low cost separator plus reduced cell impedance by addition of high surface area LTO.

While internal testing showed that the cells met many of the USABC requirements, none of the cells built were able to meet the cold-crank requirements. The cells are only capable of passing the cold cranking requirement above 60% SOC and do not show significant improvement between generations – even though electrolyte, separator, and LTO surface area were modified. Cold crank results for all three generations of cells are shown in the following Figure II - 21 and Figure II - 22 at 0.5 and 4.5 second pulses.

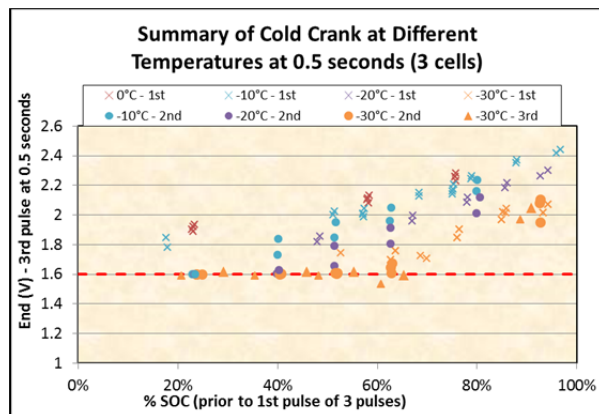


Figure II - 21: Cold Crank Results at 0.5 Seconds.

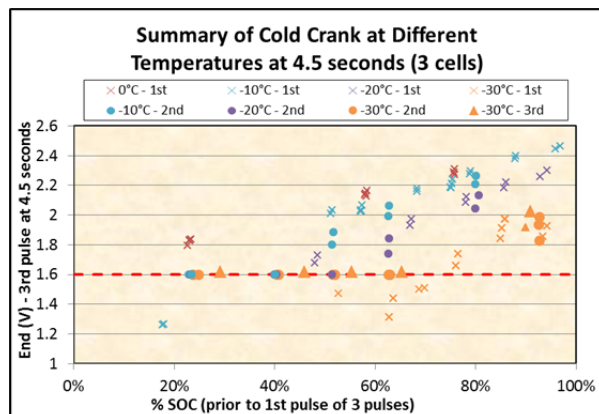


Figure II - 22: Cold Crank Results at 4.5 Seconds.

Novel Cell Assembly Development: The desired monoblock configuration, and goals for high-volume manufacturing and reduced cost, requires development

of novel assembly methods. This development involved studies of the internal bussing of electrode stacks, their feed through from within the battery to the circuit board, and eventually to the terminals on the outside of the start-stop battery. Due to the reduced program scope the cell assembly was studied on a more conceptual basis.

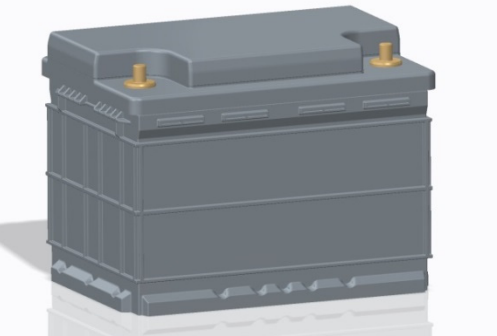


Figure II - 23: SAFT Monoblock Design Concept

Several monoblock design concepts were developed and analyzed for their ability to meet the USABC program requirements for mass, volume, and most importantly cost. The battery was also designed to comply with the IEC 60095-2 standard. (See Figure II - 23.)

The SAFT monoblock battery has a calculated volume of 6.99 liters which meets the USABC requirement of 7.0 liters max. The SAFT monoblock battery likewise meets the USABC requirement for Weight with a calculated mass of 9.77 kg.

Leveraging SAFT's large supplier base and expertise in Lithium-Ion cell production, a detailed cost analysis of the proposed monoblock battery was conducted. Using assumptions on future raw material costs, SAFT has calculated the sale price of the 12V Start-Stop battery in 2020 to be \$219.46 at 100k units per year. This projected cost meets USABC requirement of \$220.00 per unit.

Conclusions and Future Directions

Table II - 7 below shows a summary of the system level and end of project cell deliverable performance metrics gap analysis at the end of the USABC project. We have colored in green the metrics we have shown as passing. Yellow indicates that the measured value is within 10% of the target. Red is shown where the measured results do not meet the USABC target. A blank field in the gap chart indicates that the testing for that item is not completed.

Table II - 7: SAFT Gap Analysis

End of Life Characteristics	Units	USABC Target	Saft LP10P scaled Target	Saft's 1st Deliverable Cell Actual	Saft's 2nd Deliverable Cell Actual	Saft's 3rd Deliverable Cell Actual	Monoblock Calculated from 2nd Deliverable Cell Actual
		Under-hood	Under-hood	1s (LP10P)	1s (LP10P)	1s (LP10P)	5s1P, 46Ah, 11.25V
Cold cranking power at -30 °C (3- 4.5s pulses w/10s rests @ lower SOC), 0.5s followed by 4s	kW, 0.5 sec	6	1.2	0.0	0.15	0.11	3.5
	kW, 4 sec	4	0.9	0.0	0.06	0.05	1.3
Available energy (750W)	Wh	360	15.7	23.2	24.2	21.0	557
Peak Recharge Rate, 10s	kW	2.2	0.1	0.1	0.2	0.2	4.3
Cycle life, every 10% life RPT with cold crank at min SOC	Engine starts/miles	450k/150k		6.2k	In progress, 18.2k		In progress, 18.2k
Calendar Life 30°C / 45°C under hood	Years	15 at 45°C			No change @ 64d		No change @ 64d
Minimum round trip energy efficiency	%	95%		> 99%	> 99%		> 99%
Maximum self-discharge rate	Wh/day	10	0.43	0.1	0.1	0.2	2.3
Peak Operating Voltage, 10s	Vdc	15	3.0	3.0	3.0	3.0	15.0
Sustained Max. Operating Voltage	Vdc	14.6	2.9	2.9	2.9	2.9	14.6
Minimum Operating Voltage under Autostart	Vdc	10.5	2.1	2.1	2.1	2.1	10.5
Minimum Operating Voltage Under Load (below -30°C)	Vdc	8	1.6	1.6	1.6	1.6	8.0
Operating Temperature Range (available energy to allow 6 kW-1s pulse)	°C	-30 to + 75					
75 °C	Wh	360	15.7		18		414
45 °C	Wh	360	15.7		21	20	478
30 °C	Wh	360	15.7	17	18		414
0 °C	Wh	180	7.8		21		480
-10 °C	Wh	108	4.7		18		420
-20 °C	Wh	54	2.3		9		215
-30 °C	Wh	36	1.6		7		161
Survival Temperature Range (24 hours)	°C	-46 to +100					
Maximum System Weight	kg	10	N/A	N/A	N/A	N/A	9.765
Maximum System Volume (Displacement)	L	7	N/A	N/A	N/A	N/A	6.99
Maximum System Selling Price (@100 units/year)	\$	\$220	N/A	N/A	N/A	N/A	\$219.46
	Battery Scaling Factor (BSF)		5.00				
	Cell Scaling Factor (CSF)		4.60				

As can be seen in the table, the LTO-NMC cells delivered during this program and the calculated monoblock battery meet most of the performance requirements listed in the gap chart. The cells are able to pass all thermal performance tests and the cell impedance is better than Saft's original proposal. The monoblock battery is calculated to have sufficient available energy and the peak recharge rate is nearly double the requirement. There is also no excessive gas generation observed in cells fitted with pressure transducers.

However, although the DCR decreased with each build and there was ample available energy, the LTO-NMC cells were not able to pass the cold crank test after discharging 360Wh equivalent per the test manual. The cells are only able to pass cold crank above 60% SOC. We believe that NMC positive is not an appropriate material for the cold crank requirement due to the NMC/LTO open circuit potential which is too low at

minimum SOC. LMO/LTO or a blend of NMC and LMO paired with LTO are more appropriate couples. Further investigation of LMO for use in the cathode is needed.

The calendar life and cycle life of the LTO-NMC cells built during this program is not yet determined. After 45 days in storage, the cells increased slightly in 750W Discharge Energy and DCR did not change. Additional time in storage is needed to see available energy degradation. For cycling, only 2 data points are currently available. Saft observed a 6% energy fade after 7,000 cycles however more data points are needed since fade rate is not linear. Continued cycling of the cells is needed to accurately predict the cycle life.

A robust monoblock design concept was generated during this program and a significant amount of analysis was conducted which showed that the mass and volume requirements can be achieved. An extensive paper study of polymer materials candidates for the monoblock was

conducted which resulted in a short list of potential materials. Those candidates were tested for electrolyte and water compatibility and a single polymer was identified as a highly likely housing material. However, additional longer term permeation testing is needed to completely validate this polymer candidate.

An in-depth analysis of the cost of the monoblock has resulted in a projection that the USABC required sell price of \$220/unit at an annual production volume of 100k units/year in 2020 can be met. The monoblock design concept is a large enabler for meeting this critical requirement. Inclusion of LMO in the cathode also helps meet the price target while also potentially improving cold crank performance.

An extensive electrolyte study was also conducted during this program. However, it did not result in identification of a single electrolyte formulation that was statistically significantly better than any other electrolyte formulation. Saft believes that this may be related to premature failure of the seals in the coin cells used for this testing. Additional electrolyte studies are needed utilizing a more robust test vehicle.

II.A.7 Development of 12V Start-stop Microhybrid Batteries (Leyden Energy)

Chulheung Bae (USABC Program Manager)

Subcontractor: Leyden Energy, Inc.

Marc Juzkow (Program Manager)

46840 Lakeview Boulevard

Fremont, CA 94538

Phone: (510) 938-3815; Fax: (510) 445-1032

E-mail: mjuzkow@leydenenergy.com

Start Date: February 2013

Projected End Date: March 2014

Objectives

The program objective is to design, develop, and deliver 12V Start-Stop cell and pack that meet or exceed the USABC targets using the LTO-LMO electrodes and Leyden's proprietary Li-imide™ electrolyte.

Technical Barriers

Both LTO and LMO chemistries are known to have high temperature durability issues such as gassing and transition metal dissolution leading to shorter life span. Under this program, Leyden based its development on commercially available LTO and LMO materials, which were surface-treated in-house and then assembled and tested with Li-imide based electrolytes. Electrolyte development in this program required formulation of the solvent system and additive package. Main challenge of 12V Li-Ion Start-Stop battery development is low temperature performance enabling cold-cranking at -30 °C without compromising high temperature performance and life. Leyden investigated an optimum composition of electrode and electrolyte materials as well as electrode design to meet the USABC requirements.

Technical Targets

- Improve low temperature capability to meet the USABC low temperature performance targets by incrementally optimizing the LTO and LMO electrode design in conjunction with electrolyte formulation modification.
- Utilize electrolyte optimization and electrode surface treatment to reduce LTO gassing and improve high temperature life capability.

- Scale up the coating capability at Leyden and produce anodes and cathodes for the deliverables. Design and assemble 20Ah cells at XALT facility for USABC deliverables.
- Develop pack design and balancing circuitry for 12V "A" prototype pack at Flextronics.
- Deliver 2.2Ah and 20Ah cells and three 12V packs to USABC at the end of the program.

Accomplishments

- Electrode press density optimization significantly improved cold-cranking performance meeting the USABC cold-cranking target at 30% SOC. Further gradual improvement in cold-cranking is expected from solvent blend optimization.
- Significant improvement in high temperature performance enabled > 200k USABC cycles to date at 50°C and cells can survive at 85°C with minimal gassing.
- Built optimized 2.2 Ah cells by Leyden and 20 Ah prototype cells by XALT. Cells were all delivered to ANL and NREL for evaluation.
- Leyden conducted various abuse tolerance tests with 20 Ah prototype cells and obtained EUCAR Hazard Level 4 and below results.
- Three 40 Ah 12 V packs were built with optimized balancing circuit by Flextronics and delivered to National labs.



Introduction

During the course of the USABC program, Leyden has developed a technology and prototype cell design capable of meeting stringent USABC requirements for an in-cabin 12V Start-Stop battery. The technology was demonstrated in 2.2 Ah cells shipped to USABC in Jan 2014 as well as in larger 20 Ah cells assembled by XALT and processed by Leyden in 1Q of 2014. Leyden leveraged XALT's (old Dow Kokam) expertise in automated high volume cell manufacturing and Flextronics knowledge and experience in circuitry and pack development and manufacturing in order to overcome technical challenges and advance low cost, domestic manufacturing. The key elements of our program include:

- Use of an LTO/LMO couple with Leyden's Li-imide™ electrolyte to enable a system that meets target capacity, cold cranking power, cycle life, calendar life and price targets.
- Advancement of Leyden's system technical foundation and leveraging of XALT's large volume, domestic lithium-ion manufacturing footprint.
- Utilization of an innovative cell and battery design to result in a lower weight and lower volume system, approximately 7.2 kg and 6 liters.
- A rapid program timeline with development running 14 months until 3/31/14, including "A" sample prototype delivery in 14 months to designated National Labs enabling production "C" samples in 30 months.

Approach

To meet USABC targets, Leyden has focused on improvement of cold-cranking power at -30°C and high temperature life and performance of cells.

For the cold-cranking power, Leyden Energy's approach is to optimize electrode coating thicknesses and press densities and formulate a low temperature electrolyte solvent base that allows for superior low temperature operation. The LTO system is unique compared to graphite anode batteries as it does not require high melting point ethylene carbonate (EC) as a solvent. EC is the biggest impediment to good low temperature performance. Electrolyte solvent base development approach is focused on a combination of propylene carbonate and butyrolactone with linear carbonates, low melting point esters and nitriles.

Long cycle life and calendar life targets are addressed by employing Li-imide™ electrolyte with additive packages designed to improve cycle life of LTO-LMO cells and, most importantly, surface treatments of LTO material. The reduction of electrolyte on the catalytically active surface of LTO is understood to be the main reason of high temperature power fade and gassing. Cell design changes improving high temperature life and performance are evaluated at -30 C to confirm that any design change associated high temperature life and performance does not compromise the low temperature performance.

Expected target cost, large cell, and pack deliverables are addressed by close cooperation with our manufacturing partners, XALT and Flextronics.

Results

Cold cranking and power capability

As shown in Figure II - 24, Leyden has made progress in improving low temperature performance of

the LTO-LMO cells since the beginning of this program.

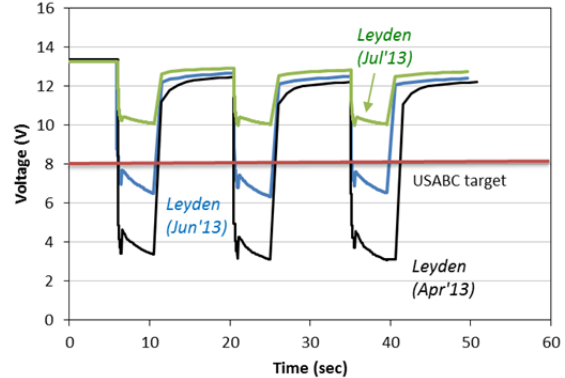


Figure II - 24: Improvements in 100% SOC -30°C cold-cranking performance over the course of the program; recalculated to pack level

Although electrolyte solvent base optimization will continue beyond the timeline of this program, cold-cranking was significantly improved by press density optimization. The study was carried out in 1.1 Ah prototype cells and the cells with thinner electrodes met cold-cranking targets at 100%, 50%, and 30% SOC which is anticipated to be the minimum target SOC after withdrawing target amount of energy at the end of life.

Improvements in cold-cranking performance were accompanied by an overall increase in rate capability that resulted in the ability of the cells to handle continuous 40C discharge (Figure II - 25) and superior power for auto-start function, i.e. ability of the system to deliver 1 sec 6kW pulses over a wide range of temperatures and SOCs (Figure II - 26).

Through low temperature performance improvement studies, electrode optimization has been completed and the designs are production ready. Leyden demonstrated that the optimized electrode formulations can be coated on high speed production slot-die equipment with excellent yields at desired thickness.

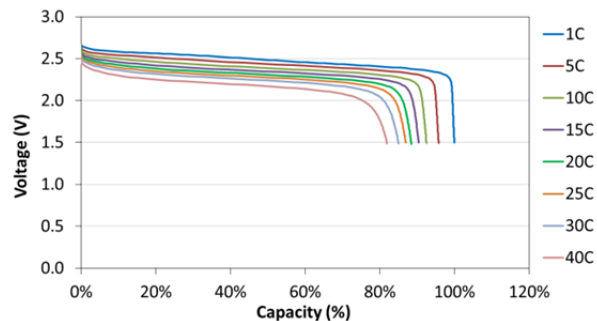


Figure II - 25: Rate performance of 2.2Ah prototype cells

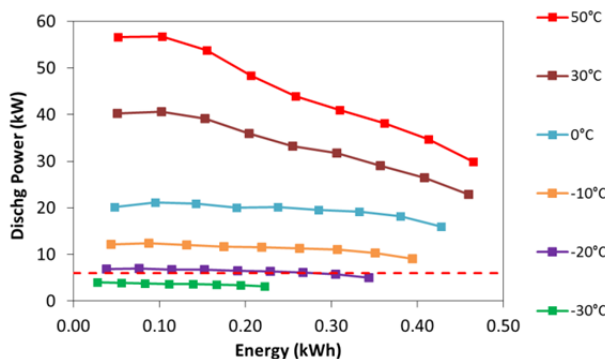


Figure II - 26: Thermal performance test on 2.2Ah prototype cells

Improvement of High Temperature Performance

Li-imide electrolyte demonstrates high temperature cycle life improvement over regular electrolyte when used in the LTO-LMO system. In addition to utilizing imide salts, Leyden has evaluated the best surface treatments from more than 15 options. A majority of the high temperature testing during the program was carried out at 50°C. In addition to USABC cycling shown on Figure II - 27, the cells from many development builds were tested at 1C/1C and 100% DOD being cycled unconstrained at 50°C. Version 3.5 cells (built in Dec. 2013) and later performed very well at this high temperature with approximated cycle life > 200k USABC cycles and > 5000 cycles at 100% DOD.

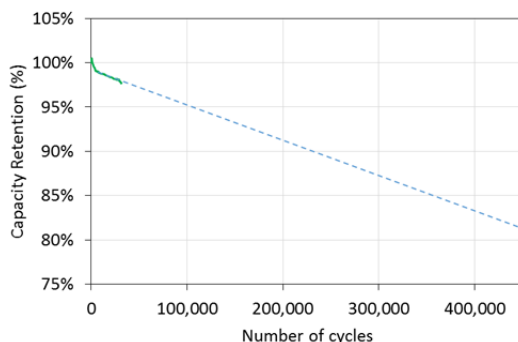


Figure II - 27: USABC cycling at 30°C on 2.2Ah cells

Correlation between USABC cycling and 1C/1C cycling patterns was determined by matching up the cycle numbers for both tests at various capacity retentions and Leyden observed that degradation on one 1C/1C cycle at 50°C correlates well to 100 USABC cycles. Based on this correlation, cells are expected to achieve 3500 1C/1C cycles to 75% of initial capacity, which translates into 350k USABC cycles at 50°C.

The calendar life of version 3.5 cells at 50°C is projected to be >12 months with cold-cranking remaining above the USABC target, which translates to

>4 years at 30°C. Leyden expects better calendar life with newer version cells under constrained condition.

Cell Scale Up

After the initial testing in 0.8 Ah prototype pouch cells, Leyden scaled up to 2.2 Ah cells to finalize some of the cell assembly and electrolyte filling parameters, which facilitated scale-up of the final 20 Ah cell size at the end of the first year. Over 350 of the 20 Ah dry cells were assembled at XALT, with completed final assembly at Leyden's facility. Cells were characterized and sorted. Several battery modules/packs have been built for internal and external testing. (See Figure II - 28.)



Figure II - 28: 2.2Ah and 20Ah cell prototype

Pack and Electronics

Flextronics led the design of the 12V 40 Ah battery pack, including a voltage balancing circuit board. They incorporated pack design features and functionality from packs and modules previously developed. The "A" sample pack (see Figure II - 29) was designed for bench testing to demonstrate the general performance of the pack.



Figure II - 29: Three USABC 12V Start-Stop battery packs

As seen in Figure II - 30, the two-cell bricks were snapped in with the compression pads positioned between the cells. Voltage balancing circuit has been optimized for accuracy of the voltage readings and balancing onset.

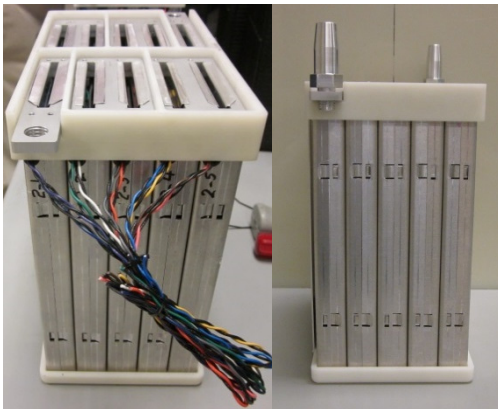


Figure II - 30: Bricks construction

Conclusions and Future Directions

Under this program, Leyden has designed, developed, and assembled 20 Ah Start-Stop cells and “A” sample 12V battery prototypes that meet the USABC targets using an LTO-LMO system and Leyden’s Li-imide electrolytes.

In particular, significant improvements in both cold-cranking and high temperature performance have been made from the start to the end of the program. The battery technology developed under this program meets the critical targets for “not under hood” applications. A strong technical path forward has been shown for further improvements in high temperature performance and survivability to meet the “under hood” set of USABC requirements.

II.A.8 2012 EV Technology Assessment Program (SKI)

Chulheung Bae (USABC Program Manager)

Subcontractor: SK Innovation

Kyungjin Park (Program Manager)

325 Expo Road, Wonchondong, Yuseongku,
Daejeon, Korea

Phone: (82) 42-609-8133; Fax: (82) 42-609-8740

E-mail: ki.park@sk.com

Start Date: November 2012

Projected End Date: January 2014

Objectives

- Develop and validate pure NCM battery system
 - High Energy density.
 - Long life performance.
 - High abuse tolerance.

Technical Barriers

One of the concerns about a pure NCM system is safety. Therefore, improved ceramic coated separator and a new electrolyte system are required.

SKI applied ceramic coated separator with superior strength and heat stability based on SK's own technology and also adjusted the electrolyte system for improved abuse tolerance.

Technical Targets

- Power density: > 460Wh/L.
- Specific power dis. at 80%DOD: 300W/kg.
- Specific power regen at 20%DOD: 150W/kg.
- Energy density C/3-rate: 230Wh/L.
- Specific energy density C/3-rate: 150Wh/kg.
- Life: 10 years.
- Cycle life -80%DOD: 1,000 cycles.

Accomplishments

- Validation of power density with over 600W/L and specific discharge/charge power with over 460W/kg/480W/kg.
- Development of 40Ah energy cell with 230Wh/L and specific energy 150Wh/kg.
- Successful life performance with over 2,000 cycles (expected).

Introduction

As the energy density and life requirements of electric-drive vehicle batteries are getting more challenging, SKI has developed and introduced a high energy 40Ah LMO-free cell. This cell, named the E400, has been delivered to USABC to be tested in the EV technology assessment program. In developing the E400, SKI set a goal of higher energy density and improved calendar life while maintaining good cycle life and stability. By removing LMO active material from the cathode, the cell can avoid Mn-dissolution which brings crucial capacity deterioration at high temperature. This change and other modifications are expected to result in improved calendar life.

SKI also applied a thermally superior ceramic coated separator and developed an electrolyte formulation with adjusted electrolyte additives for the LMO-free system. From performance validation tests, the LMO-free E400 should maintain similar electrical performance as in previously tested systems while improving calendar life.

Approach

SKI applied pure NCM as cathode material to get high energy density and to avoid crucial deterioration at high temperature. However, high Ni-content NCM is unfavorable to abuse tolerance and cycle life. In order to obtain structural stability, SKI has researched surface-coated NMC with stable materials. The surface-treated particles have shell-core morphology, that is, SC-NMC.

In addition, we enhanced the separator properties to minimize shrinkage of the separator at high temperature, and developed a new electrolyte system which is optimized for the new cathode.

Cycle life and calendar life is expected to be improved significantly after reducing the Mn-spinel.

Results

Core Test: SKI tested 18 cells in total (6 cells for cycle life and 12 cells for calendar life) and the measured average capacity is over 40Ah at current condition of C₃/3, C₂/2 and C₁/1. (See Figure II - 31.)

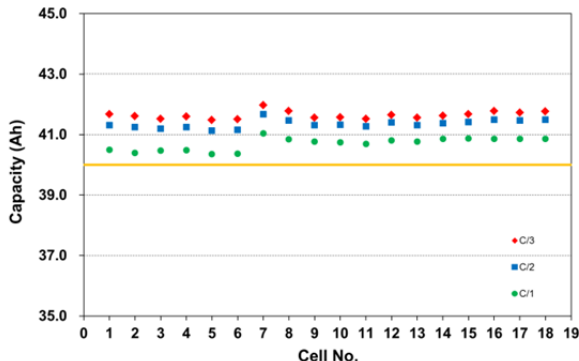


Figure II - 31: Constant Current Discharge Test for LMO free E400

The 100% DST Discharge capacity with DST power of 400W/kg is 40.8Ah on average.

The Peak power capability was calculated using the equation below and was found to be greater than 670W/kg.

$$\text{Peak power} = I_{\max} \cdot (V_{IRFree} + R \cdot I_{\max})$$

48h stand test showed very stable capacity retention after test with 0.95% capacity loss.

Life Performance: After successfully completing the core tests, six batteries have been tested for cycle life. Cycle life tests will be conducted until End of Life (EOL).

Approximately, 4 DST pattern cycles were accumulated per a day and RPTs were conducted every 100 cycles (~1/month). Figure II - 32 shows C/3 capacity retention and results show 86.1% of retention at 1,500 cycles. Similar tendency is seen in DST capacity retention (86.4%) and peak power retention (83.7%).

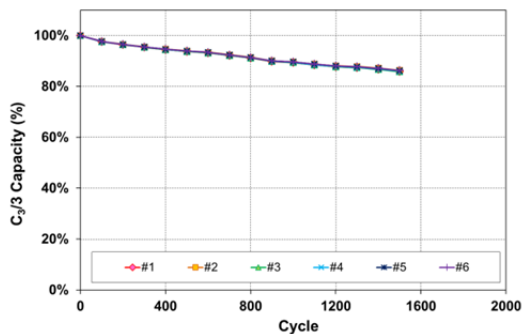


Figure II - 32: C/3 capacity retention of LMO free E400 in cycle life

Calendar life tests are ongoing at four different temperatures of 25, 35, 45, and 55°C. Each battery is charged to SOC 100% at the C/3 rate and allowed to rest

in an open circuit condition at the desired temperature for 4 weeks. At the end of 4 weeks, the batteries undergo RPTs at 30°C. Calendar life tests were conducted for 56 weeks and Figure II - 33 shows C/3 capacity retention at 25, 35 and 45°C after 56 weeks are 91.0%, 85.0% and 79.8% respectively. The 55 °C test reached EOL after 24 weeks and the result of C/3 capacity was 81.0%.

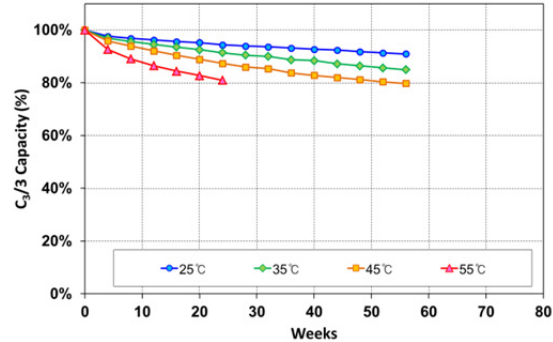


Figure II - 33: C/3 Capacity retention of LMO free E400 in calendar life

In DST capacity tests, measurement showed slightly higher capacity retention than C/3 capacity, and data after 56 weeks were 92.5%, 86.6% and 80.8% at 25, 35 and 45°C, respectively (82.2% at 55°, after 24 weeks).

In peak power degradation, comparatively high degradation is observed at high temperatures. Peak power retention after 56 weeks at 25°C and 35°C were 96.2% and 88.1%. However, it showed faster degradation at high temperatures as in 76.3% at 45°C after 50 weeks and 77% at 55°C after 24 weeks. It may be presumed that unstable SEI forms on the anode from electrolyte decomposition at high temperatures and it could have brought comparatively lower performance retention due to increased resistance especially when high current was applied.

Abuse tests were carried out and LMO-free E400 showed stable behavior after abuse tests as shown in Table II - 8. SKI followed SAND 2005-3123 abuse tests manual which was distributed by SNL, and some specific test conditions (e.g. resistance for short circuit; 1mΩ and 10mΩ) were given by SNL for this program. Abuse tests were performed and the tested cells met most of the established goals, with the exception of thermal ramp test. In the case of thermal ramp test, the objective of the test is monitoring thermal onset through temperature increase. The LMO-free cell turned out to be stable up to 180°C.

Table II - 8: Summary of abuse test results of LMO free E400

Items	Conditions	LMO free E400
Thermal Stability	SAND 2005-3123; Increasing temp. up to 200°C (hold 30min every 20°C) SOC90%	L4 (no smoke)
Thermal Ramp	SAND 2005-3123; Increasing temp. up to thermal runaway with 5°C/min SOC90%	Stable up to 180°C
Nail Penetration	SAND 2005-3123; Pin dia=3mm, Speed 80mm/s SOC100%	L3
Short Circuit	SAND 2005-3123; SOC100% (1mΩ, 10mΩ)	L3
Overdischarge	SAND 2005-3123;1C, 1.5h SOC100%	L2

Conclusions and Future Directions

SKI has carried out electrical performance tests on the LMO-free E400 and long-term life tests such as DST cycle life and calendar life tests were also conducted until RPT15. Based on capacity retention to 80%, cycle life is expected to proceed until 2,000 cycles and calendar life was measured approximately 56 weeks at 45°C and SOC 100% condition.

SKI would like to continuously develop and modify cell design including electrolyte optimization and adjustment of cathode formulation in order to improve electrochemical performance and safety further.

II.A.9 Multifunctional, Inorganic-Filled Separator Development for Large Format Li-ion Batteries (ENTEK)

Ion Halalay (USABC Program Manager)

General Motors

30500 Mound Road

Warren, MI 48230

Phone: 586-986-1497; Fax: 586-986-2244

E-mail: ion.c.halalay@gm.com

Richard W. Pekala (Project Manager)

ENTEK Membranes LLC

250 N. Hansard Avenue

Lebanon, OR 97355

Phone: 541-259-3901; Fax: 541-259-8016

E-mail: rpekala@entek-membranes.com

Start Date: August 22, 2011

End Date: January 22, 2014

- Pore Size: less than 1 μm .
- Puncture Strength: greater than 300 gf / 25.4 μm .
- Thermal Stability at 200°C: less than 5% shrinkage.
- Tensile Strength: Less than 2% offset at 1000 psi.
- No adverse effects on cell performance due to presence of fillers in the separator.

Accomplishments

- All technical targets have been met except puncture, 285 gf versus the target of 300 gf.
- Cell test results for 18650 cells with silica-filled separator are reproducible and when compared to controls built with unfilled polyolefin separator:
 - Longer cycle life.
 - Lower self discharge.
 - Higher power capability.
 - Improved low temperature performance.



Objectives

- Deliver a quantity of 18650 cells with silica filled separator and control cells with unfilled polyolefin separators to USABC.
- Continue data collection and analysis for cells still on test.
- Continue to sample battery makers interested in testing silica-filled separators in large format Li-ion batteries.

Technical Barriers

The inorganic filler loading was successful in reducing separator shrinkage at high temperature, but it also resulted in decreased mechanical strength and some inhomogeneity in the film. The focus of this last phase of the project has been to address these issues:

- (A) Improvement of puncture strength and mechanical modulus.
- (B) Production of defect free precursor films for biaxial stretching with good thickness uniformity in machine and cross machine direction as well as low polymer crystallinity.

Technical Targets

- Thickness: less than 25 μm .
- Permeability: MacMullin Number less than 11.
- Wettability: Rapid wet out in electrolytes.

Introduction

Separator shutdown is a safety feature required in nearly all commercial Li-ion cells. Shutdown results from collapse of the pores in the separator due to softening or melting of the polymer, thus slowing down or stopping ion flow between the electrodes. Nearly all Li-ion battery separators contain polyethylene as part of their construction so that shutdown begins at ~130°C, the melting point of polyethylene. However, after shutting down, residual stress and reduced mechanical strength can lead to shrinkage, tearing, or pinhole formation in the separator, potentially allowing direct contact between the electrodes.

For larger cells such as those used in hybrid, plug-in hybrid and battery electric vehicles (HEV, PHEV, EV), shutdown may or may not be required depending on specific application and system design. In HEV applications failure modes in which separator shutdown might play a role can be handled at a system level. For this reason high temperature melt integrity could be more important than shutdown.

In Phase II of this project ENTEK produced silica-filled, UHMWPE gel process separators with low impedance and excellent high temperature, mechanical and dimensional stability at pilot and production scale. The goal of Phase III of this project was to optimize processing for higher strength defect-free separator and to supply samples to battery makers who would test

silica filled separators in large format batteries in order to determine the commercial viability of this technology.

Approach

ENTEK produced separator films that were extruded and biaxially oriented with spray dried and jet milled silicas that were selected to improve dispersion and reduce defects in the film. The polymer/filler proportions were optimized to improve mechanical strength without compromising high temperature stability. A significant quantity of separator was inventoried to meet future sample needs.

Results

Deliverables

In October 2013, 18650 cells (65 each) were shipped to INL for performance testing and Sandia for abuse testing.

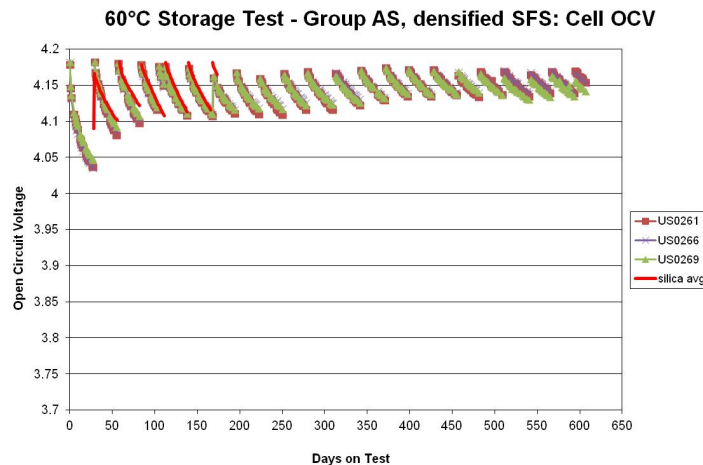


Figure II - 34: OCV fade at 60°C for 18650 cells with silica-filled separators

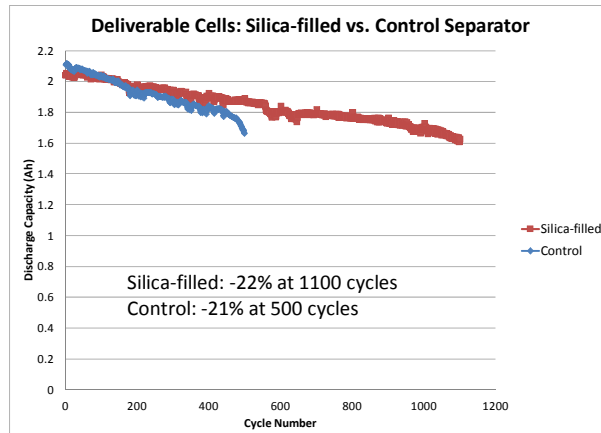


Figure II - 35: Cycle life for silica-filled separator cells compared to control PE separator cells

	Control cells	SFS cells
INL	23	20
Sandia	12	10
Total	35	30

ENTEK Cell Testing

60°C Calendar Life Test

Figure II - 34 shows excellent storage life for 18650 cells made with densified silica-filled separator. Three cells with densified SFS were on test at 60° C for 607 days, during which time the OCV fade rate between reference performance tests decreased significantly.

Figure II - 35 compares cycle life for 18650 cells made with silica filled separator and a microporous PE control separator. (100% DOD, 1C, room temp.) The cells with silica-filled separator delivered twice the cycle life of the control cells.

Large Format Cell Tests

Cells made with silica-filled separator demonstrated much higher power capability than with control separator. (Figure II - 36.)

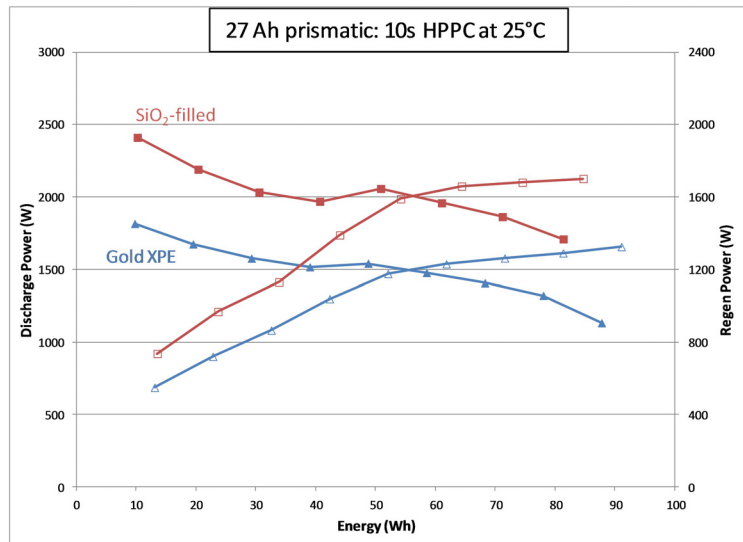


Figure II - 36: Power Capacity Plots for Cells made with silica-filled separator versus those with control separator

Conclusions and Future Directions

ENTEK has demonstrated that separators with inorganic filler can deliver enhanced performance to lithium-ion batteries:

- High temperature stability.

- High porosity for lower resistance, higher power and improved low temperature performance.
- Enhanced wettability.
- Longer cycle life.
- Improved storage life.

This material has yet to find commercial acceptance due to insufficient mechanical strength and elevated moisture content.

II.B Advanced Lithium Battery Cell Technology

II.B.1 Silicon-nanowire Based Lithium Ion Batteries for Vehicles with Double the Energy Density (Amprius)

Bruce Mixer (NETL Program Manager)

Grant Recipient: Amprius, Inc.

Ionel Stefan, PhD (Principal Investigator)

225 Humboldt Court

Sunnyvale, CA 94089

Phone: (800) 425-8803

E-mail: ionel@amprius.com

Subcontractors:

Nissan, BASF

Start Date: October 2011

Projected End Date: March 2015

Objectives

- Increase the energy and extend the cycle life of cells built with Amprius' silicon nanowire anodes.
- Identify electrolyte formulations that improve the performance of cells built with silicon nanowires.
- Design, build and test >2 Ah cells matching Amprius' silicon nanowire anodes with LCO cathodes.
- Deliver cells that meet DOE goals for energy density, specific energy, power density, cycle life, calendar life and safety.

Technical Barriers

- Development of silicon anodes capable of the long cycle life required for electric vehicles.
- Production of silicon anodes with the high amount of silicon necessary to enable high specific energy.
- Optimization of electrolyte formulations for long cycle life, high energy, and high conductivity over a wide temperature range.
- Matching of silicon anodes with LCO cathodes capable of long cycle life.
- Production of multilayer cells with silicon anodes.

Technical Targets

Amprius will match its next generation silicon nanowire anodes with LCO cathodes to produce 2-2.7 Ah cells with:

- Energy density of at least 500 Wh/l.
- Power density of at least 500 W/l.
- Cycle life of 300-1,000 cycles at 80% depth of discharge.
- Calendar life of at least 5-10 years.
- A durable design for affordable mass production.

Accomplishments

- Transitioned to building anodes on thinner and therefore lighter substrates.
- Installed, facilitated, qualified and began to operate a new tool for anode production.
- Tuned and improved anode micro- and macro-structures.
- Matched silicon anodes with high-voltage LCO cathodes with high areal loadings.
- Matched multiple layers of silicon anodes with multiple layers of LCO cathodes.
- Designed cells for higher capacity and energy.
- Delivered 24 cells that averaged >2.5 Ah, 330 Wh/kg, and 790 Wh/L at a C/3 discharge rate. The cells met the project's specific energy goal and exceeded the project's energy density goal.



Introduction

Today's lithium-ion batteries have very limited room to improve energy density or specific energy. Their active materials are used at energy capacities close to their theoretical limits and their packaging has been largely optimized. New active materials are needed to boost performance and extend electric vehicle driving range.

Amprius has proven silicon's potential as a new anode material. Silicon offers nearly 10 times the theoretical energy capacity of graphite, the traditional anode for lithium-ion batteries. However, when charged with lithium ions, silicon swells to up to four times its

volume, causing capacity fade and mechanical failure. Because of swelling, conventional approaches to silicon anodes have not produced cells with the cycle life required for electric vehicle applications.

Amprius' anode replaces graphite with silicon nanowires. Amprius' unique nanowire structure addresses swelling by enabling silicon to expand and contract internally. Amprius does not rely on particle-to-particle contact and is able to maintain high electrical conductivity. (See Figure II - 37.)

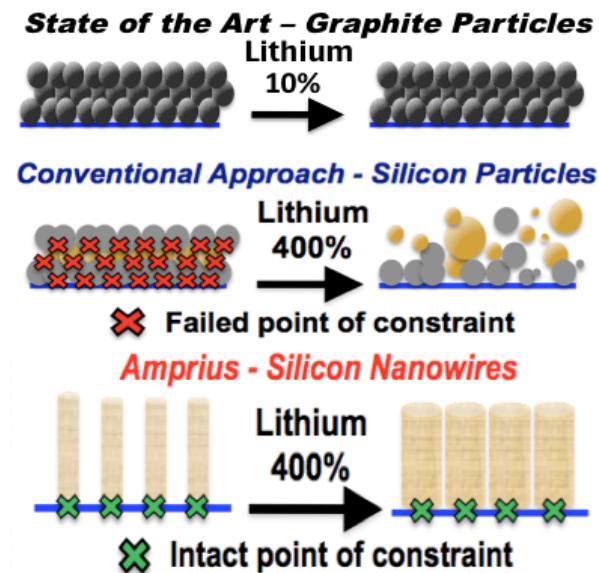


Figure II - 37: Silicon swelling causes capacity fade and mechanical failure. Amprius' nanowires address swelling by allowing silicon to swell successfully

Approach

Amprius is coordinating the three-year project and leading the anode and cell development effort. BASF supplied cathode materials. Nissan North America provided guidance regarding customer requirements.

During Phase I, Amprius conducted experiments to increase the cycle life of its silicon nanowire anode material. Amprius' work included both material and electrochemical efforts.

During Phase II, Amprius increased both the capacity and cycle life of its silicon nanowire anodes through substrate, nanowire and production process development. Amprius also built larger and double-sided silicon nanowire anodes, then matched multiple layers of those anodes with multiple layers of LCO cathodes with high areal loading. During 2013, the company delivered interim silicon-LCO cells that exceeded the project's energy targets.

During Phase III, Amprius further increased the specific energy and energy density of its silicon nanowire anode-based cells by improving anode

production and cell build processes. Amprius refined its substrate specification and built anodes on thinner and lighter foils. Amprius also continued to develop its anode production processes, tuning anode micro- and macro-structure and increasing silicon mass loading. Amprius then matched its anodes with thinner separators and high-voltage LCO cathodes. During 2014, the company delivered final silicon-LCO cells that met the project's specific energy goal and exceeded the project's energy density goal.

Results

Substrate Development: Amprius successfully transitioned to building anodes on thinner and therefore lighter substrates. Amprius began by developing a specification for thinner foils and working with foil vendors to make sure that their material met Amprius' requirements. Amprius then qualified these thinner foils and in so doing learned of another characteristic necessary for symmetrical growth of silicon nanowires. Amprius therefore refined its specification to minimize batch-to-batch variation and increase nanowire uniformity. Finally, Amprius qualified and built anodes on these thinner foils that met the company's updated specification.

Anode Production: Amprius installed, facilitated, qualified and began to operate a new tool for anode production. The new tool enabled Amprius to produce greater quantities of silicon nanowire anodes, facilitating and accelerating development efforts. The tool also helped Amprius improve its anode production processes.

Anode Development: Amprius tuned and improved anode micro- and macro-structures to enable higher specific energy and energy density cells. Amprius tuned nanowire characteristics (e.g. height), performed a design of experiments to optimize the process window for anode production, and established a robust baseline for nanowire growth. Amprius also optimized the distribution of silicon during anode production to reduce side-to-side anode variations and improved production process control and stability to increase anode uniformity.

Cell Development: Amprius improved non-anode cell components. Amprius tested several additives and electrolyte formulations, and then updated its standard formulation to extend cell cycle life. Amprius also analyzed the impact of various cell components (e.g. ceramic separators) on silicon anode-based cell performance and updated the company's cell design for the project's final deliverables.

Amprius tested single- and multi-layer cells with the company's latest anodes and non-anode cell components. Amprius built and tested single-layer and

multi-layer cells matching silicon nanowire anodes (from different production runs) with LCO cathodes.

In single-layer cells, Ampruis demonstrated >700 C/2 cycles to 80% of a cell's initial capacity. (See Figure II - 38.)

In multi-layer cells, Ampruis demonstrated >300 C/2 cycles to 80% of a cell's initial capacity. (See Figure II - 39.)

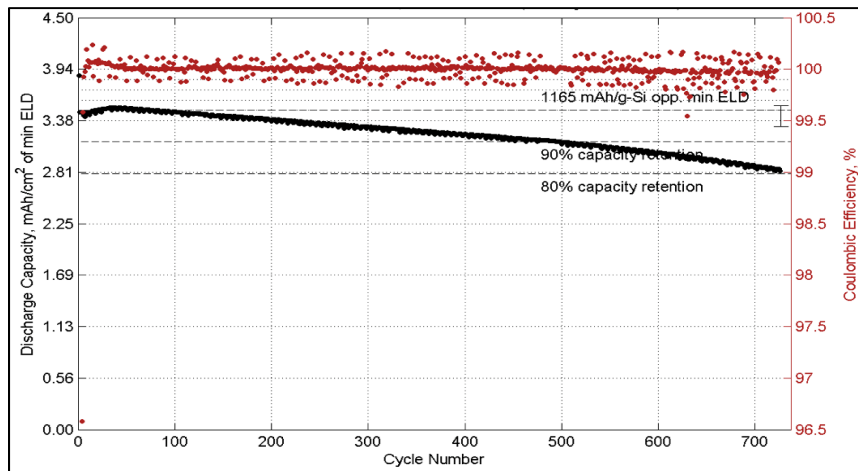


Figure II - 38: Ampruis' single-layer cell achieved >700 C/2 cycles at 100% depth of discharge

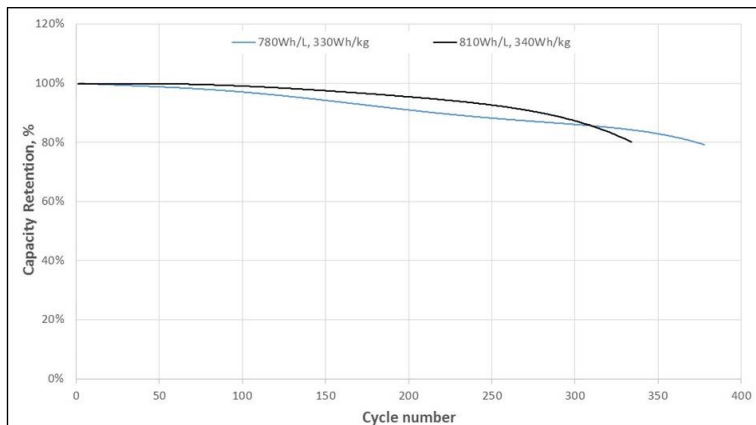


Figure II - 39: Ampruis' >2.5 Ah silicon nanowire anode-based cells achieved >330 Wh/kg, >780 Wh/L, and >300 C/2 cycles at 100% depth of discharge

Ampruis delivered 24 silicon-LCO cells that averaged >2.5 Ah, 330 Wh/kg and 790 Wh/L at a discharge rate of C/3. By decreasing the thickness of the anode substrate (i.e. current collector), optimizing the separator type and thickness, and improving pouch design, Ampruis met the project's specific energy target and exceeded the project's energy density goal.

silicon-LCO cells. Both Ampruis and INL will report their results in early 2015.

After the project, Ampruis will continue to develop silicon nanowire anodes and high-energy cells for electric vehicle applications.

FY 2014 Publications/Presentations

1. 2014 DOE Annual Peer Review Meeting Presentation.

Conclusions and Future Directions

Both Ampruis and Idaho National Laboratory will test and report on the performance of Ampruis' final

II.B.2 Development of Large Format Lithium-Ion Cells with Higher Energy Density (XALT Energy)

Christopher Johnson (NETL Program Manager)
Contractor: XALT Energy, LLC

Fabio Albano, Ph.D. (Principal Investigator)
2700 S. Saginaw Road
Midland, MI 48640
Phone: (989) 486-8501
E-mail: falbano@xaltenergy.com

Team Members:
Argonne National Laboratory
National Renewable Energy Laboratory
Oak Ridge National Laboratory
Wildcat Discovery Technologies

Start Date: October, 2011
Projected End Date: November, 2015

Objectives

The objective of this project is to research, develop, and demonstrate Li-ion battery cells that are capable of achieving an energy density of at least 500 Watt-hours per liter while maintaining comparable performance standards in terms of cycle life, calendar life, and durable cell construction and design capable of being affordably mass produced.

Technical Barriers

The energy density needed to both effectively and efficiently power EVs is not available with current lithium ion cell technology. Today's solution falls significantly short of meeting the general consumer's cost and life expectations. In order for the EV industry to be successful, a battery cell with twice the energy density must be developed.

Technical Targets

- Develop and optimize new materials and design of lithium ion cells which will double the energy density of commercially available cells from 260 – 340 Wh/L to 500 – 750 Wh/L.
- Implement these improvements to mass production system exceeding 500 Wh/L, superior overall performance and cost compared to currently

available PHEV and EV cells, and safety comparable to today's commercial Li-ion cells.

- Improve EV battery affordability by reducing cell cost to \$0.20 – 0.25/Wh.

Accomplishments

- Eighteen samples of 2.1 Ah baseline cells with NMC and graphite as the active materials were delivered to Argonne National Laboratory for evaluation.
- Both of the high capacity anode (HCA) materials tested by XALT Energy have demonstrated >2,500 mAh/g. However, satisfactory performance can be obtained only when the utilization is controlled below 1250 mAh/g. XALT Energy is testing full cells with HCA and high voltage cathode (HVC) material.
- In addition to the high capacity anode and cathode materials, XALT Energy added NMC-class high capacity cathode (HCC) materials to the list of evaluations. Leveraging the experiences learned from another program, funded by the Department of Defense (DoD), XALT Energy has demonstrated energy densities of >600 Wh/L with the HCC/graphite and HCC/HCA chemistry.
- XALT Energy has identified an HCC material that demonstrated >630 Wh/L of energy. However, it has been difficult to produce cells with cycle life above 300 cycles at 100%DOD and 1C rate of charge and discharge. In September 2014, XALT Energy decided to start working with Pneumaticoat Technologies to leverage their atomic layer deposition (ALD) technology to improve the cycle life performance of the high energy density cells. 2Ah cells with ALD coatings have been successfully manufactured and they are starting characterization. Preliminary data will be available during the month of December 2014.



Introduction

XALT Energy is developing a large format battery cell design that could double the energy density of current lithium ion cells.

According to our preliminary data from 2Ah cells, the highest energy density has been achieved by increasing the capacity of the active materials. Lithium-

rich high capacity cathode (HCC) materials are currently under investigation and against silicon-based or carbon-based high capacity anode materials. 2 Ah development cells have been produced for evaluation of the materials. 40 Ah production size cells will be produced and delivered during the course of 2015 to demonstrate that the materials can be scaled up cost effectively to a production scale manufacturing environment. Preliminary discussions with perspective customers have been initiated to develop a cell assessment program for the large format cells to be deployed in EVs.

Approach

The following approach will be taken to achieve the goals:

- Design and fabricate baseline cells in 2-Ah format. The cell design is a direct reduction of the 40-Ah production cell produced by XALT Energy.
- Develop a cell performance model to represent the behavior of the cell. This model will be used to predict the performance of cells when the novel materials described above are used.
- Evaluate those novel materials in half-cell format to understand their performance. The data will be used to design full cells with these materials as the electrodes.
- Design and construct a small-volume slot die coating system that can produce electrodes with very little material and have the same quality as production scale electrodes.
- Design and fabricate samples cells, of the 2Ah format, using HVC and HCC materials as the cathode and HCA or conventional graphite as the anode.
- Design and fabricate a full size, 40-Ah cell, that can be produced in XALT Energy's cell manufacturing facility.
- Collaborate with Pneumaticoat Technologies to develop the ALD coatings for cathode and anode materials and with Oak Ridge National Laboratory (ORNL) to characterize these materials.

Results

Baseline cell: Cells were designed, built, and tested. Test results show that these 2Ah cells behave very similarly to the 40 Ah, large format, cells XALT Energy manufactures in Midland Battery Park (MBP). Eighteen 2Ah cells have been delivered to ANL for testing in August 2014.

High Capacity Anode Material: Two silicon-based anodes were selected. The maximum specific capacities of these materials were both above 2500

mAh/g. However, if utilized above 1250 mAh/g the materials showed fast decay. It was found that matching the electrode designs between the HCA and the cathode is extremely important to the performance of the cell. Sample cells made with HVC and HCA were fabricated and tested at XALT Energy. To date, cells with >600 mAh/L energy densities have been demonstrated and cycle test results are shown in Figure II - 40. Optimization of cell design is in progress as well as development of suitable ALD coatings to extend the cycle life beyond 300 cycles and achieve program cycle life targets useful to EVs.

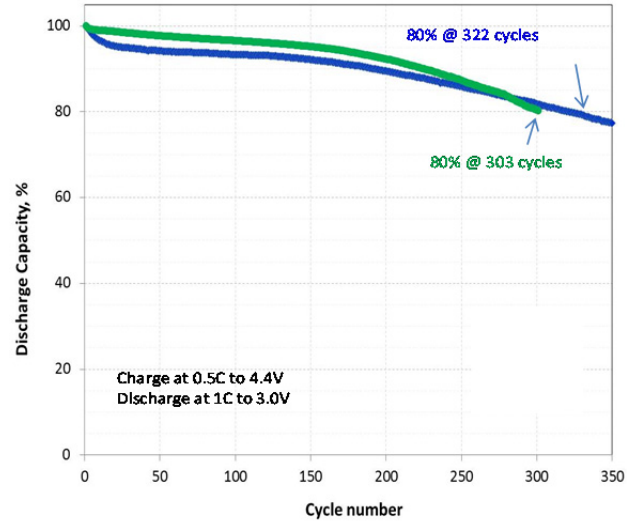


Figure II - 40: Cycle performance of an HVC / Si-based anode cell

High Voltage Cathode Material: XALT Energy has also been testing NMC-class of materials operating at higher voltages under a research program funded by the Department of Defense. Applying the knowledge gathered, XALT Energy has demonstrated 625 Wh/L of energy density using HVC with Si-based anode in a 2-Ah cell format. When charged to 4.2 and 4.4 V, the energy density of an HVC/Si-based and an HVC/graphite cell at various discharge rates is shown in Figure II - 41.

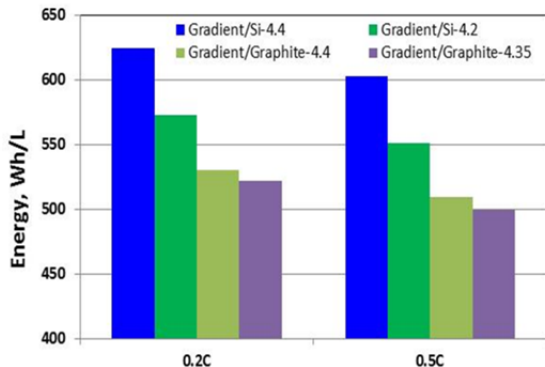


Figure II - 41: Energy density of an HVC / Si-based and Graphite sample cell

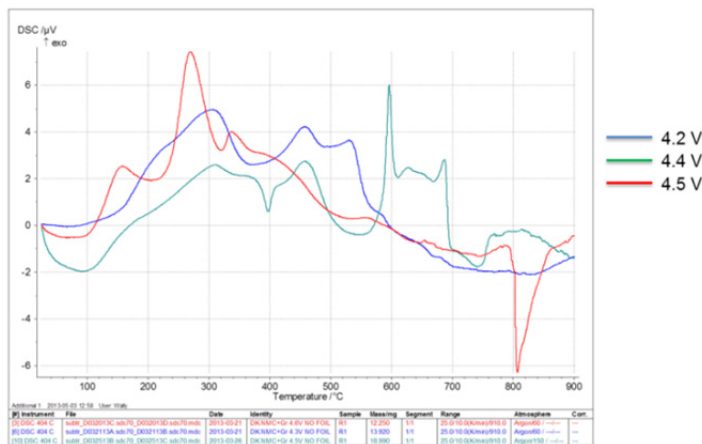


Figure II - 42: Thermal behavior of a high voltage NMC material when charged to various voltages

High Capacity Cathode Material

Given the limited resources available for this effort and the low success rate of the WDT efforts, XALT Energy has decided to stop the development of HCC synthesis techniques.

XALT Energy has sourced alternative HCC materials from commercial suppliers including BASF, Posco and other licensees of the core-shell functionally graded NMC cathode developed by ANL. XALT is leveraging the management team network to collaborate with Envia Systems for evaluating and possibly deploying their cathode materials into large format cells.

Conclusions and Future Directions

- Baseline cell test results show that the design and fabrication are suitable to produce cells in MBP. Baseline 2Ah cells have been delivered to ANL for testing.
- XALT Energy evaluated the cell performance of HCA materials and demonstrated >2500 mAh/g of specific capacity. XALT Energy will optimize the

The stability of this material as a function of the charge voltage was investigated by differential scanning calorimetry (DSC) at ORNL. It was concluded that the behavior of this NMC material, when charged to 4.4 V, is similar to when it is charged to 4.2 V below ~60°C, as shown in Figure II - 42.

electrode design to improve cell performance and explore the application of ALD coatings onto silicon anodes to extend cycle life and mitigate capacity fade.

- XALT Energy has satisfied the goal of >500 Wh/L in energy density using HVC and silicon anode. It will continue to improve the energy density and life span of cells using ALD materials and techniques that have shown promise.
- XALT Energy has stopped the work at WDT and is sourcing HCC materials from commercial suppliers.
- XALT Energy believes, from the results obtained so far, it is moving in the right direction and will continue with the development of cells with HCC and HCA improved via ALD coatings.
- Preliminary data from 2Ah HCC/HCA cells with ALD will be made available for DOE in December 2014.
- NREL will develop models with XALT Energy engineers that will inform the 40Ah large format design using the HCC and HCA materials.

- Full scale 40Ah cells based on the most promising design and high energy materials combinations will be manufactured over the summer of 2015 by Xalt Energy in MBP.
- 24 large format (40Ah) cells will be delivered to Argonne National Lab for testing in the third quarter of 2015.
- Market analysis and commercialization reports will be provided to DOE at the end of 2015 to support deployment of the large format cells in EVs.

FY 2014 Publications/Presentations

1. 2014 DOE Annual Peer Review Meeting Presentation.
2. 2014 Technical Review Meeting.
3. 2014 Materials Research Society Meeting, Boston, MA.

II.B.3 Innovative Cell Materials and Designs for 300 Mile Range EVs (OneD Material)

John Tabacchi (NETL Program Manager)
DE-EE0005443 Recipient: OneD Material, LLC

Yimin Zhu (OneD Material, LLC – PD/PI)
2625 Hanover Street
Palo Alto, CA 94304
Phone: 650-331-2232; Fax: 650-331-2199
Email: yimin.zhu@onedmaterial.com

Subcontractor:
A123 Systems
200 West Street
Waltham, MA

Start Date: October 2011
Projected End Date: March 2015

Objectives

- We propose to develop a 700~1000 mAh/g Si anode (SiNANOdeTM) with a target cycle-life of >800, and an eventual goal of achieving an energy density of 1,600 mAh/g at the end of the program. When eventually combined with a well-performing cathode in unique large format pouch cell to achieve high energy density, a target will be a cell with 350 Wh/kg and 800 Wh/L. Such a cell could be used to create a battery for an EV capable of driving 300 miles on a single charge and achieving a cell level cost target of <150 \$/kWh.

Technical Barriers

In order for EVs to achieve mass adoption and make a significant dent in U.S and global CO₂ production, the key problems of driving range per charge & cost per kWh must be addressed.

Barriers addressed:

- Performance: Low Wh/kg & Wh/L.
- Life: Poor deep discharge cycles.
- Cost: High \$/kWh.

Technical Targets

- Anode Targets: 700-1000 mAh/g and > 800 cycle; 1,600 mAh/g as needed at end of the project.
- Cathode Targets: 255 mAh/g and >800 cycles.

- Cell Targets: 350 Wh/kg, 800 Wh/L, <\$150/kWh at end of the project.

Accomplishments

- SiNANOde can be controlled in 500 ~ 1800mAh/g with an ICE of > 92%.
- We have improved pouch cell formation protocol to achieve better cycling performance.
- 700~1000 mAh/g SiNANOde has been cycled 800 cycles at 79% retention in coin cell.
- 600mAh/g SiNANOde/NCA cell has ~1000 cycles at 80% retention by third-party verification or 600mAh/g SiNANOde/LCO cell has >300 cycles at 80% retention. The improved 1100mAh/g SiNANOde/NCA cell has a slower capacity fading than 600mAh/g SiNANOde/NCA cell.
- LMR-NMC cathode achieves a reversible specific capacity of 275 mAh/g with an improved C-rate performance from 0.2C to >0.5C at high loading, which results in the pouch cells of 300~400Wh/kg using 1200mAh/g SiNANOde.
- Cathode electrode energy density has been improved by reducing inactive material content to total 2%.
- 600mAh/g SiNANOde/LCO pouch cells achieved 260Wh/kg and 600Wh/L. The pouch cells have showed acceptable cell thickness increase of < 14% over 300 cycles. The Si nanowires' expansion can be accommodated in the voids of the Si nanowire-graphite composite electrode. Our observations indicated the stable SEI formation using proprietary electrolyte can minimize the pouch cell thickness increase.
- We have developed a new electrolyte C1.1 that enables higher coulombic efficiency and hence cycling performance for SiNANOde cell.
- We delivered the high energy density cells and PHEV cells to U.S. DOE for evaluation, which has unique specific power and low temperature performance.
- SiNANOde development has been extensively explored on various graphite/carbon powder substrates using low cost precursors, which significantly reduces its production cost and shows high energy density and unique cyclability.
- SiNANOde cell's self-discharge and subsequent recharge is comparable to commercial graphite cells.

Introduction

Based on the ability to distributively generate power locally through solar and wind, more and more people believe that batteries based on Li-ion technologies are the optimal solution to electrify transportation. The cell that we propose with a novel SiNANOde™ and composite cathode, will significantly advance the current state-of-the-art in Li ion technologies.

Approach

Innovative Approach: The objectives outlined above, will be accomplished by combining a high energy cathode technology with, SiNANOde™, a Si graphite composite. Cathode materials currently being used in PHEVs and EVs have a maximum capacity of ~150 mAh/g or less. We will use the well-performed cathode or the composite cathode containing a layered component with high specific capacity. The major technology innovations will be undertaken to accomplish the objectives of this effort:

1. Improve SiNANOde™ capacity from 650 mAh/g to 700~1000 mAh/g in Phase I and to 1,600 mAh/g later. Graphite particle size and morphology will be further optimized to achieve this goal.
2. Achieve increased endurance of cycle-life from 220 to >800. To achieve this, innovative surface modification of the Si nanowire anode is required for improved stability and SEI formation. The electrolyte and binder chemistry will be optimized.
3. Achieve cell energy density of 350 Wh/kg and volumetric density of 800 Wh/L by combining the above high energy anode and cathode materials. The baseline performance of the full cell at the onset of the effort is 210 Wh/kg and 400 Wh/L
4. Achieve cost reduction resulting in <\$150/kWh (cell level). This will be achieved by moving from synthetic graphite (\$35/kg) to natural graphite which is projected to be \$5-\$10/kg. Cost reduction will also be supported through increase efficiency in manufacturing processes and scale-up of both anode and cathode.

Results

We have achieved the following progress:

Cycle Life Enhancement for 700~1000 mAh/g Anode

We have been continuously working on producing pilot-scale manufacturing quantities of SiNANOde. The specific capacity of ~650mAh/g has been achieved and the SiNANOde half cells can be cycled

more than 1200 times with a capacity retention of > 85%. Using a baseline cathode (LCO) the SiNANOde was integrated in the full cells and exhibited ~350 cycles at ~76% capacity retention, which still showed much higher anode-specific capacity over graphite anode. After 200 cycles SiNANOde full cell showed a capacity fading rate comparable to graphite full cell. (Figure II - 43.)

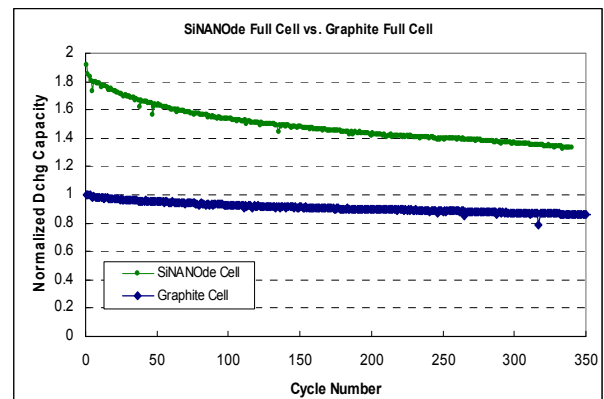


Figure II - 43: Baseline SiNANOde/LCO full cell

It is well known that OCV and SOC have relationship based on Nernst equation. SOC estimation is expected by using Nernst equation at the timing when OCV can be measured or estimated. As a peculiar problem for HEV battery, there is voltage hysteresis phenomenon, in which measured OCV after charge (discharge) is higher (lower) than estimated OCV by Nernst equation. This voltage hysteresis has been modeled by adding simple voltage modification term to Nernst equation, by using a SOC-dependent voltage source including hysteresis. These method needs history information whether battery has been charged or discharged. And SOC and OCV is no longer one-to-one relationship. Minimizing the voltage hysteresis is certainly critical. With the full cell of SiNANOde/LCO this cell voltage hysteresis has been evaluated. Our SiNANOde cell voltage hysteresis effect is much less pronounced (<0.1V). The hysteresis effect is less pronounced for 8%SiNANOde/LCO full cell in comparison with 8%Si powder-graphite/LCO full cell. (See Figure II - 44.)

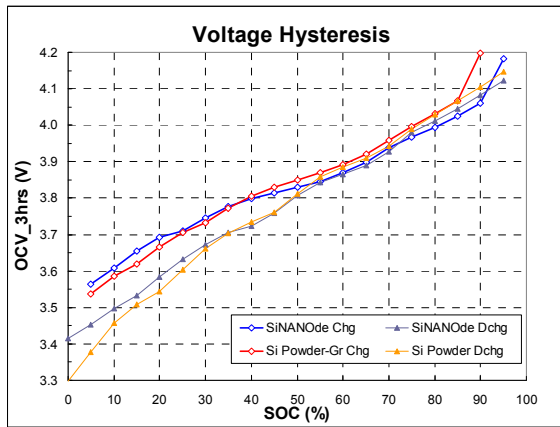


Figure II - 44: Voltage hysteresis of SiNANOde and Si powder-graphite full cells

We have made improvement in the specific capacity of SiNANOde of up to 850mAh/g of reversible capacity. We further improved the conductivity of SiNANOde to optimize the SiNANOde material, which has showed longer cycling life of ~800 cycles at 79% capacity retention at 0.3C cycling in the half cells. It should be noted that at beginning the cell has been used for various C-rate testing. (See Figure II - 45.)

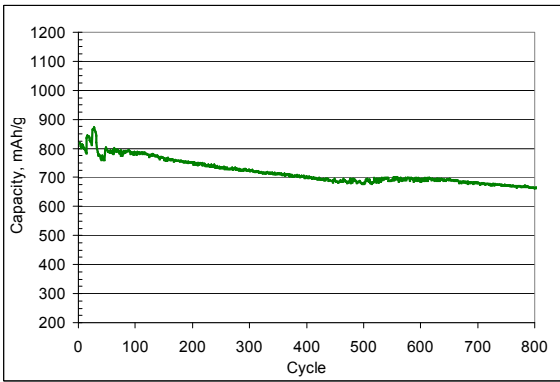


Figure II - 45: SiNANOde half cell with 700~1000mAh/g

Enhanced Si Capacity 1,600 mAh/g Anode

We are improving the high specific capacity of SiNANOde and obtained 1678mAh/g. The first coulombic efficiency is still more than 92%, Figure II - 46. Various binders have been used to achieve better cycling performance (ongoing). Even though the specific capacity has been increased up to >1600mAh/g the Si nanowires can also be uniformly distributed on the graphite powders, shown in Figure II - 47. This proves that the SiNANOde production approach allows tuning Si-content over a wide range.

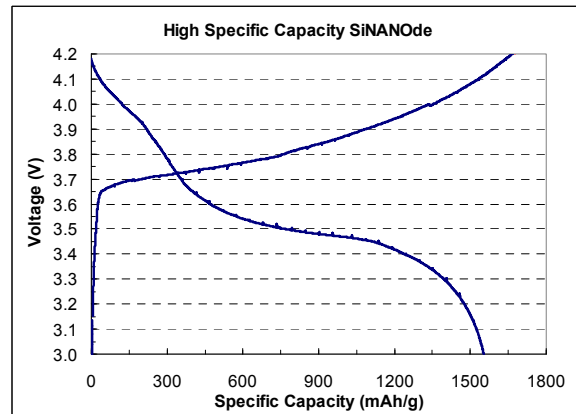


Figure II - 46: >1600mAh/g SiNANOde's voltage profile

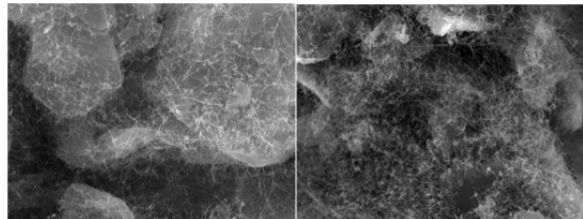


Figure II - 47: Uniform Si Nanowire distribution on graphite powders for 700mAh/g (Left) and >1600mAh/g (Right)

Optimization of Cathode Composition

We have tested Mn-rich cathode materials in coin half cells to confirm their electrochemical performance, so that the optimal cathode will be combined with Si anode, SiNANOde.

To improve the cathode materials, its surface has been modified via various ways in Figure II - 48 (Top). The ICE of the cathode electrode can be improved by optimizing its electrode composition in Figure II - 48 (Middle). Those improvements result in enhancement of its C-rate performance (Figure II - 48, Bottom).

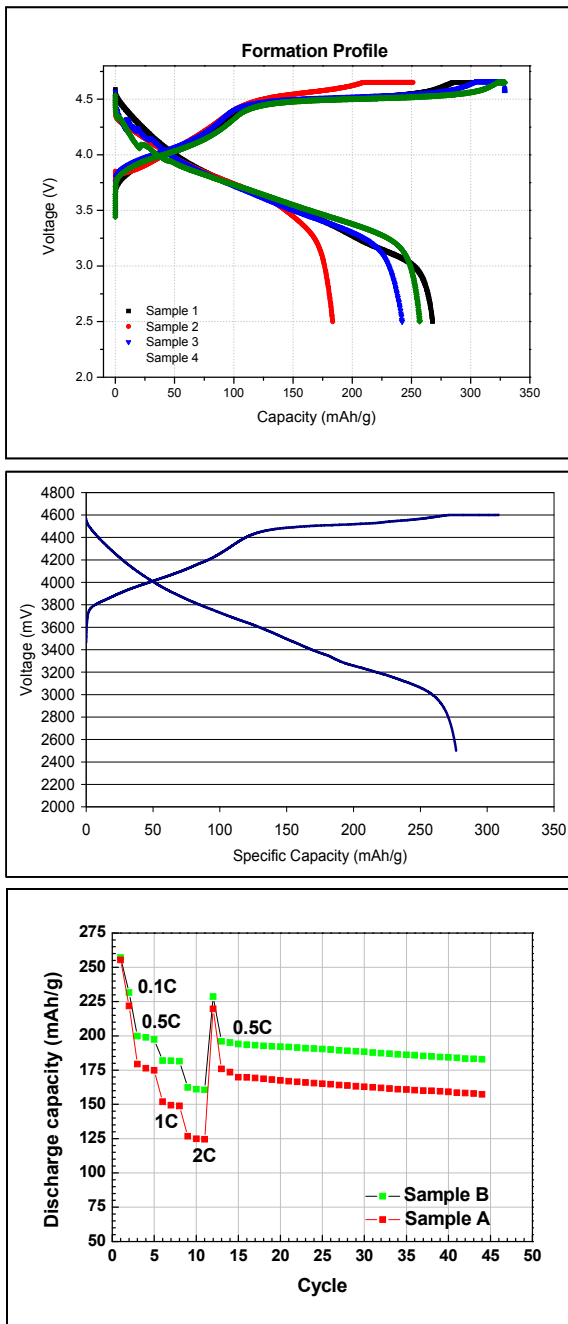


Figure II - 48: Voltage profiles and rate capabilities of cathode candidates

It is critical to identify an appropriate high voltage electrolyte to enhance the cathode cyclability. In Figure II - 49, cell #2 uses an electrolyte tailored to have high voltage stability, which shows much better cycling performance over the cell#1 using the regular electrolyte.

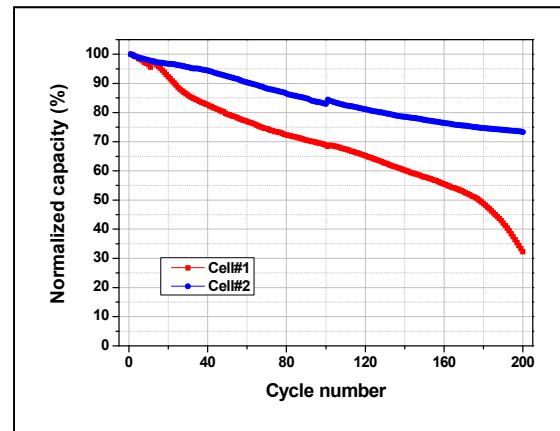


Figure II - 49: Cathode cyclability vs. different electrolyte

Feasibility Test of High Energy Cells with Mn-rich Cathode and SiNANOde

In order to demonstrate very high energy density in the cells using Mn-rich cathode and ~ 1200 mAh/g SiNANOde, various cells were designed to achieve 250, 300, 350, and 400 Wh/kg. One key finding from this work is that the rate capability needs to be improved.

The cycle life test of each cell is carried out at 0.3C under 80% DOD. In the case of 400 Wh/kg cell, its initial capacity decreases, compared with other cells. The 400Wh/kg cell showed $\sim 55\%$ capacity retention at 150th cycle (Figure II - 50).

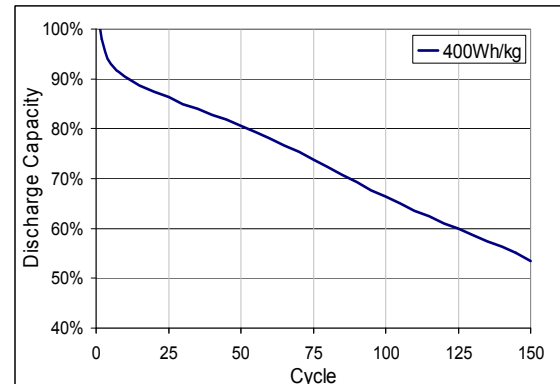


Figure II - 50: Cycle life at 0.3C rate (80% DOD)

The anode used in Figure II - 50 has a specific capacity 1000~1200mAh/g, shown in Figure II - 51a, which showed stable cycling performance. At beginning the cell formation has been done at 0.05C. The high capacity SiNANOde material shows better cycle life at 0.5C. This implies that the high capacity cathode also has negative impact on the cycle life of the full cell (Figure II - 50), which suggests that in order to evaluate SiNANOde cyclability we should select other cathodes (e.g. NCA or LCO or NCM). In addition, the reversible specific capacity of SiNANOde has been further increased up to 1200~1400mAh/g by controlling Si

nanowire content in our recently improved SiNANOde, shown in Figure II - 51b.

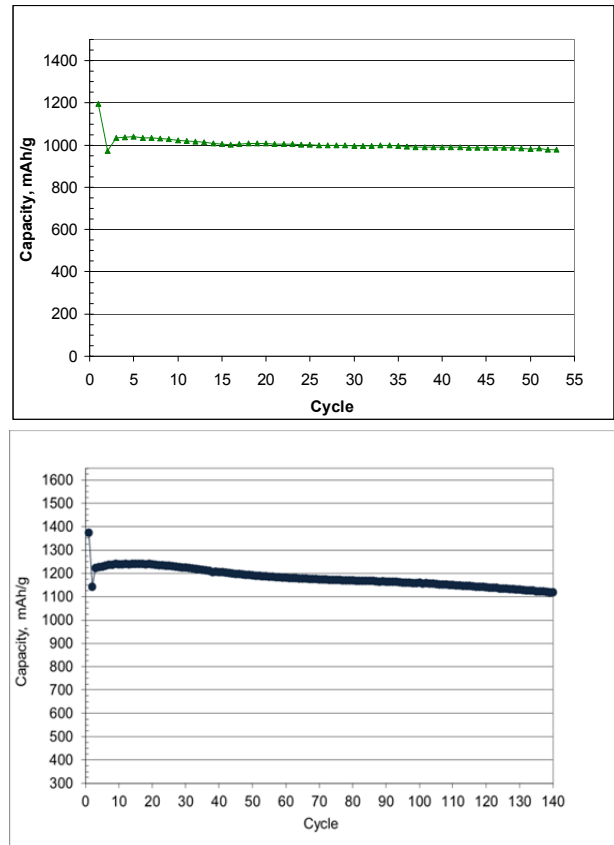


Figure II - 51: (a) 1200mAh/g SiNANOde cyclability in half cell; (b) 1400mAh/g SiNANOde cyclability in half cell

LMR-NMC indeed has a specific capacity of >270 mAh g⁻¹ in 4.6~2.5V but it requests high voltage electrolyte for its cycling otherwise its specific capacity will not be as high as NCA, NCM and LCO in 4.4~3V.

Well-established LCO, NCA or NCM has a specific capacity of 160~200mAh/g, which only uses a conventional electrolyte (Figure II - 52).

Further reducing inactive material content in the cathode electrode may increase the cell energy density. We have demonstrated good performance for NCA and LCO cathode electrode with only 2% total inactive material.

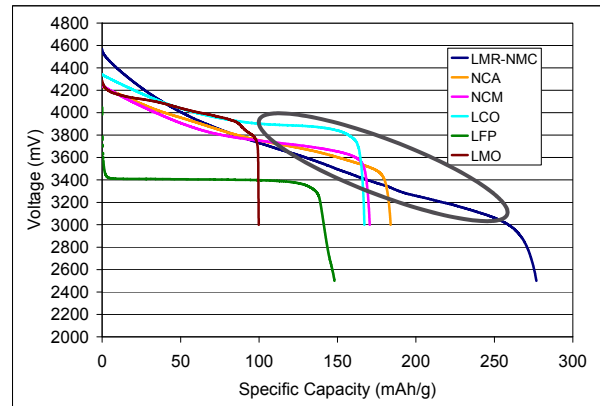


Figure II - 52: Discharge voltage profiles of various cathode materials

Cell Design Study for High Energy Cells with Well-established Cathode and SiNANOde

It is found that the electrode loading is a dominant factor in demonstrating a high energy cell with various cathodes and SiNANOde anode. The electrodes with the desired high loadings are difficult to coat on larger coater and result in the substantial increase in resistance. We have tried to prepare the electrode with higher loading through formulation work so that the pouch cells can be made in plant.

In addition, cell design study has been carried out using three different grades of Si anodes with specific capacity of 600, 800 and 1200 mAh/g, respectively. The cell operation voltage is up to 4.4 V (Table II - 9).

Table II - 9: In plant - processable high loading electrode study for high energy cell design

Loading	600 mAh/g	800 mAh/g	1200 mAh/g
Processable high loading (in plant), 4.4 V	290 Wh/kg	320 Wh/kg	330 Wh/kg
Not processable → processable high loading (in plant), 4.4 V	300 Wh/kg	330 Wh/kg	350 Wh/kg

Cycle Life Improvement of Pouch Cell with 600~1000 mAh/g Anode

Pouch cells have been built using the 600 mAh/g SiNANOde and NCA cathode (Figure II - 53). As the electrode has been heavily calendered the capacity retention is about 78% at 300th cycle. An energy density of 250~290 Wh/kg can be achieved for SiNANOde NCA pouch cells.

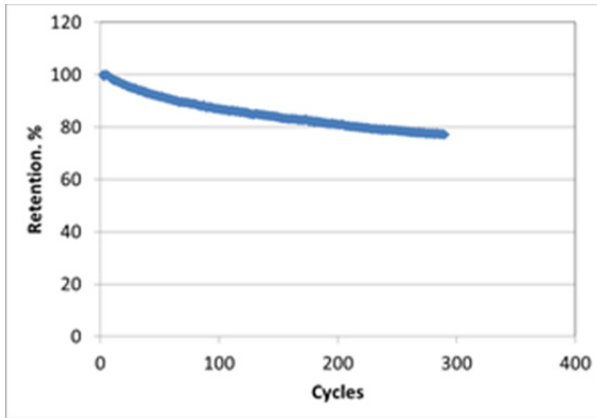


Figure II - 53: Cycle life of the pouch cell using 600 mAh/g SiNANOde at 0.5C rate (DOD 100)

The pouch cells have showed acceptable cell thickness change of < 14% cell swelling over 300 cycles (Figure II - 54).

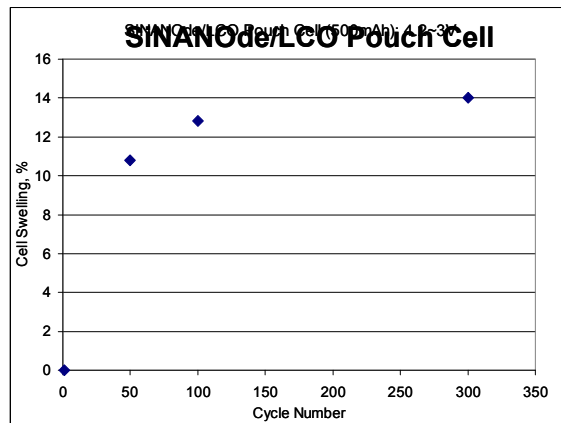


Figure II - 54: Thickness change of High Energy Density Pouch Cells: SiNANOde/LCO

Combining with the well-performed NCA cathode the SiNANOde cylindrical cell shows >1000 cycle 80% retention at +0.3C/-0.5C cycling. The relatively faster capacity reduction is observed in the beginning 100 cycles. Then the cell approaches to a more stable zone and stabilizes for 1000 cycles at 82% retention, which also shows higher anode-specific capacity over graphite anode, shown in Figure II - 55. As a reference, commercial graphite cell can be cycled 1000 times at 81% capacity retention. It demonstrates that the SiNANOde can be very stable and also can be further improved by forming more stable SEI in the first 100 cycles.

In addition, the SiNANOde/NCA combination has also demonstrated good cycle life of ~1000 cycles at 70% retention in the third party pouch cells under confidential agreement. (See Figure II - 56.)

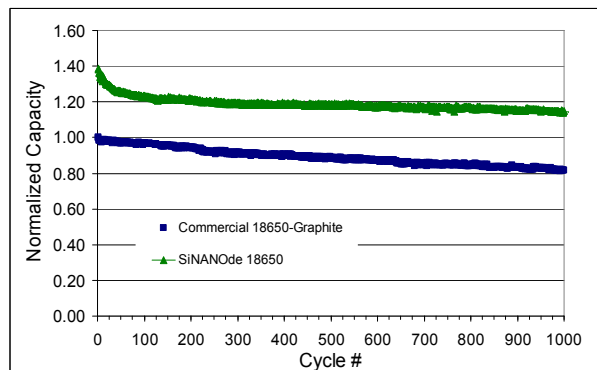


Figure II - 55: 600mAh/g SiNANOde/NCA full cell cyclability

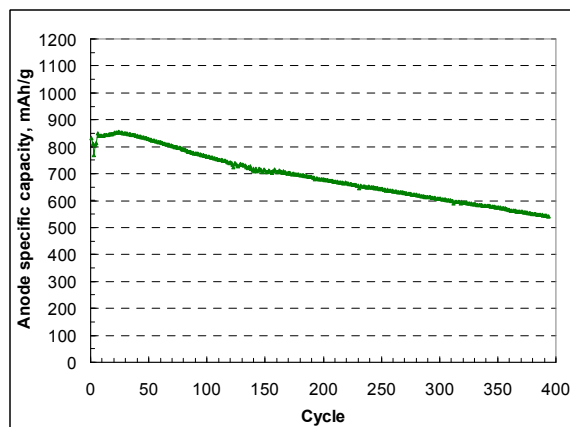


Figure II - 56: High capacity SiNANOde/LCO pouch cell performance

High capacity SiNANOde/LCO pouch cell has achieved a reversible capacity of ~ 850mAh/g. It has showed a good cycling life at +0.3C/-0.5C for the pouch cell, 210 cycles at 80% and 330 cycles at 70% retention. (See Figure II - 57.)

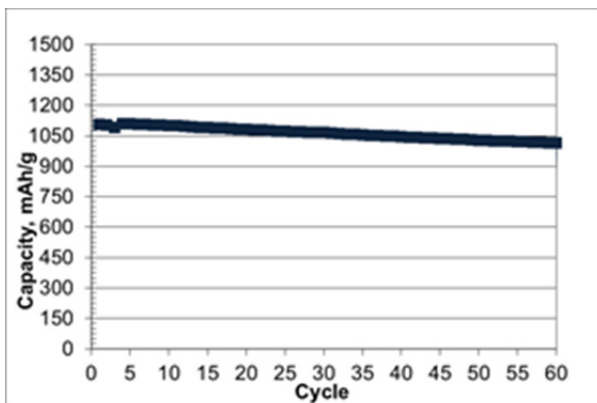


Figure II - 57: High capacity SiNANOde/NCA pouch cell performance

High capacity SiNANOde/NCA pouch cell has recently achieved a reversible capacity of ~ 1100mAh/g with a stable cycling performance in 60 cycles (ongoing) at +0.3C/-0.5C. The cell capacity is fading

slower than the 600mAh/g SiNANOde/NCA cell in Figure II - 55 because we improved the SiNANOde composite material and cell formation protocol.

At 25°C ~ -20°C, SiNANOde pouch cell shows a typical temperature-dependent performance similar to graphite pouch cell in Figure II - 58. Even at -30°C, SiNANOde cell can be charged at C/2 for 5% prior to 4.2V while graphite cell cannot be charged at C/2 as the cell voltage instantly jumps to 4.2V and starts CV charge. SiNANOde cell exhibits two discharging steps at -30 ~ -40°C, indicating that it has potential to be discharged at higher voltage if extending the first step (further investigation is ongoing).

Low Temperature Performance for SiNANOde Pouch Cells at C/2

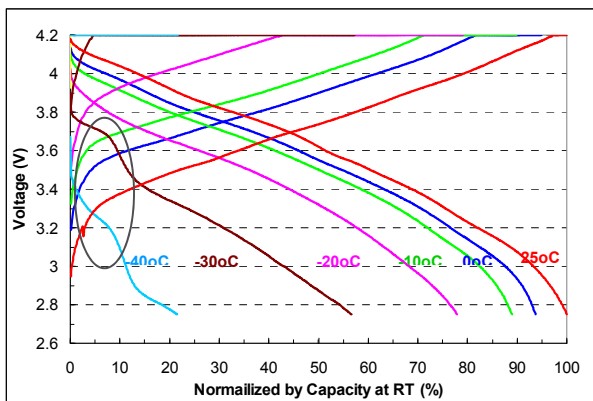


Figure II - 58: Low temperature performance of SiNANOde/NCA cell

At 0.1C ~ 1C, SiNANOde pouch cell (Top) has a specific power similar to graphite pouch cell (Bottom). At 4.5C, superior power performance can be achieved in the high energy density SiNANOde pouch cell in Figure II - 59.

Specific Power of High Energy SiNANOde Pouch Cells

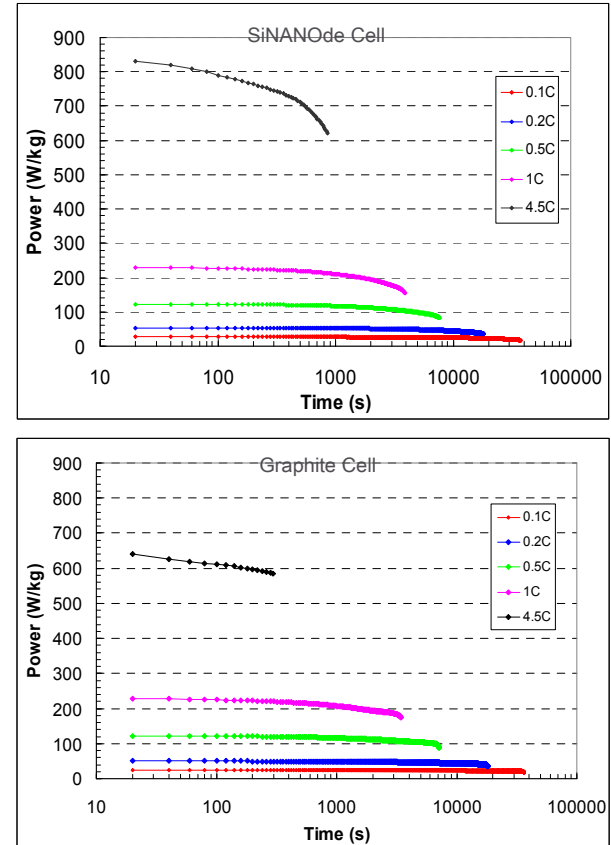


Figure II - 59: Pouch Cell Specific Power of SiNANOde vs. Graphite

SiNANOde cells' self-discharge properties have been investigated at 20°C for one month or at 60°C for one week. SiNANOde cell's self discharge and subsequent recharge is comparable to commercial graphite cell's (Table II - 10).

Table II - 10: SiNANOde Cell Self discharge

Condition	8% SiNANOde/LCO Normalized to Graphite/LCO Control
Retention % @20°C at end of 1 month	99.6%
Realized capacity upon recharge after discharging at 20°C for 1 month	98.7%
Retention % @60°C at end of 1 week	98.7%
Realized capacity upon recharge after discharging at 60°C for 1 week	99.3%

Other Development

We have developed a new electrolyte C1.1 that enables higher coulombic efficiency and hence cycling performance for SiNANOde cell with electrolyte C1.1 is better than that with electrolyte C1 over 250 cycles (Figure II - 60).

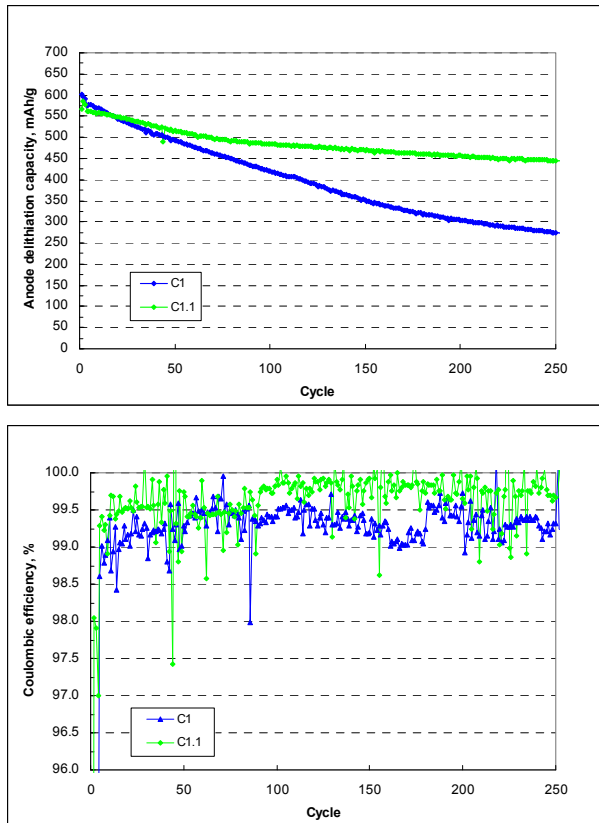


Figure II - 60: New electrolyte enables better cycling performance

SiNANOde development on different graphite substrate has been extensively explored, which results in a wide range of tunable Si nanowire density on the graphite substrate (Figure II - 61). Smaller graphite powders have higher surface area that can host more Si nanowires. It allows us to grow Si nanowires with >50%Si in the SiNANOde composite.

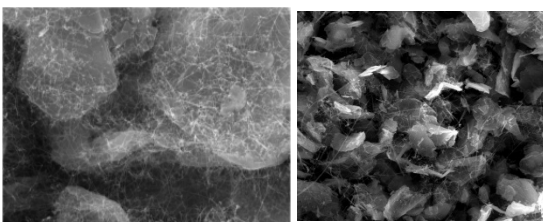


Figure II - 61: Si Nanowire grown on larger graphite powders (Left) and smaller graphite powders (Right) for >800mAh/g

The 500~700mAh/g -SiNANOde pouch cells have already showed the volumetric energy density >620Wh/L in conventional 4.2 ~3.0V range. The

SiNANOde electrode density can be as high as 1.5g/cm³ (Figure II - 62) without breaking Si nanowires.

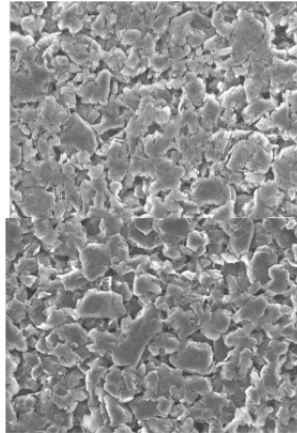


Figure II - 62: Calendered SiNANOde Anode (Left) and Graphite Anode (Right) with 1.5g/cm³

There is no crack during winding SiNANOde electrode around 0.9 mm-diameter pin (see Figure II - 63)

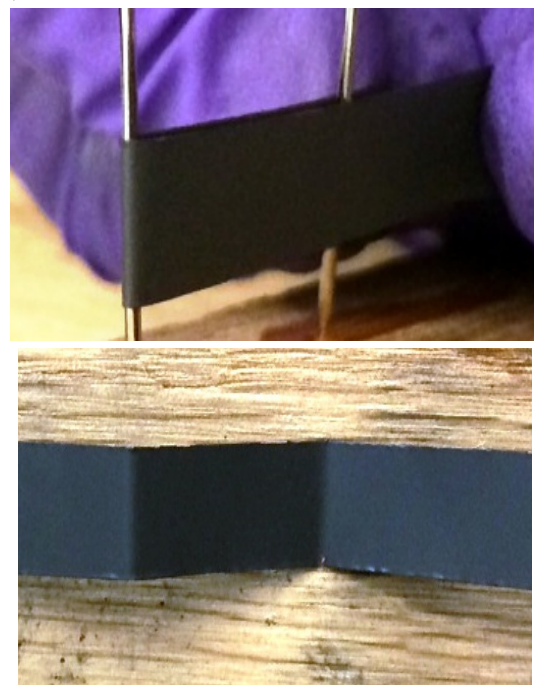


Figure II - 63: Winding on 0.9 mm diameter pin

Conclusions and Future Directions

We have made dramatic progress in Si composite anode (SiNANOdeTM), Mn-rich cathode and cell performance improvement. The specific capacity of SiNANOde can be controlled in a range of 500 to 1800mAh/g by tuning amounts of engineered silicon nanowires on the low cost graphite powders, as needed, using low cost precursors, which significantly reduces

its production cost but still shows high energy density and good cyclability. Initial coulombic efficiency has been improved up to more than 92% for all the SiNANOde products. Almost 100% utilization of Si capacity has been realized in the cells. By optimizing Si nanowire coverage and distribution on the desired graphite surface and by optimizing electrolyte and binder chemistry as well as by improving pouch cell formation protocol, cycle life has been greatly improved. We have demonstrated a cycle life of more than 800 cycles at a capacity retention of 79% for the SiNANOde with 700~1000 mAh/g in half cell. We have also demonstrated good cycling performance of >1000 cycles in the full cells combining with NCA cathodes. The improved 1100mAh/g SiNANOde/NCA cell has a slower capacity fading than 600mAh/g SiNANOde/NCA cell.

Further cathode development has achieved a reversible specific capacity of >275 mAh/g and has improved its C-rate performance from 0.2C to >0.5C even at high loading. Therefore, we are able to make full cells with high energy densities of 300~400Wh/kg using the SiNANOde of 1200mAh/g and the improved cathode materials.

We are determining the optimal Si%, electrode density and thickness so that we are able to achieve high energy density in the cells with good C-rate performance and cycling performance.

Pouch cell has showed the energy density of 250~290Wh/kg using 600 mAh/g SiNANOde and LCO or NCA cathode. The pouch cells show acceptable cell thickness increase of < 14% over 300 cycles. We have developed a new electrolyte C1.1 that enables higher

coulombic efficiency and hence cycling performance for SiNANOde cell with electrolyte C1.1 better than that with previous electrolyte C1. The stable SEI formation using this proprietary electrolyte can minimize the pouch cell thickness increase.

SiNANOde cell's self-discharge and subsequent recharge is comparable to commercial graphite cells.

The hysteresis effect is less pronounced for 8%SiNANOde full cell in comparison with 8%Si powder-graphite full cell.

We have delivered high energy density pouch cells and PHEV cells to US DOE as 2013 deliverables, which has unique specific power and low temperature performance.

The achievements have proved that the proposed technical approach is viable.

FY 2014 Publications/Presentations

1. "Innovative Cell Materials and Design for 300 Mile Range EVs", ES130_Zhu_2014_p, US DOE Vehicle Technologies AMR, 2014.
2. "Making Silicon Nanowire Battery Technology Ready for Commercialization: Materials, Processes & Cells", Yimin Zhu, 2014 Lithium Battery Power: Driving Breakthrough Energy Technologies from Lab to Market, November 11, 2014; Capital Hilton, Washington, DC.

II.B.4 Advanced High-energy Li-ion Cell for PHEV and EV (3M)

John Tabacchi (DOE Program Manager)
Subcontractor: 3M Company

Jagat D. Singh (Program Manager)
3M Center, Building 209-2C-26
St Paul, MN 55144
Phone: (651) 575-1230; Fax: (651) 736-7478
E-mail: jdsingh@mmm.com

Subcontractors:
General Motors, Umicore, Iontensity, Army Research Laboratory and Lawrence Berkeley National Laboratory

Start Date: October 2013
Projected End Date: September 2015

Objectives

Leverage a cross functional team to develop and demonstrate an Advanced High Energy Li-Ion Cell with superior performance envelope. The specific deliverables include:

- Baseline cell, based on the advanced materials developed in 3M's current contract number DE-EE0005499 titled, "High Energy Novel Cathode / Alloy Automotive Cell".
- Advanced cell >2Ah achieved by cell level integration of high capacity Si anode with $\geq 15\%$ improvement in lithiated volumetric capacity, high voltage cathode with 10% increase in Cathode Energy Factor (CEF), advanced electrolyte and advanced stable Si anode composite with novel conductive polymer binder.

Technical Barriers

Lithium-ion battery (LIB) shows a remarkable robustness as witnessed through its application in today's world of portable consumer electronics, despite being a quasi stable chemistry. The operation at high voltages helps provide high energy but comes with significant challenges in life. The development of advanced materials (anode, cathode and electrolyte) is important to address this challenge. The key technical barriers are

- Short term cycle life and low rate capability.
- High voltage electrolyte stability.
- Si alloy volume expansion over life.

Technical Targets

- Develop a >2Ah Advanced High Energy Li-Ion cell for EV and PHEV applications.
- Develop a high voltage NMC based cathode.
- Develop electrolyte for high voltage NMC and Si alloy anode.
- Develop a high capacity Si alloy anode.
- Develop advanced stable Si anode composite with novel conductive polymer binder.

Accomplishments

- Baseline cell delivered by 3M for testing at Argonne National Laboratory.
- Scaled up (100+ kg) of baseline high voltage NMC based cathode material by Umicore.
- Scaled up (100+kg) of baseline Si alloy anode material by 3M.
- Development of advanced high energy and high voltage (>4.5V) NMC based cathode material.
- Screening electrolyte additives which synergistically work with high voltage cathode and Si alloy anodes.
- Gap analysis of baseline cells by GM.
- Demonstration by Leyden Energy (now replaced by Iontensity) of excellent cycle life and low cell expansion after 600 cycles in 100% DOD window in pouch cells with Si alloy anode.
- 1st iteration of stack pouch cells assembly by Iontensity.



Introduction

LIB technology's potential to enable a commercially viable high energy density is the key to a lower \$/Wh, thereby a low cost battery. The design of a High Energy LIB (HE-LIB) with high power, safety and long life is a challenge that requires cell design from the ground up and synergy between all components. 3M Company (3M) strongly believes that this challenge can be addressed by 'teaming' key commercial businesses [General Motors (GM), Umicore and Leyden Energy (Leyden)] as well as labs [Army Research Laboratory (ARL) and Lawrence Berkley National Laboratory (LBNL)]. The technology from each team member will be complimentary and a close working relationship spanning the value chain will drive productivity. This

HE-LIB would provide more energy efficient and environmentally friendly vehicles, meeting or exceeding performance expectations and goals, making America less dependent on imported oil.

Approach

This project takes a team approach to address the project challenges. Each team member brings strong technical expertise to the table. The team consists of

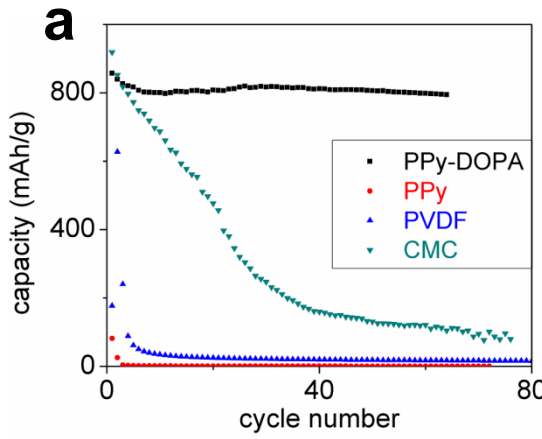
- 3M: Development of advanced cathode, anode and electrolyte. Sample 18650 cells.
- Iontensity: Design, test, diagnose and sample pouch cells.
- ARL: Development of advanced electrolytes.
- LBNL: Development of advanced conductive binder for Si alloy anode.
- General Motors: Evaluate cells and perform gap analysis vs. vehicle requirements.
- Umicore: Develop cathode synthesis and demonstrate pilot scale manufacturing.

The proposed work will be performed in two distinct phases. Phase I will focus on advanced materials development and baseline validation. Phase II will focus on iterative integration of advanced materials and testing in 18650/Pouch cells.

Results

Advanced Materials Development

Anode development: 3M team leveraged its expertise in the alloy anode technology to study



different compositions of Si alloy anode. The studied compositions targeted to achieve the highest cell energy by reducing the 1st cycle irreversible capacity. Figure II - 64 shows the lower irreversible capacity of alloys B and C when compared to base alloy A.

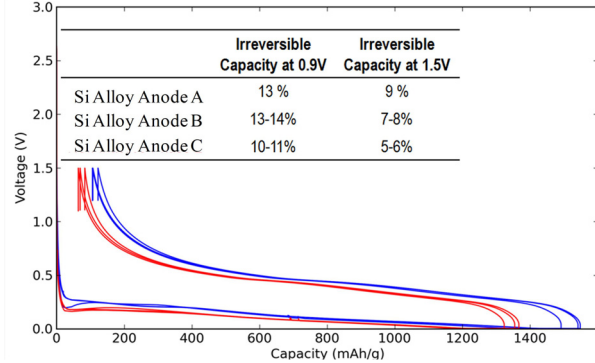


Figure II - 64: Reduction in 1st cycle irreversible capacity by compositional changes to the Si alloy anode

Anode Scale up: 3M successfully scaled up baseline anode material as well as potential advanced materials in its pilot manufacturing facility located in Cottage Grove, MN. Quantities in excess of 100 kgs were manufactured.

Binder development: LBNL applied its electrically conductive polymer binder chemistry towards the development of new binders for 3M's Si alloy anode. Figure II - 65 highlights the performance of one such binder, labeled DOPA.

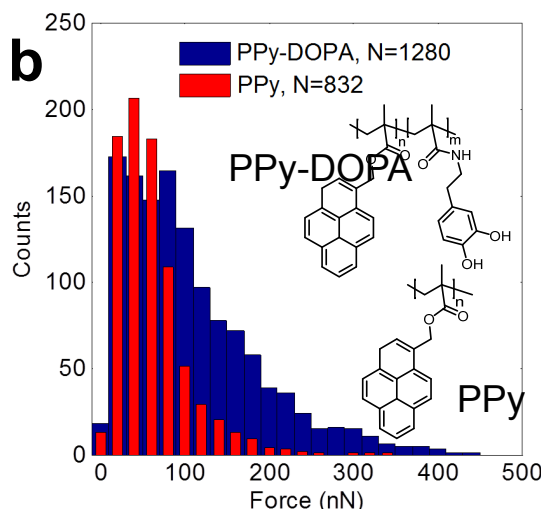


Figure II - 65: (a) Specific capacity vs. cycle number using different binders (10 wt%) with CV7 alloy (90 wt%). The half cells use EC/DEC=3/7, 30% FEC, 1.2M LiPF₆ as electrolyte at a 80 mA/g rate, with a cut-off voltage of 0.01V-1V. (b) Adhesion force between silica micron-size probe and polymer-coated silicon wafer in an atomic force microscopy tapping mode, indicating the well-improved adhesion by incorporating catechol functionality in the binder

Cathode development: 3M's has taken a bi facet approach towards the development of high voltage

(>4.5V) NMC based cathodes. One approach uses a core shell based structure and the other approach use a

surface coated NMC. Figure II - 66 compare the 18650 energy with these two cathodes when matched to Graphite and Si alloy anode composite.

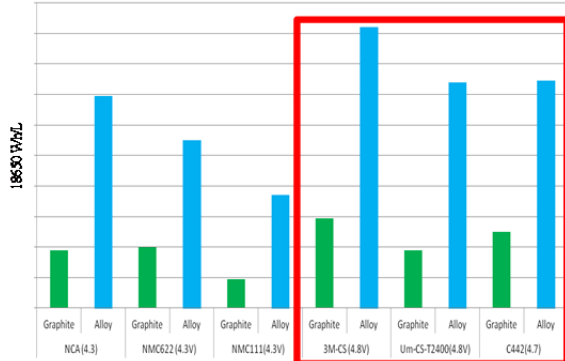


Figure II - 66: Comparison of 18650 cell energy with the different cathodes and anodes. Design with 3M lab scale C/S matched to Si anode shows the maximum energy. Umicore scaled C/S & 3M coated 442 show similar energy

Cathode Scale up: Umicore successfully applied its cathode process expertise to prepare core shell structured NMC precursor by continuous precipitation method. Precursors showed dense core and well-developed surfaces consisting of needles or plates like flowers. Some of precursors also showed quite dense surface (Figure II - 67 (a), (b)). After lithiation, the final product showed the same core-shell morphologies as precursors. However, flower-like surface has changed into hardly agglomerated rods due to sintering. Compared to the reference sample (PO332, 3M designed process, lab-scale), electrochemical properties of the pilot sample showed slightly lower performances such as capacity and cycle stability (Figure II - 68).

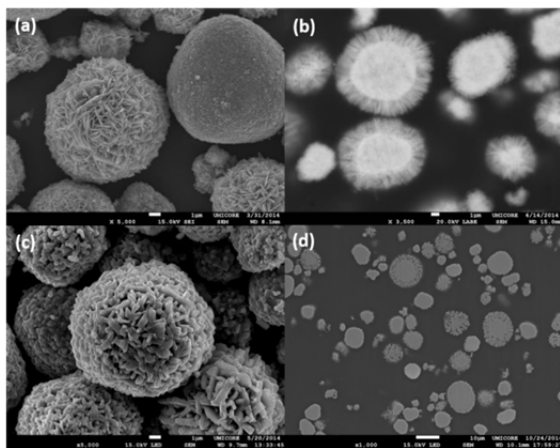


Figure II - 67: Core-shell NMC precursors of (a), (b) and their final products (c), (d)

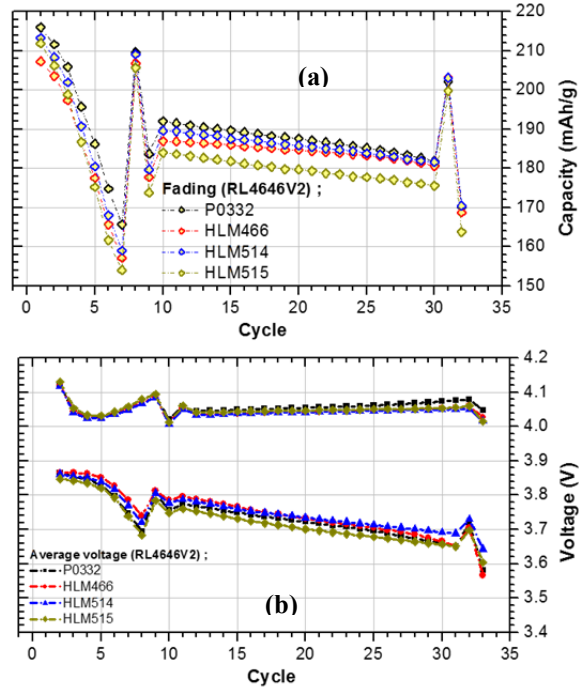


Figure II - 68: Coin cell (vs. Li) results of final products

Electrolyte development: The electrolyte development activities are being simultaneously conducted at 3M and ARL. ARL has been investigating various additives in full coin cell configurations. Thus far, the tested additives have had no positive or negative effect on the cell performance. ARL has identified six additives that have shown potentials in the initial limited cycles for improving the fade rate of the cells. However, these tests were carried out in electrolyte flooded coin cells such that the amount of electrolyte additive per unit active electrode materials might be too high. In pouch or 18650 prototype cells, the amount of electrolyte per cell is limited. The results obtained in flooded coin cells may not translate well into real cells with limited amount of electrolyte. ARL thus decided to test electrolyte additives using limited amount of electrolytes in button cells. A target amount is 12 μ L of electrolyte for 6.4 mAh button cells, which is equivalent to 2.2 g Ah used in Iontensity pouch cells, was initially chosen. However, the results were not reproducible and displayed erratic cycling behavior. It was concluded that the limited electrolyte introduced wettability issues due to non-vacuum filling and sealing. When the electrolyte amount was increased to 25 μ L, the button cells showed reproducible cycling with excellent efficiency (as high as 99.95%). Multiple button cells are being tested with various additives at varying concentrations. The results will be analyzed and the best formulations will be tested in pouch cells using only limited amount of electrolyte.

An electrolyte which not only helps to improve the cycle life of Si alloy anode but also help improve the stability with high voltage NMC cathode is key to this

project. Full coin cell with ‘Si Alloy || NMC’ and ‘High Voltage || Graphite’ as the electrochemical couples were tested with different electrolytes for performance evaluation. Figure II - 69 shows the performance of these electrolytes. L20446 may help improve the performance of a ‘Si Alloy || High Voltage NMC’ electrochemical couple.

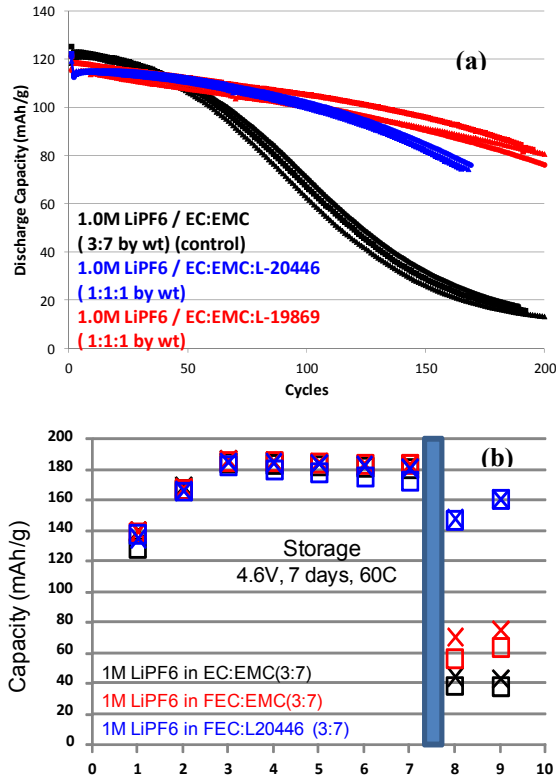


Figure II - 69: (a) Discharge Capacity vs. Cycles of ‘Si alloy||NMC’; 4.2-2.8V; 25°C; C/5. (b) Discharge Capacity vs. Cycles of ‘High voltage NMC||Graphite’; 4.6-3.0V; 25°C; C/5

Materials Testing in 18650/Pouch Cells

Baseline cells: 18650 format cells, with the advanced materials developed under the contract number DE-EE0005499 titled, “High Energy Novel Cathode / Alloy Automotive Cell”, were assembled, prescreened and shipped to ANL for testing. Figure II - 70 shows the increase in discharge energy from these baseline cells. The baseline cells utilize a high voltage NMC core shell cathode matched to high Si loading anode composite. This high voltage ($\geq 4.55V$) electrochemical couple uses a standard electrolyte (0.95M LiPF₆, 0.05M LiBOB in 35% FEC, 51%DEC & 14%PC). No high voltage electrolyte additives were used. Going forward we hope to develop additives to help improve performance at high voltage.

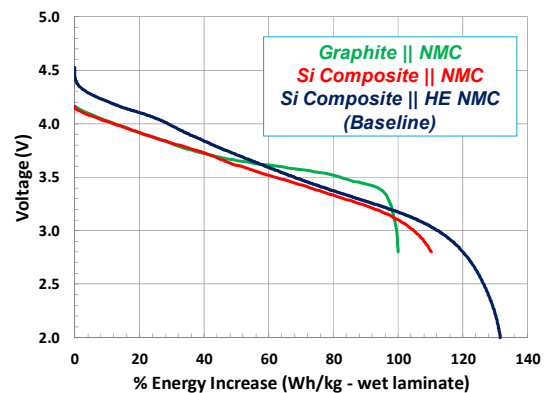


Figure II - 70: Coin cell (vs. Li) results of final products

Baseline gap analysis: 18650 format cells were sampled for performance testing and gap analysis to GM. These cells had the same cell design as the baseline cells. The cells showed acceptable rate performance at room temperature but low rate capability at 0°C and 10°C. The cells lost 35% capacity at 45th cycle. Dramatic increase in cell resistance was observed and the increase was the main reason for capacity loss. Cycled and formed cells were diagnosed to understand the degradation mechanism. SEM analysis showed that the cathode particles have variation on transition metals distribution, and the core-shell structure is not obvious for most of the particles (Figure II - 71). A thick passivation layer was observed on the cycled cathode material, which may be due to electrolyte decomposition (Figure II - 71). The passivation layer could be part of the reason for internal resistance increase.

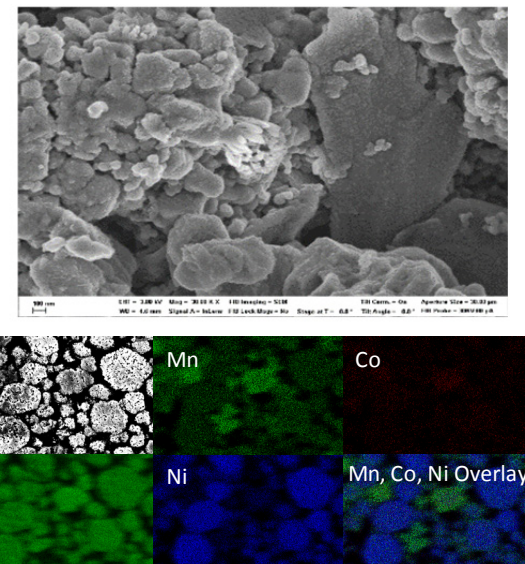


Figure II - 71: SEM and elemental analysis of cycled cathode

Binder degradation was observed in the cycled anode, which caused anode material delamination observed during cell tear down (Figure II - 72).

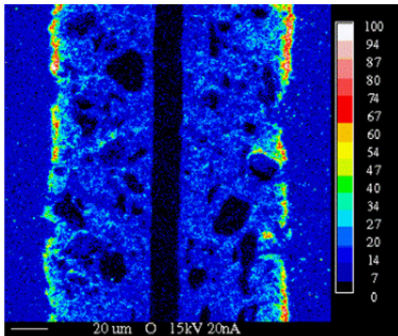


Figure II - 72: Oxygen only observed on the surface of anode

Sulfur was observed on the anode, which comes from the residue in cathode during synthesis. But it is unclear how the sulfur impacts cell performance. A thick SEI layer was observed on the cycled anode, which contains S, F, Mn, etc. These elements were mainly observed on the top layer of aged anode (Figure II - 73).

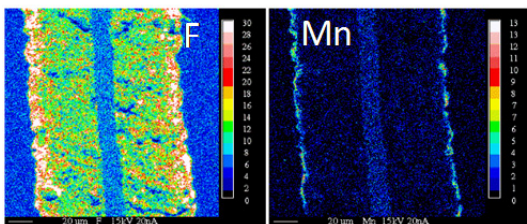


Figure II - 73: F and Mn distribution on cycled anode

Conclusions and Future Directions

Baseline cells were sampled to the DOE designated facility. Advanced materials were investigated during this period. The team is close to deciding on the advanced chemistry comprising a high capacity (low irreversible) Si alloy anode matched to a high voltage ($>4.5V$) NMC based cathode. The team is investigating high voltage electrolytes formulations that can significantly improve life performance. The team plans to build dry pouch cells (assembled by Iontensity) and sample on a regular basis to 3M & ARL. This will help enable more efficient high voltage electrolyte development.

FY 2014 Publications/Presentations

1. 2014 DOE Annual Peer Review Meeting Presentation.
2. 2014 Progress review at 3M.
3. 2014 ECS conference.

II.B.5 Solid Polymer Batteries for Electric Drive Vehicles (Seeo)

Bruce Mixer (NETL Project Manager))

Subcontractor: Seeo, Inc.

Hany Eitouni (Program Manager)

3906 Trust Way

Hayward, CA 94545

Phone: (510) 782-7336; Fax: (510) 782-7337

E-mail: heitouni@seeo.com

Start Date: October 2011

Projected End Date: September 2014

Objectives

- Develop, build, and test high-voltage solid polymer electrolyte cells with an energy density ≥ 500 Wh/l that meet USABC performance, lifetime and safety standards.
- Develop a robust commercialization plan that evaluates key risks associated with high-volume manufacturing and estimates cell production costs.

Technical Barriers

This project addresses the following technical barriers:

- Cycling of Li anodes.
- Electrolyte stability at $>4V$ cathode potentials.
- Mechanical performance of high-voltage cathode materials within solid polymer architecture.
- Interfacial performance of layered polymer electrolyte system.

Technical Targets

- Evaluation of high-voltage cathode materials within polymer electrolyte system, including electrochemical stability and mechanical properties.
- Development of polymer materials stable to potentials of high voltage cathode materials.
- Scalable, repeatable synthetic method for polymers.
- Robust, prismatic pouch cell design.
- Test and evaluation to USABC performance and abuse tolerance requirements.

Accomplishments

In 2014, the project:

- Selected a final material composition for high-voltage cells, including active material and polymer materials interfacing with cathodes.
- Optimized a technique to combine pre-formed coatings on cathode particles with additives to form a coating in-situ during cycling.
- Achieved identical charge/discharge performance of R&D size (25 mAh) with manufacturing prototype cells (1Ah).



Introduction

Achieving DOE performance targets for high energy cells requires new materials and approaches to electrochemical energy storage devices. Seeo proposes to meet these targets using high-capacity Li anodes and high-voltage cathode materials contained within a solid polymer electrolyte system, which in turn, enhances the lifetime, efficiency and safety of vehicle batteries.

Approach

The project is executed in three consecutive phases:

- Phase I: Baseline Evaluation and Material Synthesis – Deliver 2Ah baseline cells to establish stability and performance of solid polymer electrolyte cells & perform initial synthesis and characterization of high-voltage materials.
- Phase II: Material Formulation and Scale-Up – Iterate on design of high-voltage materials. Cycle laboratory-scale cells to isolate polymer-cathode couples and deliver interim design cells for technical review.
- Phase III: Cell Fabrication and Testing – Monitor stability and performance of large-area cells. Execute internal performance and abuse tests and deliver final design cells for independent verification.

Results

Material Formulation: Seeo selected NCA as the high-voltage material for the final solid polymer cell design. Focus of Phase II activities included evaluation of coatings around cathode particles to impart electrolyte stability within the solid polymer matrix. In the recent phase, Seeo evaluated an additional processing step, introducing additives to the cathode

formulation that form coatings in-situ during initial cycling of the cells.

Seeo determined that this combined approach – using pre-formed coatings along with additives that coat in-situ during cell cycling – offered the best performance due to coating conformity and thickness. Additives with bare NCA and coated NCA with no additives did not perform as well in cycle testing as the combined approach. A series of additives with coated NCA particles were tested, and a final active material formulation was determined.

Cell Fabrication: Upon achievement of the requisite R&D scale performance for high-voltage cells, Seeo's researchers focused on tuning coating and assembly processes to scale up cells from R&D size (25mAh) to manufacturing prototypes (~1 Ah) without any decline in performance. Processing results from operation of Seeo's pilot manufacturing of Li anode and LFP cathode cells were evaluated in determining the coating and assembly process for high voltage cells.

Large format high-voltage cells in a robust prismatic pouch cell design demonstrate identical charge/discharge profiles to that of R&D cells. The tuned coating and assembly processes are utilized for creation of final deliverable test cells, and economic analysis will be presented in the final project commercialization plan.

Rate (continuous and pulse), efficiency and cycling testing of final deliverable cells has been conducted by Seeo's research team. Manufacturing-scale cells will be delivered to Argonne National Laboratory for independent testing.

Conclusions and Future Directions

In Phase II, Seeo focused on improving baseline performance through incorporation of high-energy active materials and compatible solid electrolyte systems comprised of novel polymeric materials and conductive salts. In addition, Seeo investigated alternate techniques to stabilize high-voltage materials within a solid-state cell architecture.

In Phase III, Seeo isolated the most promising approach for cathode formulation, selected all materials and assembled manufacturing-scale high-energy cells for testing to USABC protocol.

It is challenging to achieve high energy densities alongside safety and long-term reliability using conventional, Li-ion cells that utilize liquid electrolytes. Seeo's novel approach incorporates the inherent safety, speed of manufacturing and robust supply chain associated with solid polymer materials, thus offering a distinct opportunity to breakthrough traditional cost barriers associated with electric drive vehicle batteries. The chemistry and prototype cells developed in this project represent Seeo's Gen II product line which will be manufactured using the same equipment and similar process as the Gen I LFP based system.

FY 2014 Publications/Presentations

1. 2014 DOE Annual Peer Review Meeting Presentation.

II.B.6 Development of High-Energy Lithium-Sulphur Battery Cells (PSU)

Christopher Johnson (DOE Program Manager)
Subcontractor: Pennsylvania State University

Donghai Wang (Program Manager)
328 Reber Building
University Park, PA 16802
Phone: (814) 863-1287; Fax: (814) 863-4848
E-mail: dwang@psu.edu

Subcontractors:
EC Power
Argonne National Lab

Start Date: September 30, 2011
Projected End Date: January 15, 2015

Objectives

- Develop a novel nanocomposite sulfur cathode for lithium-sulfur batteries with high energy density, efficiency, and cycle life.
- Develop a novel Li-rich composite anode for Li-S batteries to improve cell cycle life.
- Develop novel electrolyte and electrolyte additives for Li-S batteries to improve cell efficiency, stability, and safety.
- Design, fabricate, test, and optimize the design of Li-S batteries using the above new technologies to maximize energy, power, abuse tolerance, and other favorable traits.
- Perform thermal testing of the developed Li-S cells and materials.

Technical Barriers

- Polysulfide dissolution and shuttling, combined with degradation of the lithium metal anode and formation of an unstable SEI layer, can severely limit cell lifespan.
- High sulfur loading in the cathode is required for achieving a high energy density; however, high loading often leads to parts of the electrode becoming inaccessible to electrolyte, thereby decreasing energy density and cycle life.
- Cathodes must have high active material loading – however, the low density of sulfur and common composite materials (porous carbon, etc.) make

thin, crack-free, high-loading electrodes difficult to achieve.

- Electrolyte modifications that decrease polysulfide solubility or improve SEI layer stability often come at the cost of increased impedance and other issues.

Technical Targets

- Deliver baseline cells with energy density 280 Wh/L and 80% capacity retention after 500 cycles at 1C rate.
- Develop carbon-sulfur cathode material composed of at least 85 wt% sulfur with capacity of at least 1300 mAh/g, coulombic efficiency > 95%, and 90% capacity retention in 100 cycles at C/3 charge and discharge rate.
- Develop anode with capacity of 1500 mAh/g and capacity retention of 90% after 100 cycles at C/3.
- Full cell tests with cell irreversible capacity < 15%, coulombic efficiency > 95%, and self-discharge < 0.3% per day.
- Thermal stability characterization of the lithiated electrode via DSC.
- Scale up active material production to the 1 kg level.
- Design pouch cells with energy density > 500 Wh/L, 80% capacity retention after 300 cycles at C/2.
- Nail penetration testing at EUCAR Level 3.

Accomplishments

- Carefully analyzed dependence of cell performance on cathode structure and particle size.
- Studied the effects of lithium polysulfide chemisorption using the PSU-5 nitrogen-doped carbon/sulfur cathode.
- Investigated lithium polysulfide-based electrolyte using several diagnostic techniques.
- Investigated cathode-side SEI formation in baseline electrolyte with and without the TPPB additive and ANL-E-4 electrolyte using XPS.
- Demonstrated decreased self-discharge with ANL-E-4 and PSU-E-6 electrolytes.
- Optimized LiP anode pressing pressure.
- Studied the inherent cycling and polarization of LiP anodes in symmetric cells.
- Fabricated over 200 LiP anode pieces for use in 1 Ah pouch cells.
- Developed 1.3 Ah pouch cells with PSU-3 carbon/sulfur cathodes, LiP lithium powder-based

anodes, and ANL-E-4 fluorinated ether electrolyte which retained a capacity of 1.2 – 1.3 Ah after 40 cycles, and exhibited 80% capacity retention after 60 cycles.



Introduction

DOE goals require the development of a high-energy, high-power, high-efficiency, long-lasting, low-cost, and safe battery. This project aims to meet these goals by using the extremely promising lithium-sulfur battery chemistry. The Li-S cathode has a theoretical capacity of 1672 mAh/g with a nominal voltage of 2V. In addition, sulfur does not experience any significant size change during lithium insertion/extraction, making it very stable in principle.

The price of lithium-sulfur's great promise is the major challenges with which it is replete. Lithium polysulfides – intermediate charge/discharge states of the cathode – are highly soluble in traditional electrolytes and can move throughout the battery, experiencing redox reactions and thus causing poor efficiency and loss of active material. Additionally, the lithium metal commonly used as the anode is vulnerable to mossy lithium and dendrite growth and cannot generally form a stable SEI layer, causing further capacity loss and safety concerns. These, combined with optimization and thermal safety considerations, necessitate a significant body of work to bring the Li-S to the commercialization stage.

Approach

To design a superior lithium-sulfur battery, we will focus on several aspects of cathode, anode, electrolyte, and whole-cell study and design. On the cathode side, we aim to increase the sulfur loading, optimize the carbon framework's geometry and ability to adsorb lithium polysulfides, and enhance its practical usability and ease of production. On the anode side, our work focuses on designing and optimizing lithium powder- and silicon-based composite anodes and determining the mechanisms behind their function. Electrolyte-wise, we are working to design new systems that improve SEI stability, decrease active material loss, increase active material utilization, and ensure battery safety. Additionally, we also seek to optimize battery fabrication parameters, ensure compatibility between all battery elements, and characterize the thermal safety and abuse tolerance of our Li-S system.

Results

1. Cathode

The PSU-5 carbon/sulfur cathode material was extensively tested and characterized this fiscal year in preparation for scale-up. The PSU-5 material is composed of carbon-nanotube-interpenetrated mesoporous nitrogen-doped carbon spheres a few tens of microns in diameter. Performance testing of the PSU-5 material indicates that it can enable high-capacity, stable, high-sulfur-loading and high-areal-capacity cathodes for lithium-sulfur cells. In particular, in half-cell tests with LiNO₃-containing electrolyte (1M LiTFSI + 0.2M LiNO₃ in DOL/DME, 1:1 v/v) using the PSU-5 cathode along with a conductive interlayer composed of the carbon framework on which the PSU-5 material is based, a very stable capacity around 1200 mAh/g sulfur was achieved after 200 cycles at a current density of 1.68 mA/cm² after the first two cycles at 0.84 mA/cm². This is shown in Figure II - 74a. The electrodes in this test had 70 wt. % sulfur loading and ~5 mg S/cm², giving a high areal capacity of ~6 mAh/cm², which is very important for enabling future practical applications and use in prototype pouch cells.

Extensive characterization was conducted in order to understand the reason for this excellent performance. Ultraviolet-visible (UV-vis) spectroscopy was used to quantitatively compare the adsorption of lithium polysulfides in the carbon framework of the PSU-5 cathode material to adsorption on other adsorbents reported in the literature, including undoped mesoporous carbon and mesoporous silicon. As shown in Figure II - 74b, these tests demonstrated that adsorption on the PSU-5 framework was several times higher than on other reported adsorbents, even though some had higher surface areas than the PSU-5 framework. This indicates the critical effect of the nitrogen doping on promoting adsorption. Pair distribution function (PDF) analysis was also performed to further investigate the presence of enhanced adsorption caused by nitrogen doping. The PDF data indicated several changes in predominant interatomic bond distances, including those that may correspond to changes in bonding of surface oxygen and nitrogen functional groups. This supports the claim of strong polysulfide adsorption on the PSU-5 framework surface.

In addition to investigation of the PSU-5 cathode, the influence of more general cathode properties such as surface area, pore size, and pore volume were also investigated using an aerosol-generated mesoporous carbon material with tunable pore structure. Performance of cells using these materials as cathode frameworks showed no major dependence on surface area, but significant dependence on pore size and pore volume. This is believed to stem from improved transport of Li⁺ ions and polysulfides with

increasing pore size/volume. In addition, spherical carbon frameworks showed better performance than irregular frameworks, likely due to their decreased contact resistance. These results are highlighted in Figure II - 74c-d.

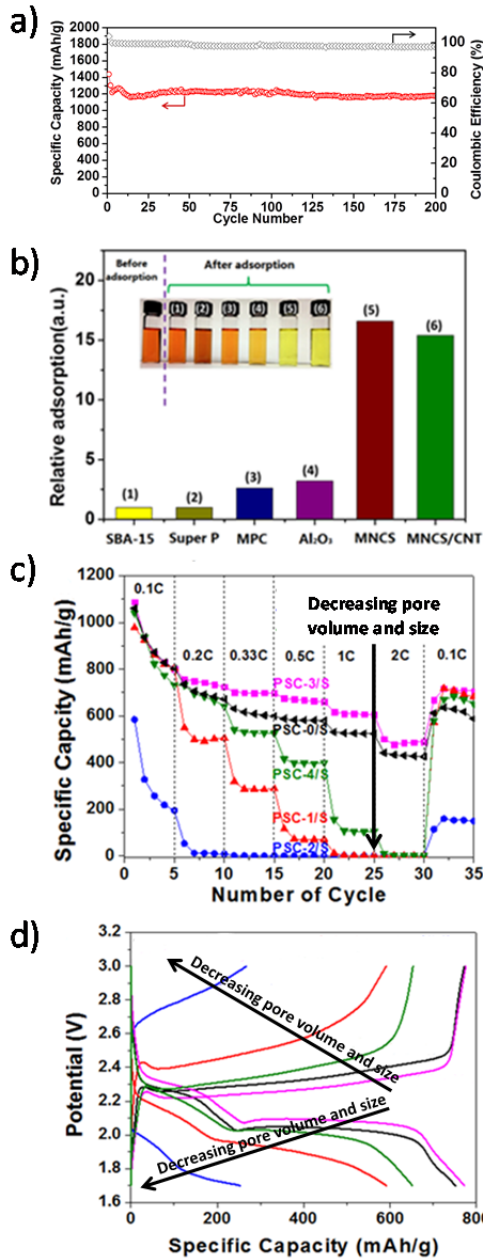


Figure II - 74: a) Performance of the high-sulfur-loading PSU-5 nitrogen-doped carbon/sulfur cathode with a PSU-5 framework-based interlayer; b) adsorption of lithium polysulfides on different adsorbents, relative to adsorption on Super P carbon; c) rate performance of carbon/sulfur cathodes with different pore properties; and d) 50th cycle voltage profiles of carbon/sulfur cathodes with different pore properties

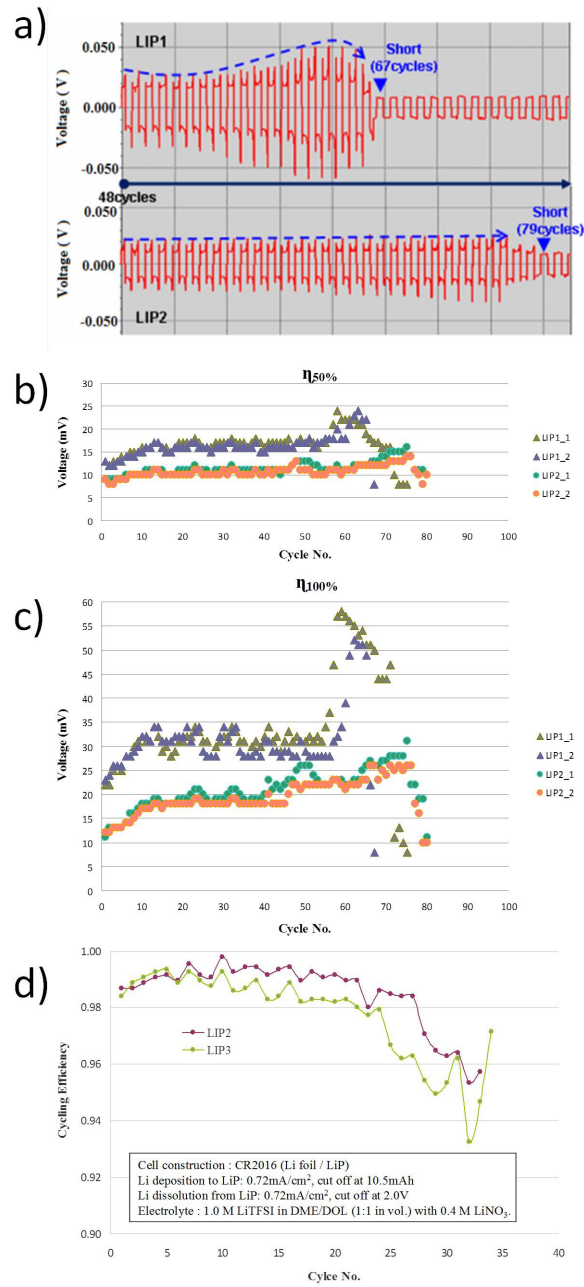


Figure II - 75: a) Charge/discharge curves,, and c) voltage at 100% state of charge for LiP1 and LiP2 cells with cycling, and d) cycling efficiency of LiP2/Li foil and LiP3/Li foil cells with cycling

2. Anode

Significant work has been dedicated to further development and optimization of lithium powder-based LiP anodes this fiscal year.

The evolution of LiP anode performance with cycling was characterized in symmetric coin cells using two different LiP electrode formulations, LiP1 (90 wt. % Li Powder + 10 wt. % binder) and LiP2 (80 wt. % Li powder + 10 wt. % carbon + 10 wt. % binder), with 1.0 M LiTFSI, 0.4 M LiNO₃, and 0.2 M Li₂S₆ in DME/DOL (1:1 v/v) as the electrolyte. These symmetric cells were charged and discharged at constant current to a capacity of 8 mAh, which is close to the Li consumption amount per cycle in LiP / S cells with an N/P ratio of 4 to 5. The voltage at 50% state of charge (SoC) on LiP1 cells increased from 12 mV to 17 mV in the initial 14 cycles and remained around 17 mV until 55 cycles, at which point it increased further to 25 mV. The voltage of LiP1 cells at the end of charge (100% SoC) increased from 22 mV to 32 mV in 10 cycles and subsequently fluctuated between 28 and 34 mV, then began increasing after 55 cycles until reaching 50 mV. After 67 cycles, the 100% SoC voltage dropped sharply to below 15 mV; this is believed to be due to internal micro-shorting of the cells due to lithium dendrite growth. Cells with LiP2 had lower voltages, with their 50% SoC voltage increasing slightly from 8 mV to 16 mV over 75 cycles and their 100% SoC voltage increasing from around 12 mV to around 26 mV over this same range. These indicate the ability of the 10% carbon additive to decrease polarization of LiP cells. Similarly to the LiP1 cells, they showed a sudden drop in voltage after 79 cycles, likely due to internal micro-shorting. These behaviors are highlighted in Figure II - 75a-c.

Cyclability of LiP cells was further studied by analyzing the cycling efficiency in a half-cell configuration, 1M LiTFSI and 0.4M LiNO₃ in DOL/DME (1:1 v/v) electrolyte, lithium foil counter electrodes, and two types of LiP electrodes (LiP2, as above, and LiP3, as 60 wt% Li powder + 20 wt% additive + 20 wt% binder). Lithium stripping of the LiP was performed to 2.0 V, when all Li powder was believed to have been stripped, followed by deposition to a capacity of 10.5 mAh; this process was repeated cyclically. The cycling efficiency (stripping capacity divided by plating capacity) of LiP2 remained above 98% for 27 cycles and decreased to 95.3% after 32 cycles, while the efficiency of LiP3 remained above 98% for 22 cycles and fell to 93.2% after 32 cycles. This is shown in Figure II - 75d.

3. Electrolyte

Extensive testing and characterization was conducted on several different electrolyte systems for Li-S batteries during this fiscal year.

The effects of the ANL-E-4 electrolyte (1M LiTFSI in DOL/TTE) on cathode surface deposition were investigated by X-ray photoelectron spectroscopy (XPS). XPS studies comparing PSU-3 cathodes cycled in ANL-E-4 electrolyte and baseline electrolyte showed

significant differences. Cathodes cycled in ANL-E-4 electrolyte had a lower presence of Li_xSO_y-type surface species; this is likely due to formation of a superior cathode-side SEI by decomposition of TTE, and helps account for the superior performance of cells in this electrolyte. In addition, peaks associated with Li₂S and Li₂S₂ can be seen to disappear after one cycle in ANL-E-4 electrolyte, but are still visible after one cycle in baseline electrolyte. This shows that the reversibility of cycling in ANL-E-4 electrolyte is superior to that in baseline electrolyte, which further explains its superior performance. XPS spectra illustrating some of these results are shown in Figure II - 76. The effects of ANL-E-4 and PSU-E-6 fluorinated electrolytes on self-discharge were also investigated, as discussed in section 4 below.

Tetraphenylphosphonium bromide (TPPB) and lithium difluoro(oxalato)borate (LiDFOB) were also investigated as electrolyte additives. Addition of 5% and 10% TPPB to 1M LiTFSI in DOL/DME electrolyte was found to significantly decrease polysulfide shuttling and improve coulombic efficiency. XPS investigation of cathodes cycled in electrolyte with and without 10% TPPB showed that the intensity of S_{2p} peaks was lower after cycling in TPPB-containing electrolyte, indicating formation of an SEI layer on the cathode surface. In addition, by comparing the intensity of peaks associated with Li₂S and Li₂S₂ species over extended cycling, it appears that a smaller amount of these insoluble species is deposited on the cathode surface with cycling. The effect of LiDFOB was also tested. Silane-based electrolyte, 1M LiPF₆ in tri(ethylene glycol)-substituted silane (1NM3), was chosen for its strong polysulfide-solvating ability, and was used in conjunction with simple ball-milled carbon-sulfur cathodes. LiDFOB-free cells showed fast capacity fading (~400 mAh/g after 50 cycles) and poor efficiency (below 60% after 10 cycles), cells with 2% LiDFOB showed much higher efficiency (> 90%) and slightly improved capacity (> 450 mAh/g after 50 cycles). Highlighted performance of cells with TPPB and LiDFOB is shown in Figure II - 77.

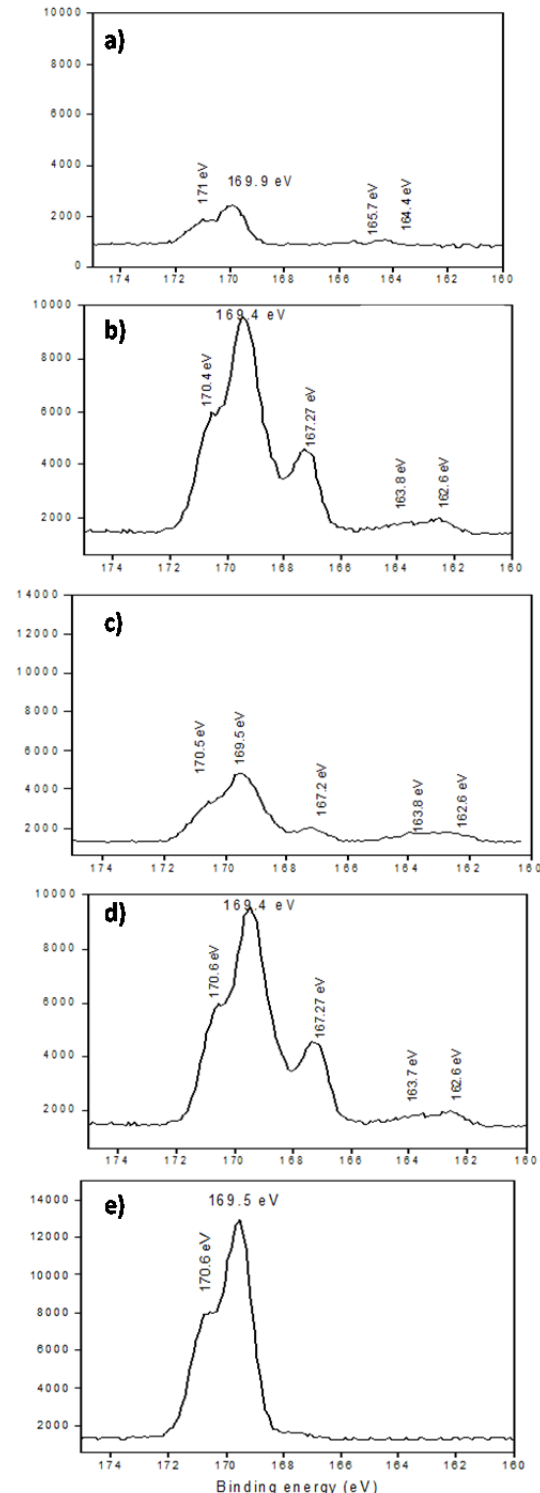


Figure II - 76: XPS S 2p spectra of PSU-3 cathodes: a) fresh, b) after 1 discharge in baseline electrolyte, c) after 1 cycle in baseline electrolyte, d) after 1 discharge in ANL-E-4 fluorinated electrolyte, and e) after 1 cycles in ANL-E-4 fluorinated electrolyte

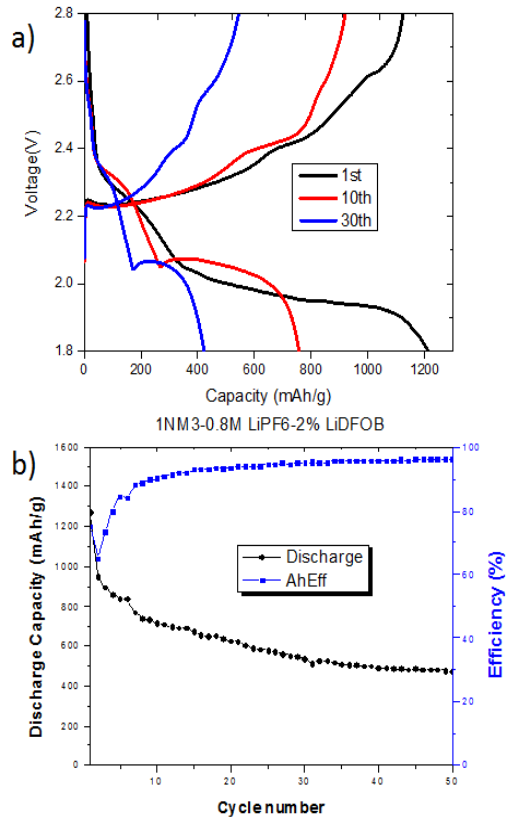


Figure II - 77: a) Charge/discharge curves of cells with 10% TPPB electrolyte additive and b) cycling and efficiency of cells with 2% LiDFOB additive

The solvation of lithium polysulfides in ether electrolyte was also fundamentally investigated through the model system of Li_2S_4 dissolved in DME. Li_2S_4 was chosen based on high-performance liquid chromatography (HPLC) tests indicating it to be the only dissolved species in this solution. Hydrogen nuclear magnetic resonance spectroscopy ($^1\text{H-NMR}$) indicated that paramagnetism may be present due to the unpaired electron on radical anions in the Li_2S_4 solution.

4. Self-Discharge

Self-discharge of cells using the ANL-E-4 fluorinated electrolyte was tested under various conditions. Cells having PSU-3 cathodes were cycled 5 times at C/10 rate, rested for 10 h at room temperature or 55°C after the 5th charge, and then discharged again to determine capacity loss – that is, self-discharge – during the rest period. Cells with ANL-E-4 electrolyte plus 0.1M LiNO_3 showed 0.7% decrease and 0.1% increase in capacity at room temperature and 55°C, respectively, while cells with baseline plus LiNO_3 electrolyte showed 3.8% and 8.4% decreases in capacity under the same circumstances. This indicates a significant reduction in self-discharge using the ANL-E-4 electrolyte. Performance of these cells is shown in Figure II - 78a-b.

Long-term self-discharge of cells using the PSU-E-6 fluorinated electrolyte (0.5M LiTFSI in DOL/DME/BTFE, 1:1:2) was also tested. Cells were cycled 5 times at C/10 rate, rested for two weeks at 45°C after the 5th charge, and then discharged again to determine the self-discharge during the rest period. The PSU-E-6 electrolyte dramatically decreased self-discharge with low-sulfur-loading cathodes from 31% (0.5M LiTFSI and 0.2M LiNO₃ in DOL/DME) to 4% (PSU-E-6 plus 0.2M LiNO₃), as shown in Figure II - 78c, and also helped high-sulfur-loading cells, decreasing self-discharge from 32% to 25% with those same electrolytes, despite a greater volume of the PSU-E-6 + LiNO₃ electrolyte being used in these cells. Self-discharge in low-sulfur-loading cells was found to be primarily due to active material loss, while self-discharge in high-sulfur-loading cells was determined to relate more to polysulfide shuttling.

5. Pouch Cell Design and Testing

Several key factors in determining pouch cell performance were studied during this fiscal year. Pouch cells were fabricated using LiP lithium powder-based anodes, PSU-3 high-sulfur-loading carbon/sulfur cathodes, and ANL-E-4 fluorinated electrolyte.

The effect of cathode porosity on pouch cell performance was studied and found to be significant. Porosity was controlled by roll pressing of cathodes, decreasing the porosity from 78-80% (unpressed) to ~60-70% depending on the chosen parameters. 0.39 Ah design capacity pouch cells using PSU-3 cathodes with 70% average porosity had a high capacity of ~0.5 Ah (~950 mAh/g S) for the first 12 cycles, and then decreased sharply to 0.2 Ah within 50 cycles. In contrast, 1.3 Ah design capacity cells with ~60% average porosity cathodes had a dip in capacity during the first several cycles, followed by an increase in capacity to around 1.3 Ah (~800 mAh/g S) with good stability and efficiency (> 90%) for at least 40 cycles. The specific energy for these cells was around 110-130 Wh/kg at the peak capacity. Capacity retention relative to this value was 80% after 60 cycles, and a capacity of 0.7-0.8 Ah was still attained after 100 cycles. This is shown in Figure II - 79a-c. A porosity of ~60% was thus selected for further work.

Anode pressing was also found to have a key effect on performance, likely because it can improve the adhesion of LiP to the current collector and decrease the electrode porosity. Pouch cells using LiP electrodes pressed at 20 MPa showed a sharp capacity decrease in the initial 10 cycles, with the S-specific capacity decreasing to below 100 mAh/g after 10 cycles. Although the cell capacity increased afterwards, and the S-specific capacity only rose to around 650 mAh/g after 30 cycles and then began to decrease again. In comparison, when the LiP was pressed at 30 MPa, pouch cells showed better cycling stability. These

differences are shown in Figure II - 79d. Accordingly, 30 MPa was selected for future pressing of the LiP electrodes.

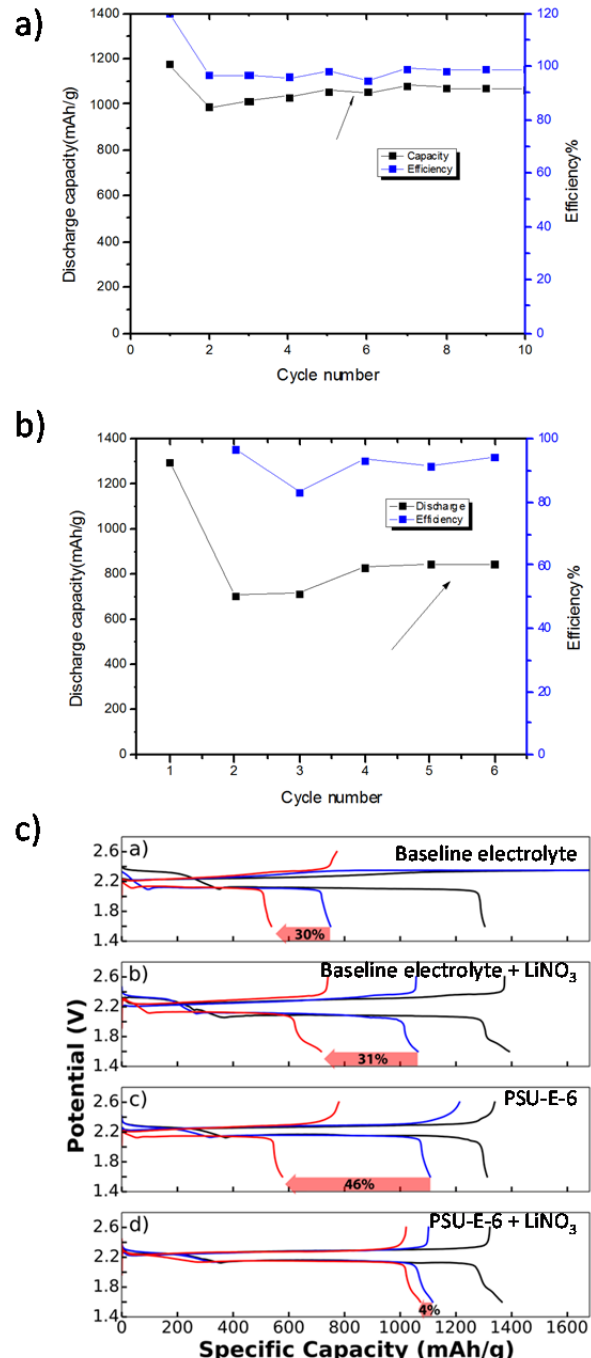


Figure II - 78: Cycling stability and efficiency of cells with ANL-E-4 electrolyte plus 0.1M LiNO₃, with a 10 h rest after the fifth charge, at a) room temperature and b) 55°C, and c) charge discharge curves of cells with baseline electrolyte, baseline electrolyte plus 0.2M LiNO₃, PSU-E-6 electrolyte, and PSU-E-6 electrolyte plus 0.2M LiNO₃, and their self-discharge after a two week rest at 45°C

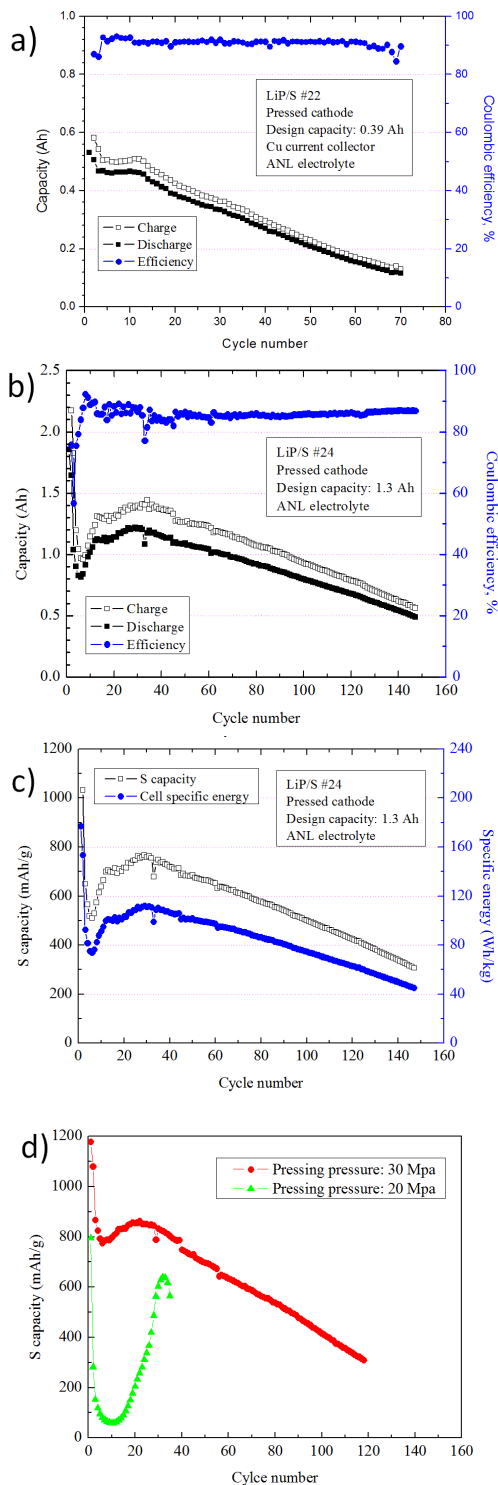


Figure II - 79: a) Capacity and coulombic efficiency of a 0.39 Ah design capacity cell with ~70% cathode porosity; b) capacity, coulombic efficiency, c) S-specific capacity, and specific energy of a 1.3 Ah design capacity cell with ~60% cathode porosity; and d) S-specific capacity of cells with LiP anodes pressed at 20 MPa and 30 MPa

Future Directions

In order to complete this project, work will focus most heavily on pouch cell development, optimization, and fabrication. We will incorporate other high-performance materials designed in this project into the 2 Ah pouch cells being developed, including scaling up MNCT/CNT cathode material production and further developing electrolytes and electrolyte additives to mitigate polysulfide shuttling and irreversible loss. We will also continue to optimize design parameters of pouch cells and pouch cell components, such as N/P ratio and electrolyte choice, and will investigate the source of the differences seen to date between coin cell and pouch cell performance. Safety evaluations, such as nail penetration and oven tests, will also be conducted.

II.B.7 Stand Alone Battery Thermal Management System (Denso)

Christopher Johnson (NETL Program Manager)
Subcontractor: DENSO International America, Inc.

Brad Brodie (Program Manager)
24777 Denso Drive
Southfield, MI 48086
Phone: (248)372-8851; Fax: (248) 350-7774
E-mail: bradley_brodie@denso-diam.com

Subcontractor:
National Renewable Energy Laboratory, Golden,
CO

Start Date: October 2011
Projected End Date: September 2015

Objectives

Reduce the vehicle battery pack size by 20% (or increase driving range by 30%) through an optimized battery thermal management system.

Technical Barriers

One of the challenges of lithium ion batteries in vehicles is their sensitivity to temperature. If batteries are exposed to high temperatures, their life is reduced. If they are exposed to low temperatures, the available power is reduced. As a result, battery packs are oversized to ensure they satisfy life (warranty) requirements and provide reasonable power at low temperatures. As the battery size is increased, the cost of the battery pack increases.

Technical Targets

- Develop a simulation program that will duplicate the battery thermal behavior in the vehicle.
- Develop a detailed thermal system design based on the information from the simulation program.
- Produce and bench test a prototype thermal system to prove the system is able to achieve the goals of the project.

Accomplishments

- Established a set of test conditions to which the battery pack will be evaluated.
- Basic cell characteristics have been identified and used for the simulation model.

- A battery simulation model was created in AMESim software which can duplicate battery behavior found in actual vehicle tests.
- The battery model was evaluated at various temperature and driving conditions with a variety of thermal system technologies to find the best solution.
- Prototype components were built and installed in a test bench to validate the results of the simulation models.



Introduction

The objective of this project is to design a thermal system that will enable a PHEV/EV Battery Pack Size Reduction by 20%. To accomplish this, DENSO proposed a dedicated stand-alone thermal system to manage the battery pack temperature efficiently. The National Renewable Energy Laboratory (NREL) is supporting the project through cell characterization, creating the battery simulation model and the life model used to calculate the life of the battery pack. Chrysler provided actual vehicle data as a baseline, test conditions, and battery pack to be used for the bench testing.

Approach

The intent of the project is to demonstrate that a thermal system could enable the reduction of the battery pack size through optimal thermal management. The key points are considering performance at cold temperatures and battery life when exposed to high temperatures.

A battery pack model was created in AMESim to simulate the battery pack. It uses equivalent circuit models (empirical) as a physics based model is too complicated for the purpose of this study. The type of Equivalent Circuit model is DC Resistance-Capacitor (RC) Circuits.

After the battery model was created in Phase I, Phase II involved incorporating the battery model with a thermal system model. This needed to include a battery management system simulation and influence of temperature from the vehicle cabin and the ambient air to the battery pack. The conditions (temperatures, drive profiles) used for the evaluation were provided by Chrysler based on their experience with specifying the battery packs for electric vehicles. Four different

thermal systems were evaluated in five different climates, and for each climate, five driving habits were evaluated which resulted in 25 scenarios to be evaluated for each thermal system concept.

Results

Four different thermal systems were evaluated, each using different technologies. They are listed in Table II - 11.

Table II - 11: Thermal System List

	Cooling Method	Heating Method	Comment
1 (PTC)	R-134a Refrigeration	PTC (electric heating)	Base System
2 (HP)	R-134a Refrigeration	R-134a Heat Pump	Improve Efficiency
3 (GIHP)	R-134a Refrigeration	R-134a Gas Injection Heat Pump	Improve low temperature performance
4 HP+PC M	R-134a Refrigeration + 10 kg PCM	R-134a Heat Pump	Add passive heat adsorption

Referring to Table II - 11, system 1 is considered our base system and is what is found in PHEV and EV vehicles currently in the market. Cooling is done using R-134a refrigeration system, and heating is provided using a high voltage PTC (Positive Thermal Coefficient) heater. The only difference is typically the R-134a system is linked to the vehicle cabin cooling system. In this study, we made it a dedicated system for only the battery. System 2 is same as system 1 for cooling, but we removed the high voltage heater and are now using the R-134a refrigeration system as a heat pump to provide heat. In this case, hot refrigerant exiting the compressor is used to heat coolant fluid flowing into the battery pack. System 3 is similar to System 2, except that it is using gas injection heat pump. This is similar to a two stage compressor system that allows for more performance at lower temperatures. Finally, System 4 is same as System 2, but we added PCM (phase change material) to provide passive cooling. This helps to smooth out peaks in temperature.

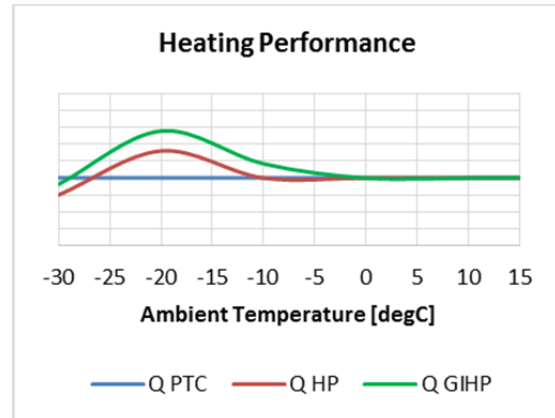


Figure II - 80: Comparing Active Heating Performance of PTC and Heat Pump Systems

The main difference in all the systems was in regards to heating the battery. In recent years, it has become clear that actively heating the cabin or battery of an electric or plug in vehicle is a large contributor to reduced driving range. In this study we compare heating using PTC heat, heat pump, and gas injection heat pump. The heating performance of each technology is shown in Figure II - 80. The PTC heater has a constant performance compared to ambient; however the heat pump systems performance will increase as ambient temperature increases. Therefore, control logic was implemented in the simulation model to limit the heat pump system to have similar performance as the PTC heater. This means that the compressor RPM is reduced in the heat pump to reduce the performance. Note that HP performance is same or higher than PTC from -25°C and warmer.

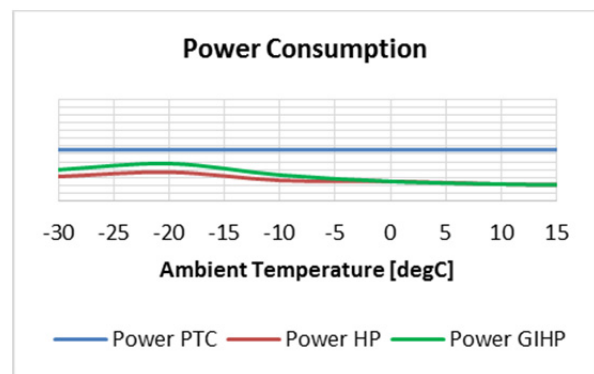


Figure II - 81: Comparing Heating System Power Consumptions

In Figure II - 81, we look at the power consumption of each system at various ambient temperatures. It is clear that the heat pump uses less power than the PTC heater but, as shown in Figure II - 80, still provides the same heating performance. The relationship between heating performance and power consumption is referred to as COP. (Coefficient of Performance)

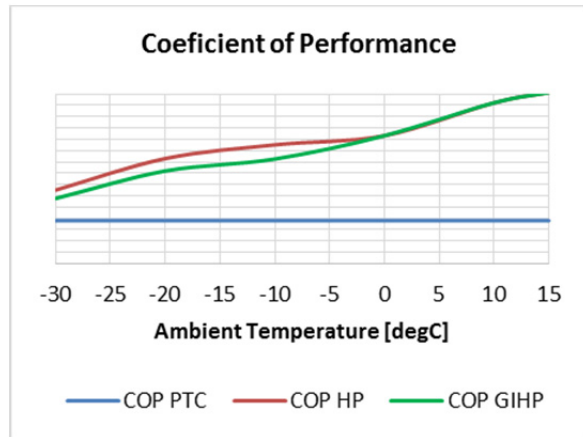


Figure II - 82: Comparing COP of various heating methods

In Figure II - 82, the COP is compared for each heating method. This shows why the heat pump system can improve driving range in cold temperatures because it consumes less energy to provide the same amount of heating to the battery pack.

After understanding the basic performance of each system, each was simulated in a driving condition at cold ambient. Figure II - 83 shows each thermal system at -20°C using UDDS and HFET driving patterns. In each case, the PTC heater was considered

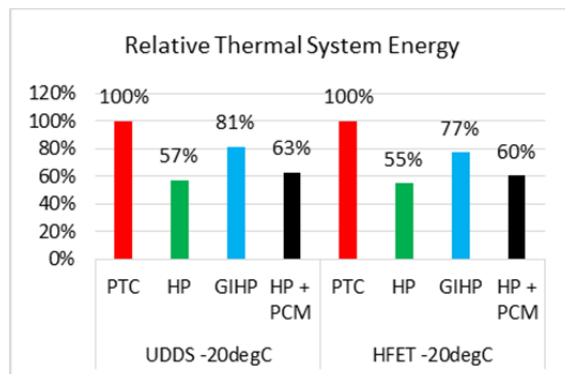


Figure II - 83: Thermal System Energy Usage at -20C Driving Conditions

The baseline and its power consumption was leveled to 100%. The power consumption of the other systems is then shown as a percentage compared to the base system. Figure II - 84 shows that a heat pump system offers a significant reduction in energy usage compared to PTC electric heating. Gas injection heat pump consumes more power than the regular heat pump, but as shown in Figure II - 81, at -20°C it also is producing more heating performance and thus heats the battery faster. Notice that the HP system with PCM requires 6% more energy than the HP system without PCM at -20°C UDDS. This is because the PCM at these temperatures acts as a thermal mass. As a result for the studies in cooling mode, the system used does not have PCM and is only R-134a A/C system.

Figure II - 84 shows basic results of cooling the battery using the different systems.

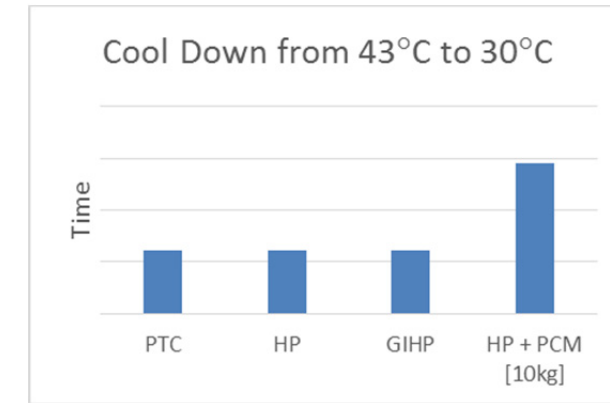


Figure II - 84: Time to Cool the Battery Pack from Hot Soak

In studying Figure II - 84 one can see the time (and energy) it takes to cool the battery pack from 43°C to 30°C is the same for PTC, HP and GIHP systems. This is because in cooling mode, the vapor compression R-134a system is basically the same for all three systems. However, the Heat Pump + PCM show an increase in time to cool down, and more energy is used. The reason is at this temperature, the PCM is only single phase and is simply more heat mass that needs to be cooled down. In this high ambient cool down condition, the PCM actually hurts performance.

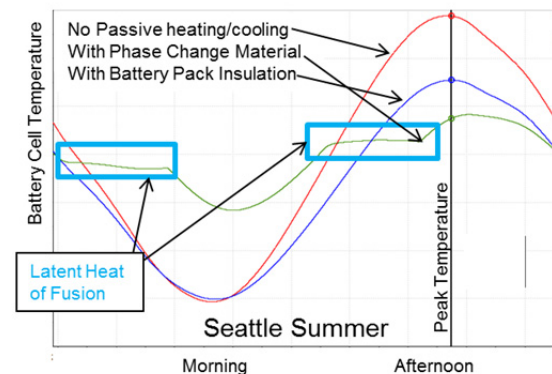


Figure II - 85: Study of passive heating and cooling; most benefit is found in mild ambient like Seattle

Phase change material does have an advantage in areas such as Seattle. The purpose for studying PCM or pack insulation is to keep the battery packs as close to optimal temperature as possible without using any energy, for example, when the vehicle is parked but not plugged in. But in extreme temperatures like Miami summer or Minneapolis winter, these temperatures are beyond the PCM melting point so there is actually only negative effect as shown in Figure II - 83 and Figure II - 84 due to the added thermal mass. Because it was difficult to decide if adding PCM or battery pack insulation was worth the added mass, cost, and

packaging space in the system, for this study it was concluded to leave them out of the study and only focus on the active cooling and heating system. However, if used correctly, PCM and insulation can have a positive influence to reduce peak temperatures in the battery cells and improve life (hot peaks) or driving range (cold peaks).

The final step in the simulations is to consider the effect on battery life. A method to do this is to measure the relative capacity of the battery pack throughout the life cycle of a battery. Figure II - 86 is a graph showing the relative capacity for minimal thermal management, aggressive thermal management and assuming the battery pack was always at a constant temperature for its entire life. Of course this is not possible in a vehicle, but is shown for comparison purposes.

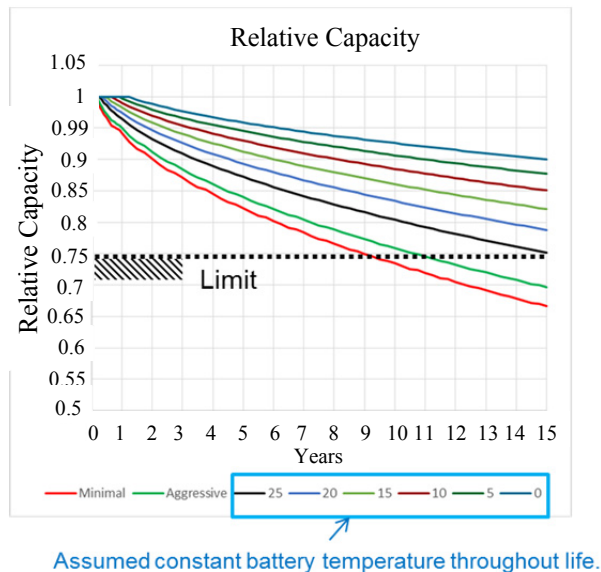


Figure II - 86: Relative Capacity of Battery Pack during Battery Life

In Figure II - 86, the goal is to keep the relative capacity greater than 75% for 8 years. Using minimal thermal management, this is achieved. Minimal thermal management is considered the base system. But, using aggressive thermal management (keeping the battery pack cooler) shown on the green line, it takes longer to achieve 75% battery life. If we know our target is 75% battery capacity after 8 years, the capacity of the battery in the beginning could be reduced to have the same capacity in the end as the base system.

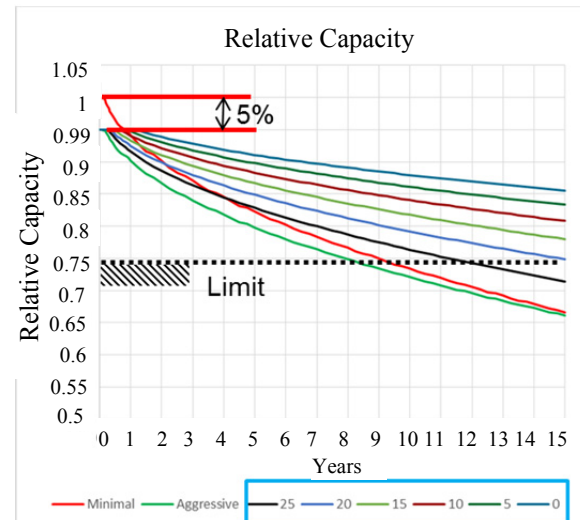


Figure II - 87: Battery Pack Capacity Can Be Reduced 5% and Achieve Life Requirements

In Figure II - 87, the capacity of the battery pack was reduced at the beginning, to have 75% capacity at the end of 8 years. The battery pack size could be reduced by 5%. This is 15% less than the objective which was 20% battery pack size reduction. However, just due to the natural aging of the battery pack, as seen from the calculations if the battery pack was at a constant temperature during its entire life, the pack size could be reduced ~10-15% from base size. The point is even if the cell is kept at optimal temperature for its entire life, just natural aging (resistance growth) in the battery cells means that achieving 20% is very difficult!

Conclusions and Future Directions

DENSO concluded from the simulation results that a gas injection heat pump system could provide a large energy savings for heating the battery at cold temperatures. The battery pack size could be reduced by 5% if aggressive thermal management is applied to keep the battery cell temperatures down.

DENSO will be setting up a test bench to check the results with actual components. Tests will include drive cycles at various ambient and battery pack cool down and warm up.

The project will be concluded by September, 2015 with final results and recommendations.

FY 2014 Publications/Presentations

1. 2014 DOE Annual Merit Review Meeting Presentation.

II.C Low-cost Processing Research

II.C.1 Low Cost Lithium-ion Cell Manufacturing Project (JCI)

Christopher Johnson (NETL Program Manager)
Subcontractor: Johnson Controls

YK Son (Principal Investigator)
5757 N Green Bay Avenue
Milwaukee, WI 53201
Phone: (414) 374-3709
E-mail: yk.son@jci.com

Subrecipients:
Maxwell Technologies
ENTEK Membranes

Start Date: October 2011
Projected End Date: March 2015

Objectives

- Research, develop and demonstrate advanced Li-ion cell manufacturing processes and techniques such as non-N-methyl-2-pyrrolidone (NMP) electrode, direct coating separator, and fast formation to reduce the existing Li-ion manufacturing costs by 50%.
- Better than 90% performance of integrated cell compared to baseline's performance.

Technical Barriers

- Integration: A key challenge related to the integration of developed technologies is a quality issue of the integrated cells due to high self discharge rate and dV variation.
- Dry processed electrode: A key challenge related to the preparation of solvent-free processed electrode is achieving scale-up to an automated continuous roll-to-roll process, and another concern is a high concentration polarization of dry cathode due to the micro-structure of dry electrode.
- Laminated separator: Continuous roll-to-roll process with uniform lamination minimizing thickness variation.

Technical Targets

- Develop dry coated cathode and anode electrodes to meet the existing wet coated electrode performance.
- Develop direct coated separator to meet the existing polyolefin separator performance.
- Develop fast formation process to meet the existing baseline formation process performance while improving cell uniformity and maintaining detectability.
- Develop a 15Ah Li-ion cell that integrates all three advanced technologies to meet a baseline NMC/Graphite cell performance, durability and safety.

Accomplishments

- Integration: 3Ah integrated cell design and process to incorporate dry coated and laminated separator technologies were developed, and delivered interim 3Ah integrated cells to DOE.
- Dry processed electrode: The cells built with optimized dry electrode demonstrate 30% lower ASI and 10% better rate capability than initial electrode design.
- Aqueous cathode: The results show 90% capacity retention at 2,500 cycles and similar performance compared to the baseline. The rate capability performance has been improved by optimizing formulation and processing.
- Laminated separator: The cells show 9% lower ASI and 27% better rate capability compared to the baseline.
- Fast formation: The new activation process shows lesser variation and better performance, and the detection process at low SOC demonstrates improved detectability and lesser cell degradation.
- Developed cost model.



Introduction

Johnson Controls proposed to develop a portfolio of advanced manufacturing technologies to reduce the manufacturing cost of large format Li-ion cells by 50%.

Three key technologies to be developed are: Non-NMP electrode, direct separator coating, and fast cell formation. The integration of these three advanced manufacturing technologies will achieve the targeted cost savings through the elimination of material, lower capital equipment expenses, and reduced energy and manufacturing costs.

Approach

During the third phase of the program we have developed and evaluated all targeted technologies – Non-NMP electrodes, laminated separator, and fast formation – in 3Ah pouch cells. The approaches that are under investigation for the final cell deliverables are:

- Dry electrode: Improve the micro-structure and morphology of the dry processed electrode and develop automated pilot processes for large format cell builds.

- Aqueous cathode: Develop an additive and new formulation for mixing and coating process improvement.
- Laminated separator: Develop roll-to-roll process for scale-up to improve lamination quality and reduce thickness variation.
- Fast formation: Develop new activation procedure to improve cell uniformity using step-charging and step-aging processes and develop an improved detection process at low SOCs. (Detection process is a process to use during formation to detect defective cells like high stand loss due to micro-short by metal contaminants.)

Results

Cell Integration

Johnson Controls has developed the cell and electrode designs to integrate the new advanced technologies into practical application as shown in Table II - 12 and Figure II - 88.

Table II - 12: 3Ah / 15Ah Integrated Cell Design

Item	Unit	Baseline		Dry Electrode (Interim)		Dry Electrode (Final)	
		Cathode	Anode	Cathode	Anode	Cathode	Anode
Active material	%	95	95	88	93	92	94
Loading weight	mg/cm ²	15.5	8.4	18.6	10.7	15.5(<17)	8.2
Thickness	um	131	141	150	180	135	140
Density	g/cc	2.8	1.33	2.85	1.35	2.85	1.35
Stacks	Number	8	9	8	9	8	9
Capacity	Ah	3.1		3.3		15	

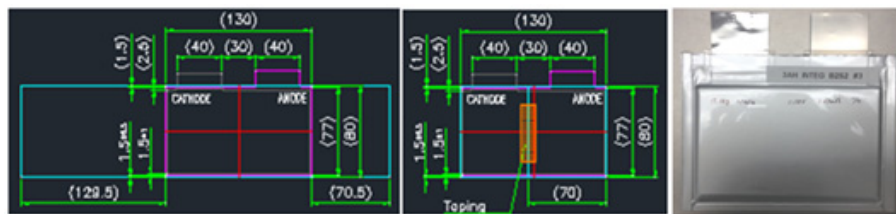


Figure II - 88: 3Ah integrated Cell

The design of the integrated cells targets PHEV applications requiring a blend of moderate energy capacity and high power performance. The integrated 3Ah cells have shown good results for DC impedance (see Figure II - 89). The 10.7 mΩ impedance for 10sec at a 5C generation pulse is 35% lower than baseline which shows 16.1 mΩ. This improvement is due to the

optimized dry electrode design and laminated separator which offer better air permeability and more uniform interface between electrodes and separators. Even though the pulse power is 35% better than baseline, it still lags the baseline's performance for high current rate capability (see Figure II - 90).

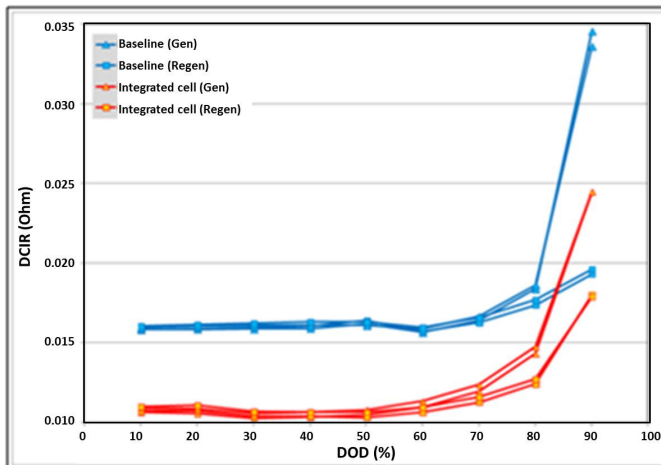


Figure II - 89: 3Ah Integrated Cell DC Impedance thru HPPC Test; Blue: Baseline cell; Red: Integrated cell

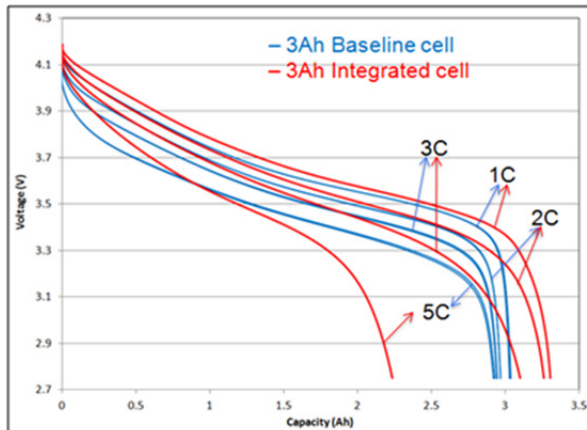


Figure II - 90: 3Ah Integrated Cell Rate Capability Test; Blue: Baseline Cell; Red: Integrated Cell

The initial IR drop and charge transfer polarization were equivalent to the baseline, but ohmic and concentration polarizations are higher than baseline. We believe the cause is higher loading weight and electrode density, particularly the micro-structure of the dry electrode. We have studied cross-sectional SEM and

porosimetry so that we can characterize the micro-structure of dry electrodes to the baseline's to improve continuous high current charge and discharge performance. The cross-sectional SEM images are shown in Figure II - 91.

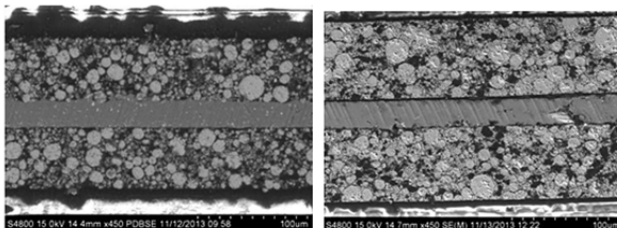


Figure II - 91: The Cross-Sectional SEM Images: Baseline Cathode Electrode (Left), Dry Cathode Electrode (Right)

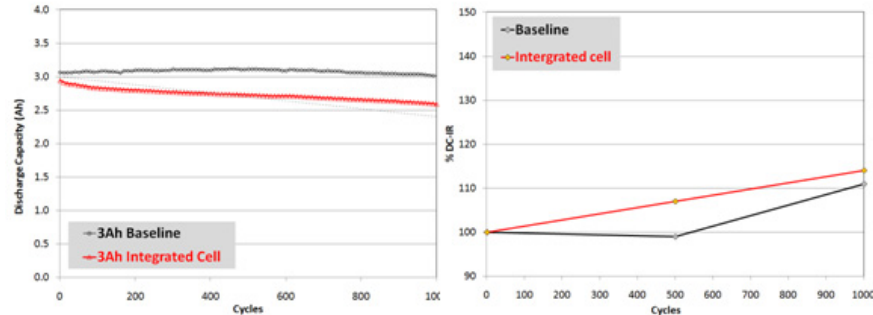
Results of porosity and average pore size are presented in Table II - 13. As shown in the cross-sectional SEM images and porosimeter results, the dry

electrodes are denser with smaller pores. The micro-structures of dry electrode are one of the main causes for higher diffusion polarization.

Table II - 13: Porosity and Average Pore Size of Dry Electrode

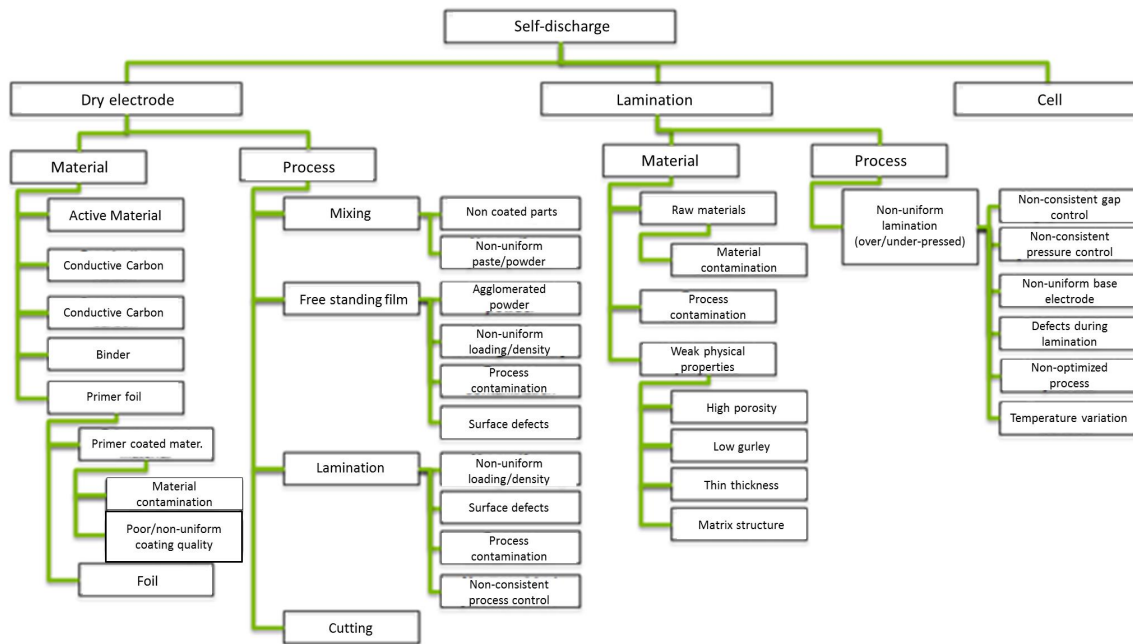
		Baseline electrode	Dry electrode
Cathode	Porosity (%)	36.4	26.9%
	Average pore size (um)	0.294	0.084
Anode	Porosity (%)	43.5	38.6
	Average pore size (um)	0.571	0.309

The data of integrated 3Ah pouch cells for 1C cycle life using 100% DOD on test gave 82% capacity retention after 1,000 cycles as shown in Figure II - 92.

**Figure II - 92: Integrated Cell Full Cycle Life Test: Capacity Retention (Left), DC Impedance (Right)**

The lot of eighteen interim cell deliverables had quality issues concerning low OCV and voltage variation due to high self-discharge rate and dV

variation. We performed a root cause analysis to minimize the variation and rate of self discharge. (See Figure II - 93.)

**Figure II - 93: FTA (Fault Tree Analysis) for High Self Discharge**

One of the major root causes is related to the lamination process; we're currently working to re-optimize the lamination process using a 2 factor, 3 level DOE (Design of Experiments).

We are now focusing all effort on improving both the performance and quality of the final cell deliverables.

Process Development

Johnson Controls has optimized the electrode notching process to accommodate the anode with the laminated separator as shown in Figure II - 94. A new stacking process eliminates the zigzag separator process by laminating the separator onto the anode improving the cell assembly rate from one to three cells per minute. By eliminating unnecessary process steps, future machines will be faster, smaller, simpler and less expensive. The concept is summarized graphically in Figure II - 95.

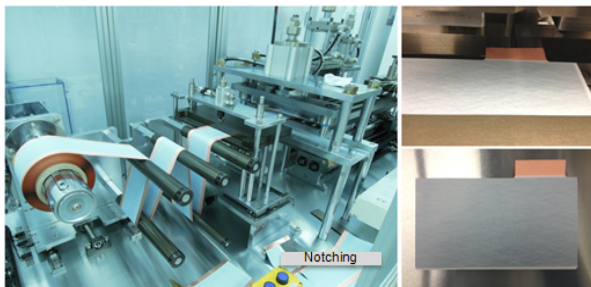


Figure II - 94: Baseline Cell Full Cycle Life Test

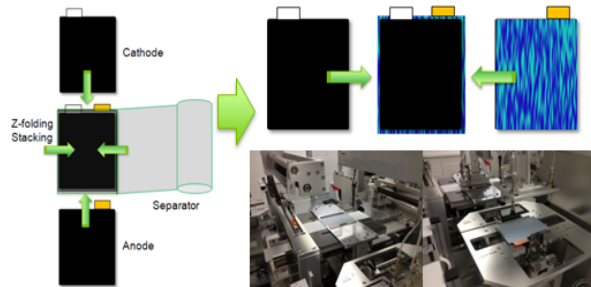


Figure II - 95: Improved Electrode notching Procedure

Dry Coated Electrodes

The dry electrode has been substantially improved based on a new optimized formulation and mixing process. The recent dry electrodes show 30% lower ASI as shown in Figure II - 96, and 20% better rate capability compared to initial dry electrodes as shown in Figure II - 97. However, it still shows reduced performance at high current rate test compared to baseline (see Figure II - 97).

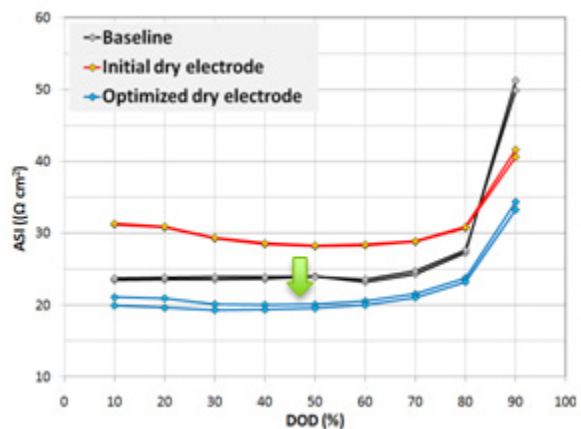


Figure II - 96: Dry Electrode Cell ASI Test thru HPPC Test; Black: Baseline; Red: Initial Dry Electrode Cell (2013); Blue: Baseline cathode and dry anode electrode

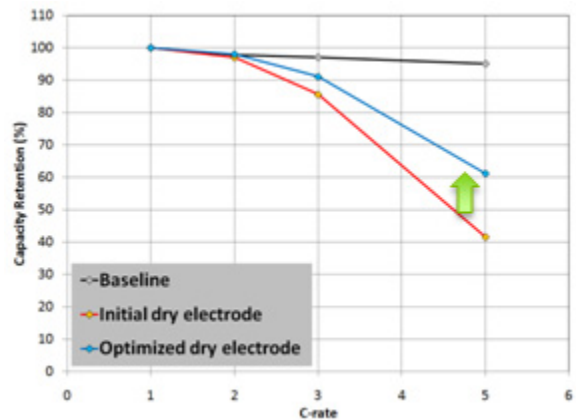


Figure II - 97: Dry Electrode Cell Rate Capability Test; Black: Baseline; Red: Initial Dry Electrode Cell (2013); Blue: Baseline cathode and dry anode electrode

Aqueous Cathode

3Ah capacity pouch cells built using aqueous binder have shown performance closer to baseline NMP based cells in terms of rate capability up to 10C, life at room temperature and 60°C, HPPC test and calendar life test at 60°C. Before building 3 Ah pouch cells with the new aqueous binder B, the design of experiments was conducted at the lab scale to optimize the binder ratio between CMC and the aqueous binder. The optimized weight percentages between CMC and binder B is reported to be 1% and 1.3% respectively. The final formulation for aqueous binder was optimized as shown in Table II - 14.

Table II - 14: Final Formulation DOE for Aqueous Binder

Test	Binder	pH balancer	Conductive agents
1	A	None	CB
2	A	0.1% additive	CB
3	A	0.2% additive	CB
4	A	0.3% additive	CB
5	B	None	CB + CG
6	B	0.1% additive	CB + CG
7	B	0.2% additive	CB + CG
8	B	0.3% additive	CB + CG

Figure II - 98 data show that the rate capability at various discharge currents for the cells based on binder B optimized formulation performed closer to the baseline. The different concentrations of oxalic acid were used to reduce the pH of the slurry and improve the slurry dispersion. HPPC studies on the 3 Ah pouch cells made with optimized binder B formulation showed closer performance to the baseline both during discharge and charge pulses as shown in Figure II - 99.

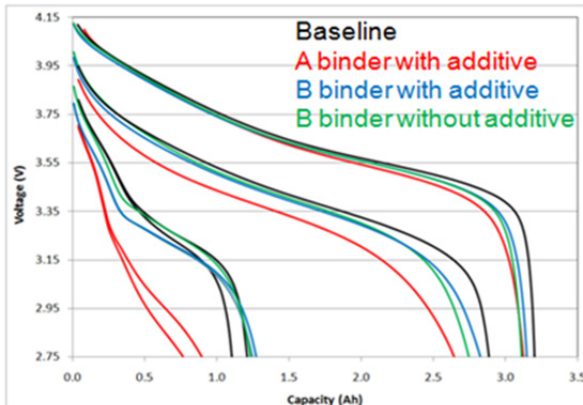


Figure II - 98: Aqueous Cathode Cell Rate Capability Results; Black: Baseline; Red: A Binder with Additive; Blue: B Binder with Additive; Green: B Binder without Additive

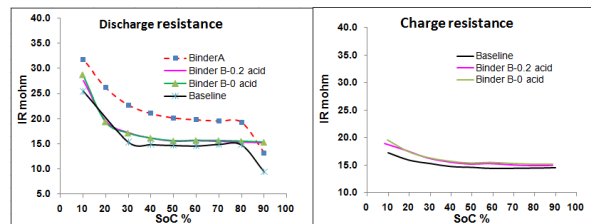


Figure II - 99: Aqueous Cathode Cell HPPC Test: Discharge IR (Left), Charge IR (Right)

The cells with aqueous cathode show much less incremental DC-IR compared to the baseline at increased storage durations. The variations of cells were also minimal in the aqueous cathode cells compared to the baseline. This is due to strong adhesion strength, controlled corrosion rate, and optimized formulation of the aqueous cathode cells which have

shown better calendar life results than the baseline as shown in Figure II - 100.

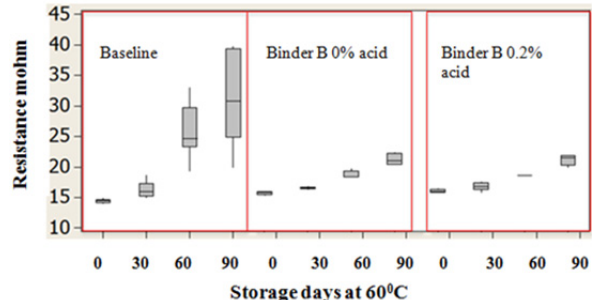


Figure II - 100: Aqueous Cathode Cell Calendar Life.

The cycle life results are shown in Figure II - 101. Indicating 92% capacity retention at 2,000 cycles.

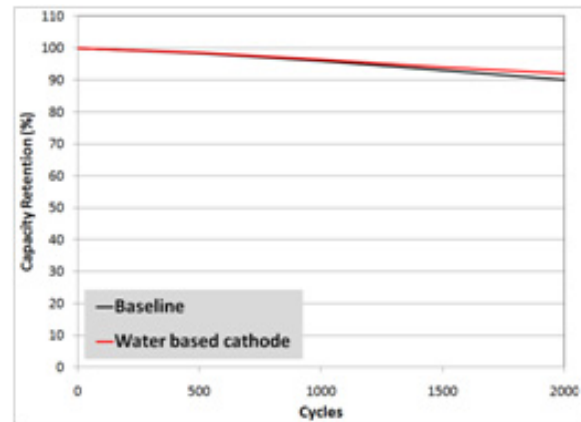


Figure II - 101: Aqueous Cathode Cell Cycle Life

Overall, aqueous cathode cells show improved performance durability in cycle and calendar life testing. One concern is the reduced processability compared to the baseline design which impacts the electrodes quality and overall performance consistency (see Figure II - 102).



Figure II - 102: Aqueous Cathode Electrode: Bumpy Surface

We are working to improve the processability of aqueous cathode with an optimized mixing process.

Direct Coated Separator

The lamination process was selected for the technology of direct coated separators based on Year 2013 studies. The cells built with laminated separator show superior power performance (Figure II - 103 and Figure II - 104). We have developed a lamination process to achieve scale-up for continuous roll-to-roll process. The optimized calendar machine enables more uniform lamination as shown in Figure II - 105.

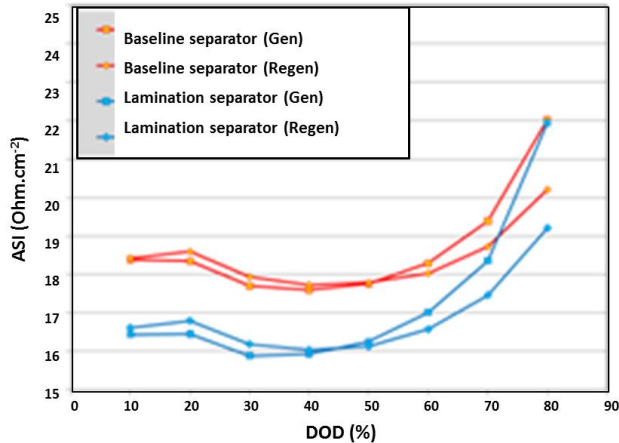


Figure II - 103: Lamination Cell ASI Results thru HPPC Test;
Red: Baseline Cell; Blue: Lamination Separator Cell

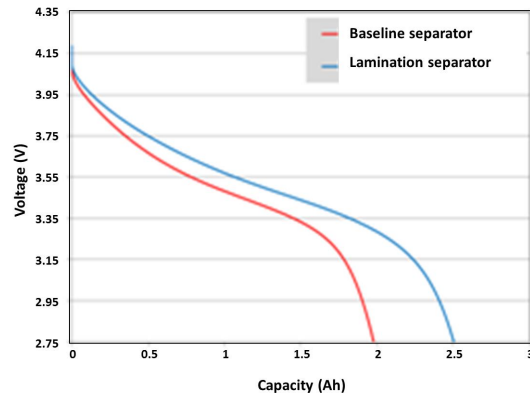


Figure II - 104: Lamination Cell 5C Rate Discharge Test;
Red: Baseline Cell; Blue: Lamination Separator Cell

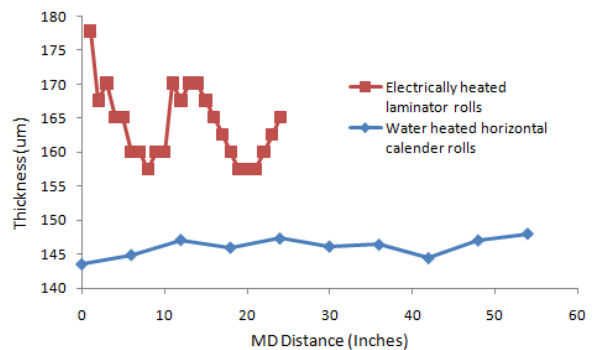


Figure II - 105: Calender Roll Effect for Lamination; Red:
Electric Heated Calender Roll; Blue: Oil Heated Horizontal Calender Roll

Fast Formation

We have developed the new activation process which combines step charging and step aging according to the concept shown in Figure II - 106. This methodology optimizes the conditions of the factors; temperature, SOC, and time using a 3 factor/ 3 level full factorial design (see Figure II - 107).

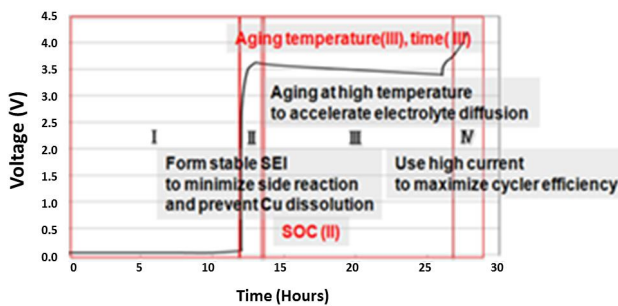
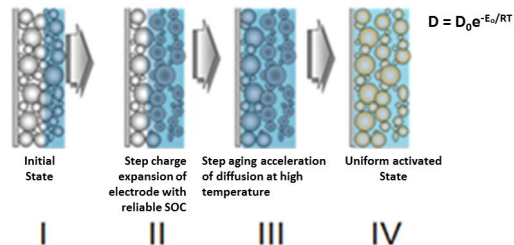
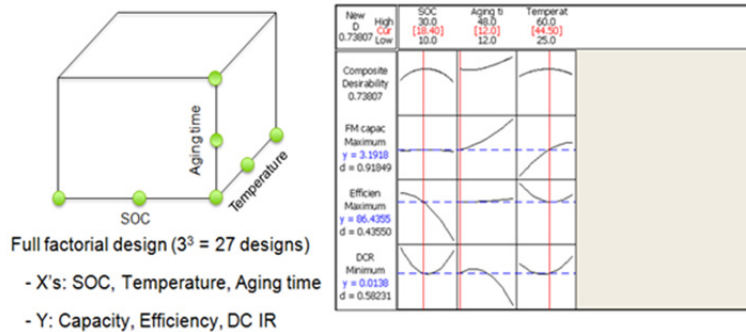


Figure II - 106: New Activation Process Concept



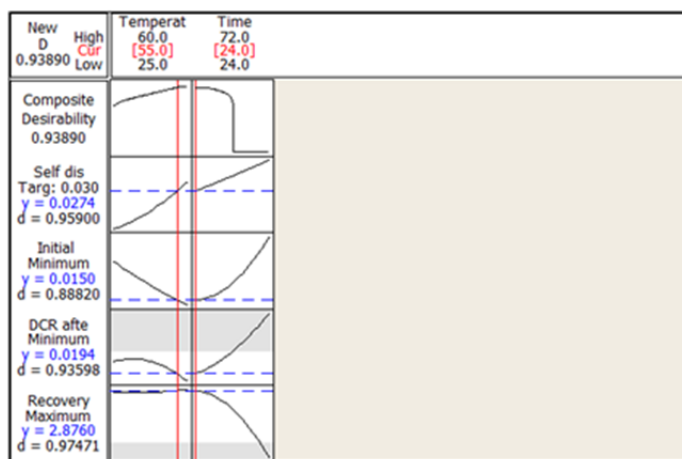
**Figure II - 107: DOE Results of New Activation Process**

In cell production the most time consuming step is the detection process due to the difficulty in detecting outliers in self discharge distribution of cells. A major thrust of the fast formation approach for this project is to shorten the stand loss storage time by

- Using a low cell SOC and higher temperature for storage.

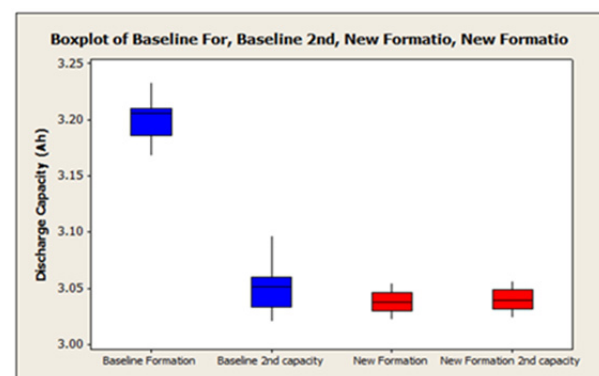
- Ensuring a SOC, temperature range and aging time at high temperature storage that minimizes cell degradation and permits faster detection.

We have developed a low SOC detection process and optimized each condition of the factors as shown in Figure II - 108.

**Figure II - 108: DOE Results of New Detection Process**

Ninety baseline cells were built using the, new formation and production process for the final validation. Figure II - 109 shows the discharge capacities of 1st and 2nd cycles. Results of new formation process show smaller capacity variation and little difference between 1st and 2nd cycle capacities. This is indicative of a stable SEI formed during activation, which minimizes irreversible capacity loss later in initial life.

The results of HPPC testing are summarized in Figure II - 110. The cells from the new formation process show better impedance and power than baseline units.

**Figure II - 109: Formation Capacity Comparison; Blue Boxes: Baseline Process; Red Boxes: New Formation Process**

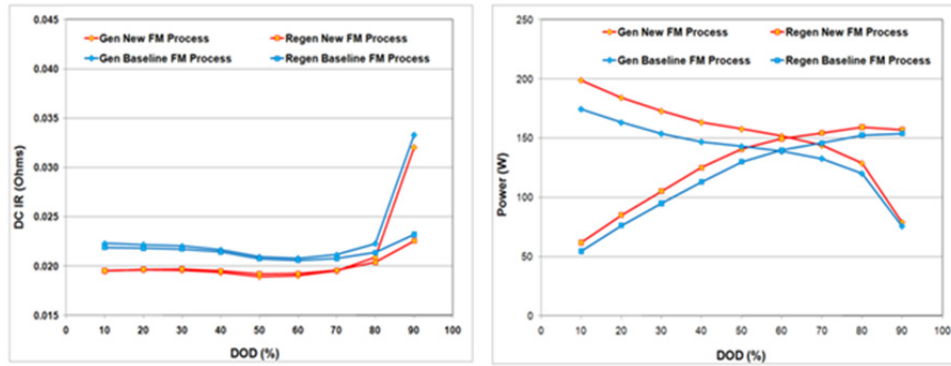


Figure II - 110: New Formation Cell of DC-IR (Left) and Power (Right); Blue Line: Baseline Process; Red Line: New Formation Process

The results of rate capability testing are shown in Figure II - 111. The new formation slightly aids rate capability at currents above 5C, and reduces IR drop and

charge transfer polarization compared to baseline formation even though they have similar capacities.

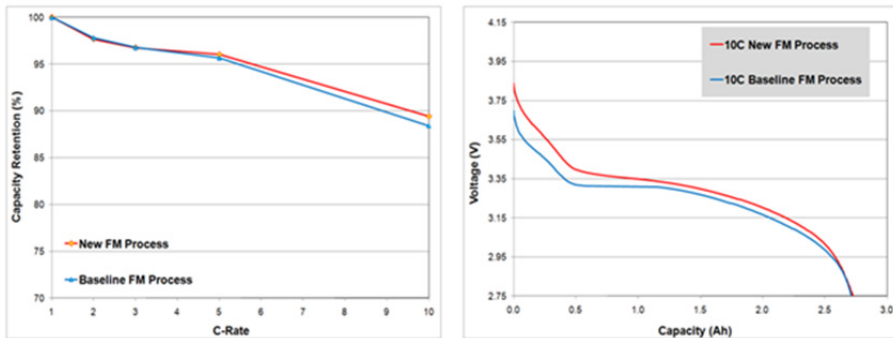


Figure II - 111: New Formation Cell Rate Capability; Blue Line: Baseline Process; Red Line: New Formation Process

The new formation process shows promising results, improving the uniformity and performance of cells. And we have studied detectability of each process with long term measurement for final validation.

Conclusions and Future Directions

In summary, the team has developed three key technologies – non-NMP coating, direct coating separator, and fast formation – and has integrated these technologies into final 15Ah deliverable cells with scale-up for large cell build.

During the third phase of program, the integration of these advanced manufacturing technologies has been achieved in 3Ah cells, we have found the technical barriers for performance and process. In the future, we're going to concentrate on overcoming these barriers.

The key future directions are listed as following:

- 15Ah final integrated cell development and delivery for evaluation.
- Final cost model including advanced technologies.

FY 2014 Publications/Presentations

1. Merit award poster presentation (6/17/2014).
2. Investigation on electrolyte transport properties in anode and cathode electrode film in lithium ion battery by wetting balance test was submitted for publication in the upcoming proceedings of the MS&T Conference, October 2014.

II.C.2 Ultraviolet Curable Binder Lithium-ion Battery Project (Miltec UV International)

John Tabacchi, NETL Program Manager

Contractor: Miltec UV International.

Gary E. Voelker (Project Director)

Dr. John Arnold (Principal Investigator)

146 Log Canoe Circle

Stevensville, MD 21666

Phone: (410) 604-2900; Fax: (410) 604-2906

E-mail: gvoelker@miltec.com; jarnold@miltec.com

Subcontractors:

Argonne National Laboratory, Argonne, IL

Oak Ridge National Laboratory, Oak Ridge, TN

Start Date: October 1, 2011

Projected End Date: May 31, 2015

Objectives

- Reduce lithium ion battery electrode and ceramic coated separator manufacturing costs by 50% by replacing thermal drying of solvent-based binders with UV curable binders.
- Demonstrate battery cells made from UV cured binder electrode coatings perform equal to or greater than equivalent cells made using solvent based binders.
- Establish the feasibility of using UV curable binder to apply a lower cost ceramic particle coating on polyolefin separators to improve safety and performance.

Technical Barriers

The technical barriers to realizing the full cost saving potential of UV curable binder technology in these applications are:

- Development of mixing techniques applicable to solvent-free slurries that ensure homogenous mixing and viscosities compatible with electrode coating techniques.
- Confirmation that the UV cured binder materials retain chemical inertness and adhesion after long term electrochemical exposure.
- Development and demonstration of high speed coating and UV curing techniques that ensure complete curing of the electrode coating.

- Demonstration of high speed precise coating of patterned ceramic particle separator coatings.

Technical Targets

- Develop a pouch cell using UV curable binder with performance equal to or greater than a reference cell made with conventional solvent based PVDF binder.
- Establish the feasibility of using UV curable binder to make a ceramic coated separator with porosity significantly greater and with less coating material than that obtained with a ceramic coating using conventional binder.

Accomplishments

- Began successful operation of a slot die coater/UV curing system capable of accommodating a 10" foil of current collector and 8" coating width and capable of speeds up to 200 feet per minute (fpm). Cathode samples were successfully prepared using the slot die coater and UV curing system and the coin cell test results were very good; essentially equal in performance to the reference baseline. As indicated in prior literature with conventional electrodes; UV curable binder electrodes demonstrate better long term cycling performance than hand drawn samples.
- The usual ratio of NMC/binder/carbon in a UV coated cathode under this contract has been 87/8/5. Miltec has successfully prepared samples at 90/5/5 and 90/7/3 with good cycle test results. Work continues to identify the potential causes of capacity loss that is slightly greater than the PVDF baseline.
- Miltec has prepared multiple 2-4 micron thick ceramic coatings on polyolefin separators using UV curable binder and high precision application technology. The results indicate the coated separators have equivalent cell performance to uncoated separators but benefit from the significant safety improvements of a coated separator with dramatically reduced processing and materials costs. Ceramic coated separators have been made with <10% increase in air permeability measured with a Gurley meter.



Introduction

Previously identified UV curable binders and associated curing technology have been shown to reduce

the time required to cure electrode coatings from tens of minutes to less than one second. This revolutionary approach can result in dramatic increases in process speeds and significantly reduced capital costs (a factor of 10 to 20) and operating costs, reduced energy requirements and reduced environmental concerns and costs due to the virtual elimination of volatile organic solvents and associated solvent dryers and recovery systems. Preliminary tests have also shown that UV curable binders can be used to replace conventional binders in the application of ceramic coatings to polyolefin separators. The use of precise coating patterns made possible by the use of instantly curable UV binder can reduce the cost and improve the performance of separators coated with ceramic particles for safety improvement reasons.

The accumulated advantages of higher speed, lower capital cost, lower operating cost, reduced footprint, lack of VOC recovery, and reduced energy cost is a reduction of 50% in the manufacturing cost of electrodes. When commercialized, the resulting cost reduction in Lithium batteries and super-capacitors will allow storage device manufacturers to expand their sales in the market and thereby accrue the energy savings of broader utilization of HEVs, PHEVs and EVs in the U.S., and a broad export market is also envisioned.

Approach

Multiple lithium ion battery cells are being fabricated using various approaches to UV curing technology; performance of the cells evaluated; and analytical testing used to further improve the performance of the cells. Final pouch cells made with UV curable binders will be submitted to the DOE for independent testing. Goals for

2014 were to continue iterative development to improve cathode sample preparation and coin cell testing using UV curable binder technology and to continue ceramic coated separator sample preparation using UV curable binder. NMC coin cells using UV curable binder have been prepared with performance at the baseline goal. Miltec began operation of a slot die coater installed on an existing UV lamp system designed for Lithium ion battery electrodes. The slot die coater is capable of coating on a 10" current collector at a width of 8" and operating at coating speeds up to 200 fpm. Initial problems with operation of the reel to reel subsystem have been corrected and extensive testing on the Slot Die/UV Curing system is underway. We anticipate seeing improved performance with Slot Die coated samples over the usual hand drawdown samples. In addition, based upon the contract amendment to extend the contract to May 2015, Miltec UV embarked on an expanded effort to investigate the preparation of ceramic coated separators using UV curable binder to replace solvent based binders now used. Miltec has procured and modified a unique coating machine to accommodate UV curing operation for the application of printed patterns of ceramic coatings on polyolefin separators.

Results

Electrode Development: The slot die web system is operational. The half-cell data in Figure II - 112 shows the slot die coater is capable of producing an excellent NMC cathode. This is a significant finding as it is the first confirmation that the slot die process is capable of running at least 125 fpm.

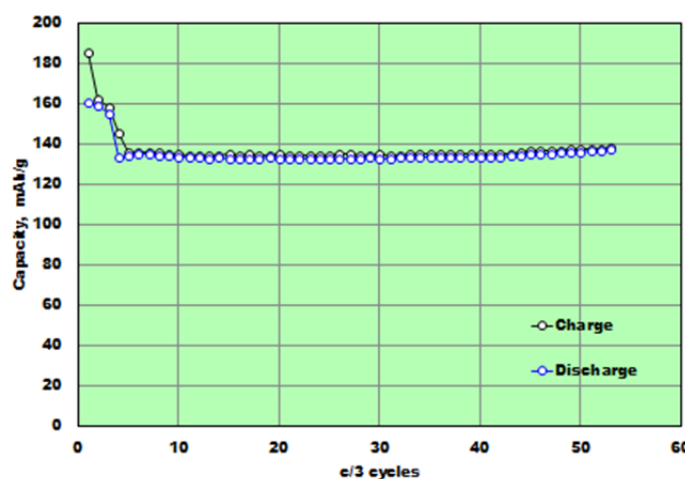


Figure II - 112: Half cell cycling of 87-5-8 (NMC-C45-UV binder) shows UV coating produced with a slot die has excellent stability and capacity

Recursive UV coating improvement has led to better electrode performance. Figure II - 113 shows the

performance of cells made using our state-of-the-art UV binder.

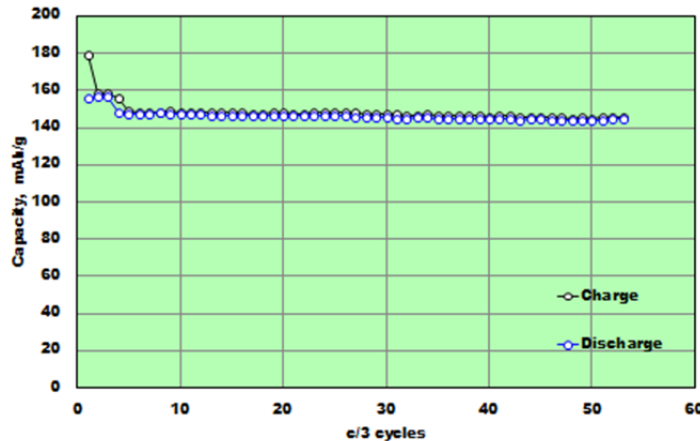


Figure II - 113: Half cell cycling of 87-5-8 (NMC-C45-UV binder). UV coating shows stable capacity with good values

Now that it has been established that the UV chemistry is stable in the environment of an operating NMC battery, the binder content is being reduced with the goal of matching commercial batteries. At this stage, 5%

binder coating behaves well in a half-cell with a respectable starting capacity and very good stability (Figure II - 114).

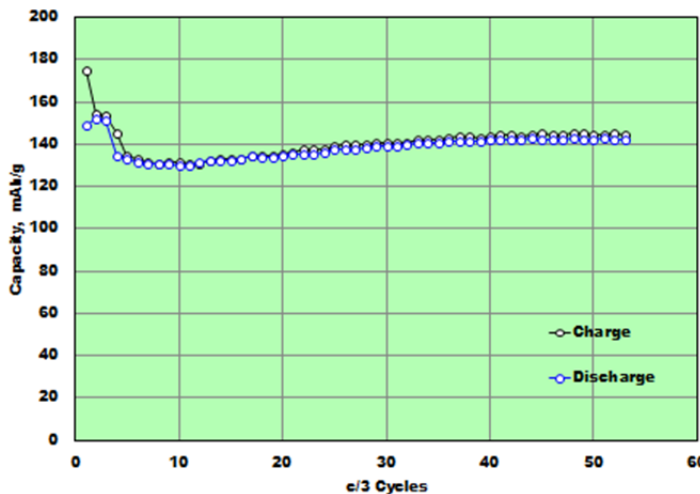


Figure II - 114: Half cell cycling of 90-5-5 (NMC-C45-UV binder). UV coating shows good capacity

Ceramic Coated Separator Development: To date, many UV chemical families for use as a ceramic binder on separators have been developed. An important aspect of this work is applying the ceramic coating in printed

patterns. For example, Figure II - 115 shows the half-cell performance of a conventional NMC cathode with a UV separator.

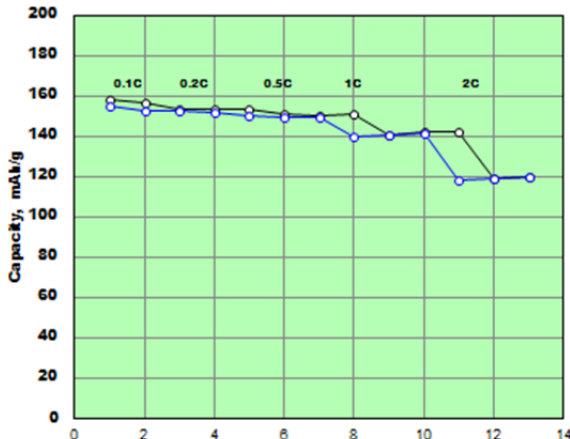


Figure II - 115: UV ceramic coated separators were found have the same capacity as the uncoated separator even at rates as high as 2C

Current work is focusing on applying these coatings with flexo press.

Conclusions and Future Directions

Miltec UV International and its subcontractors, Argonne National Laboratory and Oak Ridge National Laboratory have made significant progress toward meeting the goals of this project. A three lamp UV curing system with slot die coater and reel to reel control system capable of coating and curing at 200 feet per minute is operational. Cathode coatings of 90% NMC, 5% UV binder and 5% carbon have been prepared; made into pouch cells and cycled with performance less than 10% below the reference cells. This coating and curing system will allow Miltec UV to complete the optimization and demonstrate the full potential of this technology during the final year of the contract. During 2015, Miltec UV will deliver final pouch cells to Idaho National Laboratory for comparison testing to baseline cells to establish the performance of the cells made with a UV curable system. Miltec UV has also confirmed the feasibility of using UV curable binder to apply a precise patterned coating of ceramic particles on polyolefin separator. Miltec UV intends to vigorously pursue full development and commercialization of UV systems as applied to both Lithium ion battery electrodes and ceramic coated separators.

FY 2014 Publications/Presentations

1. 2014 DOE Annual Peer Review Meeting Presentation.

II.C.3 High Capacity Alloy Anodes (Applied Materials)

John Tabacchi (NETL Project Manager)

Grant Recipient: Applied Materials, Inc.

Sergey Lopatin (Project Director/Principal Investigator)

3100 Bowers Avenue, M/S 202

Santa Clara, CA 95052

Phone: (408) 235-4742; Fax: (408) 235-6863

E-mail: sergey_lopatin@amat.com

Subcontractors:

Lawrence Berkeley National Laboratory

Oak Ridge National Laboratory

FMC Lithium Division

Navitas Systems

Nissan Technical Center North America

Start Date: October 1, 2011

Projected End Date: September 30, 2015

Objectives

- Develop and demonstrate the feasibility of depositing alloy anode materials at high deposition rates.
- Characterize, evaluate, and optimize the resulting electrodes using pouch cells and demonstrate the low cost potential of the new manufacturing methodology.

Technical Barriers

Cycle life of alloy based anodes is one the main issues that limit their viability. We are working closely with our partners (subcontractors) to understand the underlying issues leading to the low cycle life of these anodes and then make necessary process changes to meet requirements.

Technical Targets

- Demonstrate high capacity Li-ion battery anodes capable of achieving an energy density of at least 500 Wh/l and a power density of at least 500 W/l.
- Demonstrate cycle life (300-1000 cycles at 80% depth of discharge), calendar life (5-10 years), and durable cell construction and design capable of being affordably mass produced.

Accomplishments

- Development of electro-deposition module that allows for 3D-porous structure formation in a single prototype tool for both 3DCu collector and 3DCuSnFe alloy anode.
- Development of 3DCuSnFe nano-structure alloy anode. Coulombic efficiency (CE) is improved by grain size reduction, pre-lithiation, and mitigation with combining alloy with Graphite.
- Development of modular technological steps for forming 2-4.3 mAh/cm² cells including process methodology for Graphite coating by water soluble process to achieve adhesion to the 3D-porous structures. Testing rate performance in half-cell assembly vs. Li demonstrated capacity retention advantages up to 2.5x at 5C-rate.
- Extending 3D electrode concept to the high loading alloy electrodes and testing interim pouch cell. Porous 3DCuSnFe/Graphite electrodes were assembled in single layer pouch cells with LiNi_{1/3}Mn_{1/3}Co_{1/3}O₂ (NMC111) and LiNi_{0.5}Mn_{0.3}Co_{0.2}O₂ (NMC532) cathodes. The retention capacity of 76.2% at 1280 cycles was demonstrated. These data show that the interim cell is capable of 985 cycles at 80% capacity retention at C/3 rate.
- Eighteen interim cells comprised the program's 2nd deliverable were sent to Idaho National Laboratory (INL) for further evaluation.



Introduction

Applied Materials is working on a new class of Li battery anodes with high capacity based on an innovative micro-cell porous 3DCu-Li alloy structure. Micro-cell 3DCu-Li alloy architecture of controlled thickness forms continuous and highly conductive Cu pathways for electrons through the full electrode. The technology holds great potential for electric vehicle Li-ion batteries. The electrode structure also has a very large surface to volume ratio to contact with Li-ion electrolyte. The porous 3DCu electrode can accommodate the volumetric expansion during cycling and contributes to long cycle life. The improved electrodes are assembled into prismatic battery cells and tested to demonstrate the feasibility of producing Li-ion batteries with the target energy density.

Approach

Experimental development focused on initial electro-deposition module which allows for 3D-porous structure formation. Baseline processes have been developed for (a) 3DCu current collector and (b) for Graphite coating using a water soluble process. Extending baseline electrode concept to the high loading 3DCuSnFe/Graphite alloy electrodes allowed a) low resistivity at the electrode/current collector interface, b) fast charge transfer at the electrode/electrolyte interface, and c) alloy expansion and contraction mitigated by reduced alloy grain size with Fe addition.

Modular technological steps were developed for forming 2-4.3 mAh/cm² interim cells (Figure II - 116).

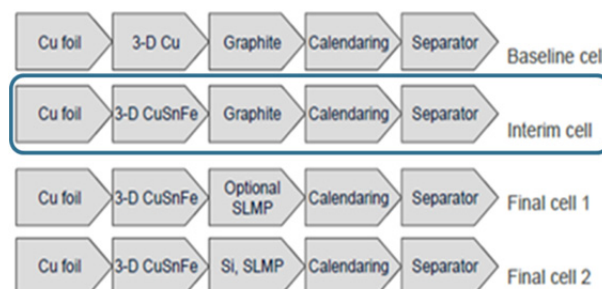
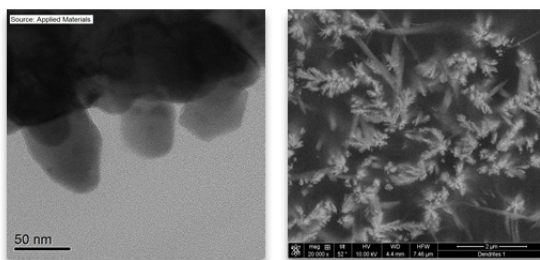


Figure II - 116: Schematic diagram of process flows for manufacturing baseline cells, interim cells and final cells with 3D current collector and alloy anodes

Results

3DCuSnFe Nano-Size Grain Material: Electrochemical deposition has been developed for forming ~50 nm grain sizes (Figure II - 117a) of alloy anode with Cu₆Sn₅(Fe) structure. Connected nano-size grains form conductive network of porous active material on Cu foil (Figure II - 117b).



a) ~50 nm grain size b) conductive network

Figure II - 117: a) Transmission Electron Microscopy (TEM) and b) high resolution Scanning Electron Microscopy (SEM) images of the 3DCuSnFe Material

3DCuSnFe/Graphite Anode: Interim cell processes have been developed for (a) 3DCuSnFe active material current collector and (b) for Graphite coating using a water soluble process. Scanning

Electron Microscopy (SEM) images of 3DCuSnFe/Graphite structures showed pore fill and crack-free coating. 3DCuSnFe/Graphite interim cell material remained unchanged with no mechanical damage as result of calendaring. Anode parameters with reduced mass and thickness for alloy anode at the same capacity vs. Graphite (both natural and artificial) are listed in Table II - 15.

Testing rate performance in half-cell assembly vs. Li demonstrated capacity retention advantages up to 2.5x at 5C-rate (Figure II - 118).

Table II - 15: Anode parameters for 3 mAh/cm² half-cell capacity including 3DCuSnFe/Graphite material with 20% thickness reduction vs. Graphite anodes (artificial and natural)

Anode	3D Alloy	Graphite	Graphite
Material	CuSn(Fe)/Graphite	Artificial	Natural
Mass loading (mg/cm ²)	9.1	10.1	10.3
Thickness (μm)	66	83	82
Delithiation capacity, 0.1C (mAh/cm ²)	3.1	3.0	2.8

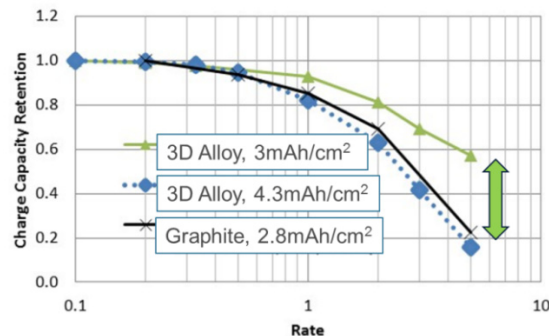


Figure II - 118: Capacity retentions at 5C for half-cells with capacities 3 and 4.3 mAh/cm² for 3DAlloy/Graphite compared to 2.8 mAh/cm² Graphite anode

Interim Cell Development: Full cells including 3DCuSnFe/Graphite vs. NMC have been assembled and tested. Modular technological steps were developed for forming 3-3.5 mAh/cm² cells including process methodology for Graphite coating by water soluble process to achieve adhesion to the 3DCuSnFe structures. Graphite was coated on 3D alloy of different loadings: 1, 1.5, 2 and 3 mAh/cm² for the 3DCuSnFe alloy. Assembly and testing of Graphite coated 3D alloy showed results of 1280 cycles having high Coulombic efficiency (Figure II - 119).

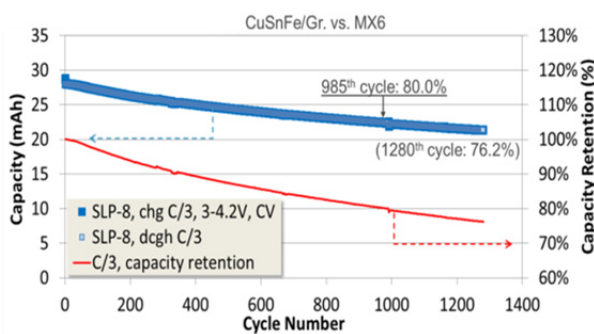


Figure II - 119: Cycling test results for 3DCuSnFe/Graphite vs. NMC. Measured 80% capacity retention is ~1000 cycles at C/3 rate

The capacity retention of 76.2% at 1280 cycles was demonstrated. These data show that the interim cell is capable of 985 cycles at 80% capacity retention at C/3 rate (Figure II - 119).

Interim Cell Testing: Full single layer pouch cells 3DCuSnFe/Graphite vs. NMC, with 34-36 mAh capacity (Table II - 16 and Figure II - 120), have been assembled and shipped to INL for testing according to the USABC manual.

Table II - 16: Single layer pouch cells (SLP) made with 3D structure CuSnFe/Graphite electrode. Eighteen cells have been shipped to INL for testing according to USABC PHEV manual

Cell	Interim SLP	Capacity
	ID	(mAh, at 0.1C)
1	JZ458-136-5-1	36.48
2	JZ458-136-5-2	35.28
3	JZ458-136-6-1	34.83
4	JZ458-136-6-2	34.88
5	JZ458-136-7-1	35.08
6	JZ458-136-8-2	35.75
7	JZ458-136-8-3	35.19
8	JZ458-136-9-1	36.31
9	JZ458-136-11-1	34.31
10	JZ458-136-11-3	35.08
11	JZ458-136-12-1	34.88
12	JZ458-136-12-2	34.34
13	JZ458-136-15-1	35.40
14	JZ458-136-16-1	33.38
15	JZ458-136-16-2	35.86
16	JZ458-136-17-2	35.02
17	JZ458-136-4-1	36.90
18	JZ458-136-4-2	36.06
	average capacity	35.28
	STDEV	0.85
	STDEV, %	2.4%

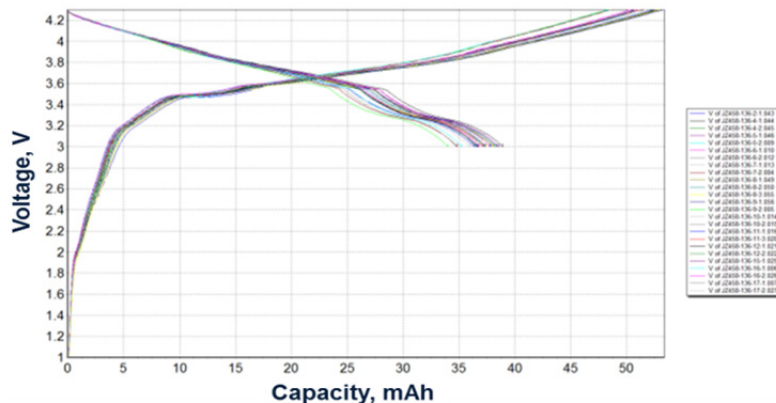


Figure II - 120: Voltage profiles of 1st formation cycle for 25 SLP cells. Eighteen cells were selected for deliverable

Coulombic efficiency (CE) of the alloy electrodes has been improved (Figure II - 119) by the following techniques: grain size reduction, pre-lithiation, and mitigation with combining alloy with Graphite. Dense and porous versions of CuSnFe alloy depositions with thickness range between 25-50 microns were developed. These 3D CuSn(Fe) electrodes were fabricated by using electroplating from acidic solutions. The mass loading, chemical composition, porosity, thickness were controlled to obtain the required loading of ~1.5

mAh/cm². These alloy electrodes were coated with Graphite to obtain 3-3.5 mAh/cm² loading. Samples were evaluated at ORNL, LBNL, Navitas Systems and Nissan TCNA in cell assemblies with different electrolytes. CE was improved by optimizing fluoroethylene carbonate (FEC) additive component in the electrolyte.

Applied Materials and project partners continue to develop alloy anode cells in order to reduce irreversible capacity loss. This task improves the cycling capability

and energy density of the system. Stanford Linear Accelerator Center (SLAC) granted beam-time for better understanding and controlling the stability of this material. Current results show that more optimizations for the cell formation protocol, ratio of alloy anode to Si-Graphite and for alloy pre-lithiation are necessary. Experimental cells including coatings of 3DCuSnFe with Si-Graphite were assembled and are being tested. Results will be included in the next technical progress report. The third deliverable, twenty four final cells, will be sent to INL after further cell optimization at the completion of the program.

Conclusions and Future Directions

Development of 3DCuSnFe nano-structure alloy anode resulted in half-cell and full cell electrode thickness reduction. Testing rate performance in half-cell assembly *vs.* Li demonstrated capacity retention advantages up to 2.5x at 5C-rate.

CE was improved by grain size reduction, pre-lithiation, and mitigation with combining alloy with Graphite. Assembling and testing full prismatic cells with 3D CuSnFe/Graphite anodes resulted in CE over 99.96% at 1000-1300 cycles. Projection from the data is that interim cell with 3DCu/Graphite anode is capable of 985 cycles at capacity retention of 80% at C/3 rate.

The second deliverable, 18 interim cells, was shipped to INL for further testing at the completion of formation protocol development including anode-cathode matching.

Equipment design concept and laboratory scale chamber prototype were developed. Plating module concept incorporated the capability to form 3D structure on both sides of the Cu foil. The individual module designs as well as module integration concepts will be fine-tuned. This will allow producing the final sets of cell deliverables for the program. These cells will incorporate the most optimal alloy anode composition. Applied Materials and project partners would like to continue development of the alloy anode to reduce irreversible capacity loss and further improve the cycling performance. This development allows the benefits of the 3DCuSnFe alloy and Si-Graphite to be utilized in a final cell with higher energy density.

FY 2014 Publications/Presentations

1. Presentation at the 2014 DOE Annual Peer Review Meeting, Arlington, VA.
2. Presentation at the 2014 Applied Materials Annual Engineering Technology (ET) Conference, Santa Clara, CA.

II.C.4 Innovative Manufacturing and Materials for Low Cost Lithium-ion Batteries (Optodot Corporation)

John G. Tabacchi (NETL Project Manager)

Subcontractor: Optodot Corporation

Steven A. Carlson (Program Manager)

100 TradeCenter, Suite G-700

Woburn, MA 01801

Phone: (781) 569-5059; Fax: (781) 569-5201

E-mail: scarlson@optodot.com

Subcontractors:

Madico Inc., Woburn, MA

XALT Energy, Lee's Summit, MO

University of Rhode Island, Kingston, RI

Ashland Inc., Wilmington, DE

Start Date: October 1, 2011

Projected End Date: September 30, 2015

Objectives

- Demonstrate technology that reduces the cell or battery inactive component weight, volume, and/or cost by at least 20% (Goal of at least 40%), while maintaining overall cell or battery performance.
- Design, develop, optimize and improve the separator, current collectors, electrolyte, termination materials, and cell casing used for manufacturing lithium ion batteries.
- Develop a simpler and faster battery coating and assembly process.

Technical Barriers

At least a two-fold reduction in the cost of manufacturing lithium ion batteries is needed for widespread adoption of electric vehicles. Even though improvements in the battery anode and cathode materials will provide significant cost reduction, it is difficult to achieve this overall two-fold level of cost reduction from incremental improvements of the current generation of battery inactive components and of battery coating and assembly processes.

Technical Targets

- Develop a high performance cell that reduces the combined cost of the battery inactive components of separator, current collectors, electrolyte, termination materials, and casing by at least 20%.

- Demonstrate a manufacturing process based on new inactive components that provides high performance cells while reducing the coating and assembly cost by at least 20%.

Accomplishments

- Developed new versions of 8 micron thick ceramic separator layers with an all-nanoporous design and of a very narrow pore size distribution with a 30 nm average pore diameter.
- Demonstrated two side slot die coating of the ceramic separator layers on two side coated reusable release film followed by a single pass through the drying ovens. This low cost process is compatible with the existing two-side electrode coating processes used for manufacturing lithium ion cells.
- The re-usable release film was optimized to eliminate any coating defects from premature release of the ceramic separator layer when it is overcoated with the electrode layer. A proprietary release coating was developed for use in this project.
- Using the Argonne National Lab battery cost model, cost savings from the 8 micron ceramic separator component including the reduced usage of electrolyte were estimated to be greater than 20% cost savings for the inactive components of the cell. This estimated savings meets the cost reduction objectives of this project from the thinner ceramic separator alone.
- 3 micron thick copper and aluminum current collector layers were sputtered onto anode/separator and cathode/separator coated stacks, respectively, and showed good cycling and conductivity. An alternative low cost proprietary process was developed for coating 2 to 6 micron thick copper and nickel current collection layers in patterns onto the electrode/separator coated stacks.



Introduction

Optodot has proposed to develop a new set of battery inactive components and a new battery coating and assembly process. These innovative materials and manufacturing process are based on the use of a thinner, safer, and lower cost ceramic separator. The proposed work comprises development of advanced ceramic

separator, current collector, and electrolyte materials and of advanced battery stack coating and current collection methods. A new system of edge termination and cell casing will be developed for use with these coated anode and cathode stacks. The boehmite all-ceramic separator layer enhances the cycle and storage life and high voltage stability of the cells. This enables the continued use of standard LiPF₆ electrolytes. Wider, two side simultaneous coating, and higher speed industrial coaters will be utilized to make the coated battery electrode stacks to obtain the cost benefits of at least a five-fold increase in coating output. The new battery manufacturing process eliminates the expensive conventional assembly equipment to precisely interleave the electrodes with free standing separators.

Approach

Optodot will characterize the performance and cost of the inactive components and assembly process of current baseline cells. Starting with a thinner ceramic separator layer for this project, Optodot and its subcontractors will overcoat this separator with conventional anode and cathode layers. Optodot will design and develop thinner and lower cost current collector layers for the anode and cathode electrodes before coating a second anode or cathode layer. Optodot is also developing a cell termination and tabbing system for use in making and demonstrating high performance 2 Ah cells of both energy and power types. With its subcontractors, Optodot is investigating the mechanism of the improved cycle life with boehmite ceramic separator layers and to optimize this property with the much thinner ceramic separator and coated battery stacks of this project. Optodot and its subcontractors will demonstrate and document the acceptable performance and overall cost reduction of these improved inactive components for lithium ion batteries and of the simpler and faster coating and assembly processes. A cost analysis report will document the cell cost reduction achieved compared to the cost of current baseline cells.

Results

The capability of overcoating the electrodes onto an 8 micron thick ceramic separator layer without penetration of the pigments of the electrode into the separator and without damage to the electrode/separator coated stacks during calendering was demonstrated in FY2012. This 8 micron ceramic separator is 40% porous with a narrow pore size distribution centered at 35 nm. In FY2014, anode/separator and cathode/separator coated stacks were manufactured with different thicknesses of the anode and the cathode layers in order to provide materials to fabricate into 2 Ah cells for both energy and power applications.

The use of an 8 micron nanoporous ceramic separator as the layer on which the electrodes and current collector layers are coated to form anode and cathode coated stacks provides significant cell cost savings of 20-25% of the inactive components of the cell, using the ANL battery cost model. The cost savings are derived from the use of the much thinner separator, a reduction in the usage of the electrolyte due to the thinner separator, and cell cost reduction in \$/kWh from the much thinner separator that allows about 5% by volume of additional active material to be used in the cell.

The heat stable ceramic separator layers with only nanopores and with very high compression strength and release substrates of this project have excellent stability to the heat and stress of the electrode coating process, as demonstrated during the machine coating of the electrodes and the subsequent calendering of the electrode/separator stacks. Safety and cell performance related features of the ceramic separator layer include dimensional stability of less than 0.5% shrinkage at 220°C, much greater compression strength than plastic separators, excellent thermal conductivity and heat dissipation, excellent cycling rate capability and low resistance from the much thinner ceramic separator, and non-flammability.

Metal current collector layers and tabbing connections are being incorporated into the electrode/separator coated stacks to produce the full anode and cathode coated stacks. Progress was made in FY2014 in developing a low cost proprietary process for coating 3 micron copper metal layers as the anode current collector layer with an electrical conductivity of about 0.5 ohms/square. The estimated cost savings for this copper current collector layer is about 40% with a large weight and volume reduction compared to the existing copper foils used as the substrate for coating the anodes.

Figure II - 121 shows cross-sections of anode and cathode coated stacks of this project. Small cells made with these coated stacks showed good cycling and high and low temperature performance.

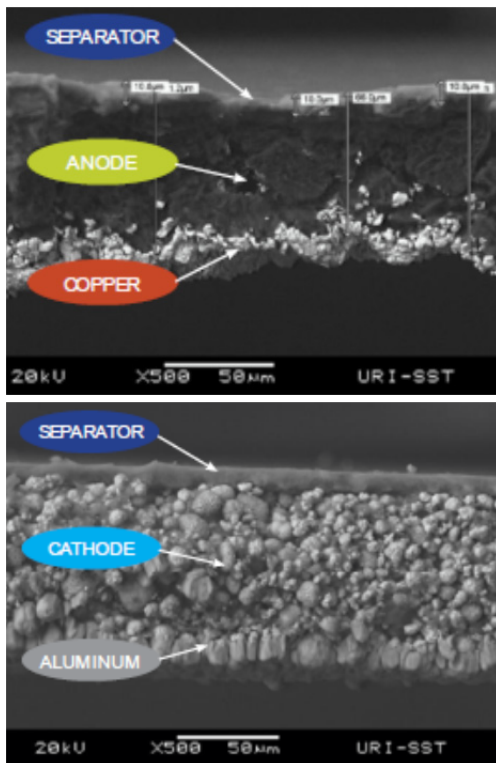


Figure II - 121: Anode electrode stack and cathode electrode stack

The new separator and current collector layers of this project are generic and compatible for use with various anode, cathode, and electrolyte materials as improved cell materials become available.

Since the much thinner boehmite ceramic separator provides increased cycle life and excellent high voltage performance with standard LiPF₆ electrolytes, URI is investigating the mechanism of this cycle life improvement with a view to finding ways to further increase the cycle life and storage stability of the cells.

Work was done in FY2014 to eliminate coating-related defects in the coated electrode stacks by developing a low cost re-usable release substrate with the preferred level of release force for the ceramic separator layer. The machine coating of the ceramic separator layer was scaled up to a full production width on a 72 inch wide production coater using slot die coating application. This project has made the anode and cathode coated stacks on machine coaters and is ready to assemble them into 2 Ah cells for cell testing compared to baseline cells. From this work, the estimated cell cost savings from coating at wider widths and higher line speeds and with a simpler cell assembly process will be determined.

Conclusions and Future Directions

- Meeting the at least 20% improved cost, volume and weight, as well as the performance requirements, for the key inactive components of Li-ion cells and developing a low cost next generation manufacturing process will help meet the DOE goals of cost reduction to \$270/kWh by 2017 for PHEVs and to \$125/kWh by 2022 for EVs.
- The use of the 8 micron thick ceramic separator alone meets the project's > 20% cost improvement objective for the inactive components, while providing 10% lighter batteries and the safety of a ceramic separator with very high dimensional stability at 220°C.

FY 2014 Publications/Presentations

1. M. Lazar, B. Sloan, S. Carlson, and B. Lucht, Analysis of integrated electrode stacks for lithium ion batteries, Journal of Power Sources, Vol. 251, 1 April 2014, Pages 476-479.
2. 2014 DOE Annual Peer Review Meeting Presentation.

II.C.5 Dry Process Electrode Fabrication (Navitas)

Christopher Johnson (NETL Program Manager)
Subcontractor: Navitas Systems, LLC

Mike Wixom (Principal Investigator)
Navitas Systems, LLC
4880 Venture Drive
Ann Arbor, MI 48108
Phone: (734) 205-1432
E-mail: mwixom@navitassys.com

Start Date: 10/01/2011
Projected End Date: 09/30/2015

- Demonstrate a prototype cell performance with the cathode and anode that meets EV rate and cycle life criteria.
- Deliver 24 cells in EV cell format.

Accomplishments

- Produced dry process cathode.
- Delivered 14 interim prototype 4Ah Li ion cells with dry process cathodes March 2014.
- Produced dry process anode August 2014.
- Demonstrated 500 cycles in a Li ion cell composing both dry process cathode and dry process anode October 2014.



Objectives

The goal of this program is to develop and demonstrate a solvent-free electrode fabrication process that will significantly reduce the cost of lithium ion batteries. This should enable the cell manufacturers to reduce the cost of large format lithium ion batteries. Navitas Systems has adapted a dry electrode process used in high volume production of ultracapacitor electrodes for use with lithium ion battery electrodes.

Technical Barriers

Conventional lithium ion battery electrodes are fabricated by casting slurries composed of active electrode powders with polymer binders and electronic conductivity additives. This approach imposes several fundamental limitations on cost and performance. Manufacturing throughput and electrode thickness are limited by the slurry drying process. Solvent removal must be precisely controlled to attain highly uniform thickness and porosity of the coated electrode, free of any blistering, delamination, skin formation or particle segregation. The slurry casting and subsequent calendering (compression) steps result in a highly tortuous pore structure that limits ion transport, and hence the rate (power) and thickness of the electrode. These barriers to increasing coating thickness ultimately limit the active material content in the cell.

Technical Targets

- Produce a dry-process cathode that can meet EV rate and cycle life criteria
- Produce a low cost anode that matches the cathode.
- Validate cost model by running pilot coating line at intended production speed.

Introduction

Conventional lithium ion battery electrodes are fabricated by casting slurries composed of active materials, conductive additives, and polymer binders. This coating process is limiting the electrode manufacturing cost and the performance.

Manufacturing throughput and electrode thickness are limited by the slurry drying process. Solvent removal must be precisely controlled to attain uniformity of the coated electrode, free of any blistering, delamination, skin formation or particle segregation. The slurry casting and subsequent calendering steps result in a highly tortuous pore structure that limits ion transport, and hence the rate (power) and thickness of the electrode. These barriers to increasing coating thickness ultimately limit the active material content in the cell.

The slurry casting process thus drives higher battery cost through at least three mechanisms:

- Solvent drying and solvent recovery steps require capital equipment and reduce throughput.
- Energy is consumed both to dry the electrode films and to recover the casting solvent.
- Electrode thickness limitations increase the cell-level costs of excess non-active materials such as current collector, separator and packaging.

In this program Navitas proposes to develop and demonstrate a solvent-free electrode fabrication process that will significantly reduce the cost of lithium ion batteries. Combined with the selected high energy, long life and safe electrode materials, the results “?..,of this

program will enable Navitas to offer a low cost, high energy, and safe EV battery.

Dry electrode processing has been commercialized for high volume manufacturing of ultracapacitors. The first goal of this program is to modify and transfer the dry process for the production of lithium battery cathodes. The baseline cathode binder is not stable at the anode. Therefore the second goal is to create a competent dry processed anode. To meet these goals we have laid out a program that will meet the following specific objectives:

1. A 20-50% reduction in cost of materials through increasing electrode coating thickness to reduce separator and current collectors.
2. Up to 80% reduction in capital equipment cost associated with electrode coating.
3. Up to 91% in energy saving by eliminating drying and solvent recovery.
4. Nearly 100% reduction in solvent emission and electrode scrap.
5. Define a binder system for dry process anode fabrication that is stable over 500+ cycles to full charge.
6. Demonstrate the dry process electrodes in an EV battery.

Approach

Phase I will extend the dry electrode process to the high energy and safe cathode material using established PTFE binder system. The cathode development approach will be to determine the thickness limit at which EV rate and cycle life criteria can be met. The phase I program will also combine sound mechanistic understanding of the dry process with understanding of anode binder chemistry/electrochemistry to down-select a binder that will enable dry process for anode.

Phase II will focus on producing a proof-of-concept dry process anode. Phase II anode approach will recapitulate the Phase I cathode development effort. In Phase II, cathode process will be optimized and scaled up. The dry process electrode production will be demonstrated and modeled to validate cost savings assumptions. The dry process electrodes will be assembled into a large format cell for EV applications.

Results

Cathode.

Navitas has developed solvent-free dry process cathode containing blended lithium metal phosphate and oxide. The active materials, process additives, and polymer binders were selected on the basis of electrochemical performance and process robustness. A cathode sheet can be prepared by being calendered to the desired thickness and porosity for EV battery. The free standing films are pressed and laminated onto an aluminum current collector. A free standing film and a laminated cathode are shown in Figure II - 122.

In the initial half cell tests, the dry process cathode is comparable to a baseline slurry-cast cathode in capacity, reversibility, and rate capability. The cathode retains 90% capacity at 1C and a loading of 3 mAh/cm² (Figure II - 123). The dry process cathode was then evaluated for cycle life in a full Li ion cell with a matching low-cost graphitic carbon anode. The cell retains 83% of initial capacity after 500 cycles at 0.5C and 100% DoD (Figure II - 124).

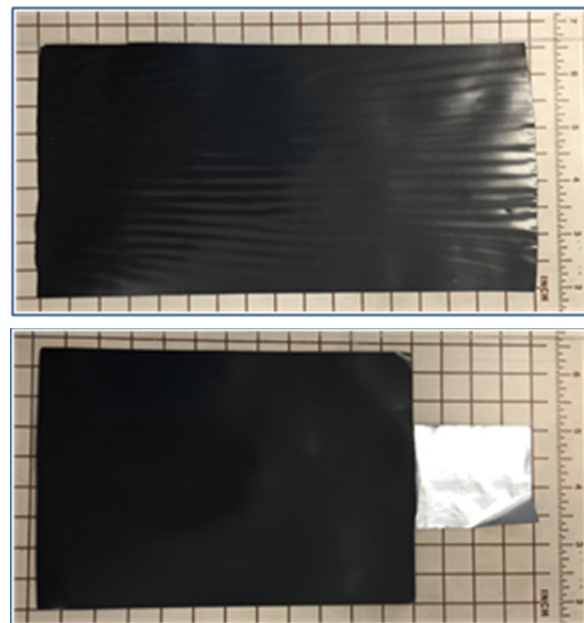


Figure II - 122: (top) a flexible free standing cathode film; (bottom) a cathode by laminating the film to an Al foil

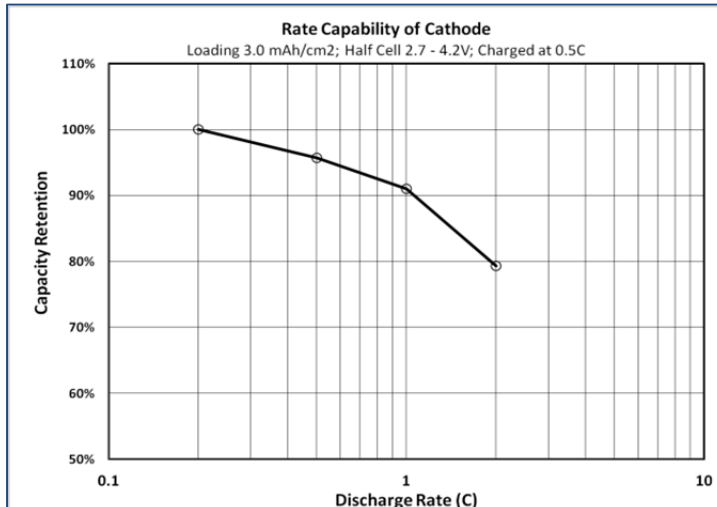


Figure II - 123: Rate capability of dry-process cathode in a half cell; the loading is 3 mAh/cm²

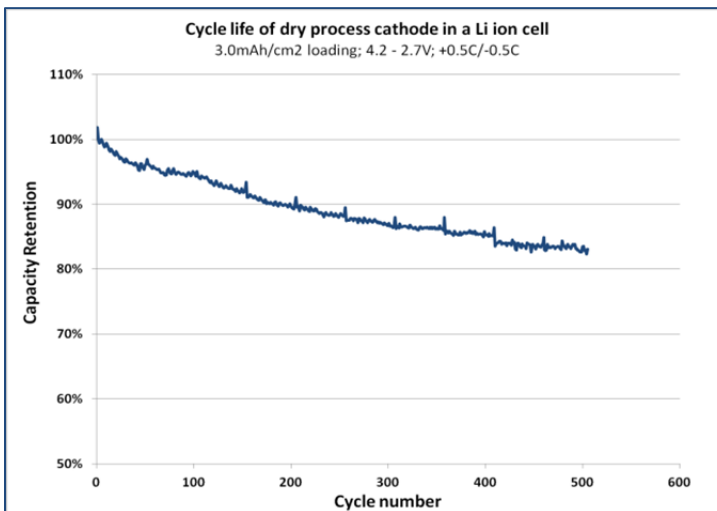


Figure II - 124: Cycle life of dry process cathode in a Li ion cell; the cell is with slurry-cast anodes and cycled at C/2 at room temperature

Anode

PTFE binder is needed to form a fibrilized network for the solvent-free cathode fabrication. However, PTFE reacts with Li (or lithiated anode) to form carbon and lithium fluoride during the first charge process. This reaction consumes cyclable lithium and results in unacceptable 32% initial capacity loss (ICL). By optimizing the anode binder formulation and fabrication condition, we were able to form a stand-alone dry process anode with ICL < 16%.

The current anode version is designated as Navitas Gen 2 anode. It has the same reversible capacity of 360 mAh/g as the baseline but has a much reduced ICL (Table II - 17).

The rate capability of the anode was evaluated in half cells over 0.7V – 0.01V. It shows 85% capacity retention at 1C at a loading of 3 mAh/cm² (Figure II -

125), comparable to the conventional slurry coated anode. This capacity retention meets the EV cell performance target.

Li ion cells (single-layer-pouch) were assembled and evaluated. 500+ cycles have been demonstrated at 0.5C and 100% DoD (Figure II - 126). It should be noted the cells include both dry process anodes and dry process cathodes. This is the first report of full Li ion cell performance combining both dry process electrodes.

Cell Prototype Assembly and Validation

Fourteen (14) 4 Ah prismatic cells containing dry process cathodes and slurry-cast anodes have been delivered to DOE as an interim deliverable. A series of tests such as peak powder, 48 hr stand, and DST will be performed towards EV battery standard.

Conclusions and Future Directions

The dry process electrodes have been developed and demonstrated in a Li ion cell that meets EV battery rate and cycle life criteria. The process is being optimized and scaled up to meet EV cell dimensional requirements. The dry process electrode production will be demonstrated and modeled to validate cost savings

Table II - 17: ICL reduction through anode optimization.

Anode	Reversible Capacity (mAh/g)	ICL %
Baseline	360	32
Gen 1	360	21
Gen 2	360	16

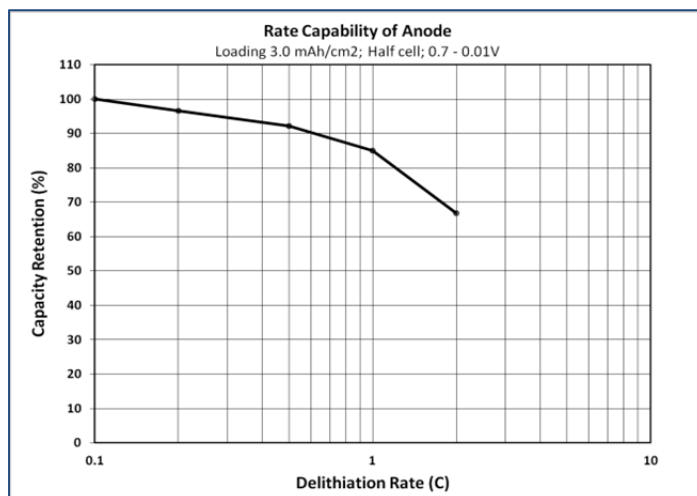


Figure II - 125: Rate capability of dry process anode in a half cell; the loading is 3 mAh/cm²

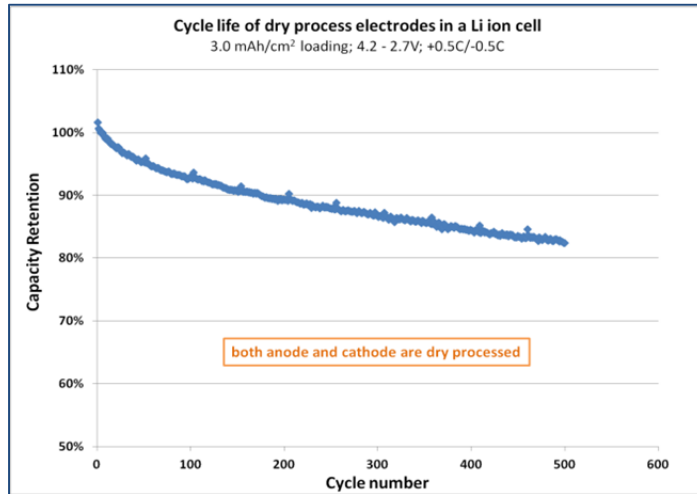


Figure II - 126: Cycle life of a Li ion cell composing both dry process anode and dry process cathode; cycled at C/2 at room temperature

assumptions. The produced electrodes will be assembled into a large format cell for EV as the final deliverable.

FY 2014 Publications/Presentations

1. 2014 DOE Annual Peer Review Meeting Presentation.

II.D Small Business Innovative Research Projects

Brian Cunningham

U.S. Department of Energy
1000 Independence Avenue, SW
Washington, DC 20585
Phone: (202) 287-5686; Fax: (202) 586-7409
E-mail: brian.cunningham@ee.doe.gov

Start Date: Ongoing

Projected End Date: Ongoing

Objectives

Use the resources available through the Small Business Innovation Research (SBIR) and Small Business Technology Transfer (STTR) programs to conduct research and development of benefit to the Energy Storage effort within the Vehicle Technologies Program Office.



Introduction and Approach

The Energy Storage effort of the Vehicle Technologies Program Office supports small businesses through two focused programs: Small Business Innovation Research (SBIR) and Small Business Technology Transfer (STTR). Both of these programs are established by law and administered by the Small Business Administration. Grants under these programs are funded by set aside resources from all Extramural R&D budgets; 2.8% of these budgets are allocated for SBIR programs while 0.35% for STTR grants. These programs are administered for all of DOE by the SBIR Office within the Office of Science. Grants under these programs are awarded in two phases: a 6-9 month Phase I with a maximum award of \$150K and a 2 year Phase II with a maximum award of \$1M. Both Phase I and Phase II awards are made through a competitive solicitation and review process.

The Energy Storage team participates in this process by writing a topic which is released as part of the general DOE solicitation. In FY12, the Energy Storage team decided to broaden its applicant pool by removing specific subtopics and allowing businesses to apply if their technology could help advance the state of the art by improving specific electric drive vehicle platform goals developed by the DOE with close collaboration with the United States Advanced Battery Consortium.

Phase II Awards Made in FY 2014.

Under the SBIR/STTR process, companies with Phase I awards that were made in FY 2013 are eligible to apply for a Phase II award in FY 2014.

Three Phase II grants were awarded in FY 2014 from eight Phase I grants that were conducted in FY 2013.

Navitas Systems, LLC. (Woodridge, IL 60517-4795) This project will develop a low cost and high capacity silicon based anode for Lithium ion batteries. This will result in new battery technology capable of reducing the cost and extending the range of electric vehicles. This addresses the two key barriers that are limiting electric vehicle adoption.

Pneumaticoat Technologies, LLC. (Westminster, CO 80021-3523) This project will implement a low-cost, lean-manufacturing approach to providing safety and stability to lithium-ion battery materials using a nanotechnology-enabling coating solution. Expected outcomes are higher retained performance under extreme conditions using statistical experimental designs, and a roadmap toward rapid commercialization and domestic production of next generation Li-ion battery materials.

Sinode, LLC: (Evanston, Illinois 60201-4488) This project will develop an advanced anode material based on a novel Si-graphene composite. This material has a high potential to overcome existing limitation on energy and power density while minimizing costs compared to alternative solutions.

Phase I Awards Made in FY 2014

Four Phase I grants were awarded in the Summer of FY 2014.

Navitas Systems, LLC. (Woodridge, IL 60517-4795) Lithium ion battery electrodes incorporate polymer binders that must serve multiple functions, including particle-to-particle cohesion, electrode-to-foil adhesion, and facile transport of lithium ions. This project will develop a novel binder system that enhances the life and reduces the cost of lithium ion batteries used in electric vehicles and consumer electronics.

Giner, Inc. (Newton, MA 02466-1311) The proposed innovation aims to develop an alternative rechargeable battery based on a novel solid electrolyte based lithium-sulfur battery that will address two barriers of conventional lithium-ion batteries for electrical vehicles, low energy density and high cost. The success of this program will significantly facilitate the commercialization of electrical vehicles.

Physical Sciences Inc. (Andover, MA 01810-1077) Higher energy density batteries are required in order to increase vehicle range and lower cost batteries are needed to make the technology affordable. This project will develop a new cell construction technique that will be demonstrated to enable the construction of cells with ~30% increase in energy density over the state of the art.

Applied Sciences, Inc. (Cedarville, OH 45314-0579) This advanced-material development effort will accelerate

the production of batteries with increased energy and power densities, with the goal of improving power sources for commercial electronics, power tools, aerospace/defense vehicles, marine applications, and making all-electric vehicles more practical. The project will position the U.S. for a sustainable competitive advantage globally.

III

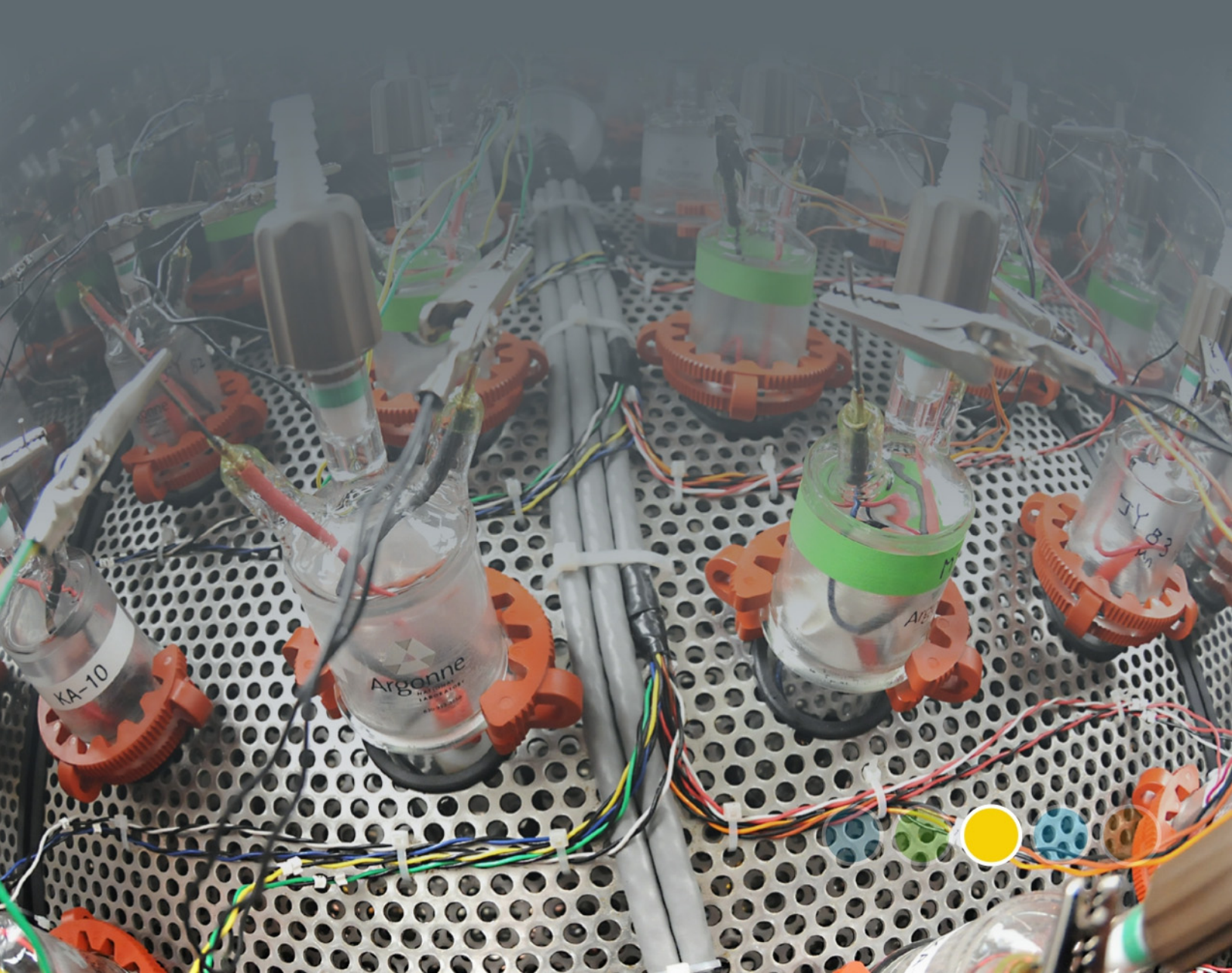
Battery Testing, Analysis and Design

Battery Testing, Analysis, and Design

Cost Assessments and Requirements Analysis

Battery Testing Activities

Battery Analysis and Design Activities



III. Battery Testing, Analysis, and Design

The Battery Testing, Analysis, and Design activity supports several complementary but crucial aspects of the battery development program. The activity's goal is to support the development of a U.S. domestic advanced battery industry whose products can meet electric drive vehicle performance targets. Within this activity, battery technologies are also evaluated according to USABC Battery Test Procedures. The manuals for the relevant PEV and HEV applications are available online. A benchmark testing of an emerging technology can be performed to remain abreast of the latest industry developments. High-level projects pursued in this area include the following topics:

- Cost Assessments and Requirements Analysis.
 - Cost modeling.
 - Secondary and other energy storage use and life studies.
 - Analysis of the recycling of core materials.
 - Requirements analysis for PEVs and HEVs.
- Battery Testing Activities.
 - Performance, life and abuse testing of contract deliverables.
 - Performance, life and abuse testing of laboratory and university developed cells.
 - Performance, life and abuse testing of benchmark systems from industry.
 - Thermal analysis, thermal testing and modeling.
 - Development of new test procedures.
 - Maintenance of current test procedures.
- Computer Aided Engineering of Batteries.
 - Development of tools for computer aided engineering of batteries.

The rest of this section lists the projects which were active for the above three key areas during FY 2014.

III.A Cost Assessments and Requirements Analysis

III.A.1 Core BatPaC Development and Implementation (ANL)

**Shabbir Ahmed, Kevin G. Gallagher,
Paul A. Nelson & Dennis W. Dees**

Argonne National Laboratory
9700 South Cass Avenue
Argonne, IL 60439-4837
Phone: (630) 252-4553
E-mail: ahmeds@anl.gov

Collaborators:

Wenquan Lu, Argonne National Laboratory
Dan Santini, Argonne National Laboratory
Fritz Kalhammer, Electric Power Research Institute
Joe McDonald, U.S. Environmental Protection Agency
Aymeric Rousseau, Argonne National Laboratory
Ram Vijayagopal, Argonne National Laboratory

Start Date: October 2012

Projected End Date: September 2016

Objectives

The objective of this task is to develop and utilize efficient simulation and design tools for advanced lithium-ion batteries capable of predicting precise overall and component weight and dimensions, as well as cost and performance characteristics.

Technical Barriers

The primary technical barrier is the development of a safe cost-effective EV battery that meets or exceeds all performance goals. The major challenge specific to this project is accurately predicting the impact of promising new battery materials on the performance and cost of advanced full-size lithium-ion batteries for transportation applications.

Technical Targets

- Develop a model for calculating the battery mass, volume, and cost from individual components.
- Evaluate the impact of battery design and manufacturing options on battery performance and its ability to meet cost targets.

- Evaluate the interplay between performance and cost for advanced materials, such as anodes and cathodes.
- Support policy making process of U.S. Government.
- Document and distribute model.

Accomplishments

- Studied the effect of electrode thickness on the accessible capacity as a function of charge/discharge rate.
- Studied the economy of scale of a plant manufacturing batteries for different types of electric (HEV, PHEV, AEV) vehicles.
- Updated the cost of materials in BatPaC.
- Revised the model to present results aligned with USABC parameters / guidelines.
- Supported the EERE-VTP program participants to quantify the effect of materials development on cost. Particular focus was on novel anode designs.
- Continued to support the EPA and DOT in refining BatPaC to enable use in the 2017-2025 rule making process for CAFE and GHG regulations. Identified and initiated critical BatPaC development pathway to support mid-term review of rule.



Introduction

The penetration of lithium-ion (Li-ion) batteries into the vehicle market has prompted interest in projecting and understanding the costs of this family of chemistries being used to electrify the automotive powertrain. Additionally, research laboratories throughout the DOE complex and various academic institutions are developing new materials for Li-ion batteries every day. The performance of the materials within the battery directly affects the energy density and cost of the integrated battery pack. To estimate the manufacturing cost of Li-ion batteries, Argonne developed a performance and cost (BatPaC) model which was peer reviewed and is available on the web. It captures the interplay between design and cost of Li-ion batteries for transportation applications. Moreover, BatPaC is the basis for the quantification of battery costs in U.S. EPA and NHTSA 2017-2025 Light-Duty

Vehicle Technical Assessment. This assessment is then used to determine what mileage (i.e., CAFE) and CO₂ emission standards are optimal from a cost-benefit analysis.

Approach

BatPaC is the product of long-term research and development at Argonne through sponsorship by the U.S. Department of Energy. Over a decade, Argonne has developed methods to design Li-ion batteries for electric-drive vehicles based on modeling with Microsoft® Office Excel spreadsheets. These design models provided all the data needed to estimate the annual materials requirements for manufacturing the batteries being designed. This facilitated the next step, which was to extend the effort to include modeling of the manufacturing costs of the batteries. The battery pack design and cost calculated in BatPaC represent projections of a 2020 production year and a specified level of annual battery production, 10,000–500,000. As the goal is to predict the future cost of manufacturing batteries, a mature manufacturing process is assumed. The model designs a manufacturing plant with the sole purpose of producing the battery being modeled. The assumed battery design and manufacturing facility are based on common practice today but also assume some problems have been solved to result in a more efficient production process and a more energy dense battery. Our proposed solutions do not have to be the same methods used in the future by industry. We assume the leading battery manufacturers, those having successful operations in the year 2020, will reach these ends by some means.

Establishing the validity of the model calculation is important in justifying the conclusions drawn from exercising the model. The design assumptions and methodologies have been documented and reported in a number of formats. The most notable of which is the 100+ page public report that accompanies the model at the BatPaC webpage. The report and model have been subjected to a public peer-review by battery experts assembled by the U.S. Environmental Protection Agency as well as many private reviews by vehicle original equipment manufacturers (OEMs) and cell suppliers. Changes have been made in response to the comments received during the peer-reviews. The public peer-review comments are available to all. The battery pack price to the OEM calculated by the model inherently assumes the existence of mature, high-volume manufacturing of Li-ion batteries for transportation applications. Therefore, the increased costs that current manufacturers face due to low scale of production, higher than expected cell failures in the field, and product launch issues are not accounted for in the calculation. BatPaC is the only model that has all of the following attributes: freely available, transparent in

methodology and assumptions, links performance and cost, and uses a bottom-up approach.

Results

Electrode Thickness: BatPaC currently has a maximum 100 micron electrode thickness limitation as a design setting for all batteries. Based upon limited information this is considered a practical limit to achieve long-lived, high-performing cells. While there appears to be no universal understanding for this limitation, possible reasons include lithium plating on the graphite negative electrode, other effects from concentration gradients within the electrodes, issues with repeated volume changes during cycling, and/or manufacturing challenges. For most lithium ion technologies the electrode thickness limitation is reached for EV and larger PHEV battery applications where the battery power to energy ratio needed for the vehicle is lower. In these cases, increasing the electrode thickness limitation would significantly reduce battery cost. Based on the potential impact of thicker electrodes on cost, being able to accurately predict the effect of thicker electrodes on performance within the BatPaC framework is an important direction for the future.

In general, batteries with thicker electrodes (i.e., higher electrode active material loadings) require less current collector foil, separator, and other associated hardware resulting in reduced battery costs. Of course, the smaller battery geometric area also reduces battery power. In addition, the higher electrode loadings increase the electrolyte current density for a given application that can limit full utilization of the electrodes. As an example during a constant current discharge, the salt concentration in the electrolyte shifts toward the negative electrode resulting in a positive electrode depleted of salt. For either high currents or thick electrodes, the salt concentration near the aluminum current collector can approach zero, thus limiting access of the ionic current to the current collector side of the electrode. BatPaC is able to accurately estimate the impact of electrode thickness on battery power. However, it does not take into account the electrode capacity utilization problem.

It is possible to solve for the salt concentration distribution in the battery electrolyte under any testing protocol and simultaneously determine the current distribution in the electrodes, thus calculating the electrode utilization. However, it generally requires solving an electrochemical model that involves a system of time-dependent multi-phase multi-scale differential equations that cannot be easily incorporated into an iterative spreadsheet platform in an efficient manner. Instead, dimensional analysis of the electrolyte salt transport equation is utilized to examine the pertinent parameters for a constant current half-cycle. Two parameters arise from the analysis, a time constant for

the electrode to come to steady state ($t_{\text{Steady State}}$) and a current penetration length ($L_{\text{Penetration}}$) for the electrode (i.e., characteristic length of the ionic current to penetrate into the electrode), given by Equations 1 and 2 respectively.

$$t_{\text{Steady State}} = \frac{(L_{\text{Electrode}})^2}{D} \quad [1]$$

$$L_{\text{Penetration}} = \frac{\left(\frac{\varepsilon}{\tau}\right) D c z_+ v_+ F}{(1-t_+^o) I} \quad [2]$$

In the equations for the electrolyte: D is the salt diffusion coefficient; c is the average salt concentration, t_+^o is the lithium ion transference number, z_+ is the cation charge number (i.e., one for lithium ions), and v_+ number of cations per salt molecule (i.e., one for lithium ions in LiPF₆). In the equations for the electrode: $L_{\text{Electrode}}$ is the electrode thickness, τ is the tortuosity, and ε is the porosity. Finally, I is the cell current density and F is Faraday's constant.

If the current penetration length could be used to estimate the fraction of electrode utilization, then the correlation could be utilized within BatPaC. An existing electrochemical model for an NCA/Graphite lithium ion cell was used to examine a wide variety of cases over a wide range of electrode thicknesses (35-385 micron). Cases examined include: various C-rates, salt concentrations, tortuosities, and porosities. The results for the simulations are given in Figure III - 1 where the fraction of electrode utilization is plotted against the ratio of electrode length to current penetration length, all for constant C-rate discharges (i.e., the electrolyte salt is depleted in the cathode during discharge). As seen in Figure III - 1, all the results fall along two lines. For the thinner electrodes ($L_{\text{Cathode}}/L_{\text{Penetration}}$ less than approximately two) the electrode utilization is effectively one. For the thicker electrodes ($L_{\text{Cathode}}/L_{\text{Penetration}}$ greater than approximately two) the electrode utilization drops off logarithmically.

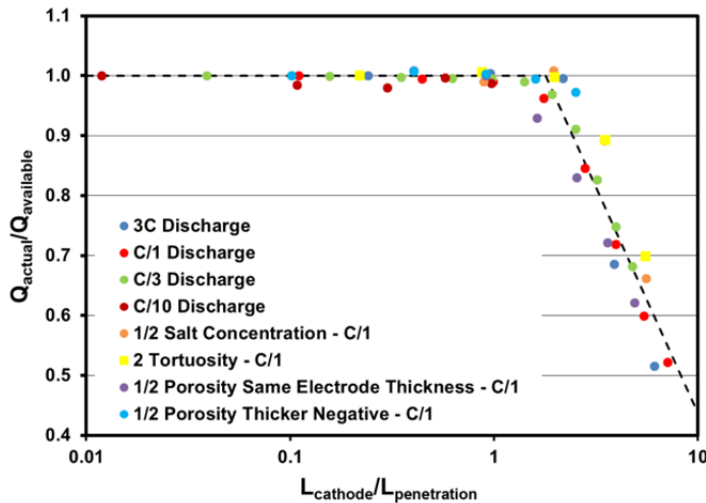


Figure III - 1: Electrochemical model simulations of cathode utilization vs. ratio of cathode length to current penetration length for constant C-rate discharges of NCA/Graphite lithium ion cell

There is very little spread in the simulation results for the thinner electrodes, but more spread for the thicker electrodes. There are several possible factors causing the spread in the thick electrode results. The current in Equation 2 is estimated from the electrode capacity and the C-rate, rather than the actual simulation current, which is more convenient for the BatPaC calculations. The transient period, which can be a significant fraction of the discharge time, for the thicker electrodes is not taken into account. Similarly, the dimensionless parameters from the other governing equations are also neglected. Nevertheless, there is a good correlation of the results for a wide range of conditions. The correlation is now being incorporated into BatPaC for the next release.

Flexible Plant: The cost of batteries is expected to come down through a combination of higher capacity materials, battery design and manufacturing process improvements, and economies of scale. The BatPaC model estimates the cost of batteries in a plant dedicated to the manufacture of a specific type of battery. The market for the different battery electric vehicles can be reasonably expected to grow in parallel but at different rates. One strategy to take advantage of high volume manufacturing is to build a plant where multiple types of batteries are produced. The BatPaC model was used to conduct a study where a plant produces 235,000 battery pack per year – 100,000 for HEVs; 60,000 for PHEV10s; 45,000 for PHEV40s; and 35,000 for EVs. Table III - 1 shows that the studied flex plant, compared to a dedicated plant, can save 9-21% of the battery

pack cost, and reduce the investment cost by 21-43%. Figure III - 2 shows the cost per battery pack, and Figure III - 3 shows the cost of energy storage for these four types of battery packs. The solid markers indicate the lower cost in a flex plant compared to the cost of an identical pack produced in a dedicated plant (lines).

Table III - 1: Distribution of product cost for flexible plant producing LMO-G batteries

Battery Type	HEV	PHEV10	PHEV40	EV	Flex Plant
Production per Year	100K	60K	45K	30K	235K
Cost of annual product, \$mil	71	97	146	245	559
Total investment, \$mil	48	67	101	176	391
Annual product / investment, ratio	1.50	1.45	1.45	1.39	1.43
Unit product cost, \$/pack	714	1,614	3,250	8,151	
Product cost, % of total	13	17	26	44	100
Product cost per area, \$-m ⁻²	24	22	22	20	21
Unit cost saving, %	21	18	14	9	14
Investment cost savings, %	43	38	31	21	28

The results show that the smaller HEV and PHEV10 batteries have the most to gain from manufacturing in the flex plant because so much of the cost is due to electrode processing, and therefore benefit from the larger production volume in the flex plant. On the other hand, the large numbers of cells and electrodes produced in the dedicated plants for the PHEV40 and EV batteries would result in large economies of scale even at the relatively low volumes at 45,000 and 30,000 packs per year, respectively.

A breakdown of the cost components showed that even though the 100,000 HEV battery packs represented the majority (43%) of the flex plant pack production rate, it was the larger EV battery packs that dominated the cost of electrode materials (58%), electrode area (46%), dry room area (38%) of the total needed for the flex plant.

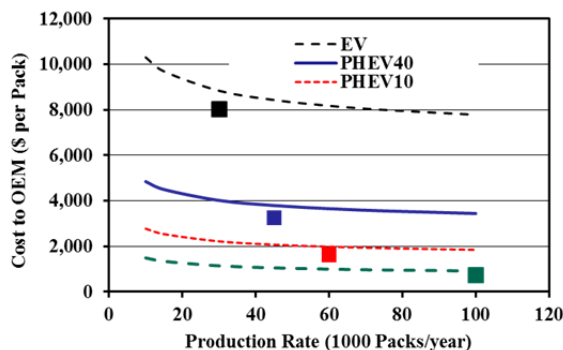


Figure III - 2: Unit cost per battery pack (including BMS) for LMO-G batteries

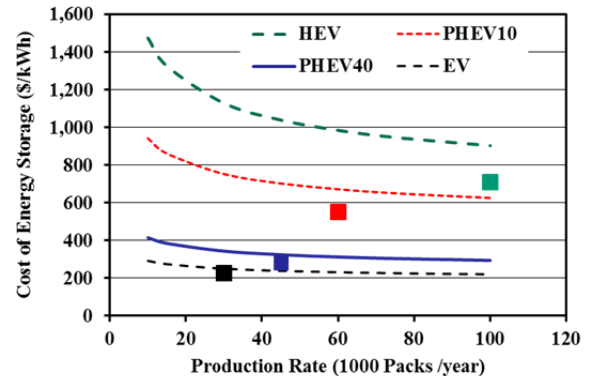


Figure III - 3: Cost of energy storage (including BMS) for LMO-G batteries. These economies of scale were derived in the flex plant by selecting uniform electrode size (length and width) to enable electrode coatings for all four battery packs. Relatively small adjustments in the coating machines can then accommodate the needed variations in coating thicknesses for the different packs. The power, capacity and voltage needs of the packs for the different types of vehicles can be further matched by changing the cell thicknesses, the numbers of cells and modules per pack, and series-parallel configurations

The flex plant study also explored a scenario where the batteries being produced and their rates were ramped up over five stages to match market demands (Table III - 2).

Table III - 2: Stages of development of a flexible plant with increases in production volume, types of batteries, and plant utilization

Stage	Pack Production Volume (thousands per year)					Plant Use, %
	HEV	PHEV10	PHEV40	EV	Flex Plant	
1	60				60	60
2	70	42			112	70
3	80	48	36		164	80
4	90	54	40.5	27	212	90
5	100	60	45	30	235	100

As shown in Figure III - 4, the cost of energy storage (\$/kWh) for the smallest capacity (the least electrode material) HEV battery pack is found to decrease the most as the production volume increases.

Material Cost Update: In a continuing effort to track the cost of materials, several updated costs have been drawn from surveys of the public domain and from private communications with experts in the field. Table III - 3 lists some of these revised costs, assuming high volume demand and production. LiFePO₄ cathode materials have dropped significantly in price as well as standard carbonate electrolyte and olefin based separator materials.

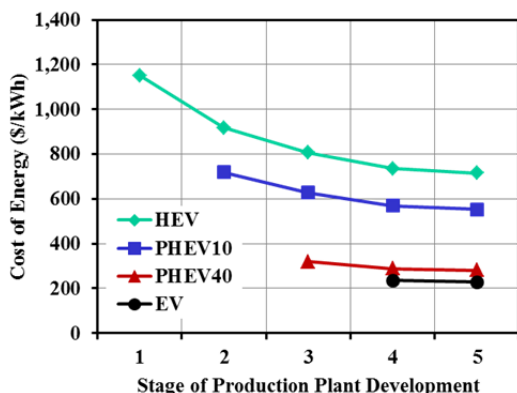


Figure III - 4: Cost of energy stored for four types of batteries as plant production level is increased in a flexible plant

Long term costs for the copper and aluminum foil are both found to decrease significantly. Projections for the manganese spinel cathode appear to be more expensive than our default assumption in BatPaC. We plan to discuss this deviation with experts in the field to understand the discrepancy before changing the value used in BatPaC.

The largest uncertainty exists with the layered oxides produced through co-precipitation and calcination. Over the next year, we will look more closely at the cost structure of these materials to better understand what a long-term cost projection should be.

Thus, we will maintain the same layered oxide costs in BatPaC until we have greater understanding.

Table III - 3. High volume cost of lithium ion battery materials

Material	BatPaC vX	BatPaC v2
Manganese spinel cathode (LMO), \$/kg	15-17	10
SV spinel cathode (LNMO), \$/kg	22	21
Phospholivine cathode (LFP), \$/kg	10-15	20
Layered oxide cathode (NCA), \$/kg	29	33-37
Layered oxide cathode (NMC333), \$/kg	23-30	31-38
Layered oxide cathode (NMC441), \$/kg	25	26-29
Li & Mn rich cathode (LMR-NMC), \$/kg	15-25	22-29
Synthetic graphite anode (SM-Gr), \$/kg	18	19
Natural graphite anode (Gr-Nat), \$/kg	10	10
Titanate spinel anode (LTO), \$/kg	12-14	12
Electrolyte (1.2 M LiPF6 EC:EMC), \$/kg	14-15	18
Olefin Separator, \$/m ²	1	2
Copper Foil, \$/m ²	1.2	1.8
Aluminum Foil, \$/m ²	0.3	0.8

Conclusions and Future Directions

Dimensional analysis of the electrolyte salt transport equation in an electrochemical lithium ion cell model has been utilized to establish a correlation for thick electrode capacity utilization. The correlation is now being incorporated into BatPaC for the next release.

Battery manufacturing plants that can produce multiple types of batteries and ramp up their production in response to market demands offer an attractive pathway to reducing the cost of batteries. The low capacity HEV batteries, which can be expected to see the earliest demand, are benefited the most from even a small volume co-production of the higher capacity batteries.

A survey of the costs of lithium ion batteries indicates some reduction. Continuing development of new materials and alternative sourcing and production methods are needed to contribute to the development of lower cost lithium ion batteries.

Future plans include further investigations into the battery and materials manufacturing methods. A cost model for the production of cathode materials will be set up in consultation with Argonne's Materials Engineering Facility (MERF). The BatPaC model will be expanded to include a blended cathode chemistry such as NMC blended with LMO. The model will also be expanded to provide more detail in the energy demands of the battery manufacturing plant. Results from these analyses will enable a more rigorous understanding of the processes and facilitate the evaluation of alternative production options.

FY 2014 Publications/Presentations

1. J. B. Dunn, L. Gaines, J. C. Kelly, C. James, and K. G. Gallagher "The significance of Li-ion batteries in EV life-cycle energy and emissions, and recycling's role in its reduction" Energy & Environmental Science, *accepted* (2014).
2. P.A. Nelson, S. Ahmed, K.G. Gallagher, D.W. Dees, "Cost Savings for Manufacturing Lithium Batteries in a Flexible Plant," to be submitted to the Journal of Power Sources.

III.A.2 Battery Ownership Model: A Tool for Evaluating the Economics of Electrified Vehicles and Related Infrastructure (NREL)

Jeremy Neubauer

National Renewable Energy Laboratory
15013 Denver West Parkway
Golden, Colorado 80401-3393
Phone: (303) 275-3084
E-mail: Jeremy.Neubauer@nrel.gov

List of Collaborators:

Eric Wood, Evan Burton, Kandler Smith, and Ahmad Pesaran
National Renewable Energy Laboratory

Start Date: FY2009

Projected End Date: FY2015

Objectives

- Identify cost-optimal electric vehicle (EV) use strategies and pathways capable of achieving national oil displacement goals in support of the DOE's EV Everywhere Grand Challenge.
- Evaluate various business models and impact of other factors such as driving patterns, geography, battery wear, and charge profiles using the National Renewable Energy Laboratory (NREL)-developed Battery Ownership Model (BOM) and Battery Lifetime Analysis Simulation Tool for Vehicles (BLAST-V).

Technical Barriers

- The economics of plug-in electric vehicles (PEVs) are highly sensitive not only to vehicle hardware and fuel costs, but also to infrastructure costs, driving patterns, all-electric range, battery wear, charging strategies, third-party involvement, and other factors. Proper analysis requires a detailed, comprehensive, systems-level approach.
- The broad range of complex EV usage strategies proposed, including battery leasing, battery swapping, fast charging, opportunity charging, vehicle-to-grid service, battery second use, etc., presents a large number of scenarios to assess.
- Battery life is typically a major factor in the total cost of ownership of EVs, but accurate modeling of battery degradation under the complex and varied

conditions of potential automotive use is challenging.

- Economics are highly sensitive to vehicle drive patterns; thus, different drive patterns require different use strategies to minimize cost. Drive pattern data sufficient for economic analysis is also in short supply.

Technical Targets

- Quantify the total cost of ownership of EVs when complex usage scenarios and business models are employed.
- Understand how battery performance, life, and usage affect cost and other engineering parameters.
- Design use strategies that achieve cost parity between EVs and gasoline-powered conventional vehicles (CVs).

Accomplishments

- Added multi-cell battery simulation capability to BLAST to study heterogeneous battery electrical, thermal, and wear response and evaluate its effect on EV performance.
- Added geospatial data to travel patterns employed in BLAST, and developed an intelligent rerouting algorithm for EVs to utilize available charging infrastructure that enables travel not otherwise achievable.
- Simulated a range of scenarios of EVs operating in the presence of real-world fast charger deployments. Found that the primary challenge for electric vehicles (EV) with fast charging is controlling maximum battery temperature resultant from repeated drive-charge cycles with minimal rests in between, which can be achieved with active battery cooling systems. Once battery temperature is controlled, we found that access to fast charge infrastructure can enable BEVs to travel 785 more miles be year on average across the travel patterns studied.



Introduction

Fast charging is attractive to EV drivers for its ability to enable long-distance travel and quickly

recharge depleted batteries on short notice. However, such aggressive charging and the sustained vehicle operation that results could lead to excessive battery temperatures and degradation. Properly assessing the consequences of fast charging requires accounting for disparate cycling, heating, and aging of individual cells in large EV packs when subjected to realistic travel patterns, usage of fast chargers, and climates over long durations (i.e., years). The resultant gains in vehicle utility afforded by fast charging under real-world conditions must also consider these factors.

The U.S. Department of Energy's Vehicle Technologies Office has supported NREL's development of BLAST-V to create a tool capable of accounting for all of these factors. In FY14, specific developments were completed to enable the realistic simulation of EVs operated in the presence of fast chargers. BLAST-V was then employed to evaluate the effects of realistic fast charger use on EV batteries and utility.

Approach

NREL's BLAST-V is an EV simulator focused on computing long-term effects of complex operational scenarios on vehicle utility and battery performance. It considers the vehicle powertrain, battery control strategy, driving and charging patterns, local climate, the vehicle-battery-environment thermal system, battery chemistry, and other factors in computing short-term vehicle and battery performance (e.g., vehicle range, battery voltage, state of charge (SOC), and temperature) and long-term vehicle utility and battery degradation.

Key to BLAST-V is the calculation of battery degradation. NREL has developed a semi-empirical life model, offering a combination of increased confidence in interpolations and projections, while maintaining simplicity of implementation and a basis in actual laboratory data. BLAST-V incorporates the NREL model for a Li-ion cell with a nickel-cobalt-aluminum cathode and graphite anode to supply a representative model of battery degradation. Recent updates enable BLAST-V to simulate individual cells within a pack, deploying this degradation model in a highly parallel fashion to investigate heterogeneous cell aging.

Another recent addition to BLAST-V is the ability to include geospatial travel data and reroute travel histories based on route efficiency and available infrastructure. This algorithm evaluates alternative routes to reach destinations using the Google Maps API, searches for available charging infrastructure within a user-defined distance from each route, selects a sequence of charging infrastructure to utilize that minimizes travel time and maintains acceptable battery SOC on each route, then selects the route and charging schedule that is most convenient to the driver.

To seed travel histories, we employ historical travel data from the Puget Sound Regional Council's Traffic Choices Study. We filter these histories to those that accrued 8,000 miles or more over a one year period for simulation to focus on higher mileage drivers. Typical meteorological year data from both moderate and hot climates (Seattle, WA and Phoenix, AZ, respectively) are employed to explore the impact of environmental temperatures. We employ a mid-size sedan with technology and performance levels anticipated for a 2020 model year vehicle that yields an 80 mile range on an approximate EPA cycle. Three battery thermal management systems (BTMS) were employed in our analyses: a passive systems, an active cooling system that operates when the vehicle is being driven, and an active cooling system that operates when the vehicle is either being driven or parked at a charger. A 6.6 kW AC level 2 charger is assumed to be installed in the vehicle owner's home and available for use at all hours of the day. A network of 50 kW DC fast chargers (DCFC) representative of the current deployment of fast chargers in the Seattle metro area was employed as well.

Results

Baseline simulations were run using the Seattle climate to check the typical usage of DCFCs resultant from our implanted methodologies and assumption. Results show that most drivers in this study use fast chargers 10 times per year or less, but extreme cases reach up to 8 times per month. This results in relatively small fractions of total EV electricity coming from DCFCs, typically less than 10%. When visiting a DCFC, we predict that drivers will stay between 10 and 22 minutes, arriving with a battery SOC of 18 to 60%. Although data on real-world usage of DCFCs is sparse, this appears to agree reasonably well with data reported by the EV Project [1, 2].

Next we compared battery response when operated in our two selected climates with and without access to a fast charger network. In Seattle, we saw that neither the use of fast chargers nor the variation of BTMS had any significant effect on time-averaged battery temperatures or capacity loss over ten years for the average driver. In Phoenix, we see similar trends when comparing the absence and presence of fast chargers, though the difference between BTMS is much more apparent – the presence of active cooling while driving, and the additional use of that system in standby mode at a charger noticeably reduces average battery temperature and capacity loss.

While the nearly negligible impact of fast charger usage on battery capacity fade may be surprising to some, it is important to point out that DCFCs are used quite sparingly by our driver histories. Where

the effect of fast charger usage is most noticeable is in the maximum battery temperature. As shown in Figure III - 5 and Figure III - 6, comparison of cases with and without fast charger availability shows that maximum battery temperatures are ~ 15 °C higher for the median driver when fast charging is employed with a passive BTMS. In fact, in the presence of fast charging our simulated maximum battery temperatures regularly exceed 45 °C in Seattle and 60 °C in Phoenix – so high that they could in fact pose a safety risk if charging and/or driving is not impeded by onboard vehicle control systems. The addition of active battery cooling, however, can significantly moderate maximum battery temperatures, especially when employed both while driving and charging.

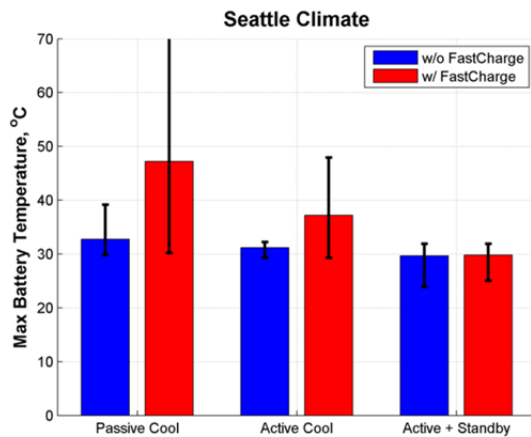


Figure III - 5: Effect of DCFCs and BTMS on battery capacity loss in Seattle

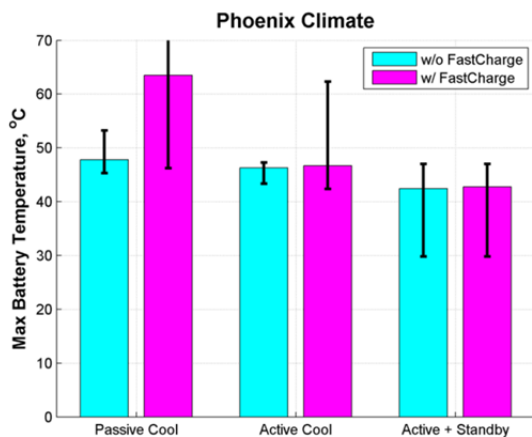


Figure III - 6: Effect of DCFCs and BTMS on battery capacity loss in Phoenix

Closer investigation of these high temperature events reveals their cause: repeated, back-to-back drive and charge events with short or no rests in between. Fast charging is shown to elevate battery temperature at a faster rate than driving (compare, for example, an estimated battery discharge power of 18 kW when

driving at 300 Wh/mi and 60 mi/hr to a fast charge rate of 50 kW), and the presence of fast charging allows the vehicles to travel further more continuously than is otherwise possible in their absence. Thus it is not unreasonable that a battery and BTMS designed for use without fast charging could overheat when this option is presented.

Subsequent simulations investigated the utility that improvements in DCFC access can afford EV drivers as a function of vehicle range. Where active BTMS is employed to manage battery maximum temperature, we find that access to fast chargers can enable EVs to travel 785 more miles per year on average across the travel patterns studied for our baseline 80 mile EV. In extreme cases, though, drivers can achieve several thousand additional miles with the use of fast charging. Clearly, the impact of travel patterns can be high. We also observe that the benefits of fast charging for the average driver falls slowly to 409 miles per year as vehicle range increases to 218 miles. Travel patterns that make use of fast charging infrastructure most frequently are found to fall much more sharply as vehicle range increases. (See Figure III - 7.)

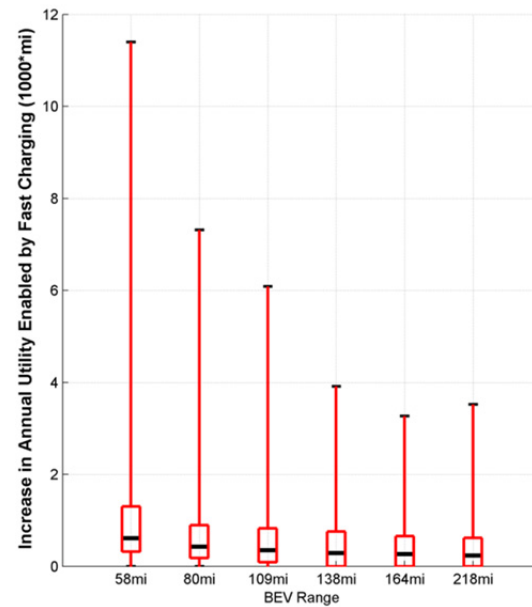


Figure III - 7: Additional mileage enabled by fast charger access as a function of vehicle range

Conclusions and Future Directions

BLAST-V has been employed to study the impact of realistic fast charging on simulated battery electrical, thermal, and degradation response, as well as the resultant gains in vehicle utility. We have found that the largest challenge presented by fast charging to the battery is its effect on maximum battery temperature. In

the presence of a passive BTMS, maximum battery temperatures can exceed safe operating limits due to repeated drive-charge sequences with short or no rests in between. This can be controlled, however, via the employ of BTMS with active cooling capabilities, or onboard vehicle controllers limiting charging and driving activities. The prior is expected to be much more attractive in terms of driver satisfaction.

Where active BTMS is employed to manage battery maximum temperature, we find that access to fast chargers can enable EVs to travel 785 more miles per year on average across the travel patterns studied for our baseline 80 mile EV. This benefit is found to decrease as vehicle range increases, as would be expected.

References

1. Fast DC Charging for Electric Vehicles, Navigant Research Webinar, April 9, 2013.
navigantresearch.com/webinar/fast-dc-charging-for-electric-vehicles
2. Smart, J. "Latest Insights from The EV Project and ChargePoint America PEV Infrastructure Demos," presented at GITT meeting, Idaho National Laboratory, August 12, 2014.

FY 2014 Publications/Presentations

1. Neubauer, J.; Pesaran, A.; Bae, C.; Elder, R.; Cunningham, B. "Updating United States Advanced Battery Consortium and Department of Energy Battery Technology Targets for Battery Electric Vehicles," *Journal of Power Sources*, Volume 271, 20 December 2014, Pages 614–621. NREL Report No. JA-5400-62265.
2. Neubauer, J; Wood, E. "Thru-life impacts of driver aggression, climate, cabin thermal management, and battery thermal management on battery electric vehicle utility," *Journal of Power Sources*, Volume 259, 1 August 2014, Pages 262–275. NREL Report No. JA-5400-61311.
3. Neubauer, J; Wood, E. "The impact of range anxiety and home, workplace, and public charging infrastructure on simulated battery electric vehicle lifetime utility," *Journal of Power Sources*, Volume 257, 1 July 2014, Pages 12–20. NREL Report No. JA 5400-61036.

III.A.3 PEV Battery Second Use (NREL)

Jeremy Neubauer

National Renewable Energy Laboratory
15013 Denver West Parkway
Golden, Colorado 80401-3393
Phone: (303) 275-3084
E-mail: Jeremy.Neubauer@nrel.gov

List of Collaborators:

Eric Wood, Evan Burton, Kandler Smith, and
Ahmad Pesaran
National Renewable Energy Laboratory

Subcontractors:

California Center for Sustainable Energy,
UC San Diego, UC Davis,
San Diego Gas and Electric

Partners:

Southern California Edison and BMW USA

Start Date: FY2009

Projected End Date: FY2015

Objectives

- Identify, assess, and verify sustainable applications for the second use of plug-in electric vehicle (PEV) lithium-ion (Li-ion) traction batteries after their end of useful life in a vehicle.
- Collaborate with industry and others through cost-share subcontracts to demonstrate and evaluate the potential and expected performance of used batteries in real applications.

Technical Barriers

- High cost of Batteries is a barrier to wide adoption of PEVs.
- PEV end-of-service burdens (battery recycling, disposal) could impede PEV deployment. Re-using PEV batteries in secondary applications and delaying recycling can shift these burdens away from the automotive industry.
- Finding suitable second-use applications for the large quantity of used PEV batteries that could become available from automotive markets.
- Assessing the value of post-automotive applications for PEV batteries is challenged by uncertain

electrical demands, complex and difficult-to-assess revenue streams, and prohibitive regulatory structures.

- The processes of repurposing PEV batteries are yet to be identified and could have a major impact on the viability of second use strategies.
- Uncertainty in the longevity of repurposed batteries in post-automotive applications.
- Battery degradation in both automotive and post-automotive use is notoriously difficult to ascertain, yet has a strong impact on the potential end-user acceptability and profitability of secondary use strategies.

Technical Targets

- Identify and demonstrate sustainable second use applications for PEV Li-ion traction batteries.
- Conduct testing on aged PEV batteries to ascertain their longevity for second use applications.
- Devise optimized use strategies for automotive traction batteries to facilitate their second use, maximizing their value and reducing cost to the automotive consumer and also preventing premature recycling of otherwise useable batteries.

Accomplishments

- Continued field testing of aged automotive batteries with California Center for Sustainable Energy (CCSE) to demonstrate viability of identified second-use applications and quantify long term degradation. Field testing expected to be completed in January 2015.
- Continued laboratory testing of aged automotive batteries at NREL.
- Developed a partnership with BMW and supported test planning for a large pre-commercial stage second-use energy storage system.
- Completed detailed analysis of behind-the-meter demand charge management (DCM) as a potential application for second use batteries.



Introduction

Accelerated market penetration of PEVs as targeted by the DOE's *EV Everywhere* Grand Challenge is presently limited by the high cost of Li-ion batteries. It has been estimated that a 50%-75 % reduction in battery

cost may be necessary to equalize the current economics of owning PEVs and conventionally fueled vehicles. Further, both vehicle manufacturers and consumers are concerned about end-of-service costs associated with proper handling of the battery.

One strategy that can positively affect both topics is battery second use – allocating a retired automotive battery to be reused in other applications where it may still have sufficient performance to be valuable. By extracting additional services and revenue from the battery in a post-vehicle application, the total lifetime value of the battery is increased. This increase could be credited back to the automotive consumer, effectively decreasing automotive battery costs. Further, it transfers the cost of battery recycling or disposal from the automotive community to the second use industry.

There are several current and emerging applications where PEV battery technology may be beneficial. For example, the use of renewable solar and wind technologies to produce electricity is growing, and their increased market penetration can benefit from energy storage, mitigating the intermittency of wind and solar energy. New trends in utility peak load reduction, energy efficiency, and load management can also benefit from the addition of energy storage, as will smart grid, grid stabilization, low-energy buildings, and utility reliability. The prospect of extremely low-cost energy storage via second use batteries is attractive to these industries.

In past years, NREL has created a detailed framework for analyzing the second use of advanced automotive batteries, addressing repurposing costs, sale price, automotive discounts, and second use applications. The application of this framework to Li-ion PEV batteries has highlighted the need for efficient repurposing strategies, and identified a promising market for repurposed batteries. It has also found that the most pressing remaining uncertainty is the longevity of repurposed batteries in post-automotive applications.

To address this uncertainty, NREL has acquired aged batteries, developed a long-term field test site and strategy, and initiated long-term testing via a subcontract with CCSE, leveraging a 50-50 cost share partnership with industry. NREL has also acquired additional aged batteries for on-site laboratory testing. Additionally, NREL has worked with Southern California Edison to evaluate the potential of second use batteries in community energy storage applications, and with BMW to demonstrate a pre-commercial second-use battery system.

Approach

Four aged automotive batteries have been deployed for field testing at UCSD, executed by CCSE. Two applications have been the focus of testing to date:

regulation energy management (REM), and demand charge management (DCM). Though testing protocols for the latter have been developed specifically for a behind-the-meter scenario, it is more broadly applicable to generalized peak shaving applications as well. For both applications, we have developed both prescribed duty cycle and real-time testing modes. The objective of this testing is to characterize battery degradation in likely second use applications and begin demonstration of the feasibility of aged automotive batteries in such applications.

In parallel, NREL has initiated laboratory life tests to further characterize second-use battery degradation. Included is a 10-kW pack that has been substantially cycled to an automotive use duty cycle and that has been disassembled to the cell level. Cells from this pack are being tested individually to provide insight into the variation in degradation across a single battery pack, as well as the response of cells to different duty cycles. Four ~4-kWh modules have also been acquired following extensive automotive cycling to the same state of health, albeit via different conditions (temperatures and number of cycles). A life test using a regulation energy management profile has been designed and initiated for these modules to answer the question of whether simple state data or full pack history data are necessary at the point of repurposing to quantify a battery's value.

In addition to the application-specific duty cycles, all batteries undergo regular reference performance tests at defined intervals. The results of these tests will be used to track loss of capacity and growth of resistance within each battery.

Results

Figure III - 8 shows an example response of a battery in the field testing system at UCSD performing real-time DCM. It illustrates the complexity of such an algorithm, requiring the inclusion of accurate solar power, building load, and battery performance prediction.

As noted previously, both real-time and prescribed REM and DCM testing is being performed on multiple packs at the UCSD test site. A full analysis will be prepared on test results when testing completes in FY15.

Figure III - 9 shows the change in capacity of 30 cells under test at NREL taken from an aged 10 kW battery pack. The test conditions vary considerably across this data set, with DODs ranging from 40% to 80%, temperature ranging from 0° to 45 °C, cycle frequency ranging from once to twice per day, and duty cycles including grid-specific, automotive specific, and constant power profiles. The presented data represents the cells' state of health after one year of cycling at NREL. Initial results suggest that degradation rates for

these conditions are relatively low. A full analysis of the data will be prepared in FY15 after additional cycling has been completed.

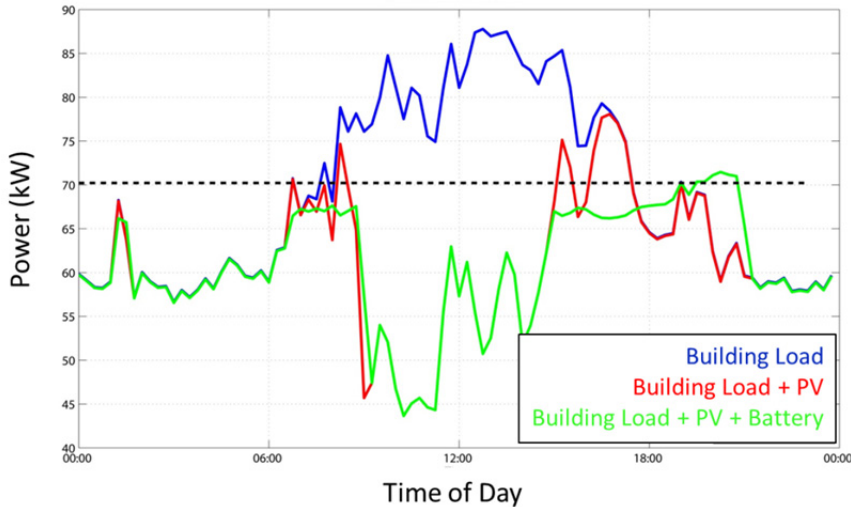


Figure III - 8: Real-time DCM field test response.

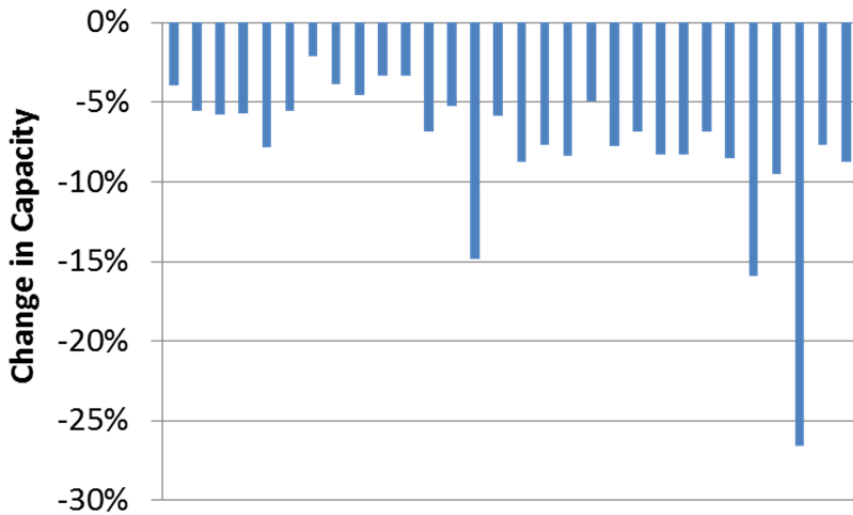


Figure III - 9: Change in capacity of 30 cells under test at NREL taken from an aged 10 kW battery pack

Conclusions and Future Directions

NREL has performed comprehensive analyses and testing to assess the feasibility of PEV battery in a second use. The study has found that implementation of battery second use strategies will be a viable means to offset end-of-service battery costs for PEV owners (e.g., battery removal, disposal, recycling), while offering secondary markets extremely large supplies of low cost energy storage. This could have drastic effects on the electricity grid, improving quality of service and

reducing emissions. However, these efforts have also ascertained that the rate of battery degradation in second use applications is a large uncertainty that must be resolved to enable such a future. NREL is at present addressing these issues with multiple long term battery testing and analysis efforts.

In FY15, NREL will complete its battery life testing efforts, perform detailed analysis on results, and publish reports to disseminate their findings. NREL will also publish a comprehensive report on its second use analyses.

III.A.4 Battery Life Trade-Off Studies (NREL)

Kandler Smith (NREL)

National Renewable Energy Laboratory
15013 Denver West Pkwy, Golden, CO 80401
Phone: (303) 275-4423
E-mail: kandler.smith@nrel.gov

Subcontractor:
Texas A&M University, College Station, TX
Prof. Partha Mukherjee

Start Date: October 2008
Projected End Date: December 2014

Objectives

- Develop physics-based battery life prediction models that quantify battery longevity over a range of real-world temperature and duty cycle conditions.
- Extend cell life models to pack-level, capturing impacts of temperature non-uniformity, cell performance and aging variability on system lifetime.
- Perform tradeoff studies to quantify potential battery lifetime extension and cost reduction achievable via advanced systems, controls, and operating strategies for electric drive vehicle battery packs.

Technical Barriers

- Multiplicity of degradation modes (10+) faced by Li-ion battery cells in automotive environment.
- Lack of models and methods to accurately quantify battery lifetime.
- Lifetime uncertainty leading to conservative, oversized batteries in order to reduce warranty risk.

Technical Targets

- 10-15 year battery life for electric drive vehicles in disparate geographic environments and duty cycles.
- Battery lifetime predictive models validated against real-world data with less than 10% error.
- Thermal and other control systems that reduce cell energy content while still meeting 10-15 year lifetime.

Accomplishments

- Integrated 10+ degradation mechanisms into a statistical framework for diagnosing degradation mechanisms and predicting lifetime from cell experimental data.
- Validated cell-level life models with pack-level life measurements using multi-cell pack-level electrical-thermal degradation model.
- With Texas A&M, applied high order continuum physics transport/fracture models to develop reduced order models of electrode particle damage that can be used to interpret experimental data.



Introduction

Battery aging behavior directly impacts to what degree an EDV battery must be oversized to achieve desired service life across applications and environments. Eliminating extra cost associated with oversizing would positively benefit market acceptance of EDVs. Automotive batteries face large variability in thermal environment and duty cycle, with 10+ degradation factors that must be considered to predict lifetime. Worst-case cell aging conditions within a multi-cell battery pack drives the need to oversize battery cell energy content.

Physics-based models describing cell- and pack-level aging processes are needed to support engineering optimization of next generation batteries. Cell life models must capture a multiplicity of degradation modes experienced by Li-ion cells, such as interfacial film growth, loss of cycleable lithium, loss of active material, degradation of electronic and ionic pathways, with dependence on temperature, state-of-charge, depth-of-discharge, C-rate and other duty cycle factors. In particular, the mechanical damage induced by high C-rate and depth-of-discharge electrochemical cycling is a poorly understood degradation mechanism which we seek to clarify with physical models. Pack-level life models must capture effects leading to non-uniform cell aging, including temperature imbalance, cell performance and aging variability, and interaction with balance of plant systems such as cell balancing.

Approach

In FY14, NREL's existing life model framework developed for NCA, FeP, and NMC chemistries was extended to an additional NMC chemistry and validated at both the cell- and pack-level. The SEI microcracking model of Deshpande et al., *J. Electrochem. Soc.* (2012), was extended to capture mixed modes of cycling and calendar degradation. That model successfully describes mid-life degradation for the FeP chemistry, to be described in a forthcoming journal article.

To describe resistance and capacity changes with lifetime for multiple Li-ion technologies, NREL's life modeling framework includes multiple degradation mechanisms:

- Side reactions forming electrode impedance films and consuming Li, such as at the negative electrode solid electrolyte interface (SEI) layer.
- Lithium plating at low temperatures.
- Binder degradation at high temperatures.
- Electrolyte decomposition at high temperatures and voltages.
- SEI microcracking and regrowth.
- Particle and electrode fracture/fatigue/isolation due to electrochemical-thermal-mechanical cycling.
- Separator pore closure due to viscoelastic creep caused by cycling.
- Gas pressure buildup.
- Break-in processes releasing excess Li and enhancing reaction/transport initially at beginning of life.

During model development, multiple degradation hypotheses can be proposed, guided by knowledge of cell chemistry and cell teardown experiments when available. Mechanism hypotheses are confirmed/refuted based on regression statistics of model versus data.

Of the above degradation mechanisms, the least understood mechanism is particle and electrode fracture/fatigue/isolation due to electrochemical-thermal-mechanical cycling. The model framework presently relies on empirical formulas to capture this degradation as a function of temperature, C-rate, and depth-of-discharge. To reduce this empiricism, NREL initiated a project with Texas A&M to explore a wide range of electrode particle fracture simulations using their physics-based lattice spring (or discrete element) model. From these computationally-expensive simulations, we extract low order fatigue models that can be applied to cell-level lifetime simulations and validated with experimental data.

Results

Particle Fracture Model

In previous work, Texas A&M developed an electrochemical/thermal model of an electrode active material particle coupled with solid mechanics (Barai, et al., *J. Electrochem. Soc.*, 2013). The model captures Li transport inside the particle, stress and fracture due to transport-limited concentration gradients, and impact of fracture on further limiting Li transport. The model is unique in that it predicts damage evolution dependent on charge/discharge condition and also captures the impact of that damage on subsequent performance of the battery. The model is too computationally-expensive, however, to run large-scale cell or pack lifetime simulations. In FY14, NREL and Texas A&M ran a large matrix of simulation cases for various temperatures, constant currents, and drive cycles. We then tested various models from the fatigue literature to come up with low order models that describe the damage evolution across all operating conditions. Figure III - 10 shows the magnitude of concentration gradient, C, versus cumulative strain energy, CSE. By non-dimensionalizing independent and dependent variables and applying scaling laws, the 20 simulation cases reduce down to a single damage evolution path shown in the bottom panel of Figure III - 10. The scaling laws, derived from constant current charge/discharge simulations, are separately validated against more complex drive cycle charge/discharge simulations. This is significant, as the low order scaling model provides practical guidance as to what aspects of high rate current pulses cause the most damage during drive cycles. The results will be published in an upcoming paper.

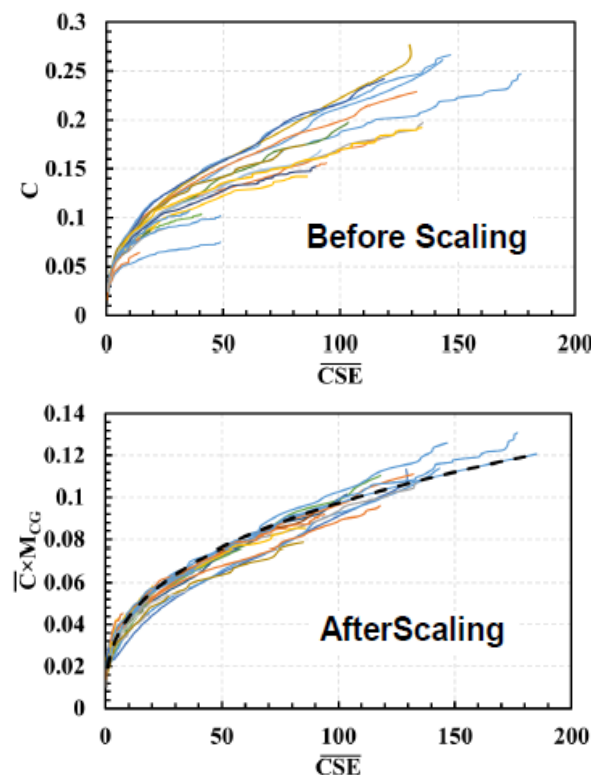


Figure III - 10: Damage evolution for 20 constant current discharge/charge simulations using particle fracture model, reduced to a single trend line using fatigue scaling laws

SEI Microcracking Model

In FY13, NREL developed a life predictive model for the graphite/FeP chemistry based on aging data for the A123 26650 2.2 Ah cell. A particular focus was to capture end-of-life effects, where capacity suddenly fades at a high rate due to cycling-related conditions. But the model required additional refinement in order to more accurately capture mid-life capacity fade, where calendar fade has a weak coupling with cycling condition.

The SEI microcracking model of Deshpande et al., *J. Electrochem. Soc.* (2012), enhances the typical chemical degradation/SEI growth model by including mechanical damage to the SEI due to cycling. The damage is caused as high tensile stresses build in the SEI layer during delithiation, resulting in microcracks in the SEI. These microcracks expose fresh negative electrode sites for new SEI to form, consuming additional lithium from the system and degrading capacity.

Unlike the Deshpande model, which tracked capacity fade versus number of cycles, in FY14, we extended that model to capture mixed modes of cycling- and calendar- or time-driven degradation. That model successfully describes mid-life degradation for the FeP

chemistry, to be described in a forthcoming journal article.

Dissemination and Validation

To date, the NREL battery life model has been licensed to more than ten external companies, labs, and universities to apply in their own research studies. The life model is a critical component in NREL's electric vehicle techno-economic analysis model, Battery Lifetime Assessment Tool (BLAST) described elsewhere in this report. The BLAST model predicts the lifetime of batteries in electric vehicles for various driver behaviors, charge behaviors, climates, battery thermal management designs, and cell balancing systems. Two journal articles were published in FY14.

Under a cooperative research and development agreement (CRADA) with Eaton Corporation, the NREL life model is being integrated into Eaton's real-time hybrid electric vehicle (HEV) supervisory controller. By including the life prognostic model, the controller is able to maximize fuel economy and satisfy constraints on battery lifetime. The general method allows for increased vehicle performance even with a less expensive, downsized battery. For the CRADA project, NREL carried out life tests of Eaton's graphite/NMC cells under more than 20 aging conditions in order to develop a cell life model for that technology. Separately, NREL ran one-year aging tests on two Eaton HEV packs with substantially different duty cycles and at multiple environmental chamber temperatures representing different seasons of the year. The cell life model, together with a pack thermal model capturing temperature distributions in the packs, was able to predict the outcomes of these two packs within 3% and 5% of measured capacity and resistance, respectively, over the course of the one-year test. This validation provides further confidence in the approach for physics-based modeling of battery lifetime at the cell- and pack-levels.

Conclusions and Future Directions

A robust framework for modeling a multiplicity of degradation mechanisms in Li-ion cells has been developed. Models of multiple chemistries are now available and are being applied in multiple system and control design studies to lower the cost and extend the life of Li-ion battery systems. The parameterization of these life models remains a burden however, requiring 6-12 months of expensive testing for each new cell technology. As such, the models arrive too late in the design process to apply more directly in the cell design optimization process. Pending resources, future work will therefore focus on developing 3D multiphysics models of degradation processes consistent with the Computer-Aided Engineering of Batteries (CAEBAT) program at DOE. Goals of the models are to provide

engineering feedback for cell design optimization, allow for accurate lifetime prediction with less test data, and help enable next generation Li-ion chemistries.

FY 2014 Publications/Presentations

1. K. An, P. Barai, K. Smith, P.P. Mukherjee, “Probing the Thermal Implications in Mechanical Degradation of Lithium-Ion Battery Electrodes,” *J. Electrochem Soc.* 161 (6) A1058-A1070, 2014. <http://dx.doi.org/10.1149/2.069406jes>
2. D.R. Diercks, M. Musselman, A. Morgenstern, T. Wilson, M. Kumar, K. Smith, M. Kawase, B.P. Gorman, M. Eberhart, C.E. Packard, “Evidence for Anisotropic Mechanical Behavior and Nanoscale Chemical Heterogeneity,” *J. Electrochem. Soc.* 161 (11) F3039-F3045, 2014. <http://dx.doi.org/10.1149/2.0071411jes>
3. A. Hoke, A. Brisette, K. Smith, A. Pratt, D. Maksimovic, “Accounting for Lithium-Ion Battery Degradation in Electric Vehicle Charging Optimization,” *IEEE J. Pwr. Electronics*, 2013. <http://dx.doi.org/10.1109/JESTPE.2014.2315961>
4. K. Smith, E. Wood, S. Santhanagopalan, G.-H. Kim, A. Pesaran, “Advanced Models and Controls for Prediction and Extension of Battery Lifetime,” Large Lithium Ion Battery Technology & Application Symposia Advanced Automotive Battery Conference, Atlanta, GA, February 4-6, 2014. [NREL Report No. PR-5400-61037](#)
5. K. Smith, E. Wood, S. Santhanagopalan, G.-H. Kim, Y. Shi, A. Pesaran, “Predictive Models of Li-ion Battery Lifetime,” IEEE Conference on Reliability Science for Advanced Materials and Devices, Golden, Colorado; September 7-9, 2014. [NREL Report No. PR-5400-62813](#)

III.A.5 Battery Production and Recycling Materials Issues (ANL)

Linda Gaines and Jennifer Dunn

Center for Transportation Research
Argonne National Laboratory
9700 S. Cass Avenue
Argonne, IL 60439
Phone: (630) 252-4919, Fax: (630) 252-3443
E-mail: lgaines@anl.gov

Start: Spring 2008

Projected Completion: Ongoing

Objectives

- Examine emissions to air, water, and land from acquisition of current and future battery materials.
- Analyze active materials production from metals and other precursors.
- Identify barriers in development of active material supply chain.
- Identify precursors of greatest concern in the supply chain.
- Estimate material demands for Li-ion batteries.
 - Identify any potential scarcities.
- Calculate theoretical potential for material recovery.
- Evaluate real potential for recovery using current recycling processes.
- Determine potential for recovery via process development.
- Characterize ideal recycling process.
- Develop improved process to maximize material recovery.
- Determine how each of these factors changes with battery chemistry (or mixtures of chemistries).
- Determine how reuse of batteries will impact recycling processes and economics.
- Identify economic and regulatory factors impacting battery recycling.
- Formulate actions to make recycling happen.

Technical Barriers

- Nickel and cobalt are energy intensive to produce and have significant environmental impacts, including SO_x emissions, but the need to access virgin supplies could be reduced by recycling, thereby reducing the local impacts of metals mining.

- Scarcity could increase costs for battery materials.
 - Recycling could increase effective material supply and keep costs down.
 - Current processes recover cobalt, use of which will decline.
 - Recycling economics in doubt because of low prices for lithium and other materials.
- Some reports have indicated that battery assembly may be the most energy intensive step in the battery supply chain, limiting the utility of recycling from an energy conservation perspective.
- Material recovered after use may be obsolete.
- Producers may be reluctant to use recovered materials.
- Mixed streams may be difficult to recycle.
- Process data are not published and may in fact not be known yet.
- Future battery chemistry is not determined.

Technical Goals

- Estimate energy use/emissions for current material processes.
- Estimate energy use/emissions for current battery assembly processes.
- Characterize current battery recycling processes.
- Estimate impacts of current recycling processes.
- Evaluate alternative strategies for additional material recovery.
- Develop improved recycling processes.
- Screen new battery materials for potential negative impacts from production or problems in recycling.

Accomplishments

- Compared critical material demand to supply out to 2050 for maximum penetration of EVs.
- Compiled information on local environmental burdens of metal production.
- Analyzed cradle-to-gate impacts of producing four new cathode materials and one new anode material.
- Determined and characterized current production and recycling methods for lithium-ion batteries.
- Performed battery production and recycling lifecycle analysis to compare impacts and identify ideal recycling processes.
- Determined roles battery chemistry plays in both environmental and economic benefits of recycling.
- Identified institutional factors that can enable or hinder battery recycling.

- Presented and published analyses and recycling process comparison.
- Released update to GREET battery module, incorporating four new cathode materials and one new anode material.
- Participated in IEA HEV Task 19, SAE, and USCAR working groups



Introduction

Examination of the production of batteries from raw material acquisition to assembly illuminates the stages of this supply chain that incur the greatest energy and environmental burdens. Recycling of material from spent batteries will be a key factor in alleviating potential environmental and material supply problems. We are examining battery material production, battery assembly, and battery recycling processes that are available commercially now or have been proposed. Battery materials, assembly and recycling processes are being compared on the basis of energy consumed and emissions, suitability for different types of feedstock, and potential advantages relating to economics and scale. We are comparing the potential of several recycling processes to displace virgin materials at different process stages, thereby reducing energy and scarce resource use, as well as potentially harmful emissions from battery production. Although few automotive batteries have been produced to date, work is under way to develop the best processes to recycle these batteries when they are no longer usable in vehicles. Secondary use of the batteries could delay return of material for recycling.

Approach

In our initial work, we developed cradle-to-gate energy consumption and air emissions for electric vehicle batteries with an LiMn_2O_4 cathode. These data were incorporated into Argonne's Greenhouse gases, Regulated Emissions, and Energy use in Transportation (GREET) model and released in GREET1_2014. We also estimated the maximum reasonable demand for battery materials, based on extremely aggressive scenarios for penetration of electric-drive vehicles. We combined vehicle demand growth with detailed battery designs and looked at how lithium demand might grow world-wide. We also estimated how much material could be recovered by recycling, thus reducing demand for virgin materials. We determined that cumulative world demand for lithium to 2050 would not strain known reserves. Although cobalt supplies, and possibly those of nickel, could be significant constraints by 2050,

the envisioned move away from chemistries containing these elements would obviate potential problems.

Now, life cycle analysis (LCA) of batteries with other cathode materials based on detailed process data is being used to further identify potential environmental roadblocks to battery production, and to compare energy savings and emissions reductions enabled by different types of recycling processes. The cathode materials that are the focus of current work are lithium cobalt oxide (LiCoO_2), lithium iron phosphate (LiFePO_4), nickel manganese cobalt ($\text{LiNi}_{0.4}\text{Co}_{0.2}\text{Mn}_{0.4}\text{O}_2$), and an advanced cathode that has been the subject of research at Argonne, $0.5\text{Li}_2\text{MnO}\cdot0.5\text{LiNi}_{0.44}\text{Co}_{0.25}\text{Mn}_{0.31}\text{O}_2$ (LMR-NMC). The anode paired with each of these cathode materials is typically graphite, although we have also developed an analysis for silicon.

Results

Battery Production: Roughly half of battery mass consists of materials (Cu, steel, plastics, Al) that have been extensively documented in previous analyses. Therefore, our focus was on the active battery materials that are not as well-characterized, and their fabrication into finished cells. Our earliest work emphasized production of the raw materials and their conversion to active materials. In order to understand the impact of our dependence on imported raw materials, we compared energy use and emissions from lithium carbonate production in Chile to domestic production in Nevada. Domestic production was determined to have somewhat greater impacts, but not enough to cause concern. Our focus then shifted to component manufacture and battery assembly, which must be repeated even if recycled materials are used. Previous work on Ni-MH batteries had suggested that these steps could be energy intensive.

Argonne's LCA of lithium-ion batteries is based upon a model of lithium-ion battery assembly that Nelson et al. (2011) developed. This peer-reviewed model provides an inventory of battery components and describes the equipment and steps involved in assembling these components into a battery at a manufacturing facility. The dry room was found to consume 1.3 MJ/kg battery or 60% of the total manufacturing energy, in the forms of electricity and natural gas. Total energy for the manufacturing stage of overall battery production from cradle-to-gate is estimated to be only 2.2 MJ/kg, compared to over 130 MJ/kg for the material production (all steps that precede manufacturing) for a battery with a LiMn_2O_4 cathode. Therefore, recycling has the potential to save a very large fraction of the total battery production energy. Earlier in 2014, a publication in *The Journal of Industrial Ecology* (Ellingsen et al., 2014) reported a much higher energy intensity of battery assembly that ranged from 100 MJ/kg to 400 MJ/kg. If battery

assembly were that energy intensive, the benefit of using battery components recovered from recycling would likely be minimal from an energy savings perspective. A close examination of this report revealed that the facility was operating at low throughput (up to 30% of capacity) and had several opportunities to improve energy efficiency. Energy intensity of assembly is strongly dependent upon throughput because the dry room, which is energy-intensive to operate, likely consumes a relatively even amount of energy regardless of throughput. A low throughput yields a high energy intensity. In a mature industry, we expect that a battery assembly facility would operate closer to capacity, reducing the energy intensity of battery assembly. In a publication (Dunn et al., 2014), we advocated for evaluation of lithium-ion batteries on a mature industry basis, rather than emerging industry basis, especially when comparing EVs with conventional vehicles that are produced with mature technology.

Based on our analysis, recycling does provide energy conservation benefits and reduces the local impacts of metal recovery and purification. Recycling is even more beneficial when cathode materials contain nickel or cobalt. Cathode materials with these metals have higher cradle-to-gate energy consumption and greenhouse gas (GHG) emissions than LiMn_2O_4 (30 MJ/kg LiMn_2O_4). The greater energy intensity of cobalt and nickel-containing cathode materials is evident when the cradle-to-gate energy consumption for different cathode materials are compared side-by-side as in Figure III - 11. In the case of LiCoO_2 , the recovery and purification of the metal dominates the overall energy consumption of producing this cathode material.

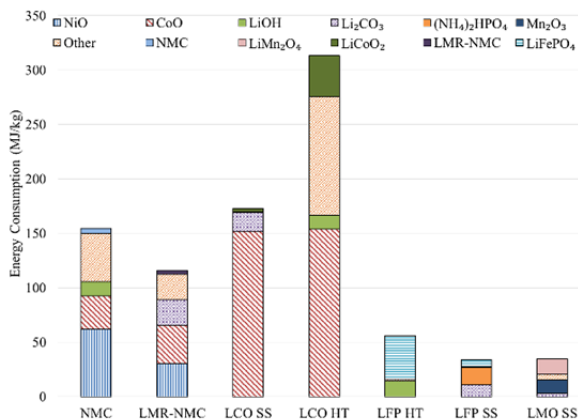


Figure III - 11: Cradle-to-gate energy consumption for different cathode materials (NMC= $\text{LiNi}_{0.4}\text{Co}_{0.2}\text{Mn}_{0.4}\text{O}_2$, LMR-NMC=0.5 $\text{Li}_2\text{MnO}_3\cdot0.5\text{LiNi}_{0.44}\text{Co}_{0.25}\text{Mn}_{0.31}\text{O}_2$, LCO= LiCoO_2 , LFP= LiFePO_4 , HT=hydrothermal preparation, SS=solid state)

Figure III - 12 compares cradle-to-gate energy of producing batteries with different cathode types. Batteries with cobalt- and nickel-containing cathode materials have the greatest energy consumption on a per mass of battery basis. On a per battery basis, the battery containing a LMR-NMC cathode and graphite anode has approximately the same cradle-to-gate energy consumption as a battery with an LMO cathode. LMR-NMC is about three times as energy intensive to produce as LMO but about 41% less of it is needed in the battery (when both batteries use graphite as the anode material) because its capacity is 250 mAh/g, 2.5 times greater than that of LMO.

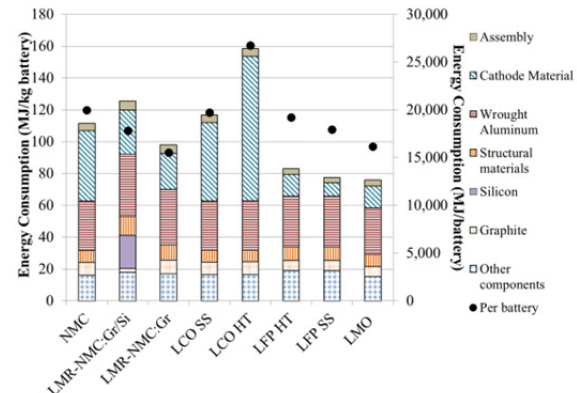


Figure III - 12: Cradle-to-gate energy consumption for batteries with different cathode materials (NMC= $\text{LiNi}_{0.4}\text{Co}_{0.2}\text{Mn}_{0.4}\text{O}_2$, LMR-NMC=0.5 $\text{Li}_2\text{MnO}_3\cdot0.5\text{LiNi}_{0.44}\text{Co}_{0.25}\text{Mn}_{0.31}\text{O}_2$, LCO= LiCoO_2 , LFP= LiFePO_4 , HT=hydrothermal preparation, SS=solid state)

Recycling Processes: Recycling can recover materials at different production stages, from elements to battery-grade materials. Figure III - 13 shows how some battery production processes can be avoided by the use of materials recovered by different recycling processes.

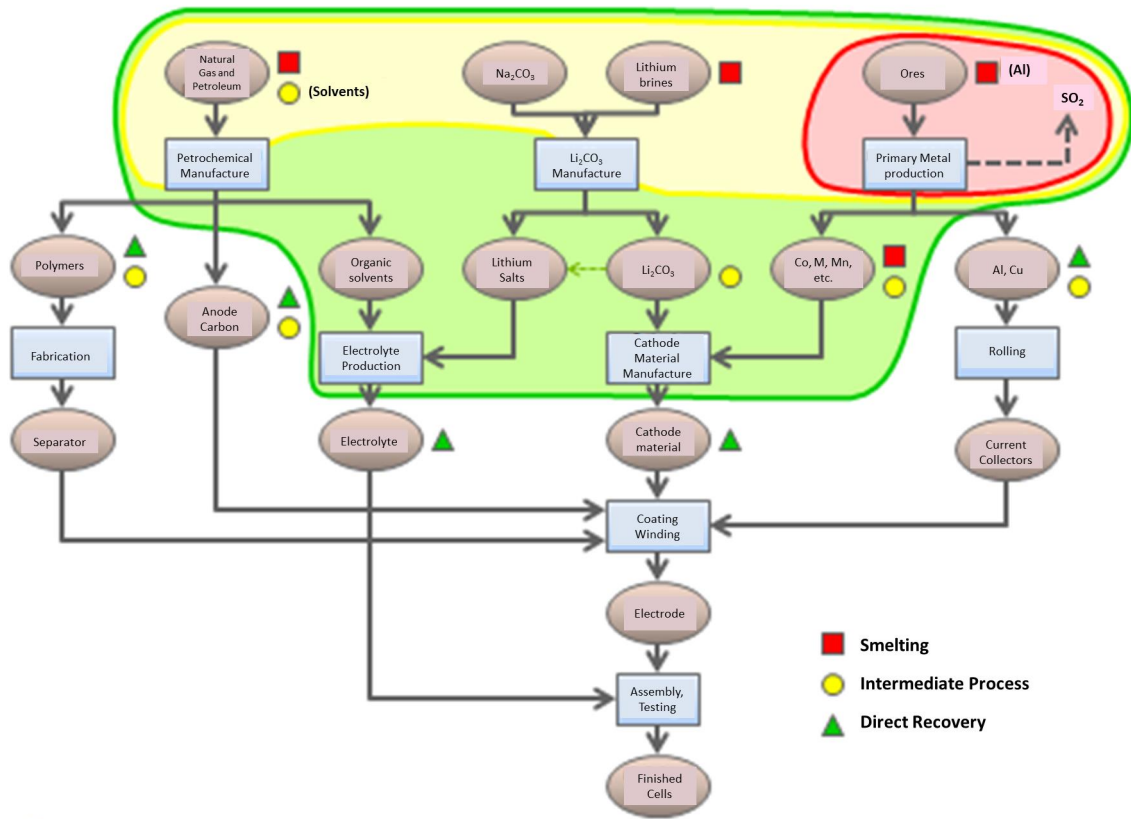


Figure III - 13: Schematic of Processes Avoided by Recycling

At one extreme are pyrometallurgical (smelting) processes that recover basic elements or salts. Smelting is operational now on a large scale in Europe, processing both Li-ion and Ni-MH batteries. At high temperature, all organics, including the electrolyte and carbon anodes, are burned as fuel or reductant. The valuable metals (Co and Ni) are recovered and sent to refining so that the product is suitable for any use. If these are not contained in the batteries, the economic driver for smelting disappears. The other materials, including Al and Li are contained in the slag, which is now used as an additive in concrete. The lithium could be recovered, if justified by price or regulations, but the impacts of Li recovery from slag could be greater than those from primary production. Smelting chemistry could be changed to keep the lithium out of the slag or make the slag easier to handle. Note that the rare-earths from Ni-MH smelting slag are now being recovered.

At the other extreme, direct recovery of battery-grade material by a physical process has been demonstrated. This process requires as uniform feed as possible, because impurities jeopardize product quality. The valuable active materials and metals can be recovered. It may be necessary to purify or reactivate some components to make them suitable for reuse in new batteries. If cathode material can be recovered, a high-value product can be produced, even if the

elemental value of the constituent elements is low. This is a big potential economic advantage for direct recycling (see Table III - 4). Only the separator is unlikely to be usable, because its form cannot be retained. This is a low-temperature process with a minimal energy requirement. Almost all of the original energy and processing required to produce battery-grade material from raw materials is saved. The quality of the recovered material must be demonstrated, and there must be a market for it in 10 or more years, when cathode materials may be different. Direct recovery, which is expected to be economical on a small scale, could be used for prompt scrap from battery production now without these concerns.

Table III - 4: Comparison of element values to cathode price

Cathode	Price of Constituents (\$/lb)	Price of Cathode (\$/lb)
LiCoO ₂	8.30	12–16
LiNi _{1/3} Co _{1/3} Mn _{1/3} O ₂	4.90	10–13
LiMnO ₂	1.70	4.50
LiFePO ₄	0.70	9

Intermediate or hydrometallurgical processes, such as the one funded by DOE under the Recovery Act

(Toxco, now Retriev Technologies), are between the two extremes. These do not require as uniform a feed as direct recovery, but recover materials further along the process chain than does smelting. If battery materials are treated hydrometallurgically, the Li is easy to get out, in comparison to pyrometallurgical processing, which traps it in the slag, making it very difficult and expensive to recover. Although the Li can be recovered (as the carbonate), the high value of the cathode material is not preserved.

Figure III - 14 compares estimated GHG emissions reductions from producing recycled cathode material by the pyrometallurgical process (Umicore), intermediate process (Toxco), and by direct recycling to the energy needed for virgin cathode production. It can be seen that direct recycling offers the greatest potential GHG savings. It is important to note, however, that the results in Figure III - 14 are based on engineering calculation estimates of the energy and material intensity of these recycling processes, which in some cases are at the bench scale and in all cases not yet widely used for automotive lithium-ion batteries. Figure III - 15 illustrates how, in the case of batteries with an LMO cathode, production energy for the entire battery can be minimized by the use of recycled metals as well as recycled cathode material.

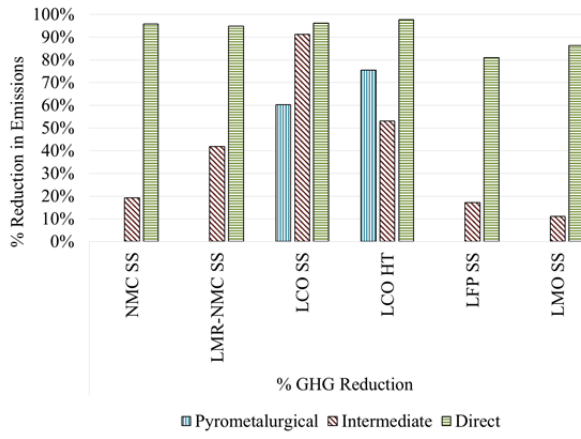


Figure III - 14: GHG emissions associated with producing cathode material

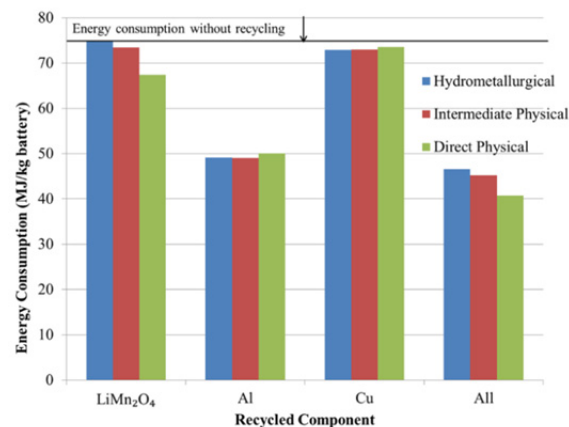


Figure III - 15: Energy required to produce battery

Sulfur Emission Reductions by Recycling:
Several of the metals used in batteries are smelted from sulfide ores, leading to significant emissions of SO_x. These constitute a significant fraction of the vehicle's life-cycle emissions (see Figure III - 16). Recycling produces no such emissions, and thus cathode materials made from recycled materials would have lower production emissions, as can be seen in Figure III - 17.

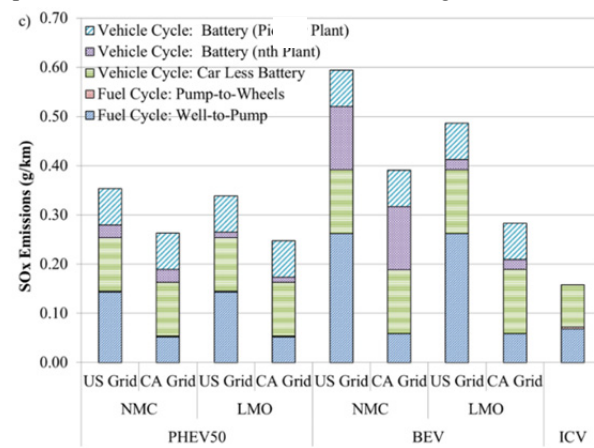


Figure III - 16: Batteries contribute a significant fraction of life-cycle sulfur emissions. Pioneer plant energy intensity based on Ellingsen et al. Nth plant assembly energy intensity based on Dunn et al. (2012) and reflects mature, high-throughput battery assembly facilities

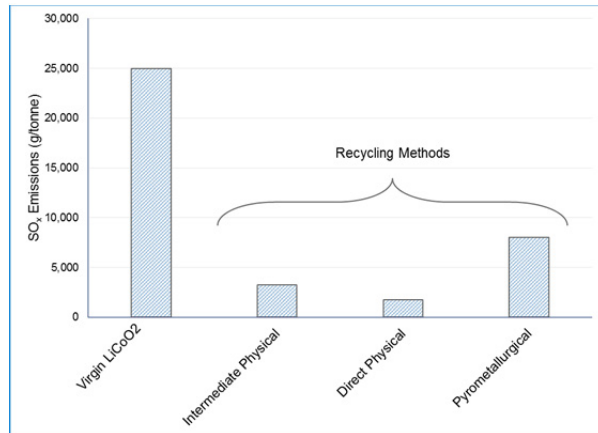


Figure III - 17: Cathodes made from recycled materials minimize sulfur emissions

Enablers of Recycling and Reuse: Material separation is often a stumbling block for recovery of high-value materials. Therefore, design for disassembly or recycling would be beneficial. Similarly, standardization of materials would reduce the need for separation. In the absence of material standardization, labeling of cells would enable recyclers to sort before recycling. Argonne staff contributed heavily to the draft labeling standards being proposed by SAE. They also participated in several U.S. and international working groups to help enable recycling. Standardization of cell design, at least in size and shape, would foster design of automated recycling equipment. Standardization would also be beneficial to reuse schemes, where cells from various sources would be tested and repackaged in compatible groups for use by utilities. It and proper labeling also help mitigate the emerging problem of Li-

ion batteries disrupting secondary lead smelter operation.

Relative Life-Cycle Energy Consumption and GHG of EVs Compared to ICEVs

Figure III - 18 compares life-cycle energy consumption on a per-km basis among BEV, PHEV50, and internal combustion engine vehicles (ICV) and breaks out the energy consumption in the fuel and vehicle cycles. The pioneer plant energy consumption for battery assembly is based on Ellingsen et al. (2014) while the *n*th plant energy consumption is based on Dunn et al. (2012). The latter is more reflective of a mature industry with assembly facilities operating at or near capacity. In all cases, even with the pioneer plant assembly energy intensity, EVs have lower life-cycle energy consumption than ICVs. The same is true for life-cycle GHG emissions. As Figure III - 19 shows, however, life-cycle SO_x emissions are higher in the case of EVs. The low sulfur content of gasoline is one reason why life-cycle SO_x emissions are lower for ICVs. Additionally, SO_x emissions from cathode material production contribute significantly to EV life-cycle SO_x emissions, but this impact can be reduced through integrating recycled materials into cathode material production (Figure III - 17). One key approach to reducing EV life-cycle GHG emissions is to use less carbon-intensive sources of electricity as Figure III - 19 illustrates. These results show that when EVs charge up with purely coal-derived electricity and have batteries that are produced in pioneer plants, their life-cycle GHG emissions are higher than those of ICVs. As the carbon intensity of the grid decreases, the relative GHG emissions are grow smaller compared to those of an ICV.

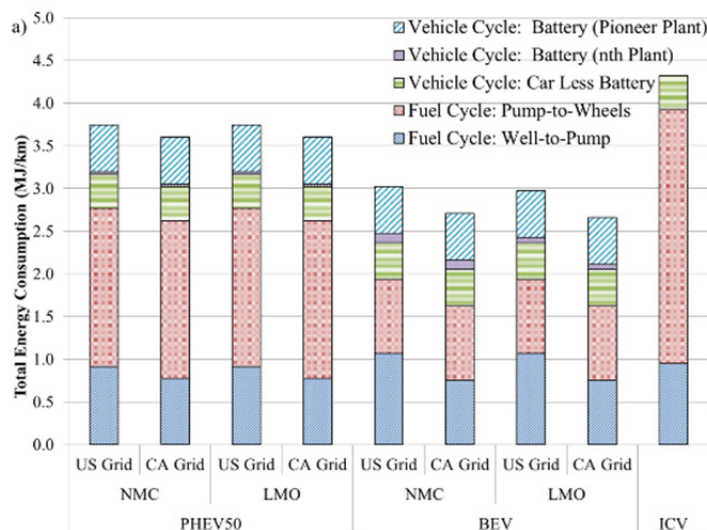


Figure III - 18: Fuel cycle and vehicle cycle total energy consumption for BEVs, PHEV50s, and ICVs. The PHEV50 (km) is modelled as being in charge-depleting (CD) and charge-sustaining (CS) modes during 47.5% and 52.5% of operation, respectfully. The PHEV50 is

assumed to have a fuel economy of 3.2 and 8.5 gasoline equivalent L/100 km in CD and CS modes, respectively. The BEV is assumed to have a fuel economy of 2.9 gasoline equivalent L/100 km mpg while the ICV operates at 23 mpg. The liquid fuel used by the ICV and the PHEV30 during CS mode is conventional gasoline, 4% of which derives from oil sands recovered via in-situ production

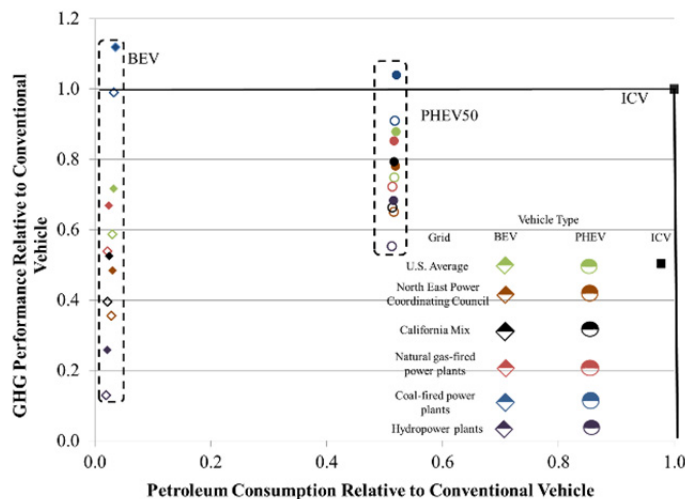


Figure III - 19: Relative performance of BEV (NMC cathode) and PHEV50 (LMO cathode) as compared to ICV. Green, orange, black, red, blue, and purple points represent results for vehicles powered with the average U.S. grid, North East Power Coordinating Council regional grid, the California grid, exclusively natural gas-fired power plants, exclusively coal-fired power plants, and hydropower plants, respectively. Hollow and full points represent results generated with the at capacity and low-throughput battery assembly energies, respectively

FY2014 Presentations and Publications

Presentations

- Impacts of Plug-In Hybrid Electric Vehicle Charging Choices in 2030. IEA Task 19 Workshop (October 15–16, 2014).
- Enabling Future Li-Ion Battery Recycling*, European Lead Battery Conference, (September 10–12, 2014).
- Life Cycle Analysis of Vehicle and Fuel Systems with the GREET Model, Chemie Paris Tech (May 7, 2014).
- The Future of Automobile Battery Recycling*, NAS Committee on Overcoming Barriers to Electric Vehicle Deployment (February 25, 2014).
- A Step-by-Step Examination of Electric Vehicle Life Cycle Analysis, LCA XIII (October 1–3, 2013).
- Can Automotive Battery Recycling Help Meet Critical Material Demand?*, IEA HEV Task 19 Workshop, (October 9–10, 2013) (during shutdown—script written for surrogate presenter).
- A Look Through the Crystal Ball at the Future of Automobile Battery Recycling, International Battery Seminar, (March 10–13, 2014).
- Recycling of Lithium-Ion Batteries*, Plug-In 2013 (Sept. 30–October 2, 2013).

Papers, Book Chapter, and Reports

- Dunn, J.B., Gaines, L., Kelly, J. C., James, C., Gallagher, K.G. (2015) “The significance of Li-ion batteries in electric vehicle life-cycle energy and emissions and recycling’s role in its reduction.” *Energy and Environmental Science*, doi: 10.1039/C4EE03029J.
- Dunn, J.B., James C., Gaines, L., Gallagher, K. “Material and Energy Flows in the Production of Cathode and Anode Materials for Lithium-Ion Batteries.” Argonne National Laboratory Technical Report ANL/ESD-14/10.
- Gaines, L. (2014), The Future Of Automotive Lithium-Ion Battery Recycling: Charting A Sustainable Course, *Sustainable Materials and Technologies* <http://dx.doi.org/10.1016/j.susmat.2014.10.001>
- Lithium-Ion Battery Environmental Impacts*, in *Lithium-Ion Batteries: Advances and Applications*, Elsevier (2014) (book chapter).
- Life Cycle Assessment of Electric Vehicles – Key Issues of Task 19 of the International Energy Agency (IEA) on Hybrid and Electric Vehicles (HEV), G. Jungmeier, J.B. Dunn, A. Elgowainy, L. Gaines, S. Ehrenberger, E.D. Özdemir, H.J. Althaus, R. Widmer, Transport Research Arena 2014, Paris (paper).

References

1. Dunn, J.B., Gaines, L., Sullivan, J., Wang, M. (2012). "Impact of recycling on cradle-to-gate energy consumption and greenhouse gas emissions of automotive lithium-ion batteries." *Environmental Science and Technology*, 46: 12704-12710.
2. Dunn, J.B., Gaines, L., Kelly, J.C., James, C., Gallagher, K.G. (2015) "The significance of Li-ion batteries in electric vehicle life-cycle energy and emissions and recycling's role in its reduction."
3. Ellingsen, L.A., Majeau-Bettez, G., Singh, B., Srivastava, A.K., Valøen, L.O., Strømman, A.H. (2014) "Life Cycle Assessment of a Lithium-Ion Battery Vehicle Pack." *Journal of Industrial Ecology*, 18:113-12.
4. Nelson, P., Gallagher, K., & Bloom, I. (2011). Modeling the performance and cost of lithium-ion batteries for electric-drive vehicles. Argonne National Laboratory.

III.B Battery Testing Activities

III.B.1 Battery Performance and Life Testing (ANL)

Ira Bloom (Primary Contact)

John Basco, Panos Prezas,
David Robertson, Lee Walker
Argonne National Laboratory
9700 South Cass Avenue
Argonne, IL 60439
Phone: (630) 252-4516; Fax: (630) 252-4176
E-mail: ira.bloom@anl.gov

Start Date: September 1976

Projected End Date: Open

Objectives

- Provide DOE, USABC, and battery developers with reliable, independent and unbiased performance evaluations of cells, modules and battery packs.
- Benchmark battery technologies which were not developed with DOE/USABC funding to ascertain their level of maturity.

Technical Barriers

This project addresses the following technical barriers as described in the USABC goals [1, 2, and 3]:

- (A) Performance at ambient and sub-ambient temperatures.
(B) Calendar and cycle life

Technical Targets

PHEV Technical Targets

- 15-y calendar life.
- 5,000 CD cycles.

Other technical targets exist for EV, HEV, PHEV and LEESS applications

Accomplishments

Tested battery deliverables from many developers (see Table III - 5):

- Determine the effect of the Fast-Charge Test, which is in the USABC EV Test Manual [3], on battery performance.
- Compare EV battery test protocols used in the U.S. and in China (Argonne lead; in progress).

Table III - 5: Summary List of Tested Batteries

Developer	Application	Status
Johnson Controls, Inc.	PHEV20 PHEV20 PHEV20 PHEV20 PHEV20 HEV	On-going Complete On-going On-going On-going On-going
SKI	EV	complete
Actacell	LEESS	complete
DowKokam	EV	
Optodot	EV	On-going
Sakti3	EV	Complete
3M	EV Based on EV+PHEV	On-going On-going
Seeo	EV-cell EV-module	On-going On-going
Tiax	Based on EV+PHEV	On-going
Leyden Energy	12V Start/Stop	On-going
Navitas	EV	On-going



Introduction

Batteries are evaluated using standard tests and protocols which are transparent to technology. Two protocol sets are used: one that was developed by the USABC [1, 2], and another which provides a rapid screening of the technology. The discussion below focuses on results obtained using the standard protocols.

Approach

The batteries are evaluated using standardized and unbiased protocols, allowing a direct comparison of performance within a technology and across technologies. For those tested using the USABC methods, the performance of small cells can be compared to that of larger cells and full-sized pack by means of a battery scaling factor [1, 2].

Results

With further vehicle electrification, consumers would want battery charging to take about the same amount of time as refueling an internal-combustion-engine-powered vehicle currently does at a service station. This “fueling” does not have to be a full charge, but can be a partial charge. The Fast-Charge Test, in the USABC EV Manual [3], was designed to measure the impact of charging a battery from 40 to 80% SOC at successively faster rates, starting from about twice the overnight rate. Since the manual was written for nickel-metal hydride technology, this test may have to be adjusted for the higher-performing, lithium-ion cells.

ANL determined the effect of this test on performance using two commercially-available, lithium-

ion cell chemistries, A and B, in the form of 18650-sized cells. There were two levels of charging, 0 to 100% SOC and between 40 and 80% SOC. Both levels of charging used the manufacturer’s rate (~1C rate), and 2-, 4-, and 6-C rates. After every 100 cycles, the cells were recharacterized in terms of C/1 capacity and resistance from the Peak PowerTest [3]. The experiment is complete using cell chemistry A, but is still in progress using chemistry B; therefore, only the results from chemistry A will be reported here.

In cell chemistry A, the effect of charging between 0 and 100% SOC on cell capacity is shown in Figure III - 20. The rate of capacity fade depended on charge rate, but there was not a simple, linear relationship between the two.

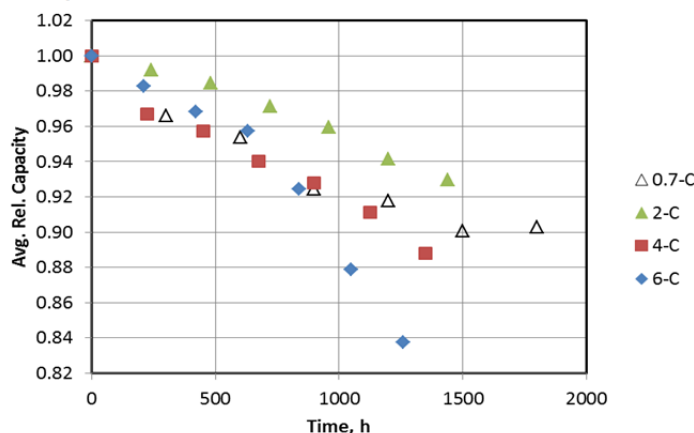


Figure III - 20: Average, relative capacity of cell chemistry A with time and charge rate. The cells were charged from 0 to 100% SOC at the rates given in the legend

The effect of charge rate on cell resistance using 100% charge returned was also non-linear. As shown in Figure III - 21, the rate of resistance rise depended on

charge rate and the rate of resistance rise also accelerated with time.

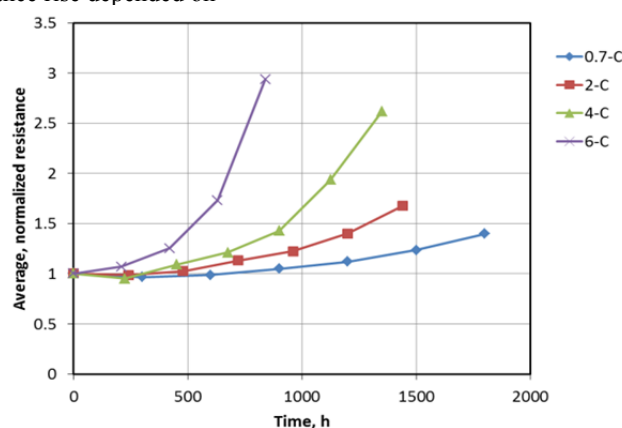


Figure III - 21: Average, normalized resistance vs. time and charge rate. The cells were charged from 0 to 100% SOC at the rates given in the legend

The effect of decreasing the amount of charge returned, 40 to 80% SOC, on cell resistance is shown in Figure III - 22. The same trends shown in

Figure III - 21 were also seen, but on a shorter time scale. For example, in the 6-C data, the relative cell resistance approached 3 in about 700 h in Figure III -

21, but, in Figure III - 22, this occurred around 500 h. With less charge returned, the overall cycle time was shorter than with 100% SOC returned. The shorter cycle

did not allow the cell to cool as much. Thus, the higher cell temperature, most likely, caused cell resistance to increase faster.

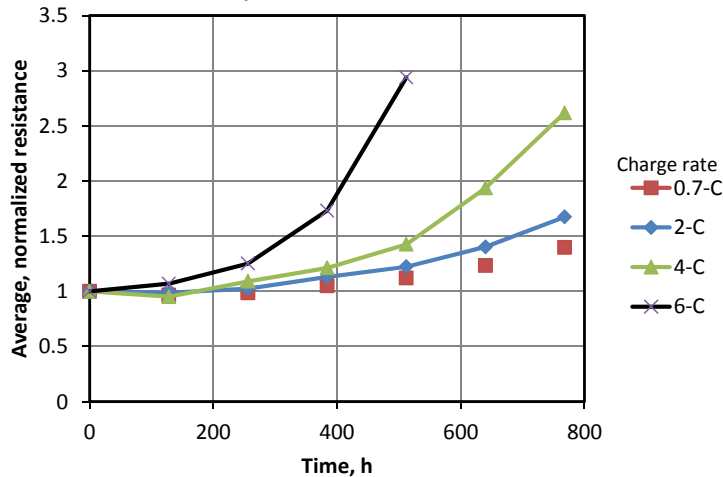


Figure III - 22: Average, normalized resistance vs. time and charge rate. The cells were charged from 40 to 80% SOC at the rates given in the legend

Conclusions and Future Directions

Testing has been shown to be a useful way to gauge the state of a developer's technology and to estimate the life of a battery.

For the future, we plan to:

- Continue testing HEV contract deliverables.
- Continue testing PHEV contract deliverables.
- Continue testing EV contract deliverables.
- Begin testing LEESS contract deliverables.
- Continue acquiring and benchmarking batteries from non-DOE sources.
- Aid in refining standardized test protocols.
- Upgrade and expand test capabilities to handle increase in deliverables.
- Complete the fast-charge experiment.
- Explore other possibilities for test protocol comparison and, perhaps, standardization with Europe, Japan and China.

List of Abbreviations

- HEV: hybrid electric vehicle
- PHEV: plug-in hybrid electric vehicle
- EV: electric vehicle
- LEESS: Low-Energy Energy Storage System
- USABC: United States Advanced Battery Consortium (DOE, GM, Chrysler and Ford)
- SOC: state of charge
- ANL: Argonne National Laboratory
- RPT: reference performance test

DST: dynamic stress test, see reference 3.

FY 2014 Publications/Presentations

1. 2014 AMR Presentation.
2. *Battery Testing for EV Applications: A Comparison between US- and China-Based Protocols*, J. P. Christoperson, T. Bennett, D. Robertson, and I. Bloom, Advanced Automotive Battery Conference, Feb 3-7, 2014, Atlanta GA.
3. *A Comparison of US and Chinese EV Battery Testing Protocols and Results*, I. Bloom, D. Robertson, J. Christoperson, T. Bennett, F. Wang and S. Liu, 8th US-China EV and Battery Technology Workshop, August 18-19, 2014, Seattle, WA.
4. *Effects of Fast Charging Lithium-Ion Cells*, P. Prezas, J. K. Basco, L. Somerville, T. Duong, and I. Bloom, IEA IA-HEV Meeting, September 22-23, 2014, Nice, France

References

1. FreedomCAR Battery Test Manual for Power-Assist Hybrid Electric Vehicles, DOE/ID-11069, October 2003.
2. FreedomCAR Battery Test Manual for Plug-In Hybrid Electric Vehicles, June 2010.
3. Electric Vehicle Battery Test Procedures Manual, Revision 2, January 1996.

III.B.2 Battery Performance and Life Testing (INL)

Jon P. Christophersen, PhD (PI)

Idaho National Laboratory

P.O. Box 1625

Idaho Falls, ID 83415

Phone: (208) 526-4280; Fax: (208) 526-3150

E-mail: jon.christophersen@inl.gov

Christopher J. Michelbacher

Matthew G. Shirk

Sergiy V. Sazhin

INL Contract Number: DE-AC07-05ID14517

Start Date: September 1983

Projected End Date: Open Contract

Objectives

- Provide high fidelity science-based performance and life testing, analysis, modeling, reporting, and other support related to electrochemical energy storage devices under development by the Department of Energy's Vehicle Technologies Program.
- Develop test methodologies and analysis procedures for various alternative vehicle applications in conjunction with the U.S. Advanced Battery Consortium (USABC).

Technical Barriers

The successful adoption of cost-effective, safe, reliable and environmentally sustainable alternative vehicles remains a challenge. Performance and life testing of energy storage devices (e.g., batteries) in a controlled, laboratory environment is a critical component of DOE's mission to support the development of electric drive vehicle and component technology. Battery testing at the Idaho National Laboratory (INL) addresses all of the primary technical barriers: performance, life, cost, abuse tolerance and reliability. Accumulated test data are useful to gauge battery capability relative to the established USABC targets as a function of aging as well as for developing battery life and cell-to-cell error models for advanced life and health prognostic tools. Performance and life testing are also useful for battery manufacturers as they develop lower-cost systems that can still meet the established targets. Finally, fresh and aged test articles

are useful for abuse testing and thermal analysis in collaboration with other national laboratory efforts.

Technical Targets

- Battery performance and life testing in FY-14 at INL primarily focused on USABC technical targets for Plug-in Hybrid Electric Vehicles (PHEV), Electric Vehicles (EV), Low-Energy Energy Storage Systems (LEESS), 12 V Start/Stop (12V S/S), and power-assist Hybrid Electric Vehicles (HEVs).
- Technical targets for each of these automotive applications are available in the published manuals located on the USABC website (uscar.org/guest/article_view.php?articles_id=86).

Accomplishments

- Performance and life testing for USABC Programs:
 - 294 cells.
 - 6 modules.
 - 3 packs.
- Performance and life testing for Benchmark Programs:
 - 101 cells.
 - 14 modules.
- Performance and life testing for FOA-2011 Programs:
 - 82 cells.
- Performance and life testing for FOA-ARRA (American Recovery and Reinvestment Act) Programs:
 - 10 cells.
 - 3 modules.
- Performance and life testing for Applied Battery Research Programs:
 - 48 cells.
- Published Revision 3 of the Plug-In Hybrid Electric Vehicle Manual (September 2014).
- Published Revision 0 of the 12V Start/Stop Vehicle Manual (November 2013).



Introduction

Advancing alternative transportation is a top priority within the Department of Energy (DOE) given its potential to reduce U.S. dependency on oil. The INL

Battery Testing Center is a world leader in science-based performance testing and assessment of advanced electrochemical energy storage technologies, primarily for automotive applications. It has been designated by DOE as a core capability and the lead test facility for USABC activities. The development of batteries and other energy storage devices requires validation testing from an independent source to accurately characterize the performance and life capability against the established USABC technical targets for HEVs, PHEVs, EVs, and other electric drive system applications.

Approach

High quality testing, validation, and analysis of electrochemical energy storage systems are critical for the successful adoption of alternative vehicles. The INL Battery Testing Center (BTC) has over 20,000 square feet of laboratory space and is equipped with over 700 test channels for advanced energy storage testing at the cell-level (e.g., up to 7V, 300A), module-level (e.g., up to 65V, 250A), and pack-level (e.g., 500-1000V, 500A). The test equipment can be programmed to perform any test profile while simultaneously monitoring constraints such as voltage, current and temperature limits. Batteries and other energy storage devices are typically subjected to a test sequence while housed inside thermal chambers to ensure consistent and repeatable results. All of the temperature chambers cover a broad range (e.g., -70 to 200°C) for enhanced testing and modeling capability.

Successful performance testing and accurate life modeling are highly dependent on the accuracy of the acquired test data. The INL BTC has developed advanced calibration verification and uncertainty analysis methodologies to ensure that the voltage, current, and temperature measurements are within the tolerance specified by the manufacturer (e.g., 0.02% of the full scale). These measured test parameters are subsequently used in various mathematical combinations to determine performance capability (e.g., resistance, energy, power, etc.). INL has also quantified the error associated with these derived parameters using the accuracy and precision of the relevant measured parameter (e.g., voltage) to ensure high-quality and repeatable results.

The INL BTC capability has also been enhanced with additional equipment for advanced characterization of battery technologies. For example, a Ling Dynamic Systems V8-640 SPA56k shaker table (installed in FY13) is being considered within select USABC Programs for non-destructive reliability and system robustness testing. Unconventional and untested cell designs are the key drivers behind the interest in using a vibration system to perform mild abuse testing at INL. Options for safety shielding and/or installation of a

thermal chamber on the shaker table for controlled vibration testing are presently under investigation.

Results

INL Testing Activities: The INL BTC continues to test articles of various sizes and configurations using standardized test protocols. Table III - 6 and Table III - 7 summarize the testing activities under the USABC and Benchmarking Programs, respectively, for FY-14. The purpose of the USABC testing activities is to evaluate a candidate technology against the specified targets (EV, PHEV, etc.) and, where applicable, previous generations of test articles from the same manufacturer. The purpose of the Benchmark Program is to evaluate devices that do not have existing contracts in place, but have technologies that are of interest to DOE and/or USABC. In some cases, a Benchmark Program is also used to validate newly developed test procedures and analysis methodologies (e.g., the modified HPPC test for the new PHEV Manual revision, see below).

Table III - 6: Testing activities under the USABC Program

Manufacturer	Type	# of Articles	Application
LG/CPI	Cells	20	HEV
	Cells	43	PHEV
	Packs	2	PHEV
Envia	Cells	37	EV
K2	Cells	40	EV
Saft	Cells	12	HEV
	Cells	32	12V S/S
Quallion	Modules	6	EV
Maxwell	Cells	30	LEESS
	Pack	1	LEESS
Entek	Cells	40	PHEV
Leyden	Cells	20	EV
Farasis	Cells	20	EV

Table III - 7: Testing activities under the Benchmark Program

Manufacturer	Type	# of Articles	Application
Lishen	Cells	10	EV
Axion	Modules	12	HEV
Hydroquebec	Cells	16	HEV
Smart Battery	Modules	2	12V S/S
Sanyo	Cells	45	PHEV
EIG	Cells	30	12V S/S

Table III - 8 and Table III - 9 summarize the INL testing activities under the FOA-2011 and FOA-ARRA Programs, respectively, for FY-14. The FOA-2011 (i.e., 2011 Advanced Cells and Design Technology For Electric Drive Batteries awards) focuses on developing high performance cells for electric drive vehicles that significantly exceed existing technology, in regards to both cost and performance. Technologies addressed include EV, PHEV, and HEV applications; the INL focus in FY-14 was on PHEV cells (a total of 82 cells with advance materials were evaluated). The FOA-ARRA (i.e., 2009 Electric Drive Vehicle Battery and Component Manufacturing Initiative) focuses on battery and battery material manufacturing plants and equipment for advanced vehicle batteries. All deliverables under FOA-ARRA have completed the scheduled testing at INL and final reports are being provided to the relevant parties.

Table III - 8: Testing activities under the FOA-2011 Program

Manufacturer	Type	# of Articles	Application
Miltec ANL	Cells	18	PHEV
Nanosys	Cells	16	PHEV
PSU	Cells	16	PHEV
Applied Materials	Cells	16	PHEV
Ampruis	Cells	16	PHEV

Table III - 9: Testing activities under the FOA-ARRA Program

Manufacturer	Type	# of Articles	Application
EnerG2	Ultracap	5	Ucap
Enerdel	Cells	5	PHEV
Exide Bristol	Modules	3	Idle/Stop Start/Lighting Ignition

The INL BTC tested a total of 561 devices in FY-14, including 535 cells, 23 modules, and 3 packs. Table III - 10 summarizes the anticipated INL testing activities for FY-15, including cells from the Applied Battery Research (ABR) Program, see below. USABC and Benchmark Program testing on existing deliverables are expected to continue and new USABC deliverables will be added as well, including Envia EV, Ampruis EV, and possibly others. For the FOA-2011 Program, INL expects to test three generations of deliverables from each awardee. Typical reference performance tests include static capacity tests and cycle life testing, along with high and low temperature capacity testing. Some deliverables will be pulse tested, while others will not, depending on the maturity of the technology.

Table III - 10: Anticipated testing activities for FY15

Program	Type	Manufacturer
USABC	Cells	LG/CPI, Maxwell, Envia, K2, Leyden, Entek, Farasis, Saft, Ampruis
	Packs	LG/CPI
Benchmark	Cells	Hydroquebec, Sanyo, EIG, Toshiba
	Modules	Axion
ABR	Cells	ANL, Envia, Farasis, PSU
FOA-2011	Cells	Miltec ANL, Ampruis, Applied Materials, Nanosys, PSU

Applied Battery Research Program: The purpose of ABR is to assess core performance, cycle life and accelerated calendar life of advanced lithium-ion cell chemistries. Table III - 11 summarizes the INL ABR testing activities in FY-14. Testing is underway on the baseline cell chemistries with final deliverables scheduled to be shipped to INL in early FY-16. The testing will benchmark the performance capability of the cells relative to the established PHEV-40 or EV targets. A total of 12 cells will be subjected to life testing, with 3 cells undergoing cycle-life aging at 30°C and nine cells undergoing calendar-life aging (3 each at 30, 40, and 50°C). All cells are initially characterized with constant current discharges at the C₁/1, C₁/2 and C₁/3 rates, an HPPC test, a 48-hr stand test, and impedance spectroscopy measurements. During life testing, the cells are also periodically interrupted for reference performance tests at 30°C to track degradation rates compared to the targets.

Table III - 11: Testing activities under the ABR Program

Manufacturer	Type	# of Articles	Application
Envia	Cells	12	PHEV
Farasis	Cells	12	EV
PSU	Cells	12	EV
ANL	Cells	12	EV

PHEV Testing and Analysis: Revision 3 of the PHEV Manual was published in FY-14 (INL/EXT-14-32849). The manual was reviewed thoroughly for clarity and consistency with the intent of using it as the standard for future manual development or edits. Significant modifications include an updated glossary and a new appendix that defines how to fill in a USABC Gap Analysis chart. The PHEV-10 condition was eliminated and a new xEV-50 Mile Application was added to the targets. A survival temperature test was added to the manual to assess the capability of the energy storage device to withstand extreme hot and/or cold temperatures for extended periods of time (e.g.,

while the battery is being shipped across the ocean). The HPPC test was also modified to ensure more consistency with actual vehicle operations.

For the modified HPPC test, the first step was to better define of the required voltages. Figure III - 23 shows the various voltage limits based on the new approach. The electrochemical range of the energy storage device is between $V_{max_{100}}$ and V_{min_0} and this is used to establish the rated (nominal) capacity. However, the electrochemical range is not typical of the operational range, so the maximum and minimum operating voltage limits are also defined as $V_{max_{op}}$ and

$V_{min_{op}}$. Other than static capacity tests, all testing will now begin at $V_{max_{op}}$. The minimum operating voltage, $V_{min_{op}}$, is a variable term that is based on the appropriate amount of energy removed during a Charge Depleting cycle and typically has a minimum value specified by the manufacturer that is greater than V_{min_0} . Voltage limits are also defined for pulses that are less than or equal to 10 seconds, (i.e., $V_{max_{pulse}}$ and $V_{min_{pulse}}$). Finally, a minimum pulse voltage limit for test temperatures less than or equal to 0°C is defined as $V_{min_{LowT}}$.

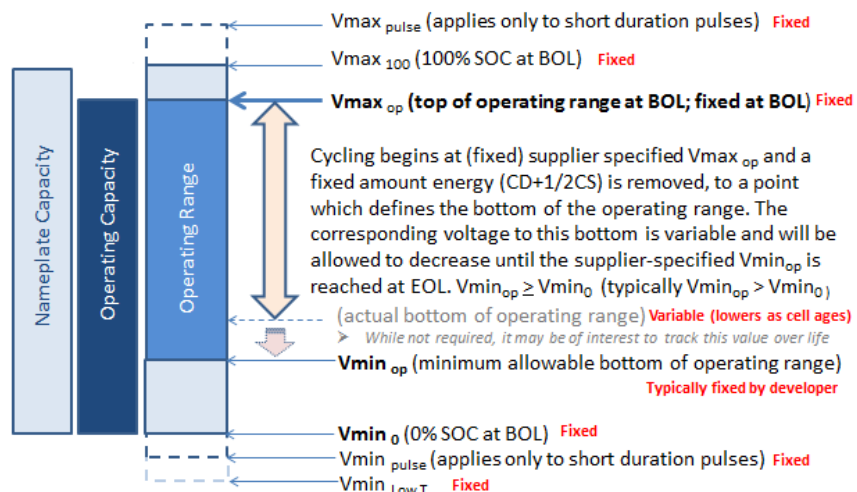


Figure III - 23: PHEV Voltage Definitions and Key Concepts

Previous HPPC tests required a full charge to $V_{max_{100}}$ followed by a 1-hour rest at an open-circuit voltage (OCV) condition and a discharge step that removed 10% depth of discharge (DOD). After another 1-hour rest at OCV, the pulse profile shown in Figure III - 24 is conducted using specified currents. This process was repeated at each 10% DOD increment until the test article reached full discharge (i.e., V_{min_0}). In the new approach, the test article is only charged up to the maximum operating voltage ($V_{max_{op}}$). Consequently, after a 1-hour rest at OCV, the HPPC pulse is conducted prior to the initial 10% drop in rated capacity. The new test sequence is shown in Figure III - 25, including the initial constant power discharge at the 10-kW rate.

The 10% drops between HPPC pulses are based on the rated capacity. For example, a cell with a rated capacity of 1 Ah between $V_{max_{100}}$ and V_{min_0} will result in a removal of 0.1 Ah between HPPC pulses. One disadvantage of starting at $V_{max_{op}}$ instead of $V_{max_{100}}$ is

that the true DOD condition of the test article is not known. However, the HPPC analysis is based on pulse power capability as a function of the cumulative energy removed, so knowledge of the actual DOD prior to each HPPC pulse is not strictly necessary. Note also that the discharge and regen pulse power capabilities are now relative to the pulse voltage limits, $V_{max_{pulse}}$, $V_{min_{pulse}}$, in this version of the manual (previous versions used $V_{max_{100}}$ and V_{min_0} instead).

An advantage of this new approach is that the cumulative energy removed is directly measured to determine the useable energy for the Charge Depleting and Charge Sustaining modes. In the previous version, an initial 10% DOD discharge was required prior to the initial pulse and the cumulative energy removed needed to be corrected for this initial discharge. Since this initial 10% DOD swing was based on the rated capacity, the level of correction also increased with aging. In the new approach, the initial discharge is always zero.

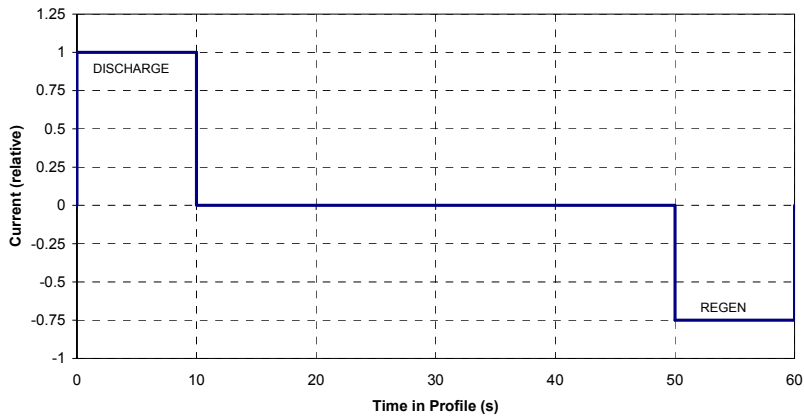


Figure III - 24: HPPC Test Profile

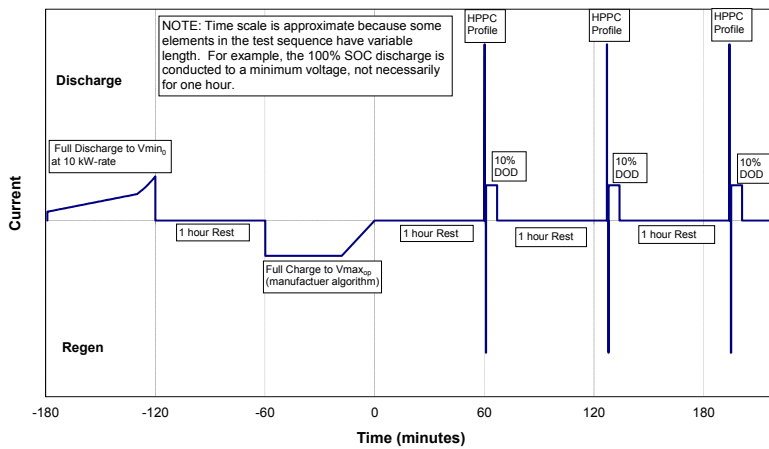


Figure III - 25: HPPC Test Sequence

Conclusions and Future Directions

Battery performance and life testing is critical for the successful adoption and implementation of advanced alternative vehicles. The INL provides a DOE core capability that is well equipped to conduct accelerated aging protocols on battery technologies of various sizes and shapes while ensuring high quality, repeatable results as an independent source of science-based performance assessment for DOE, the automotive industry, and the battery manufacturers. In FY-15, INL plans to continue accelerated aging protocols for existing and new devices designated for the USABC, Benchmarking, ABR, FOA-2011, and FOA-ARRA Programs. In addition to testing and life modeling, INL will also continue developing and refining standard test protocols and analysis procedures in collaboration with USABC.

FY 2014 Publications/Presentations

1. *Battery Test Manual for Plug-In Hybrid Electric Vehicles*, Revision 3, INL/EXT-14-32849, September 2014.
2. *Battery Test Manual for 12 Volt Start/Stop Vehicles*, Revision 0, INL/EXT-12-26503, November 2013.

III.B.3 Battery Abuse Testing (SNL)

Christopher J. Orendorff, Joshua Lamb, and Leigh Anna M. Steele
Sandia National Laboratories
P. O. Box 5800, Mail Stop 0614
Albuquerque, NM 87185-0614
Phone: (505) 844-5879; Fax: (505) 844-6972
E-mail: corendo@sandia.gov

Collaborators:
USABC Contractors/TAC
Ahmad Pesaran, NREL
Jon Christophersen, INL
Ira Bloom, ANL

Start Date: October 2013
Projected End Date: September 2014

Objectives

- Serve as an independent abuse test laboratory for DOE and USABC.
- Abuse testing in accordance with the USABC abuse testing manual.
- Successful testing of all deliverables from developers under USABC contracts.
- Test the propensity towards propagation of cell failure through multiple cell batteries.
- Provide mechanical testing support to develop and validate mechanical models for EV batteries.
- Evaluate the effect of cell age on abuse response

Technical Barriers

- Abuse tolerance of energy storage devices is identified as a barrier in USABC and DOE battery development programs.
- The failure modes for lithium-ion batteries are complex and need to be evaluated for all types of chemistry, design, packaging and systems for PHEV/EV applications.
- Lack of understanding of how single cell or cell group failures propagate and what the primary drivers are for different battery designs.
- Limited knowledge on how cell level abuse tolerance changes over the age of a cell or battery.

Technical Targets

- Perform abuse testing and evaluation of cells and modules delivered from contractors to USABC.
- Perform failure propagation testing and evaluation.
- Static mechanical testing of cells and batteries.
- Identify a cell age target for characterization and analysis > 20% fade.
- Report results to DOE, the USABC TAC, and contractors to USABC.

Accomplishments

- Successful testing of cell and module deliverables through USABC contracts including
 - Entek.
 - Farasis.
 - LG Chem.
 - Maxwell.
 - JCI.
 - Leyden Energy (Start/Stop).
 - Saft (Start/Stop).
- Performed multi-cell pack propagation testing with varying electrical configurations and worked with NREL to model this response
- Age cells to >40% fade for characterization and analysis



Introduction

Abuse tests are designed to determine the safe operating limits of HEV/PHEV/EV energy storage devices. The tests are performed to yield quantitative data on cell/module/pack response to allow determination of failure modes and help guide developers toward improved materials and designs. Standard abuse tests are performed on all devices to allow comparison of different cell chemistries and designs. New tests and protocols are developed and evaluated to more closely simulate real-world failure conditions.

In scaling from the cell to the battery level, it is important that understanding safety performance includes a detailed understanding of cell interactions. Single point failures from a single cell or group of cells can be initiated by a number of triggers including an internal short circuit, misuse or abuse, or a component failure at the battery or system level. Propagation of that

single failure event (regardless of the initiation trigger) through an entire battery, system or vehicle is an unacceptable outcome. Our work focuses on evaluating the propagation of a single cell thermal runaway event through a battery using a variety of design considerations.

While robust mechanical models for vehicles and vehicle components exists, there is a gap for mechanical modeling of EV batteries. The challenge with developing a mechanical model for a battery is the heterogeneous nature of the materials and components (polymers, metals, metal oxides, liquids). Our work will provide some empirical data on the mechanical behavior of batteries under compressive load to understand how a battery may behave in a vehicle crash scenario. This work is performed in collaboration with the U.S. Council for Automotive Research (USCAR).

Many development efforts directed toward improving safety performance are designed and evaluated using fresh cells. However, it is important to understand how reliable a materials or design improvement will be over time or if there is a “tipping point” somewhere along the age of a battery. Our work is directed toward understanding the effects of cell age on the safety performance, thermal stability and abuse tolerance.

Approach

Abuse tolerance tests are performed which evaluate the response to expected abuse conditions.

- Test to failure of energy storage device.
- Document conditions that cause failure.
- Evaluate failure modes and abuse conditions using destructive physical analysis (DPA).
- Provide quantitative measurements of cell/module response.
- Document improvements in abuse tolerance.
- Develop new abuse test procedures that more accurately determine cell performance under most likely abuse conditions.

Possible tests that can be performed cover three main categories of abuse conditions:

- Mechanical Abuse - Controlled crush, penetration, blunt rod, drop, water immersion, mechanical shock and vibration.
- Thermal Abuse - Thermal stability, simulated fuel fire, elevated temperature storage, rapid charge/discharge, thermal shock cycling.
- Electrical Abuse - Overcharge/overvoltage, short circuit, overdischarge/voltage reversal, partial short circuit.

Batteries for failure propagation evaluation are based on 3 Ah LiCoO₂ pouch cells in either a 5-cell

series (5S1P) or 5-cell parallel (1S5P) configuration. Cell failure and thermal runaway are initiated by a mechanical nail penetration into a single cell. Batteries for mechanical testing are based on 5Ah LiCoO₂ pouch cells in a 12-cell parallel (1S12P) configuration.

Results

Battery Abuse Testing. The actual USABC testing results are Protected Information and are prohibited from public release. However, representative data is shown below for an overcharge abuse test of a commercial-off-the-shelf (COTS) cell purchased on the open market.

One type of mechanical abuse test that is performed on cell deliverables is the blunt rod test, where a 3 mm diameter steel rod with a rounded tip is pressed into a cell. Figure III - 26 shows a representative force/displacement curve for a COTS cylindrical cell subjected to a blunt rod test. At ~4 mm deflection, the cell package was ruptured at ~820 N, causing a hard short circuit and the cell goes into an energetic thermal runaway. Figure III - 27 also shows a still photograph of the test where the blunt rod is penetrated into the face of the pouch cell.

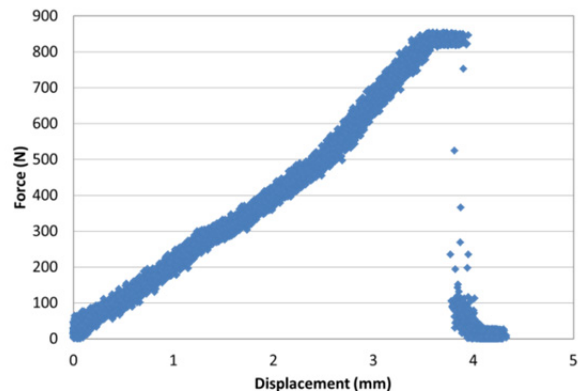


Figure III - 26: Force-displacement curve for a blunt rod test of a COTS cylindrical cell

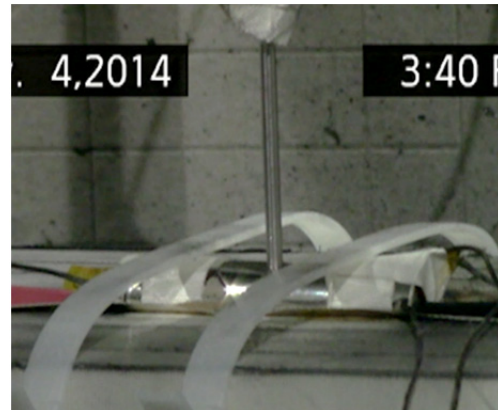


Figure III - 27: Still photograph of a COTS cylindrical cell blunt rod test

Another type of test commonly performed on cell deliverables is a thermal ramp test. The intent of the test is to thermally ramp a cell to force a thermal runaway under controlled conditions in order to understand the failure characteristics of a cell including venting/rupture behavior, onset temperature for self-heating, thermal runaway characteristics, and the likelihood for self-

ignition. Figure III - 28 shows cell voltage and temperature for a thermal ramp test of a COTS cylindrical cell. The cell voltage drops at 110°C, begins to self-heat at 180°C, and goes into thermal runaway at 200°C. In this example, the cell self-ignites and the runaway is energetic enough to result in a peak cell skin temperature of 620°C.

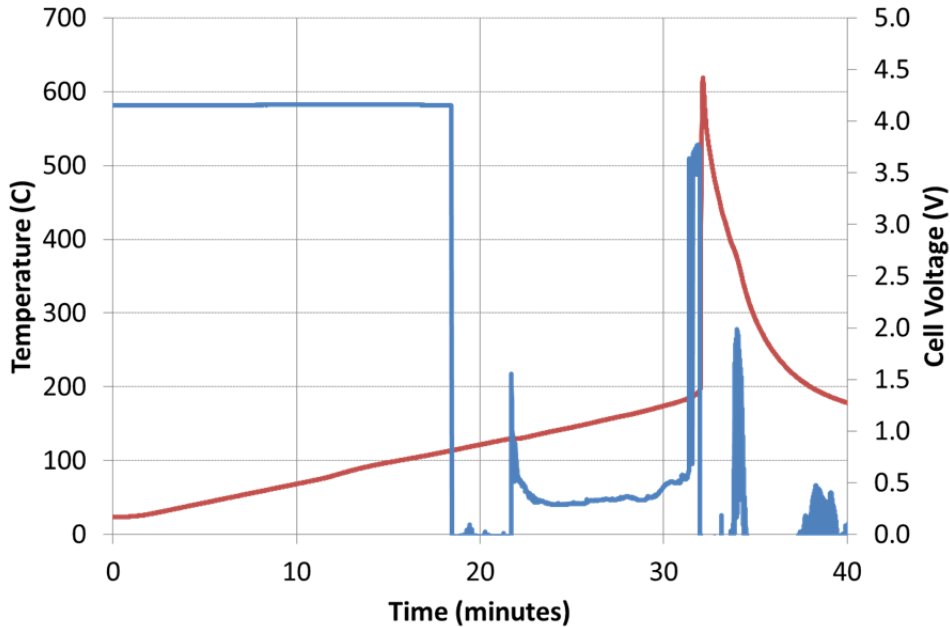


Figure III - 28: Voltage and temperature as a function of time for a thermal ramp abuse test of a COTS cylindrical cell

Propagation Test Development: A number of studies on the response of single cells to field and abusive failures have been conducted at Sandia, however less attention has been paid to how a battery system responds to the energetic failure of a constituent cell. A single cell failure may be a relatively rare occurrence, but the consequence of that failure can be significantly greater if these failures propagate through the entire battery. To study this further, we have tested a series of small batteries constructed with COTS cells.

In our experimental work, batteries consisting of 3 Ah pouch cells were constructed in fully parallel (1S5P) and fully series (5S1P) configurations. These were stacked together such that the largest area faces of the cells were in contact with each other and the battery tabs were all colocated on the same side of the pack. Failure initiation was performed on central cell as well as the outside edge cell. In all cases the failure propagated through the entire battery within roughly the same time frame (50-60 s) and with similar runaway temperatures (600-700°C). In the parallel configuration, the short circuit current was

measured for each cell and show that ~200 A is passed through the shorted cell. Even with the additional short circuit current in the parallel configuration, the results compared to the series configuration tests are not significantly different. This suggests that response is dominated by thermal transfer from cell-to-cell because of the large contact surface area.

The results for these tests were modeled in collaboration with NREL using multiscale thermoelectrochemical simulations. Figure III - 29 shows the simulated temperature rise through the entire battery to > 700°C in 35 s. Figure III - 30 shows the experimental and simulated temperature response of each cell as a function of time during the failure propagation. The simulation follows the response of the first 3 cells reasonably well, and then over predicts the response of the last two. This is due to physical changes to the battery, including possibly broken electrical connections, which decrease the thermal conductivity over time which are not considered in the model. Work will continue with NREL to further develop and validate this predictive capability.

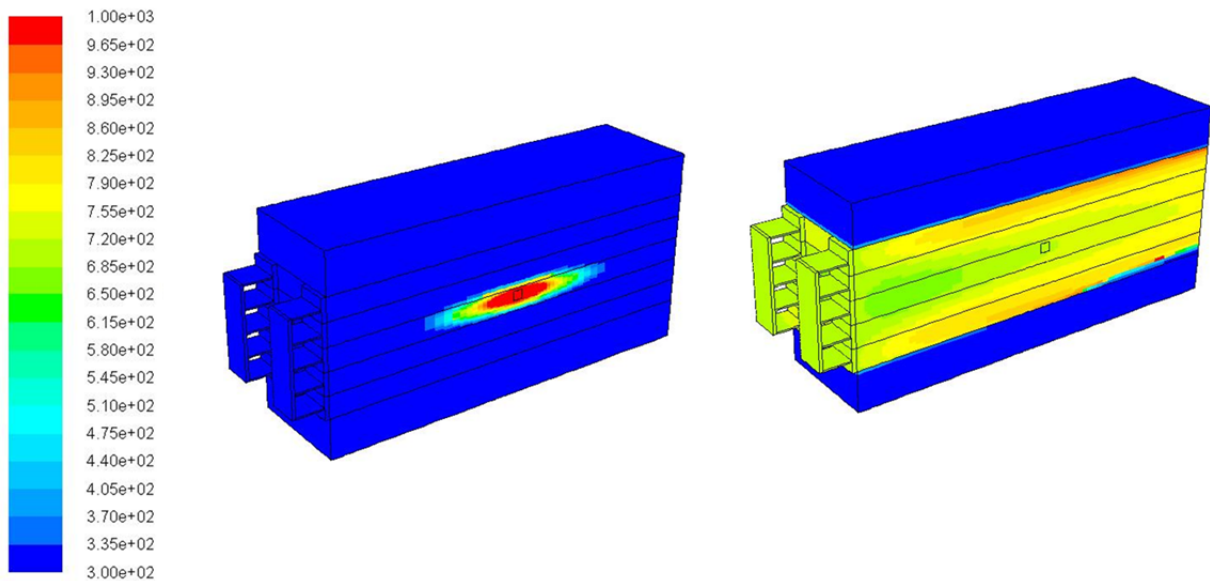


Figure III - 29: Simulated temperature rise from Cell 3 through all five cells in a 1S5P battery (NREL)

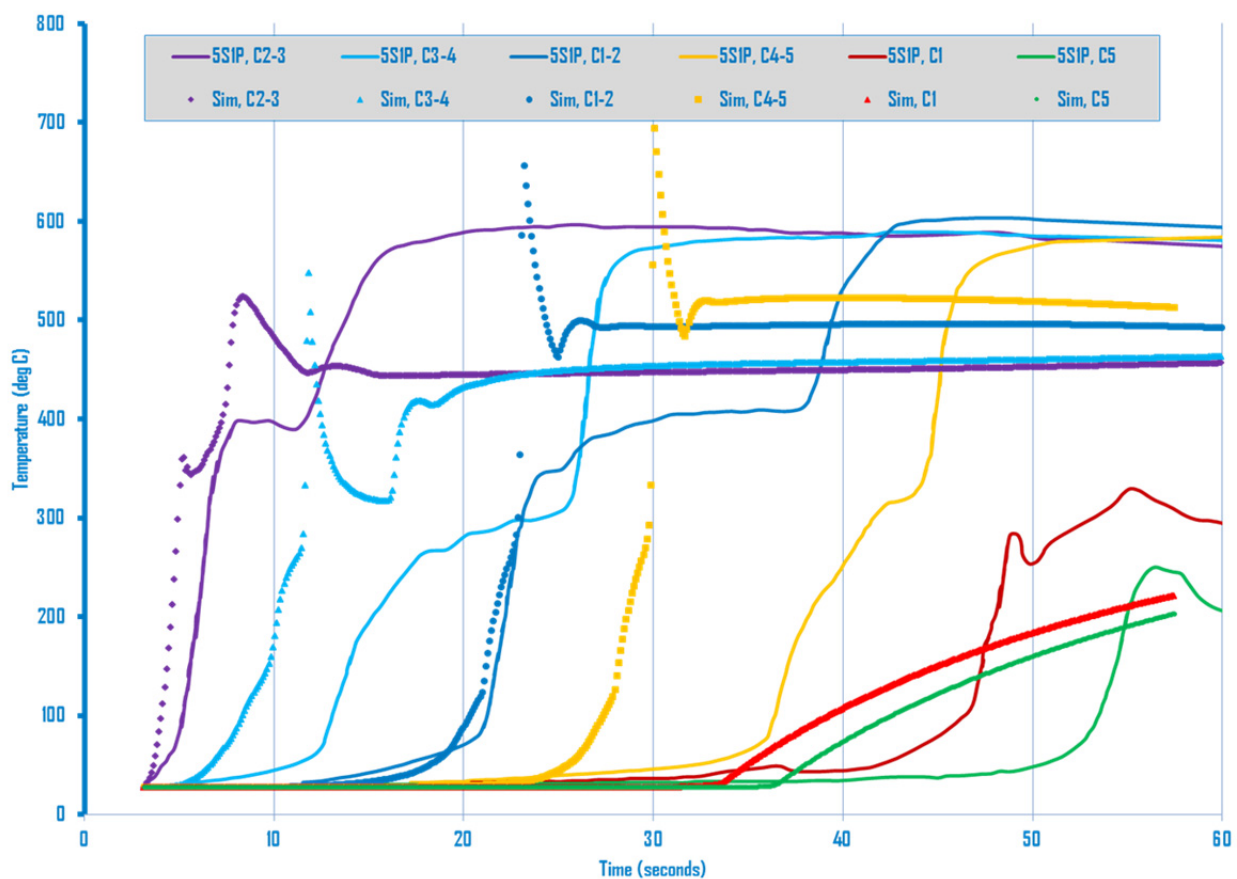


Figure III - 30: Experimental (solid lines) and simulated (dotted lines) cell temperature during a propagation test of a 1S5P battery (NREL)

We have also published a report that describes the failure propagation testing procedure and provides representative data (C.J. Orendorff et al. “Propagation Testing of Multi-Cell Batteries” SAND2014-17053). Our hope is that this procedure benefits testing organizations, becomes incorporated into testing standards, and provides value in understanding failure propagation of battery systems to regulatory agencies and battery developers.

Mechanical Testing: This project is focused on providing mechanical testing support to the USCAR Crash Safety Work Group (CSWG) to set boundary parameters for mechanical models and to validate predictions made by the numerical models. In FY13, the relationship between USCAR and UnIII. of Michigan ended and the focus shifted from cell level testing to battery testing. Batteries are tested in two orientations: (1) end – into the face of the cells with a flat plate and (2) side – into the side of the battery with a 45 mm diameter ram to mimic an FMVSS pole impact test at the vehicle level. The testing focus in FY14 has been on fully constrained batteries to provide the most well defined experimental data set for the mechanical model. Figure III - 31 shows batteries in the end (left) and side



Figure III - 31: Photographs of batteries in the sleeve constraint for mechanical testing in the end and side orientations

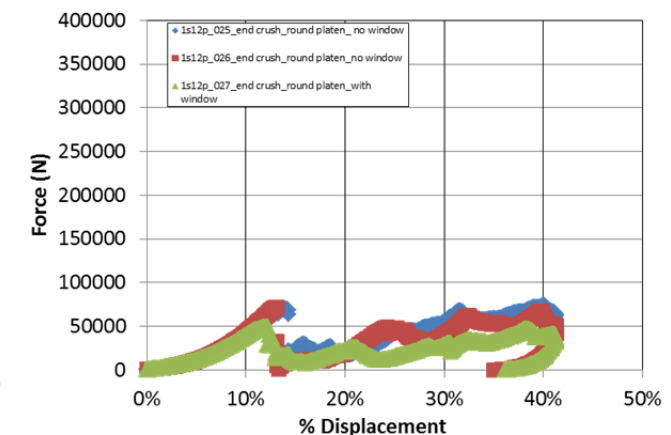
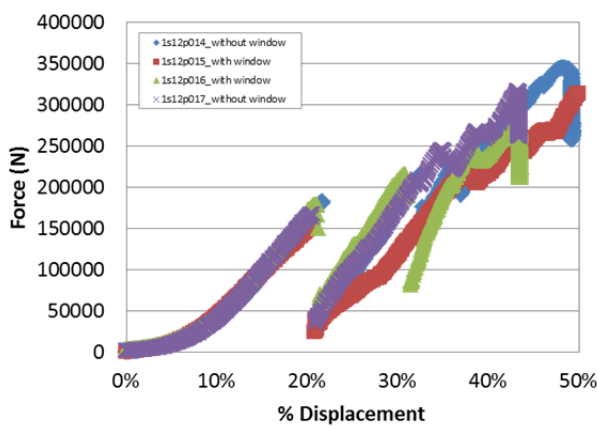


Figure III - 32: Force-displacement curves for batteries crushed in the end orientation using a flat plate (left) and a cylindrical impactor (right)

(right) orientations in sleeves to constrain the cells in the stack when loaded in either orientation. The intent of the sleeve with the window is to be able to view the mechanical buckling or fracture of the battery while acquiring the test data as shown in Figure III - 32.

Figure III - 32 and Figure III - 33 show force-displacement curves for experiments in both the end and side orientations using the cylindrical ram and a flat platen. For the batteries tested in the end orientation with the flat platen, results are very reproducible from battery-to-battery and show a shear failure of the battery at ~20% displacement. Results for batteries in the side orientation impacted using a flat platen show somewhat more variability from battery-to-battery because of the less well defined battery structure in the edge orientation. Moreover, there is only deformation and elastic compression observed and no mechanical failure of the battery up to 40% displacement into the battery in the side orientation. Similarly, with the cylindrical impactor, there is also some variability from battery-to-battery and the peak loads observed are significantly less than with the flat plate impactor.

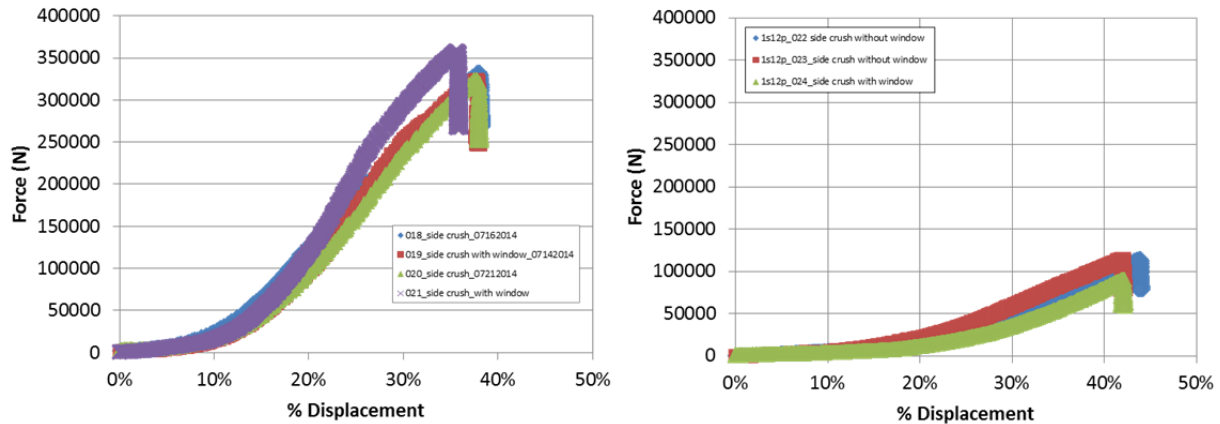


Figure III - 33: Force-displacement curves for batteries crushed in the side orientation using a flat plate (left) and a cylindrical impactor (right)

Aged Cells. While significant attention has been paid to cell performance over time (capacity fade, available power, etc.) there is very little known about how a cell failure, in particular thermal runaway profiles, may change over time. Moreover, while measurable progress has been made in cell safety and advanced materials, there is surprisingly very little data on whether or not these materials improvements observed at the beginning of cell life will continue to have the same positive benefit as these cells age. This is important not only in understanding cell behavior, but also in designing thermal management controls for battery systems. Since these are designed for new or fresh cells in a battery, we must understand how the runaway response may change over cell lifetime and how cell-to-cell variations in thermal response may change over time and also impact the system response.

We have previously studied COTS NMC cells aged to 20% power fade. Calorimetry and abuse testing results on 20% faded cells show only slight differences with the control cells at 100% SOC and significantly greater cell-to-cell variability. Working with INL, cells were calendar aged to 50% capacity fade in FY14.

Figure III - 34 shows accelerating rate calorimetry data

for a representative fresh cell at 100% SOC, a fresh cell at 50% SOC, and a cell aged to 50% capacity fade at 100% SOC. The peak heating rate of the aged cell is $\sim 120^{\circ}\text{C}/\text{min}$ with an estimated runaway enthalpy of $\sim 13 \text{ kJ/Ah}$, while the fresh cell at 100% SOC runaway is measured to have a peak heating rate of $220^{\circ}\text{C}/\text{min}$ and a runaway enthalpy of $\sim 19 \text{ kJ/Ah}$. While this trend of a less energetic runaway for the 50% aged cell is expected, the absolute magnitude of the runaway reaction, even at 50% capacity fade/100% SOC is somewhat surprising. Also, Figure III - 34 contains an ARC profile for a fresh cell at 50% SOC, which is effectively the same stored energy capacity as the aged cell, however, the runaway reactivity measured by ARC is significantly diminished. One might expect the runaway reactions of both a fresh cell at 50% SOC and an aged cell at 50% capacity fade/100% SOC to be more comparable. It is also important to note that the aged cell is measured at 4.2 V and the 50% SOC fresh cell is measured at $\sim 3.6\text{V}$, which could contribute to the discrepancy between the two cell types. Work will continue in FY15 to evaluate the thermal runaway characteristics of aged cells.

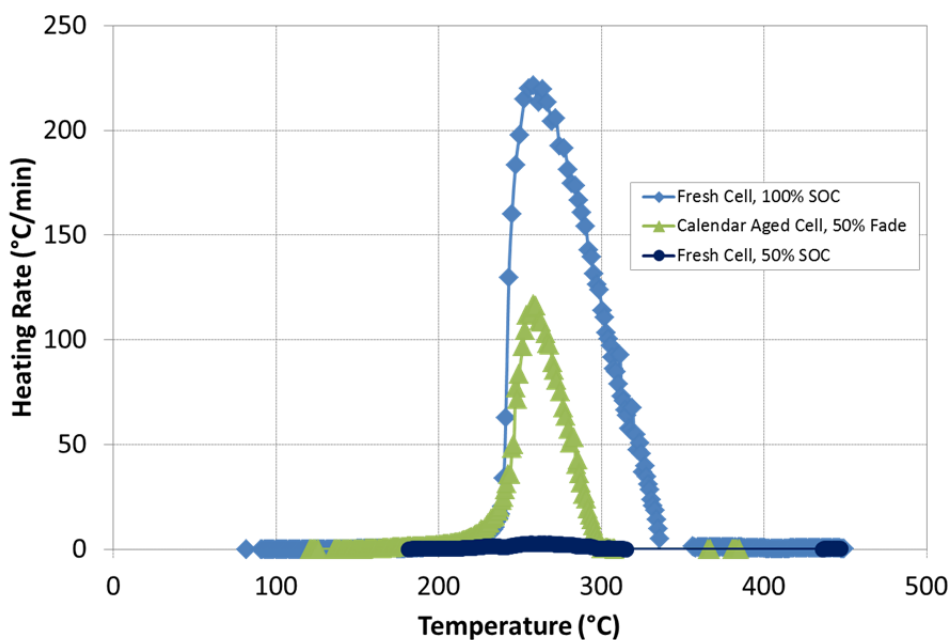


Figure III - 34: Cell heating rate (°C/min) as a function of temperature for the following representative cells: a fresh cell at 100% SOC, a calendar aged cell to 50% capacity fade, and a fresh cell at 50% SOC measured by accelerating rate calorimetry (ARC).

Conclusions and Future Directions

Testing has continued on larger format cells, modules and packs for USABC cell developers. This has required careful control and monitoring of tests with the potential of high energy release. This has provided critical information to cell developers to aid in the development of increasingly abuse tolerant cell chemistries and module designs. This independent testing is also necessary to perform objective evaluations of these various designs and chemistries by the DOE and U.S. automobile manufacturers. Testing will continue in FY 15 on new module and cell designs from USABC contractors.

Initial work on failure propagation highlights the contributions of battery configuration to the ability of a single point failure to propagate through a battery. Our initial effort at modeling the propagation behavior shows good agreement with experimental results. Future work on this project includes evaluating different cell chemistries, passive design changes, and active temperature management. We will also continue to work with our colleagues to model this failure propagation behavior in order to develop a predictive design capability.

Mechanical testing of batteries under well controlled experimental conditions provides baseline input parameters to modify existing continuum mechanical models for batteries. Future work will focus on dynamic (high impact rate) testing and experiments to validate mechanical models.

Cells calendar aged to 50% capacity fade show a measureable reduction in the thermal runaway reactivity, relative to fresh cells. Future directions for the aged cell abuse response work includes evaluating a greater population of aged cells and cells at reduced SOC and numerical analysis of the aged cell data to better

FY 2014 Publications/Presentations

1. J. Lamb, C. J. Orendorff, *J. Power Sources* 247 (2014) 189-196. “Evaluation of mechanical abuse techniques in lithium ion batteries”.
2. USABC TAC, February 2014.
3. USABC TAC, May 2014.
4. 2014 DOE Annual Peer Review Meeting Presentation.
5. USABC TAC, July 2014.
6. C. J. Orendorff et al. “Propagation Testing of Multi-cell Batteries” SAND2014-17053.
7. L.A.M. Steele et al. “Understanding Lithium-ion Battery Fires” 89th Lithium Battery Technical/Safety Group Meeting, September 2014.
8. C. J. Orendorff “Battery Safety R&D at Sandia National Laboratories” 89th Lithium Battery Technical/Safety Group Meeting, September 2014.
9. J. Lamb et al., *Journal of Power Sources* (2014), <http://dx.doi.org/10.1016/j.jpowsour.2014.10.081>

III.B.4 Battery Thermal Analysis and Characterization Activities (NREL)

Matthew Keyser (NREL)

National Renewable Energy Laboratory
15013 Denver West Parkway
Golden, CO 80401
Phone: (303) 275-3876; Fax: (303) 275-4415
E-mail: mattthew.keyser@nrel.gov

Collaborators:

Aron Saxon, Ying Shi, Shriram Santhanagopalan,
Ahmad Pesaran, GM, Ford, Chrysler

Partners:

USABC, JCI, LG CPI, SK Innovations,
Leyden, Saft, Envia, and Farasis

Start Date: October 1, 2009

Projected End Date: September 2015

Objectives

- Thermally characterize battery cells and evaluate thermal performance of battery packs provided by USABC developers.
- Provide technical assistance and modeling support to USDRIVE/USABC and developers to improve thermal design and performance of energy storage systems.
- Quantify the impact of temperature and duty-cycle on energy storage system life and cost.

Technical Barriers

- Decreased battery life at high temperatures.
- High cost due to an oversized thermal management system.
- Cost, size, complexity and energy consumption of thermal management system.
- Decreased performance at low temperatures.
- Insufficient cycle life stability to achieve the 3,000 to 5,000 "charge-depleting" deep discharge cycles.

Technical Targets

- Battery operating temperature from -30°C to 52°C without degradation in performance or life.
- 15-year calendar life at 30°C.

Accomplishments

- Obtained cells from various USABC battery partners including Johnson Controls Incorporated (JCI), LG-CPI, SK Innovation, Leyden, and Farasis.
- Obtained infrared thermal images of cells provided by USABC battery developers and identified any areas of thermal concern.
- Used NREL's unique calorimeters to measure heat generation from cells and modules under various charge/discharge profiles in order to design the appropriate thermal management system.
- Obtained thermal and electrical performance data of cells under HEV, PHEV and EV power profiles.
- Determined that the energy efficiency of most lithium ion cells is above 93%.
- Evaluated thermal performance of a PHEV pack.
- Presented results of cell thermal characterization and pack thermal evaluation at USABC/battery developers review meetings.



Introduction

The operating temperature is critical in achieving the right balance between performance, cost, and life for both Li-ion batteries and ultracapacitors. At NREL, we have developed unique capabilities to measure the thermal properties of cells and evaluate thermal performance of battery packs (air or liquid cooled). We also use our electro-thermal finite element models to analyze the thermal performance of battery systems in order to aid battery developers with improved thermal designs.

Approach

Using NREL's unique R&D 100 Award-winning calorimeters and infrared thermal imaging equipment, we obtain thermal characteristics (heat generation, heat capacity, and thermal images) of batteries and ultracapacitors developed by USABC battery developers and other industry partners. NREL supports the Energy Storage Technical Team by participating in various work groups such as the JCI, LG CPI, SK Innovations, Leyden, Saft, Envia, and Farasis USABC Working Groups.

Results

Calorimeter Testing

Figure III - 35 shows the efficiency of cells tested in FY14 at NREL at a calorimeter temperature of 30°C. The Li-ion cells were fully discharged from 100% SOC to 0% SOC under C/2, C/1, and 2C currents. It should be noted that the cells in the figure are for both power and energy cells and have been developed for the HEV, PHEV, EV, or the LEESS programs with USABC. The figure shows that most of the Li-ion cells, A-C, are very efficient over this cycling regime – typically greater than 93%. The range of efficiencies at a 2C discharge rate is between 93% and 97%. A 4% difference in

efficiency may not appear to be of concern; however, if you consider a 50 kW pulse from the battery in an electrified advanced vehicle, then a 1% difference in efficiency results in an additional 500 Watts of heat for the pulse duration – taking the example further, a 4% difference results in 2000 Watts of additional heat. The efficiency differences between the cells will require the thermal management system to be tailored to the cell thermal characteristics so as not to affect the cycle life of the cells. Finally, Cell D shows a fairly low efficiency as compared to many of the other cells tested in FY14 and could benefit from design improvements to the cell. NREL's calorimeter can identify these outliers but can also help determine if the inefficiency is due to chemistry or cell design.

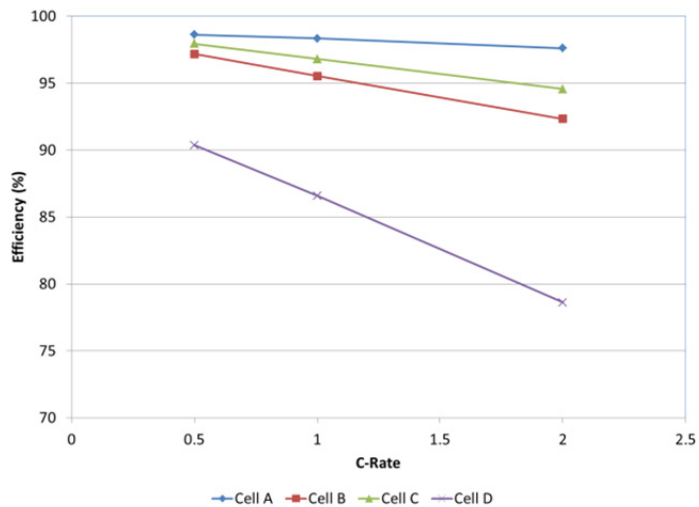


Figure III - 35: Efficiency of cells tested at 30°C in NREL's calorimeter during FY14

Figure III - 36 compares the efficiency of multiple generations of a cell from the same manufacturer. The cells were all discharged under a constant C-rate current from 100% to 0% SOC. The efficiency of the first generation cell is the highest whereas the fourth generation cell has the lowest efficiency. The efficiency differences between successive generations of cells may be due to many different factors – different material suppliers, different additives, cathode or anode thickness

changes, or the cell is tweaked to be an energy cell versus a power cell. The NREL calorimeters help the battery manufacturers to understand how their design changes and improvements affect the efficiency and heat generation of their cells. Battery manufacturers use the data from the calorimeter to ensure that the cell has the desired efficiency over the usage range while making trade-offs on other aspects of the cell design such as low temperature operation, safety, cost, and ease of manufacturing.

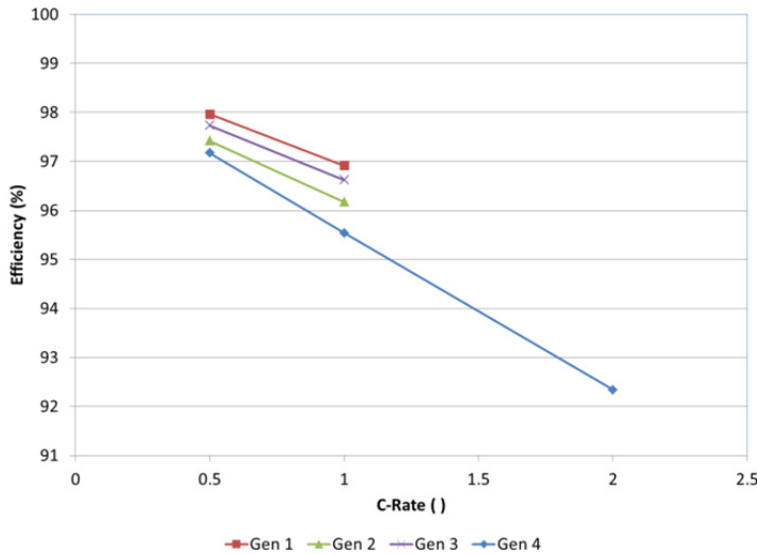


Figure III - 36: Efficiency of four generations of cells tested at 30°C under a constant current discharge from 100% to 0% SOC

NREL's calorimeters are designed to be accurate enough to measure the electrochemical response from batteries under test. As car manufacturers progress from HEVs to PHEVs and EVs, the design of the battery pack will also change. For instance, an HEV battery pack is cycled within a very narrow band—typically within a window encompassing 10% of the overall energy window of the pack. In contrast, a PHEV and EV battery is typically cycled over a much wider range – typically, 80-90% of the battery's capacity. Figure III - 37 shows the normalized heat rates of four different cells tested during FY14. The batteries in this figure were cycled from 0% to 100% DOD at a very low

current. As shown in the figure, the battery undergoes endothermic and exothermic heat generation over the cycling range. The figure also shows how the battery chemistry affects the entropic signature of the battery. Cell 1 is endothermic at the beginning of the discharge as compared to cells 2 and 3 which are exothermic. The fourth cell is the most inefficient cell of the group tested – some of this inefficiency is due to the design of the electrical paths in the cell. The figure also shows where a cell is most inefficient – below 80% DOD for Cells 1-3 and below 50% DOD for Cell 4. The data from this graph helps manufacturers and OEMs to understand where to cycle their battery and which areas to avoid thereby increasing the cycle life of the battery.

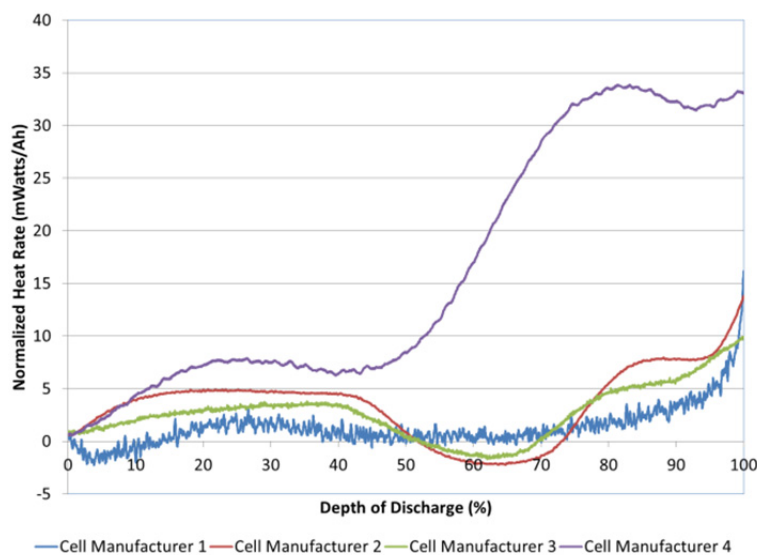


Figure III - 37: Normalized heat rate at 30°C for cells discharged from 0% to 100% DOD

Infrared Imaging

NREL performs infrared (IR) thermal imaging of battery manufacturer's cells to determine areas of thermal concern. IR thermal imaging is conducted under a set of prescribed procedures and environments to minimize the error from different sources such as reflective cell surfaces, radiation from surrounding surfaces, and cooling from the power cables attached to the cell. NREL combines the IR imaging equipment with a battery cycler to place the cells under various drive cycles, such as a US06 charge depleting cycle for a PHEV, to understand the temperature differences within the cell. We then make recommendations to the battery manufacturers and USABC on how to improve the thermal design of the cell to increase its cycle life and safety.

Figure III - 38 shows the thermal image of a PHEV cell under a constant current discharge. The figure contains a thermal image of the cell at the end of the constant current discharge as well as plot indicating horizontal contour lines across the face of the cell – L01, L02, L03, and L04. Figure III - 38 shows a hot

spot in the upper left hand corner of the thermal image of the cell which corresponds to the positive (aluminum) terminal of the cell. The positive terminal will typically be warmer due to the difference in electrical conductivity between the aluminum and copper - the negative terminal of the cell is usually nickel coated copper. When following a contour line from left to right, the temperature generally decreases as is expected. One interesting phenomena associated with the thermal image of this cell is the temperature increases from top to bottom under the negative terminal (right side) of the cell. The current density of the cell is highest near and between the two terminals. Thus, we expected the L01 contour line to be hotter than the L04 contour line. In the end, the cell was imaged under an aggressive constant current discharge and the cell shows good temperature uniformity across its face – a difference of only 3.0°C. When the cell temperature is uniform and consistent, all areas within the cell age at the same rate leading to a better cycle life. NREL is working with battery developers to understand how temperature non-uniformities affect the efficiency and cost of the cell over its life.

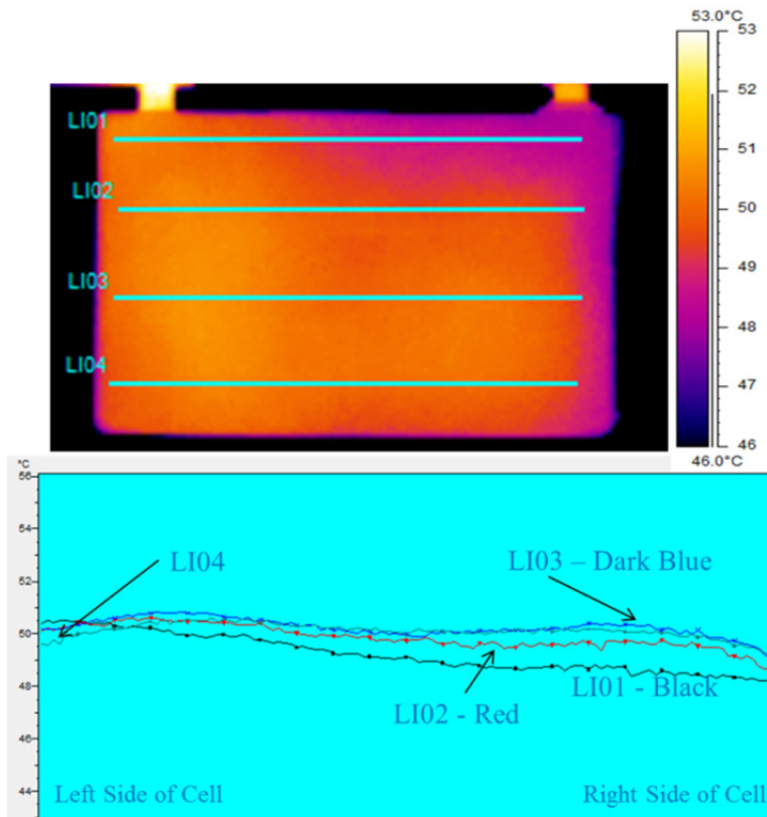


Figure III - 38: Thermal image of a lithium-ion cell at the end of a constant current discharge from 100% to 0% SOC

Pack Thermal Studies

In FY14, NREL evaluated air, liquid, and vapor compression cooled packs for USABC battery developers. We measure the temperature rise and

difference between corresponding cells as well as the voltage of each cell within the pack. Testing is performed at temperatures between -20°C and 30°C with drive cycles pertinent for the battery under test –

PHEV or EV. It has been shown that a 2-3% difference in cell temperature can have a 2-3% effect on fuel economy. Also, the higher temperature cells within a pack are typically more efficient and therefore work harder than the cells at lower temperatures – higher temperature cells typically provide more power. When different cells within the pack provide different amounts of energy over time, then the cells age differently and may cause imbalances with the pack and warranty issues may be a result.

The pack shown in Figure III - 39 was tested under a US06 charge depletion (CD) cycle followed by a US06 charge sustaining cycle. Figure III - 39 is divided into two graphs. The top graph shows the measured cell temperatures of the pack as a function of time. The bottom graph shows the cell temperatures at one point in time which, for this graph, is at the end of the CD portion of the US06 cycle - 20 minutes into the test. At

the end of the CD cycle, a number of interesting conclusions can be drawn. The temperature difference across all the cells in the pack is around 11.8°C . As noted previously, temperature differences between cells cause the cells to age differently which affects the longevity of the pack. We typically recommend a cell temperature difference across the pack of only 3°C and not higher than 5°C . Figure III - 39 also shows that the terminal temperatures are the highest in the pack and that the cell temperatures closest to the cooling plate are the lowest. In this pack, we are not only creating cycle life age differences between individual cells but we are also aging portions of a single cell differently – top versus the bottom of the cell. As the thermal data is collected, we work with the battery developers and OEMs to improve the temperature uniformity of the cells within a pack and the effectiveness of the thermal management system.

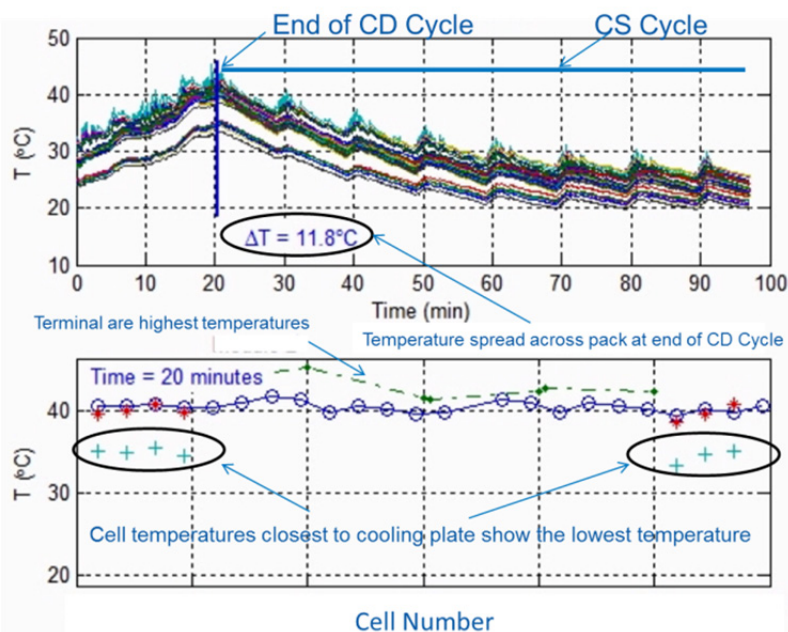


Figure III - 39: Average cell temperature in a pack with and without cooling. The pack underwent a US06 CD cycle followed by a US06 CS cycle

Conclusions and Future Directions

NREL has thermally tested cells, modules, and/or packs from JCI, LG CPI, SK Innovations, Leyden, and Farasis. We've provided critical data to the battery manufacturers and OEMs that can be used to improve the thermal design of the cell, module, pack and their respective thermal management systems. The data included heat generation of cells under typical profiles for HEV, PHEV, and EV applications, which is essential for designing the appropriate sized battery thermal management system. We found that the

majority of the cells tested had a thermal efficiency greater than 93% when cycled under a 2C constant current discharge. During the thermal imaging of the cells, we identified areas of thermal concern and helped the battery developers improve the thermal design of their cells. Finally, we evaluated multiple packs during FY14 and determined that all aspects of the design need to be evaluated for the best thermal performance of the pack and the longest life.

In FY15, NREL will continue to thermally characterize cells, modules, packs for USABC, DOE, and USDRIVE.

FY 2014 Publications/Presentations

1. 2014 DOE Annual Peer Review Meeting Presentation.
2. "The NREL Large-Volume Battery Calorimeter – A Crucial Tool for the Development of Batteries for Electric-Drive Vehicles", CALCON 2014, New Mexico, July, 2014.
3. "Using the NREL Large-Volume Battery Calorimeter for the Thermal Development of Battery Technologies for Advanced Vehicles" SAE Thermal Management Systems Symposium, Denver, September, 2014.

III.C Battery Analysis and Design Activities

III.C.1 Battery Multiscale Multidomain Framework & Modeling (NREL)

Gi-Heon Kim (Principal Investigator)

National Renewable Energy Laboratory
1617 Cole Boulevard
Golden, CO 80401
Phone: (303) 275-4437
E-mail: gi-heon.kim@nrel.gov

Collaborators:

Peter Graph, National Renewable Energy Laboratory

Objectives

- Continue updating the NREL multiscale multidomain (MSMD) battery performance model to run faster.
- Develop a code from the NREL's baseline MSMD battery model in an open-source programming language to provide wider portability and accessibility to public.

Technical Barriers

Battery cost, performance, life and safety are barriers to wide adoption of plug-in electric vehicles. Fast, accurate multiphysics battery computer tools would accelerate development of batteries addressing these barriers.

NREL developed the multiscale multiphysics battery model framework that became a cornerstone for the initiation of CAEBAT program. The code realization of the model was mostly done in a commercial scripting language, MATLAB. This has limited the computational speed of the model simulations and the portability of the codes to existing software in different programming platforms. Utilization of the high performance computing (HPC) resources was also restricted.

Technical Targets

- Restructure the MSMD MATLAB codes.

- Port the baseline MSMD model codes into an open source programming language platform (such as C or C++).
- Enhance the expandability of new developments.
- Accelerate collaboration with external expertise.
- Support battery community in reduced amount of time, helping with advanced modeling capability to address their daily engineering problems.

Accomplishments

- Standardized the model input-output, and the data structure for particle domain (PD), electrode domain (ED) and cell domain (CD) models in the MSMD platform.
- Restructured the MATLAB code structure of the baseline MSMD model codes.
- Completed the porting of PDM and EDM in C++.
- Completed the prototype porting of the CDM to C++.
- Verified the newly developed C++ model codes performance against the corresponding MATLAB codes.



Introduction

Expandable Multiscale Multiphysics Modular Framework – MSMD: Physicochemical processes in Li batteries occur in intricate geometries over a wide range of time and length scales. As the size of the battery increases to meet the system demands of high-energy and high-power energy storage in electric vehicle applications, macroscopic design factors in combination with highly dynamic environmental conditions significantly influence the electrical, thermal, electrochemical, and mechanical responses of a battery system. Without better knowledge of the interplays among interdisciplinary multiphysics occurring across varied scales in the battery systems, it is costly to design long-lasting, high-performing, safe, large battery systems. (See Figure III - 40.)

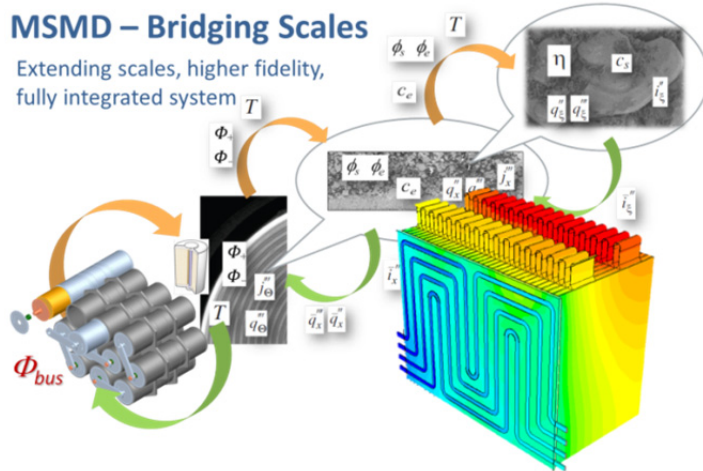


Figure III - 40: NREL's MSMD provides modular architecture, facilitating flexible integration of multiphysics submodels

NREL pioneered the MSMD model, overcoming challenges in modeling the highly nonlinear multiscale response of battery systems. The model resolves the battery geometry into three coupled computational domains. The MSMD provides high extent flexibility and multiphysics expandability through its modularized architecture, as well as computational efficiency to enable the model to run on standard desktop PCs by providing selective, finer meshes for low hierarchical subdomains. Model domain separation for the physicochemical process interplay is carried out where the characteristic time or length scale is segregated. The MSMD particle-domain models (PDMs) solve collective response of electrically and ionically connected particle-batteries which are collocated in the electrode-domain. The electrode-domain models (EDMs) solve collective behavior of PD-batteries, considering polarization through electrolyte and composite matrices. The cell-domain models (CDMs) of the MSMD solves single- or multi-cell battery response by resolving collective behavior of paired plate batteries, considering polarization caused by non-uniform temperature and electric potential fields across cell volume.

Approach

MSMD Baseline Submodels: The MSMD baseline submodels are identified and ported into C++. Here are summarized the descriptions of the submodels in each scale domain.

PDM resolves lithium transport in solid electrode particles, interfacial reaction kinetics, and charge conservation at the interfaces. NREL has developed the discrete diffusion particle model (DDPM) as a baseline PDM for MSMD multiscale model, to better address the impacts of particulate morphology, size distribution, surface modification, contact resistances, mixture

composition of active particles (see Figure III - 41). A system of particles is considered electronically continuous, but ionically discrete. An arbitrary number of quantized discrete particles can be given as a user input. Thermodynamic, Kinetic, transport, electrical and geometrical model parameters of each discrete particle can be independently determined.

EDM solves electronic and ionic charge conservation respectively in composite electrodes and electrolyte, and species conservation in electrolyte. Assuming existence of a local in-plane ensemble average in a finite volume of cell-domain, one dimensional porous electrode model is chosen for a baseline EDM.

CDM solves for temperature and electronic current in current collectors and other passive pathways across cell dimensions. An orthotropic cell composite model is a baseline CDM for MSMD multiscale model. Battery cell-composite has intricate stratified structures, and the assembly units of paired electrode layers are stacked or wound to build prismatic or cylindrical cells. Macroscopic designs for electrically and thermally configuring cell components greatly affect the physicochemical processes occurring in a battery. Treating the cell-composite as a homogeneous orthotropic continuum can significantly reduce numerical complexity of a model. For example, the single potential-pair continuum (SPPC) model treats the stratified cell-composite as homogeneous continuum with orthotropic transport properties, and resolves temperature and a pair of current collector phase potentials in the volume of the continuum with distinguished in-plane and transverse conductivities for heat diffusion and electrical current conduction.

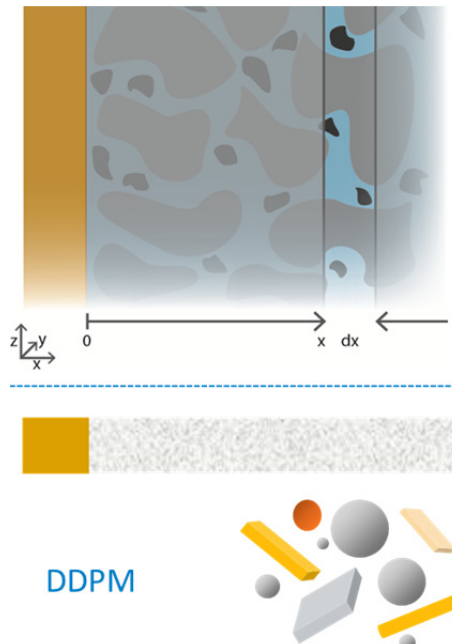


Figure III - 41: Discrete diffusion particle model, a baseline PDM for MSMD multiscale model for better representing complex dynamic behaviors from particulate attributes on kinetics and diffusion dynamics

Results

Standalone Models and Standard Input Files: In the MSMD hierarchical architecture, PDMs become a subscale domain model to EDMs, and in turn EDMs do the same to CDMs. However, PDMs or EDMs can also be run in standalone mode without being integrated into their upper hierarchical parent models. Standard input files define batteries (physicochemical properties and design parameters) in each scale, define the usage, and provide the required numerical set-up for the models. This MSMD input file structure sustains well the MSMD modularity, See Table III - 12. Each input file can be independently modified or replaced for corresponding changes in materials or designs of a system.

Model Application: The ED model captures the impact of application characteristics on inhomogeneous use of electrode materials for a mixed chemistry battery. Figure III - 42 compares the experimentally measured open circuit potential (OCP) curve from LCO and NMC (1:1) mixed cathode and the computed OCP from the OCPs of component materials.

Table III - 12: Comparison of model input file lists to run a standalone PDM, EDM and CDM

	PDM	EDM	CDM
Define Batteries			
posptcltbl.inp, negptcltbl.inp	0	0	0
edparm.inp		0	0
cdparm.inp			0
Define Usage (Load Profile)			
ELprfl.inp	0	0	0
Define Model			
setup.inp	0	0	0

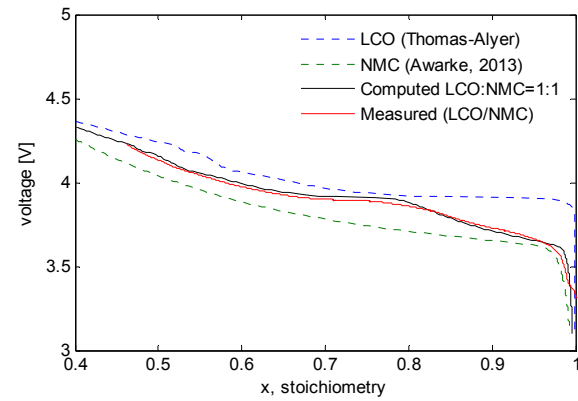


Figure III - 42: Comparison of measured and computed open circuit potential curves for 1:1 LCO-NMC cathode

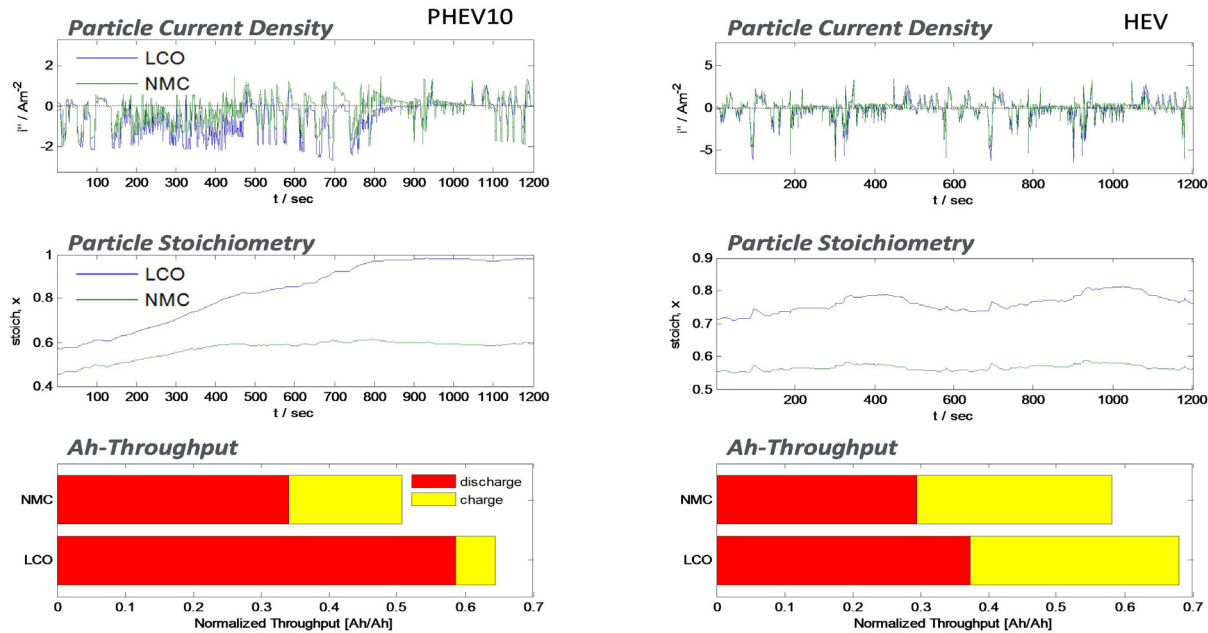


Figure III - 43: Utilization of LCO and NMC particles in 1:1 mixed cathode during 20-minute US06 profile drive of midsize sedan; in PHEV10 (left) and HEV (right) applications

Utilization of LCO and NMC particles in 1:1 mixed cathode during 20-minutes US06 profile drive of midsize sedan are compared. The results for PHEV10 (left) application and HEV (right) application cases are presented in Figure III - 43. When the mixed cathode battery is used in PHEV application, the battery is operated over a wide range of SOC in charge depleting mode. Local thermodynamic equilibria among the mixture components substantially vary, and so does the usage of the materials. Lithium content difference between LCO and NMC grows during the drive. In charge sustaining mode (after ~ 800 sec), the battery is cycled with LCO nearly saturated. Overall charge transfer current throughput is larger with LCO particles. Especially discharge throughput is much larger in LCO particles, but NMC takes more current in charging events. However, the usage pattern among the mixed material components changes greatly with application characteristics. In HEV, while discharge and charge throughputs are balanced for the both components, LCO is used more than NMC by about 17% in terms of charge throughput.

code now can become available to the battery community for use in any platform which accepts compiled C++ code.

Conclusions and Future Directions

NREL's baseline MSMD model codes developed in MATLAB have been successfully restructured and ported into C++. The ported codes were verified against the corresponding MATLAB codes. Standard experimental and computational procedure to identify the MSMD model inputs will be developed and documented. This

III.C.2 Computer Aided Engineering of Batteries – CAEBAT (NREL)

Ahmad Pesaran

National Renewable Energy Laboratory

15013 Denver West Parkway

Golden, CO 80401

Phone: (303) 275-4441; Fax: (303) 275-4415

E-mail: ahmad.pesaran@nrel.gov

Collaborators:

G.H. Kim, K. Smith, S. Santhanagopalan, NREL
S. Pannala, J. Turner, ORNL

Subcontract Teams:

General Motors, ANSYS, and ESim
EC Power, Ford, JCI, and PSU
CD-adapco, Battery Design, A123Systems, and JCI

Start Date: April 2010

Projected End Date: September 2015

Objectives

The overall objective of the Computer-Aided Engineering of Electric Drive Vehicle Batteries (CAEBAT) project is to develop electrochemical-thermal software tools to accelerate design and simulate the performance, life, and safety of electric drive vehicle batteries. As part of this effort, the NREL objectives are:

- Coordinate the activities of CAEBAT for DOE.
- Develop battery modeling tools to enhance understanding of battery performance, life, and safety to enable development of cost-effective batteries for electric drive vehicles.
- Support the U.S. vehicle battery industry with cost-shared subcontracts to develop battery modeling tools to simulate and design cells and battery packs in order to accelerate development of improved batteries for hybrid, plug-in hybrid, and electric vehicles.
- Technically manage the performance of the three subcontract teams led by General Motors, CD-adapco, and EC Power.
- Collaborate with Oak Ridge National Laboratory (ORNL) in their development of Open Architecture Software (OAS) to link various battery models developed under the DOE Energy Storage R&D program.

Technical Barriers

- Cost, life (calendar and cycle), high performance at all temperatures, and safety are barriers for widespread adoption of lithium-ion batteries in electric drive vehicles (EDVs).
- Large investments and long lead times in cell and pack research, design, prototyping, and testing—and then repeating the design-build-test-break cycle many times—increase production costs.
- There is a lack of advanced computer-aided engineering tools to optimize cost-effective electrical-thermal-chemical-mechanical solutions for battery packs in EDVs under various conditions.

Technical Targets

- Develop suites of software tools that enable automobile manufacturers, battery developers, pack integrators, and other end-users to design and simulate the electrochemical and thermal performance of cells and battery packs in order to accelerate development of energy storage systems that meet the requirements of electric drive vehicles.

Accomplishments

- NREL enhanced its battery multi-physics, multi-scale, multi-domain (MSMD) platform for CAEBAT and developed a stand-alone version of the MSMD in open-source C++ for ease of use by any party (this activity is further discussed in Section III.C.2.1 of this report).
- Three subcontract teams (CD-adapco, EC Power, and General Motors) continued developing CAEBAT software tools and validating them.
- NREL continued monitoring the technical performance of the three subcontract teams through monthly progress conference calls, quarterly review meetings, and annual reporting with DOE/HQ.
- Each subcontract team has been successful in delivering CAEBAT software tools to the public and their many clients (specific progress reports for the subcontract teams are provided from Sections III.C.4 to III.C.6).
- The following are major accomplishments from each subcontract team in FY14:
 - CD-adapco completed the framework for electrochemical and thermal modeling of spirally-wound prismatic and cylindrical cells in its widely-used commercial simulation

- platform STAR-CCM+; the model was validated with experimental data from Johnson Controls, Inc. (JCI).
- EC Power completed the final version of its commercial software tool AutoLion, developed based on CAEBAT versions of the ECT3D model; PSU provided data for validation; more than 30 licenses are using these software tools, including Ford.
 - General Motors supported ANSYS to release the CAEBAT software tool in the leading simulation platform: Fluent-15.



Introduction

In April 2010, DOE announced a new program activity called Computer-Aided Engineering of Electric Drive Vehicle Batteries (CAEBAT) to develop software tools for battery design, R&D, and manufacturing. The objective of CAEBAT is to incorporate existing and new models into battery design suites/tools with the goal of shortening design cycles and optimizing batteries (cells and packs) for improved performance, safety, long life, and low cost. The goal is to address the existing practices with which battery and pack developers operate: tediously experimenting with many different cell chemistries and geometries in an attempt to produce greater cell capacity, power, battery life, thermal

performance, and safety, and lower cost. By introducing battery simulation and design automation at an early stage in the battery design life cycle, it is possible to significantly reduce the product cycle time and cost, and thus significantly reduce the cost of the battery. When the project started three years ago, NREL had already developed an electrochemical-thermal model of lithium-ion cells with three-dimensional geometries. However, those tools were not integrated into a 3D computer-aided engineering platform, which automotive engineers routinely use for other components. In many industries, including automotive and combustion engine development, CAE tools have been proven pathways to:

- Improve performance by resolving relevant physics in complex systems;
- Shorten product development design cycles, thus reducing cost; and
- Provide an efficient manner for evaluating parameters for robust design.

DOE initiated the CAEBAT project to provide battery CAE tools to the industry. The CAEBAT project is broken down into four elements, as shown in Figure III - 44.

- Material- and component-level models.
- Cell-level models.
- Pack-level models.
- Open architecture software for interfacing and linking all models.

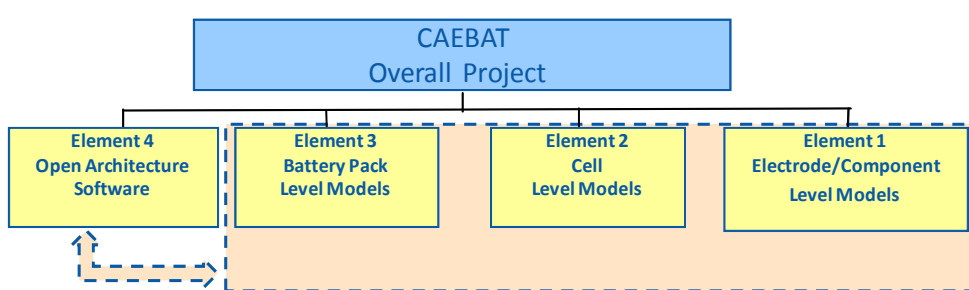


Figure III - 44: The four elements of CAEBAT activity

The goal of the CAEBAT activity is to “develop suites of software tools that enable automobile manufacturers, battery developers, pack integrators, and other end-users to simulate and design cells and battery packs in order to accelerate the development of energy storage systems that meet the requirements of the electric drive vehicle.” So, the involvement of industry (automakers, battery developers, and software producers) in the CAEBAT activity, particularly for Elements 2 and 3 (Development of Cell and Pack Models) was essential. In 2010, DOE’s major strategy was to solicit active participation of the industry in developing cell and pack software suites for the design of batteries.

To oversee the successful execution of the CAEBAT program, NREL was assigned to coordinate the industry and academic activities on Cell-Level Modeling and Pack-Level Modeling. The Open Architecture Software element was assigned to ORNL. In order to engage serious involvement of industry, NREL, with guidance from DOE, issued a Request for Proposals (RFP) in FY10 to seek development of cell and pack battery design tools for a period of three years with 50-50% cost sharing. The CD-adapco, GM, and EC Power teams were awarded in the middle of 2011. The three subcontract teams started technical work in July 2011, made steady progress, and have either met their milestones or are on track to complete them in early FY15 after no-cost extensions.

In addition, NREL continued working on developing and further improving its 3D electrochemical-thermal models. NREL also collaborated with ORNL in their development of the Open Architecture Software as part of Element 4.

Results

Subcontracts with Industry

In FY14, NREL continued to monitor the technical performance of the three subcontract teams through monthly progress conference calls, quarterly review meetings, and annual reporting with DOE/HQ. Quarterly review meetings took place at the subcontractor sites, NREL, or near DOE/HQ.

Significant progress has been reported by each subcontractor. CD-adapco completed its project, according to plan, by the end of July 2014, and delivered the final version of the battery electrochemical-thermal models for spirally-wound cells in its Star-CCM+ flagship simulation platform to various clients. Progress on the CD-adapco subcontract is described in Section III.C.5 of this report. EC Power, although finished with all deliverables, including the commercial version of their CAEBAT tool, requested a no-cost extension to deliver all final reports by the end of December 2014. Section III.C.6 of this report provides details on the progress by EC Power. The General Motors team has released the latest version of their CAEBAT tool in ANSYS Fluent-15 and will complete their subcontract in December 2014. More details about GM's subcontract progress may be found in Section III.C.4 of this report. A summary of the major accomplishments for each subcontractor is provided below.

CD-adapco

- The project has successfully delivered the overall modeling framework, both electrochemical and thermal, as described above, into the computer-aided engineering tool STAR-CCM+, produced by CD-adapco.
- An enhanced electrochemistry model has now been created; the original model is based on the work of Newman, et al.; this model has been significantly extended to include the effect of concentration dependence of the solid phase diffusion coefficient and also multiple active materials, as often found in contemporary lithium-ion cell design.
- Electrochemical and thermal datasets have been created and validated within the project for the spiral cells listed below; these have been created after the provision of cell-specific data from JCI (see Figure III - 45 and Figure III - 46); a process to extract the unknown electrochemical properties from specific test work has been developed.

- A dataset of contemporary electrolytes has been added to the simulation environment; the dataset contains molarity, conductivity, diffusion coefficient, transport number, activity coefficient, density, and viscosity for 12 electrolytes; all values are concentration- and temperature-dependent within appropriate ranges.
- An approach to simulating aging within lithium-ion cells has been formulated which considers SEI layer growth and associated capacity fade driven by lithium loss; this model is based on the work of H. Ploehn.
- The Star-CCM+ flagship commercial software of CD-adapco's was released with battery modeling modules developed under this CAEBAT project; many users worldwide are already adopting this tool for accelerating battery design.

EC Power

- Delivered final version of the large-format software tool “Electrochemical-Thermal Coupled 3-Dimensional Li-ion Battery Model” (ECT3D) to partners during FY14; recent updates to the software included additional technical features, enhanced robustness and execution speed, and upgrades based on Ford, JCI, and NREL user feedback.
- Completed property characterization for materials database.

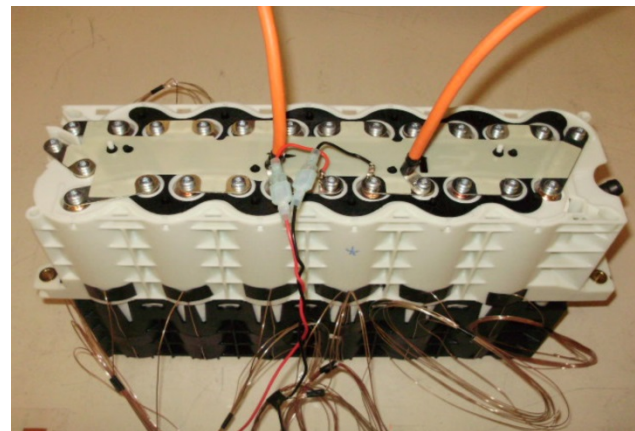


Figure III - 45: Johnson Controls' 12-cell module, used for validating the Star-CCM+ Battery Model

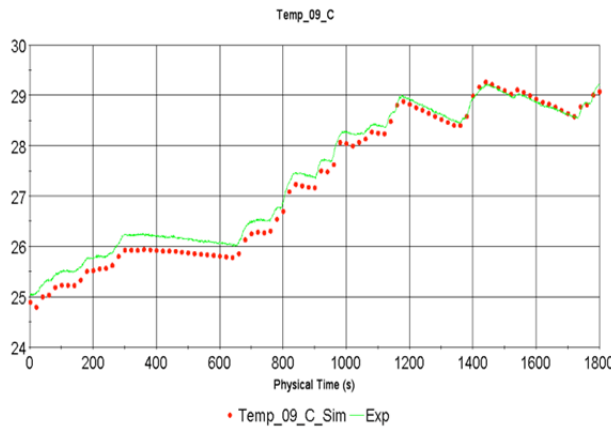


Figure III - 46: Thermal result for a cell within the VL6P module using a standard drive cycle (red dots are simulation, green line is experiment)

- Completed final validation (see Figure III - 47).
- Demonstrated advanced coupling of ECT3D with third party software via Open Architecture Software developed by Oak Ridge National Laboratory.

- Delivered eighteen high-impact publications and presentations over the course of the project.
- The AutoLion™ commercial software developed, in part, under this project has been well received, with approximately 30 licensees employing the software.
- AutoLion™ software is now being applied in markets beyond automotive, including batteries designed for personal and wearable electronic devices and large-scale energy storage.

General Motors

- Continued implementation of NREL's MSMD framework in FLUENT with three electrochemistry sub-models.
- Released official public version of ANSYS battery tools in Fluent - Release15.
- Developed ANSYS Battery Design Tool (ABDT) utilizing the ANSYS Workbench framework.

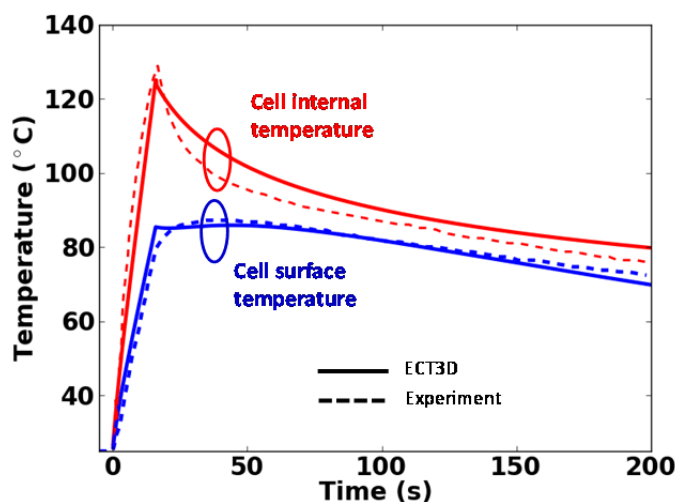


Figure III - 47: Validation of externally-shorted 1.6 Ah NMC/graphite 18650 cell; experimental data acquired using RTS sensor

- Completed reduced-order models (LTI/LPV) for system-level simulations and performed demonstration on an entire pack.
- Developed cycle life model for LG CPI cell based on continuous fading equivalent circuit model by adding SEI side reaction.
- Included newly-developed NREL user-defined function for multiple particle/multiple active material models.
- Validated full 3D electrochemical and thermal model with a 24-cell liquid-cooled module with satisfactory results in comparison with test data (see Figure III - 48).

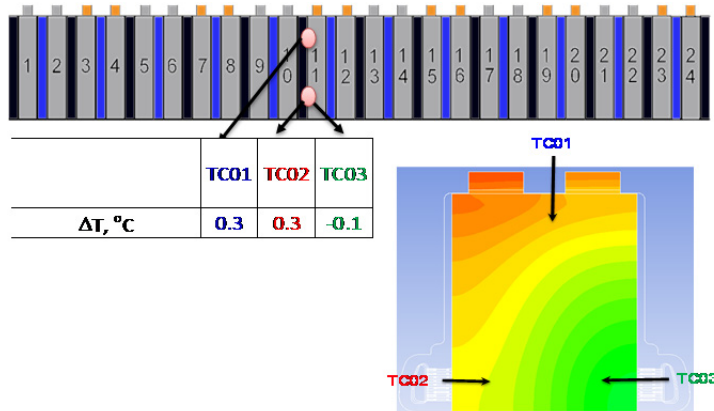


Figure III - 48: Temperature difference between simulation and test data at three thermocouple locations.

Collaboration with ORNL on Open Architecture Software

NREL and ORNL held meetings to discuss the best approach and strategy for Open Architecture Software (OAS). This included collaboration on battery input, battery state, wrappers, and translators. CAEBAT subcontractors were engaged with ORNL for interfacing with OAS. Further details about ORNL's progress may be found in Section III.C.2 of this report.

Development of Multi-Physics Battery Models at NREL

NREL standardized the model input-output, and the data structure for particle domain (PD), electrode domain (ED), and cell domain (CD) models in the MSMD platform, and restructured the MATLAB code structure of the baseline MSMD model codes. The porting of PDM and EDM in C++ and prototype porting of the CDM was completed. The newly-developed C++ model code performance was verified against the corresponding MATLAB codes. (This activity is further discussed elsewhere in this report).

- NREL collaborated with ORNL on development of the OAS to link developed and existing models.
- CD-adapco completed its project and subcontract in July 2014.
- EC Power has completed its project and will finalize reporting in December 2014.
- General Motors has completed its project and will finalize reporting in December 2014.
- The original CAEBAT project will be complete in early FY15; this project has been successful in delivering three stand-alone computer-aided battery engineering tools for accelerating the electrochemical and thermal design of electric drive vehicle batteries.
- The second phase of CAEBAT activity, called CAEBAT-2, will be coordinated directly by DOE/HQ with competitive procurements through Funding Opportunity Announcements; the focus will be on understanding the behavior of batteries under abuse conditions such as crash-induced crush, thermal ramp, and sharp object penetration.

Conclusions and Future Directions

- The three CAEBAT subcontract teams lead by CD-adapco, EC Power, and General Motors made significant progress toward achieving their project objectives.
- Experimental data are being collected by each team to validate the models; simulation results of CAEBAT tools show good agreement with the experimental data.
- Each subcontractor released a mature version of their CAEBAT software tools to the public—CD-adapco in Star-CCM+, EC Power with AutoLion™, and General Motors in ANSYS Fluent-15.
- NREL enhanced its battery MSMD platform for CAEBAT and developed a stand-alone version of MSMD in C++ for ease of use by any party.

FY 2014 Publications/Presentation

1. Ahmad Pesaran, Gi-Heon Kim, Kandler Smith, Shriram Santhanagopalan, "Multi-physics Computational Models for Accelerated Design of Batteries," Conference Proceedings, Batteries 2014, September 24-September 26, 2014, Nice, France NREL/CU team.

III.C.3 Computer Aided Engineering of Batteries Effort (ORNL)

Brian Cunningham (DOE Program Manager)
Subcontractor: Oak Ridge National Laboratory

John A. Turner (Program Manager)
Computational Engineering and Energy Sciences Group
Oak Ridge National Laboratory
Phone: (865) 241-3943; Fax: (865) 241-4811
E-mail: turnera@ornl.gov

Collaborators:
S. Pannala, S. Allu, W. Elwasif, S. Simunovic,
J. Billings, and S. Kalnaus

Start Date: July 2010
Projected End Date: September 2014

Objectives

- Develop a flexible and scalable computational framework that can integrate multiple physics models at various scales (battery pack, cell, electrodes, etc.), and provide a predictive modeling tool under the auspices of the CAEBAT program.
- Coordinate with partners across the program on requirements and design of the framework so as to preserve the investment in existing models.
- Ultimately, the detailed simulation capability will model coupled physical phenomena (charge and thermal transport; electrochemical reactions; mechanical stresses) across the porous 3D structure of the electrodes (cathodes and anodes) and the solid or liquid electrolyte system while including nanoscale effects through closures based on resolved quantities.
- The simulation tool will be validated both at the full-cell level and at the battery-pack level, providing an unprecedented capability to design next-generation batteries with the desired performance and the safety needs for transportation.

Technical Barriers

Given the complex requirements for development of electrical energy storage devices for future transportation needs, a predictive simulation capability which can guide rapid design by considering performance and safety implications of different

chemistry and materials choices is required. This capability must leverage existing investments and integrate multiple physics models across scales in order to (1) provide feedback to experiments by exploring the design space effectively, (2) optimize material components and geometry, and (3) address safety and durability in an integrated fashion. Such models do not currently exist.

Technical Targets

Develop a computational framework that will integrate both existing and new models developed by CAEBAT subcontractor teams that span the battery pack, modules, cells, etc. to provide an integrated design tool for battery manufacturers to optimize performance and safety in an accelerated fashion.

Accomplishments

- Final release of the CAEBAT-Open Architecture Software (OAS) framework together with VIBE (Virtual Integrated Battery Environment), and the Integrated Computational Environment (ICE).
- Cell to module to pack capabilities with automated mesh generation.
- Two-way tight coupling between thermal and electrochemical components.
- Full 3D capability for electrochemistry.



Introduction

Computational tools for the analysis of performance and safety of battery systems are not currently predictive, in that they rely heavily on fitted parameters. While there is ongoing experimental research at various length scales around the world, computational models are primarily developed for the lower-length scales (atomistic and mesoscopic), which do not scale to the system-level. Existing models at the macroscopic or system-level are based on electrical circuit models or simple 1D models. Currently there is no design tool for batteries that can leverage the significant investments in modeling efforts across DOE and academia. An open and flexible computational framework that can incorporate the diverse existing capabilities and new capabilities coming through CAEBAT partners can provide a foundation for a predictive tool for the rapid design and prototyping of batteries.

Approach

We are developing a flexible, robust, and computationally scalable open-architecture framework that integrates multi-physics and multi-scale battery models. The physics phenomena of interest include charge and thermal transport, electrochemical reactions, and mechanical stresses. They operate and interact across the porous 3D structure of the electrodes (cathodes and anodes), the solid or liquid electrolyte system and the other battery components. The underlying lower-length processes are accounted for through closure equations and sub-models that are based on resolved quantities.

Results

Virtual Integrated Battery Environment (VIBE)

A hierarchical process to construct meshes for battery packs has been developed. In the automated script-based geometry and mesh construction procedure a single prismatic cell is replicated to form a module which in turn is replicated to obtain a battery pack (Figure III - 49). This produces significant savings in time and effort in creating geometry for simulations.

Mechanics simulations were performed with the goal of replicating the pinch test with a rigid sphere. Unlike other approaches for modeling battery response to an external load, where cell properties are homogenized over multiple domains, in this approach all layers are resolved. This allows application of failure criteria to each of the domains (electrode, current collector, separator, pouch material) independently, which in turn facilitates determination of the precise location of short circuits. Example results showing Von Mises stress on a deformed mesh in a pouch cell are shown in Figure III - 50.

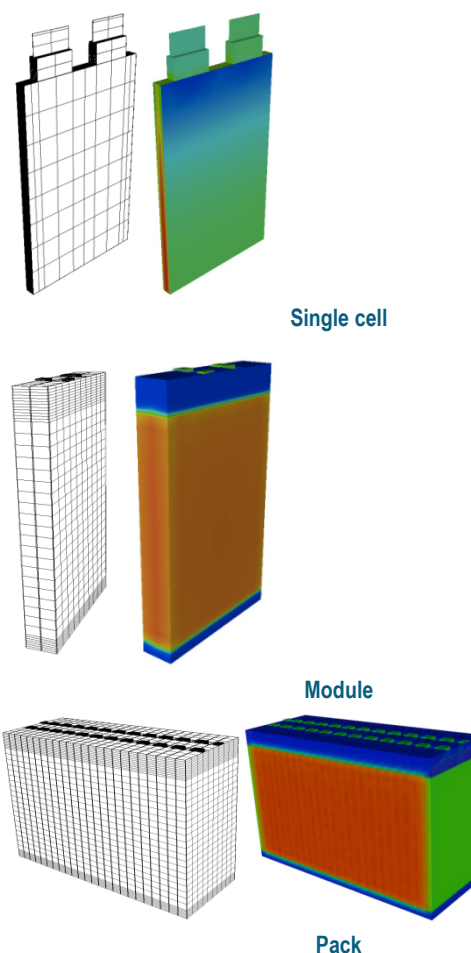


Figure III - 49: Automated mesh generation from cell to pack level with corresponding results of thermal solution

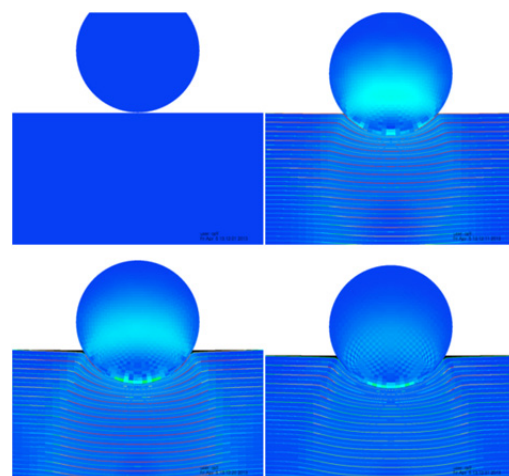


Figure III - 50: Von Mises stress distribution in different domains of a pouch cell under external mechanical loading

Battery State

The battery state file format was expanded by addition of local state of charge as a variable in addition

to local temperature, resistance, and heat source. This accomplishes the goal of including gradients in remaining capacity within the 3D domain of a cell (module, battery pack). When coupled with a thermal component this allows modeling of the influence of cooling strategies and temperature gradients on battery health. Module-level coupling allowed performing simulations of modules consisting of 4 pouch cells connected either in parallel or in series. Simulations of uneven cooling conditions on the module surface show that the potential difference in the cells on two sides can be as high as 2.5 mV. The results for a 4P module are shown in Figure III - 51.

OAS: Tight coupling between thermal and electrochemical components was realized by introducing a Picard iteration scheme into OAS. The corresponding simulation driver and component driver have been improved to include a convergence criterion at each time step. A pseudo 2D model (DualFoil) was coupled to the thermal solution using the example geometry of an unrolled Li-polymer cell. Temperature-dependent diffusivities and Butler-Volmer kinetics provide coupling with the thermal component. Rapid convergence of Picard iterations was observed – typically within 4 iterations. Improved solution accuracy is observed for higher discharge rates (Figure III - 52).

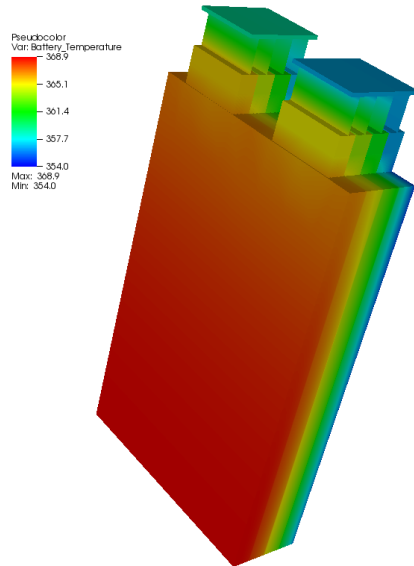


Figure III - 51: Temperature distribution in a module with asymmetric cooling

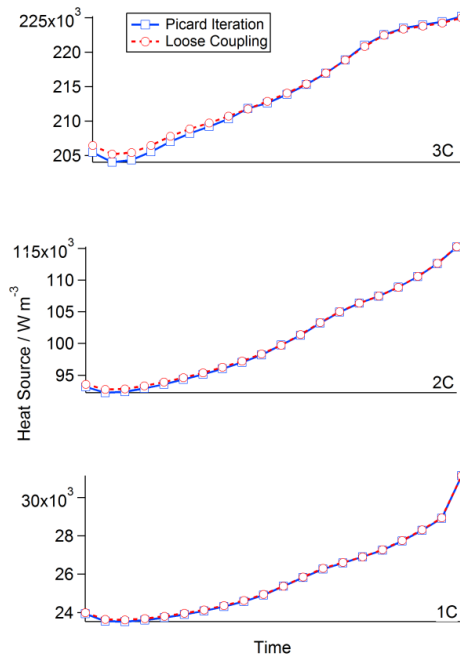


Figure III - 52: Calculated volumetric heat source using loosely and tightly coupled scenarios

Graphical User Interface and Integrated Workflow Environment: The development of a tool for simulation launch and post-processing of the results was based on ICE project for workflow and data management. ICE currently allows:

- Editing of OAS input setup files.
- Editing of BatML files.
- Local and remote job launch.
- Multi-file upload and download of VIBE data.
- 3D visualization of output.

A screen shot of CAEBAT-ICE environment is shown in Figure III - 53. The tool provides easy model setup with drop-down menus for model (component) selection, simulation control parameters and input of the material properties.

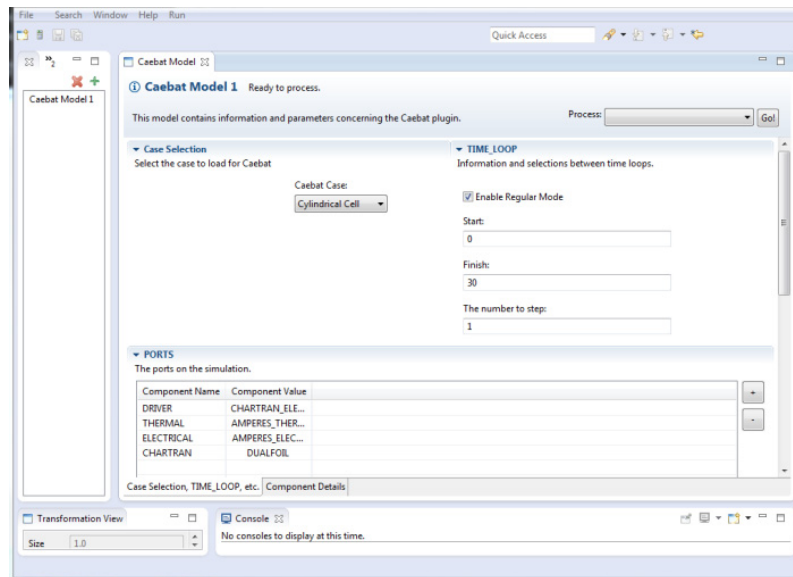


Figure III - 53: CAEBAT-ICE workflow environment for simulation setup, job launch and data post-processing

Conclusions and Future Directions

The CAEBAT OAS framework core is stable and has been released together with VIBE, ICE, BatML, and Battery State. Components for electrochemical, electrical, and thermal modeling have been successfully integrated with different coupling strategies.

The coming year will be primarily focused on user outreach, support and maintenance. Primary objectives are:

- Outreach and user support.
- BatML/Battery State revisions based on community feedback.
- Bug fixes and updates as necessary.

FY 2014 Publications/Presentations

1. Allu, S., Kalnaus, S., Elwasif, W., Simunovic, S., Turner, J.A., and Pannala, S., 2014, "A New Open Computational Framework for Highly-Resolved Coupled Three-Dimensional Multiphysics Simulations of Li-ion Cells," *Journal of Power Sources*, **246**, pp. 876-886.
2. Turner, J.A., Allu, S., Elwasif, W., Kalnaus, S., Simunovic, S., and Pannala, S., "Safer batteries through predictive simulation", *Battery Safety 2013*, San Diego, CA, Nov., 2013.
3. Allu, S., Pannala, S., Nanda, J., Simunovic, S., and Turner, J.A., "A Generalized 3D Multiphysics Model for Li-Ion Intercalation Batteries," *ECS 226th Meeting*, Cancun, Mexico, Oct. 5 – 9, 2014.
4. Simunovic, S., Stershic, A., Kalnaus, S., Allu, S., Pannala, S., and Turner, J.A., "Mesoscale models

for mechanics of active materials in LIBs," *ECS 226th Meeting*, Cancun, Mexico, Oct. 5 – 9, 2014.

III.C.4 Development of Computer Aided Design Tools for Automotive Batteries (GM)

Gi-Heon Kim (NREL Technical Monitor)

Subcontractor: General Motors LLC

Taeyoung Han (Principal Investigator)

30500 Mound Road

Warren, MI 48090

Phone: (586) 986-1651; Fax: (586) 986-1647

E-mail: taeyoung.han@gm.com

Partners:

ANSYS Inc. and ESIM LLC

Start Date: June 2011

Projected End Date: Dec 2014

Objectives

- As one of the subcontract teams, support the DOE/NREL Computer Aided Engineering for Batteries (CAEBAT) activity to shorten the product development cycle for EDVs and to reduce the cost associated with the current hardware build and test design iterations.
- Provide simulation tools that expand the inclusion of advanced lithium-ion battery systems into ground transportation. Validate advanced lithium-ion battery systems using GM's six-step model verification and validation approach.
- Participate in the Open Architecture Software program led by Oak Ridge National Lab to develop a flexible and scalable computational framework to integrate multiple battery physics sub-models produced by different teams.

Technical Barriers

- Existing design tools are not practical for realistic battery pack design and optimization.
- Various cell physics sub-models exist, but they have not been integrated in a single framework in commercial code.
- Current engineering workstations do not have the computational power required to simulate pack-level thermal response coupled with electrochemistry. System-level analysis or Reduced Order Modeling (ROM) is required to simulate integrated pack-level physics. However, ROM

approaches for battery packs are not well established.

- Collaboration to date has been difficult since software developer's commercial code, automaker's electrification strategies, and battery developer's cell designs and chemistry are all well guarded intellectual property.

Technical Targets

To be useful to automotive engineers, battery cell and pack design tools should have the following analytical capabilities:

- Evaluate battery pack thermal management strategies by predicting max intra/inter-cell temperature difference under various drive-cycles.
- System simulations with ROM that allow trade off studies between the cooling cost and the battery pack warranty cost in the early stage of vehicle development.
- Real-time system simulation speed that can support BMS development and enhancement.

Accomplishments

First version of the battery software was officially released to public with Release 15 of FLUENT in winter of 2014

Software development

- The ANSYS Battery Design Tool (ABDT) has been developed by utilizing the ANSYS Workbench framework.
- LTI/LPV system level model was completed and demonstrated for the entire pack.
- Cycle life model has been developed for an LG cell based on a continuous fading equivalent circuit model by adding an SEI side reaction.
- NREL has developed a user-defined function for multiple particle/multiple active material models.

Cycle life test

- Cycle life test at an elevated temperature was completed.
- Physics-based cycle life model has been developed.

Pack level validation

- Field simulation has been validated with satisfactory results in comparison with the test data.

- System-level model was completed and validated compared to the full field simulation and the test data; comparisons are satisfactory.
- Linear Time-Invariant (LTI) system-level ROM model approach has been validated in comparison with the full field simulation results.
- Thermal abuse and runaway model has been implemented and demonstrated for the thermal propagation in a pack.



Introduction

The principal objective of the GM team is to produce an efficient and flexible simulation tool that predicts multi-physics responses for battery pack thermal management and predicts an optimum cell energy capacity in terms of electrical performance, cooling requirements, life, safety, and cost. GM has assembled a CAEBAT Project Team composed of GM researchers and engineers, ANSYS software developers, and Prof. R.E. White of the University of South Carolina and his ESim staff. In partnership with DOE/NREL, the Project Team has interacted with the CAEBAT working groups to integrate and enhance existing sub-models, develop cell- and pack-level design tools, and perform experimental testing to validate the simulation tools. The GM team has also created

interfaces to enable these new tools to interact and interface with current and future battery models developed by others. NREL has provided the technical consultations and monitored the overall progress. ORNL has provided the standard for Open Architecture Software (OAS). With a rapid deployment to industry, these project results will contribute to accelerating the pace of battery innovation and development for future electric-drive vehicles.

Approach

The project objective is to develop an open, flexible, efficient software tool for multi-scale, multi-physics battery simulation based on the ANSYS Workbench framework. ANSYS is leveraging and enhancing its existing commercial products to provide both field-level (Fluent) and system-level (Simplorer) capabilities, including novel ROM methods and with other battery tools through the OAS interface. Figure III - 54 shows the conceptual view of the ABDT architecture which is the basis for ANSYS software development. The essential role of the ABDT is to automate, integrate, and enhance the ANSYS simulation tools to tailor the various components for cell and pack capabilities. (See Figure III - 54.)

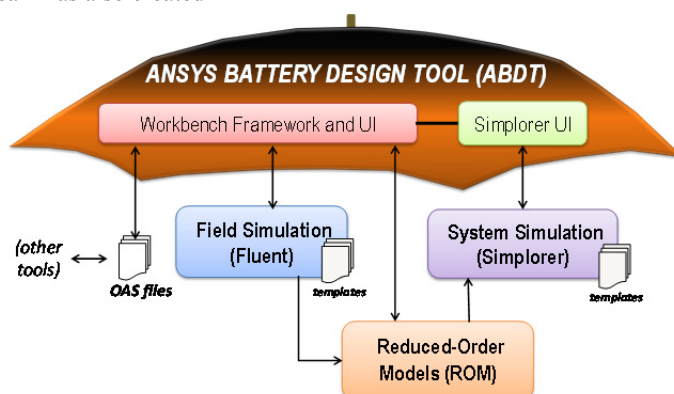


Figure III - 54: Conceptual view of the ANSYS Battery Design Tool

GM engineers and ESim engineers tested the sub-models, evaluated the ABDT tools, and provided further enhancements. The GM team also has built prototypes for a battery module and a pack and performed experimental testing to validate these tools. At the pack level, the tools have been significantly advanced by the development of innovative reduced-order models, derived and calibrated from the cell-level models and carefully validated through experiments.

Results

New features were added to the ANSYS Fluent battery model that offer additional functionality and flexibility to the user. The electric load profile can now be provided as a *time-scheduled* or as an *event-scheduled* function according to the user's choice (Figure III - 55 and Figure III - 56). Both methods allow users to change the electric load type and electric load value during the simulation.

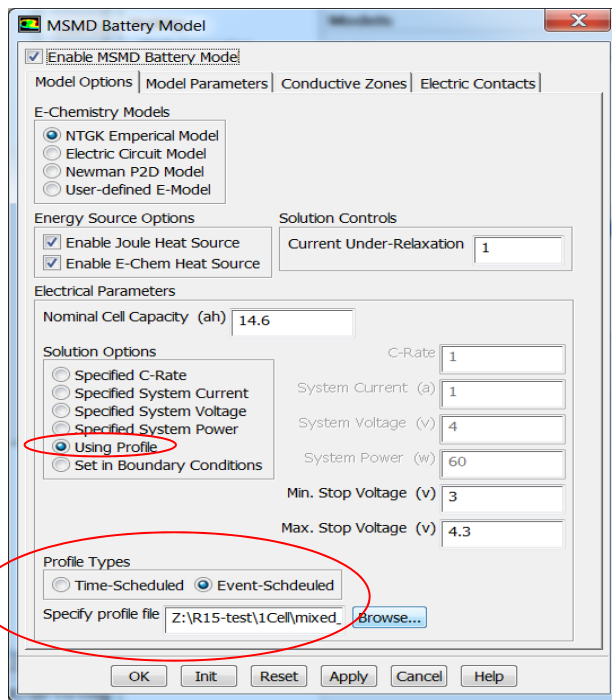


Figure III - 55: Profile Types Selection

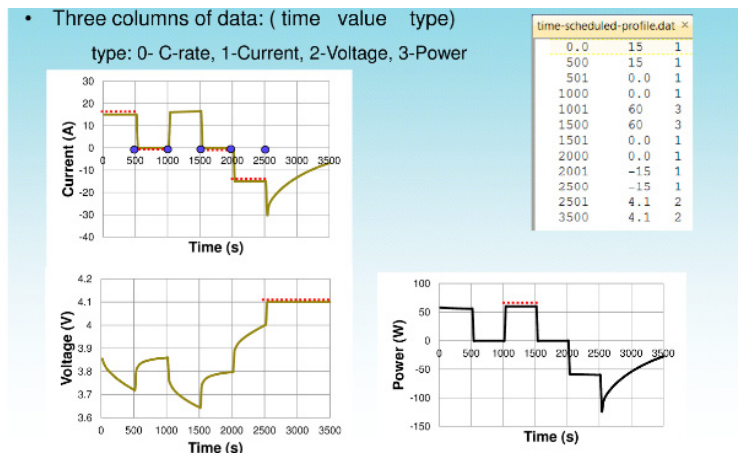


Figure III - 56: Time-Scheduled Profile

The team has also developed a model parameter estimation tool (Figure III - 57) for the NTGK and ECM electrochemistry sub-models. These model parameters are battery-specific and the user needs to

estimate them by curve fitting data points from experimental measurements of the battery's electric behavior.

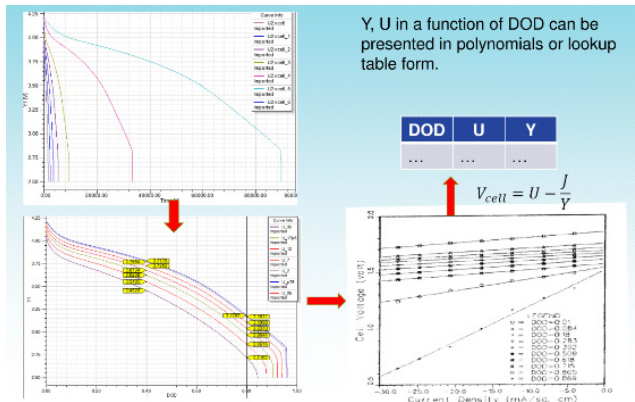


Figure III - 57: NTGK Model Parameter Estimation Procedure

Typically, battery cells are connected either in parallel or series in a module or pack, and highly conductive busbars are used to connect cell tabs. However, a busbar is usually very thin and meshing becomes a challenging task especially in large and complex arrangements. A simpler battery connection

technique (Figure III - 58) has been researched and ANSYS has developed a virtual battery connection that avoids physically modeling the connectors. The Fluent solver sets up the connections accordingly by automatically associating conductive zones with each cell.

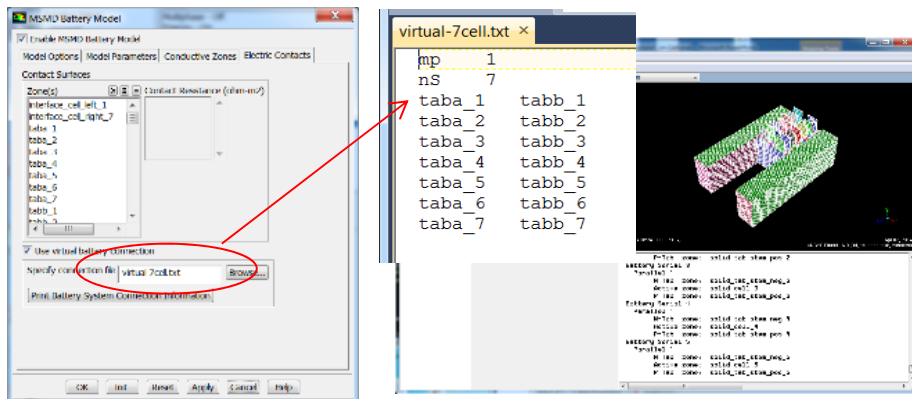


Figure III - 58: Virtual Battery Connection

Occasionally battery cells are abused due to accident or extreme conditions. The associated chemical side reactions and potential for thermal runaway are important safety considerations. To evaluate the tolerance of battery packs in such abuse conditions, a thermal abuse model has been developed in the Fluent solver through a user defined function and corresponding interface (Figure III - 59) for editing model parameters.

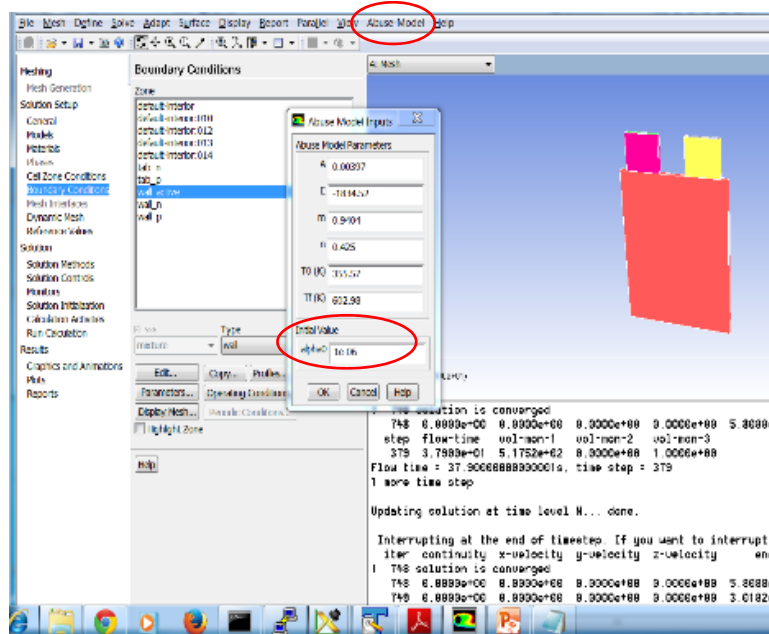


Figure III - 59: Thermal Abuse Model in Fluent

The team continued making progress on simulating battery packs with reduced order models (ROM). The LTI ROM algorithm has been automated within the ABDT environment. In parallel, the development of a robust Linear Parameter Varying (LPV) macro-model has been continued with the algorithm being validated on a 20-cell module with time-varying coolant flow rate. ANSYS has also continued to explore the use of POD (Proper Orthogonal Decomposition) ROMs for simulating battery packs in a more direct method. This method extracts thermal, electrical, and electrochemical matrix information, based on the finite-volume mesh and the representative solution and builds a high-quality ROM. The method has been applied to a large test case and will be extended to include variable coolant flow rates.

Regarding the battery life model, Deshpande's model has been evaluated with the LG cell OPCAP data (every 500 cycles) by ESim. However, Deshpande's model has three limitations: first, the model does not work for cells with varied cycling protocols; second, the model only predicts the capacity for full charge/discharge and cannot be used for incomplete charge/discharge cycles; third, the model cannot be used to predict the power fade of a cell. Due to the above-mentioned limitations, ESim developed a continuous fading equivalent circuit model by adding an SEI side reaction branch to an equivalent circuit model as shown in Figure III - 60.

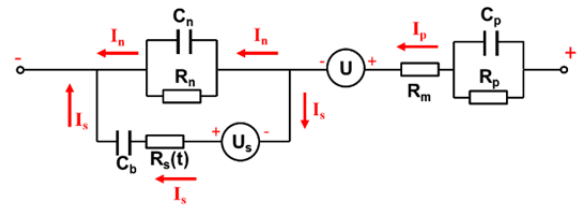


Figure III - 60: The equivalent circuit model with an SEI formation branch.

In the SEI formation branch, U_s denotes the open-circuit potential for the deposition reaction, R_s stands for the sum of the ohmic and kinetic resistances, and C_b is a balancing capacitor. Due to the deposition reaction, the resistance of the SEI increases with time through the following correlation:

$$\frac{dR_s}{dt} = K_u I_s \quad (\text{for } I_s > 0) \quad \frac{dR_s}{dt} = 0 \quad (\text{for } I_s \leq 0) \quad (1)$$

where K_u ($\Omega \text{ m}^4/\text{C}$) is a parameter that relates the side reaction current density, I_s , to the film resistance, R_s , ($\Omega \text{ m}^2$), with $R_s(t=0)$ as a parameter. The initial values for the circuit components (C_p , R_p , C_n , R_n , and R_m) were obtained by validating the model with the discharge data at different rates for fresh cells at 25°C. The initial fitting results are presented in Figure III - 61. Equivalent circuit components (C_p , R_p , C_n , R_n) take the following expression:

$$\Psi = \left(\frac{1}{a \cdot \text{DoD}^2 + b \cdot \text{DoD} + c} \right)^2 \quad (\text{where } \Psi = R_n, C_n, R_p, C_p) \quad (2)$$

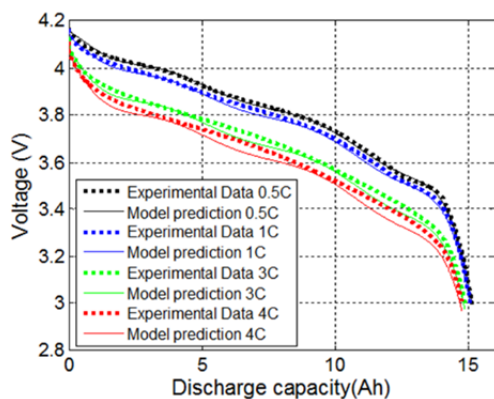


Figure III - 61: Fit of the ECM life model at the beginning of life

Comparison of the simulated and experimental capacity values during the first 500 cycles was used to determine the fade parameters ($R_s(t=0)$, C_b , U_s , and K_u), and the results are presented in Figure III - 62. In each cycle, the cell was charged at 30 A (2C) to 4.091 V followed a CV charge to 0.75 A (0.05 C), then discharged at 45 A (3C) to 3.513 V. The continuous ECM life model shows good agreement with experimental data. (See Figure III - 62.)

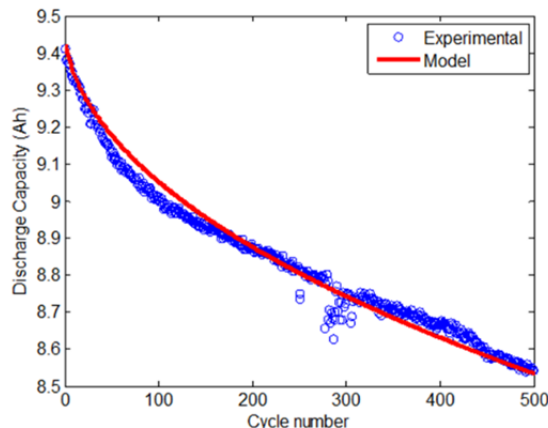


Figure III - 62: Comparisons between the ECM life model and experimental cycling data

GM has built a 24-cell module with a liquid-fin cooling system (Figure III - 63). Thermocouples were located at various places in the module to validate the full field CFD simulations. A CFD model was constructed by GM engineers and has been validated to compare the simulation results with the test data for a 1 sec charge/discharge pulse case at a 3.5 C-rate. The state of the charge stayed at a constant value of 50%. This is a simple test case with a constant heat generation rate to validate the model. The battery surface temperature predictions are within 0.5°C accuracy at a steady state (Figure III - 64 and Figure III - 65).

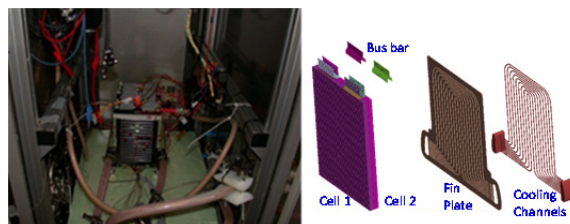


Figure III - 63: A 24-cell module validation test set up for full field simulation against test data for a high-frequency charge/discharge pulse case

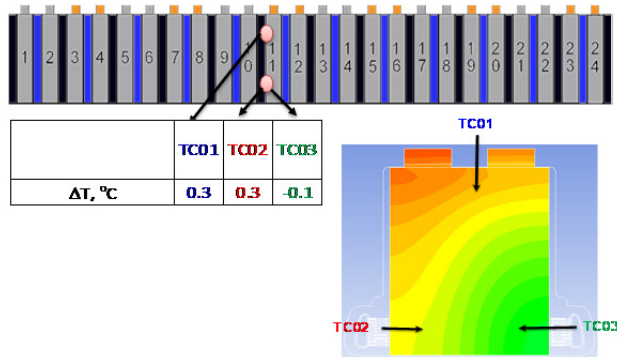


Figure III - 64: Temperature difference between the simulation and the test data at 3 thermocouple locations

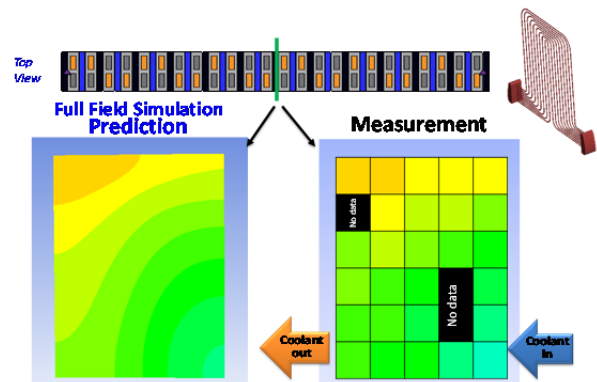


Figure III - 65: Comparison of temperature distribution on the battery surface located in the middle of the module

In 2014, the GM team continued making progress on simulating battery packs and developing system-level simulations with and without ROM. In order to validate the system-level model without ROM approach, GM engineers constructed the system model from an automated ABDT user interface as shown in Figure III - 66. For the high frequency charge/discharge pulse case shown in Figure III - 64 and Figure III - 65, the system simulation (Figure III - 67) required a total CPU time less than 1 minute (Dell Z800 PC) compared to the full field simulation that took 4-5 days on a 64-processor HPC cluster.

The team has also developed a procedure to obtain empirical parameters from HPPC test data that predicts

accurately the load voltage, and hence the heat generation, in cells under various drive-cycles. GM engineers also validated the system-level approach for a realistic USO6 driving cycle as shown in Figure III - 68. The validation of the system simulations for the 24-cell module was completed and the predicted temperatures

were within 0.5°C in comparison with the test data as shown in Figure III - 68. Simulation of 5 back-to-back USO6 drive cycles for a total of 30 minutes driving simulation took less than a few seconds of computational time with the system model.

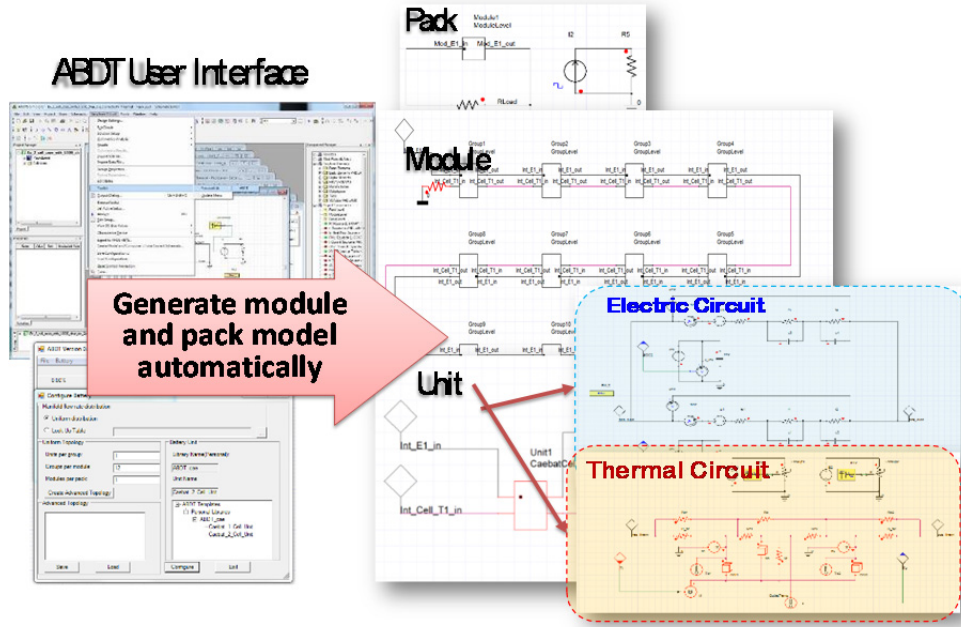


Figure III - 66: Automatic construction of the system model for the 24 cell module from ABDT interface

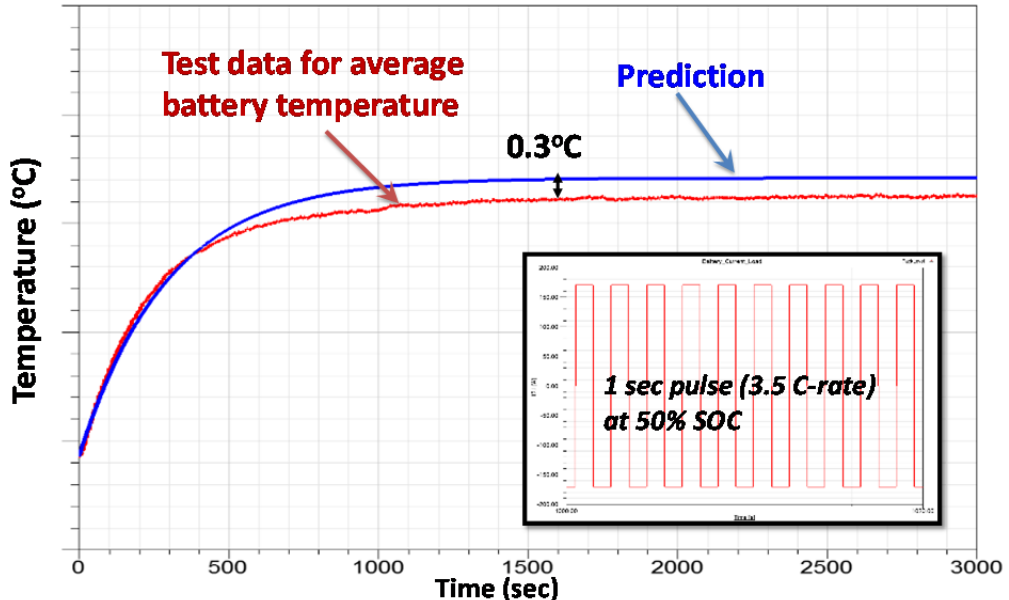


Figure III - 67: Prediction of the battery temperature due to internal heat generation by 1 sec charge/discharge pulses at 3.5 C-rate

The agreement for the pack total heat generation is satisfactory compared with the measured coolant total heat rejection rate and temperature difference between

the inlet and the outlet as shown in Figure III - 68. We demonstrated that the system simulation accurately characterizes the thermal behavior of the cells in the 24-

cell module. Activity also has been initiated to leverage the existing battery-pack CAE models and test data sets for further validation of the new tools.

Finally, as the team continues to develop new simulation tools to be in compliance with OAS, ANSYS

has issued a related product license for Oak Ridge National Lab. ORNL is now actively assisting to ensure OAS compatibility for ANSYS tools.

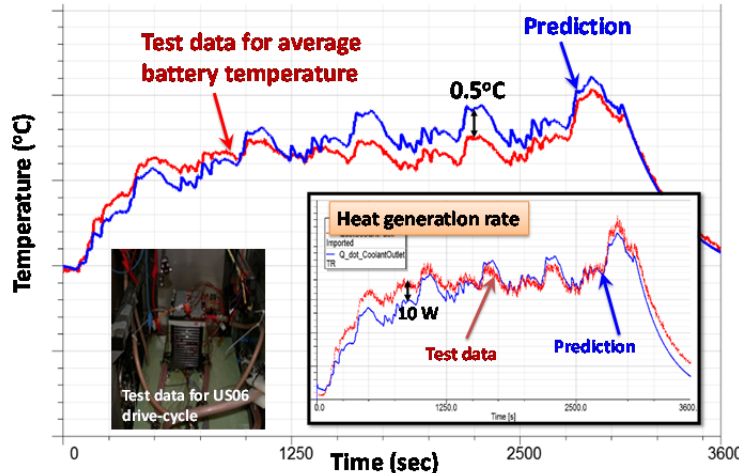


Figure III - 68: Comparison of cell temperatures during US06 Drive-Cycle and the heat generation comparison between the test and the prediction

Conclusions and Future Directions

Overall, the project is on-track and technical progress is consistent with the project plan. A first version of the battery software was officially released to the public with Release 15 of FLUENT in winter of 2014.

Two tasks remain to be completed by the end of 2014.

- 1) Complete the battery life model based on an equivalent circuit model by adding an SEI side reaction branch.
- 2) Complete pack-level validation for the production battery packs to meet the future capability matrix for pack-level CAE.

Acknowledgement

Supported by the Department of Energy, specifically Dave Howell and Brian Cunningham.

FY 2014 Publications/Presentations

1. M. Guo and R. E. White, "Mathematical Model for a Spirally-Wound Lithium-Ion Cell," Journal of Power Sources 250 (2014), also presented at the ECS meeting, spring 2014, Orlando, FL.

2. R. Rebba, J. McDade, S. Kaushik, J. Wang, T. Han, "Verification and Validation of Semi-Empirical Thermal Models for Lithium Ion Batteries," 2014 SAE World Congress, Detroit, MI.
3. G. Li, S. Li, "Physics-Based CFD Simulation of Lithium-Ion Battery under a Real Driving Cycle", Presentation at 2014 ECS and SMEQ Joint International Meeting, Oct 5-9, 2014, Cancun, Mexico.
4. G. Li, S. Li and J. Cao, "Application of the MSMD Framework in the Simulation of Battery Packs", Paper IMECE2014-39882, Proceedings of ASME 2014 International Mechanical Engineering Congress & Exposition, IMECE 2014, Nov 14-20, 2014, Montreal, Canada.
5. Y. Dai, L. Cai, and R. E. White, "Simulation and Analysis of Inhomogeneous Degradation in Large Format LiMn₂O₄/Carbon Cells," Journal of The Electrochemical Society, 161 (8), 2014
6. T. Han, G. Kim, R. White, D. Tselepidakis, "Development of Computer Aided Design Tools for Automotive Batteries," ANSYS Convergence conference, Detroit, MI, June 5, 2014.
7. T. Han, M. Fortier, L. Collins, "Accelerating Electric-Vehicle Battery Development with Advanced Simulation," Aug 21, 2014, Webcast seminar organized by SAE International, sae.org/magazines/webcasts

III.C.5 Development of Computer Aided Design Tools for Automotive Batteries (CD-Adapco)

Kandler Smith (NREL Technical Monitor)

Subcontractor: CD-adapco

Steve Hartridge (Principal Investigator)

CD-adapco, New York

60 Broadhollow Road

Melville, NY 11747

Phone: (631) 549-2300; Fax: (631) 549-2654

E-mail: steve.hartridge@cd-adapco.com

Subcontractor:

Battery Design LLC

2277 DeLucchi Drive

Pleasanton, CA 94588

E-mail: rspotnitz@batdesign.com

Partners:

Johnson Control Inc and A123 Systems

Start Date: August 2011

Projected End Date: July 2014

Objectives

- As one of the subcontract teams, support the DOE/NREL Computer Aided Engineering for Batteries (CAEBAT) activity.
- Develop battery CAE software that reduces design cycle time, reduces the cost and enhances the performance, life and safety of large format automotive cells and packs.
- Specifically develop a numerical simulation model which can resolve the appropriate phenomena required to create a coupled thermal and electrochemical response model.
- Apply advanced numerical techniques to expedite the solution of the governing fundamental equations within lithium ion battery cells.
- In partnership with commercial battery suppliers, validate the accuracy of the numerical models for multiple automotive cell designs and module thermal configurations.

Technical Barriers

One of the major challenges of this project is to include the important aspects of the rapidly maturing lithium ion battery simulation field in to an easy to use, widely accepted computer aided engineering tool. This implementation should be flexible and extensible to ensure the methods can move forward as the level of understanding in the fundamental physics evolves.

Another significant challenge is the creation of a modeling concept for spirally wound cells and their underlying architecture. Spiral cells can be grouped into several categories and hence flexible templates were created, the user then provides appropriate data to populate such templates creating a complete electrochemical and thermal cell model. The creation of such electrochemical and thermal templates and overall method is a significant part of this project.

It should also be stated that obtaining some of the modeling parameters used within such electrochemical models has proved a challenge. Part of proliferating the use of such a coupled thermal-electrochemical tool is to present a process to obtain such parameters to users so there is confidence in results obtained from such models.

Technical Targets

- Create a spiral cell analysis framework that includes the two electrodes wound together to create the spiral jellyroll. This method should resolve the planar electrical/thermal gradients along the length and height of the electrodes as well as the overall performance of the electrode pair.
- Validate the created cell simulation models against test work provided by sub-contractors including both cylindrical and prismatic forms of spiral cells.
- Use the validated methods within a larger framework to create simulations of battery modules including such cells. These methods will be validated against electrical and thermal results from appropriate battery modules.

Accomplishments

- The project has successfully delivered the overall modeling framework, both electrochemical and thermal, as described above in to the computer aided engineering tool STAR-CCM+, produced by CD-adapco.

- An enhanced electrochemistry model has now been created. The original model is based on the work of Newman et al¹⁰. This model has been significantly extended to include the effect of concentration dependence of the solid phase diffusion coefficient¹¹ and also multiple active materials as often found in contemporary lithium ion cell design.
- Electrochemical and thermal datasets have been created and validated within the project for the spiral cells listed below. These have been created after the provision of cell specific data from Johnson Controls Inc. A process to extract the unknown electrochemical properties from specific test work has been developed.
- A dataset of contemporary electrolytes has been added to the simulation environment. The dataset contains molarity, conductivity, diffusion coefficient, transport number, activity coefficient, density, and viscosity for 12 electrolytes. All values are concentration and temperature dependent within appropriate ranges.
- An approach to simulating aging within lithium ion cells has been formulated which considers SEI layer growth and associated capacity reduction driven by lithium loss. This model is based on the work of H. Ploehn¹².
- The Star-CCM+ flagship commercial software of CD-adapco was released with battery modeling module developed under this CAEBAT project. Many around the world use this tool for accelerating battery design.



Introduction

Department of Energy established the Computer Aided Engineering for Electric Drive Vehicle Batteries (CAEBAT) activity to develop multi-physic design tools. NREL, with guidance from DOE, co-funded three

¹⁰ Simulation and Optimization of the Dual Lithium Ion Insertion Cell, T. Fuller, M. Doyle, J. Newman, J. Electrochem. Soc. 141 (1994) 1-10

¹¹ Concentration dependence of lithium diffusion coefficient in LiCoO₂, Young-II Jang, Bernd J. Neudecker, and Nancy J. Dudney, Electrochemical and Solid-State Letters, 4 (6) A74-A77 (2001)

¹² Solvent diffusion model for aging of lithium-Ion battery cells, Ploehn, P Ramadass & R. White J. Electrochem. Soc A456-A462(2004).

subcontractors including CD-adapco, to develop software tools for CAEBAT. CD-adapco has extended its class leading computer aided engineering code, STAR-CCM+, to analyze the flow, thermal and electrochemical phenomena occurring within spirally wound lithium ion battery modules and packs. This coding has been developed in collaboration with Battery Design LLC who is a sub-contractor to CD-adapco and has considerable experience in the field of electrochemistry modeling. As well as resolving the electrochemically active regions in a spiral cell the model accounts for the tabbing of the electrode in the overall performance.

The created electrochemical model has now been applied to the lithium ion cells listed below, excluding the pouch cell where an empirical model has been used.

Manufacturer	Format	Capacity
JCI	Cylindrical	7Ah (HP)
JCI	Cylindrical	40Ah (HE)
JCI	Prismatic	6Ah (HP)
JCI	Prismatic	27Ah (HE)
A123	Pouch	20Ah

Approach

Detailed design information was obtained from Johnson Controls Inc. to describe the dimensions of the electrode, the details of the can and finally details of the electrode chemistry used in each of the designs. These cell models also used the appropriate electrolyte formulation from the newly integrated dataset provided by K. Gering at INL (also part of this project). Tightly controlled cell level test work was specified to enable the remaining modeling parameters to be extracted. This has now been done for all 4 spiral cells. The project now has a high level of confidence in the overall process, including cell test work specification and parameter extraction. This is borne out by the validation results presented below.

Results - Electrochemistry

Electrochemistry: A validation of the voltage response from the created models was completed. This validation used either a charge-sustaining or charge-depleting load as appropriate for the cell in question and compared with experimentally obtained voltage curves. Validation results are shown below.

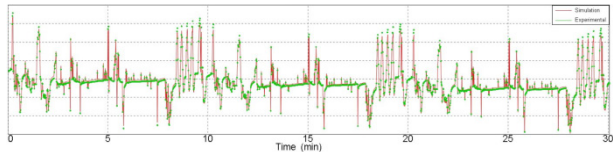


Figure III - 69: Voltage response from the created electrochemical model for the JCI VL6P cell over a 30min drive cycle compared to test work (Voltage scale removed)

The mean squared error for the VL6P simulation model (Figure III - 69) over the 30 minute drive cycle is 9 mV. Similar error levels are seen in the other models for various cell sizes. (See Figure III - 70 and Figure III - 71)

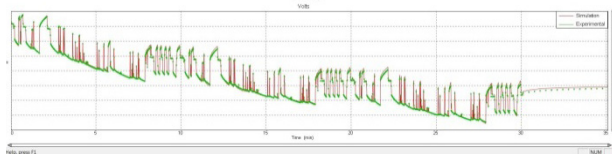


Figure III - 70: Voltage response using the electrochemistry model for the JCI VL41M high energy cell over a 30min drive cycle compared to test work (Voltage scale removed)

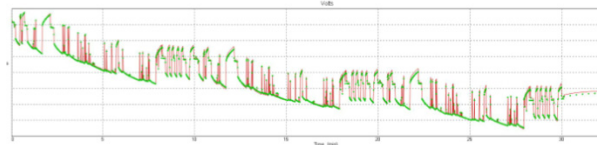


Figure III - 71: Voltage response using the electrochemistry model for the PL27M cell over a 30min drive cycle compared to test work (Voltage scale removed)

The above validation work was completed using a ‘lumped’ electrochemistry model. This essentially means a single temperature for the whole cell is assumed. The cell representations were then transferred in to STAR-CCM+ and complex three dimensional models of the cell were created. This model now accounts for the internal anisotropic thermal conductivity of the jelly roll as well as its thermal interfaces with neighbor components such as mandrels and external cans. The electric conductivity of the current collectors is also included in the model. Figure III - 72 compares the simulation results for the VL6P electrochemistry model using the lumped model and the 3D model. The mean difference is 8mV over the 30 minute drive cycle. Differences are expected within the results due to the 3D model having a distribution of temperature within the jelly roll, hence a differing response. Overall we can conclude that the voltage response of the cell is well captured within both lumped and 3D modeling domains hence engineers can use the same cell data within either modeling framework, lumped or detailed 3D.

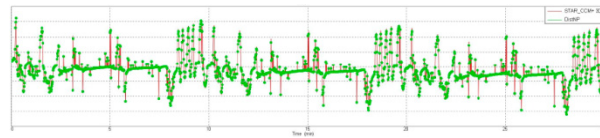


Figure III - 72: Comparison of lumped electrochemistry model vs three dimensional electrochemistry model over a 30min drive cycle (Voltage scale removed)

Thermal: The thermal validation was completed using the 3D model within STAR-CCM+. Module test work for all the cells has now been complete. Figure III - 73 shows the VL6P 12 module that is used within the module tests. This arrangement is liquid-cooled.

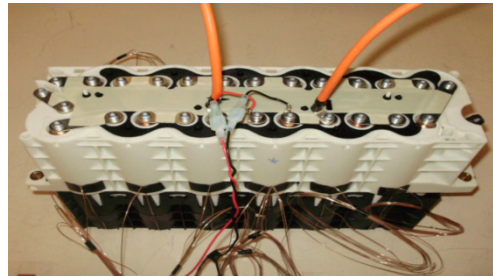


Figure III - 73: Johnson Controls 12 cell module ready for testing

The main thermal validation test used the same drive cycle input condition as used in the lumped model and cell can surface temperatures were monitored.

A high fidelity finite volume model was created within STAR-CCM+ including all cell components (jelly rolls, current collection designs, outer cans) as well as current carrying straps and coolant system. (See Figure III - 74.)

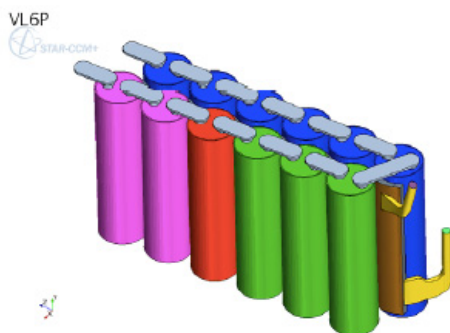


Figure III - 74: High fidelity finite volume model within STAR-CCM+

A number of thermal couples were located on the cell of interest and Figure III - 75 shows one result compared to the appropriate test result. These thermocouples were located on the outer surface of the cell can.

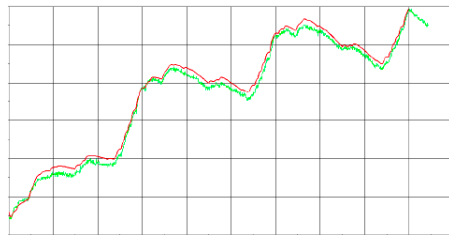


Figure III - 75: Thermal result for a cell within the VL6P module (red line is simulation, green line is experiment)

The spatial distribution around the cell is considered by having a number of thermocouples and this was used to validate the simulation model. Due to the confidential nature of the commercial cells and modules used for validation more extensive plots cannot be shown within this report.

Blind Test: As well as the original US06 drive cycle experiments towards the end of the project it was decided to expand the scope and do several blind tests on a different drive cycle. This tested the flexibility and general applicability of the model. The second drive cycle chosen was a worldwide harmonized light vehicles test procedure (abbreviated to WLTP) and this was performed on the VL6P also. Figure III - 76 and Figure III - 77 show electrical and thermal performances of the model.

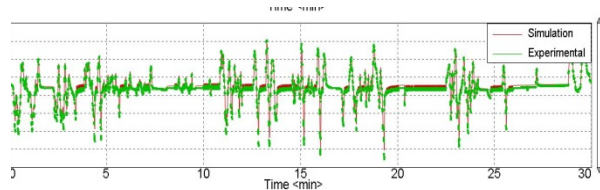


Figure III - 76. Voltage prediction for WLTP drive cycle as a blind test (Voltage scale removed)

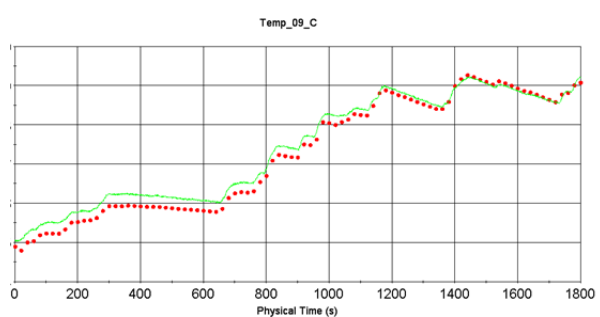


Figure III - 77. Thermal result for a cell within the VL6P module using WLTP drive cycle (red dots are simulation, green line is experiment)

Conclusions and Future Directions

The breadth of lithium ion cells covered by this work and the addition of the WLTP drive cycle demonstrate that coupled electrochemical and thermal highly resolved 3D simulations are now possible within a mainstream CAE framework. Although a significant proportion of the cell specific details remained confidential the learning and method development covering how to conduct studies and the critical points to focus on is now openly available from CD-adapco and its project partners. Star-CCM+ with battery modeling methods developed under the DOE CAEBAT activity can be licensed from CD-adapco. These methods are already being used outside of this project to add value to other lithium ion applications.

The project is now complete (July 2014) and final reports have been issued. A dedicated team at CD-adapco continues to move these methods forward and expand the coverage of the tool to address other lithium ion applications.

Acknowledgments

The subcontractors would like to acknowledge the contribution and input that the National Renewable Energy Laboratory has made, particularly Kandler Smith and the support of the Department of Energy, specifically Dave Howell and Brian Cunningham. The authors would like to acknowledge the subcontractors, namely JCI, Inc and A123 Systems, support in sharing some of the results from this work.

III.C.6 Development of Computer Aided Design Tools for Automotive Batteries (EC Power)

Shriram Santhanagopalan (NREL Technical Monitor)

Subcontractor: EC Power

Christian Shaffer (Project Manager)

341 N. Science Park Road
State College, PA 16803

Phone: (814) 861-6233; Fax: (814) 861-6234
E-mail: ceshaffer@ecpowergroup.com

Partners:

Ford Motor Company
Johnson Controls, Inc.
Penn State University

Start Date: June 2011

End Date: December 2014

Objectives

The objectives of this work, in support of the DOE/NREL CAEBAT activity, are:

- Develop a commercial electrochemical-thermal coupled model and associated computer code for large-format, automotive Li-ion cells and packs.
- Create a novel computational framework that allows for rapid and accurate performance/safety simulations. Algorithms will span several length scales, ranging from particle size, to an electrochemical unit cell, to a 3D battery, and finally to an entire battery pack. This computational framework will be able to model both wound and stacked cell geometries.
- Develop a comprehensive materials database that is critical for accurate modeling and simulation of large-format Li-ion batteries.
- Test and validate the developed cell and pack models against a wide range of operating conditions relevant to automotive use, such as extreme temperature operation, complex power profiles, etc.

Technical Barriers

The large format nature of automotive Li-ion batteries presents a unique set of challenges that set them apart from the batteries used in cell phones,

laptops, and other consumer goods. For example, high rates of charge and discharge, in combination with the large surface area of the cell, lead to widely varied temperature distributions on the cell and throughout the packs. This non-uniformity causes a number of serious issues, including poor battery performance, increased degradation effects, potential safety concerns, and the inability to fully utilize the active material inside the battery. Creating actual cells and packs is time consuming and extremely expensive, which makes an efficient, high fidelity simulation tool very desirable.

However, the strongly coupled nature of electrochemical and thermal physics, the relevant scales of a battery cell or pack (ranging from sub-microns to meters), and the need for a comprehensive materials database, makes the creation and development of a Li-ion battery model a unique and challenging task.

Technical Targets

- Development of an extensive database of material properties for accurate model input.
- Creation of a multi-dimensional, electrochemical-thermal coupled model, complete with an easy to use, intuitive graphical user interface (GUI).
- Development of fast, scalable numerical algorithms enabling near real-time simulation of batteries on a single PC, and packs with thermal management systems on a small computer cluster.
- Experimental validation of the model and corresponding software.

Accomplishments

- Delivered final version of our large-format software tool, "Electrochemical-Thermal Coupled 3-Dimensional Li-ion Battery Model" (ECT3D) to partners during FY2014. Recent updates to software included additional technical features, enhanced robustness and execution speed, and upgrades based on Ford, JCI, and NREL user feedback.
- Property characterization for materials database complete.
- Final validation complete.
- Demonstrated advanced coupling of ECT3D with third party software via Open Architecture Standard developed by Oak Ridge National Laboratory.

- Eighteen high-impact publications and presentations from the team over the course of the project.
- The AutoLion™ commercial software developed in part under this project has been well received, with approximately 30 licensees employing the software.
- AutoLion™ software is now being applied in markets beyond automotive, including batteries designed for personal and wearable electronics devices and large-scale energy storage.



Introduction

In order to reduce greenhouse gas emissions and reduce the U.S. dependence of foreign oil, the development of hybrid electric, electric, and plug-in electric (HEV, EV, PHEV) vehicles is extremely important. The Li-ion chemistry used in automotive batteries can store large amounts of energy, while maintaining a low weight (relative to other battery chemistries).

The design, build, and testing process for batteries and packs is extremely time consuming and expensive. The Computer Aided Engineering for electric drive Batteries (CAEBAT) activity was initiated by DOE and monitored by NREL to develop software tools to accelerate the development and design of batteries.

EC Power's code, ECT3D, directly addresses the issues related to the design and engineering of these cells. Many technical characteristics of batteries and packs that are critical to battery performance and safety are impossible to measure experimentally.

However, these same characteristics are easily analyzed using ECT3D in a virtual environment. The use of advanced software such as ECT3D allows the design engineer to gain unique insights into the performance of his/her system that would be inaccessible via experimental measurements. Furthermore, the analysis is done completely in a virtual environment, eliminating the need for any physical production of test cells.

Approach

EC Power has developed the large-format, li-ion battery simulation software, ECT3D to analyze battery cells and packs for electrified vehicles (EV, PHEV, HEV). Team member Penn State University was primarily responsible for performing materials characterization experiments and diagnostic experiments for multi-dimensional validation. The materials characterization experiments supplied data for the extensive materials database incorporated into ECT3D.

Industrial partners Ford Motor Company and Johnson Controls, Inc. are currently testing and validating ECT3D to ensure its utility for industrial use. The overarching goal of the project is to produce a world-class, large-format lithium-ion cell and pack design tool that drives innovation and accelerates the design process for electric vehicles and their power systems.

Results

Figure III - 78 highlights the validation of the external shorting safety model developed during the course of the project. In addition to external shorting, we also developed models to simulate internal shorting and nail penetration. Specifically in these figures, we note overall good agreement for simulated and experimental voltage, current, and local temperature over the entire shorting process. A maximum error of approximately 2% was observed for voltage, 10% for current, and ~4% error for local temperatures at the peak time (~16s). The cell-internal temperature measurement was made using a novel reaction temperature sensor (RTS). These results emphasize the importance of measuring or predicting the local cell-internal temperature as an appropriate metric for safety. As observed below, a difference in peak temperature of 45°C was observed. A local (surface) temperature of 85°C does not indicate safety concerns, but a temperature of 130°C (internal temperature) may be on the verge of thermal runaway.

Figure III - 79 illustrates a good example of how the software can be applied to enhance cell design efficiency and materials utilization. The cell's normalized energy is shown on the y axis, and the x axis gives the cell time-averaged current density non-uniformity factor (CDNUF). Details can be found in reference [15], but the CDNUF is generally a metric used to measure how non-uniform the current density is within a large-format cell; typically the larger this value, the poorer the active materials utilization, and the less energy can be usefully extracted from the same amount of active material. Specifically, Figure III - 79 shows the results of simulated cells with various numbers of tabs in both symmetric and asymmetric format, along with experimental data from 2.4Ah cells with various tab designs. Clearly, the results show that a larger number of tabs can increase the energy efficiency of the cell by more than 50%. Note that while continuous tabs are widely used to reduce the CDNUF, they can also add substantial weight to the cell; this multi-tab design is an example of lean engineering. Further, this highlights one example of how to increase a large format cell's energy density not through material innovations, but rather by cell engineering.

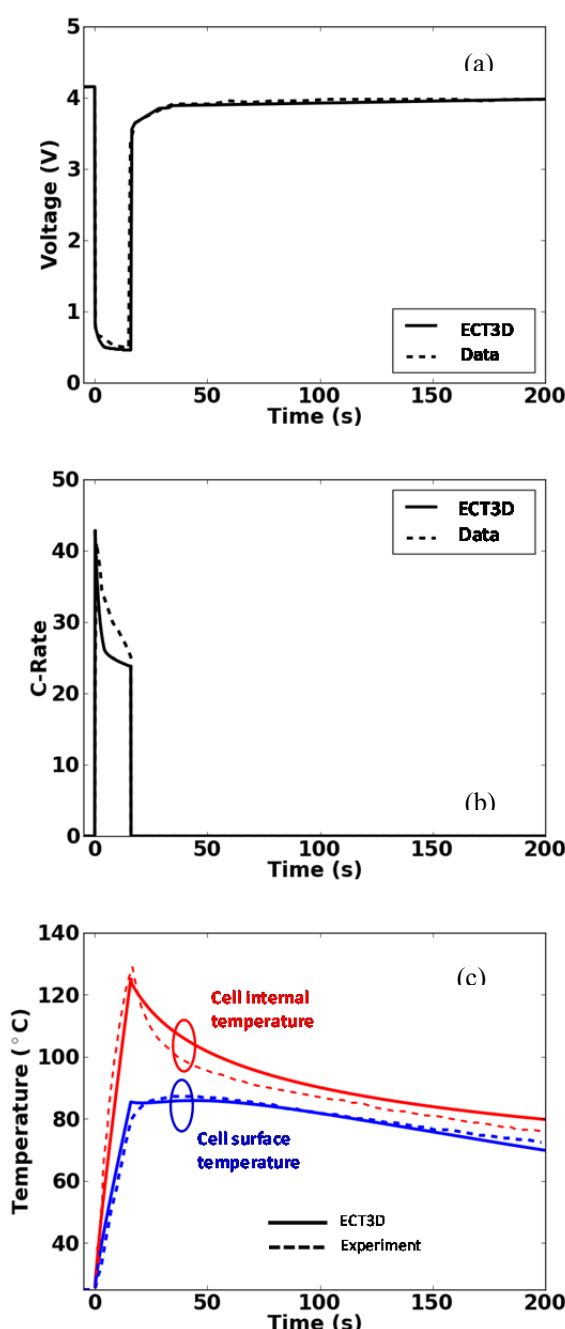


Figure III - 78: Validation of externally shorted 1.6 Ah NMC/graphite 18650 cell; experimental data acquired using RTS sensor [14,16,17]. (a) voltage, (b) current (C-rate), and (c) cell-internal and surface temperatures

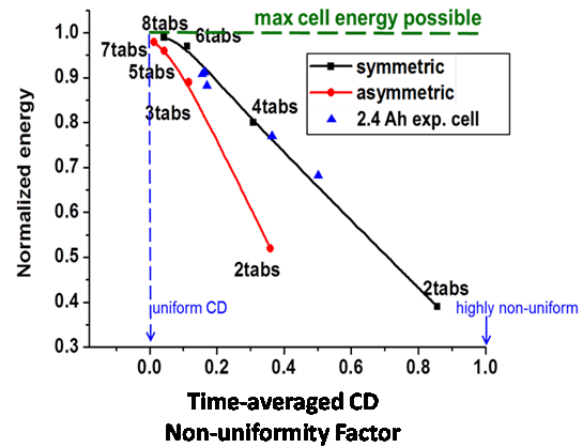


Figure III - 79: Cell normalized energy vs. time-averaged current density non-uniformity factor for cells with various tab designs (experiment and simulation results shown) [15]

Conclusions and Future Directions

EC Power has completed the project successfully, accomplishing all goals set forth at the outset. The final version of the ECT3D software contains an extensive materials database, including NMC, LFP, LMO, and LCO cathode materials, along with graphite and LTO anode materials characterized between $-30^{\circ}\text{C} < T < 60^{\circ}\text{C}$. The validated software accurately predicts the coupled thermal and electrochemical response of large-format batteries, and has been used to investigate enhanced cell design for reduced weight, volume, and cost, enhanced safety, and life prediction under real-world driving conditions. The pack model has likewise been used in the design of advanced thermal management strategies. AutoLion™ commercial version of ECT3D software is offered commercially and 30 licensees are employing the software to design battery cells and packs for various applications.

Project Term Publications/Presentations

- Wei Zhao, C.Y. Wang, Gang Luo, Christian E. Shaffer, “New Findings on Large Li-ion Battery Safety through Computer Simulation”, Battery Safety 2011- Advancements in System Design, Integration, & Testing for Safety & Reliability, November 9-10, 2011, Las Vegas, NV.
- G. Luo and C.Y. Wang, A Multi-dimensional, Electrochemical-Thermal Coupled Li-ion Battery Model, Chap.6 in Lithium-Ion Batteries: Advanced Materials and Technologies, CRC Press, 2012.
- Yang, Xiao Guang, Miller, Ted and Yu, Paul, Ford Motor Company, “Li-Ion Electrochemical Model,” 2012 Automotive Simulation World Congress, October 30-31, 2012, Detroit, MI

4. Shaffer, C.E., Wang, C.Y., Luo, G. and Zhao, W., "Safety Analysis Design of Lithium-ion Battery EV Pack through Computer Simulation," Battery Safety 2012, Knowledge Foundation Conference, December 6-7, 2012, Las Vegas, NV.
5. Shaffer, C.E. and Wang, C.Y., "Thermal Management for Start-up of Li-Ion Batteries," 222nd Meeting of The Electrochemical Society (PRiME 2012), Honolulu, HI, October 7-12, 2012
6. Luo, Gang, Shaffer, C.E. and Wang C.Y., "Electrochemical-thermal Coupled Modeling for Battery Pack Design," 222nd Meeting of The Electrochemical Society (PRiME 2012), Honolulu, HI, October 7-12, 2012.
7. G.S. Zhang, L. Cao, S. Ge, C.Y. Wang, C. E. Shaffer, C. D. Rahn, In Situ Measurement of Li-Ion Battery Internal Temperature, 224th ECS Meeting, Abstract #538, San Francisco, CA, U.S., Oct. 27 - Nov. 01, 2013.
8. Kalupson, J., Luo, G. and Shaffer, C., "AutoLion™: A Thermally Coupled Simulation Tool for Automotive Li-ion Batteries," SAE Technical Paper 2013-01-1522, 2013, doi: 10.4271/2013-01-1522. SAE International World Congress and Exhibition, April 16, 2013, Detroit, MI.
9. Ji, Y., Zhang, Y., and Wang, C.Y. (2013). "Li-Ion operation at low temperatures," Journal of the Electrochemical Society, 160(4), A636-A649.
10. Zhang, G., Shaffer, C. E., Wang, C. Y., & Rahn, C. D. (2013). "In-situ measurement of current distribution in a li-ion cell," Journal of the Electrochemical Society, 160(4), A610-A615.
11. Ji, Y., Wang, C.Y. (2013). "Heating strategies for Li-ion batteries operated from subzero temperatures," *Electrochimica Acta*, 107, 664-674.
12. Zhang, G., Shaffer, C.E., Wang, C.Y., and Rahn, C.D. (2013), "Effects of Non-uniform Current Distribution on Energy Density of Li-ion Cells," *Journal of the Electrochemical Society* 160(11), A2299-A2305.
13. W. Zhao, G. Luo and CY Wang, "Modeling Nail Penetration Process in Large-Format Li-ion Cells," submitted to *J power sources* (2014).
14. Zhang, G., Cao, L., Ge, S., Wang, C.Y., Shaffer, C.E. and Rahn, C.D. (2014). "In Situ Measurement of Radial Temperature Distributions in Cylindrical Li-Ion Cells," *Journal of the Electrochemical Society*, 161, A1499-A1507.
15. W. Zhao, G. Luo, and C.Y. Wang, "Effect of Tab Design on Large-format Li-ion Cell Performance," *Journal of Power Sources* 257 70-79 (2014).
16. G. Zhang, L. Cao, S. Ge, C. Y. Wang, C.E. Shaffer, and C.D. Rahn, "In Situ Measurement of Temperature Distribution in Cylindrical Li-Ion Cells," 226th ECS Meeting, Cancun, Mexico, October 9, 2014.
17. Guangsheng Zhang, Lei Cao, Shanghai Ge, Chao-Yang Wang, Christian E. Shaffer, and Christopher D. Rahn, "Reaction temperature sensing (RTS)-based control for Li-ion battery safety," submitted for publication in *Nature Communications* (2014).
18. Qing Wang, Christian Shaffer, and Puneet Sinha, "Implications of Cell Design on Safety of Large-format Li-ion Batteries Undergoing Nail Penetration," submitted for publication in *Journal of Power Sources* (2014).

III.C.7 Coupling of Mechanical Behavior of Cell Components to Electrochemical-Thermal Models for Computer-Aided Engineering of Batteries Under Abuse (NREL, MIT, ANSYS)

Ahmad Pesaran (Principal Investigator)

National Renewable Energy Laboratory
15013 Denver West Parkway MS 1633
Golden CO 80401
Phone: (303) 275-4441; Fax: (303) 275-4415
E-mail: Ahamd.Pesaran@nrel.gov

NREL Collaborators:

Shriram Santhanagopalan, Gi-Heon Kim, Chuanbo Yang, Chao Zhang, Michael A. Sprague

Subcontractor:

Massachusetts Institute of Technology
Ansys, Inc.

Start Date: October 2013

Projected End Date: September 2015

Objective

- The main objective is to develop a model to couple the electrochemical-thermal (ECT) behavior of a lithium-ion cell to its structural behavior after rapid mechanical deformation.
- A second objective is to develop a model to predict the thermal response of cells to thermal ramp.
- A supporting objective is to make the models compatible with CAEBAT-1 and its Open Architecture Software (OAS) for wider proliferation of their use.

Technical Barriers

- Non-availability of a standard experimental approach that is widely accepted by the industry to characterize the mechanical response of a lithium ion cell, and resulting implications for battery safety.
- Limited understanding of physical phenomena that take place within a lithium ion cell just before and after introduction of a short-circuit.
- Inability of simplified safety models to identify the mechanism behind a variety of short-circuit responses observed following a mechanical crush of a lithium ion cell.

Technical Targets

The major technical targets for this effort include:

- Creation of an experimentally validated mechanical deformation model for a lithium ion cell.
- Development of a mechanism to understand the interaction between the mechanical effects and the run-away reactions that occur within the cell.
- Implementation of the coupling between mechanical and electrochemical-thermal models on the ANSYS software platform.

Accomplishments

- Built two types of material models for electrode assemblies, the isotropic and the anisotropic one, to simulate local deformation and damage of batteries.
- Used experimental results to calibrate the new anisotropic model.
- Developed a coupled modeling methodology encompassing the mechanical, thermal and electrical response for predicting short circuit mechanism of a cell under external load.



Introduction

During the first phase of CAEBAT, performance models simulating the electrochemical and thermal performance of lithium ion batteries were developed and incorporated into commercially available software tools. Efforts towards modeling abuse response were initiated. The existing models in the literature as well as those developed under the previous phase of CAEBAT assume a predetermined value for the short circuit resistance when calculating the heat generation rate during thermal runaway events. Thus, depending on the value of contact resistance chosen for a particular simulation case, the outcome of the cell response can be varied arbitrarily. Thus, the existing models are limited in their ability to predict the outcome of an internal short circuit or mechanical crush.

In the current effort, we develop a methodology to couple the mechanical response of the different cell components (such as the anode, cathode, separator, etc.) with NREL's Electrochemical Thermal Models, to

provide a comprehensive set of tools that will allow us to compute properties such as the nature of the short-circuit or the evolution of the short resistance as a function of the chemical composition, thermal and electrical properties, as well as the mechanical constraints on the material, thereby accounting for experimental observations using realistic modeling tools.

Approach

Simulating simultaneous mechanical, electrochemical, and thermal response of a cell due to crush is very complex and requires modeling simplifications. Our approach is to assume that crush is rapid (e.g., the cell is damaged in less than a fraction of a second). We also assume that electrochemical and thermal response of a cell takes longer than seconds - this allows us to couple the mechanical aspect with the thermal aspect in a sequential, one-way fashion.

- In order to identify the location of cracks originating within the cell during a compression test, two mechanical models – one isotropic and another non-isotropic, were developed by MIT.
- Comparisons to experimentally measured load versus displacement curves as well as CT scans were used to verify the validity of the models.
- A comparison between the solution of thermal/electrochemical models on the deformed geometry versus the use of an effective resistance to characterize the mechanical damage, will be performed.
- Additional tests required to calibrate the new material properties associated with the anisotropic model will be performed in FY15.

Results

Mechanical Simulations: Figure III - 80 shows the different simplifications to the mechanical representation of a lithium ion cell: the representative volume element (RVE) approach uses one effective layer with equivalent mechanical properties to represent the composite stack of active material, current collectors and separator. The representative sandwich (RS) modeling approach retains the properties of the individual layers; but uses one sandwich, with the thickness values scaled, to represent the repeat units of the different components within the cell.



Figure III - 80: Simplified representations of a lithium ion cell used in the mechanical/electrical simulations: the RVE approach is efficient in calibrating the cell response to measured values of the mechanical response of individual layers. The RS model is useful to simulate electrical short-circuit across the different components on the deformed geometry

Figure III - 81 shows crack orientations for a small pouch cell under hemispherical loading, assuming three trial failure strains for the RVE. The load versus displacement calibration shows good agreement with the test results.

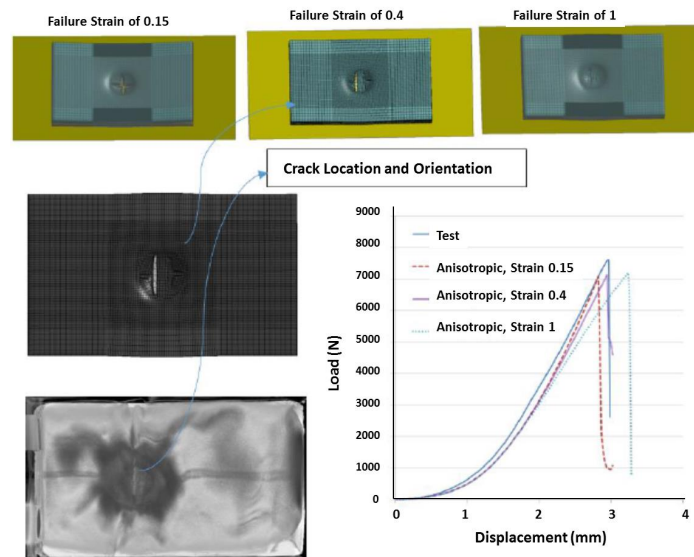


Figure III - 81: Location of crack and comparison of load-displacement curves. Simulations were performed with anisotropic pouch cell model using the RVE at assumed failure strains of 0.15, 0.4 and 1.0

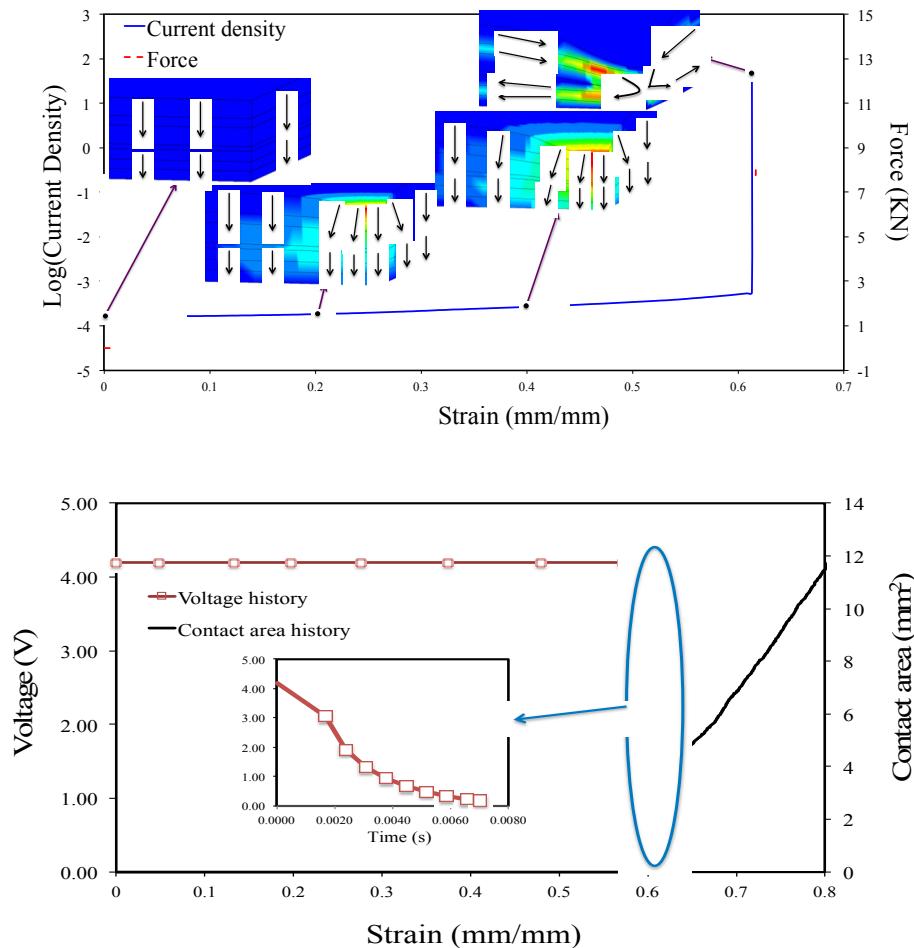


Figure III - 82: Current density across the active material before and after a short-circuit at different levels of total strain and the corresponding plot of current vectors during an indentation on a prismatic cell similar to the test shown on the previous figure: the RS model was used to calculate voltage history and evolution of the short-circuit area during the crush

Figure III - 82 shows the current density and voltage with the progression of the short circuit, and evolution of the short-circuit area across the different layers as a function of time, predicted based on the electrical and mechanical properties of the different layers.

Conclusions and Future Directions

Two different representations for the cell geometry – the layer-by-layer model and the representative sandwich model, were developed. Comparisons with experimental data from MIT indicate that the representative sandwich model adequately captures the mechanics of deformation of a cell. This approach expedites the mechanical simulations considerably. Different approaches to couple mechanical response of the cell to thermal/electrical response were developed. Results from the first implementation, that involves performing the electrical simulations on the deformed mesh in LS-DYNA were discussed in this report.

Future work will involve building a robust coupling methodology between existing thermal-electrochemical models for lithium-ion cell abuse, with the origin and evolution of a short-circuit as shown in this report.

FY 2014 Publications/Presentations

1. T. Wierzbicki and E. Sahraei, “Homogenized mechanical properties for the jellyroll of cylindrical Lithium-ion cells,” *J. Power Sources*, Vol. 241, pp. 467-476, 2013.
2. E. Sahraei E., J. Meier, T. Wierzbicki, “Characterizing mechanical properties and onset of short circuit for three types of lithium-ion pouch cells,” *J. Power Sources*, Vol. 247, pp. 503–516, 2014.
3. C. Yang, G-H.Kim, S. Santhanagopalan, A. Pesaran, “Multiphysics Modeling of Thermal

- Runaway in a Li-Ion Battery”, Presented at the 225th ECS Meeting, May 2014, Orlando FL.
4. S. Santhanagopalan, “Mathematical Modeling of Battery Safety under Crush”, Presented at the Discussion of Issues Related to Safety of Batteries in Hybrid and Electric Vehicles by the International Energy Agency, January 2014, Washington, D.C.
 5. C. Zhang, S. Santhanagopalan, M. Sprague, A. Pesaran, “Coupled Mechanical-Electrical-Thermal Modeling for Lithium-ion Batteries”, *J. Power Sources*, Under Review.

III.C.8 Mechanistic Modeling Framework for Predicting Extreme Battery Response: Coupled Hierarchical Models for Thermal, Mechanical, Electrical and (Electro)chemical Processes (SNL, ORNL, Col School of Mines)

Tony Geller (Sandia Program Manager)

Sandia National Laboratories

Albuquerque, NM 87185-0836

Phone: (505) 844-7795; Fax: (505) 844-4523

E-mail: asgelle@sandia.gov

Harry Moffat (PI)

Phone: (505) 844-6912; Fax: (505) 844-9297

E-mail: hkmoffa@sandia.gov

Subcontractor:

S. Pannala, Oak Ridge National Labs, TN

R. Kee, Colorado School of Mines, CO

Start Date: Oct 2013

Projected End Date: September 2015

Objectives

- Address root cause and implications of thermal runaway of Li-ion batteries by delivering a software architecture solution that can lead to the development of predictive mechanisms that are based on identification of species.

Technical Barriers

Key technical risks involve the lack of mechanistic understanding of interfacial layers associated with electrodes in the Li-ion system.

Additionally barriers involving the development of mechanistic understanding of degradation mechanisms and detailed kinetics of solid phase processes and liquid phase secondary reactions abound with the Li-ion battery community.

Technical Targets

- Implement 1DElectrode capability within CAEBAT and verify.
- Implement partially saturated porous flow and solid mechanics modeling within 1DElectrode.
- Develop consistent thermodynamic/transport models of the entire cell using CANTERA. Add

partial saturation and solid mechanics models to CAEBAT. Build SEI models that can predict the autocatalytic temperature behavior experimentally observed.

- Implement upscaling ideas from microstructure models within CAEBAT using both averaged results and perhaps statistical distributions.
- Exercise new capability by developing new models for thermal runaway processes with 1DElectrode / CAEBAT.

Accomplishments

- Linked 1DElectrode model into CAEBAT architecture, running thermal and electrical simulations using AMPERES/1DElectrode.
- Validated models against Dualfoil model within 1DElectrode/CAEBAT.
- Developed microstructural electrode models from experimental FIB-SEM and X-ray tomography reconstructions.
- Effective electrode properties are extracted from microscale models, which can be used in CAEBAT cell-scale models.
- 1DElectrode model improvements include real thermodynamics based chemistry, Stefan-Maxwell non-dilute diffusion, and consistent enthalpy-based, multi-species energy conservation. This is new to battery modeling software.
- A formulation for two-phase, multispecies electrochemical transport in porous electrodes has been developed for subsequent implementation into 1DElectrode. This is also new to the battery modeling community.
- Successfully reconstructed 3D microscale digital models of Li-ion cathodes from FIB-SEM images and developed electrochemical transport models with Faradaic and Ohmic internal heat generation.
- Successfully simulated a 1C discharge rate in a cathode using the reconstructed 3D microscale model showing reasonable cell potential and Joule heating curves over full discharge cycle.



Introduction

We are expanding the functionality of the CAEBAT-I architecture developed at Oak Ridge National Laboratory by incorporating advanced speciation models. These models are built on the Cantera open-source software library for elementary thermodynamic, transport and kinetic processes. We will be implementing this modeling capability to address two key aspects of Li-Ion battery chemistry that will support the existing CAEBAT-I program.

- 1) Modeling the processes that transform chemical energy to thermal energy in abusive scenarios and the associated heat release for both normal operation and abusive conditions. In doing this we focus on interactions between electrode-particle scale physics present within our Cantera-based approach and the cell-level physics already present within the CAEBAT framework. We will add models that can capture the autocatalytic temperature rise observed at elevated temperatures, fitting data from Sandia's BATLab program.
- 2) Modeling thermo-electro-mechanical interactions within porous materials that determine the heat, mass and electrical transport processes, addressing cell-level structural evolution under normal operation and abusive conditions. This will include modeling gasification mechanisms by adding partial saturated flow to battery models so that mechanisms for gasification may be envisioned and applied in at least a 1D context.

Our modular approach will emphasize hierarchical approaches to modeling the detailed chemistry system and onset of thermal abuse from a species-specific point of view. These represent a natural extension to the current CAEBAT architecture currently developed at ORNL. We will also develop upscaling algorithms to bring information from subgrid variations in microstructure developed by Prof. Bob Kee at the Colorado School of Mines to the macrohomogeneous scale. This approach to incorporating detailed chemistry and fundamental processes into the CAEBAT OAS is based on the open-source program Cantera. Our first goal is to advance the state of the art in modeling chemical processes within the battery community using open software standards. Because the battery community has lacked such an infrastructure, fundamental quantitative comparisons of chemistry have not occurred to a significant extent within the community. We expect to emulate what has occurred within the combustion community with programs such as Chemkin, which brought together experimentalists and computational scientists to create an infrastructure,

which was then used to quantitatively understand and predict mechanistic details.

Approach

We have two complimentary goals within this project. The first goal is to advance the state of the art in modeling chemical processes within the battery community using open software standards. This is an important and often misunderstood goal. Because the battery community has lacked such an infrastructure, fundamental quantitative comparisons of chemistry have not occurred to a significant extent within the community. We hope to emulate what has occurred within the combustion community with programs such as Chemkin, which brought together experimentalists and computational scientists to create an infrastructure which was then used to elucidate mechanistic details.

The second goal of the project is to start populating this infrastructure with models of various levels of fidelity that may address the thermal runaway process observed to occur within Li-ion batteries. Ideally this would involve understanding the formation of the SEI layer and its evolution as a function of temperature. Although the mechanistic details of this process as well as inputs for constitutive models that would make a model for this are not available for engineering-level capabilities; we will propose starting with those models and then refine them using the experimental data from Sandia's BATLab program to interpret the thermal runaway process from an engineering perspective. Furthermore, we will expand the engineering details into more sophisticated level that will track individual species in mechanisms that closely resembles the corrosion processes based on our current understanding of the stability of the passivating layers. This would necessarily involve determining the stability and thermodynamics of components of the SEI layer as a function of temperature and pressure.

An unappreciated feature of batteries is the need to understand the thermo-mechanical interactions of the porous materials as a function of the state of discharge and as a function of the number of cycles. We at Sandia have started to address this issue within our codes and would like to transfer some of the technology to the CAEBAT architecture with collaboration from ORNL. This involves solving the partially saturated flow equations, which are important for some battery systems, and represent failure mechanisms in others. And we also propose to include the poroelastic stress constitutive equations using the effective stress principles. This concept is essentially new to batteries, though we have extensively used it in other contexts with Sandia codes such as Goma, which can model the mechanical environments found in drying porous media or porous media in contact with continuum fluids that undergo external stresses.

Key technical risks associated with the proposal involve the lack of mechanistic understanding of interfacial layers associated with electrodes in the Li-ion system. We will pursue upscaling of information from DFT or ab-initio, or MD atomistic calculations to the continuum level to address this area where absolutely needed and the sensitivity to model parameters is very high.

The impact of this project will be far-reaching. By the end of the project we will have created infrastructure for the inclusion of detailed mechanistic models for thermochemical processes that are important to battery performance and safety. Additionally, the mechanistic understanding of thermal runaway processes in Li-ion batteries will be advanced. This capability can be linked to existing cell, module and pack-level capabilities being developed under CAEBAT-I.

Results

Model Development

We have expanded the list of electrode objects that can be used with 1DElectrode to include diffusional objects with and without the total arbitrary Lagrangian Eulerian (TALE) capability.

We have added the capability to employ arbitrary fitted OCV curves into the electrode object (which is the industry norm) in order to compare against Dual foil, which uses this method exclusively. The default method for specification of the OCV within 1DElectrode is to calculate the OCV from the specification of the electrochemical potentials of all of the species involved in the interfacial kinetics reaction, and this is the method that will eventually lead to the greatest progress in understanding degradation methods.

We have added to Cantera the ability to combine the concepts of a generalized Butler-Volmer formulation for charge-transfer reactions at interfaces with an affinity formulation, which is used extensively in the geochemistry community and which with the addition of the voltage-dependent modification of the activity energy can be made to look like a generalization of the B-V reaction..

Comparison to Dualfoil

In order to validate our model we have carried out a validation exercise against Dualfoil. Figure III - 83 demonstrates that we can duplicate Dualfoil calculations fairly well when the problem statement is specified. Additional work on the transport formulation within 1DElectrode was pointed out to be demonstrated by this exercise.

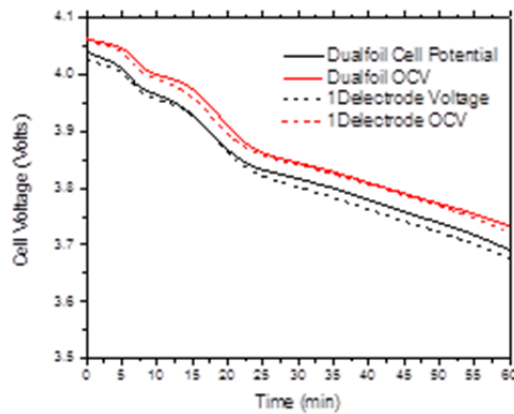


Figure III - 83: Comparisons of Dualfoil to 1DElectrode using the OCV fitting capability and recently installed generalized Butler-Volmer implementation within Cantera

CAEBAT Development

One of the primary tasks is to integrate the 1D electrode model based on cantera into Virtual Integrated Battery Environment (VIBE). We have successfully integrated this new software into the suite of components for modeling electro-chemistry inside VIBE. Below we show an existing example to demonstrate the capability to swap the dualfoil with the 1D electrode component and perform a coupled electrochemical, electrical and thermal simulation. In FY15, we will perform some detailed validation and comparison of the cell level simulations.

Example: Cylindrical Cell (Electrochemical-Electrical-Thermal)

This example contains the electro-chemistry, electrical and thermal transport components in a rolled cylindrical cell. Figure III - 84 shows the geometry and the finite element mesh used to resolve the geometry of the cylindrical cell and the current collectors. The top hierarchy model has 168 (56 each for the cell-sandwich and positive and negative current collectors) zones in 4 quadrants. The zones describe different current collector and cell sandwich regions. The simulation uses 56 concurrent 1D Electrode simulations for different cell-sandwich zones. Typical results are shown in Figure III - 85. The maximum temperature occurs at the cell core as expected.

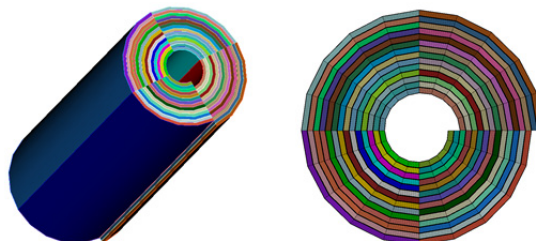


Figure III - 84: Geometry and mesh of the simulated cylindrical cell

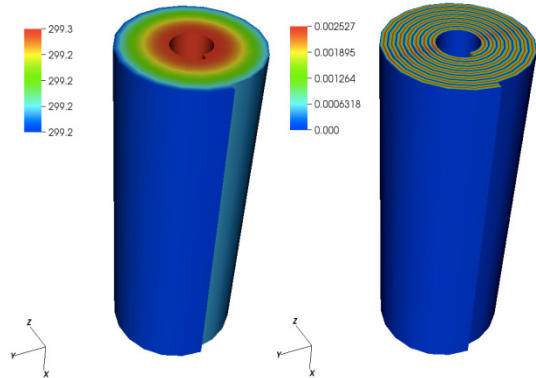


Figure III - 85: Sample results for cylindrical cell (temperature on the left and the electrical potential on the right)

Effective Properties from Microscale Electrode Calculations

Accurately predicting electrical and thermal performance of lithium-ion batteries and pack assemblies is of great importance. By understanding fundamental electrochemical and thermal behaviors at the electrode microscale, and upscaling the results, macroscale models can be improved. Many previously published models approximate the electrode microstructures as packed spheres. However, actual electrode microstructures can differ significantly from the spherical approximation. Figure III - 86 illustrates a small segment of a graphite anode that has been reconstructed using X-ray tomography.

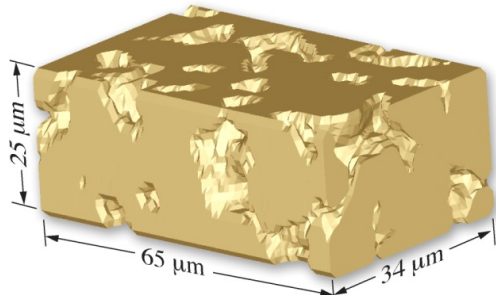


Figure III - 86: Reconstructed anode microstructure from an X-ray tomography experiment (X-ray data courtesy of Prof. Scott Barnett, Northwestern University)

Models developed at CSM predict the electrochemical and thermal behaviors at the electrode microscale. These models are based upon microstructural geometries that are reconstructed from either FIB-SEM or X-ray tomography experiments. The modeling itself is implemented with extensions of the ANSYS FLUENT software.

To date, the microstructural modeling has focused on the cathode, assuming an ideal anode. Both the electrode and electrolyte phases are resolved in three dimensions, using millions of finite control volumes. The models solve conservation equations for lithium concentrations and electrostatic potentials within the

electrode and electrolyte phases. Electrochemical charge transfer at the phase interfaces is represented in Butler-Volmer form. The thermal models represent both Faradaic and Ohmic contributions. A new algorithm has been developed to model accurately the Ohmic heating, which is very sensitive to computational noise in evaluating the local electrostatic-potential gradients.

The microscale models are being extended to fully couple the full anode-separator-cathode assembly at the microscale. Additionally, the binder phases are being incorporated into the electrode models.

Upscaling Ideas -Microstructurally Derived Heat-Generation Tables

Upscaling is important aspect of the microscale modeling. Extracting effective physical properties, such as mass density, heat capacity, and thermal conductivity, is relatively straightforward. However, evaluating the local heat-release rates is much more challenging. One objective of the microscale effort is to predict and communicate effective properties into cell- and module-scale models using the CAEBAT architecture. Figure III - 87 is an example of a heat generation table idea. The heat generation values will override the native heat-generation functions where necessary within the macrohomogeneous representation of the material. The tables will be parameterized as a function of internal state variables such as local temperature, SOC, and C-rate.

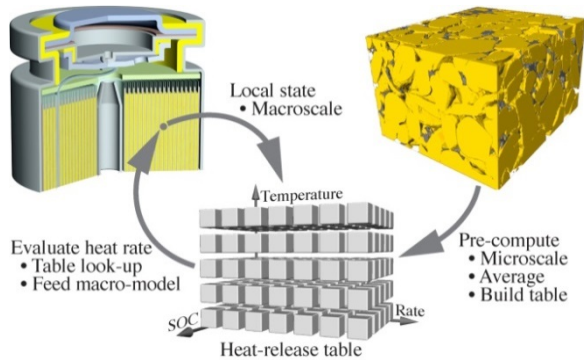


Figure III - 87: Methods of upscaling of heat generation tables are being evaluated

Conclusions and Future Directions

In addition to the partially saturated porous flow and solid mechanics modeling efforts which we have planned, we have started to design new models for the SEI layers based on analogs to corrosion system, whose formulation reactions are thermodynamically reversible, so that they may be designed to dissipate under some conditions. Combining these models with traditional thermal models for thermal runaway, we will then attempt to fit these against Sandia's Batlab data.

FY 2014 Publications/Presentations

1. 2014 DOE Annual Peer Review Meeting Presentation.
2. 89th Lithium Battery Technical/Safety Group Meeting, Sandia Labs, Sept 2014.

III.C.9 Efficient Safety and Degradation Modeling of Automotive Li-ion Cells and Packs (EC Power, Penn State U)

Brian Cunningham (DOE Project Manager)
Subcontractor: EC Power

Christian Shaffer (PI)
341 N. Science Park Road
State College, PA 16803
Phone: (814) 861-6233; Fax: (814) 861-6234
E-mail: cshaffer@ecpowergroup.com

Subcontractor:
Penn State University, University Park, PA 16802

Start Date: October 2013
Projected End Date: September 2015

Objectives

- Develop an efficient & robust pack-level safety model.
- Develop abuse and refined life models.
- Perform life, abuse, and safety tests to acquire data for validation.
- Expand extensive materials database by characterizing and adding NCA material.
- Perform co-simulation of our software with structural mechanics software via the Open Architecture Standard (OAS).
- Support DOE CAEBAT activity.

Technical Barriers

Key barriers to more widespread adoption of hybrid and electric vehicles include challenges in the design of large-format Li-ion cells and packs related to performance, safety, life, and abuse. In the ongoing work of this project, we are developing and refining a commercial physics-based software tool that is directly aimed at helping cell manufacturers and automakers overcome these design challenges and barriers through an accurate and fast computer aided engineering tool.

Technical Targets

- Develop and validate physics-based (non-empirical), predictive pack-level safety model.

- Develop and validate mechanism-based, fundamental models for accurately predicting degradation of Li-ion batteries.
- Develop and validate mechanism-based abuse models.
- Experimentally characterize NCA cathode material under automotive-relevant and wide ranging conditions (e.g., $-40^{\circ}\text{C} < T < 60^{\circ}\text{C}$).

Accomplishments

- Successfully validated cell-level safety model with experimental data.
- Successfully completed implementation of pack-level safety model, with coupled electrochemical-thermal physics, which allows user to predict safety of pack using software.
- Investigated ramifications of cell design on safety through large-matrix numerical experiments.
- Completed initial validation of safety and abuse models.
- NCA characterization $> 50\%$ complete ($-40^{\circ}\text{C} < T < 60^{\circ}\text{C}$).



Introduction

The overarching objective of the ongoing work is to develop experimentally validated, robust, and easy-to-use computation models for Li-ion battery (a) pack-level safety and abuse simulation and (b) advanced and accurate degradation modeling. The commercial need for an efficient pack-level safety and abuse model is best highlighted by the recent Boeing 787 Li-ion battery pack fires, where there has been much debate as to the root cause of the fires, how the failure subsequently spread through the battery pack, and how to avoid such a scenario in the future via enhanced design. The pack-level safety model addresses precisely this type of scenario, yielding great insight as to how an initially local safety-related event such as nail penetration or internal short spreads throughout the pack both thermally and electrically/electrochemically. In addition to pack safety simulation, our team is developing additional chemistry-specific life and abuse models for simulation of blended electrode life and overcharge, for example. The models developed are being extensively validated using in-house data from a variety of advanced

diagnostics tests. Finally, the team is experimentally characterizing commercially widely-used NCA cathode material ($-40^{\circ}\text{C} < T < 60^{\circ}\text{C}$) and adding that information to the previously developed extensive material database.

Approach

The EC Power-led team is working to develop physics-based Li-ion battery and pack design software, leveraging EC Power's demonstrated expertise in multi-physics modeling. This physics-based modeling approach results in a predictive design software focused on addressing life, safety, and performance barriers over automotive-relevant wide-ranging operating conditions (e.g., $-40^{\circ}\text{C} < T < 60^{\circ}\text{C}$), which will lead to more widespread adoption of Li-ion batteries in this application. To ensure model accuracy, we also leverage the expertise of the Penn State University team in materials characterization, safety, and life testing, in order to validate the software developed.

Results

Figure III - 88 highlights the temperature contours from the simulation of a pack-level nail penetration event. This type of a safety test is carried out on new products to ensure safety, and is required for several product safety certifications. When the local temperature inside any cell reaches a dangerous level, thermal runaway will ensue. The predictive design software developed under this project allows users to quickly, cheaply, and safely iterate through various cell and pack designs to optimize safety before a cell is ever built, leading to a more refined and ultimately safer product.

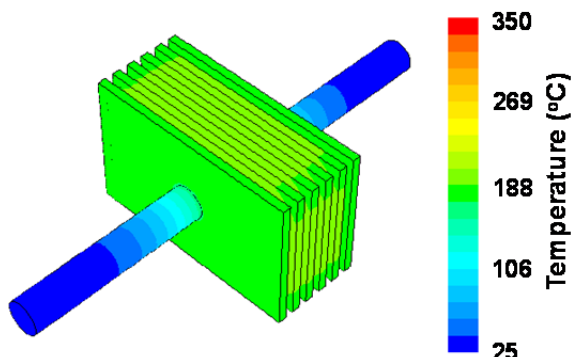


Figure III - 88: Temperature contours of 6 cell module undergoing nail penetration

Figure III - 89 gives an example of the validation of the design software. Figure III - 89(a) shows the experimental and simulated voltage of a 4Ah cell which has been penetrated with a stainless steel nail; Figure III - 89 (b) gives the temperature inside of the

nail and at one location on the cell surface. Overall, good agreement is observed, with the largest discrepancy between experimental and simulated results with nail temperature. Further investigation is ongoing as to the cause of this discrepancy, which could be attributable to experimental noise, given the wavy nature of the observed nail temperature. We expect this unprecedented capability of Li-ion battery cell and pack safety simulation will empower manufacturers and automakers to reduce time and cost in developing safe Li-ion battery packs.

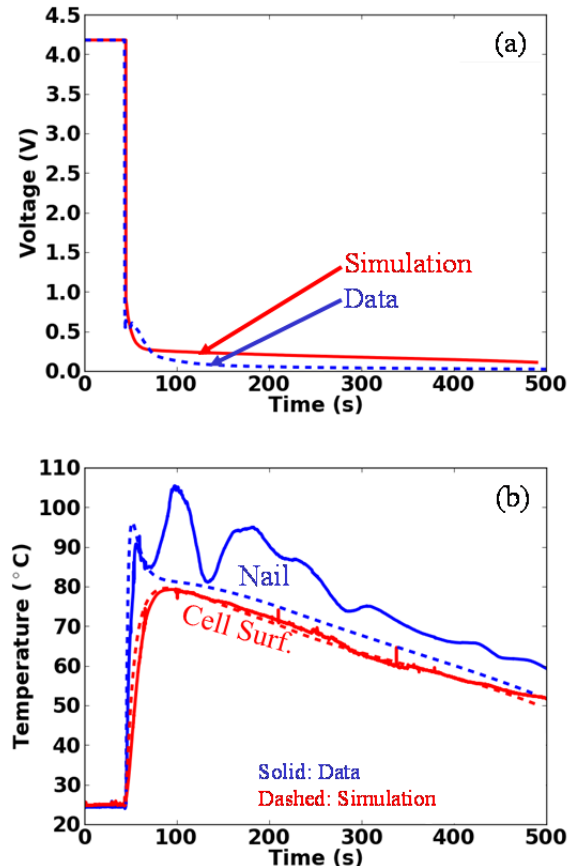


Figure III - 89: Validation of nail penetration model comparing simulation and experimental data, (a) cell voltage, (b) temperature in nail (blue) and at surface of cell approximately halfway between nail and edge (red)

Finally, as an example of the characterization of NCA cathode material, Figure III - 90 shows the solid diffusivity of NCA over full depth of discharge (DoD), and at various temperatures ($-40^{\circ}\text{C} < T < 60^{\circ}\text{C}$). Note that logarithmic y-axis highlights up to a four orders of magnitude difference in diffusivity over these automotive-relevant conditions; this fact emphasized the importance of the characterization work ongoing in this project, in addition to the software's temperature-dependent materials database developed under previous work.

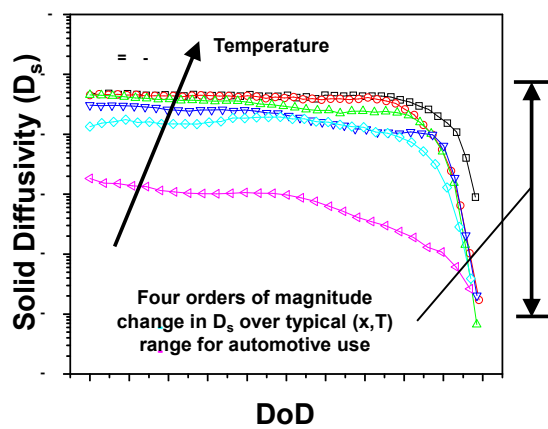


Figure III - 90: Solid diffusivity of NCA cathode material over full depth of discharge (DoD) and temperature

FY 2014 Publications/Presentations

1. 2010 DOE Annual Peer Review Meeting Presentation.
2. Kalupson, J., Wang, Q., Zhao, W., Sinha, P., Shaffer, C. and Wang, C.Y., "Cell- and Pack-Level Simulation of Large-Format Li-Ion Battery Safety Events," 225th ECS Meeting, Abstract# 160, Orlando, FL, U.S., May 11-15, 2014.

Conclusions and Future Directions

EC Power has completed initial software implementation of the models developed under this project, including those related to safety, abuse, and life. Additionally, by working with our partners at Penn State, we have completed our first set of validation testing. The second year of the project will focus on more extensive validation and model refinement, along with completion of the NCA materials characterization. The ultimate goal at the conclusion of the project is to have refined commercial Li-ion battery design software that cuts cost and time from the design phase of automotive Li-ion batteries and packs.

III.C.10 Significant Enhancement of Computational Efficiency in Nonlinear Multiscale Battery Model for Computer-Aided Engineering (NREL, ANSYS, MIT)

Gi-Heon Kim (Principal Investigator)

National Renewable Energy Laboratory
1617 Cole Boulevard
Golden, CO 80401
Phone: 303-275-4437
E-mail: gi-heon.kim@nrel.gov

Collaborators:

Kandler Smith, Peter Graf, Myungsoo Jun,
Chuanbo Yang, National Renewable Energy
Laboratory

Subcontractor:

ANSYS Inc. (Genong Li, Amit Hotchman,
Dimitrios Tselepidakis)

Objectives

- Improve computation speed of tools developed in CAEBAT-1.
- To develop a computational methodology for a significant enhancement in computation speed of nonlinear multiscale battery modeling while maintaining or improving the solution accuracy from the most advanced state-of-the-art models.

Technical Barriers

- The inevitable nested iteration, ensuring self-consistency in the state-of-the-art multi-scale multiphysics (MSMD) battery modeling, becomes a factor limiting further improvement of computation speed.
- The traditional multiphysics approach, collapsing scales into a single, large, differential algebraic equation system, renders the system impractically large and stiff, sacrificing modularity.
- As soon as the reduced order model (ROM) basis is acquired in a reduced dimension space, physical interpretations are easily lost.
- The ROM basis is restricted to reuse in the system where its characteristics are evolving, such as the battery aging process.
- The ROM build process becomes computationally costly, especially with an increased number of parameters.

- Most state-of-the-art efficient battery models addressed coupling battery physics only within limited scales.
- The state-of-the-art ROMs suggested for battery models lose validity when severe nonlinearities arise.
- The model applicability can be limited for varied design, environment, and operation conditions.

Technical Targets

- Develop an innovative multiscale coupling method using time-scale separation and variable decomposition to eliminate several layers of nested iteration, while still keeping the modular framework architecture that is critical to battery behavior simulations.
- Establish a new technique to identify low order State Variable Model (SVM) that is adaptive to system evolution, such as during aging.
- Design a new ROM that does not fail under severe nonlinear condition and achieves speeds that are compatible with state-of-the-art ROMs for battery models.
- Construct multiple options of modular component models for various subsystems.

Accomplishments

- Increased the computational speed of running electrode domain model by a factor of 100 without any loss in accuracy.
- Reformulated the model equations using time-scale separation and partial linearization.
- Prototyped ED-GHMSMD and CD-GHMSMD on MATLAB.
- Completed evaluating promising methods for adaptive-SVM.
- Implemented VECTFIT open-source software that improves stability and speed of look-up table identification.
- Developed a method using interconnection-of-systems approach for time-domain realization of nested transfer functions.
- Performed full look-up table identification of all transfer functions associated with Newman model electrode potentials & concentrations.

- Developed API to use NREL's SVM and LPD library in ANSYS/FLUENT's CAEBAT module.
- Completed GH-PDM and GH-EDM implementation.
- Demonstrated stack cell model in the new model framework.
- Carried out EDM benchmark tests; $\times 100$ speed-up was achieved with the new model framework.
- Performed testing a-SVM prototype code in MATLAB to evaluate tradeoffs in computational efficiency, memory vs. full order model.



Introduction

Background and Motivation: DOE's Computer Aided Engineering for Electric Drive Vehicle Battery (CAEBAT) program has focused on developing innovative modeling capabilities to help industries accelerate mass-market adoption of electric-drive vehicles (EDVs). NREL pioneered the multiscale multidomain (MSMD) model, overcoming challenges in modeling the highly nonlinear multiscale response of battery systems. The MSMD provides high extent flexibility and multiphysics expandability through its modularized architecture, as well as computational efficiency. (See Figure III - 91.) NREL also served as a technical advisor/coordinator in transforming the MSMD for industrial use in the first phase of CAEBAT.

However, there are still remaining challenges. Significant efforts continue being invested to improve energy-power capability and reliability of batteries through engineering at the material level by controlling particulate morphology and size, modifying the particle surface, or other approaches. Due to the complex nonlinear interactions across a wide range and scale of physics, computational cost becomes excessively high

to quantify such improvements in device level response even with the state-of-the-art models. The CAEBAT program has resulted in software packages providing 3-D battery pack simulation modeling capability. Because of the system's extreme complexity, the computational cost of simulating a battery pack response is still very high.

Therefore, further improvement of computational efficiency is needed, and the intrinsic nonlinearity of battery physics must be resolved properly. This would enable the use of models in design and management tradeoff studies of performance/life in large vehicle battery systems, which are typically composed of several hundred large-format individual cells.

In this project, we develop a computational methodology for a significant improvement in computational efficiency of nonlinear multiscale battery modeling while maintaining or enhancing the solution accuracy from the most advanced state-of-the-art models. The project objectives are to:

- 1) Significantly improve the computation speed and stability of multiscale model framework by eliminating several layers of nested iteration through innovative multiscale coupling methodology, while still keeping the modular framework architecture. (See Figure III - 91.)
- 2) Provide a new ROM that is adaptive to system evolution and identifiable with fewer compound parameters, which is critically needed to improve non-uniformly evolving large battery system life predictions.
- 3) Provide a new ROM that will not fail under severe nonlinear conditions and can achieve compatible speed-up against the state-of-the-art ROMs for battery models.
- 4) Provide multiple options for efficient submodules to improve overall simulation speed while accommodating high-fidelity physics models.

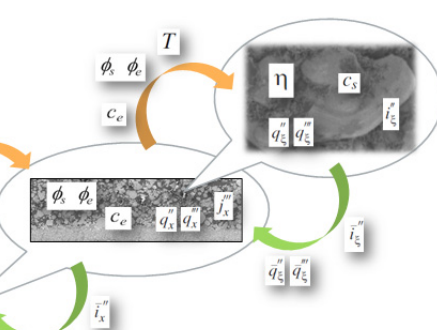
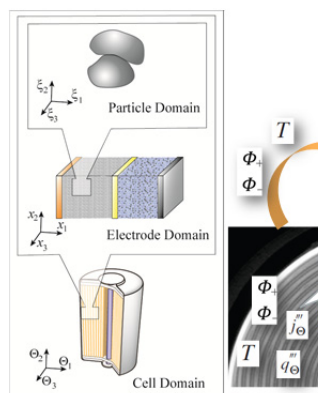


Figure III - 91: A diagram of intra- and inter-domain coupling protocols used in NREL's MSMD framework, integrating widely varied scale battery physics in a computationally efficient manner with hierarchical modular architecture (particle, electrode, and cell domains)

Approach

The project target will be achieved through complementary parallel efforts in framework efficiency improvement and component efficiency improvement. The team applies an innovative multiscale coupling methodology (so called, GH-MSMD) using time-scale separation, eliminate several layers of nested iteration, significantly improve the speed and stability upon the original MSMD, and retain the modular framework architecture that is critical to battery behavior simulations. We also develop advanced ROMs for the component models. Computational time is often invested in advance to find reduced order basis in a much lower dimension than that of the full ordinary differential equation systems derived from spatial discretization of the partial differential equation systems. NREL researchers pioneered a reduced-order state space representation of the one-dimensional porous electrochemical model, the State Variable Model (SVM), already having improved the computational speed of the present MSMD model. The ROM basis is typically restricted to reuse in the system where its characteristics are evolving, such as the battery aging process. In this project, the team develops a new ROM that adapts to system evolution and is identifiable with fewer compound parameters. The state-of-the-art ROMs for battery modeling lose validity when severe nonlinearities arise in the system. In a parallel effort, the team also explores a new ROM that does not fail under severe nonlinear condition. The project team plans to have the models available to industrial users on a commercial software platform by implementing them in the ANSYS CAEBAT-1 software.

Results

In order to improve the computation speed and stability of multiscale model framework by eliminating several layers of nested iteration through innovative multiscale coupling methodology, the original MSMD

model governing equations were reformulated using time-scale separation, and variable decomposition. In addition, we established a new technique to identify low order State Variable Model (SVM) that is adaptive to system evolution, such as during aging.

Framework Efficiency Improvement: An innovative new framework, GH-MSMD, has been developed and implemented up to electrode domain model (EDM) by the end of FY14. Recent benchmark tests performed at EDM level demonstrates that the new GH-MSMD framework could achieve 100x increase in speed while maintaining model accuracy and the modular architecture. The results from EDM benchmark test are presented in Figure III - 92.

Adaptive ROM Development: In this task we extend previous work that developed a reduced order model in state variable model form by fitting frequency response of transfer functions representing distributed electrochemical dynamics and use numerical and/or analytical approaches to eliminate the cumbersome pre-processing step required to fit frequency responses and compile results into look-up tables usable only for one battery design at one state of health. Full look-up table identification of all transfer functions associated with Newman model electrode potentials and concentrations has been performed. Adaptive-SVM code has been prototyped in MATLAB to evaluate tradeoffs in computational efficiency, memory versus full order model.

API Development Integrating New Models in CAEBAT Platform: An application programming interface has been established to integrate NREL's newly developed, computationally efficient physics-based electrochemical model in the ANSYS's CAEBAT-1 software. This opens possibility for industry users to access the most updated NREL's state-of-arts models while using commercially available CAE software suite.

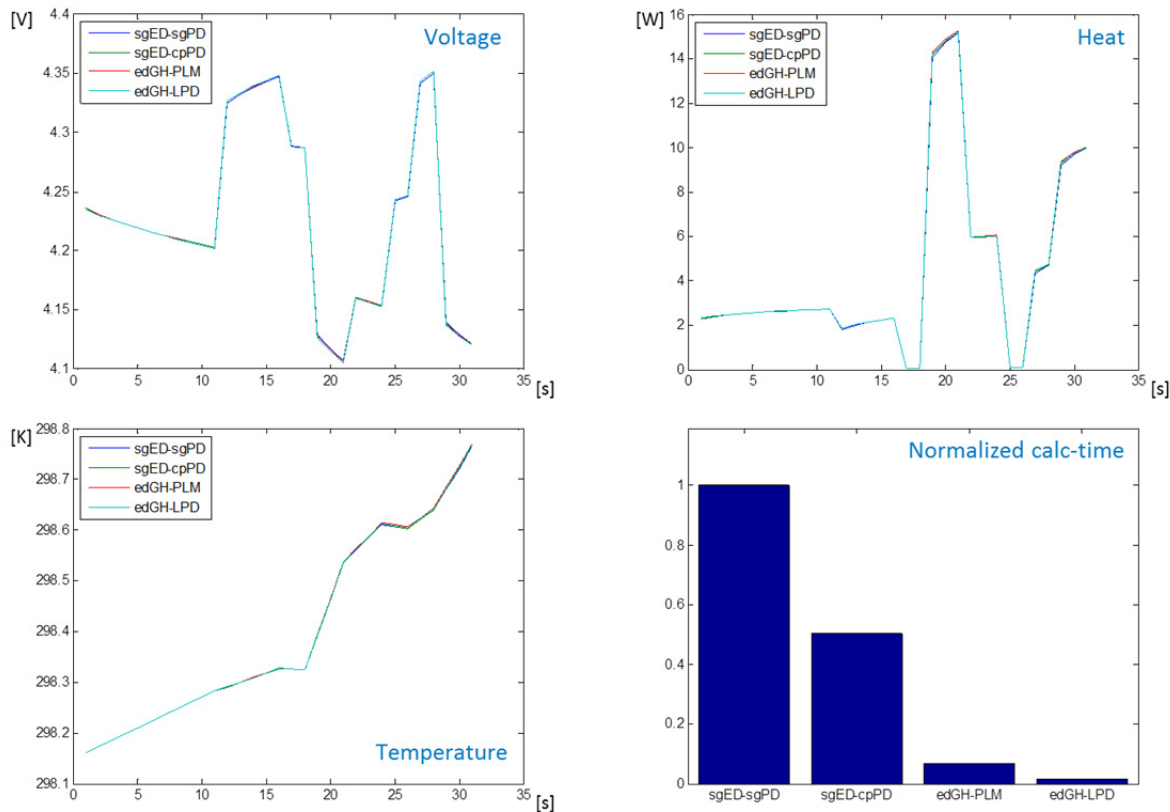


Figure III - 92: EDM benchmark results show that, without losing accuracy, x100 speed-up is achieved with the new GH-MSMD framework when the most efficient PDM and EDM submodel combination is chosen

Conclusions and Future Directions

As part of CAEBAT-2 activity, a new quasi-explicit nonlinear multiscale model framework GH-MSMD has been developed and implemented up to the EDM level demonstrating a 100x increase in speed while maintaining model accuracy. In FY15, the model framework will be further refined and extended to cell domain models (CDMs). We will also identify further order reduction opportunities, while developing an algorithm to utilize non-dimensional form and scaling to circumvent frequent lookup table search or reduce computation upon changes in the parameters.

FY 2014 Publications/Presentations

1. 2014 DOE Annual Peer Review Meeting Presentation.
2. M. Jun, K. Smith, P. Graf, "State-space Representation of Li-ion Battery Porous Electrode Impedance Model with Balanced Model Reduction." J. Power Sources.

III.C.11 Crash Propagation Simulation and Validation (NREL)

Shriram Santhanagopalan

National Renewable Energy Laboratory
15013 Denver West Parkway MS 1633
Golden CO 80401

Phone: (303) 275-3944; Fax: (303) 275-4415
E-mail: shriram.santhanagopalan@nrel.gov

NREL Collaborators:

Chao Zhang, Michael A. Sprague

Subcontractor:

Ford Motor Company

Start Date: December 2013

Projected End Date: December 2015

Objective

- To simulate the electrical, thermal, and mechanical responses of a lithium-ion battery subjected to a sudden mechanical impact, such as a crash, focusing largely on the module- to pack-level phenomena.

Technical Barriers

- PEV battery safety during abuse conditions.
- Lack of experimental data and analytical models for understanding battery response during crash-induced crush.

One of the most commonly encountered field safety events for PEV batteries is related to mechanical failure. However, the abuse response of batteries to mechanical failure is not very well understood.

Limited experimental studies on the modes of propagation, as well as the arbitrary nature of crash conditions, also limit the understanding of how failure at the individual cell level translates to implications for the safety of the module or the pack.

The computational intensity of coupled simulations due to the inherently non-linear nature of the physics, as well as the need for explicit solvers for high-speed mechanical crush, has traditionally prevented battery simulation in commonly available software.

Technical Targets

This effort aims to develop mechanical models that can be coupled with thermal and electrochemical aspects of failure propagation in lithium-ion batteries. The emphasis is on single-cell to multi-cell propagation.

The technical target is to develop simulation capability in this area for individual cells and cell strings that shows good agreement with experimental data for coordinates of the origin of failure.

Accomplishments

- Established the approach to import CAD geometries for individual cells to modules into LS-DYNA, to generate a mesh to perform calculations in a reasonable time frame and export the results back to CFD software (e.g., ANSYS).
- Performed crash simulations on different cell formats (prismatic versus cylindrical, stacked versus wound) under various impact conditions (slow crush versus impact load) to demonstrate the versatility of the approach; some case studies involving multi-cell simulations were also performed to demonstrate scalability of these models.
- Built an approach to calculate short circuit area from the deformed geometries.
- Initiated comparison with experimental results; the validation task is underway.



Introduction

NREL has actively participated in building mathematical models to simulate performance and life of lithium-ion batteries as part of the DOE/VTO CAEBAT activity. These models accommodate a wide variety of physics, including thermal and electrochemical aspects. In FY13, simulations showing the effect of different chemical species on the overcharge response of these cells were carried out. These models assumed that the contributions from the mechanical constraints imposed on the cells were limited. Physical deformation of the cells due to thermal/electrochemical events was not considered.

Existing thermal/electrochemical models in the literature assume a short circuit resistance when calculating the heat generation rate and temperature evolution during thermal runaway events, and are thus limited in their ability to predict the outcome of mechanical crash. On the other hand, existing mechanical simulations of vehicle batteries treat the batteries as passive components and do not include the energetics that ensues from mechanical failure of a battery. Thus, design of structural components based on these calculations is not straightforward.

In the current effort, we are developing a modeling approach that incorporates the effects of mechanical failure (e.g., during a crash) on the energetics that follow the event.

Approach

- The dynamic impact response of structures typically has a short time constant, on the order of microseconds to milliseconds. However, the full battery discharge/thermal event can continue over much longer time scales. Taking advantage of this wide disparity in the time scales for these processes, we simulate the mechanical changes following an impact as a step process, which happens instantaneously.
- Secondly, the simulation of individual layers within a cell is computationally expensive; so, we have built cell-level and multi-cell simulations using a representative sandwich model, which lumps the mechanical response of the multiple layers within the cell to one electrode-pair with an equivalent set of properties.
- The subsequent development of the electrical and thermal pathways is treated as a separate set of events that take place under a quasi-steady state.

Results

Cell-Level Simulations

The response of individual cells subjected to mechanical crush was simulated using LS-DYNA, a software package commonly utilized by the automotive industry to perform explicit dynamics simulations. We have established the ability to simulate mechanical events at the single cell level: these models are versatile in simulating different form factors of cells - prismatic can versus pouch, stacked versus wound, etc. (See Figure III - 93). These simulations can be performed on CAD geometries imported into LS-DYNA in a reasonable time frame. The deformed geometries can be exported to CFD software (e.g., ANSYS) for use in short-resistance calculations. Simplifications to the thermal/electrochemical calculations after impact are currently being validated.

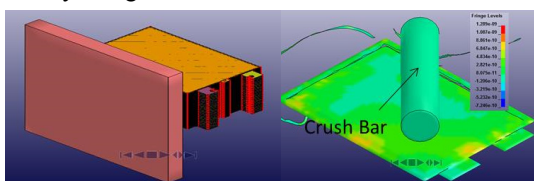
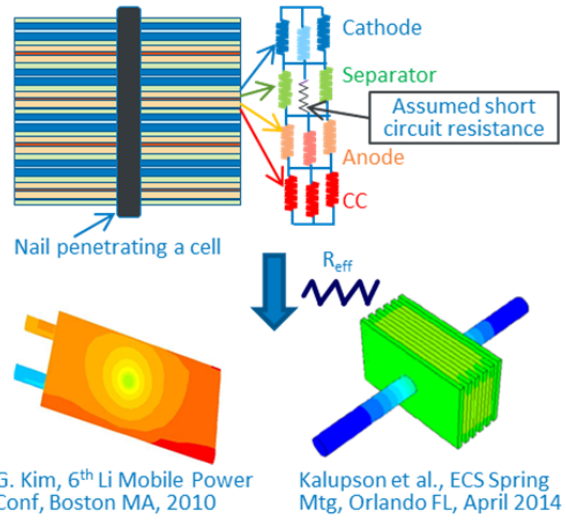


Figure III - 93: Model versatility - crush response of different types of cells under various load conditions can be studied using the tools developed under this effort; left, a prismatic cell crush on a wall; right, deformed pouch cell geometry after crush

Short-Circuit Characterization

Traditional short circuit simulations assume a short area and compute the resultant thermal response of the cells. Under the current effort, the electrical simulations are performed on the deformed geometry, resulting in calculation of the short circuit contact area. A simple schematic comparing the two approaches using a circuit analogy is shown in Figure III - 94.

(a). Regular Short (Previously Reported Approach):



(b). Irregular Short (Current Approach):

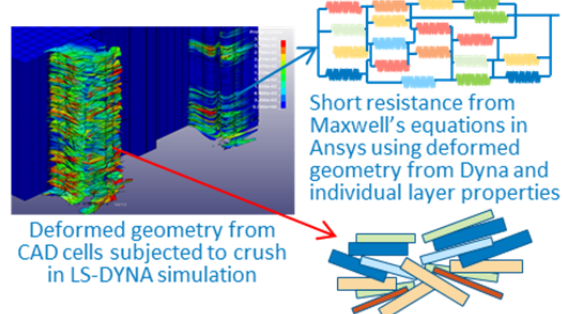


Figure III - 94: Short circuit propagation under crash - the conventional approach (a) does not consider the impact of mechanical deformation; so, crash simulations must consider (b) the evolution of geometry along with the thermal/electrical effects that ensue following a crash event

Multi-Cell Simulations

The lumped modeling approach enables us to simulate crush in a multi-cell module. These results can then be used to assess the extent of deformation across the different cells for a given impact scenario. Some results are shown in Figure III - 95 and Figure III - 96.

One example is the thermal response of the module when heat exchange fins of different designs are used for thermal management of cells. In the second case

study, two load scenarios on the first fin design (lateral and normal impact) are considered.

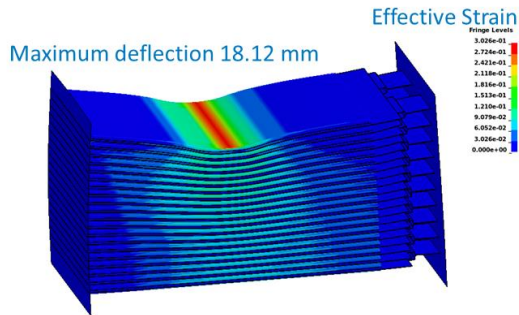


Figure III - 95: Propagation of mechanical failure across multiple cells in a module containing 20 prismatic stacked cells (15 Ah each) of the NMC chemistry

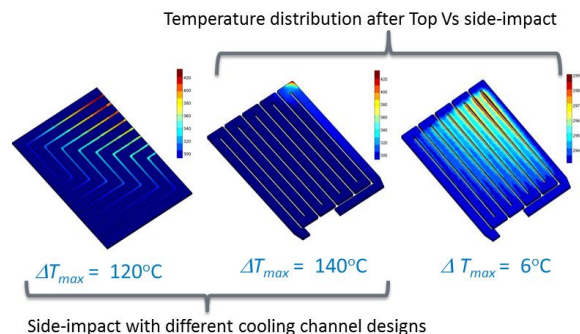


Figure III - 96: Demonstration of the utility of multi-cell crash-response simulations - two case studies are shown, the first comparing the effect of different locations of impact on temperature rise, and the second comparing two different cooling-fin designs

Conclusions and Future Directions

Simulation tools that couple mechanical response of a battery subjected to crash with the thermal/electrical response of the cells were developed. Several case studies to demonstrate the versatility and scalability of these models were performed. We are in the process of validating the model results against experimental data. This effort will continue through FY15, together with some module-level simulations. The effect of the evolution of short-circuit with time on the propagation of failure from individual cells to other areas within the pack will be studied. Approaches to integrate these simulations within the CAEBAT framework will be proposed.

FY 2014 Publications/Presentations

1. S. Santhanagopalan, C. Yang, G.H. Kim, M. Keyser and A. Pesaran, "Impact Response of Lithium Ion Batteries", Presented at the 224th ECS Meeting, November 2013, San Francisco, CA.
2. S. Santhanagopalan, "Mathematical Modeling of Battery Safety under Crush", Presented at the Discussion of Issues Related to Safety of Batteries in Hybrid and Electric Vehicles by the International Energy Agency, January 2014, Washington, D.C.
3. S. Santhanagopalan, "Pushing the Envelope on Battery Safety - Some Simulation Tools", Presented at the Battery Show, September 2014, Novi, MI.
4. C. Zhang, S. Santhanagopalan, M. Sprague, A. Pesaran, "Coupled Mechanical-Electrical-Thermal Modeling for Lithium-ion Batteries", *J. Power Sources*, Under Review.